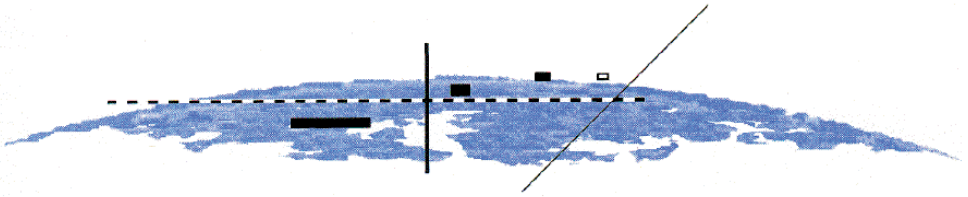

GeoForschungsZentrum Potsdam

in der Helmholtz-Gemeinschaft

Oliver Ritter

Die Abbildung von Bewegungsbahnen in Deformationszonen der Erde mit elektrischen Methoden

Scientific Technical Report STR05/10

Impressum

GeoForschungsZentrum Potsdam
in der Helmholtz-Gemeinschaft
Telegrafenberg
D-14473 Potsdam

e-mail: postmaster@gfz-potsdam.de
www: http://www.gfz-potsdam.de

Gedruckt in Potsdam
Juni 2005

ISSN 1610-0956

Die vorliegende Arbeit ist in elektronischer Form erhältlich unter:
http://www.gfz-potsdam.de/bib/zbstr.htm

Oliver Ritter

Die Abbildung von Bewegungsbahnen in Deformationszonen der Erde mit elektrischen Methoden

---

Habilitationsschrift
in Verbindung mit publizierten
Forschungsergebnissen

Freie Universität Berlin
Fachbereich Geowissenschaften (Fachrichtung Geophysik)
Malteserstr. 74-100 12249 Berlin

angefertigt: im Mai 2004
Erteilung der Lehrbefähigung für Geophysik: 11. Mai 2005

Scientific Technical Report STR05/10

Scientific Technical Report STR 05/10

GeoForschungsZentrum Potsdam

Inhaltsverzeichnis

Abbildungsverzeichnis

Vorwort

Mit der vorliegenden Arbeit werden voneinander unabhängige Experimente zur Untersuchung der elektrischen Leitfähigkeit im Untergrund miteinander verknüpft, mit dem Ziel, das Potenzial der Methode Magnetotellurik für das Abbilden aktiver und fossiler tektonischer Systeme aufzuzeigen. Die Magnetotellurik hat sich in den letzten zehn bis fünfzehn Jahren zunehmend zu einem zuverlässigen und aussagekräftigen Tiefensondierungsverfahren entwickelt. Dieser positive Entwicklungsprozess wird auch durch meine Forschungsergebnisse dokumentiert, die in verschiedenen Projekten während meiner Zeit am GeoForschungsZentrum entstanden sind. Eine Übersicht über die verwendeten Arbeiten befindet sich in Tabelle 1.1. Große geophysikalische Feldexperimente, wie die hier beschriebenen Magnetotellurikprojekte, lassen sich nur im Team durchführen. Im akademischen Bereich bedeutet dies die Integration von Studenten und Doktoranden bei den Feldmessungen und der anschließenden Bearbeitung der Daten. Entsprechend gehen einige der in Tabelle 1.1 aufgeführten Arbeiten auf Diplomarbeiten oder Promotionsschriften zurück, die von mir mitbetreut wurden. Bei anschließender Veröffentlichung der Arbeiten habe ich als Co-Autor mitgewirkt.

Die beiliegenden Veröffentlichungen enthalten eine Einführung in die Methode der Magnetotellurik und gegebenenfalls die Beschreibung neu entwickelter Methoden. Eine allgemeine Darstellung der theoretischen Grundlagen der Magnetotellurik findet man z.B. in (Kaufman & Keller, 1981; Nabighian, 1987; Weaver, 1994).

Am Ende der Arbeit befindet sich ein Glossar, in dem einige Begriffe und Abkürzungen erklärt werden.

Danksagung

Volker Haak hat meinen wissenschaftlichen Werdegang über viele Jahre begleitet und natürlich auch geprägt. Unser beider gemeinsames Bestreben, die Magnetotellurik zu dem zuverlässigen und anerkannten Tiefensondierungsverfahren zu machen, das sie heute (zunehmend) ist, hat uns immer verbunden. Sehr dankbar bin ich ihm dafür, dass er die Möglichkeiten, die das GFZ bietet, so an uns weitergegeben hat, dass wir nahezu perfekte Bedingungen für inspiriertes und konzentriertes Forschen hatten. Über die Jahre ganz besonders zu schätzen gelernt habe ich seine Art, die Dinge von einer ganz anderen Seite zu sehen, sie humorvoll zu hinterfragen, und mich immer wieder mit gänzlich unerwarteten Einfällen zu überraschen.

Gleich zu Beginn meines Wirkens am GFZ hatte ich das Glück, dass zwei sehr talentierte Studenten zu unserer Arbeitsgruppe stießen, die heute beide PostDocs sind. Ute Weckmann und Arne Hoffmann-Rothe haben gerade in letzter Zeit meine Arbeit entscheidend mit vorangetrieben, wofür ich beiden von ganzem Herzen danken möchte. Ute Weckmann hat an fast allen, immer sehr anstrengenden Messfahrten teilgenommen und mit ihrer Kraft und Zuversicht nicht nur mich persönlich unterstützt, sondern wesentlich zum Erfolg der gesamten Projekte beigetragen. Auch Paul Bedrosian möchte ich für seine Mithilfe beim Publizieren und der Projektarbeit danken.

Michael Weber danke ich für die Unterstützung im DESERT Projekt, vor allem aber dafür, dass er als Seismologe von Anfang an offen für die Magnetotellurik war. Ali Schulze möchte ich für die gute Zusammenarbeit im Rahmen des Gerätepools und bei mancher Messfahrt danken. Mittlerweile existieren erfreulich viele kollegiale Bande „sektionsübergreifend“ am GFZ, und mein Dank in diesem Sinne geht an Bob Trumbull, Frank Schilling, Ernst Huenges, Trond Ryberg, Klaus Bauer, Christian Haberland, Nils Maercklin, Stephan Sobolev und Christoph Janssen.

Große Anerkennung und Dank gebührt den Niemegker Kollegen, die mitgeholfen haben, den MT-Teil des Geophysiklischen Gerätepools Potsdam aufzubauen und zu pflegen: Eberhard Pulz, Manfred Schüler, Carsten Müller, Richard Winkler und Willi Poggendorf. Dank für die Unterstützung auch an Monika Korte und Hans-Joachim Linthe.

Mit Graham Dawes und seinen MT Geräten bin ich seit meiner Zeit in Edinburgh immer in Verbindung geblieben. Ohne seine Ideen und harte Arbeit wäre die „moderne MT“ nicht möglich geworden.

Im Rahmen des DESERT Projekts habe ich Abdel-Rhman Abueladas als zuverlässigen und sehr liebenswerten Kollegen schätzen gelernt. Zvi Garfunkel und Yossi Bartov danke ich für zahlreiche Anregungen und Diskussionen.

Bedanken möchte ich mich bei allen, die in den verschiedenen Feldprojekten mitgeholfen haben. Bisher noch nicht genannt habe ich: Svetlana Byrdina, Andre Jung, Juliane Hübert, Heiko Thoss, Judith Schwarte, Annika Steuer, Katja Schiffbauer, Katrin Mai, Gabbi Haim, Issam Qabbani, Hani Al-Amoush,

Tahsin Talat, Gassan Sweidan, Uli Kalberkamp, Jan Schmidt, Achim Helm, Guido Bengel, Ulrich Knieß, Rudolf Knieß und Conny Hammer. Dank für die gute Zusammenarbeit auch den Kollegen der Magnetfeldgruppe der Sektion 2.3 am GFZ und besonders den ehemaligen Kollegen der MT Gruppe: Fritz Echternacht, Markus Eisel, Katrin Schwalenberg, Patrick Denny und Guido Öttinger.

Bei Henri Brasse möchte ich mich für die Zusammenarbeit in unserer seit Jahren gemeinsam veranstalteten „MT AG“ bedanken. Für die zahlreichen und unersetzlichen Anregungen und Diskussionen in diesem Forum danke ich allen Mitwirkenden.

Vor allem in unserer nationalen Gruppe „Kolloquium Elektromagnetische Tiefenforschung“, aber auch im „Internationalen Induction Workshop“ der IUGG habe ich mich immer „zuhause“ gefühlt. Meinen Dank allen Beteiligten.

Kapitel 1

Einleitung

Die äußere Schale der Erde, die Lithosphäre, besteht aus Platten, die sich relativ zueinander bewegen. In Bereichen von Plattenrändern wird kinetische Energie von bewegten Plattenfragmenten in großräumige Deformation der Lithosphäre umgewandelt. Die Konzentration von Deformation führt zur Ausbildung von Scherzonen in der Erdkruste, die unter Umständen die gesamte Lithosphäre durchdringen. Scherzonen sind tektonische Bewegungsbahnen, die über viele Millionen Jahre aktiv sein können. Scherzonen wirken heute in vielen Regionen an der Formung der Erdoberfläche mit, können aber auch als fossile Spuren einstiger Aktivität in geologischen Strukturen archiviert sein. Instabile dynamische Bruchvorgänge, die in Störungssystemen ablaufen, können Erdbeben auslösen und stellen damit ein erhebliches Gefährdungspotenzial für den Menschen dar. Lokalisierter[1], deformationsgesteuerter Fluidfluss kann andererseits aber auch zur Ausbildung von Erzlagerstätten führen und damit nützlich für die Menschheit sein. Die Entwicklung von Scherzonen in unterschiedlichen Niveaus der Erdkruste hängt wesentlich von Verformungsraten sowie den vorherrschenden Druck- und Temperaturbedingungen ab. Scherzonen stehen dabei in einer komplizierten und bisher nur unvollständig verstandenen Wechselwirkung der mineralogischen Zusammensetzung des deformierten Materials, dessen mechanischen Eigenschaften sowie Massen- und Stofftransportprozessen. Die Erforschung von Deformationszonen ist und bleibt daher ein vorrangiges Ziel für die Geowissenschaften und dominierte auch seit seinem Bestehen die wissenschaftlichen Ziele des GeoForschungsZentrums.

Prominente Deformationszonen, wie die San Andreas Verwerfung in Kalifornien, die Tote Meer Verwerfung im Nahen Osten oder die Nordanatolische Verwerfung, lassen sich auf Satellitenbildern leicht über hunderte oder tausende von Kilometern an der Erdoberfläche verfolgen. Informationen über Eigenschaften und Strukturen von Verwerfungszonen in großer Tiefe lassen sich jedoch nur indirekt, im Wesentlichen aus geophysikalischen Messungen, ableiten.

[1] im Sinne von engl. *localize – begrenzen, konzentrieren* und nicht von engl. *locate – orten (Lokalisation)*

Es ist eine große Herausforderung für die geophysikalischen Tiefensondierungsverfahren, sub-vertikale Strukturen von der Erdoberfläche bis in den Erdmantel hinein scharf abzubilden. Neben der Existenz vertikaler Strukturen, die nicht unbedingt an der Erdoberfläche zu erkennen sein müssen, gilt es deren Breite und Tiefenerstreckung zu bestimmen, auf Materialeigenschaften, wie z.B. dem Vorhandensein von Brüchen oder deren Füllung, zu schließen und strukturelle Merkmale, wie Verzweigungen etc. zu erkennen. Mit zunehmender Tiefe ändern sich das Spannungs- und Verformungsverhalten der Gesteine und damit auch die relevanten physikalischen und petrologischen Parameter.

Generell unterscheidet man zwischen sprödem Verhalten der Gesteine in der oberen Erdkruste mit dominierend bruchhafter Deformation der Gesteine und plastischem oder duktilem Verhalten in der tieferen Kruste. Störungszonen der oberen Kruste können dabei in unterkrustale Scherzonen übergehen. Die Art und Weise wie dieser Übergang vonstatten geht, ist allerdings noch weitgehend unverstanden. Wie später noch gezeigt wird, können elektrische Leitfähigkeitsuntersuchungen an Scherzonen aber wesentlich zur Klärung des Problems beitragen. Im Folgenden wird der Begriff Scherzone allgemein für die Beschreibung von Bewegungsbahnen im Bereich von Deformationszonen verwendet.

Ein physikalischer Ausdruck rezenter Bewegung von Litosphärenplatten sind Erdbeben. Die weltweite Verteilung von Epizentren macht dabei auch die großen Scherzonen „sichtbar“, wie z.B. die San Andreas Verwerfung. Die meisten Erdbeben in rezent deformierenden kontinentalen Gebieten ereignen sich in den oberen $15\,km$, dem Sprödbereich der Erdkruste. Allerdings gibt es auch so genannte leise Scherzonen, bzw. leise Erdbeben (silent earthquakes) (Beroza & Jordan, 1990; Dragert et al., 2001; Ozawa et al., 2003), bei denen die Bewegungsenergie als Rutschereignis (slip event) ohne große Erdbeben frei wird. Erdbeben sind hauptsächlich an heute aktive Scherzonen gekoppelt. Ein Fenster von bis zu 10000 Jahren in vergangende Aktivität gewinnt man mit Hilfe der Paläoseismologie und der Neotektonik (siehe z.B. Grant-Lisa & Lettis-William, 2002). Die räumliche Orientierung der Bruchflächen bei einem Erdbeben, und damit indirekt die bevorzugte Bewegungsrichtung einer Scherzone, kann mit Herdflächenlösungen bestimmt werden. Bewegungsraten von Scherzonen in der Größenordnung von $1\,cm/Jahr$ können heute satellitengestützt mit kontinuierlich messenden GPS Netzwerken oder Radar Interferometrie direkt bestimmt werden (z.B. Goldstein et al., 1993; Khazaradze & Klotz, 2003). Strukturgeologische Aufnahmen ermöglichen bei entsprechend günstiger Aufschlusssituation eine Rekonstruktion der Kinematik beliebig alter Scherzonen.

Scherzonen sind oft mit einer Konzentration von Fluiden und Mineralen verbunden, die die elektrische Leitfähigkeit gegenüber dem Nebengestein wesentlich erhöhen. Besondere Aufmerksamkeit haben in den letzten Jahren die Arbeiten von (Unsworth et al., 1997, 1999, 2000; Unsworth & Bedrosian, 2004) im Bereich der San Andreas Verwerfung erlangt, die für die obere Erdkruste

einen klaren Zusammenhang zwischen Zonen erhöhter Leitfähigkeit, strukturellen Merkmalen der Verwerfung und Seismizität ergaben. Das Vermögen mit der elektrischen Leitfähigkeit Scherzonen abzubilden, steht im Mittelpunkt dieser Arbeit und wird im Weiteren noch ausführlich dargelegt.

Die Ausbreitung seismischer Wellen wird in Bereichen stark deformierter Gesteine der Störungszone durch Effekte wie Anisotropie, starke Dämpfung, Streuung und geführte Wellen (wave guides) beeinflusst (Ben-Zion & Sammis, 2003). Mit speziellen Versuchsanordnungen aktiver seismischer Experimente kann man diese Effekte zum Abbilden struktureller Eigenschaften von Störungszonen nutzen (DESERT Group et al., 2004; Haberland et al., 2003; Maercklin et al., 2004; Rümpker et al., 2003). Das direkte Abbilden vertikaler Strukturen mit Hilfe der Seismik ist aufgrund der ungünstigen Reflexionsbedingungen eigentlich nicht möglich. Störungen lassen sich in der Regel nur indirekt, als Versätze in horizontalen Schichtabfolgen ausmachen. Es gibt aber Ansätze mit Hilfe spezieller Versuchsanordnungen und Abbildungsalgorithmen (Steep-Dip Seismic Imaging) sub-vertikale Reflektoren direkt abzubilden (Hole et al., 2001).

Mit magnetischen und gravimetrischen Verfahren können am ehesten Signaturen von lithologischen Kontrasten entlang von Störungen flächig kartiert werden. Petrologische und mineralogische Analysen erlauben Rückschlüsse auf Herkunft und Zusammensetzung von deformationsveränderten Gesteinen. Die Genese von Scherzonen in Abhängigkeit von den geodynamischen Randbedingungen kann mit Hilfe von Analogmodellen oder durch thermo-mechanische numerische Modellierungen simuliert werden.

Aus diesen Überlegungen wird deutlich, dass zur Erkundung deformationsgesteuerter Prozesse und der damit verbundenen Phänomene eine Vielzahl verschiedener Herangehensweisen notwendig ist. Zonen rezenter Deformation, aber auch der fossil überlieferten Deformation, sind Objekte, aus denen sich Modelle für die Evolution der Lithosphäre ableiten lassen. Geophysikalische Verfahren können entscheidende Informationen über den Verlauf und Zustand von Scherzonen in verschiedenen Tiefenlagen der Litosphäre liefern. Der Einsatz elektrischer Verfahren ist deshalb erfolgversprechend, weil die Konzentration von Fluiden und Mineralen in Scherzonen zu einer gegenüber dem Nebengestein wesentlich erhöhten elektrischen Leitfähigkeit führt. Die elektromagnetischen Induktionsverfahren (Magnetotellurik) erlauben Aussagen über die Verteilung der elektrischen Leitfähigkeit von der gesamten Erdkruste bis in den oberen Erdmantel hinein. Moderne MT Experimente, wie die weiter unten beschriebene Untersuchung der Tote Meer Verwerfung in Jordanien und Israel, beruhen heutzutage auf hunderten von Messstationen. Daraus lassen sich klare Abbilder der elektrischen Leitfähigkeit im Untergrund erstellen, die Rückschlüsse auf das Zusammenwirken von Gesteinswässern (Fluide), elektrischer Leitfähigkeit und strukturellen Einheiten der Verwerfungszone zulassen.

Jahr	Feldexperiment / Art der Arbeit	Publikation(en)	Thema / wesentliche Ergebnisse
1996	Münchberger Gneiss, Bayern	Ritter et al., 1999	Interpretation der extrem hohen Leitfähigkeiten unterhalb des Münchberger Gneisskomplexes als graphitisierte Scherbahnen, die durch horizontale Transportprozesse entstanden sind.
1997	Java, Indonesien	Ritter et al., 1998a; Hoffmann-Rothe et al., 2001	Zonen hoher Leitfähigkeiten in Zentral-Java, Indonesien stehen in Verbindung mit Vulkanismus und aktiven Störungssystemen.
1997	Südliches Schottland, UK	Tauber et al., 2003	Im Inneren der Iapetus Suturzone in den Southern Uplands in SW Schottland befinden sich in der oberen und mittleren Erdkruste sub-vertikale Zonen hoher Leitfähigkeit, die mit kartierten Störungssystemen an der Oberfläche korellieren.
1998 1999	Damara Mobile Belt, Namibia	Ritter et al., 2003b; Weckmann et al., 2003a	Zonen hoher und anisotroper elektrischer Leitfähigkeit im Damara Belt in Namiba spiegeln ein regionales Schersystem wider, in dem oberkrustale listrische Störungen in einen Abscherhorizont übergehen.
2000	West Fault, Chile	Hoffmann-Rothe et al., 2004	Der Vergleich strukturgeologischer Aufnahmen mit der MT zeigt eine räumliche Übereinstimmung der Breite des "Fault Zone Conductors" mit dem Bereich stark veränderten Gesteinsmaterials, mit auffälliger Fluidalteration.
2000 2001 2002 2003	Dead Sea Verwerfung, Jordanien und Israel	Ritter et al., 2003a	Im Abbild der elektrischen Leitfähigkeit erscheint die Tote Meer Verwerfung als impermeable Barriere für Fluide in der oberen Kruste. Der scharfe Leitfähigkeitskontrast korreliert mit seismischen Geschwindigkeitssprüngen.
	Übersicht	Ritter et al., 2004	Vergleich hochauflösender MT Experimente an aktiven und fossilen Störungssystemen. Untersuchung auf Unterschiede und Gemeinsamkeiten im Hinblick auf strukturelle, hydrogeologische und dynamische Prozesse.
	methodische Arbeit	Ritter et al., 1998b	Entwicklung von Breitband MT Geräten und neuen Verfahren in der Datenanalyse.
	methodische Arbeit	Weckmann et al., 2003b	Entwicklung eines Abbildungsverfahrens für eine komplizierte Verteilung der elektrischen Leitfähigkeit im Untergrund.

Tabelle 1.1: Auflistung der in Verbindung mit der Habilitationsschrift publizierten Forschungsergebnisse

Kapitel 2

Scherzonen und die Magnetotellurik

Untersuchungen der elektrischen Leitfähigkeit des tiefen Untergrundes begannen in den 50er und 60er Jahren zunächst ausschließlich mit magnetischen Variationsmessungen (Wiese, 1962; Parkinson, 1962; Schmucker, 1970; Gough, 1973). Nach Veröffentlichung von Bauplänen für portable 3-Komponenten Variometer (Gough & Reitzel, 1967) wurden diese erschwinglich, und es konnten erstmals in größerem Umfang Messungen mit temporären Netzwerken durchgeführt werden. Auf fast allen Kontinenten wurden dabei im Laufe der Jahre Magnetometernetzwerke mit Stationsabständen in der Größenordnung von zehner bis hundert Kilometer installiert. Auffallendes Ergebnis vieler dieser Studien waren langgestreckte Leitfähigkeitsanomalien (elongated anomalies), die sich zum Teil über Tausende von Kilometern verfolgen ließen (Gough, 1983; Haak, 1985). Viele dieser klassischen Leitfähigkeitsanomalien sind auch heute noch Gegenstand der Forschung: die North American Central Plains Anomalie (Reitzel et al., 1970; Alabi et al., 1975; Jones et al., 1997), die Karpathen Anomalie in Europa (Ritter, 1975; Cerv et al., 1984; Stanica et al., 1999), die Carpentaria Anomalie in Australien (Lilley & Bennett, 1972; Chamalaun et al., 1999), der Southern Cape Conductive Belt (de Beer et al., 1975) in Südafrika, der Damara Conductive Belt in Namibia (de Beer et al., 1982; Ritter et al., 2003b; Weckmann et al., 2003a), die Southern Uplands Anomalie in Südschottland (Hutton et al., 1980; Banks et al., 1983; Tauber et al., 2003) und die Fennoscandian Shield Anomalie (Pajunpää, 1984; Pajunpää et al., 2002).

Alle diese Leitfähigkeitsanomalien wurden ohne auffällige Oberflächenmerkmale in heute tektonisch stabilen Schilden gefunden. Bereits Haak & Hutton (1986) folgerten aber, dass diese „elongated anomalies“ mit erloschener tektonischer Aktivität in Verbindung stehen und Relikte alter Subduktionszonen abbilden könnten. Die reinen magnetischen Variationsmessungen waren vor allem zum Aufspüren solcher großräumigen Leitfähigkeitsanomalien wertvoll. Die Modellierung einer beliebigen Verteilung der elektrischen Leitfähigkeit im

Untergrund wurde aber erst durch die zusätzliche Messung von Erdströmen, der sogenannten tellurischen Methode, möglich.

Die Magnetotellurik wurde ursprünglich von Tikhonov (1950) und Cagniard (1953) als Methode zur Bestimmung der elektrischen Leitfähigkeit eines horizontal geschichteten Untergrundes entwickelt. Elektromagnetische Felder weit entfernter Quellen induzieren horizontale Ströme in die elektrisch leitfähige Erde. Misst man mit geeigneten Sensoren horizontale magnetische ($B\,[T]$) und elektrische ($E\,[V/m]$) Wechselfelder an der Erdoberfläche, kann aus dem Verhältnis $E/i\omega B$ eine komplexe Eindringtiefe berechnet werden (mit $\omega = 2\pi f\,[Hz]$). Die Eindringtiefe der induzierten Felder und damit auch die Sondierungstiefe hängen sowohl von deren Frequenz als auch von der Leitfähigkeit des Untergrunds ab (Skineffekt). Aus dem Verhältnis E/H ($H = \frac{1}{\mu_0}B$) lässt sich die Impedanz $Z\,[m/s]$ und daraus der elektrische Widerstand $\rho\,[\Omega m]$, bzw. die elektrische Leitfähigkeit $\sigma\,[S/m]$ eines homogenen Untergrunds berechnen.

Der Begriff Eindringtiefe ist dabei insofern irreführend, als sich elektromagnetische Felder in alle Raumrichtungen, also auch lateral, gleichermaßen ausbreiten; aus diesem Grund spricht man besser vom Induktionsraum. Befinden sich im Induktionsraum laterale Leitfähigkeitskontraste, werden diese erfasst, und man erhält an der Erdoberfläche räumlich inhomogene Feldverteilungen. Misst man zu einander orthogonale Feldkomponenten (B_x, B_y, E_x und E_y) lässt sich die Impedanz als tensorielle Größe bestimmen. Durch geeignete Modellierungsverfahren kann man aus den für viele Frequenzen und an vielen Messorten bestimmten Impedanztensoren die Verteilung der elektrischen Leitfähigkeit im Untergrund rekonstruieren. Allerdings können die entsprechenden Differentialgleichungen nur für eine homogene oder geschichtete eindimensionale (1D) Verteilung der Leitfähigkeit analytisch gelöst werden.

Numerischer Verfahren zur Lösung des elektromagnetischen Induktionsproblems in zwei Dimensionen (2D) entstanden um das Jahr 1970 (Jones & Price, 1971; Coggon, 1971; Schmucker, 1971). Bei einem 2D Modell kann sich die Leitfähigkeit mit der Tiefe und in einer horizontalen Raumrichtung ändern. Den allgemeinen dreidimensionalen (3D) Fall löste Weidelt (1975) für die Magnetotellurik. Allerdings ist es erst seit dem Ende der 90er Jahre Standard, MT Daten zweidimensional zu interpretieren, seit leistungsfähige Computer und numerische Verfahren zuverlässige 2D Inversionsverfahren ermöglichen. Bis dahin basierten Untersuchungen der Leitfähigkeitsverteilung des Untergrunds entweder auf Schichtmodellen (1D Inversion) oder aber auf sehr zeitaufwendigen (trial-and-error) 2D Vorwärtsmodellierungen. 3D Untersuchungen der elektrischen Leitfähigkeit beruhen auch heute noch überwiegend auf Modellstudien, bei denen zwar bestimmte Aspekte eines Datensatzes beleuchtet werden können, nicht aber eine Anpassung der gesamten Daten durch ein Modell erreicht wird. Dies liegt zum einen am hohen Rechenaufwand und zum anderen an der Schwierigkeit, Datensätze mit einer entsprechend hohen lateralen Stationsdichte zu gewinnen. Die Magnetotellurik liefert dabei von der

Theorie her eindeutige Lösungen der Leitfähigkeitsverteilung; die Methode ist also nicht wie die Potenzialverfahren (Gravimetrie, Magnetik) prinzipiell mehrdeutig. Wie bei (fast) allen anderen geophysikalischen Verfahren erhält man aber aufgrund der nicht-perfekten Datenbasis immer eine gewisse Vieldeutigkeit, sogenannte Äquivalenzmodelle, die die Daten im Rahmen ihrer Messfehler und der zugrunde liegenden Annahmen über die Leitfähigkeitsverteilung gleichermaßen (gut oder schlecht) anpassen.

Im 1D Fall lässt sich die beste Modellanpassung prinzipiell mit Modellen erreichen, die aus einer Abfolge von perfekten Leitern und Isolatoren (sogenannte D^+ Modelle) zusammengesetzt sind (Parker & Booker, 1996). Da solche Modelle kaum geologisch interpretierbar sind, wird die Modellfindung a priori durch eine bestimmte Inversionsstrategie oder durch Zusatzinformation gesteuert (z.B. die Vorgabe einer Schichtanzahl). Die meisten modernen 2D Inversionsalgorithmen finden sogenannte „minimum structure“ Modelle, die nur Strukturen enthalten, welche für die Datenanpassung unbedingt erforderlich sind. Ein Nachteil dieser Methode besteht darin, dass die Inversion scharfe Strukturgrenzen nicht immer wiederherstellt, sondern diese verschmiert erscheinen. 2D Vorwärtsmodellierungen werden oft benutzt, um die Sensitivität der gemessenen Daten auf Modifikationen bestimmter Bereiche eines (Inversions-) Modells zu untersuchen (Schwalenberg et al., 2002). Durch solche Modellstudien kann man auch die Auflösungstiefe feststellen, d.h. ab welcher Tiefe Modelländerungen in den Daten nicht mehr festgestellt werden können. „Constrained inversion“, in denen Teile eines Modells während der Inversion festgehalten werden, erlauben Rückschlüsse auf die Notwendigkeit von Lage und Größe modellierter Leitfähigkeitsstrukturen (siehe z.B. Hoffmann-Rothe et al., 2004; Ritter et al., 2004).

Einhergehend mit verbesserten Interpretationsverfahren wurde auch eine neue Messtechnik notwendig. Die wesentlichen Neuerungen beruhten dabei vor allem auf zwei Dingen: höhere Stationsdichte und besseres Signal / Rauschverhältnis.

Im Falle einer eindimensionalen Erde ist der Leitwert, das Produkt aus Leitfähigkeit und Schichtdicke, der am besten aufgelöste Parameter (engl. conductance). Unabhängig von ihrem Abstand, erreicht man durch zusätzliche Stationen keinen zusätzlichen Informationsgewinn, da innerhalb des jeweiligen Induktionsraums die gleiche Leitfähigkeitsverteilung vorliegt. Sobald sich aber laterale Leitfähigkeitskontraste im Induktionsraum befinden, ändert sich die Situation: Messstationen in der Nähe eines Leitfähigkeitskontrasts erfassen diesen bei höheren Frequenzen als weiter entfernt liegende Stationen. Bei gleicher Frequenz ist der Induktionsraum in einem schlecht leitenden Untergrund größer als im guten Leiter. Benachbarte Stationen tragen also in diesem Fall unterschiedliche Informationen. Durch überlappende Induktionsräume wird die Modellfindung stabilisiert, da es weniger äquivalente Modelle gibt. Der Effekt, dass „viel messen viel bringt“, verstärkt sich bei verrauschten Messdaten. Aus ähnlichen Überlegungen werden z.B. auch digitale Audio CDs mit „oversamp-

ling“ aufgenommen (digitalisiert).

In der Geophysik lassen sich überlappende Induktionsräume am ehesten mit der Migration reflexionsseismischer Daten vergleichen, die auf einer räumlichen Überabtastung beruht. Im Gegensatz zu horizontalen Schichten reflektieren einfallende Schichten seismische Energie zur Seite. Mit nur einem einzelnen Seismometer kann man nicht entscheiden aus welcher Richtung die reflektierten Wellen ankommen. Trägt man die seismischen Spuren einfach unterhalb des Aufzeichnungsortes ab, werden einfallende Reflektoren seitlich ihrer eigentlichen Position abgebildet. Durch die Migration werden Reflektoren in ihre richtige Lage gebracht und ihre Einfallswinkel korrigiert. Für eine erfolgreiche Migration benötigt man neben einer hohen Stationsüberdeckung gut bestimmte seismische Geschwindigkeiten oberhalb des Reflektors.

Mitte der 90er Jahre wurden die ersten Breitband-MT Instrumente entwickelt. Die von der Universität Edinburgh gebauten S.P.A.M. MkIII Geräte (Ritter, 1995) ermöglichten Abtastraten im Bereich von einigen kHz, eine Echtzeitanalyse der gesammelten Daten, das Abspeichern großer Datenmengen (Zeitreihen), das Synchronisieren getrennt registrierender Geräte mittels GPS Signal und niedriges Geräterauschen bei gleichzeitig niedriger Leistungsaufnahme, die auch einen Betrieb als Datenlogger mit kontinuierlichen Registrierintervallen von mehreren Tagen erlaubten. Erst mit solchen Geräten wurden Messanordnungen mit großer Stationsdichte und hohem Messfortschritt möglich; sie sind Vorraussetzung für die hochauflösenden, magnetotellurischen Untersuchungen, wie wir sie heute kennen.

Mindestens genauso wichtig war der Aufbau des Geophysikalischen Geräte Pools Potsdam (GIPP). Seit dem Bestehen des GeoForschungsZentrums wurde dabei über die Jahre hinweg eine homogene Infrastruktur mit einer großen Anzahl moderner geophysikalischer Messgeräte und Sensoren geschaffen, die zumindest für die Magnetotellurik weltweit einzigartig ist.

Fortschritte gab es auch bei der Datenanalyse, die im Wesentlichen auf neuen statistischen Verfahren (multivariate, robuste Methoden) und auf Korrelationsanalysen zwischen zeitgleich registrierenden Stationen beruhen (vgl. Ritter et al., 1998b). Durch diese Verfahren wurde es möglich, elektromagnetische Störsignale, die insbesondere in dicht besiedelten Gebieten MT Messungen stark beeinträchtigen können, wirkungsvoll zu unterdrücken. Als ein Beispiel hierfür können die Messungen in der Münchberger Gneismasse (MüMa) angeführt werden (Ritter et al., 1999), die nur wenige Jahre zuvor, im Rahmen der KTB Voruntersuchung, an den in der Oberpfalz herrschenden Rauschverhältnissen gescheitert waren.

Die MüMa ist ein Beispiel für Deckentektonik, in der Scherzonen als subhorizontale Strukturen erhöhter Leitfähigkeit abgebildet werden. Scherzonen, die im Zusammenhang mit dem Mosaik tektonischer Platten entstehen, verlaufen in der oberen Kruste vornehmlich sub-vertikal. Typische Gesteine für den spröden Bereich von Scherzonen sind diskrete Störungen, unter Umständen begleitet von Brekzien oder Kataklasiten, je nach Zerrüttungsgrad des Aus-

gangsgesteins. Scherzonen kann man daher als Schwächezonen der Erdkruste erachten: Zonen, in denen das Umgebungsgestein nachhaltig und bis in große Tiefen durch Brüche und Klüfte geschwächt wird. Ab einer bestimmten Tiefe, der spröd-duktilen Grenze im Bereich von $10 - 15\,km$, kommt es im Bereich von Scherzonen nicht mehr zu Brüchen, sondern zu plastischer Verformung des Gesteins.

Scherzonen sind sehr dynamische Systeme, gebunden an Prozesse, die in einer komplizierten Wechselwirkung von Lithologie, Fluidversorgung, Permeabilität und Geometrie von Störungen stehen. In die Bruchsysteme einer Störung können Wässer eindringen, die entweder meteorischen Ursprungs sind oder auch von chemischen Reaktionen des Umgebungsgesteins (Metamorphose) herrühren. Durch die im Bruchnetzwerk zirkulierenden Wässer kann es zu chemischen Ausfällungen kommen, die dazu beitragen, bestehende Brüche wieder zu schließen (Zementierung). Abhängig vom vorhandenen Ausgangsmaterial und den vorherrschenden Druck und Temperaturbedingungen können aber auch Ton- oder Erzminerale entstehen. Verheilen Brüche durch Zementierung in Phasen vorübergehender tektonischer Ruhe oder durch Erhöhung des Umgebungsdrucks, ist die Entstehung nicht-permeabler Barrieren für Flüssigkeiten möglich. Zuzementierte Brüche sind oft härter als das Umgebungsgestein; bei erneuter tektonischer Aktivität kann die Störung daher an einer anderen Stelle aufreißen, was eine Verbreiterung der Störungszone zur Folge hat.

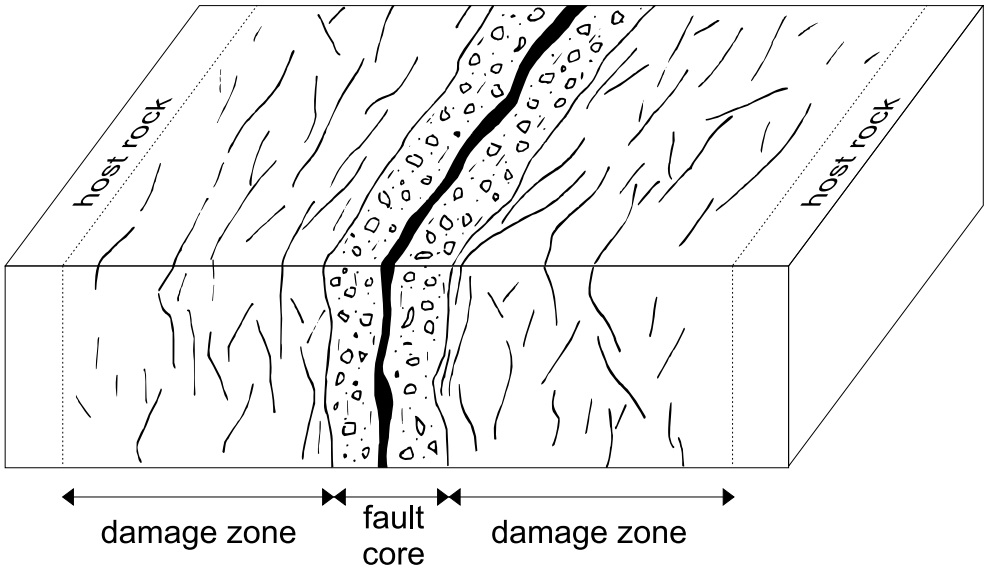

Abbildung 2.1: prinzipielle Strukturmerkmale einer Störungszone (Hoffmann-Rothe, 2002)

Abb. 2.1 zeigt prinzipielle Strukturmerkmale einer Störung für den Bereich der spröden Kruste. Generell wird zwischen dem Kern der Störung (fault core), einer Zerrüttungszone (damage zone) und dem unveränderten Umgebungs-

gestein unterschieden. Im Störungskern, der die Hauptbewegungsenergie aufnimmt, befinden sich die am stärksten zerstörten und veränderten Gesteine. Die Zerrüttungszone weist eine mit wachsender Entfernung vom Störungskern abnehmende Bruchhäufigkeit auf. Die Breite einer Störungszone ist demnach dadurch definiert, dass sich die Anzahl der Brüche noch vom Umgebungsgestein unterscheidet.

Die elektrische Leitfähigkeit von Gesteinen variiert wie kein anderer physikalischer Parameter über viele Größenordnungen. Es gibt allerdings keine eindeutige Zuordnung eines Gesteinstyps zu einer bestimmten Leitfähigkeit. Die Gesamtleitfähigkeit eines Gesteins wird im Wesentlichen vom Poreninhalt und der Vernetzung der Poren bestimmt. Während die Gesteinsmatrix in der Regel schlecht leitend ist, können salzhaltige Wässer in Poren und Brüchen oder dünne verbundene metallische Flächen zu einer stark erhöhten Gesamtleitfähigkeit eines Gesteins führen (siehe z.B. Guéguen & Palciauskas, 1994). Demnach ergeben sich folgende Möglichkeiten für Leitfähigkeitsanomalien im Bereich von Störungszonen: (i) die Nebeneinanderstellung geologischer Einheiten mit unterschiedlichen Leitfähigkeiten, (ii) das Entstehen permeabler Fließwege für Elektrolyte (Wasser) in zerrütteten Bereichen der Störungszone, (iii) eine tonreiche Störungslette (fault gouge) und (iv) die Ausfällung oder Konzentration elektronisch leitfähiger Phasen wie Graphit oder Vererzungen.

Um diese ineinander verzahnten Prozesse verstehen und voneinander unterscheiden zu können, wäre es notwendig, Scherzonen in-situ, von der Oberfläche bis in den Erdmantel hinein beobachten zu können. Welchen Beitrag können geophysikalische Verfahren hier leisten? Welche Bereiche von Störungszonen werden abgebildet und warum? Bilden verschiedene geophysikalische Verfahren unterschiedliche Bereiche von Scherzonen ab? Wie genau sind die Abbildungen, vor allem in großer Tiefe?

Kapitel 3

Fallbeispiele tektonisch aktiver Systeme

3.1 Java, Indonesien

Die Insel Java ist Teil des Sunda Bogens, der auf einer Länge von 5600 km der Grenze zwischen der indisch/australischen Lithosphärenplatte (subduzierend) und der Eurasischen Platte (überschiebend) folgt (Hoffmann-Rothe et al., 2001, Fig. 1). Die Central Java Fault (CJF) markiert eine krustale Schwächezone im Zentrum Javas, die vom Übergang des alten, kratonisierten Sunda Land im Westen zu junger ozeanischer Kruste im Osten herrührt (Hoffmann-Rothe et al., 2001, Fig. 14). Zu beiden Seiten der Störung ändern sich die Dichte und Ausrichtung tektonischer Lineamente und die Verteilung der Vulkane. So sind die Vulkane westlich der CJF zufällig verteilt, während sie östlich einer vulkanischen Achse folgen. Auch die Vulkane Merapi und Merbabu befinden sich auf der vulkanischen Achse im Kreuzungspunkt zweier Störungssysteme.

MT Daten wurden 1997 entlang eines NS verlaufenden, 150 km langen Profils an acht Stationen im Frequenzbereich $1\,kHz - 0.1\,mHz$ gemessen (Hoffmann-Rothe et al., 2001, Fig. 2). Bereits in einer ersten, auf Schichtmodellen basierenden Analyse der Daten wurde im Zentrum Javas eine Zone stark erhöhter elektrischer Leitfähigkeit mit Werten unter $1\,\Omega m$ festgestellt (Ritter et al., 1998a, Fig. 1). Mit Hilfe eingehender 2D und 3D Vorwärtsmodellierungen der Daten konnten die anomalen Anteile des hochleitfähigen Indischen Ozeans abgespalten und insgesamt drei leitfähige Bereiche auf Java identifiziert werden (Hoffmann-Rothe et al., 2001, Fig. 8a). Im nördlichen Teil des Profils erscheint die Central Java Störungszone als Zone erhöhter Leitfähigkeit in der oberen Erdkruste. Interessanterweise befinden sich die Zonen mit den niedrigsten Widerständen von $0.2\,\Omega m$ in einem Bereich nördlich der Vulkankette, der auch durch ein Schwereminimum gekennzeichnet ist. Widerstände von $1\,\Omega m$ und darunter können nicht ausschließlich auf junge, unverfestigte vulkanische Sedimente zurückgeführt werden, sondern stehen vermutlich in Zusammenhang mit

erhöhter geothermischer Aktivität, möglicherweise auch mit Gesteinsschmelzen.

Eigenschaften der Unterkruste oder des oberen Erdmantels, die mit Prozessen der Subduktionszone in Verbindung stehen, können auf Grund des abschirmenden Effekts der hochleitfähigen oberen Kruste nicht aufgelöst werden.

3.2 Die West Fault, Chile

Das Präkordilleren Störungssystem (PS) ist eine breite Scherzone, die sich auf einer Länge von 2000 km parallel zur chilenischen Küste erstreckt. Die West Fault (WF) in Nordchile entstand als Teil dieses Systems im Eozän, im Zuge schiefwinkliger Konvergenz der Nasca und der Südamerika Platte. Der PS/WF kommt deshalb besondere Bedeutung zu, da aufsteigende hydrothermale Lösungen zur Formation der wirtschaftlich bedeutenden Kupferlagerstätten Chiles führten (z.B. Chuquicamata). Außerdem zeigten regionale MT Studien (Echternacht et al., 1997; Brasse et al., 2002), dass das PS möglicherweise die gesamte Lithosphäre des Forearc durchdringt.

Im Jahr 2000 wurde im Bereich der WF ein Messgebiet ausgewählt, das sich sowohl für magnetotellurische Messungen als auch für strukturgeologische Aufnahmen eignete. Die MT Stationen wurden in zwei Parallelprofilen mit Längen von 4 km und 2.5 km gemessen; der Stationsabstand des 4 km langen Hauptprofils betrug 100 m.

Das 2D Inversionsmodell des Hauptprofils zeigt im Bereich der Störung eine sub-vertikale, mit 70° nach Osten einfallende Zone erhöhter Leitfähigkeit (Hoffmann-Rothe et al., 2004, Fig. 7). Solche Zonen erhöhter Leitfähigkeit im Bereich von Störungen werden mit FZC (engl. Fault Zone Conductor) abgekürzt. Auflösungsuntersuchungen mit 2D Vorwärtsmodellen ergaben, dass die Tiefe dieser Struktur mindestens 1100 m beträgt. Ein noch tiefer reichender FZC widerspricht den Daten nicht, ist aber zur Modellanpassung nicht notwendig.

Der Vergleich mit den strukturgeologischen Aufnahmen zeigt eine gute räumliche Übereinstimmung der Breite des FZC mit dem Bereich stark veränderten Gesteinsmaterials mit auffälliger Fluidalteration (Hoffmann-Rothe et al., 2004, Fig. 12). Sekundäre Störungen und Brüche in der Alterationszone fallen spitzwinklig mit 70° nach Osten hin ein, also in die gleiche Richtung wie der FZC aus den Leitfähigkeitsmodellen. Meteorische Wässer, die in den Bruchsystemen der Scherzone zirkulieren, können die erhöhte Leitfähigkeit erklären. Porositätsabschätzungen nach Archie (1942) in Verbindung mit Salinitätsbestimmungen des Grundwassers weisen auf eine Abnahme der Porosität von 20 % an der Oberfläche auf etwa 1 % in einer Tiefe von 200 m hin (Hoffmann-Rothe et al., 2004, Fig. 12).

3.3 Die Tote Meer Verwerfung, Jordanien und Israel

Die Tote Meer Verwerfung (DST, Dead Sea Transform) ist eine linkslaterale, transkontinentale Seitenverschiebung, die die afrikanische von der arabischen Kontinentalplatte trennt. Die DST erstreckt sich auf einer Länge von 1500 km vom Roten Meer im Süden bis in das Taurus Kollisionsgebirge im Norden (Ritter et al., 2003a, Fig. 1). Seit Beginn der Aktivität im Miozän beläuft sich der Gesamtversatz auf 105 km, die jährlichen Versatzraten liegen bei etwa 4 mm pro Jahr. MT Daten wurden in vier aufeinander folgenden Messkampagnen an mehr als 250 Stationen in den Jahren 2000-2003 gesammelt. Die Messungen konzentrierten sich dabei zum einen auf ein etwa 10 km^2 großes Gebiet im Arava Tal, mit der Arava Fault (AF) als lokalem Vertreter der DST, und zum anderen auf ein regionales, 200 km langes Profil, das sich von Jordanien, über das Arava Tal bis nach Israel hinein erstreckte (siehe Abb. 3.1). Alle Daten wurden im Rahmen des DESERT (DEad SEa Rift Transect) Projekts auf gemeinsamen Profilen mit der Seismik gesammelt (DESERT Group et al., 2004).

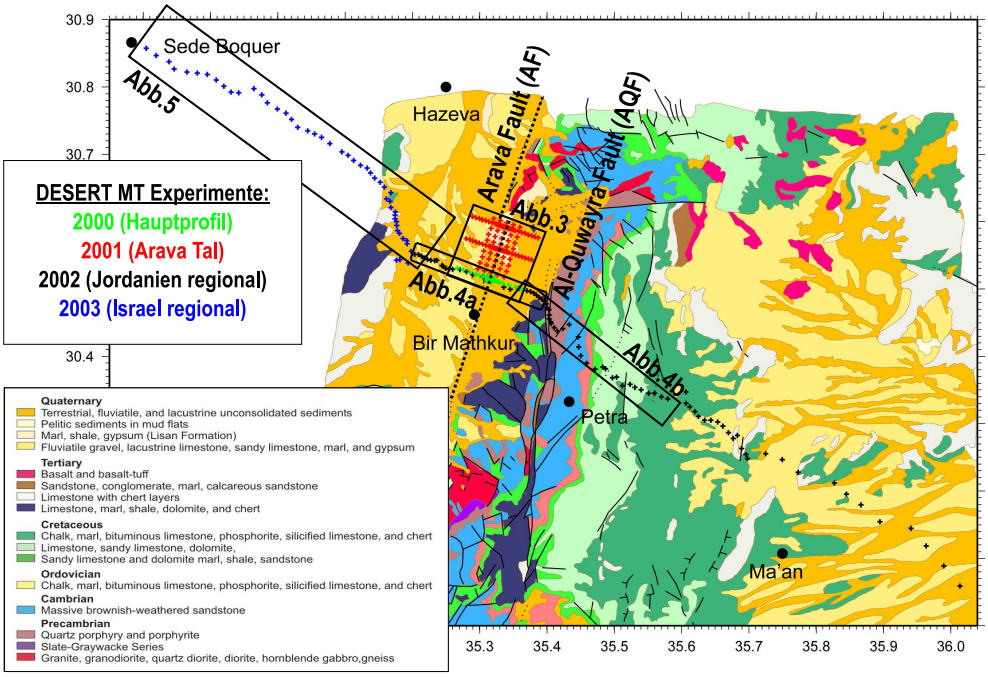

Abbildung 3.1: Lagekarte der in Israel und Jordanien gemessenen MT Profile. Insgesamt wurden in 4 aufeinanderfolgenden Experimenten in den Jahren 2000-2003 mehr als 250 Stationen gemessen. Für den jordanischen Teil ist die Karte mit der Oberflächengeologie unterlegt. (Es existiert keine „grenzüberschreitende“ Karte zwischen Israel und Jordanien mit einheitlich bezeichneten geologischen Formationen.)

Da die letzten Daten erst im November 2003 gewonnen wurden, sind noch nicht alle Ergebnisse in Fachzeitschriften veröffentlicht. In diesem Kapitel werden deshalb auch einige vorläufige, bisher unveröffentlichte Ergebnisse gezeigt, die für die Diskussion wichtig sind.

Die ersten MT Daten wurden 2000 entlang eines $10\,km$ langen Segments des seismischen Hauptprofils im Arava Tal gemessen. Der Stationsabstand betrug innerhalb eines $2\,km$ breiten Bereichs im Zentrum über die AF $100\,m$ und in größerer Entfernung von der Störung $500\,m$. Ritter et al. (2003a, Abb. 2) stellen zweidimensionale MT Inversionsergebnisse zusammen mit einem seismischen P-Wellen Geschwindigkeitsmodell dar. Im Bereich der oberen Kruste (Modelltiefe ist $5\,km$) zeigen beide Modelle signifikante laterale Änderungen der entsprechenden physikalischen Parameter im Bereich der Störung. Oberflächennah enthält das Leitfähigkeitsmodell eine horizontale, etwa $100\,m$ dicke Schicht die sich von der AF nach Osten erstreckt. Die auffälligste Struktur ist eine westlich der Störung gelegene, leitfähige Schicht ($2-4\,\Omega m$) in einer Tiefe von etwa $1.3-1.5\,km$, deren östliche Begrenzung mit der AF an der Erdoberfläche übereinstimmt. Die hohen Leitfähigkeiten in dieser Schicht sind vermutlich auf salinare Wässer in Sedimenten zurückzuführen. In Verlängerung dieses guten Leiters kommt es auf der anderen Seite der Störung zu einem signifikanten Anstieg der P-Wellen Geschwindigkeiten auf Werte bis zu $5\,km/s$. Die gemessenen hohen seismischen Geschwindigkeiten östlich der AF sind typisch für kristallines Gestein, während die beobachteten Widerstandswerte von nur 20 bis $80\,\Omega m$ (weiter östlich bis $250\,\Omega m$) zu niedrig für unverwittertes Kristallingestein sind. Kristallines Gestein mit fluidhaltigen Brüchen könnte gleichzeitig die moderaten elektrischen Leitfähigkeiten und die hohen P-Wellen Geschwindigkeiten erklären.

Auffälligstes Merkmal im Abbild der elektrischen Leitfähigkeit ist die abrupte laterale Begrenzung der leitfähigen Schicht(en) im Bereich der Störung. Rührt die hohe Leitfähigkeit der tieferen Schicht von Fluiden her, scheint es entweder durch die Störung selbst oder durch den lithologischen Kontrast zu einer Barriere für Fluidtransport zu kommen. Abb. 3.2 zeigt die Verteilung der elektrischen Leitfähigkeit entlang von drei $10\,km$ und sieben $5\,km$ langen Parallelprofilen, die 2001 gemessen wurden. Das südlichste Segment entspricht dem in Ritter et al. (2003a) beschriebenen Profil. Zwar wurde hier noch eine ältere Version des Inversionsalgorithmus verwendet, der keine Anpassung der vertikalen Magnetfelder erlaubte, doch erkennt man deutlich, dass die wesentlichen Leitfähigkeitsstrukturen erhalten bleiben. Alle Modelle zeigen die von Westen her kommende, elektrisch leitfähige Schicht, die im Bereich der AF in einer Tiefe von etwa $1.3-1.5\,km$ abrupt unterbrochen wird. Die Auflösung auf den kurzen Zwischenprofilen, die jeweils nur von fünf Stationen mit einem Stationsabstand von $1\,km$ besetzt sind, ist deutlich geringer. Im nördlichen Bereich, besonders beim nördlichsten Profil, weisen die Leitfähigkeitsmodelle mehr Heterogenitäten auf. Inwieweit die Geometrie und Lage dieser kleinräumigeren Strukturen wirklich festliegen, muss in weiteren Modellstudien noch

untersucht werden.

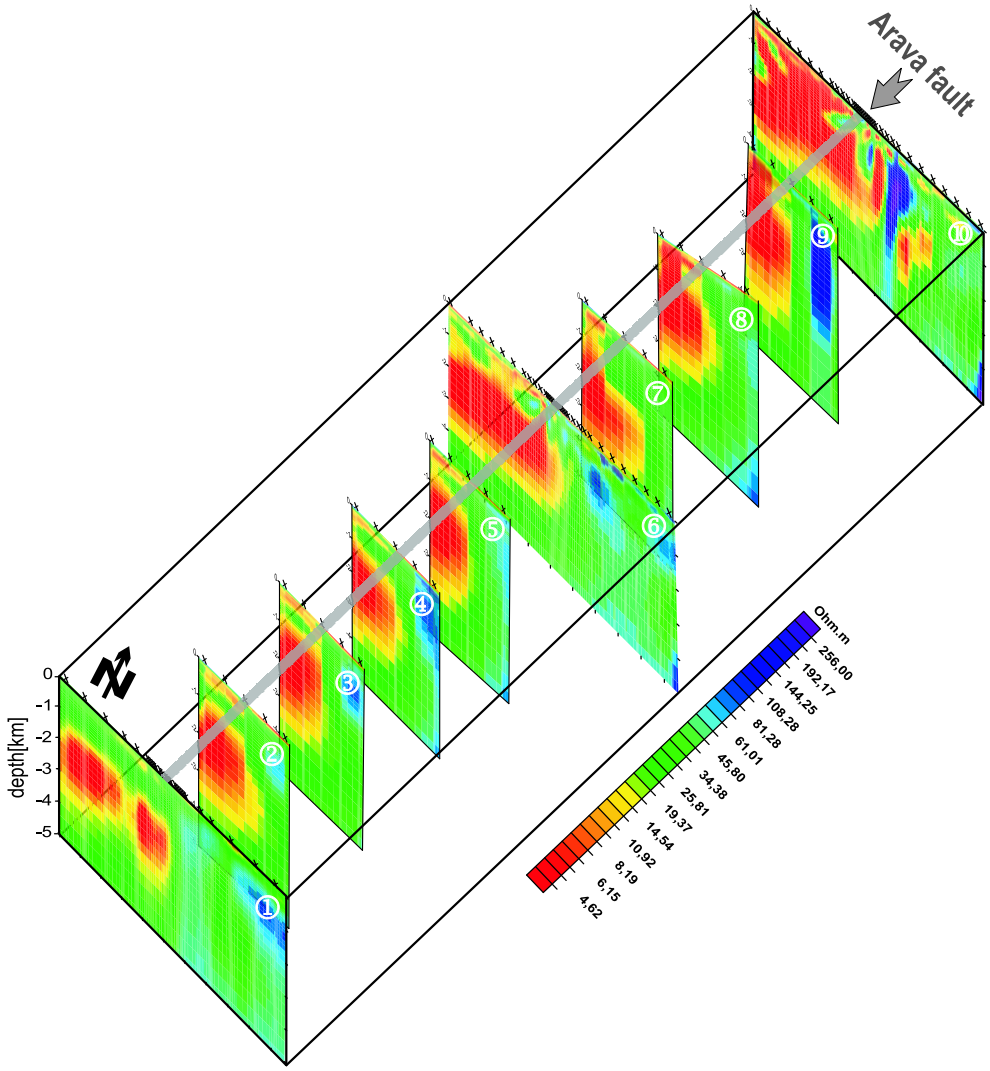

Abbildung 3.2: Verteilung der elektrischen Leitfähigkeit entlang von drei 10 km und sieben 5 km langen Parallelprofilen im Arava Tal, Jordanien (pers. Mitteilung U. Weckmann). Die Bereiche hoher elektrischer Leitfähigkeit erscheinen in gelben und roten Farben. Durch die Störung selbst oder aufgrund des lithologischen Kontrast entlang der Störung scheint es zu einer Barriere für Fluidtransport zu kommen. Siehe Abb. 3.1 für die Lage der Messstationen.

Auch die Daten der regionalen Profile in Jordanien (2002, 82 Stationen) und Israel (2003, 42 Stationen) sind zu diesem Zeitpunkt noch nicht abschließend bearbeitet. Trotzdem möchte ich einige Modelle zeigen, die erste Aufschlüsse über die tieferen Strukturen zulassen. Aufgrund der starken Topographie und der damit verbundenen numerischen Schwierigkeiten bei der Modellgittergene-

rierung musste das Gesamtprofil zunächst in mehrere Teile zerlegt werden. Im oberen Teil der Abb.3.3a (pers. Mitteilung U. Weckmann) erkennt man ein etwa $30\,km$ langes Teilstück, das von der jordanisch-israelischen Grenze bis zum östlichen Rand des Arava Tals reicht. Deutlich zu erkennen ist der oben bereits diskutierte sub-horizontale Leiter in der oberen Kruste. Weiterhin erkennt man im Bereich der AF eine etwa $3-5\,km$ breite sub-vertikale leitfähige Zone, die die gesamte Erdkruste bis in eine Tiefe von $30\,km$ durchdringt. Eine genauere Betrachtung zeigt, dass der östliche Rand der leitfähigen Zone - also nicht dessen Zentrum - mit der Lage der AF an der Erdoberfläche übereinstimmt. Das Modell ist im Sinne der Inversion ein „minimum structure“ Modell, d.h. es passt die Daten an, ohne a-priori Information zu verwenden. Trotzdem sollte die Signifikanz struktureller Details nicht überinterpretiert werden, bevor diese nicht durch entsprechende Auflösungstests bestätigt wurden. Robuste Parameter scheinen aber die Breite und Lage der leitfähigen Zone zu sein, während deren absolute Tiefenerstreckung und die Leitfähigkeiten unsicher sind. Es steht aber fest, dass sich die Tiefe der Zone erhöhter Leitfähigkeit im Bereich von zehner Kilometern bewegt.

Zum weiter östlich gelegenen zweiten Profilsegment gehören die Stationen des Escarpments, einem topographischen Anstieg von Meeresspiegelniveau bis auf etwa $1800\,m$. Im Gegensatz zum Arava Tal, das von jungen Sedimenten bedeckt ist, ist die Aufschlusssituation in diesem Gebiet ausgezeichnet. Man erkennt in der geologischen Karte (Abb. 3.1), dass das Profil mehrere Äste der Al-Quwayra Störungszone (AQF) kreuzt. Im 2D Inversionsergebnis (Abb. 3.3b) korreliert dieses Gebiet mit einer etwa $3\,km$ breiten Zone erhöhter Leitfähigkeit in der mittleren bis unteren Kruste. Im Bereich der AQF verläuft das Profil allerdings nicht senkrecht zur Störungszone, was für eine 2D Interpretation eigentlich notwendig wäre. Erste Tests zeigen aber, dass die leitfähige Zone in der Tiefe zur Anpassung einer ganzen Reihe von Messstationen notwendig ist. Existenz und ungefähre Lage der leitfähigen Zone scheinen robuste Parameter zu sein. Sicher scheint auch, dass die Oberkante des guten Leiters in der mittleren Kruste liegt. Die Breite der leitfähigen Zone und die absoluten Leitfähigkeiten sind dagegen weniger gut aufgelöst.

Über die Bedeutung der Al-Quwayra Störung im Zusammenhang mit der regionalen Tektonik ist bisher wenig bekannt. Nach Süden hin kann die AQF über mehrere hundert Kilometer bis nach Saudi Arabien weiterverfolgt werden. In unserem Messgebiet verbindet sich möglicherweise ein Ast der Störung mit der AF, wobei es allerdings keine Anzeichen für rezente Aktivität der AQF gibt. Längerfristig fehlende Aktivität kann dazu führen, dass sich Brüche in einer Störung schließen. Dies könnte erklären, warum die AQF nicht mit einer signifikanten Erhöhung der Leitfähigkeit in der oberen Kruste in Verbindung steht.

Das im Westen der DST auf israelischer Seite liegende Segment des regionalen Profils in Abb. 3.4 (pers. Mitteilung P. Bedrosion) zeigt die westliche Begrenzung des in $1.3-1.5\,km$ Tiefe liegenden leitfähigen Horizonts. Die-

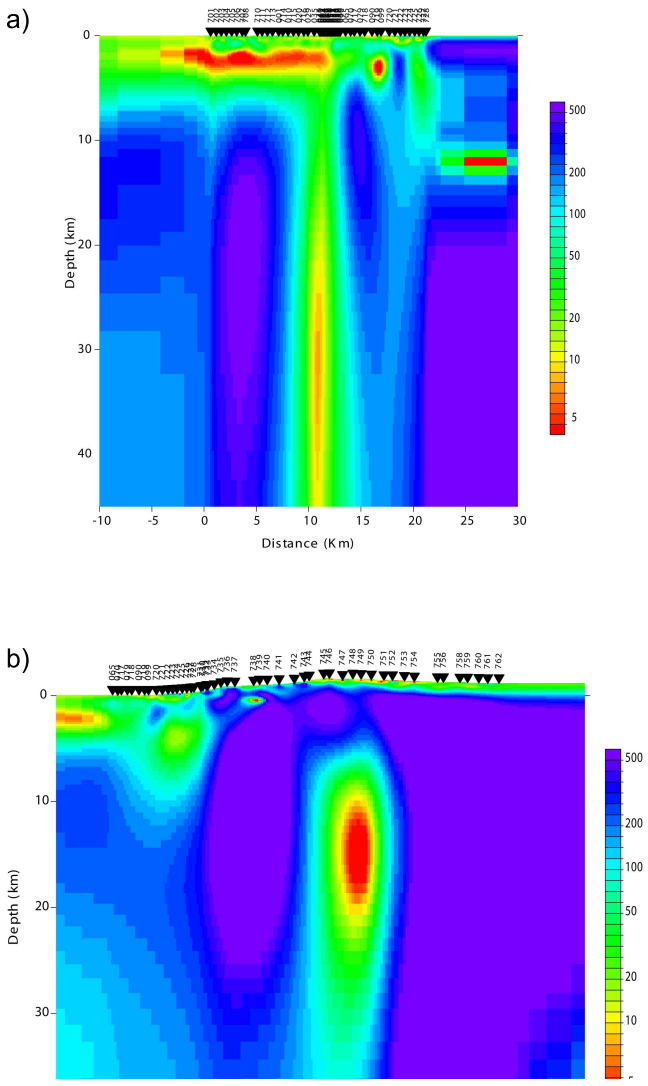

Abbildung 3.3: Regionale Leitfähigkeitsmodelle in Jordanien: a) Arava Tal: die AF / DST erscheint als eine etwa $3-5\,km$ breite sub-vertikale leitfähige Zone, die die gesamte Erdkruste bis in eine Tiefe von $30\,km$ durchdringt. b) Escarpment: die AQF erscheint als eine etwa $3\,km$ breite Zone erhöhter Leitfähigkeit in der mittleren bis unteren Kruste. Siehe Abb. 3.1 für die Lage der Messstationen.

se Grenze stimmt ungefähr mit der Lage der Zofar Störung überein. In der westlichen Hälfte des Modells erscheint eine vermutlich durchgängige, muldenförmige, leitfähige Schicht in einer Tiefe von $0.5 - 1.5\,km$. Die Bereiche hoher Widerstände (blau in Abb. 3.4) in einer Tiefe von $2.5 - 3\,km$ stimmen sehr gut mit den aus der Vp Tomographie (Ritter et al., 2003a, Fig. 2) und der Weitwinkelseismik (DESERT Group et al., 2004) bestimmten Tiefenlage für das Grundgebirge überein. Die Topographie der Oberkante des schlechten Leiters könnte großräumige Faltenstrukturen im Grundgebirge wiedergeben.

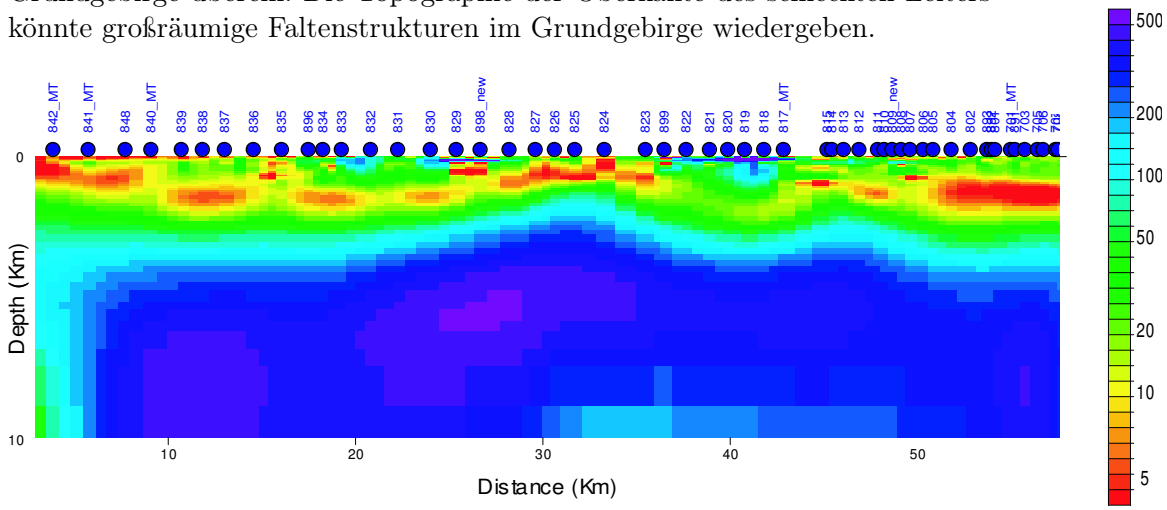

Abbildung 3.4: Regionales Leitfähigkeitsmodell für das israelische Segment. Man erkennt die westliche Begrenzung des in $1.3-1.5\,km$ Tiefe liegenden leitfähigen Horizonts im Bereich der Zofar Störung. Die Topographie der Oberkante des schlechten Leiters könnte großräumige Faltenstrukturen im Grundgebirge wiedergeben. Siehe Abb. 3.1 für die Lage der Messstationen.

Kapitel 4

Beispiele fossiler Systeme

4.1 Die Münchberger Gneismasse

Für die Rekonstruktion fossiler tektonischer Prozesse spielen kristalline Klippen eine wichtige Rolle. Tektonische Klippen sind durch allochthone Gesteine charakterisiert, d.h. Gesteine, die durch tektonische Prozesse über große Distanzen lateral transportiert wurden (Deckentektonik). Das Münchberger Massiv (MüMa) in Bayern ist eine solche Klippe; sie besteht aus einer Folge von Gneisen, die im Zuge der Variskischen Orogenese in ihre heutige Position befördert wurden. Die tektonische Interpretation dieser Gneise, die eine invertierte metamorphe und stratigraphische Abfolge aufweisen, ist außerordentlich kompliziert und beschäftigt Geologen seit mehr als 100 Jahren. Die Interpretation der MüMa Formationen spielte für die Lokation der Kontinentalen Tiefbohrung (KTB), die letztlich 80 km weiter südöstlich abgeteuft wurde, eine wichtige Rolle. So wurde die MüMa 1981 im Rahmen der KTB Voruntersuchung, neben vielen anderen geophysikalischen Verfahren, auch mit magnetotellurischen Messungen im Frequenzbereich ($1\,kHz - 1\,Hz$) an 20 Messorten untersucht (Haak et al., 1985). Hochfrequente MT Messungen wurden zu dieser Zeit gerade technisch machbar, allerdings zeigte sich später, dass diese frühen Daten aufgrund der starken elektromagnetischen Störsignale nicht auswertbar waren.

Die MT Daten von Ritter et al. (1999) wurden 1996 in drei Stationsclustern mit jeweils drei (über Kabel!) synchronisierten Messstationen gewonnen. Der Abstand zwischen den Stationsclustern betrug 4, bzw. $8\,km$. Bei der Datenanalyse wurde das in Ritter et al. (1998b) vorgestellte Verfahren eingesetzt, das neben einer robusten Statistik darauf beruht, dass nur diejenigen Signalanteile in den Eingangskanälen (normalerweise den horizontalen Magnetfeldkomponenten) zur Analyse herangezogen werden, die zwischen den Stationen kohärent und stationär sind. Aufgrund des hohen Rauschpegels sind die neuen Messergebnisse zwar immer noch gestört (vgl. Ritter et al., 1999, Fig. 4), allerdings bleiben die Daten interpretierbar. So zeigen alle Messstationen steil abfallende scheinbare Widerstandskurven, die auf eine stark erhöhte elektrische Leitfähig-

keit im Untergrund hinweisen. Eine Modellierung der Daten mit Schichtmodellen ergibt Widerstände von unter $1\,\Omega m$ in Tiefen von 2.5 bis $3.5\,km$.

Zumindest für die Stationen im Zentrum der MüMa stimmt die Tiefe der leitfähigsten Horizonte mit dem Einsetzen starker seismischer Reflektivität überein. Während dieser Tiefenbereich zwischen 2.5 und $5.5\,km$ nach seismischen Geschwindigkeitsmodellen mit hochmetamorphen oder granulitischen Gesteinen assoziiert wird, weist die unterste leitfähige Schicht in Modell 1 (Ritter et al., 1999, Fig. 7) in dieser Tiefe einen Leitwert von mehr als $19000\,S$ auf! Der Versuch solche Leitfähigkeiten ausschließlich durch elektrolytische Leitung (Fluide) zu erklären, führt zu Modellen mit völlig unrealistischen Porositäten oder Schichtdicken. Nur Elektronenleiter, wie z.B. Graphit, können die gemessenen hohen Leitfähigkeiten vernünftig erklären, allerdings nur dann, wenn diese metallischen Leiter genügend stark vernetzt sind (siehe z.B. auch Jödicke et al., 2004). Gesteinsproben mit bedeutender Graphitvernetzung wurden in der KTB nur in Bereichen von Scherzonen gefunden. Es ist deshalb sehr wahrscheinlich, dass die extrem hohen Leitfähigkeiten unterhalb der MüMa von graphitisierten Scherbahnen hervorgerufen werden, die wiederum auf subhorizontale Transportprozesse der MüMa Formationen zurückzuführen sind.

4.2 Die Iapetus Suturzone

Die Iapetus Suturzone (ISZ) ist ein breites Schersystem, das im Zuge der Schließung des Iapetus Ozeans im Ordovizium und Silur entstand. An der Erdoberfläche ist die ISZ durch eine Vielzahl NE-SW verlaufender Scherzonen gekennzeichnet, von denen die Southern Upland Fault vielleicht die bekannteste ist. Die ISZ ist auch durch eine, aus magnetischen Variationsmessungen abgeleitete, regionale Leitfähigkeitsanomalie vom Typ „elongated conductor“ gekennzeichnet (Banks et al., 1983, 1996); eine aktualisierte Kompilation dieser Daten zeigt Tauber et al. (2003, Fig. 1). Mit der 1997 durchgeführten magnetotellurischen Untersuchung der Southern Uplands im Südwesten Schottlands sollten strukturelle Details innerhalb dieser leitfähigen Zone in der oberen bis mittleren Erdkruste aufgelöst werden.

Die MT Messungen wurden an etwa 40 Stationen entlang mehrerer Profile in einem ca. $40\,km^2$ großen Gebiet in der Gegend von Galloway durchgeführt (siehe Tauber et al., 2003, Fig. 2). Der mittlere Stationsabstand entlang der Profile betrug ca. $1-2\,km$. Das 2D Leitfähigkeitsmodell in Tauber et al. (2003, Fig. 17) zeigt bis in etwa $4\,km$ Tiefe eine generell schlecht leitende, obere Erdkruste in Übereinstimmung mit den dort aufgeschlossenen metasedimentären und metamorphen Gesteinen. In größerer Tiefe löst das Modell verschiedene leitfähige Strukturen auf, die zum Teil klar mit tektonischen Merkmalen an der Erdoberfläche korrelieren. Die höchsten Leitfähigkeiten befinden sich in zwei circa $4\,km$ breiten vertikalen Blöcken, die sich jeweils in einer Tiefe von 4 bis $12\,km$ erstrecken und deren Ränder mit Störungen an der Erdoberfläche

übereinstimmen. Im Modell der elektrischen Leitfähigkeit erscheinen die Störungen als vertikale Strukturen, die andere Merkmale des Modells bis in Tiefen von 15 km durchschneiden. Diese Beobachtung bestätigt die Ansicht, dass die Störungen während der Schließung des Iapetus reaktiviert wurden. Die erhöhte elektrische Leitfähigkeit könnte wiederum durch graphitisierte Scherbahnen hervorgerufen worden sein. Im Bereich der Störungszonen befinden sich einige (kohlenstoffhaltige) Schwarzschieferaufschlüsse.

4.3 Der Damara Gürtel in Namibia

Auch im Damara Gürtel in Namibia wurde bereits in den 70er Jahren ein ungefähr ost-west verlaufender „elongated conductor“ gefunden (de Beer et al., 1982). Die Anomalie lässt sich in östlicher Richtung bis nach Botswana verfolgen, wo ihre Lage mit dem Verlauf der transkontinentalen Mwembeshi Scherzone korreliert (Daly, 1986).

Unsere MT Experimente in Namibia wurden in zwei Phasen 1998 und 1999 durchgeführt, wobei sich das erste Experiment auf wichtige großtektonische Strukturen des Damara Orogens konzentrierte. Das 200 km lange Profil durchquerte dabei den historischen „elongated conductor“ und mehrere tektonisch stratigraphische Zonengrenzen des Damara Gürtels (Ritter et al., 2003b, Figs. 1 und 2). Das aus diesen Messungen abgeleitete regionale 2D Leitfähigkeitsmodell in Ritter et al. (2003b, Fig. 9) zeigt eine generell schlecht leitende, obere Erdkruste, die an zwei Stellen von sub-vertikalen Zonen erhöhter Leitfähigkeit durchbrochen wird. Die Lage dieser vertikalen Leiter stimmt an der Erdoberfläche mit großen Störungszonen überein, der Autseib Fault (AuF) und der Waterberg Fault/Omaruru Lineament (WF/OL). Die Tiefenerstreckung der vertikalen Leiter reicht bis in die mittlere Erdkruste hinein, die im gesamten südlichen Teil des Profils gut leitend ist. Die Geometrie der leitfähigen Strukturen könnte ein regionales Schersystem wiederspiegeln, in dem oberkrustale listrische Störungen in einen Abscherhorizont (detachment) übergehen (vgl. Ritter et al., 2003b, Fig. 11).

Die zweite Messkampagne konzentrierte sich auf eine detaillierte Untersuchung der WF/OL. Zu diesem Zweck wurde ein 18km langes Profil mit einem Stationsabstand von 500 m, ein Parallelprofil mit einem Stationsabstand von 2000 m sowie an einigen weiteren, lateral verteilten Stationen gemessen (Weckmann et al., 2003a, Fig. 1). Das daraus abgeleitete Leitfähigkeitsmodell zeigt eine komplizierte Überlagerung verschiedener Strukturen (siehe Weckmann et al., 2003a, Fig. 21): (i) die WF/OL, die als eine 10 km breite Zone mit anisotroper elektrischer Leitfähigkeit erscheint, (ii) eine sehr gut leitende, ringförmige Struktur in der oberen Kruste im nördlichen Teil des Messgebiets und (iii) eine steilwinklig zum Hauptprofil verlaufende Lineamentzone. Zur Unterscheidung dieser komplizierten Leitfähigkeitstrukturen wurde ein neues Abbildungsverfahren entwickelt (Weckmann et al., 2003b), mit dem die Information

des Impedanztensors direkt in Form von Widerstandsellipsen umgesetzt werden kann. Bei ausreichend hoher Stationsüberdeckung, lassen sich mit diesem Verfahren sowohl isotrope als auch anisotrope Leitfähigkeitsanomalien direkt abbilden.

Das 2D anisotrope Leitfähigkeitsmodell in Weckmann et al. (2003a, Fig. 18) zeigt, dass die leitfähige Zone bis in eine Tiefe von $14\,km$ reicht. Trotz seiner einfachen Blockstruktur ist dieses Modell in der Lage, die innere Struktur der WF/OL aufzulösen, da der ungewöhnliche Verlauf der Sondierungskurven nur wenige äquivalente Modelle zulässt. Das Verhältnis von orthogonaler zu störungsparalleler Leitfähigkeit ist $1:10$, mit einer Streichrichtung von N70°E, sub-parallel zum Profil. Das regionale (isotrope) und lokale (anisotrope) Modell sind in Ritter et al. (2004, Fig. 8) einander gegenübergestellt. Die Unterschiede rühren hauptsächlich vom ungleichen Auflösungsvermögen der angewandten Techniken her. Isotrope 2D Inversion versucht die beiden Nebendiagonalelemente des Impedanztensors (vgl. Ritter et al., 2004, Fig. 3) gleichzeitig für alle Perioden und Stationen anzupassen, kann aber nicht die beobachteten Hauptdiagonalelemente erklären. Aus der 2D anisotropen Vorwärtsmodellierung erhält man zwar einen vollständig besetzten Impedanztensor, allerdings bleibt die Anwendung aus praktischen Gründen auf prinzipielle Modellstudien beschränkt. Im Vergleich der beiden Modelle stimmen die Tiefenerstreckung und laterale Ausdehnung des anisotropen Blocks gut mit dem sub-vertikalen Leiter des regionalen Modells überein. Auch die Widerstände der beiden Modelle sind vergleichbar; im regionalen Modell repräsentieren sie einen azimutalen Mittelwert der anisotropen Widerstandsverteilung des lokalen Modells.

Kapitel 5

Diskussion

Die oben beschriebenen Fallbeispiele belegen, dass Scherzonen häufig mit Zonen erhöhter elektrischer Leitfähigkeit korrelieren. Als Ursachen für die erhöhten Leitfähigkeiten wurden (i) in die Störung eindringende Oberfächen- und Formationswässer (Elektrolyte) oder (ii) Graphitisierungen entlang von Scherbahnen (elektronische Leiter) diskutiert, wobei beide Leitfähigkeitsmechanismen gleichzeitig (aber räumlich voneinander getrennt) wirksam sein können.

Typisch für viele aktive Störungssysteme sind FZC (fault zone conductor), die an das Vorhandensein von Fluiden im Bereich der Störungen, d.h. deren Zerrüttungszone, gebunden sind. Ausgeprägte FZC sind neben der West Fault in Chile (WF) (Hoffmann-Rothe et al., 2004) auch an aktiven Segmenten der San Andreas Verwerfung (SAF) (Unsworth et al., 2000; Bedrosian et al., 2002) oder an der Yamasaki Störung in Japan festgestellt worden (Handa & Sumitoma, 1985). Hingegen fehlt ein FZC im Abbild der elektrischen Leitfähigkeit der Tote Meer Verwerfung (DST/AF) (Ritter et al., 2003a). Wodurch wird das Ausmaß erhöhter Leitfähigkeit im Bereich der Zerrüttungszone von Störungen kontrolliert? Um dieser Frage nachzugehen, muss das komplizierte Zusammenspiel von elektrischer Leitfähigkeit, Lithologie, Permeabilität und Störungsgeometrie näher untersucht werden.

Die FZC der SAF und der WF haben Breiten in der Größenordnung von einigen hundert Metern und Tiefenerstreckungen von 1.5 bis $8\,km$ (siehe Ritter et al., 2004, Figs. 5 und 6). Die lateralen Leitwerte der FZC im Bereich der SAF betragen in Hollister $600\,S$, in Parkfield $250\,S$ und in Carrizo Plain nur $20\,S$. Während zur Erklärung der hohen lateralen Leitwerte in Hollister und Parkfield salinare Wässer im Bereich der Zerrüttungszone der Verwerfung herangezogen werden müssen (Unsworth & Bedrosian, 2004), reicht eine schmale Zerrüttungszone mit geringen Mengen meteorischer Wässer aus, um die Leitfähigkeiten von Carrizo Plain zu erklären (Unsworth et al., 1999). Meteorische Wässer, die durch den Verlauf der Topographie in die Störungszone hinein transportiert werden, können auch die lateralen Leitwerte von $5\,S$ an der WF erklären (Hoffmann-Rothe et al., 2004).

Die Größe der lateralen Leitwerte scheint auch mit der regionalen Seismizität zu korrelieren (siehe Ritter et al., 2004, Tab. 1). Die SAF bei Hollister zeichnet sich durch starke Mikroseismizität, dem Fehlen großer Erdbeben (Magnitude > 5), aseismisches Kriechen und dem größten lateralen Leitwert aus. Das als arretiert (locked) beschriebene Segment der SAF bei Carrizo Plain ist charakterisiert durch starke Erbeben und die niedrigsten lateralen Leitwerte. Parkfield liegt zwischen dem kriechenden (creeping) Segment im Norden und dem arretierten Segment der SAF im Süden und weist auch mittlere laterale Leitwerte auf. Die gegenwärtig inaktive West Fault ist durch niedrige laterale Leitwerte gekennzeichnet, und auch die aktive, aber FZC freie DST weist ein fast völliges Fehlen rezenter Seismizität auf.

In konzeptionellen Modellen von Störungszonen (siehe Abb. 2.1) werden drei strukturelle, mechanische und hydrologische Einheiten unterschieden: (i) das unveränderte Ausgangsgestein (protolith), (ii) die Zerrüttungszone (damage zone), eine bis zu mehrere hundert Meter breite, normalerweise permeable Zone mit stark erhöhter Bruchdichte und (iii) der Strörungskern (fault core), einer schmalen, in der Größenordnung von Zentimeter bis Meter breiten, oftmals impermeablen Zone stark deformierter Gesteine, die den größten Teil der Bewegungsenergie aufnimmt (Chester & Logan, 1986; Caine et al., 1996). Eigenschaften des Fluidtansports hängen von der Geometrie und den Permeabilitätskontrasten der Störung ab.

In welchem Zusammenhang stehen die beobachteten Leitfähigkeitsanomalien mit diesen strukturellen Einheiten von Störungszonen? Die FZCs, die auf drei parallelen Profilen über die SAF in Parkfield (Unsworth et al., 2000) abgebildet wurden, geben einen deutlichen Hinweis darauf, dass die SAF zumindest lokal kontinuierlichen Fluidtransport parallel zur Störung ermöglicht. Allerdings zeigen auch zwei $20\,km$ voneinander entfernte MT Profile in Hollister ausgeprägte FZCs (Bedrosian et al., 2002). Dies könnte bedeuten, dass die SAF auch auf regionalem Maßstab im gesamten mittleren Kalifornien als Fluidleiter wirkt.

Für den scharfen Widerstandskontrast über die SAF hinweg (Ritter et al., 2004, Fig. 5) kann der lithologische Kontrast zwischen Graniten (Salinian) im Westen und den Metasedimenten (Franciscian) im Osten verantwortlich sein. An der WF erhalten wir ein ähnliches Bild (Ritter et al., 2004, Fig. 7): der FZC scheint sich kontinuierlich entlang der Störung fortzusetzen und ist jeweils zur westlichen Seite der Störung hin scharf begrenzt. Quellen, die im Bereich der WF austreten, deuten ebenfalls darauf hin, dass Fluidtransport senkrecht zur Störung verhindert wird.

Das Leitfähigkeitsmodell über die Arava Fault (AF) in Jordanien zeigt zwei hochleitfähige Zonen, die abrupt an der Störung unterbrochen werden (Ritter et al., 2004, Fig. 6). Besonders auffällig ist dabei die von Westen her kommende Schicht in einer Tiefe von $1.3 - 1.5\,km$. Abb. 3.2 zeigt, dass sich dieses Bild über eine Länge von $10\,km$ entlang der Störung weiter nach Norden verfolgen lässt. Ein lithologischer Kontrast von phanerozoischen Sedimenten (Kalk- und

Sandsteine) zum präkambrischen metamorphen Grundgebirge könnte für diesen Leitfähigkeitskontrast verantwortlich sein. Allerdings dürften dann die zur Erklärung der relativ hohen Leitfähigkeiten geforderten, fluidgefüllten Klüfte nicht mit dieser Schicht verbunden sein. Weiterhin wird auch eine von Osten kommende, oberflächennahe Schicht an der Störung unterbrochen, wobei sich hier zu beiden Seiten der Störung ähnliche Lithologien (alluviale Sedimente) befinden. Es könnte also sein, dass in diesem Fall der Störungskern der AF direkt als Fluidbarriere wirkt, wobei dieser Eindruck noch durch das Fehlen eines FZC verstärkt wird.

Bei den anderen großen Störungssystemen führten die in die Zerrüttungszonen eingedrungenen Wässer zur Ausbildung der FZCs. Ausgehend von einem Gesamtversatz von 105 km, würde man nach Skalierungsregeln für Störungen (Scholz, 1987; Scholz et al., 1993) auch für die AF/DST eine Zerrüttungszone in der Größenordnung von bis zu 1 km Breite erwarten. Wodurch könnte dieser Widerspruch, also das Fehlen eines FZC bzw. einer Zerrüttungszone, erklärt werden?

1. Die alluvialen Sedimente an der Oberfläche haben nur über eine kurze Zeitspanne hinweg Versatz aufgenommen. In diesem Fall würden wir einen FZC in einer Tiefe erwarten, in der das Grundgebirge durchschnitten worden ist. „Constrained Inversions“ zeigen, dass ein FZC oberhalb von 1.5 km ausgeschlossen werden kann; in noch größerer Tiefe, wäre ein FZC mit den Daten vereinbar, aber nicht erforderlich.

2. Die Deformation findet entlang bisher noch nicht entdeckter Seitenäste der Störung statt. In seismischen Sektionen finden sich zwar Hinweise auf die Existenz von parallelen Störungen, allerdings gibt es kaum Hinweise auf nennenswerte laterale Versatzraten.

3. Es gibt keinen FZC oder er ist zu schmal, um aufgelöst werden zu können: Das bedeutet, er hat eine Breite von weniger als 50 m. Diese Schlussfolgerung wird von seismischen „fault guided wave“ Experimenten unterstützt, die eine Niedriggeschwindigkeitszone von nur $3 - 10\,m$ Breite im Bereich der Störung ergaben (Haberland et al., 2003). Auch in geologischen Geländeaufnahmen ließ sich keine breite und intensiv zerklüftete Zerrüttungszone nachweisen.

Der letzte Punkt würde bedeuten, dass die Verformung (strain) auf eine sehr schmale Zerrüttungszone konzentriert sein muss. Prozesse, die im Zusammenhang mit der Verhärtung oder Schwächung von Störungen stehen (fault hardening and weakening), kontrollieren, ob eine Störungszone im Laufe der Zeit breiter wird oder lokalisiert bleibt (Mitra & Ismat, 2001). In diesem Sinne wäre es möglich, dass die AF Zyklen zur vollständigen Wiedererlangung der Störungsfestigkeit (strength recovery) nicht oder nur unvollständig durchlaufen hat. Die ausgeprägten Zonen struktureller Deformation an der SAF und WF,

entwickelten sich hingegen in wiederholten Zyklen von Störungsverheilung, Festigkeitswiedererlangung und anschließendem Versagen. Alternativ könnte es sein, dass an Störungen mit starkem Festigkeitskontrast der jeweils schwächere Block stärker und weitläufiger strukturell deformiert wird (z.B. die SAF bei Hollister). Der fehlende FZC an der AF könnte demnach einfach bedeuten, dass es keinen ausgeprägten Festigkeitskontrast zwischen den Formationen östlich und westlich der Störung gibt.

Festzustehen scheint, dass mit der MT die Zerrüttungszone einer Störung – sofern diese existiert – teilweise oder in ihrer Gesamtheit abgebildet werden kann, während der Störungskern unsichtbar bleibt. Die Zerrüttungszone einer Störung wird deshalb sichtbar, weil die Bruchsysteme in der Regel von Fluiden durchdrungen werden. In diesem Sinne erhält man aus den Leitfähigkeitsmodellen indirekt Informationen über die lokale Fluidversorgung und die Permeabilität der Störungszone. Im Gegensatz zur MT kann man mit Hilfe der Seismologie den Kern einer Störung bestimmen, während man keine Informationen über die Zerrüttungszone erhält. Am ehesten kann deshalb aus der Kombination von räumlicher Verteilung der Hypozentren (Störungskern), FZC (Zerrüttungszone) und geologischen Aufnahmen auf strukturelle Einheiten von Störungszonen geschlossen werden. Abb. 5.1 erläutert diesen Zusammenhang:

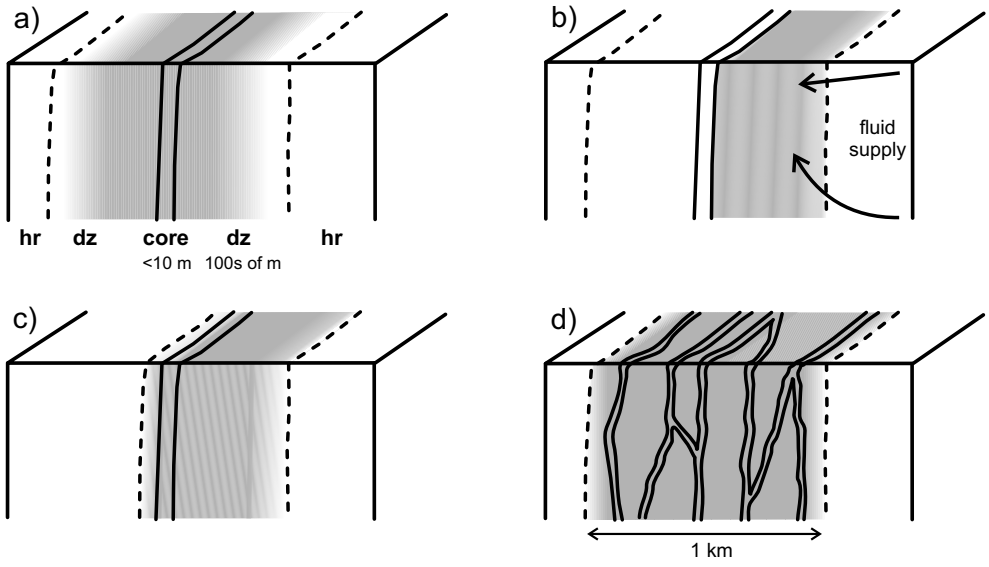

Abbildung 5.1: Zusammenhang zwischen Zonen hoher Leitfähigkeit (FZC) und strukturellen Merkmalen von Störungen (aus Ritter et al., 2004, Fig. 9).

1. Klassische, symmetrische Störungszone (Abb. 5.1a). Seismizität und Austritt der Störung an der Erdoberfläche liegen im Zentrum des FZC. Der FZC spiegelt die gesamte permeable Zerrüttungszone wieder. Strukturgeologische Aufnahmen würden eine symmetrische Bruchhäufigkeitsver-

teilung mit einem Maximum über dem Störungskern ergeben. Dieses Szenario ähnelt der Situation in Parkfield, obwohl strukturelle Aufnahmen aufgrund der fehlenden Aufschlüsse hier nicht möglich sind.

2. Symmetrische Zerrüttungszone mit einem impermeablen Störungskern (Abb. 5.1b). Seismizität und Austritt der Störung an der Erdoberfläche liegen nicht im Zentrum, sondern an einem Rand des FZC. Wie im vorhergehenden Fall würde eine strukturgeologische Aufnahme wiederum eine symmetrische Bruchhäufigkeitsverteilung ergeben. Aufgrund der Fluidbarriere im Zentrum der Störung dringen Fluide aber nur in eine Seite der Zerrüttungszone ein. Dieses Szenario scheint für eine ganze Reihe der beobachteten Leitfähigkeitsmodelle relevant zu sein. Entlang der WF wurde eine symmetrische Bruchhäufigkeitsverteilung festgestellt sowie Fluide, die aufgrund der topographischen Verhältnisse nur von einer Seite in die Störung eindringen. Auch an der AF in Jordanien werden leitfähige Schichten an einer impermeablen Barriere zurückgehalten. In diesem Fall stehen die hohen Leitfähigkeiten jedoch nicht im Zusammenhang mit einem FZC. Die SAF bei Hollister ist ähnlich wie die WF durch einen Störungskern gekennzeichnet, der mit einem Rand des FZC übereinstimmt. Allerdings gibt es hier keine strukturgeologischen Daten.

3. Asymmetrische Störungszone (Abb. 5.1c). Eine asymmetrische Störungszone entsteht durch einen ausgeprägten Festigkeitskontrast. Nach Schulz & Evans (2000) zeigt die Punchbowl Fault in Südkalifornien an einigen Abschnitten eine asymmetrische Störungszone. Die räumliche Verteilung von Seismizität und FZC wäre ähnlich dem vorhergehenden Beispiel in (Abb. 5.1b), wobei der FZC die mechanisch schwächere und vermutlich permeablere Seite wiederspiegeln würde. Nur durch eine strukturgeologische Aufnahme könnte man beide Fälle voneinander unterscheiden. Die SAF bei Hollister, mit dem starken lithologischen Kontrast zwischen den Graniten auf der einen und dem stark deformierten Franciscan Komplex auf der anderen Seite, könnte in diese Kategorie fallen.

4. Anastomotische Störungszone (Abb. 5.1d). Faulkner et al. (2003) entwickelten ein Störungszonenmodell mit einer breiten Zone anastomotischer Bänder von Störungslette in schichtsilikatreichem Material. Die Verteilung der elektrischen Leitfähigkeit für diese Art von Störungszone ist schwer vorherzusagen, da sie sowohl von der räumlichen Verteilung der Bänder als auch von deren relativer Permeabilität innerhalb der Störungszone abhängen wird. Es ist allerdings möglich, dass eine solche Störungszone durch starke anisotrope Leitfähigkeit gekennzeichnet ist, ähnlich wie sie für die fossile Waterberg Fault / Omaruru Lineament (WF/OL) in Namibia auftrat.

Bisher konzentrierte sich die Diskussion auf Modelle von Störungszonen in

der oberen (spröden) Kruste. Um die tieferen Stockwerke einer Scherzone elektrisch abzubilden, gibt es prinzipiell zwei Möglichkeiten: Einerseits versucht man die tiefen Strukturen einer aktiven Störung mit ausreichend langen Perioden und Profilen direkt aufzulösen, was in Anbetracht des abschirmenden Effekts oberflächennaher Leiter und dem mit der Tiefe abnehmenden Auflösungsvermögen der Methode schwierig sein kann. Andererseits untersucht man eine exhumierte, fossile Scherzone in der heutigen oberen Kruste. Im zweiten Fall kann man mit hoher Auflösung abbilden, da man sich relativ nah am Untersuchungsobjekt befindet. Allerdings können im Vergleich zu den aktiven Zeiten der Scherzone andere Leitfähigkeitsmechanismen wirksam sein, bzw. alte Strukturen überprägt worden sein.

Fig. 10 in Ritter et al. (2004) zeigt eine Adaption einer Übersicht von Sibson (1983) über den Verlauf von großen Scherzonen in der Tiefe, zusammen mit einer Reihe von publizierten regionalen Modellen. Eine der wichtigen offenen Fragen ist dabei, ob Verformung (shear) im duktilen Bereich lokalisiert bleibt (a) oder mit zunehmender Tiefe auf einen breiteren Bereich wirkt (c). (Molnar et al., 1999) vermuten, dass es im duktilen Bereich zu kontinuierlicher Deformation mit vertikaler Abkopplung kommen könnte (d). Die Abb. (e-f) zeigen vereinfacht Beispiele, die aus der Interpretation seismischer Daten für die Unterkruste des San Andreas Systems gewonnen wurden und deren Ergebnisse nicht unbedingt im Einklang miteinander stehen. So werden Störungssysteme gefordert, die entweder in der unteren Kruste zusammenlaufen (f), über ein Detachment in der mittleren Kruste verbunden sind (g) oder separat die gesamte obere und untere Erdkruste durchdringen (Parsons & Hart, 1999; Brocher et al., 1994; Henstock et al., 1997).

Das vorläufige Modell in Abb. 3.3 zeigt die tieferen Strukturen der DST im Arava Tal. Bemerkenswert ist die nur etwa $3 - 5\,km$ breite Zone erhöhter Leitfähigkeit, die sich unterhalb der AF bis in große Tiefen durch die gesamte mittlere und untere Kruste erstreckt, wobei der östliche Rand der leitfähigen Zone mit der Lage der AF an der Erdoberfläche übereinstimmt. Als Ursachen für die hohen Leitfähigkeiten in der unteren Kruste kommen prinzipiell wieder Fluide und/oder Vererzungen in Frage. Hinweise für Aufschmelzungen gib es nicht. Vermutlich steht die unterkrustale Leitfähigkeitsanomalie jedoch nicht im Zusammenhang mit einer dem Sprödbereich zugeordneten Zerrüttungszone der Störung. Die Lage und Geometrie der Zone erhöhter Leitfähigkeit legen den Schluss nahe, dass sich die Störung ähnlich wie in Ritter et al. (2004, Fig. 10a) angedeutet, auch in der mittleren und unteren Kruste sub-vertikal und stark lokalisiert bis in große Tiefen hin fortsetzt.

Ein verwandtes Bild ergibt sich auch für die WF/OL-Zone in Namibia, eine prominente Störungszone des Damara Orogens, die im Laufe der Erdgeschichte viele Male reaktiviert wurde. Das Leitfähigkeitsmodel in Ritter et al. (2004, Fig. 8) zeigt die WF/OL nicht als einzelne Störung, sondern als eine anisotrope Zone mit erhöhter Leitfähigkeit parallel zur Störung. Mit der Magnetotellurik lässt sich grundsätzlich nicht zwischen makroskopischer und intrinsischer

Anisotropie unterscheiden. Die im Bereich der Störung gefundenen, graphithaltigen Marmore könnten Graphitanreicherungen in Lamellen oder dünnen Filmen entlang von Scherbahnen ermöglichen. Die Langzeitstabilität von Graphit macht ihn dabei zu einem idealen Kontrastmedium für Abbildungszwecke.

Die Tiefe der anisotropen Zone in Ritter et al. (2004, Fig. 8) beträgt mindestens $14\,km$. Unter der Annahme, dass die ehemalige obere Kruste bereits erodiert wurde, bedeutet dies, dass die WF/OL die gesamte Kruste durchdrungen hat. Ähnlich wie bei der DST/AF deutet dieses Leitfähigkeitsmodell also auf eine Scherzone hin, in der Verformung auf ein etwa $10\,km$ breites Band beschränkt blieb. Die Anisotropie der elektrischen Leitfähigkeit könnte bedeuten, dass die Verformung, als semi-kontinuierliche Deformation in der mittleren und unteren Kruste, auf dünne, anastomosierende sub-vertikale Bänder konzentriert blieb.

MT Messungen von fossilen Scher- und Suturzonen, wie z.B. auch die oben beschriebenen Untersuchungen der Iapetus Suturzone oder des Münchberger Gneiskomplexes erlauben also durchaus Einblicke in die duktile Erdkruste. Allerdings sollte man sich klar machen, dass man gute Abbilder der früheren Unterkruste nur dann erhält, wenn man die rezente obere Kruste mit der dazu notwendigen hohen Stationsüberdeckung untersucht. Viele der MT Studien in solchen Gebieten, z.B. die im kanadischen Schild (Jones, 1999; Jones et al., 2003), sind aber ausschließlich auf regionale Leitfähigkeitsstrukturen ausgelegt. Während mit diesen Experimenten Anomalien der tiefen Lithosphäre ergründet werden können, bleiben die Spuren fossiler Scherzonen in der heutigen oberen Kruste weitgehend unbestimmt.

Kapitel 6

Zusammenfassung und Ausblick

Scherzonen zeigen im Abbild der elektrischen Leitfähigkeit Gemeinsamkeiten aber auch wesentliche Unterschiede. Typisch für viele der aktiven Scherzonen sind sub-vertikale Zonen erhöhter elektrischer Leitfähigkeit im Bereich der oberen Kruste, die mit der Zerrüttungszone der Störungen in Verbindung stehen. Generell können Fluide, die im Bruchnetzwerk der Zerrüttungszone verteilt sind, diese FZCs (Fault Zone Conductor) erklären. Zumindest für die San Andreas Fault scheint es auch eine Korrelation zwischen der Größe (dem lateralem Leitwert) der FZC und der lokalen Seismizität zu geben. Das kriechende Segment der SAF bei Hollister ist durch die höchsten Leitfähigkeiten und starke Mikroseismizität gekennzeichnet. Im Gegensatz dazu gibt es beim arretierten Segment der SAF bei Carrizo Plain vergleichsweise geringe Leitfähigkeiten und starke Erdbeben. Die schwach ausgeprägten FZC der West Fault (WF) und der SAF bei Carrizo Plain könnten in diesem Sinne auf ein sich schließendes Bruchnetzwerk hindeuten, also auf ein Störungssystem, in dem Zementations- und Abdichtungsprozesse im Gange sind bzw. die Überhand haben.

Das elektrische Abbild der Arava Fault (AF) in Jordanien fällt durch das Fehlen eines FZC aus dem Rahmen. Allerdings gibt das Leitfähigkeitsmodell Hinweise auf eine Barriere für Fluidtransport, die entweder durch einen impermeablen Störungskern oder durch den lithologischen Kontrast an der Störung hervorgerufen wird. Das Fehlen des FZC ist ungewöhnlich, da an der SAF und der WF solche Zonen mit Breiten von einigen hundert Metern gefunden wurden. Dies ist in Übereinstimmung mit den aus Skalierungsgesetzen abgeleiteten Breiten für Zerrüttungszonen großer Störungen. Nach Mitra & Ismat (2001) können Störungszonen in wiederholten Zyklen von Verheilung, Wiedererstarken und Versagen in ihrer Breite anwachsen. Die fehlende oder nur meterdicke Zerrüttungszone der AF könnte daher auf eine Scherzone hinweisen, in der Verformung auch über lange Zeiträume extrem lokalisiert ist.

Die Fallbeispiele machen deutlich, dass FZC nicht unmittelbar bestimmten strukturellen Einheiten in konzeptionellen Modellen von Störungszonen zugeordnet werden können. FZC können entweder die gesamte Zerrüttungszone ei-

ner Störung abbilden (SAF bei Parkfield) oder nur einen Teil davon (WF, SAF bei Hollister). Um ein vernünftiges Gesamtbild zu erhalten, bietet sich an, die Abbilder der MT (Zerrüttungszone) mit denen der Seismologie (Störungskern) und der Strukturgeologie (Bruchdichte) zu verbinden.

Durch magnetotellurische Untersuchungen an exhumierten, fossilen Scherzonen können Einblicke in Prozesse von Scherzonen in der Unterkruste gewonnen werden. In Abwesenheit größerer Fluidmengen scheinen die erhöhten Leitfähigkeiten in fossilen Systemen von graphitisierten Scherbahnen verursacht zu werden. Strukturelle Details können allerdings nur dann bestimmt werden, wenn die Messungen so konzipiert werden, dass die heutige obere Kruste mit hoher Auflösung erfasst wird. Die fossile WF/OL in Namibia erscheint als eine $10\,km$ breite und $14\,km$ tiefe Zone anisotroper Leitfähigkeit. Nach heutigem Exhumierungsgrad bedeutet dies vermutlich, dass die Scherzone die gesamte Erdkruste auf relativ schmalen Raum durchdrungen hat.

Die Untersuchung aktiver und fossiler Scher- und Störungszonen wird auch in der Zukunft ein zentrales Thema geowissenschaftlicher Forschung bleiben. Moderne objektorientierte Forschungsansätze, bei denen das Verständnis geodynamischer Prozesse im Vordergrund steht, verlangen eine interdisziplinäre Herangehensweise bei der Beobachtung und Interpretation geowissenschaftlicher Daten. Dem genauen Abbilden von elektrischen Leitfähigkeitsanomalien im tiefen Untergrund in Verbindung mit anderen geowissenschaftlichen Verfahren kann dabei eine Schlüsselrolle zukommen.

Literaturverzeichnis

Alabi, A. O., Camfield, P. A., & Gough, D. I., 1975. The North American Central Plains conductivity anomaly, *Geophys. J. R. astr. Soc.*, **43**, 815–833.

Archie, G. E., 1942. The electrical resistivity log as an aid in determining some reservoir characteristics, *Transactions of the American Institute of Mining, Metallurgical and Petroleum Engeneers*, **146**, 54–62.

Banks, R. J., Beamish, D., & Geake, M. J., 1983. Magnetic variation anomalies in northern England and southern Scotland, *Nature*, **303**, 316–318.

Banks, R. J., Livelybrooks, D., Jones, P., & Longstaff, R., 1996. Causes of high crustal conductivity beneath the Iapetus Suture Zone in Great Britain, *Geophys. J. Int.*, **124**, 433–455.

Bedrosian, P. A., Unsworth, M. J., & Egbert, G., 2002. Magnetotelluric imaging of the creeping segment of the San Andreas Fault near Hollister, *Geophys. Res. Lett.*, **29**(11), 10.1029/2001GL014119.

Ben-Zion, Y. & Sammis, C. G., 2003. Characterization of fault zones, *Pure and Applied Geophysics*, **160**, 677–715.

Beroza, G. C. & Jordan, T. H., 1990. Searching for slow and silent earthquakes using free oscillations, *J. Geophys. Res.*, **95**, 2485–2510.

Brasse, H., Lezaeta, P., Schwalenberg, K., Soyer, W., & Haak, V., 2002. The Bolivian Altiplano Conductivity Anomaly, *J. Geophys. Res.*, **107**(5), 10.1029/2001JB000391.

Brocher, T. M., McCarthy, J., Hart, P. E., Holbrook, W. S., Furlong, K. P., McEvilly, T. V., Hole, J. A., & Klemperer, S. L., 1994. Seismic evidence for a lower-crustal detachment beneath San Francisco Bay, California, *Science*, **265**, 1436–1439.

Cagniard, L., 1953. Basic theory of the magneto-telluric method of geophysical prospecting, *Geophysics*, **18**, 605–645.

Caine, J. S., Evans, J. P., & Forster, C. P., 1996. Fault zone architecture and permeability structure, *Geology*, **24**(11), 1125–1128.

Cerv, V., Pek, J., & Praus, O., 1984. Models of induction anomalies in Czechoslovakia, *J. Geophys.*, **55**, 161–168.

Chamalaun, F., Lilley, F., & Wang, L., 1999. Mapping the Carpentaria conductivity anomaly in northern Australia, *Phys. Earth Planet. Int.*, **116**, 105–115.

Chester, F. M. & Logan, J. M., 1986. Implications for mechanical properties of brittle faults from observations of the Punchbowl fault zone, California, *Pure and Applied Geophysics*, **124**(1/2), 79–106.

Coggon, J. H., 1971. Electromagnetic and electrical modeling by the finite element method, *Geophysics*, **36**, 132–155.

Daly, M. C., 1986. Crustal shear zones and thrust belts: their geometry and continuity in Central Africa, *Phil. Trans. R. Soc.*, **317**(A), 111–128.

de Beer, J. H., Gough, D. I., & van Zijl, J. S. V., 1975. An electrical conductivity anomaly and rifting in southern Africa, *Nature*, **225**, 678–680.

de Beer, J. H., Huyssen, R. M. J., & van Zijl, S. J. V., 1982. Magnetometer array studies and deep Schlumberger soundings in the Damara orogenic belt, South West Africa, *Geophys. J. R. astr. Soc.*, **70**, 11–29.

DESERT Group, Weber, M., Abu-Ayyash, K., Abueladas, A., Agnon, A., Al-Amoush, H., Babeyko, A., Bartov, Y., Baumann, M., Ben-Avraham, Z., G.Bock, Bribach, J., El-Kelani, R., Förster, A., Förster, H.-J., Frieslander, U., Garfunkel, Z., Grunewald, S., Götze, H. H., Haak, V., Haberland, C., Hassouneh, M., Helwig, S., Hofstetter, A., Jäckel, K., Kesten, D., Kind, R., Maercklin, N., Mechie, J., Mohsen, A., Neubauer, F. M., Oberhänsli, R., Qabbani, I., Ritter, O., Rümpker, G., Rybakov, M., Ryberg, T., Scherbaum, F., Schmidt, J., Schulze, A., Sobolev, S., Stiller, M., Thoss, H., Weckmann, U., & Wylegalla, K., 2004. The crustal structure of the Dead Sea Transform, *Geophys. J. Int.*, **156**, 655–681.

Dragert, H., Wang, K., & James, T. S., 2001. A silent slip event on the deeper Cascadia subduction interface, *Nature*, **292**, 25 – 28.

Echternacht, F., Tauber, S., Eisel, M., Brasse, H., Schwarz, G., & Haak, V., 1997. Electromagnetic study of the active continental margin in northern Chile, *Phys. Earth Planet. Int.*, **102**, 69–87.

Faulkner, D. R., Lewis, A. C., & Rutter, E. H., 2003. On the internal structure and mechanism of large strike-slip fault zones: field observations of the Caboneras fault in southeasten Spain, *Tectonophysics*, **367**, 235–251.

Goldstein, R. M., Engelhardz, H., Kamb, B., & Frolich, R. M., 1993. Satellite radar interferometrie dfor monitoring ice sheet motion: application to an Antarctic ice stream, *Science*, **262**, 1525–1530.

Gough, D. I., 1973. The geophysical significance of geomagnetic variation anomalies, *Phys. Earth Planet. Int.*, **7**(3), 379–388.

Gough, D. I., 1983. Electromagnetic geophysics and global tectonics, *J. Geophys. Res.*, **88**(B4), 3367–3377.

Gough, D. I. & Reitzel, J. S., 1967. A portable three-component magnetic variometer, *J. Geomag. Geoelectr.*, **19**(3), 203–215.

Grant-Lisa, B. & Lettis-William, R., 2002. *Paleoseismology of the San Andreas fault system*, Seismological Society of America. Berkeley, CA, United States.

Guéguen, Y. & Palciauskas, V., 1994. *Introduction to the Physics of Rocks*, Princeton University Press, UK.

Haak, V., 1985. *Anomalies of the electrical conductivity in the earth's crust and upper mantle, in Landolt-Bornstein: Numerical data and funtional relationships. In Angenheister, G. (ed.) Science and Technology. New Series*, chap. 2.3.2, pp. 397–436, Springer Verlag, Berlin.

Haak, V. & Hutton, V. R. S., 1986. Electrical resistivity in continental lower crust, in *The Nature of the Lower Continental Crust*, edited by J. B. Dawson, vol. 24, pp. 35–49.

Haak, V., Blümecke, T., Fischer, G., Schnegg, P., & Rath, V., 1985. Electrical conductivity studies, Oberpfalz, *Abstract in 2nd International Symposium on Observation of the Continental Crust through Drilling, Seeheim*, **55**.

Haberland, C., Agnon, A., El-Kelani, R., Maercklin, N., Qabbani, I., Rümpker, G., Ryberg, T., Scherbaum, F., & Weber, M., 2003. Modeling of seismic guided waves at the Dead Sea Transform, *J. Geophys. Res.*, p. 10.1029/2002JB002309.

Handa, S. & Sumitoma, N., 1985. The geoelectric structure of the Yamasaki and the Hanaori faults, Southwest Japan, *J. Geomag. Geoelectr.*, **37**, 93–106.

Henstock, T., Levander, A., & Hole, J., 1997. Deformation in the lower crust of the San Andreas Fault system in northern California, *Science*, **278**, 650–653.

Hoffmann-Rothe, A., 2002. *Combined structural and magnetotelluric investigation across the West Fault zone in the Andes of northern Chile*, Ph.D. thesis, University of Potsdam, http://www.gfz-potsdam.de/bib/pub/str0212/0212.htm.

Hoffmann-Rothe, A., Ritter, O., & Haak, V., 2001. Magnetotelluric and geomagnetic modelling reveals zones of very high electrical conductivity in the upper crust of Central Java, *Phys. Earth Planet. Int.*, **124**, 131–151.

Hoffmann-Rothe, A., Ritter, O., & Janssen, C., 2004. Correlation of Electrical Conductivity and Structural Damage at a Major Strike-Slip Fault in Northern Chile, *J. Geophys. Res.*, pp. 000–000 (in revision).

Hole, J. A., Catchings, R. D., Clair, K. C. S., Rymer, M. J., Okaya, D. A., & Carney, B. J., 2001. Steep-dip seismic imaging of the shallow San Andreas Fault near Parkfield, *Science*, **294**, 1513–1515.

Hutton, V. R. S., Ingham, M. R., & Mbipom, E. W., 1980. An electrical model of the crust and upper mantle in Scotland, *Nature*, **287**, 30–33.

Jödicke, H., Kruhl, J. H., Ballhaus, C., Giese, P., & Untiedt, J., 2004. Syngenetic, thin graphite-rich horizons in lower crustal rocks from the Serre San Bruno, Calabria (Italy), and implications for the nature of high-conducting deep crustal layers, *Phys. Earth Planet. Int.*, **141**, 37–58.

Jones, A. G., 1999. Imaging the continental upper mantle using electromagnetic methods, *Lithos*, **48**, 57–80.

Jones, A. G., Katsube, T., & Schwann, P., 1997. The longest conductivity anomaly in the world explained: sulphides in fold hinges causing very high electrical anisotropy, *J. Geomag. Geoelectr.*, **49**, 1619–1629.

Jones, A. G., Lezaeta, P., Ferguson, I. J., Chave, A. D., Evans, R. L., Garcia, X., & Spratt, J., 2003. The electrical structure of the Slave craton, *Lithos*, **71**(2-4), 505–527.

Jones, F. W. & Price, A. J., 1971. Geomagnetic effects of sloping and shelving discontinuities of earth conductivity, *Geophysics*, **36**, 58–66.

Kaufman, A. A. & Keller, G. V., 1981. *The Magnetotelluric Sounding Method*, Elsevier Scientific Puplishing Company.

Khazaradze, G. & Klotz, J., 2003. Short- and long-term effects of GPS measured crustal deformation rates along the south central Andes, *J. Geophys. Res.*, **108**(6), 5–1 – 5–15.

Lilley, F. E. M. & Bennett, D. J., 1972. An array experiment with magnetic variatiometers near the coast of south-east Australia, *Geophys. J. R. astr. Soc.*, **29**, 49–64.

Maercklin, N., Haberland, C., Ryberg, T., Weber, M., Bartov, Y., & DESERT Group, 2004. Imaging the DEAD SEA Transform with scattered seismic waves, *Geophys. J. Int.*, **0**, 0–0.

Mitra, G. & Ismat, Z., 2001. Microfracturing associated with reactivated fault zones and shear zones: what can it tell us about deformation history?, in *The Nature and Tectonic Significance of Fault Zone Weakening*, edited by R. E. Holdsworth, R. A. Strachan, J. F. Magloughlin, & R. J. Knipe, vol. 186, pp. 113–140, Geol. Soc. London Spec. Publ.

Molnar, P., Anderson, H. J., Audoine, E., Eberhart-Philips, D., Gledhill, K. R., Klosko, E. R., McEvilly, T. V., Okaya, D., Savage, M. K., Stern, T., & Wu, F. T., 1999. Continuous Deformation versus faulting through the continental lithosphere of New Zealand, *Science*, **286**, 516–519.

Nabighian, M. N., 1987. *Electromagnetic methods in applied Geophysics*, vol. 1 and 2, Society of Exploration Geophysicists.

Ozawa, S., Miyazaki, S., Hatanaka, Y., Imakiire, T., Kaidzu, M., & Murakami, M., 2003. Characteristics silent earthquakes in the eastern part of the Boso peninsula, Central Japan, *Geophys. Res. Lett.*, **30**(6), 16–1 – 16–4.

Pajunpää, K., 1984. Magnetometer array studies in Finland – determination of single station transfer functions, *J. Geophys.*, **55**, 153–160.

Pajunpää, K., Lahti, I., Olafsdottir, B., Korja, T., & BEAR working group, 2002. Crustal conductivity anomalies in central Sweden and southwestern Finland, *Geophys. J. Int.*, **150**, 695–705.

Parker, R. L. & Booker, J. R., 1996. Optimal one-dimensional inversion and bounding of magnetotelluric apparent resistivity and phase measurements, *Phys. Earth Planet. Int.*, **98**(3-4), 269–282.

Parkinson, W., 1962. The influence of continents and oceans on geomagnetic variations, *Geophys. J.*, **2**, 441–449.

Parsons, T. & Hart, P. E., 1999. Dipping San Andreas and Hayward faults revealed beneath San Francisco Bay, California, *Geology*, **27**(9), 839–842.

Reitzel, J. S., Gough, D. I., & Anderson, H. P. C. W., 1970. Geomagnetic deep sounding and upper mantle structure in the western United States, *Geophys. J. R. astr. Soc.*, **19**, 213–235.

Ritter, E., 1975. Results of geoelectromagnetic deep soundings in Europe, *Gerlands Beitr. Geophysik Leipzig*, **84**, 261–273.

Ritter, O., 1995. *An audiomagnetotelluric investigation of the Southern Upland Fault: novel instrumentation, field procedures and 3D modelling*, Ph.D. thesis, Univ. of Edinburgh.

Ritter, O., Hoffmann-Rothe, A., Müller, A., Dwipa, S., Arsadi, E. M., Mahfi, A., Nurnusanto, I., Byrdina, S., Echternach, F., & Haak, V., 1998. A magnetotelluric profile across Central Java, Indonesia, *Geophys. Res. Lett.*, **25**(23), 4265–4268.

Ritter, O., Junge, A., & Dawes, G., 1998. New equipment and processing for magnetotelluric remote reference observations, *Geophys. J. Int.*, **132**, 535–548.

Ritter, O., Haak, V., Rath, V., Stein, E., & Stiller, M., 1999. Very high electrical conductivity beneath the Münchberg Gneiss area in southern Germany: Implications for horizontal transport along shear planes, *Geophys. J. Int.*, **139:2**, 161–170.

Ritter, O., Ryberg, T., Weckmann, U., Hoffmann-Rothe, A., Abueladas, A., Garfunkel, Z., & DESERT Research group, 2003. Geophysical images of the Dead Sea Transform in Jordan reveal an impermeable barrier for fluid flow, *Geophys. Res. Lett.*, **30**(14), 1741, doi:10.1029/2003GL017541.

Ritter, O., Weckmann, U., Vietor, T., & Haak, V., 2003. A magnetotelluric study of the Damara Belt in Namibia 1. Regional scale conductivity anomalies, *Phys. Earth Planet. Int.*, **138**, 71–90, doi:10.1016/S0031–9201(03)00078–5.

Ritter, O., Hoffmann-Rothe, A., Bedrosian, P. A., Weckmann, U., & Haak, V., 2004. Electrical conductivity images of active and fossil fault zones, in *Microstructural Evolution and Physical Properties in High-Strain Zones*, pp. 000–000, Geol. Soc. London Spec. Publ. (accepted for publication).

Rümpker, G., Ryberg, T., Bock, G., & DESERT Seismology Group, 2003. Boundary-layer mantle flow under the Dead Sea transform fault inferred from seismic anisotropy, *Nature*, **425**, 497 – 501.

Schmucker, U., 1970. *Anomalies of Geomagnetic Variations in the Southwestern United States*, Univ. of California Press, Berkeley.

Schmucker, U., 1971. Neue Rechenmethoden zur Tiefensondierung, *Protokoll Kolloquium Elektromagnetische Tiefensondierung, 14.-16. Sept. 1971 Rothenberge/Westf.*.

Scholz, C. H., 1987. Wear and gouge formation in brittle faulting, *Geology*, **15**, 493–495.

Scholz, C. H., Dawers, N. H., Yu, J.-Z., Anders, M. H., & Cowie, P. A., 1993. Fault growth and fault scaling laws: preliminary results, *J. Geophys. Res.*, **98**(B12), 21951–21961.

Schulz, S. E. & Evans, J. P., 2000. Mesoscopic structure of the Punchbowl fault, southern California and the geologic and geophysical structure of active strike-slip faults, *Journal of Structural Geology*, **22**, 913–930.

Schwalenberg, K., Rath, V., & Haak, V., 2002. Sensitivity studies applied to a two-dimensional resistivity model from the Central Andes, *Geophys. J. Int.*, **150**(3).

Sibson, R. H., 1983. Continental fault structure and the shallow earthquake source, *Journal of the Geological Society*, **140**, 741–767.

Stanica, M., Stanica, D., & Marin-Furnica, C., 1999. The placement of the Trans-European Suture Zone on the Romanian territory by electromagnetic arguments, *Earth, Planets and Space*, **51**, 1073–1078.

Tauber, S., Banks, R., Ritter, O., & Weckmann, U., 2003. A high-resolution magnetotelluric survey of the Iapetus Suture Zone in southwest Scotland, *Geophys. J. Int.*, **153**, 548–568.

Tikhonov, A. N., 1950. Determination of the electrical characteristics of the deep strata of the earth's crust, *Dokl. Akad. Nauk SSSR*, **73(2)**, 295pp.

Unsworth, M. & Bedrosian, P. A., 2004. Electrical resistivity at the SAFOD site from magnetotelluric measurements, *Geophys. Res. Lett.*, **accepted**.

Unsworth, M. J., Malin, P. E., Egbert, G. D., & Booker, J. R., 1997. Internal structure of the San Andreas fault at Parkfield, California, *Geology*, **25**(4), 359–362.

Unsworth, M. J., Egbert, G., & Booker, J., 1999. High-resolution electromagnetic imaging of the San Andreas fault in Central California, *J. Geophys. Res.*, **105**(B1), 1131–1150.

Unsworth, M. J., Bedrosian, P., Eisel, M., Egbert, G., & Siripunvaraporn, W., 2000. Along strike variations in the electrical structure of the San Andreas Fault at Parkfield, California, *Geophys. Res. Lett.*, **27**(18), 3021–3024.

Weaver, J., 1994. *Mathematical Methods for Geo-electromagnetic Induction*, Research Studies Press LTD.

Weckmann, U., Ritter, O., & Haak, V., 2003. A Magnetotelluric study of the Damara Belt in Namibia 2. MT phases over 90° reveal the internal structure of the Waterberg Fault / Omaruru Lineament, *Phys. Earth Planet. Int.*, **138**, 91–112, doi:10.1016/S0031–9201(03)00079–7.

Weckmann, U., Ritter, O., & Haak, V., 2003. Images of the magnetotelluric apparent resistivity tensor, *Geophys. J. Int.*, **155**, 456–468.

Weidelt, P., 1975. Electromagnetic induction in Three-Dimensional Structures, *Journal of Geology*, **41**, 85–109.

Wiese, H., 1962. Geomagnetische Tiefentellurik Teil II: die Streichrichtung der Untergrundstrukturen des elektrischen Widerstandes, erschlossen aus geomagnetischen Variationen, *Geofisica pura e applicata*, **52**, 83–103.

Glossar

Archie-Gleichung	von Archie (1942) aufgestellte empirische Beziehung, die den spezifischen elektrischen Widerstand mit dem Formationswasser eines Gesteins verbindet.
AF	Arava Fault (Jordanien)
AQF	Al-Quwayra Fault (Jordanien)
AuF	Autseib Fault (Namibia)
CJF	Central Java Fault (Indonesien)
DST	Dead Sea Transform (Naher Osten)
Epizentrum	Punkt auf der Erdoberfläche, der sich direkt oberhalb des Hypozentrums befindet
Forearc	Rand der Oberplatte zwischen der Plattengrenze in der Tiefseerinne und der vulkanischen Front
Formationswasser	in Gesteinsporen enthaltenes Wasser (oder allgemein für Fluide)
FZC	(Fault Zone Conductor) Sub-vertikale Zone erhöhter elektrischer Leitfähigkeit im Bereich einer Störung
ISZ	Iapetus Suturzone (Südschottland / Nordengland)
GIPP	Geophysical Instrument Pool Potsdam
Hypozentrum	Lage des als punktförmig angenommenen Erdbebenherdes innerhalb des Erdkörpers
KTB	Kontinentale Tiefbohrung (Windischeschenbach, Bayern)
Lithosphäre	die äußere, etwa 100-200 km mächtige Schale der Erde
MT	Magnetotellurik
lokalisiert	räumlich konzentriert
WaF/OL	Waterberg Fault / Omaruru Lineament (Namibia)
MüMa	Münchberger Gneismasse (Oberpfalz, Bayern)
PS	Präkordilleren Störungssystem (Chile)
robuste Statistik	statistisches Verfahren, das den Einfluss von Ausreißern bei der Bestimmung von Schätzwerten minimiert
SAF	San Andreas Fault (Kalifornien)
S.P.A.M. MkIII	Magnetotellurik Apparatur: Short Period Automatic Magnetotelluric (Mark III)
Variszikum	(Variszіden) östlicher Teil eines europäisch-nordamerikanischen Gebirgsgürtels des jüngeren Paläozoikums
WF	West Fault (Chile)

Auflistung der in Verbindung mit der Habilitationsschrift publizierten Forschungsergebnisse

1. **Ritter, O.**, Haak, V., Rath, V., Stein, E., & Stiller, M., 1999. Very high electrical conductivity beneath the Münchberg Gneiss area in southern Germany: Implications for horizontal transport along shear planes, *Geophys. J. Int.*, **139:2**, 161–170.
2. **Ritter, O.**, Hoffmann-Rothe, A., Müller, A., Dwipa, S., Arsadi, E. M., Mahfi, A., Nurnusanto, I., Byrdina, S., Echternach, F., & Haak, V., 1998. A magnetotelluric profile across Central Java, Indonesia, *Geophys. Res. Lett.*, **25**(23), 4265–4268.
3. Hoffmann-Rothe, A., **Ritter, O.**, & Haak, V., 2001. Magnetotelluric and geomagnetic modelling reveals zones of very high electrical conductivity in the upper crust of Central Java, *Phys. Earth Planet. Int.*, **124**, 131–151.
4. Tauber, S., Banks, R., **Ritter, O.**, & Weckmann, U., 2003. A high-resolution magnetotelluric survey of the Iapetus Suture Zone in southwest Scotland, *Geophys. J. Int.*, **153**, 548–568.
5. **Ritter, O.**, Weckmann, U., Vietor, T., & Haak, V., 2003. A magnetotelluric study of the Damara Belt in Namibia 1. Regional scale conductivity anomalies, *Phys. Earth Planet. Int.*, **138**, 71–90, doi:10.1016/S0031–9201(03)00078–5.
6. Weckmann, U., **Ritter, O.**, & Haak, V., 2003. A Magnetotelluric study of the Damara Belt in Namibia 2. MT phases over 90° reveal the internal structure of the Waterberg Fault / Omaruru Lineament, *Phys. Earth Planet. Int.*, **138**, 91–112, doi:10.1016/S0031–9201(03)00079–7.
7. Hoffmann-Rothe, A., **Ritter, O.**, & Janssen, C., 2004. Correlation of Electrical Conductivity and Structural Damage at a Major Strike-Slip Fault in Northern Chile, *J. Geophys. Res.*, **109**, B010101, doi:10.1029/2004/B003030.
8. **Ritter, O.**, Ryberg, T., Weckmann, U., Hoffmann-Rothe, A., Abueladas, A., Garfunkel, Z., & DESERT Research group, 2003. Geophysical images of the Dead Sea Transform in Jordan reveal an impermeable barrier for fluid flow, *Geophys. Res. Lett.*, **30**(14), 1741, doi:10.1029/2003GL017541.
9. **Ritter, O.**, Hoffmann-Rothe, A., Bedrosian, P. A., Weckmann, U., & Haak, V., 2004. Electrical conductivity images of active and fossil fault zones, in *Bruhn, D. & Burlini, L. (eds), High-Strain Zones: Structure and Physical Properties, Geol. Soc. London Spec. Publ.*, **245**, 165–185.
10. **Ritter, O.**, Junge, A., & Dawes, G., 1998. New equipment and processing for magnetotelluric remote reference observations, *Geophys. J. Int.*, **132**, 535–548.
11. Weckmann, U., **Ritter, O.**, & Haak, V., 2003. Images of the magnetotelluric apparent resistivity tensor, *Geophys. J. Int.*, **155**, 456–468.

Geophys. J. Int. (1999) **139,** 161–170

Very high electrical conductivity beneath the Münchberg Gneiss area in Southern Germany: implications for horizontal transport along shear planes

Oliver Ritter,[1] Volker Haak,[1] Volker Rath,[2] Eckardt Stein[3] and Manfred Stiller[1]

[1] *GeoForschungsZentrum, Telegrafenberg,* D-14473 *Potsdam, Germany. E-mail:oritter@gfz-potsdam.de.*
[2] *Technische Universität Berlin, Institut für Angewandte Geophysik, Petrologie und Lagerstättenkunde, Ackerstrasse* 71–76, D-13355 *Berlin, Germany*
[3] *Institut für Mineralogie, Technische Universität Darmstadt, Schnittspahnstrasse* 9, D-64287 *Darmstadt, Germany*

Accepted 1999 May 28. Received 1999 May 28; in original form 1998 August 13

SUMMARY

New magnetotelluric data from the Münchberg Gneiss complex in Southern Germany reveal a zone of extremely high electrical conductivity. 1-D modelling of the data is justified in the period range 0.01 to 10 s. At least three layers are required to explain the steepness of the apparent resistivity curves, and the best-fitting models comprise four layers with successively higher conductivities. The layers of highest conductivity at depths between 2.2 and 3.6 km correlate with pronounced bands of high seismic reflectivity (profile DEKORP 85-4N). The Münchberg complex is today widely recognized as a tectonic klippe, consisting of rocks whose metamorphic and stratigraphic order is inverted rather than overturned. The material was transported into its present position by predominantly horizontal tectonic forces along shear zones. We interpret the high conductivity and high reflectivity as remnants of this transport process.

Key words: DEKORP85-4N, electrical conductivity, magnetotellurics, Münchberg Gneiss complex, shear zones, Variscan orogeny.

INTRODUCTION

Crystalline nappes play an important role in the reconstruction of fossil tectonic processes of the basement. Nappes are characterized as allochthonous rock assemblages that have been transported laterally by tectonic processes. The distance over which the rocks are transported can reach hundreds of kilometres. The Münchberg Massif (MüMa) in Southern Germany is such a nappe; it consists of an assemblage of gneissic rocks, which were transported to their present location in NE Bavaria during the Variscan orogeny (Franke 1980). The tectonic interpretation of this gneiss complex, however, has been disputed among geologists for more than 100 years, and there have been problems in deciding how and which geophysical methods should be deployed to support the interpretations.

Renewed interest in the area arose within the framework of recent research of the Mid-European Variscan Belt (e.g. DEKORP & Orogenic Processes Research Groups 1998; Schäfer 1997; Franke *et al.* 1995; Behr & DEKORP Research Group (B) 1994; Weber & Behr 1983). In order to understand the regional geology, it is essential to decide how the MüMa deep crustal, high grade rocks (the highest grade metamorphic facies comprise eclogite, which is created under *PT* conditions of the Earth's mantle) arrived at their present position.

The interpretation of the MüMa formations also played a major role in the choice of the final location for the German deep drilling project KTB, which is located 80 km further southeast. In this context, and also as part of the German DEKORP programme, the MüMa was investigated with reflection seismics and numerous other geophysical methods. In 1981, audiomagnetotelluric (AMT) measurements were carried out at 20 locations across the MüMa (Haak *et al.* 1985). At that time, AMT instruments that could record data at high frequencies (1000–1 Hz) were just becoming technically feasible; however, a wide variety of electromagnetic noise sources, combined with high surface resistivities, prevented an accurate assessment of the data quality. Although the noise problem has worsened over the last 15 years, there have been considerable improvements in geophysical instrumentation and data processing tools (Egbert & Booker 1986; Larsen *et al.* 1996; Egbert 1997; Ritter *et al.* 1998). These developments provided the impetus to re-investigate the MüMa with modern equipment.

A large number of electrical conductivity anomalies have been detected in the Earth's crust around the world. There is no clear consensus as to the causes and origins of these anomalies, particularly in crystalline regimes. However, in the light of the 9.1 km deep KTB drill hole, we now have evidence that high electrical conductivity can be linked with shearing processes. At the KTB site, zones of high electrical conductivity

have been found to be connected with fractured sections of the crust, while the 'wet' but intact crust is very resistive (ELEKTB 1997).

GEOLOGICAL BACKGROUND

The Münchberg Massif represents an exotic klippe as part of a former widespread, continuous nappe complex which has been preserved from erosion by its protected position in the Vogtland syncline. It consists of four low to high grade metamorphic thrust sheets, overlying an allochthoneous, weakly metamorphosed metasedimentary unit which itself can be separated into three thrust sheets. The tectonometamorphic units from top to bottom are (see Fig. 1): Hangend series, Liegend series, Randamphibolite series and Phyllit-Prasinit series.

The Hangend series shows a variegated lithology, comprising hornblende gneisses, amphibolites and paragneisses with interlayers of calcsilicate rocks and marbles. At the base, bodies of serpentinite, eclogite and eclogite-amphibolite with diameters from tens of metres to several kilometres are abundant. The metamorphic peak conditions are displayed by the eclogites, with $P_{max} > 2.5$ GPa and $T_{max} \sim 650\,^{\circ}$C, whereas the metamorphic imprint of gneisses of the Hangend series show only amphibolite facies conditions, with pressures of about 1.2 GPa and related temperatures of $\sim 650 \pm 30\,^{\circ}$C (O'Brien 1996). The age of the high-pressure metamorphism is still under discussion,

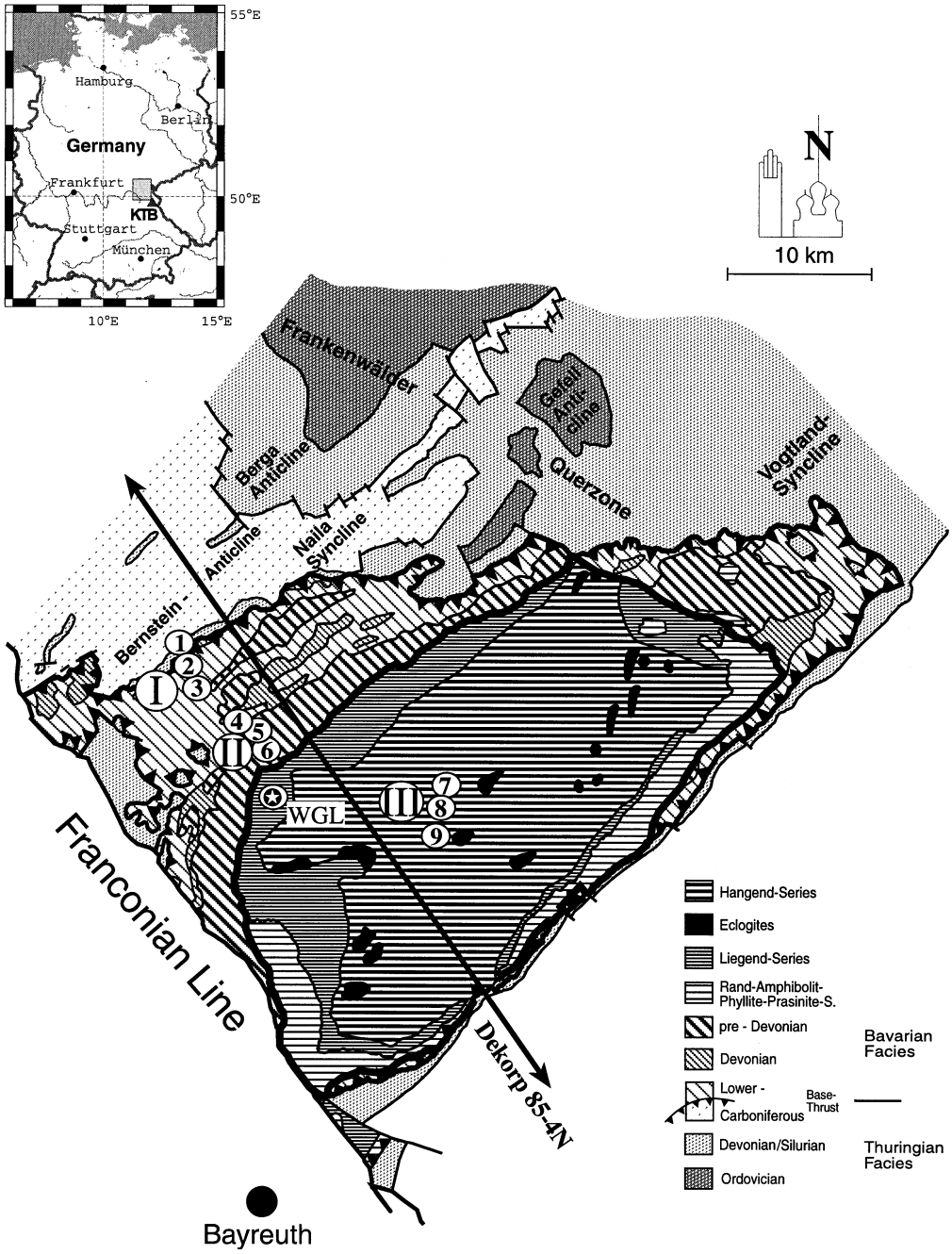

Figure 1. Location map of the MT sites and simplified geological map of the Münchberg Massif. Each station array (labelled I–III) consists of three AMT sites (labelled 1–9). Site WGL was measured in a previous survey (see text).

but the latest published data (Sm/Nd, whole rock–pyroxene–garnet core) from Stosch & Lugmair (1990) show an isochrone age of 395 ± 4 Ma.

Compared with the Hangend series, the Liegend series shows a monotonous lithology, consisting of paragneisses, which are intercalated with an orthogneiss sheet and a few lenses of metagabbros. The peak-metamorphic conditions, of $P \sim 1.2$ GPa and $T \sim 650\,^{\circ}$C determined at a metagabbro, are similar to the amphibolite facies conditions of the Hangend series; no evidence for high-pressure metamorphism has been identified in these rocks so far (O'Brien 1996). According to Müller-Sohnius *et al.* (1987), both units were spatially separated until about 385 Ma, with a common subsequent cooling history starting at about 380 Ma (K/Ar, Ar/Ar: hornblende and muscovite).

The Randamphibolite series is built up solely by amphibolites, which may be massive, banded or schistose. Their mineral assemblages point to lower amphibolite facies metamorphic conditions. A characteristic feature is the intense mylonitization at the tectonic contacts to the over-and underlying units.

The Prasinit-Phyllite series consists of an alternation of basic to intermediate lavas and pyroclastics with silty shales which are metamorphosed under greenschist facies conditions and which is overprinted by brittle deformation at the contact to the underlying nappe. Microfossils in the phyllites indicate a Proterozoic protolith age (Pflug & Reitz 1987).

Mineral lineations and mineral-stretching lineations in mylonites and ductile shear zones as well as other kinematic markers indicate an accretion of the metamorphic nappes in an east–west direction with transport towards the west.

The underlying, unmetamorphosed to anchimetamorphic tectonic units from top to bottom are the Randschiefer series, with a lithology similar to the Prasinit-Phyllite series but Ordovician in age (fossil dated), Silurian and Devonian cherts, and lower Carboniferous flysch sediments. All these allochthoneous metasedimentary thrust sheets belong to the Bavarian facies, which is overthrusted onto the autochthoneous sediments of the Thuringian facies at the basal thrust, and each of these units is separated from the others by tectonic contacts.

Brittle deformations with NW–SE-orientated slickensides on the thrust planes, including the basal thrust, clearly point to a NW–SE-directed accretion of the metasedimentary thrust sheets with a final, NW-directed emplacement of the entire nappe unit in a superficial, shallow environment.

Summarizing the geological constraints, the Münchberg nappe pile consists of two tectonic thrust sheet units:

(1) A metamorphic one, which clearly shows a medium- to high-pressure metamorphic imprint with an inverse zonation of the baric isograde and an accretion and transport toward the west.

(2) A (meta-)sedimentary thrust sheet complex, with an inverse, but not overturned, stratigraphic sequence typical for thrust sheets, with an accretion and final emplacement toward the northwest.

MAGNETOTELLURIC AND SEISMIC DATA

Both the GeoForschungsZentrum Potsdam and the Technische Universität Berlin use a new generation of instruments called SPAM (short-period automatic magnetotellurics) MkIII, developed at the University of Edinburgh (Dawes 1990). SPAM MkIII operates as a networked instrument in such a way that compatible parts of the system can be interconnected in many different ways. The information from neighbouring sites can be used in data processing schemes to reduce the influence of noise. For the data analysis we applied a method which uses the coherency and expected uniformity of the magnetic source field as quality criteria (Ritter *et al.* 1998). Data are rejected (i) if the horizontal magnetic field components at two given sites have a low coherence (coherency criterion) or (ii) if the response functions are considerably different from unity (target criterion). Time segments with inconsistent horizontal magnetic field data are thereby removed, leaving a reduced but cleaned data set for the estimation of robust, remote referenced, magnetotelluric response functions.

Overall, we recorded at three station arrays, each consisting of three sites. The station arrays are labelled I to III in Fig. 1; the approximate distances between arrays I and II, and II and III are 4 and 8 km, respectively. Array III was located at the centre of the gneiss complex, near the town of Münchberg, while arrays I and II were installed close to the boundary to the Carboniferous sediments of the Bavarian facies. The site locations are summarized in Table 1.

Fig. 2 shows the results from sites I/3, II/6 and III/9 as apparent resistivity and phase curves, calculated from orthogonal components of the electric and magnetic fields in a geographical coordinate system. In this convention, the *XY*-polarization curves in Fig. 2 correspond to an electric field measured in a NS direction, and the *YX*-polarization to an electric field measured in an EW direction. The data of site II/6 are extended with long-period results (100–10 000 s) from site WGL (see Fig. 1), which were recorded in 1992 by the Free University of Berlin (Gürtler & Schuarz 1994; Börner 1995). It is worth mentioning that the data from the two sites coincide and overlap, in spite of the fact that sensors, loggers, processing and personnel were all different. All apparent resistivity and phase curves show very similar patterns. The apparent resistivity curves decrease over more than three decades at an angle of almost 45°, while the phases are consistently above 45°, reaching values of up to 85°. Diverging apparent resistivity and phase curves for the long-period data of site WGL in Fig. 2 indicate more complicated structures as the induction range widens. Induction arrows, as indicators for lateral conductivity variations, are relatively small (<0.25) in the relevant period range between 0.01 and 10 s. However, the reversed orientation of the real induction arrows, as plotted at a frequency of 5.7 Hz in Fig. 3, hint at a zone of higher conductivity between station arrays I and III.

Table 1. Locations of the magnetotelluric sites, as plotted in Fig. 1.

Site No	Gauß-Krüger Easting	Northing	Geographic Longitude	Latitude
I/1	4466.5500	5570.6250	E11°31′31.06″	N50°16′18.24″
I/2	4466.7750	5570.1750	E11°31′43,76″	N50°16′03.65″
I/3	4467.2150	5569.4500	E11°32′06.47″	N50°15′39.73″
II/4	4470.1375	5566.7125	E11°34′56.47″	N50°14′12.16″
II/5	4470.6625	5566.2875	E11°35′27.53″	N50°14′02.03″
II/6	4470.7500	5565.9375	E11°35′31.76″	N50°13′47.03″
III/7	4481.4125	5561.5000	E11°44′22.86″	N50°11′28.39″
III/8	4481.4250	5560.9250	E11°44′23.49″	N50°11′06.08″
III/9	4481.1000	5560.1875	E11°44′07.62″	N50°10′43.38″

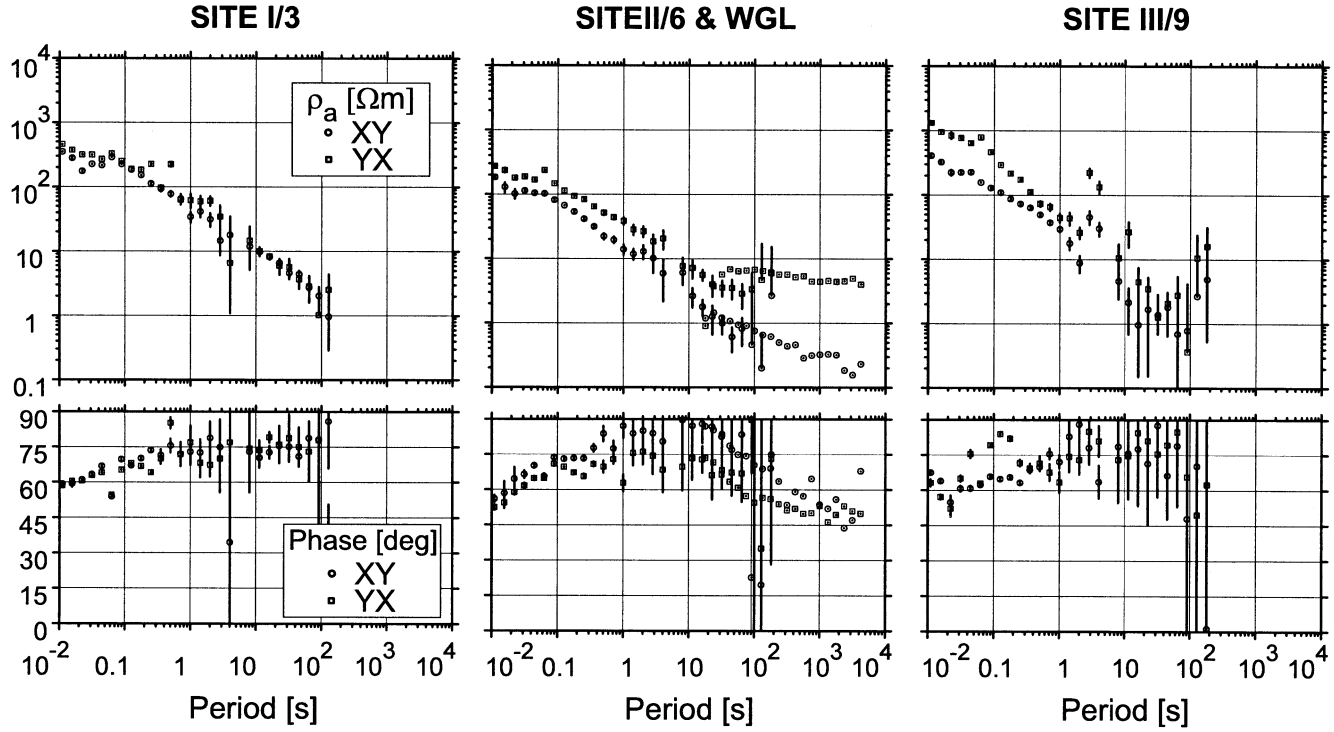

Figure 2. *XY*- (circles) and *YX*- (squares) polarizations of the apparent resistivity (ρ_a) and phase (Φ) curves. Each station array is represented by one site. Site II/6 is extended with long-period data from site WGL. Steeply decreasing ρ_a curves indicate a high electrical conductivity anomaly at depth.

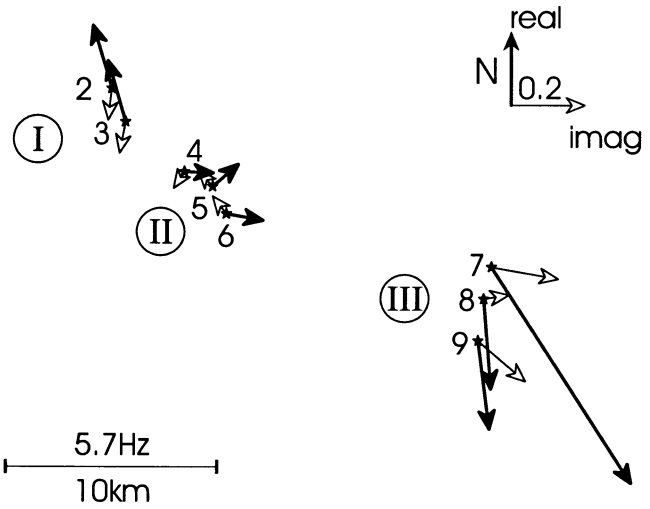

Figure 3. Real and imaginary induction arrows plotted at a frequency of 5.7 Hz. In Wiese convention the arrows tend to point away from the conductive side of a nearby conductivity contrast. See Fig. 1 for comparison with surface geology.

Fig. 4(a) shows the result of a 2-D Occam inversion (DeGroot-Hedlin & Constable 1990). The model responses and measured data from seven sites–sites I/1 and III/7 could not be used—are given in Fig. 4(b). For the inversion, the impedance tensor and vertical magnetic field transfer function data are rotated by $-60°$, as the sites align along a profile striking S60°E (compare with Fig. 1). Because of the irregular site distribution and large error bars in some frequency bands, this data set is not really suitable for a 2-D inversion. While the model should therefore not be over-interpreted, it is useful to discuss some of the main features of the data in Fig. 4(a): (1) the upper crust is resistive (100–1000 Ω m) beneath station arrays I, II and III; (2) the entire lower crust becomes very conductive (≤ 1 Ω m) from depths of between 2.5 and 3.5 km; and (3) between station arrays II and III a conductive zone reaches the surface. This zone is probably most clearly expressed in the data by the reversed vertical magnetic field response functions between arrays II and III. The model responses shown in Fig. 4(b) are the results of an inversion which seeks to fit all data—the vertical magnetic field responses, TE, and TM mode—without static shift correction. The initial model for each inversion was a 100 Ω m homogeneous half-space.

The unconstrained 2-D Occam inversion generates a model showing resistivities of 1 Ω m for the entire lower crust and upper mantle (to a depth of 300 km!), which is not geologically plausible. A comparison of Figs 2 and 4(b) shows that the apparent resistivity and phase curves are similar at all sites, for both the rotated and unrotated data sets. The fact that the *XY*- and *YX*-polarizations of apparent resistivity and phase curves are approximately parallel at all sites also indicates a predominantly 1-D character of the subsurface. This observation is supported further by qualitative measures, such as small skew values and undetermined rotation angles for both conventional tensor analysis (Swift criterion) and tensor decomposition methods (Bahr 1988; Groom & Bailey 1989). To discuss alternative conductivity models we resort therefore to 1-D modelling procedures.

A wide variety of tools for forward and inversion calculations is available for 1-D modelling of magnetotelluric data. However, each has its own philosophy for deciding how much structure (i.e. number of layers and their thickness) is necessary

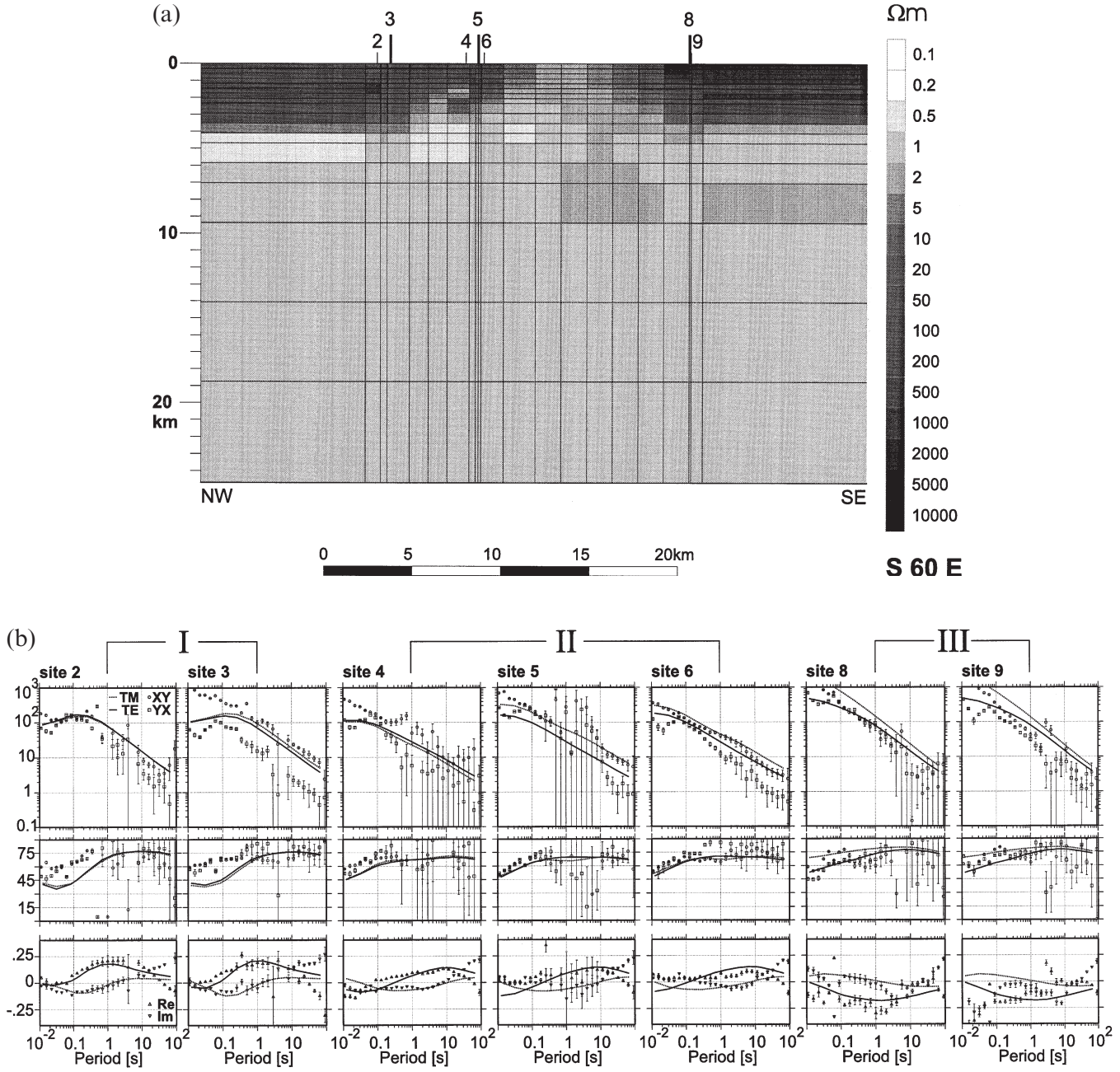

Figure 4. (a) Result of a 2-D Occam inversion of seven sites: the regularization grid is 74 × 31 nodes. Dark shaded areas indicate resistive blocks; light greys indicate conductive cells. The model shows resistivities of 1 Ω m for the entire lower crust and upper mantle. (b) Comparison of model responses (lines) with field data (symbols). The field data are rotated by −60°. The panels show apparent resistivity at the top, phase in the middle, and vertical magnetic field response functions at the bottom.

to understand the subsurface reality or sufficient to explain a certain data set. Most of our model calculations in this paper are based on a standard Marquardt–Levenberg least-squares fitting method which is part of the GEOTOOLS data interpretation package (Geotools 1997). To fit the data we calculate apparent resistivity and phase curves from rotationally invariant, averaged impedances: $Z_{\mathrm{avg}} = (Z_{xy} - Z_{yx})/2$.

Fig. 5 demonstrates that a simple two-layer model of a resistor over a conducting half-space is not suitable to fit the data. The diagram shows 1-D responses of five different two-layer models. The top layer has a fixed resistivity of 256 Ω m, while the resistivities of the second, more conductive layer vary between 128 and 0.25 Ω m. On the right-hand side of Fig. 5 the model responses are plotted together with the averaged apparent resistivity and phase curves of site II/6. Model 3, with a resistivity ratio of 1 : 32, can partially explain the data but a more conductive second layer worsens the fit. While a model with at least three layers is required to represent the data, we observe consistently smaller misfits with four-layer models. Fig. 6 compares four-layer 1-D inversion responses with the measured data of sites I/3, II/6 and III/9; the modelling results are shown in Fig. 8 and Table 2. Obviously, the models suggest continuously increasing conductivity with depth at all sites.

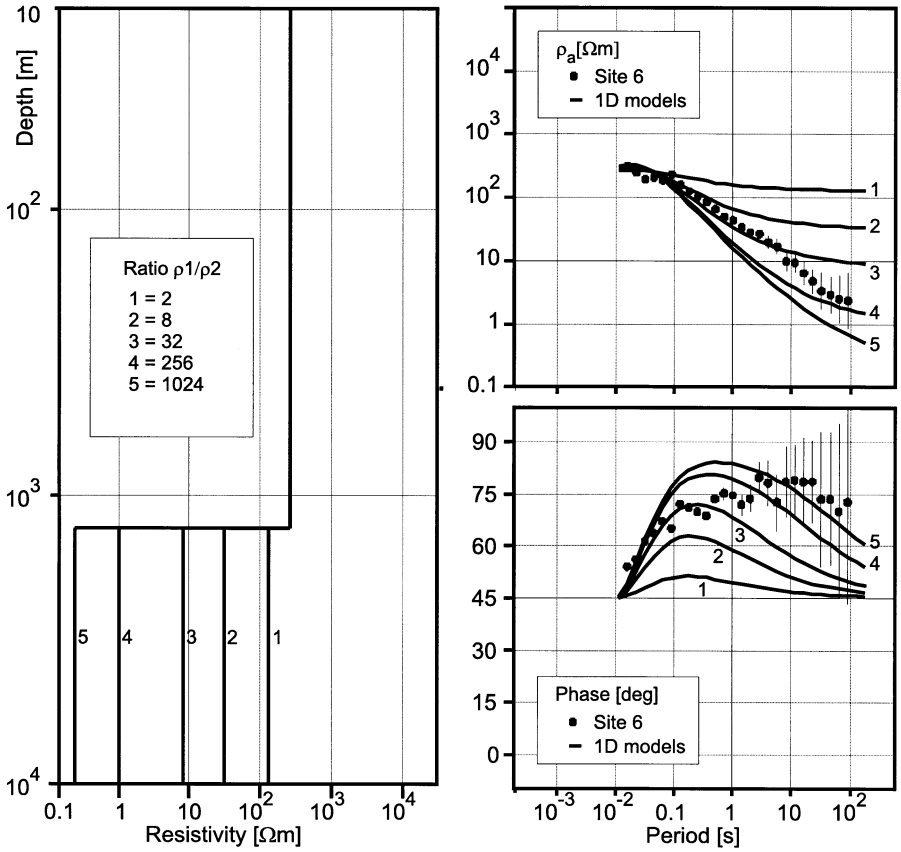

Figure 5. The slope of the steeply decreasing apparent resistivity curves cannot be explained by simple two-layer models composed of a resistive top over a conductive half-space. At least three layers are required to fit the data.

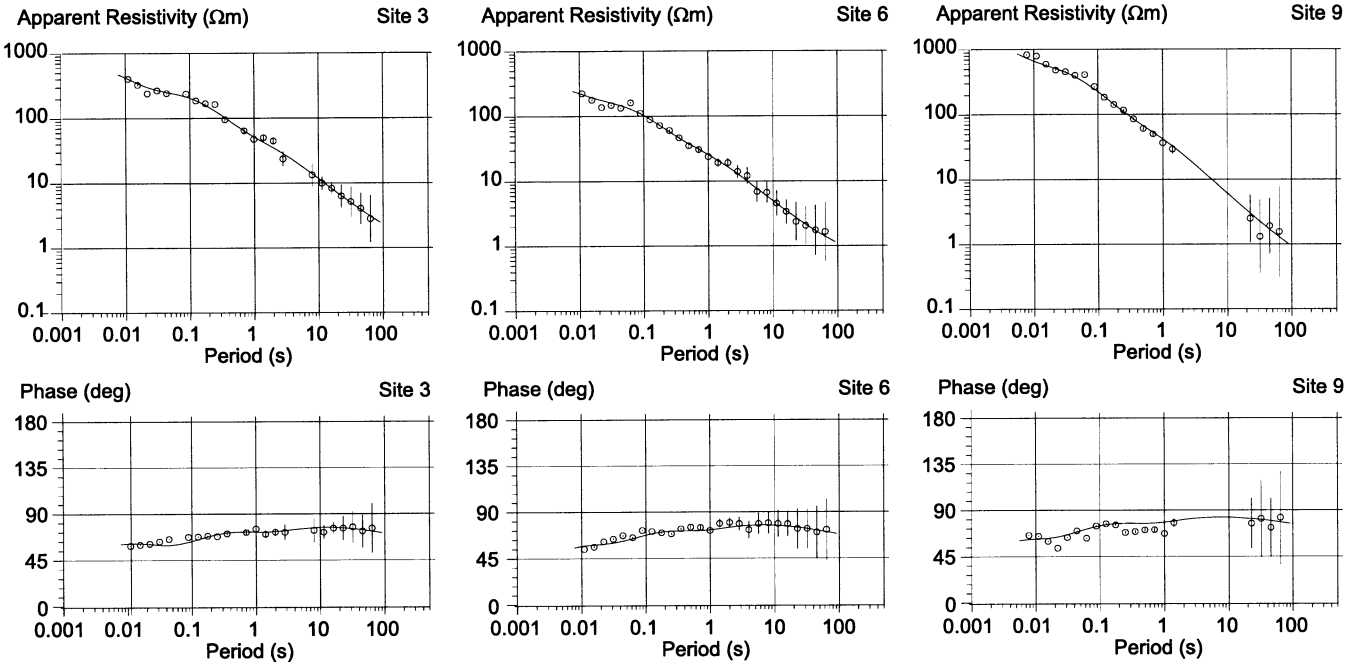

Figure 6. Rotationally invariant, averaged apparent resistivity and phase curves (circles), together with the responses of the best-fitting four-layer 1-D models (solid line). The conductivity models are plotted in combination with the seismic reflection data in Fig. 8.

Table 2. Summary of four-layer 1-D Marquardt–Levenberg inversion results. Depth values specify the distances to the top of the layers.

Site I/3 Resistivity [Ω m]	Depth [m]	Site II/6 Resistivity [Ω m]	Depth [m]	Site III/9 Resistivity [Ω m]	Depth [m]
634	0	261	0	1017	0
97	590	50	514	118	759
4.8	2043	3.7	1245	2.8	1701
0.26	3751	0.27	2215	0.16	2458
rms ($\ln \rho_a$)	rms (Φ)	rms ($\ln \rho_a$)	rms (Φ)	rms ($\ln \rho_a$)	rms (Φ)
4.59	9.52	2.88	3.33	6.57	17.58

In Fig. 7 we examine a variety of inversion strategies in an attempt to fit the data of site II/6. All models are constrained to include a resistive bottom layer of 1000 Ω m whose depth is a free parameter. From geological considerations it is reasonable to include such a layer because we expect a resistive basement beneath the Münchberg nappes. Judging from the MT data alone, its inclusion is less certain as the phases stay above 45° even at the longest periods of site WGL. While a resistive bottom layer may not be required to fit the data, it does not cause a contradiction, makes comparison of the different models easier, and provides some idea about the total conductance. Fig. 7(a) shows four different 1-D models. Model 1 comprises four layers with continuously increasing conductivity (plus the bottom layer of 1000 Ω m). Only the number of layers is determined *a priori* for the inversion, while resistivities and depths are free parameters. Model 2 is similar to Model 1, but with an additional thin layer of fixed thickness (250 m) and resistivity (0.01 Ω m). Model 3 is similar to Model 2, but comprises a stack of alternating thin conductive and resistive layers. Again, thicknesses (250 m) and resistivities (0.1 and 1000 Ω m, respectively) are fixed parameters. Model 4 is the result of a 1-D OCCAM inversion. Residuals of resistivity and phase over period and rms misfits are given in Fig. 7(b) for each model. The diagrams show that the rms misfits are mainly controlled by a few scattered data points with small error bars in the period range between 0.01 and 0.1 Hz (see Fig. 2 for the error bars). The residuals are calculated from the formulas

$$\mathrm{resid}(\ln \rho) = [\ln(\rho_{\mathrm{avg}}) - \ln(\rho_{\mathrm{mod}})]/\Delta\ln(\rho_{\mathrm{avg}}),$$

$$\mathrm{resid}(\Phi) = (\Phi_{\mathrm{avg}} - \Phi_{\mathrm{mod}})/\Delta\Phi_{\mathrm{avg}}.$$

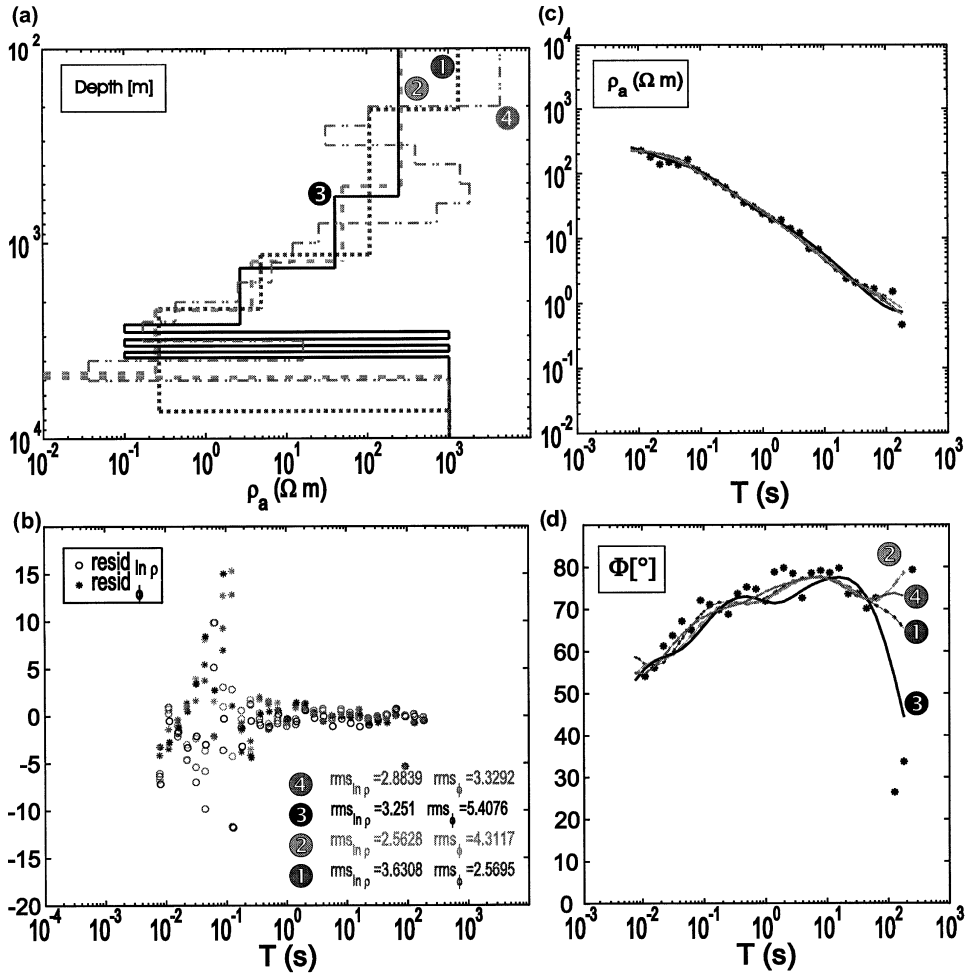

Figure 7. Comparison of various strategies to invert the averaged apparent resistivity and phase data of site II/6 (see text). (a) shows the models, (b) gives residuals (resid) and rms misfits, and (c) and (d) give model responses together with the field data. Obviously, only the general trend of continuously decreasing resistivities is common to models 1–3, while the geometry of the deepest conducting layer cannot be resolved. The bottom layer of model 1 indicates a total conductance of 19 000 S.

ρ_{avg}, $\Delta\rho_{avg}$ and Φ_{avg}, $\Delta\Phi_{avg}$ are the apparent resistivity and phase values, calculated from averaged impedances, and their respective absolute errors. ρ_{mod} and Φ_{mod} are 1-D modelling results. The rms misfits for n estimates of ρ_{avg} and Φ_{avg} are

$$\mathrm{rms}(\ln \rho) = [\Sigma_n \,\mathrm{resid}(\ln \rho)^2/n]^{1/2},$$

$$\mathrm{rms}(\Phi) = [\Sigma_n \,\mathrm{resid}(\Phi)^2/n]^{1/2}.$$

If the 1-D model responses are compared with the apparent resistivity and phase data in Figs 7(c) and (d), it becomes evident how alike these dissimilar models are in terms of model responses. The main common feature in the models is continuously increasing conductivity with depth. However, we cannot distinguish between a thin, very conductive layer, a stack of thin conductors, and a thick conductive layer.

To gain more structural information, which is obviously difficult from the magnetotelluric data alone, we can turn to the relevant section of the DEKORP 85-4N seismic reflection profile. The MüMa was investigated by reflection and refraction experiments. The most prominent seismic features are a highly reflective upper crust and a zone of very high velocities, rising from 5.6 km s^{-1} at a depth of 2 km to 7 km s^{-1} at about 5 km depth (Lang & Gebrande 1993). Behr *et al.* (1994) interpret the coherent reflectivity as due to the occurrence of mafic stratiform rocks in a metasedimentary assemblage deformed by low-angle thrusting. New geophysical data suggest that the high-velocity zone is not restricted to the MüMa formations but might extend as far as the SW margin of the Bohemian Massif (DEKORP & Orogenic Processes Research Groups 1999).

The depths of seismic reflectors imaged in migrated TWT-sections depend largely on the assumed near-surface seismic velocity structure, which is complicated and not very well known in the area. The 2-D velocity structure that was used to calculate the interface depths in the seismic section in Fig. 8 is a combination of a model estimated directly from rms velocities of the reflection data and a 1-D model derived from expanded spread seismic experiments for MVE90-CMP1 (Lang & Gebrande 1993) with significantly higher *P*-wave velocities. An individual application of these two different velocity models results in a depth variability of up to 1 km.

Fig. 8 shows the seismic reflection data in combination with the best-fitting four-layer models of sites I/3, II/6, and III/9. Each of the sites represents one station array; corresponding depths, resistivities and misfits are summarized in Fig. 6 and Table 2. Site III/9, at the centre of the MüMa, shows the highest resistivity for the top layer and the lowest resistivity for the bottom layer. This behaviour corresponds generally with the sandwich-type structure of the decreasing metamorphic grades of the MüMa rocks. Site II/6, located on Palaeozoic magmatic rocks at the boundary of the MüMa formations with the Bavarian facies, shows a more modest resistivity structure and, seen in conjunction with site III/9, rising interface depths. Site I/3, on the other hand, is situated on a NE–SW-trending band of outcropping Silurian and Cambrian metasedimentary rocks, which may explain the relatively high surface resistivities. At site I/3, the bottom layer with the highest conductivity is reached at about 3.5 km.

The band of the highest, most coherent reflectivity in Fig. 8 is found in the depth range between 2.5 and 5.5 km. Referring to the MVE90-CMP1 (Lang & Gebrande 1993) v_p velocity model for a petrological interpretation of this depth range, velocities of up to 7 km s^{-1} would indicate rocks of a high metamorphic or granulitic composition which are not usually associated with high conductivity. A more detailed discussion of the apparent discrepancy in the seismic velocities is beyond the scope of this paper.

UNDERSTANDING HIGH ELECTRICAL CONDUCTIVITY

Electrical resistivity is a property of rocks, as is, for example, their density. There is, however, a clear difference between the

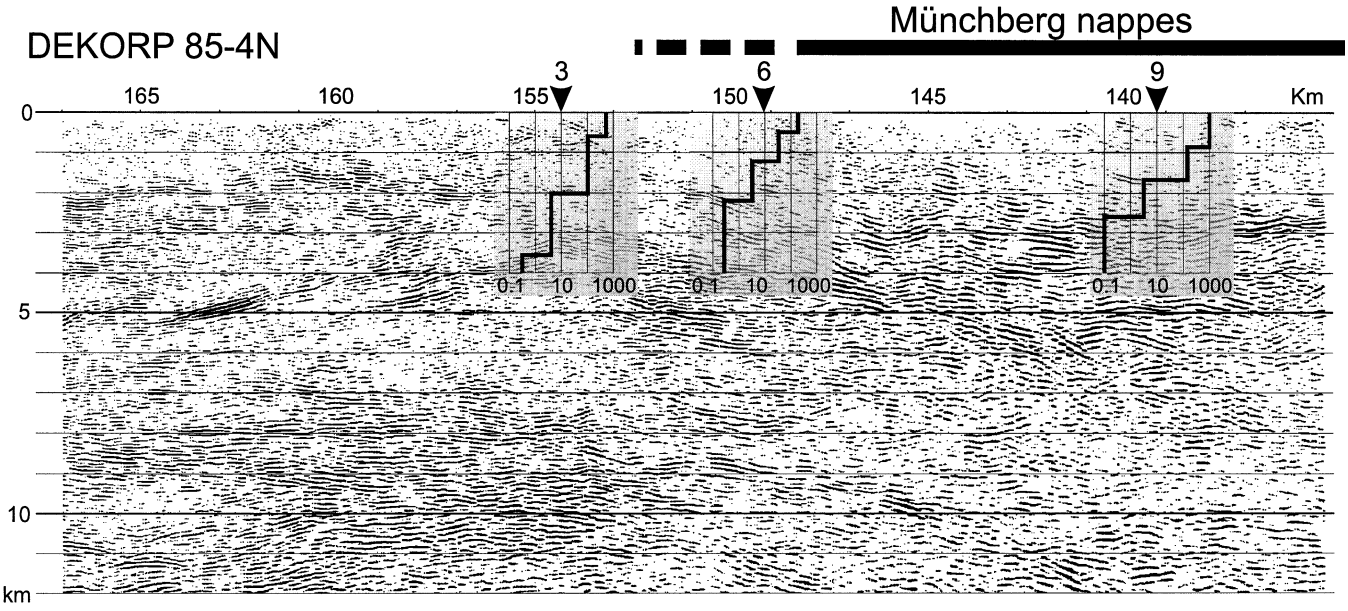

Figure 8. DEKORP 85-4N migrated seismic reflection line together with the best-fitting four-layer 1-D models of three MT sites. The depth to the best conducting layer at the MüMa sites II/6 and III/9 seems to correlate with the beginning of strong seismic reflectivity. The total overall conductance indicates that fluids alone cannot explain such high conductivity. Metallic conduction is a more consistent explanation, probably in the form of graphite, which was smeared-out along shear planes during transport of the MüMa nappes.

two properties. Density characterizes the type of rock, since it depends on the type of minerals of which the rock consists. The electrical resistivity, on the other hand, is usually not controlled by the major rock-building minerals but by the material in between these minerals: fluids, graphite, and ore minerals. It also depends on the interconnectivity of the materials. Intact rocks, in particular high grade metamorphic rocks, are usually highly resistive, with resistivities exceeding 10 000 Ω m.

These values remain the same under *in situ* conditions, demonstrated by the continuous measurements in the KTB Deep Drill hole which show resistivity values in excess of 100 000 Ω m at 9 km depth. Rock samples from the drill hole, mainly gneisses, contain even connate graphite and high-salinity fluids, which do not decrease the electrical resistivity. In the case of the KTB, interconnected, highly conductive phases exist only in shear zones in which the resistivity drops by seven orders of magnitude. High conductivity is caused both by high-salinity fluids and interconnected graphite, usually on slickensides (ELEKTB 1997).

The shearing has two functions with respect to the increase in conductivity. First, it creates space for the invasion of fluids. Second, the shearing process provides the tribochemical energy to form graphite from hydrocarbon-bearing fluids via the reaction $CO_2 + CH_4 \leftrightarrow 2H_2O + 2C$ (Kontny *et al.* 1997). The graphite is thereby actively deposited from this mixture of fluids by the shearing process. Further shearing causes smearing-out of formed graphite, and eventually interconnected films of graphite, as is the case in the slickensides. Graphite could also originate from the shearing of carbon layers in the sedimentary rock assemblages due to the transport of nappes; such 'internal' graphite enables the shearing but is not generated by the shearing.

In summary, we consider the dynamic processes associated with shear zones to be the primary source for high electrical conductivity, while the type of conductive material in shear zones is of secondary importance.

DISCUSSION AND CONCLUSIONS

With modern MT equipment and data processing tools it has become feasible to achieve reasonable results in electrically contaminated areas. Our data, collected at three station arrays along a profile across the Münchberg Massif, support this finding. The new data are of significantly better quality than those measured more than 15 years ago. Common to all sites are steeply decreasing apparent resistivity curves which indicate very high electrical conductivity with increasing depth.

1-D inversion of the apparent resistivity and phase curves results in layered models with continuously decreasing resistivities. The bottom layers yield resistivities below 1 Ω m at approximately 2.5–3.5 km depth at all sites. The 1-D models can explain most aspects of the apparent resistivity and phase data at shorter periods (< 100 s). The relatively sparse site spacing hinders construction of a more detailed structural electrical image of the MüMa, although there is some evidence in the vertical magnetic field transfer functions for a lateral change in conductivity between station arrays II and III. From the MT data alone it is not possible to decide whether the conductivity at depth is caused by a thin, very conductive layer, a stack of thin conductors, or an extended, thick conductive layer. However, at least for the sites close to or on the MüMa, the depth of the best conducting layer coincides with the beginning of strong seismic reflectivity (DEKORP85 4N) at a depth between 2.5 and 5.5 km. From the MVE90-CMP1 v_p velocity model, this depth range is associated with rocks of a high metamorphic or granulitic composition.

The metamorphic rock complex of the MüMa is an allochthonous part of the Variscan basement in NE Bavaria which has been identified as a crystalline nappe for a number of geological and petrological reasons that are beyond the scope of this paper. If the MüMa is a crystalline nappe, it must have been pushed to its present position by a tectonic process several hundred million years ago. What traces are left behind from this process? What are the geoscientific methods suitable to detect such traces?

Our magnetotelluric experiment discovered zones of high electrical conductivity in the uppermost crust beneath or within the highly resistive metamorphic rocks of the MüMa, not deeper than 1–3 km. The lower boundary of the deepest high-conductivity layer is not well resolved (see Table 2). Periods longer than 100 s are required to resolve the total conductance. However, it is plausible to conclude that the conductance of the deepest conducting layer of model 1 in Fig. 7 represents a lower limit of the true conductance. The conductance of this layer exceeds 19 000 S! If we take this value, assume high-salinity fluids of $\rho_0 = 1/100$ Ω m and a porosity (F) of 10 per cent, then, according to Archie's law ($\rho_a = \rho_0 F^{-2}$), a conductance of 19 000 S would require a layer 19 km thick. This thickness contradicts our modelling results in Fig. 7. More realistic values ($\rho_0 = 1/10$ Ω m, 1 per cent porosity) would result in an even thicker layer (1900 km!) of high conductivity. This result means that saline fluids alone cannot explain our observations. There is no realistic explanation other than to assume metallic conduction, perhaps in combination with electrolytic conduction. The electrical conductivity of graphite is several orders of magnitude higher than that of saline fluids, and, if intensively interconnected, requires a layer thickness of less than 1 km. The lesson we learned from the KTB study (ELEKTB 1997) was that connate graphite in the gneisses does not increase the electrical conductivity at all, because it is not interconnected. It is the graphite formed on shear planes that is well interconnected and thus highly conductive.

Graphite is a very effective lubricating element. If the results from the KTB can be transferred to the MüMa, then the shear planes and the graphite on them were created in the deep Variscan crust. Thus, the movement along shear zones seems to be responsible for this high-conductivity anomaly; the mere existence of the conducting material is insufficient. Materials (like graphite) which increase the electrical conductivity may also increase the mobility, which would imply a common origin of conductivity and mobility.

Furthermore, the 1-D, layered character of the conductivity anomaly could hint at a new, more complicated, two-phase scenario for the accretion of the MüMa nappes: the Randamphibolite represents the basal part of the crystalline thrust sheets which were accreted towards the west and later overthrust towards the northwest onto the sediments of the Bavarian facies as a complex of thrust sheets, from the Randamphibolite as its footwall to the Hangend Serie as hanging wall. There are no indications for metamorphic events after 365 Ma and temperatures must have been below 300 °C since then. This means that the lower Carboniferous sediments

could not have been deposited at that time. Therefore, there must have been a second, compressional tectonic event after the lower Carboniferous sedimentation, with an accretion of the (meta-)sedimentary thrust sheets and their final emplacement towards the northwest. The crystalline thrust sheets were transported passively as an entire complex. Such a two-phase tectonic environment could have left two major shear planes which we might have detected as electrical conductors. In that respect, magnetotelluric measurements can give us insight today into dynamic processes of the Earth's history.

ACKNOWLEDGMENTS

We would like to thank Uli Kalberkamp, Achim Helm, and Markus Himmerich for their help during the field work. We are grateful for the very helpful comments of two anonymous referees.

REFERENCES

Bahr, K., 1988. Interpretation of the magnetotelluric impedance tensor: regional induction local telluric distortion, *J. Geophys.,* **62,** 119–127.

Behr, H.-J. & DEKORP Research Group (B), 1994. Crustal structure of the Saxothuringian Zone: Results of the deep seismic profile MVE-90 (East), *Z. geol. Wiss.,* **22,** 647–769.

Börner, R.-U., 1995. Die Leitfähigkeitsverteilung der Erdkruste zwischen Frankenwald und Harz—abgeleitet aus der Inversion magnetotellurischer Messungen, *PhD thesis,* Technische Universität Bergakademie Freiberg.

Dawes, G.J.K., 1990. Feasibility study for a transputer-based upgrade of the Short-Period Automatic Magnetotelluric S.P.A.M.-system, NERC report F3/G6/S43, University of Edinburgh.

DeGroot-Hedlin, C. & Constable, S., 1990. Occam's inversion to generate smooth two dimensional models from magnetotelluric data, *Geophysics,* **55,** 1613–1624.

DEKORP & Orogenic Processes Working Groups, 1999. Structure of the Saxonian Granulites—geological and geophysical constraints on the exhumation of HP/HT rocks in the mid-European Variscan belt, *Tectonics,* in press.

Egbert, G.D., 1997. Robust multiple-station magnetotelluric data processing, *Geophys. J. Int.,* **130,** 475–496.

Egbert, G.D. & Booker, J.R., 1986. Robust estimation of geomagnetic transfer functions, *Geophys. J. R. astr. Soc.,* **87,** 173–194.

ELEKTB Group, 1997. KTB and the electrical conductivity of the crust, *J. geophys. Res.,* **102** (B8), 18 289–18 305.

Franke, W., 1984. Variszischer Deckenbau im Raume der Münchberger Gneismasse- abgeleitet aus der Fazies, Deformation und Metamorphose im umgebenden Paläoziokum, *Geotekt. Forsch.,* Vol. 68, Nägele & Obermüller, Stuttgart.

Franke, W., Kreuzer, H., Okrusch, M., Schüssler, U. & Seidel, E., 1995. Saxothuringian Basin: exotic metamorphic nappes: stratigraphy, structure, and igneous activity, in *Pre-Permian Geology of Central and Western Europe,* pp. 277–294, eds Dallmeyer, R.D., Franke, W. & Weber, K., Springer-Verlag, Heidelberg.

Geotools, 1997. *Geotools MT Users's Guide,* Geotools Corp., Austin, TX.

Groom, R.W. & Bailey, R.C., 1989. Decomposition of magnetotelluric impedance tensors in the presence of local three-dimensional galvanic distortion, *J. geophys Res.,* **94** (B2), 1913–1925.

Gürtler, J. & Schwarz, G., 1994. Interpretation of a MT Profile from the Frankenwald to the Harz Mountains, *Potokoll Kolloquium Elektromagnetische Tiefenforschung,* eds Bahr, K. & Junge, A., Hoechst (in German).

Haak, V., Blümecke, Th., Fischer, G., Schnegg, P. & Rath, V., 1985. Electrical conductivity studies, Oberpfalz, in *Abstract 2nd Int. Symp. on Observation of the Continental Crust through Drilling,* p. 55, Seeheim, Germany.

Kontny, A., Friedrich, G., Behr, H.J., de Wall, H., Horn, E.E., Möller, P. & Zulauf, G., 1997. Formation of ore minerals in metamorphic rocks of the German continental deep drilling site (KTB), *J. geophys. Res.,* **102** (B8), 18 323–18 336.

Lang, M. & Gebrande, H., 1993. Seismische Geschwindigkeiten in der Münchberger Gneismasse, *Z. geol. Wiss.,* **21,** 172–177.

Larsen, J.C., Mackie, R.L., Manzella, A., Fiordelisi, A. & Rieven, S., 1996. Robust smooth magnetotelluric transfer functions, *Geophys. J. Int.,* **124,** 801–819.

Müller-Sohnius, D., Von-Drach, V., Horn, P. & Koehler, H., 1987. Altersbestimmungen an der Münchberger Gneismasse, Nordost-Bayern, *Neues Jahrbuch fuer Mineralogie,* Abhandlungen, E. Schweizerbart'sche Verlagsbuchhandlung, Stuttgart, **156 (2),** 175–206.

O'Brien, P., 1996. Eclogites and related rocks in the Münchberg Massif.–6, *EMPG Tagung, Exkursionsführer 13.4.96,* University of Bayreuth.

Pflug, H.D. & Reitz, E., 1987. Palynology in metamorphic rocks: indication of early land plants, *Naturwissenschaften,* **74,** 386–387.

Ritter, O., Junge, A. & Dawes, G.J.K., 1998. New equipment and processing for magnetotelluric remote reference observations, *Geophys. J. Int.,* **132,** 535–548.

Schäfer, F., 1997. Krustenbilanzierung eines variscischen Retrokeils im Saxothuringikum, *PhD thesis,* Freie Universität Berlin.

Stosch, H.G. & Lugmair, G.W., 1990. Geochemistry and evolution of MORB-type eclogites from the Muenchberg Massif, southern Germany, *Earth planet. Sci. Lett.,* **99,** 230–249.

Weber, K. & Behr, H.J., 1983. Geodynamic interpretation of Mid-European Variscides; case studies in the Variscan Belt of Europe and the Damara Belt in Namibia, in *Intracontinental Fold Belts,* pp. 427–469, eds Martin, H. & Eder, F.W., Springer Verlag, Heidelberg.

GEOPHYSICAL RESEARCH LETTERS, VOL. 25, NO. 23, PAGES 4265-4268, DECEMBER 1, 1998

A magnetotelluric profile across Central Java, Indonesia

O. Ritter,[1] A. Hoffmann-Rothe,[2,8] A. Müller,[1] S. Dwipa,[3] E. M. Arsadi,[4]
A. Mahfi,[5] I. Nurnusanto,[6] S. Byrdina,[7,8] F. Echternacht,[1] V. Haak [1]

Abstract. Along a N30°E striking profile in central Java, Indonesia we recorded broadband magnetotelluric data at 8 sites in the period range 0.01 s - 10000 s. A preliminary analysis of apparent resistivity, phase and magnetic transfer function data favours a one-dimensional interpretation of most sites for the upper 3-5 km of the crust and a two- or three- dimensional structure for the lower crust. Several conductive features can be distinguished: (i) a strong "ocean effect" at the southern most site, (ii) a zone of very high conductivity in the central part of the profile, and (iii) a conductor in the north that cannot be caused by the shallow Java sea. We discuss tentatively causes for these anomalies. The conductor in the central part of the profile is probably connected with volcanic or geothermal activity, while the anomaly in the north could be an expression of processes associated with an active fault zone.

Introduction

This magnetotelluric investigation was carried out within the framework of an Indonesian - German research program to study the high risk volcano Merapi in Central Java. Electromagnetic measurements are widely used to explore the electrical conductivity structure of the Earth's crust from depths of a few meters down to several tens of kilometers. The electrical resistivity of crustal rocks does not depend on the resistivity of the minerals but on the material between the minerals: saline fluids, graphite, ore minerals and on the interconnectivity between these materials. The goals in this project are twofold: (i) The detection of electrical anomalies which can be linked directly with volcanic activity (i.e. hydrothermal fluids or the hot melt) and (ii) to better understand the connection between regional scale electrical anomalies and the development of the volcanic regime.

In this letter we present results from the regional conductivity study. We give a preliminary interpretation of the data and discuss briefly the significance of structures to the geology of the region.

Geological background

Figure 1 shows the locations of the MT sites in central Java and the boundaries of lithospheric plates. The whole tectonic setting of southeast Asia is controlled by subduction processes [e.g. *Hamilton,* 1979; *Hutchison,* 1989; *Lee and Lawver*, 1995] . The present configuration of Indonesia is believed to have developed since late Neogene times due to the interaction of three major lithospheric plates: the NW-moving Philippine Sea Plate; the NNE- moving Indo-Australian plate and the stationary Eurasian Plate [*Simandjuntak and Barber*, 1996]. In the Java trench, the convergence (67 ± 7 mm/yr) between the Indian Ocean Plates and the SE Asian plates is normal to the subduction trace [*Tregoning et al.*, 1994,]. *Widiyantoro and van der Hilst* [1996] suggest that the lithospheric slab dips at an angle of $\approx 60°$ in a northern direction and penetrates to a depth of at least 1500 km. The volcanic arc which forms the backbone of Java is constructed on continental crust in West Java, on accretionary complexes in Central and East Java, and on oceanic crust in Sumbawa and Flores [*Katili*, 1974].

Much research has focused on the subduction zone itself, but comparatively little is known about the tectonic framework of Central Java. An asymmetric anticlinorium (Kendeng zone) follows the north of the axial ridge with the Neogene to recent volcanoes and their sediments. This region developed out of a backarc basin setting when the stress regime changed to a compressional system in the Late Neogene [*Simandjuntak and Barber*, 1996]. The northern flanks of the anticlinorium are very steep, in places vertical or reversed, and northward thrustfaults are frequent [*De Genevraye and Samuel*, 1973]. This zone can be correlated with a backthrust trending west-east in the northern part of the Java island arc (Barbaris Kendeng thrust [*Simandjuntak and Barber*, 1996]). The west-east trending lineaments of the anticlinorium are cut by several younger NE-SW trending sinistral strike-slip faults observable in Landsat satellite images [*Chotin et al.*, 1980].

Data and preliminary interpretation

Along the profile, shown in Figure 1, we recorded broadband magnetotelluric data at 8 sites in the period range 0.01 s to 10000 s. The total length of the profile is 150 km, the average site spacing is 21 km. Data was collected using 2 different kinds of instruments: S.P.A.M. MkIII real time systems [*Ritter et al.*, 1998] were used to record the short period (AMT) data (0.01 s to 100 s), while RAP data loggers were used for the long period (LMT) data (100 s - 10000 s). Along the northern part of the profile, the data quality was generally satisfactory. Most recordings at sites close to or on the volcano, on the other hand, were severely disturbed by electromagnetic noise. Java is one of the most densely populated countries in the world, and most of the population live in small villages all of which have electric-

[1]GeoForschungsZentrum Potsdam, Germany.
[2]Rheinische Friedrich-Wilhelm Universität Bonn, Germany.
[3]Volcanological Survey of Indonesia, Bandung, Indonesia.
[4]Indonesian Institute of Science, Bandung, Indonesia.
[5]Gadjah Mada University, Yogyakarta, Indonesia.
[6]Volcanological Technology Research Center BPPTK, Indonesia.
[7]Technische Universität Berlin, Germany.
[8]Also at GeoForschungsZentrum Potsdam, Germany.

Paper number 1998GL900158.
0094-8276/98/1998GL900158$05.00

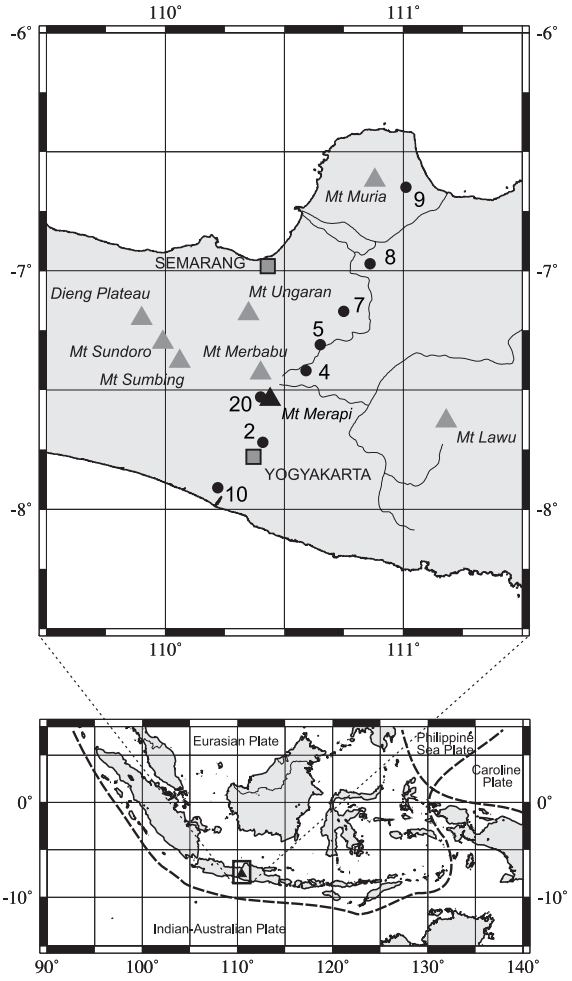

Figure 1. a) Location of Java in southeast Asia with boundaries of lithosperic plates. b) MT profile, striking approximately N30°E, across Central Java. Volcanoes are marked with triangles.

ity, including the villages on Mount Merapi. Because one of our AMT systems was permanently installed at the (noisy) Merapi volcano we could not use it as a remote reference site for the processing of short period data. For the long period data, however, this was feasible. The magnetotelluric responses are generally more affected by noise than the geomagnetic transfer functions. The most disturbed segments of the apparent resistivity and phase curves are the intermediate period ranges between 1 s and 50 s, while the short and long period ends are mostly of good quality.

Figure 2 shows apparent resistivity and phase curves of site 8 as an example of the data quality. The following features are representative for the other sites: (i) at the shortest periods – small penetration depths of the electromagnetic fields into the Earth – the resistivities are generally quite low, (ii) similar XY- and YX polarisation curves indicate one-dimensional structure for the period range 0.01 s to about 10 s, (iii) minimum apparent resistivities of 1 Ωm or below are observed between 10 s and 100 s, and (iv) the apparent resistivity curves rise steeply between 100 s and 10000 s.

With the exception of site 20, which is located about 1000 m above sea level on Mount Merapi, we generally observe small skew values and small induction arrow magnitudes in the period range 0.01 s to about 10 s. As these are further indicators for one-dimensionality, we present a preliminary interpretation of the data in Plate 1. The diagram shows a resistivity versus depth cross section of Bostick transformed averaged impedances: $Z_{avg} = \frac{1}{2}(Z_{xy} - Z_{yx})$. Z_{avg} is a rotational invariant. The plot is cut-off at a depth of 25 km which corresponds to the largest penetration depth of the EM fields at the best conducting site. It should be noted that the conductivity structure of the deeper crust (> 5 km) is influenced by lateral conductivity variations which are not accounted for by the Bostick transformation. The lowest resistivities in Plate 1 are found north of Mount Merapi at sites 4,5 and 7. The northernmost part of the cross-section at sites 8 and 9 is still conductive, showing resistivities of 10 Ωm or below. The region south of the volcano appears to be more resistive (sites 10, 2 and 20) when compared with the other sites. This observation is unlikely to be a result of static shift as a very similar pattern is revealed by the phase curves. The southern and northern sites indicate phases between 55° and 70° at short periods which can easily be distinguished from phases close to 45° at the central sites. The XY- and YX- polarisation apparent resistivity curves of sites 4,5, and 7 vary only within a band between 3 and 8 Ωm at a period of 0.01 s.

However, as mentioned before, more complicated conductivity structures than in the previous model are required to explain the induction arrows at longer periods in Figure 3. Induction arrows are particularly useful to map lateral conductivity variations. In the Wiese convention [*Hobbs*, 1992], the real arrows point away from the high conductivity side of a nearby conductivity contrast. No vertical magnetic field

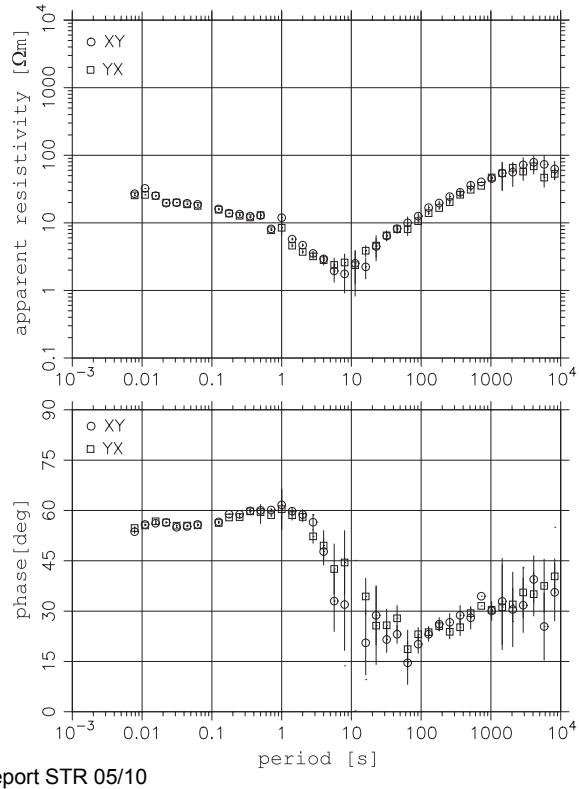

Figure 2. Apparent resistivity and phase curves of site 8, rotated by N30°E into the direction of the profile.

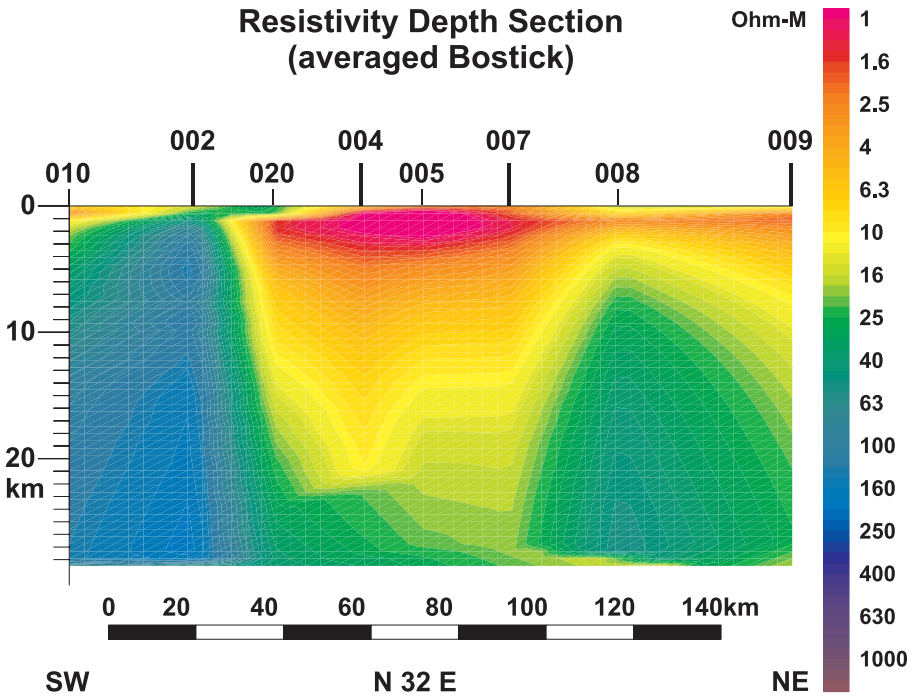

Plate 1. Preliminary one-dimensional interpretation of the magnetotelluric data as a Bostick resistivity versus depth section which shows a zone of high conductivity in Central Java with minimum resistivities below 1 Ωm. The horizontal to vertical exaggeration is 3:1.

component, and hence no induction arrow, is generated in the absence of lateral contrasts or above the centre of two equally well conducting features. In Figure 3 the induction arrows are plotted along the profile in Java at two periods (50 s and 2000 s) while Figure 4 shows diagrams of the induction arrows versus period at sites 8 and 4. At the southernmost site (10) in Figure 3, the induction arrows point away from the deep sea trench. The arrows become larger for the longer periods because as the induction range widens, a greater volume of the highly conducting sea water is sampled. It is interesting to note, that the arrows at site 9 point towards the conductive Java sea which covers an area of several thousand square kms but is on average only 60 m deep. The induction arrows at site 9 must therefore be caused by a much stronger conductivity anomaly to the south. At site 8, we see a reversal of the induction arrows: a conductor to the north, between sites 8 and 9, is suggested at 50 s, while the arrows point away from the central Java conductivity anomaly at 2000 s. Sites 7 and 4 probably mark the northern and southern boundaries of the anomaly; the arrows at 50 s of these three sites are small because the subsoil is conductive in all directions at the respective penetration depths. The reversal of the induction arrows between sites 20 and 2 at 50 s is connected with a local conductivity anomaly at Mount Merapi. Induction arrows with a distinctive eastern component are observed at sites 2, 20 and 4 at longer periods. It is possible that they are aligned with the chain of volcanoes indicated in Figure 1.

Discussion

The geomagnetic and magnetotelluric data from Central Java indicate several east-west orientated conductivity contrasts and, on a wider scale, an additional conductor striking obliquely, in north-south direction. The lengths of the induction arrows at site 10 suggest that sites further inland could at least partly be influenced by the deep ocean. In these circumstances the induction arrows represent a superposition of crustal conductivity anomalies and of the ocean

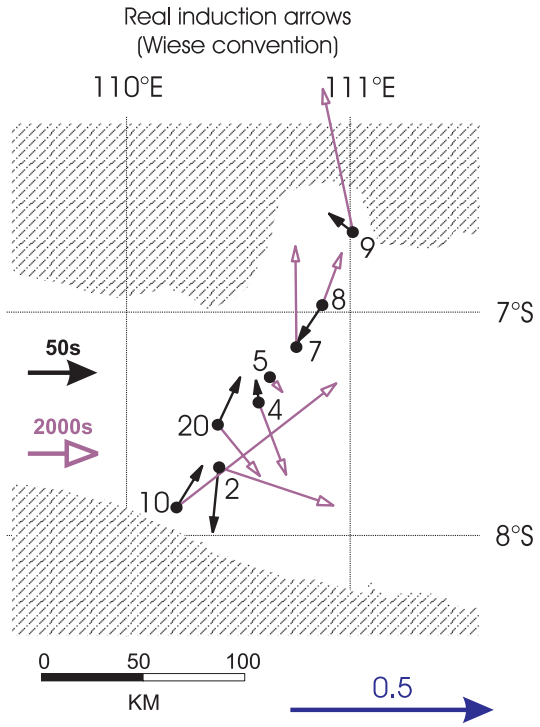

Figure 3. Real parts of induction arrows in Wiese convention for periods of 50 s and 2000 s. The electrical conductivity structure becomes more complex with increasing induction range (see text).

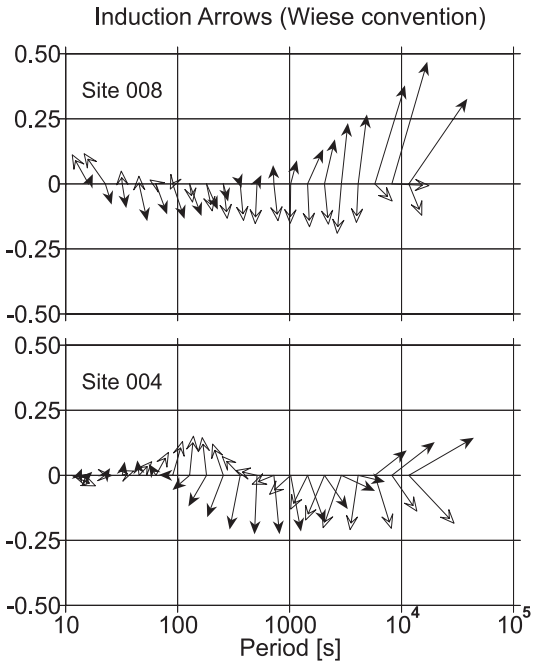

Figure 4. Real (filled arrow heads) and imaginary (outlined arrow heads) induction arrows versus period in Wiese convention of sites 8 (top) and 4 (bottom).

effect. Two- and three- dimensional modeling of the data is necessary to work this out in more detail, but this is beyond the scope of this paper.

The most important feature in the data is the Central Java conductivity anomaly which is certainly created inland and not caused by an ocean effect. *Green et al.* [1981] correlate a secondary gravity depression, approximately in the position of the Kendeng zone, with a zone of thick Tertiary sediments. *De Genevraye and Samuel* [1973] found that sediments of the Oligocene to Pliocene reach an average thickness of 1500 m and volcanoclastics are highly abundant in the Ungaran volcano region. However, it is unlikely that sediments alone are responsible for resistivities below 1 Ωm. *De Genevraye and Samuel* [1973] postulate a fault with important vertical displacement just south of site 7 where the oldest outcrops of the Late Oligocene are found. There are also signs of geothermal activity, like the mud volcanoes near Sangiran, which in combination with hydrothermal fluids could be responsible for high conductivity [e.g. *Haak et al.,* 1989]. The cause of the conductivity anomaly in the north might be connected with zones of crustal weakness. *Simandjuntak et al.* [1996] suggest that compression across the Indian ocean and Eurasian plates subduction system has resulted in backarc thrusting. Some segments of the backarc thrust are currently active [*Kertapati et al.*, 1972].

Acknowledgments. This research was supported by the Volcanological Survey of Indonesia and the German Science Foundation DFG (Ha1210/18). We would like to thank Malcolm Ingham and two anonymous referees for their helpful comments.

References

Chotin, P., A. Giret, and J.P. Rampnoux, Java island, a record of tectonic movements up a subduction zone, *Bull. Soc. Geol. France, Suppl., 22(5)*, 175-177, 1980.

De Genevraye, P., and L. Samuel, Geology of the Kendeng Zone, *Proc. Ann. Conv. - Indon. Petrol. Assoc., 1*, 17-30, 1973.

Green, R., J.S. Adkins, H.J. Harrington, and M. Untung, Bouguer Gravity Map of Indonesia, *Tectonophysics, 71*, 267-280, 1981.

Haak, V., O. Ritter, and P. Ritter, Mapping the Geothermal Anomaly on the Island of Milos by Magnetotellurics, *Geothermics, 18*, 533-546, 1989.

Hamilton, W., Tectonics of the Indonesian Region, *Geol. Surv. Prof. Paper, 1078*, US Gov. Printing Office, Washington, 1979.

Hobbs, B.A., Terminology and Symbols for Use in Studies of Electromagnetic Induction in the Earth, *Surveys in Geophys., 13*, 489-516, 1992.

Hutchison, C.S., Geological Evolution of South-east Asia, *Oxford Monogr. on Geol. and Geophys., 13*, Clarendon Press, Oxford, 1989.

Katili, J.A., Volcanism and Plate Tectonic in the Indonesian Island Arcs, *Tectonophysics, 26*, 165-188, 1974.

Kertapati, E. K., A. Soehami, and A. Djuhanda, Seismotectonic Map of Indonesia, *Geol. Res. and Dev. Centre Bandung*, 1972.

Lee, T. Y., and L. A. Lawver, Cenocoic plate reconstruction of Southeast Asia, *Tectonophysic, 251*, 85-138, 1995.

Ritter, O., A. Junge, and G.J.K. Dawes, New equipment and processing for magnetotelluric remote reference observations, *Geophys. J. Int., 132*, 535- 548, 1998.

Simandjuntak, T.O., and A. J. Barber, Contrasting tectonic styles in the Neogene orogenic belts of Indonesia, in *Tectonic Evolution of Southeast Asia*, edited by R. Hall and D. Blundell, *Geol. Soc. spec. Publ., 106*, pp. 185- 201, 1996.

Tregoning, P., F. K. Brunner, Y. Bock, S. O. Puntodewo, R. McCaffrey, J. F. Genrich, E. Calais, J. Rais, and C. Subarya, First geodetic measurements of convergence across the Java Trench, *Geophys. Res. Lett., 21(19)*, 2135- 2138, 1994.

Widiyantoro, S., and R. van der Hilst, Structure and Evolution of Lithospheric Slab Beneath the Sunda Arc, Indonesia, *Science, 271*, 1566-1570, 1996.

O. Ritter, GeoForschungsZentrum, Telegrafenberg, D-14473 Potsdam, Germany. (e-mail: oritter@gfz-potsdam.de)

(Received July 13, 1998; revised October 14, 1998;
accepted October 19, 1998.)

ELSEVIER

Physics of the Earth and Planetary Interiors 124 (2001) 131–151

PHYSICS OF THE EARTH AND PLANETARY INTERIORS

www.elsevier.com/locate/pepi

Magnetotelluric and geomagnetic modelling reveals zones of very high electrical conductivity in the upper crust of Central Java

Arne Hoffmann-Rothe, Oliver Ritter*, Volker Haak

GeoForschungsZentrum, Telegrafenberg, D-14473 Potsdam, Germany

Received 18 January 2000; received in revised form 30 November 2000; accepted 23 December 2000

Abstract

We present results of two- and three-dimensional modelling of magnetotelluric and geomagnetic data from Central Java, Indonesia. We adopt a hypothesis testing approach, where we examine the influence of individual structural elements of competing models on the total model responses. The models show that ocean anomalies do not overwhelm the signal due to strong electrical conductivity anomalies within Java. These highly conducting regions with resistivities of below 1 Ω m are located in the central and northern parts of the island. Fitting of the geomagnetic data requires that the innermost parts of both regions consist of material with extremely low resistivity (0.2 Ω m). Young sediments, tephra and their alteration products can be responsible for some of the low resistivity regions at shallow depths. The two zones of extremely high conductivity, however, are best explained as consequences of geothermal activity in the vicinity of active volcanism (Mt. Merapi) in Central Java and by fluid or graphite enrichment along shear zones in northern Java. Subduction zone related processes in a depth range of 70–400 km cannot be resolved because the highly conductive regions at shallow depths effectively screen deeper structures.

Keywords: Magnetotellurics; Geomagnetic induction; Java, Indonesia; Shear zones; Merapi volcano

1. Introduction

The island of Java is part of the Sunda Arc system which extends for more than 5600 km between the Andaman islands in the Northwest to the lesser Sunda islands in the east (Fig. 1). The Sunda arc system follows the boundary between the subducting Indian–Australian lithospheric plate and the overriding Eurasian plate.

In Ritter et al. (1998a), we published preliminary results of a broadband magnetotelluric survey recorded in 1997 at eight sites in the period range 0.01–10000 s along a N30°E striking profile in Central Java (Fig. 2). One-dimensional interpretation of the data revealed a zone of very high conductivity in the central part of the profile. From analysis of the induction arrow data, it was inferred that the southernmost site was strongly influenced by the ocean effect, whereas the conductive zone in the north of the island was not caused by the shallow Java Sea. In this paper, we complement our previous interpretation with extensive two- and three-dimensional modelling of the data.

The non-uniqueness of derived models is a common problem in the interpretation of geophysical data sets and affects EM induction methods particularly adversely. The problem can be inherent to the method (e.g. potential field methods), it can be caused by incompleteness of the particular data set (e.g. noise,

* Corresponding author. Tel.: +49-331-288-1257; fax: +49-331-288-1235.
E-mail address: oritter@gfz-potsdam.de (O. Ritter).

0031-9201/01/$ – see front matter
PII: S0031-9201(01)00196-0

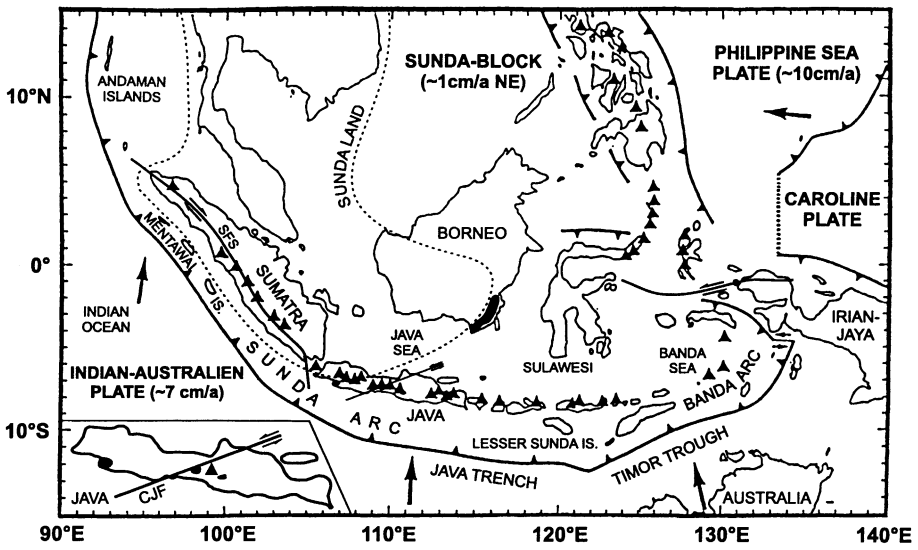

Fig. 1. Lithospheric plates and tectonic units of the Indonesian region, modified after Puspito and Shimazaki (1995). Arrows indicate plate convergence (Chamot-Rooke and Le Pichon, 1999; Simandjuntak and Barber, 1996); data on Sunda Land are taken from Hutchison (1989), Metcalfe (1996) and Soeria-Atmadja et al. (1998); triangles denote active volcanoes; SFS: Sumatra Fault System. Outcrops of Pre-Tertiary ophiolitic mélanges on Borneo and Java are marked in grey (Hamilton, 1979). The inset magnifies the melanges, the Central Java Fault (CJF) System (Chotin et al., 1984a) and the position of the Merapi volcano on Java.

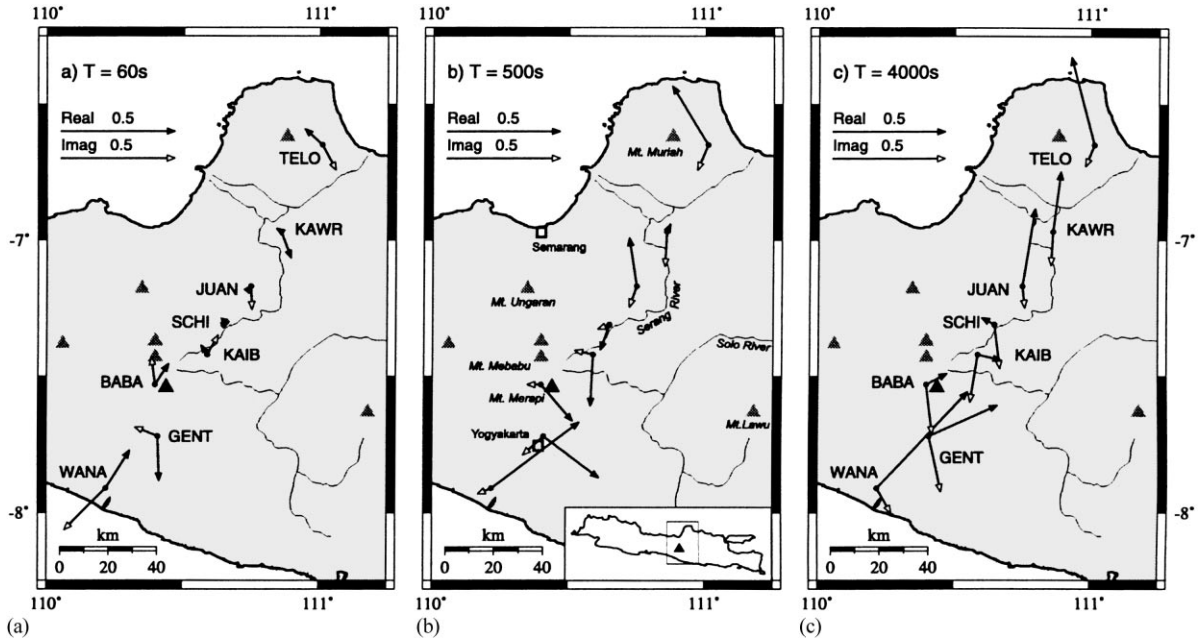

Fig. 2. Site map with induction arrows for periods $T = 60$ (a), 500 (b) and 4000 s (c). The real arrows (solid) in the Wiese convention (Hobbs, 1992) point away from the high conductivity side of a nearby conductivity contrast. Triangles mark volcanoes. Geographic names are included in (b). Note the different real arrow responses at sites close to the southern and northern coasts, respectively.

limited site spacing, limited frequency range of the observations, etc.), or by trying to fit data to the wrong model (e.g. the attempt to fit a 3D data set by means of 2D modelling) or — and this is most likely — by some combination of the above. It is therefore good practice to evaluate any derived model for the significance of structural elements. The method we propose here is to reduce the structural diversity of a 2D inversion model to the most relevant features and resort to forward modelling studies for further hypothesis testing. Removal or inclusion of relevant structural elements will alter the total model response significantly. By comparing these results with the measured data we can work out those parts of a model that are required. This is important information that cannot easily be extracted from the inversion result. The strategy will lead to models containing robust features, rather than "best fitting" models.

For the modelling procedure we put the emphasis on a combined interpretation of the MT impedance and induction arrow data. The vertical magnetic field data are sensitive to lateral changes in conductivity and fitting both data sets helps to pinpoint positions and strengths of conductivity contrasts. This is particularly useful in our case, with a data set containing a limited number of widely spaced sites. Finally, we discuss our modelling results in view of other published geophysical and geological data.

2. Geological background

The Sunda arc (Fig. 1) developed since the Mid Tertiary due to the subduction of the northward moving Indian–Australian plate beneath the — relative to Eurasia — slowly northeastward progressing Sunda Block (Chamot-Rooke and Le Pichon, 1999; Soeria-Atmadja et al., 1998). Present day subduction processes manifest in an island arc that hosts some of the most active volcanoes in the world, including the Merapi volcano in Central Java (Fig. 1 inset). The convergence at Central Java is approximately frontal with a steeply dipping Benioff zone of $\sim 60^{\circ}$ (Widiyantoro and van der Hilst, 1997).

The SE Asian continental parts of the Sunda block/Eurasian plate with Pre-Tertiary basement are collectively called Sunda Land (Fig. 1). This stable, cratonized core of SE-Asia is believed to have formed by accretion of Pre-Cretaceous terranes and sutures (Metcalfe, 1996). The boundary of Sunda Land marked in Fig. 1 indicates that the island arc in Sumatra and West Java is build on continental crust whereas the volcanic arc of the Eastern part of the Sunda system is situated on young oceanic crust. Refraction seismic experiments indicate a crustal thickness of 20–30 km in Sumatra and 8–10 km for the eastern Sunda arc (Kieckhefer et al., 1980).

Beneath Central and East Java the crustal composition is probably best described as a transition from continental to oceanic. The transition zone is manifested in a trace of Pre-Tertiary melanges (Daly et al., 1991; Soeria-Atmadja et al., 1998) and ophiolites (Hamilton, 1979) reaching from SE-Borneo via the basement of the Java Sea towards Java itself (cf. Fig. 1). This mesozoic accretionary complex (Simandjuntak and Barber, 1996) is the relic of an Upper Cretaceous NE trending subduction zone (Daly et al., 1991; Soeria-Atmadja et al., 1998; Chotin et al., 1984b).

Many of the prominent fault systems in Java are related to this transition zone. Marked in Fig. 1 is an important strike-slip fault zone (hereafter called the Central Java Fault (CJF)) trending N70°E from Cilacap at the southern coast of Java towards the eastern foot of Mt. Muriah and apparently extending off-shore into the extensional Pati (Bawean) trough (Chotin et al., 1980, 1984b). Sinistral movement over a distance of kilometres and a vertical displacement of ~ 2 km is indicated by the shift of basin/volcanic axes and the outcrops of ophiolitic melanges of the Pre-Tertiary basement along the faults, respectively (Sano et al., 1978; Chotin et al., 1980, 1984b).

3. Interpretation of the magnetotelluric and geo-magnetic data

The magnetotelluric method (MT) is based on the observation of orthogonal components of time-varying horizontal electromagnetic fields at the surface of the earth:

$$\begin{pmatrix} E_x \\ E_y \end{pmatrix} = \begin{pmatrix} Z_{xx} & Z_{xy} \\ Z_{yx} & Z_{yy} \end{pmatrix} \begin{pmatrix} B_x \\ B_y \end{pmatrix} \quad (1)$$

with $\boldsymbol{E}$ being the electric field in (mV/km), $\boldsymbol{B}$ the magnetic field in (nT) and Z_{ij} the components of the impedance tensor $\boldsymbol{Z}$ which contains information on the

conductivity structure of the sub-surface. The factors x, y, and z are defined to be positive when pointing towards north, east and downwards, respectively.

A vertical magnetic field component is generated in addition to the horizontal electric fields if lateral conductivity variations are of the order of the induction range of the observations. The geomagnetic depth sounding method (GDS) is based on the analysis of vertical magnetic field variations. The geomagnetic response functions T_x, T_y are defined similarly to Eq. (1):

$$B_z = T_x B_x + T_y B_y \tag{2}$$

The T_x and T_y response functions are usually presented in the form of induction arrows to map lateral conductivity variations. In the Wiese convention (Hobbs, 1992), which is employed in this paper, the real arrows tend to point away from the high conductivity side of a nearby conductivity contrast.

3.1. Data acquisition and processing

This field experiment from Central Java was carried out as part of a German–Indonesian research programme to study the Merapi volcano (Fig. 1). We used two different types of instruments to collect the data. The short period data in the range from 0.01 to 100 s were recorded with S.P.A.M. MkIII real time systems (Ritter et al., 1998b) and Metronix induction coils while the long period data (>50 s) were gathered with RAP data loggers and Magson flux gate magnetometers. All data were analysed using the robust, remote reference processing algorithm described in Ritter et al. (1998b).

Due to a variety of operational difficulties, the available dataset is not ideal. Java is one of the most densely populated countries in the world and most of the population lives in numerous small villages all of which have electricity. High noise levels in combination with short recording times resulted in a wide band (0.1–10 s) of biased and poorly determined estimates of the MT impedance and GDS results. The long period recordings were usually discontinuous as we experienced reliability and timing problems with the RAP loggers and also with our power supplies (batteries, solar panels). Timing problems in particular with the long period systems meant that remote reference processing usually failed to improve the quality of the data at long periods. However, robust single site processing of the data gave generally reliable and reasonable quality results for long periods between 40 and 4000 s and for short periods between 0.01 and 0.1 s (see Figs. 3 and 4). Fig. 4 shows real and imaginary parts of the T_x component of the vertical magnetic field response functions. While they are generally small and noisy at periods less than 10 s, they have much higher quality at longer periods. For periods greater than 10 s, the response curves vary smoothly and consistently with period at most sites. The error bars are generally small and bivariate coherencies are mostly above 0.8 (not shown).

Although the MT and GDS data are severely hampered by electromagnetic noise in the period band between 0.1 and 10 s, the general trend of the response curves is still recognisable at most sites. Better data quality at shorter and longer periods can be used to partly reconstruct missing parts of the curves as we know from theory that MT and GDS sounding curves must vary smoothly and continuously with period. Several sites show, for example, phases above 45° at periods less than 1 s and below 45° at long periods, thereby indicating a conductive zone sandwiched between resistive regions above and below.

3.2. Dimensionality and directionality

The (electrical) complexity of the sub-surface can be assessed by calculating parameters for dimensionality and directionality. These parameters are derived from the tensor nature of the MT observations (see Eq. (1)) and from the induction arrows (Eq. (2)). Over a 1D earth induction arrows vanish and the impedance tensor is rotationally invariant with $Z_{xy} = -Z_{yx}$ and $Z_{xx} = Z_{yy} = 0$. Impedance tensor data acquired over a 2D earth have vanishing diagonal elements only if the electromagnetic fields are either recorded in or mathematically rotated to a co-ordinate system which is perpendicular to the electric strike. Older methods for optimum electrical strike angle determination (Swift, 1967) rely on the magnitude information in the impedance tensor elements while modern tensor decomposition methods (see Jones, 1998 for a recent review) are based also on their phase information (Bahr, 1988; Groom and Bailey, 1989). Real and imaginary induction arrows, on the other hand, point

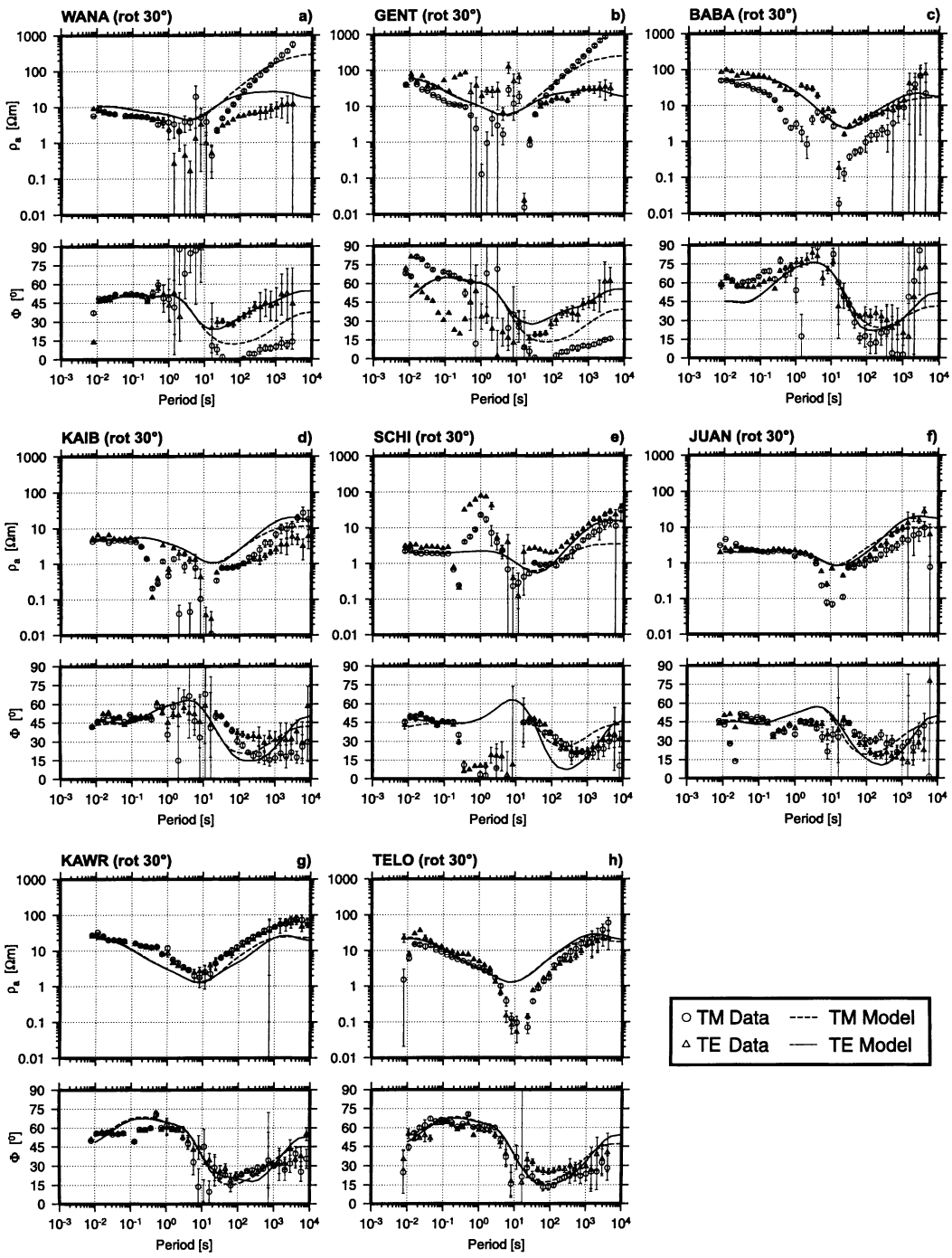

Fig. 3. Apparent resistivity and phase data (rotated 30°E) together with the Java model responses (see Section 3.3). Circles and dashed lines refer to TM-mode, triangles and solid lines to TE-mode data. Error bars in this and following figures are one standard deviation.

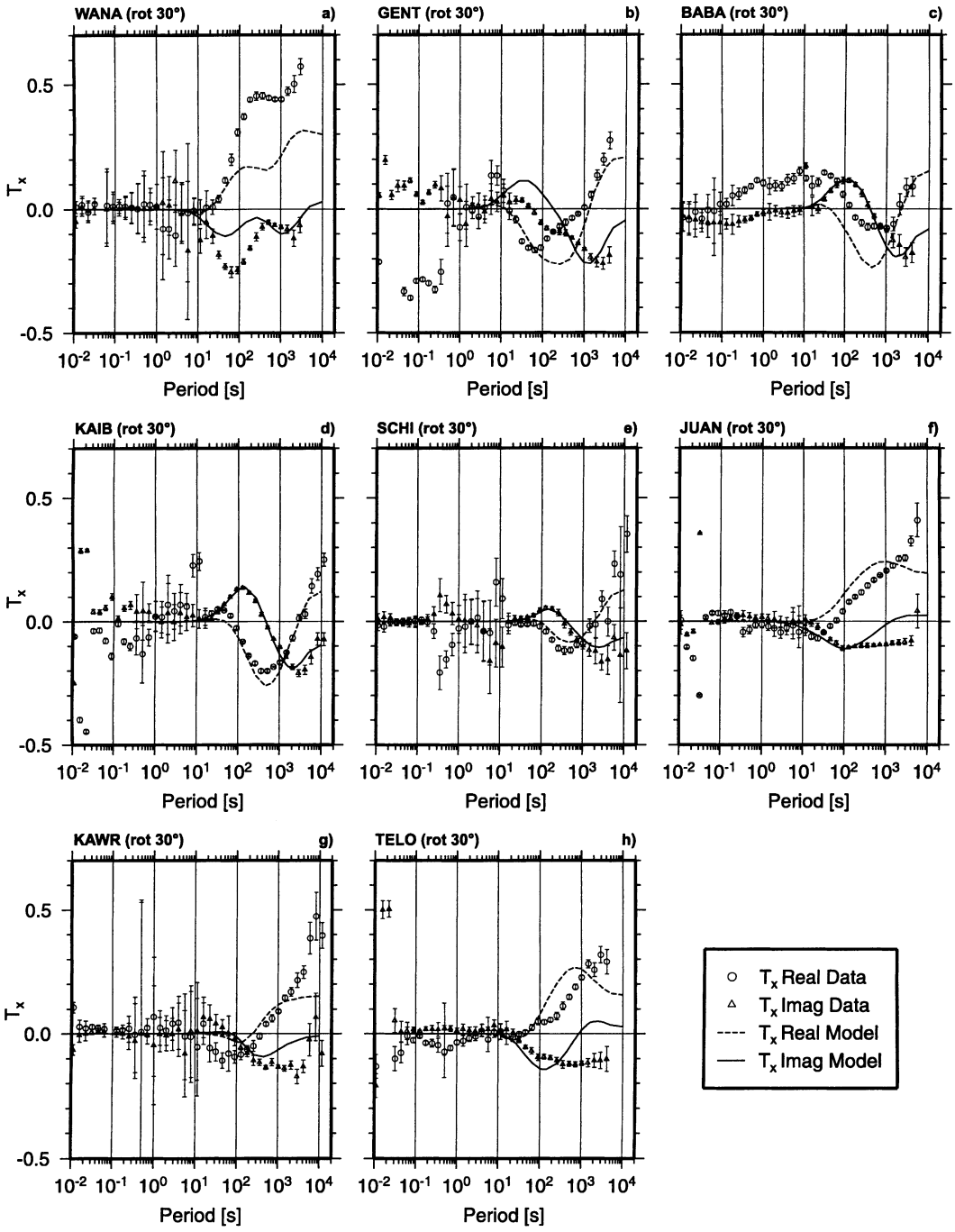

Fig. 4. Magnetic transfer functions of the 30°E rotated data together with the *Java model* responses. The magnetic field is oriented parallel to the profile for the T_x-component. Thus, positive T_x-values generate induction arrows pointing N30°E. Circles and solid lines are the real part, triangles and dashed lines the imaginary part. Refer to Fig. 9 for a presentation in the form of induction vectors.

perpendicular to the strike of a two-dimensional structure and parallel or anti-parallel to each other. Obliquely pointing induction arrows and non-zero diagonal elements of the impedance tensor hint generally at a more complicated, three-dimensional distribution of the sub-surface conductivity.

The skew of the impedance tensor is a measure of the ratio of its diagonal to off-diagonal elements and is used as an indicator of the complexity of the subsurface. Normal (Swift) and phase-sensitive (Bahr) skew values are plotted in Fig. 5. The skew values are below 0.2 for $T < 1$ s at most sites. Very large skew values in the band between $1 < T < 10$ s are caused by noise in the data. The Bahr skew values appear to be larger than the normal skews but it is difficult to decide if this is caused by noise in the data

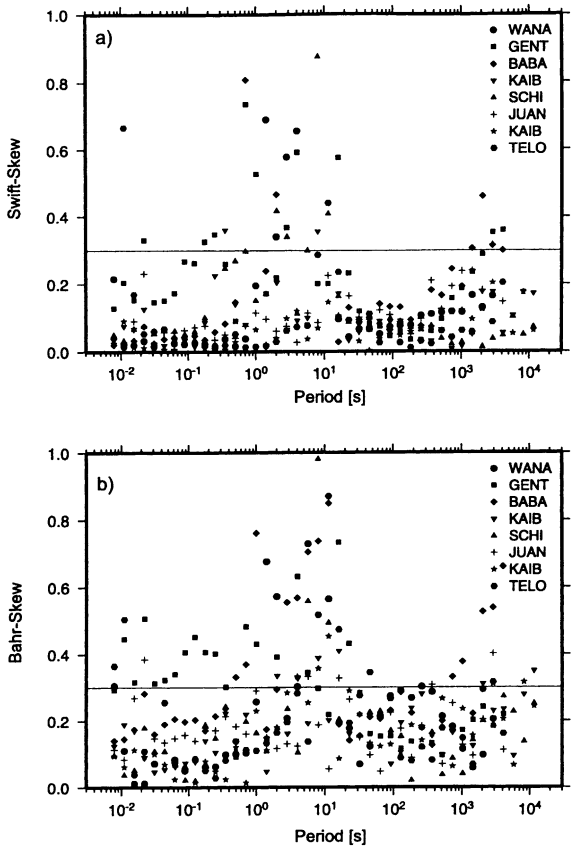

Fig. 5. Swift (a) and Bahr (b) skew values for all sites. The 'dead-band' from 1 to 10 s with little electromagnetic signal energy produces strongly scattered skew values. The skew values are below 0.3 (horizontal line) for $T < 1$ s at most sites.

or by the geological setting. In general, values remain below 0.3 at longer periods. Skew values above 0.3 indicate that the data cannot be represented by a 1D or 2D sub-surface (Bahr, 1991). Smaller skew values are compatible with a 1D or 2D earth but certain 3D geometries cannot be ruled out. Small skew values would be observed, for example, above the centre of a ball shaped anomaly.

Swift- and *Bahr* electrical strike angles for all sites are plotted as rose diagrams for three different period ranges (Fig. 6). For periods less than 1 s, strike angles are mostly undetermined. This indicates that the short period data are compatible with a 1D shallow sub-surface, as do matching XY- and YX polarisations of apparent resisitivity and phase curves (Fig. 3), small GDS response functions (Fig. 4) and small skew values (Fig. 5) at short periods. For the period band with good data quality between 10 and 1000 s the rose diagrams indicate a concentration of the electric strike angles at approximately 20° for the Swift criterion and at approximately 30° using the Bahr method. The Bahr angles at periods greater than 1000 s indicate a strike direction of approximately 70°. Closer inspection of the data (not shown) reveals that this is predominantly caused by the four northern most sites.

The induction arrows are shown in Fig. 2 along the profile across Java at periods of 60, 500 and 4000 s as examples. The real arrows at site WANA in the south point away from the deep and highly conductive Indian ocean. The arrow lengths rise with increasing period as the induction range widens (skin depth phenomenon of electromagnetic waves). At site TELO in the north, we observe north pointing induction arrows at 4000 s which cannot be caused by the shallow Java Sea but must originate from a (stronger) conductivity anomaly inland. The south pointing real arrow at site GENT in Fig. 2a indicates a conductor to the north of that site. South pointing arrows are also observed at sites GENT, BABA, KAIB and SCHI in the period range 100–3000 s. The directions of the real induction arrows reverse between sites SCHI and JUAN, suggesting a conductive region in-between. The north pointing arrows at the three northern sites JUAN, KAWR and TELO are consistent with a highly conductive zone in Central Java. Eastward pointing induction arrows at the southern sites WANA, GENT, and BABA at periods longer than 200 s indicate the influence of a conductor further west.

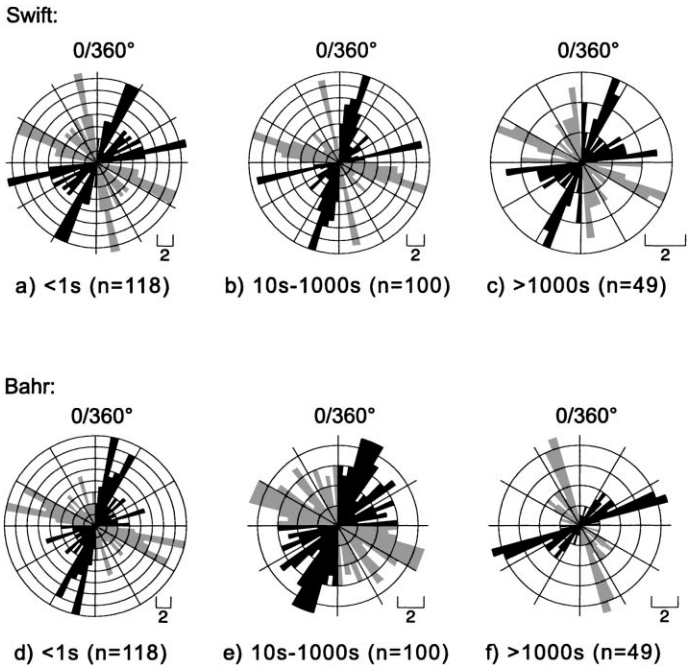

Fig. 6. Rose diagrams of Swift (a–c) and Bahr (d–f) electric strike angles at different period ranges derived from the MT data. The strike angles have an ambiguity of 90° (black and grey roses). Here, *n* denotes the number of data within each frequency band; each frequency is treated independently. While electric strike is mostly undetermined for periods less than 1 s, a concentration of strike angles at approximately 30° is indicated in the period range of 10–1000 s. A different strike of about 70° is implied for the longest periods in figure (f).

Induction arrows indicating a true 2D situation with parallel or anti-parallel pointing real and imaginary arrows can only be recognised at a few sites, for example, at JUAN and KAWR at 4000 s or at WANA between 60 and 500 s in Fig. 2. However, induction arrows pointing approximately along the direction of the profile are observed at most sites over a wide period range. This is consistent with electrically conductive structures striking approximately perpendicular to the profile.

3.3. Two-dimensional interpretation of the data

The reasonably good quality long period data (periods above 10 s) are suitable for a regional interpretation of the data. The tensor decomposition analysis of Section 3.2 shows that these data are compatible with an earth model of a predominantly regional two-dimensional structure. For the period band 10–1000 s, the Bahr analysis reveals that the electrical strike direction is N30°E or N60°W (Fig. 6). The direction of the induction arrows, however, confirms that the strike direction is N60°W. In order to interpret the measured data by means of 2D modelling it is necessary to first rotate the MT and GDS response functions into the co-ordinate system of the strike. The rotated XY- and YX polarisations are then called TE- and TM-mode. In the TE-mode the electric current flow is parallel to the strike of the conducting feature, in the TM-mode the current flow is perpendicular to the strike.

The short period (0.01–0.1 s) apparent resistivity and phase data are primarily useful to determine the electrical conductivity of the very shallow subsurface in close vicinity to the sites. But these data also indicate that static shift does not appear to be a major problem with this data set. As discussed already in Ritter et al. (1998a) the main conductivity anomalies are clearly expressed in the magnetotelluric phase data and in the induction arrows which are not affected by static shift. The XY- and YX polarisations of the apparent resistivity curves of the most conductive sites

KAIB, SCHI, and JUAN vary only within a narrow band between 3 and 8 Ω m at the shortest period of 0.01 s. Static shift corrections are therefore not considered in any of the models discussed.

Fig. 7 shows the result of a 2D inversion (RLM2DI; Rodi and Mackie, 2001) of TE- and TM-mode apparent resistivity and phase data. The initial model for the inversion was designed with a 100 Ω m homogeneous half space in which the bounding Indian Ocean in the SW and the Java Sea in the NE were included as zones of 0.2 Ω m. The model shows low resistivity values between 1 and 10 Ω m for the whole of Java's shallow subsurface (<2 km). Regions of highest conductivity are found between BABA and JUAN (A) and beneath TELO (B) at depths of about 1100 m. The model in Fig. 7 does not account for topography. The more resistive areas near BABA and GENT (C) and between KAWR and TELO (D) therefore correspond to a downward projection of the topographic heights of Mt. Merapi and the Rembang hills which consist of more resistive massive igneous rocks. Other interesting features in the model are the deeper conductor beneath SCHI (E), its possible connection with zone A and the laterally extended resistive layer (F).

Fig. 8a shows a two-dimensional electrical resistivity model that we call the *Java model*. Vertical and lateral extensions of the *Java model* are illustrated in Fig. 8b. This model was derived using the outcome of several 1D and 2D inversion programs and very many 2D forward modelling studies. Most modern 2D inversion codes generate so-called smooth models which compromise between a best fit and lateral coherence between the resistivity of neighbouring grid cells. It is almost impossible though, to assess the significance of structural elements in these smooth models. The *Java model* includes only features which have a demonstrable impact on the model response. In a way, it represents a *minimum* features model. The *Java*

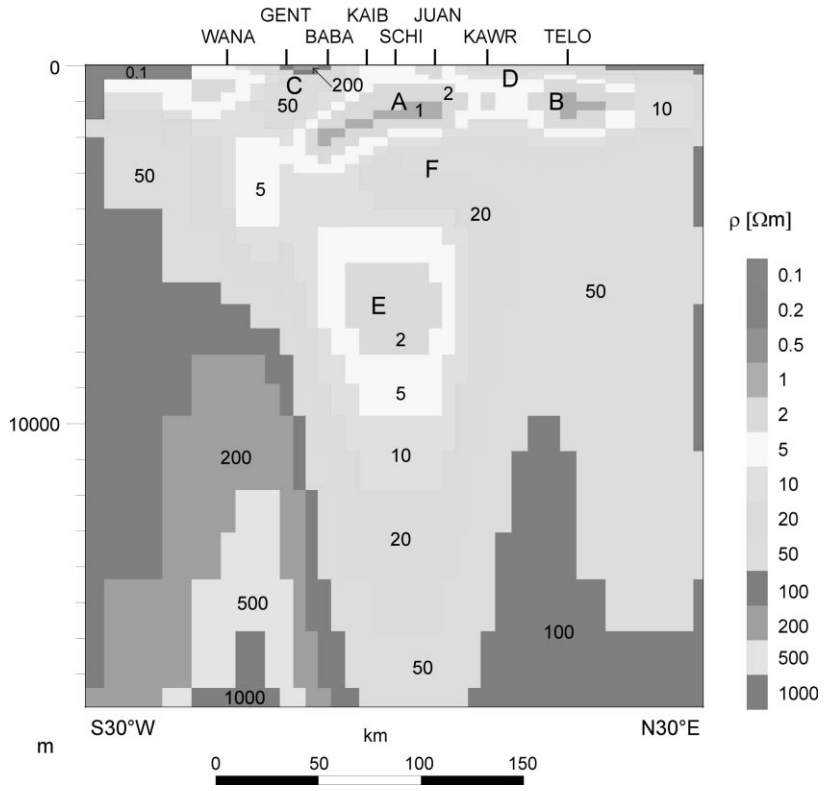

Fig. 7. Result of 2D inversion of TE- and TM-mode impedances. The impedance data have been rotated by 30°E. Letters A to F mark important structures discussed in the text. Numbers are resistivities in Ω m. Vertical exaggeration: 17.5.

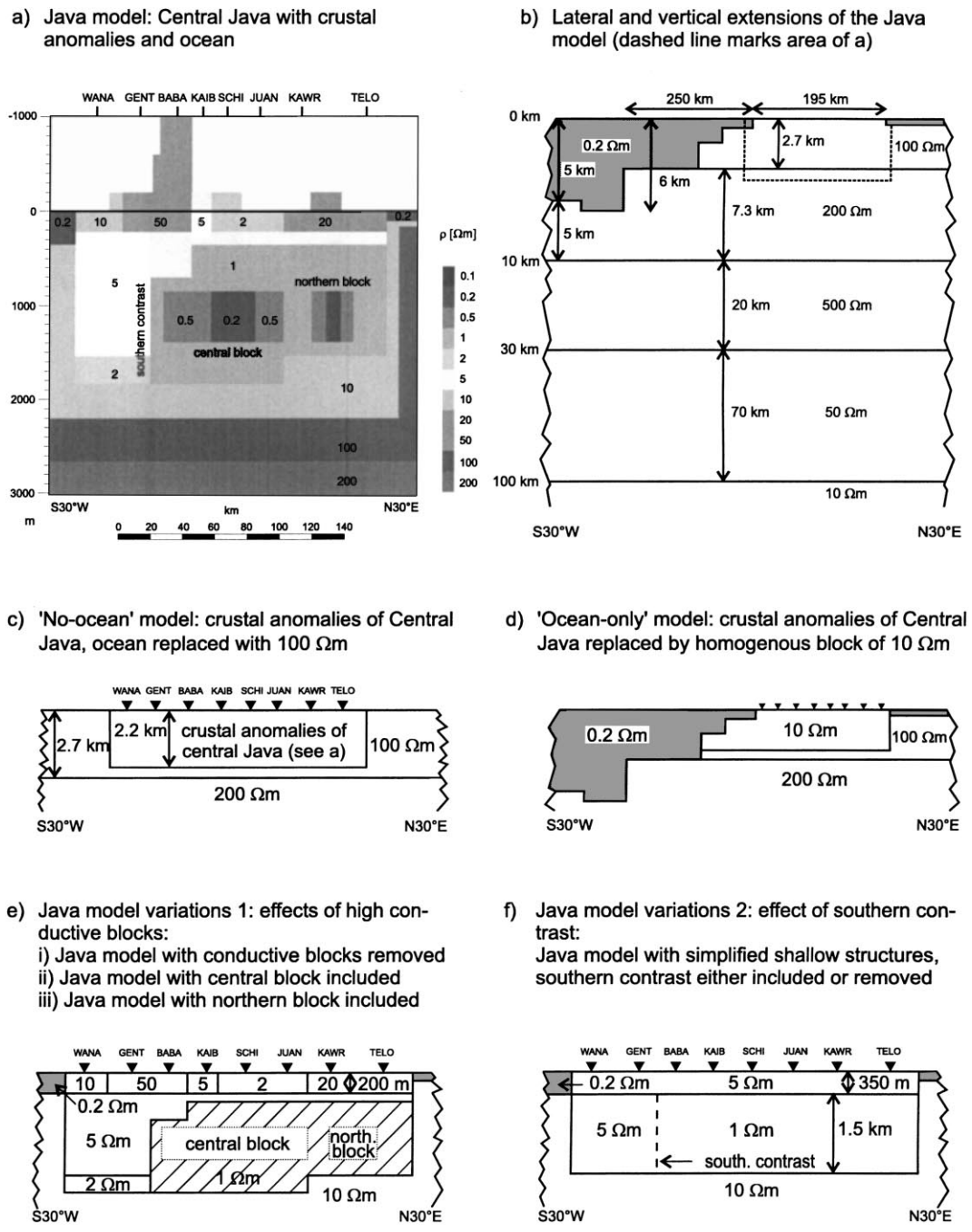

Fig. 8. (a) Core of the 2D forward *Java model* model with topography taken into account. The lateral and vertical extensions of the model are illustrated in 8b. Numbers mark resistivities in Ω m. The model shows a generally very conductive upper crust (to a depth of about 2 km). (c) The *no-ocean model* comprises only the crustal anomaly structure of Central Java, without the surrounding sea water. (d) The *ocean-only* model consists of a 10 Ω m block instead of the conductive features shown in 8a; (e) and (f) are further model variations (see text).

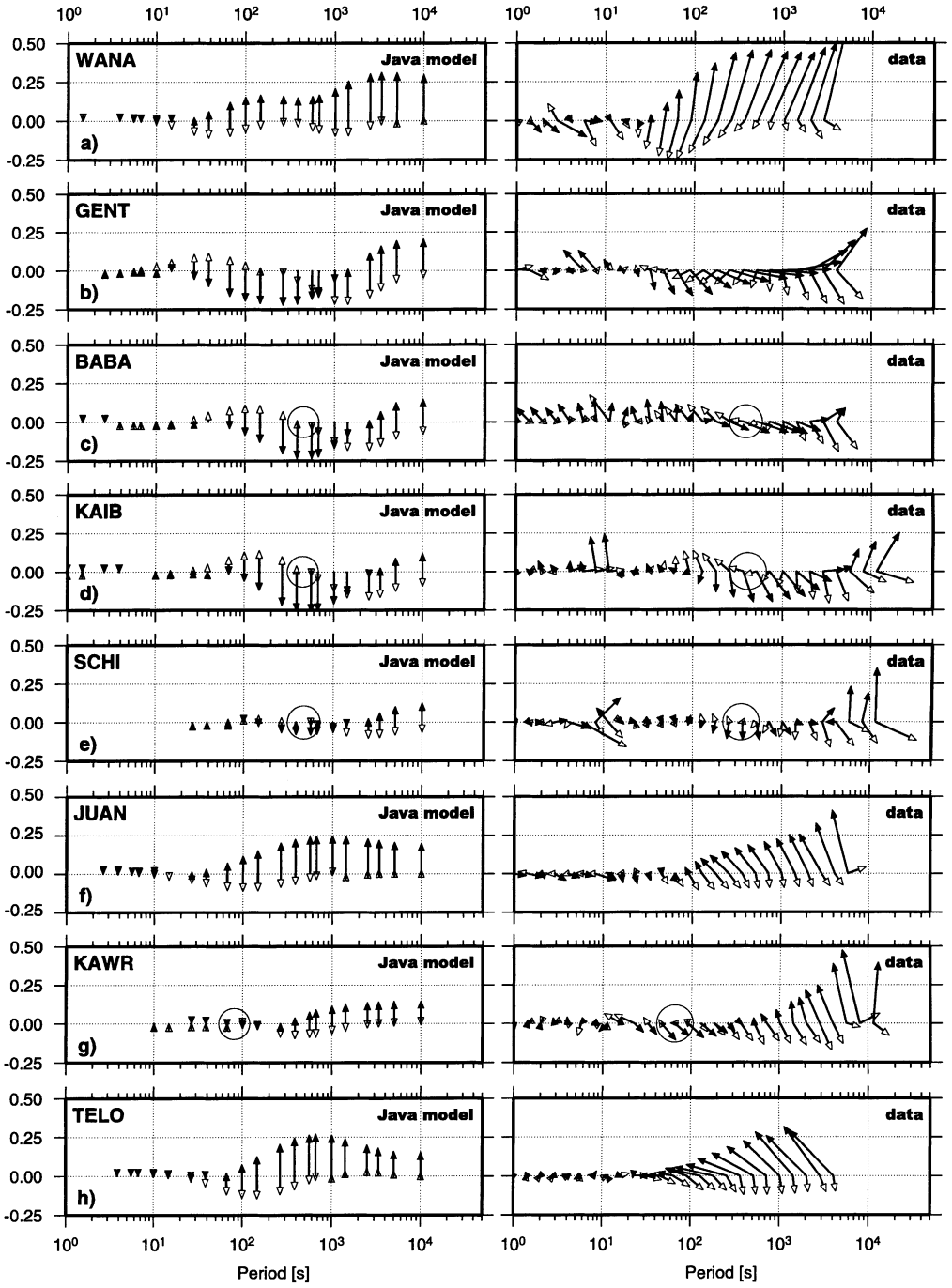

Fig. 9. Modelled (left) and measured (right) induction arrows in Wiese convention (solid: real part, hollow: imaginary part). Note: the induction arrows are plotted in a (N30°E) rotated co-ordinate system, i.e. upright arrows point NE. Circles mark the range of the characteristic period T_c (see text).

model includes a priori information on topographic heights and bathymetry. Major upper crustal conductive features are labelled (i) the southern *contrast*; (ii) the *central block* (compatible to zone A in the inversion model of Fig. 7) and (iii) the *northern block* (zone B). Fig. 3 shows the model responses together with measured TE and TM-mode apparent resistivity and phase data. The respective GDS data are plotted as induction arrows in Fig. 9 and as magnetic transfer functions of the relevant T_x-component in Fig. 4.

Many of the structural details in the *Java model* were only introduced because they are required by the GDS data. The main aspects to look for are: reversed arrow directions between sites, the trend in the arrow lengths over period and the ratios of real to imaginary arrows. Comparison of measured and modelled induction arrows shows that reversals between sites WANA and GENT (Fig. 9a and b) and between SCHI and JUAN (Fig. 9e and f) are well reproduced in the correct period range. The model responses also show increasing arrow lengths with increasing periods but the absolute magnitudes of the modelled induction arrows are sometimes too small (e.g. at WANA or GENT). Even the behaviour of the imaginary arrows is convincingly duplicated. Marked by circles in Fig. 9 is the period range of vanishing imaginary arrows (the turning point of their orientation) which coincides with maximum real arrows, the so-called characteristic period T_c (Agarwal and Dosso, 1993). Good agreement between modelled and measured T_c can be recognised at sites BABA, KAIB, SCHI, and KAWR.

In the following sections, we will discuss structurally reduced models that deal with specific aspects, such as the ocean effect and lateral changes of conductivity within the island.

3.3.1. The ocean effect

It is clear that the electromagnetic data are influenced by the conducting sea water of both the Indian Ocean and the shallow Java Sea (average depth 100 m). To demonstrate the effects of the ocean on the data from the island of Java we compare the results of two model variations which we called the *no-ocean model* (Fig. 8c) and the *ocean-only model* (Fig. 8d). In the latter, the whole of Java is considered as a homogeneous block of 10 Ω m, thereby reducing the *Java model* to the effects of the ocean only. For the *no-ocean model* we keep the island's crustal structure of the *Java model* but replace the bounding sea water with resistive cells of 100 Ω m. The effects of these model variations are shown at three representative sites, located at both coasts and at the centre of Java, in the top row of Fig. 10.

The *ocean-only model* can explain separating apparent resistivity and phase curves at longer periods of the *Java model* (and consequently the measured data) in the bottom part of Fig. 10. The effect is most evident at the southern most site WANA (Fig. 10a); the effect is still visible but reduced at site JUAN (Fig. 10b) at the centre of the profile. The apparent resistivity and phase curves at TELO (Fig. 10c) in the north, are influenced by both the Indian Ocean and the Java Sea and consequently, we observe the onset of separation of the two polarisations at shorter periods.

Comparison of the *Java model* responses in Fig. 10b, d and f with those of the *no-ocean model* in Fig. 10a, c and e reveals that the sea water (which is removed in the *no-ocean model*) affects mainly the TM-mode. Particularly, sites JUAN and TELO have almost identical TE-mode curves which must be controlled by crustal conductivity structures. The model responses in Fig. 10 show furthermore that the *Java model* represents a superposition of the *ocean-only* and the *no-ocean models*. It is remarkable that the resulting apparent resistivity and phase curves at TELO have a one-dimensional appearance despite the strong 2D character of the respective *ocean-only* and *no-ocean model* responses.

The *ocean-only* and *no-ocean* conductivity anomalies also influence the GDS response functions. Fig. 11a shows the ocean effect on the GDS response function T_x. The amplitude of $\Re e(T_x)$ controls the length of the induction arrows, a positive sign generates N30°E pointing arrows, a negative sign S30°W pointing arrows. The largest $\Re e(T_x)$ values (or induction arrow lengths) are always observed at sites closest to the coast. The negative sign of T_x in the period range 10–1000 s at the three northern most sites is caused by the Java Sea. All sites, however, show positive T_x values at longer periods which are caused by the Indian Ocean. The period for which positive T_x values first appear depends on the distance of a site from the southern coast. Sites far away from the southern coast see the ocean effect at longer periods than sites close to the shore.

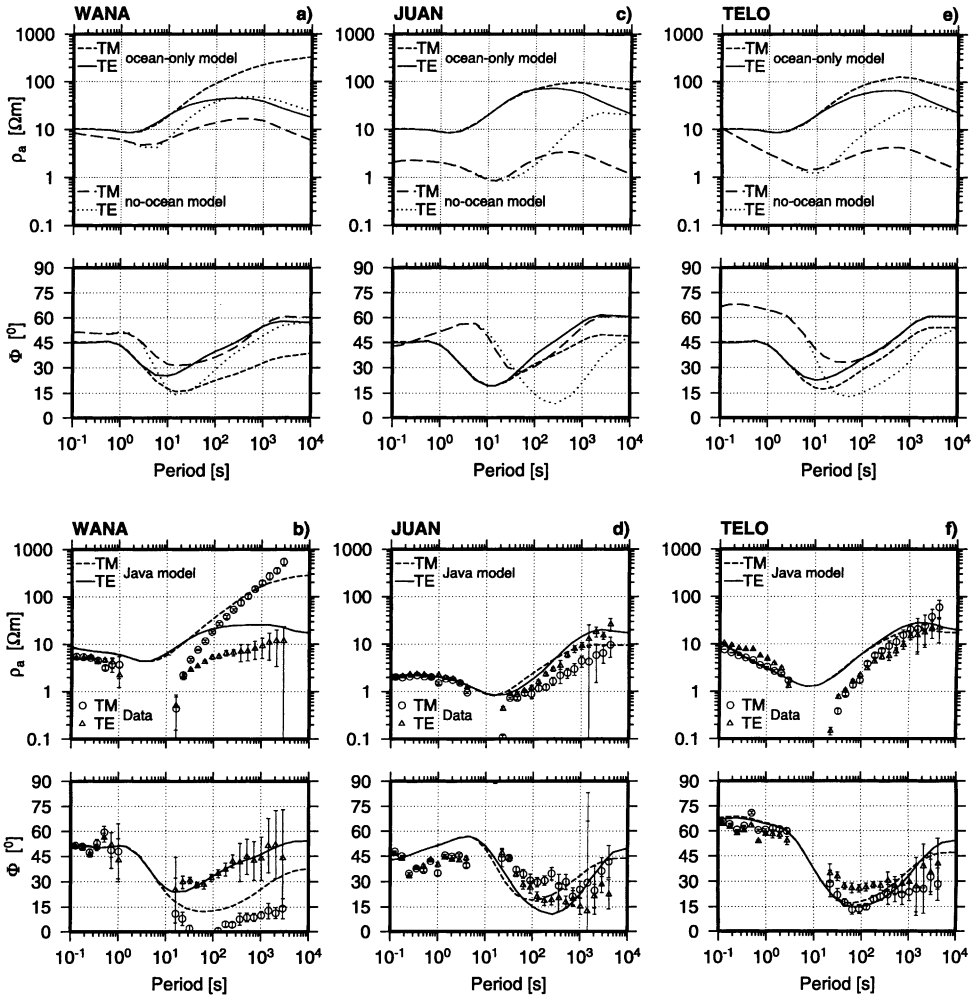

Fig. 10. Impedance data derived by 2D forward modelling for the *ocean-only model* and the *no-ocean model* of sites (a) WANA; (c) JUAN and (e) TELO. The figures in the bottom row (b, d and f) show the model responses of the *Java model* at the same sites together with the measured data (some of the extremely noisy data are omitted). The *Java model* is the combination of the *ocean-only* and the *no-ocean* model.

The GDS responses of the *no-ocean model* in Fig. 11b, on the other hand, explain the southward pointing induction arrows at GENT as the anomaly caused by the *southern contrast* exceeds that of the Indian Ocean. The lengths of these south pointing arrows decrease continuously towards the sites further inland (up to site SCHI, compare Fig. 2b). We also learn from these models that the induction arrows between sites WANA to SCHI point northward at the longest periods because of the dominating influence of the Indian Ocean, while the arrows point northward between sites JUAN to TELO because of the effects of the *central block* anomaly.

3.3.2. Lateral and deep conductivity contrasts on Java

In this section, we examine the significance of the high conductivity zones at a depth of about 900–1400 m, labelled *central block* and *northern block* in Fig. 8 and the *southern contrast*, situated between sites GENT and BABA. Fig. 12 shows diagrams of $\Re e(T_x)$ response functions of the *Java model*

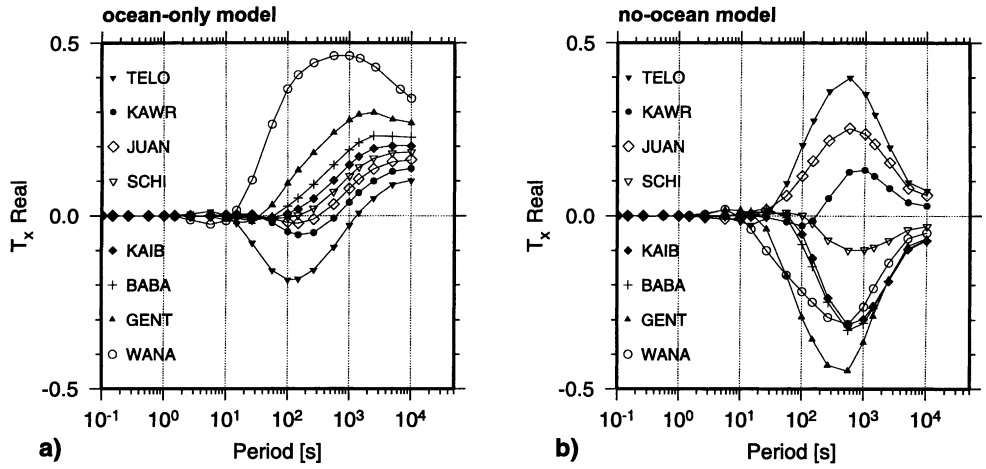

Fig. 11. Amplitude of the real parts of the GDS response functions T_x of (a) the *ocean-only model* and (b) the *no-ocean model*. Positive values correspond to real induction arrows pointing N30°E, while negative values indicate S30°W pointing arrows. The narrow period range of negative T_x values at the northernmost sites in the *ocean-only model* indicates that the data are hardly affected by the shallow Java Sea. The *no-ocean model*, on the other hand, shows large negative values (southward pointing induction arrows) at the southern sites which are generated by lateral conductivity contrasts within Java.

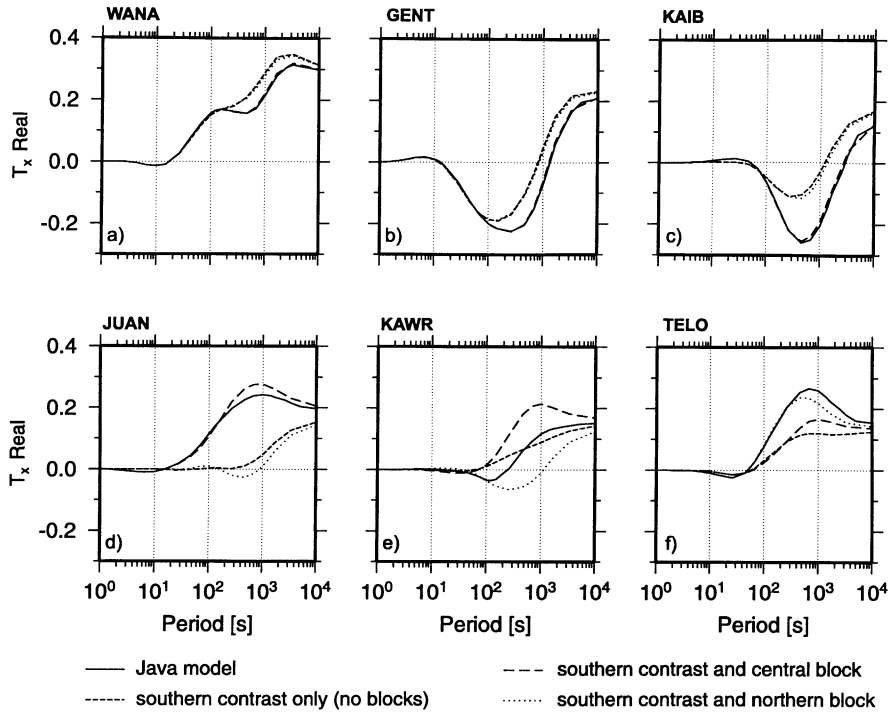

Fig. 12. Comparison of amplitudes of $\Re e(T_x)$ GDS response functions of the *Java model* with three model variations in which the conductivity structures of the *central* and *northern blocks* are successively removed. The model variations correspond to Fig. 8e. The results show the importance of the *southern contrast* for explaining the sign reversal between sites WANA and GENT. At site KAWR it becomes evident how the combined effect of all three structures produces the response of the *Java model*.

together with three model variations (Fig. 8e): (i) Java is modelled as a homogeneous block of 1 Ω m with a transition to 5 Ω m beneath sites GENT and BABA (*southern contrast*); (ii) the anomalous *central block* structure is added to the *southern contrast*; and (iii) the *northern block* structure is added.

The *southern contrast*, with its lateral change from 1–5 Ω m, is mostly responsible for the reversal of the magnetic response functions between sites WANA and GENT (Fig. 12a and b). To rule out that any other conductivity contrast causes the negative $\Re e(T_x)$ values of site GENT, the model was further simplified (Fig. 8f). The only vertical contrast left within the conductivity structure of Central Java is the*southern contrast*. Only the removal of this structure causes negative $\Re e(T_x)$ values at GENT to disappear. At site KAIB, the effect of the *southern contrast* is reduced but the influence of the *central block* anomaly becomes increasingly more important. This is expressed by the large negative $\Re e(T_x)$ values in Fig. 12c. The positive maximum at JUAN is almost entirely caused by the *central block* anomaly (Fig. 12d); the transition from 0.5 to 0.2 Ω m within the *central block* is required to generate the desired induction arrow lengths. The shape of the $\Re e(T_x)$ curve at KAWR is formed by superposition of *central block* and *northern block* anomalies (Fig. 12e); it is not caused by the Java Sea although the *ocean model* response curves in Fig. 11a are almost identically shaped. The north pointing induction arrows at TELO in Fig. 12f are predominantly generated by the *northern block* anomaly with an additional contribution from the *central block*. The inclusion of a 0.2 Ω m conductive core within the *northern block* is necessary to obtain correct amplitude/period relations.

We have also tested the influence of subduction-zone related features at greater depth. A conductive down-going slab, following the suggestions for the JUAN de Fuca subduction zone (Kurtz et al., 1986) or a block of partial melt at a depth of 100 km due to water released by dehydration reactions have no effect on the data, at least not at periods less than 10000 s. A crustal scale *central block* anomaly of 10 Ω m reaching down to 30 km depth which might represent pathways of rising magma produced in the lower crust, on the other hand, is compatible with the observed data and cannot be ruled out. Such a mid to lower crustal feature could be indicated by zone E in the inversion model (Fig. 7). However, as this conductor is not compulsory to fit the data it is omitted in favour of a minimum features model.

3.4. Three-dimensional modelling

Earlier, we discussed the fact that the data do not fully comply with the requirements of a two-dimensional model. Deviations from two-dimensionality are noticeable in the vicinity of the volcanic chain (BABA, GENT) and in the north between sites TELO and KAWR. Inductive features situated subparallel or obliquely to the profile cannot be correctly addressed by 2D modelling (cf. 'side-sweep' effect in Simpson, 2000). For the northern location between sites TELO and KAWR we test qualitatively what kind of 3D situation could be responsible for producing some of the observed effects. Fig. 13b shows induction arrows in a geographic co-ordinate system for the two sites. At TELO, the real arrows point towards the NW in the period range 30–1000 s, whereas SSE pointing real induction arrows are observed at KAWR in the period range from 20 to 400 s. A two-dimensional interpretation of these induction arrows would infer a SW–NE striking conductive zone between the two sites.

We used the 3D forward algorithm of Mackie et al. (1994) to model the behaviour of the induction arrows at longer periods. The model comprises the surrounding sea water (Fig. 13a) and the inner Javanese conductivity anomalies as derived from the 2D *Java model*. The *northern block* is now replaced with an elongated N70°E trending conductor, while the *central block* remains in position. The extensions of the model's inner core (Fig. 13a) are 228 km × 228 km horizontally and 8.3 km (plus some homogeneous layers) vertically. The grid lines of the 3D model are 4 km apart in both horizontal directions; more complex models exceed computational resources.

Fig. 13b and c compare the measured data of sites KAWR and TELO with 3D modelling results at six sites located north and south of the obliquely striking conductor. The modelling responses for periods up to 1000 s allow comparison with the data. The lengths of the induction arrows for periods greater than 2000 s are not fitted because the overall conductance of the Indian Ocean is too high to be modelled properly. At site 1 the real induction arrows are dominated by the Java Sea to the north. Only 12 km further south,

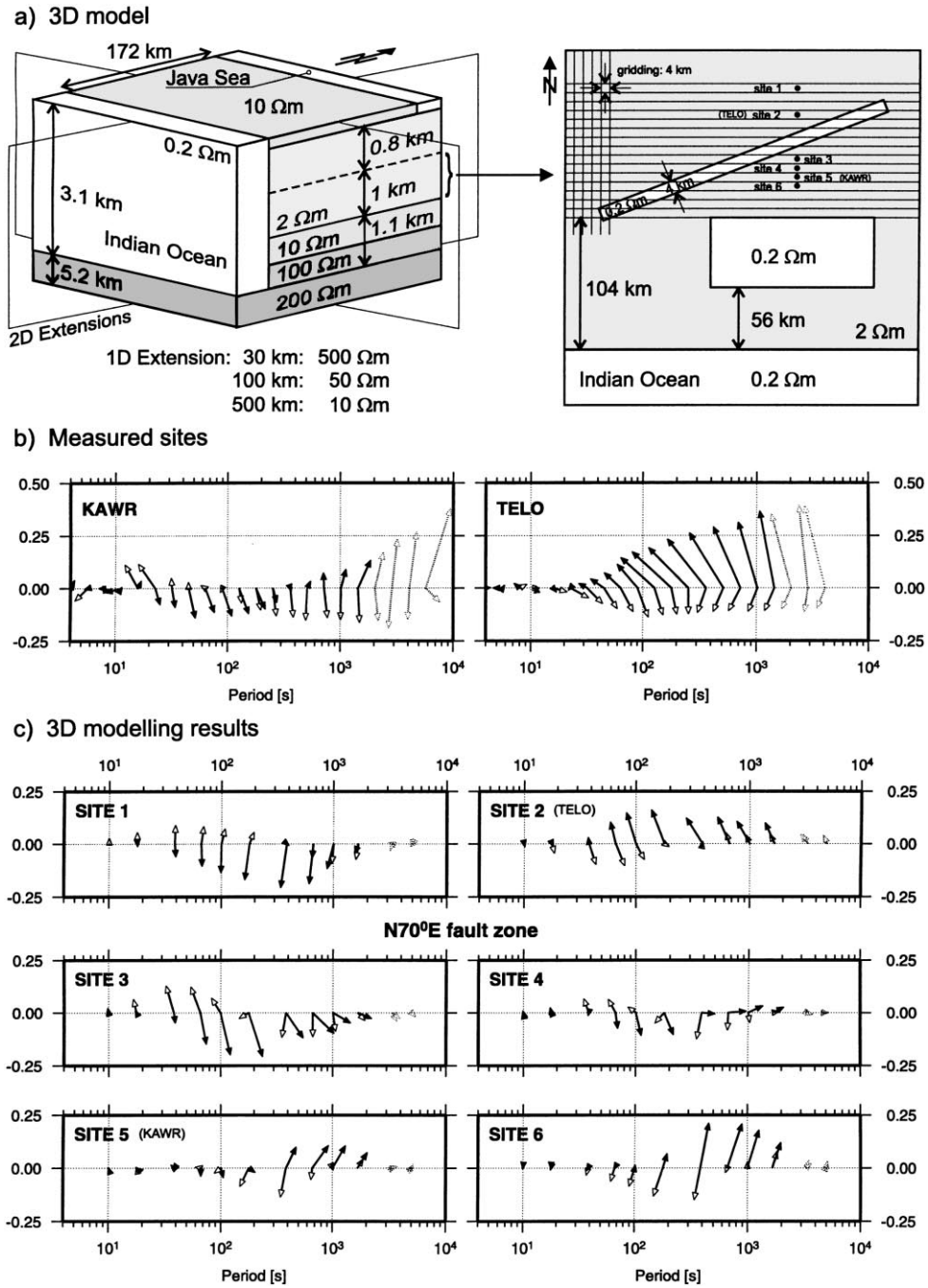

Fig. 13. Three dimensional modelling study that includes an obliquely striking conductor in the northern part of the island. The strike angle was chosen in agreement with the trend of the CJF (Fig. 1) and the Bahr angles at long periods (Fig. 6f). (a) 3D image of the model core. The 2D extensions expand the conductivity anomalies in N-S and E-W directions, respectively. The plan view shows a section of the model representing the situation at a depth of 2 km. The grid is homogenous, though only some of the grid lines are shown. (b) Measured induction arrows in Wiese convention for sites KAWR and TELO. The data are *not* rotated, hence upright arrows point towards the north. A much larger 3D core would be required to properly model the induction arrows at the longest periods (marked by dotted arrows). (c) Results of the 3D calculations: model sites 2 and 5 show some characteristics of sites TELO and KAWR, respectively.

at site 2 which corresponds to TELO, the arrows are reversed and clearly indicate the strike direction and position of the NE trending conductor. The influence of the obliquely-striking structure becomes smaller (shorter arrows) with increasing distance from it while the effects of the *central block* and the Indian Ocean begin to show up in north pointing real arrows at longer periods. The imaginary arrows reverse their orientation when the south pointing real arrows reach their maximum lengths. Site 5 resembles KAWR with SE pointing arrows between 40 and 200 s and NNE pointing arrows for longer periods. At site 6 the effect of the obliquely-striking conductor is no longer obvious. The longer period arrows (300–2000 s) straighten up because of the increasing influence of the EW striking structures to the south.

It should be noted that only the arrows of sites 3 and 4 in close vicinity to the conductor show a distinct three-dimensional behaviour, which is in agreement with our assumption of local distortion of a regional 2D conductivity structure across Java.

4. Discussion of the MT/GDS results in view of other geological and geophysical data

The results presented here indicate that the whole of Central Java is remarkably conductive. Within Java we can distinguish three conductivity anomalies, the *southern contrast*, the *central* and the *northern block*. What significance do these findings have in view of the geological and tectonic development of Java? Our compilation of other important geological and geophysical data is shown in Fig. 14.

The electrical conductivity of rocks depends mainly on the amount, connectivity and contents of the pore volume, whereas the matrix of the rock itself is very resistive. Generally, we would associate high conductivity with young marine and volcanoclastic sediments with little compaction, especially volcanic ashes. The massive, less porous igneous rocks of the Merapi and Muriah volcanic edifices, on the other hand, could be expected to be more resistive. Alteration of volcanic ashes and tuffs can result in the formation of clay minerals with a high capability to store water in the mineral lattice (montmorillonitic clays, bentonite). Clay layers of this kind can have resistivities below 10 Ω m (Jones and Dumas, 1993).

Low resistivity values between 1 and 10 Ω m which are typical for the shallow subsurface of Java (cf. Fig. 8a) can partly be explained by the thick Cenozoic sedimentary cover of marine and pyroclastic sequences (Van Bemmelen, 1949a,b; Hamilton, 1978). Their thickness, however, can only be estimated from surface geological observations. Natori (1978) assumes less than 1000 m for the southern part of Central Java. Via the intervolcanic lowland further to the north, with its Quartenary volcanic and continental-sedimentary series and the active volcanic axis (Van Bemmelen, 1949a), the sediment thickness rises to about 3000 m (marine sands, clays, marls and intercalated pyroclasts) in the northern part of the profile (Hamilton, 1978, 1979). The transition from 10 to 100 Ω m at a depth of approximately ∼2000 m in the *Java model* could therefore represent an averaged depth for the top of the basement. However, sediments alone cannot explain the observed regions of very high conductivity in Central Java.

In Section 3.3.2, we stressed that the inclusion of the *southern contrast*, with a lateral decrease in resistivity from 5 to 1 Ω m between sites GENT and BABA, was necessary for the two-dimensional interpretation of the data. It seems plausible that the higher conductivity is related to an increased geothermal gradient and/or the presence of melts as the profile approaches the axial volcanic ridge. Due to the wide site spacing however, we cannot be very exact on the position of this transition zone, nor can we decide if the change is more gradual or abrupt.

Interestingly, the highly conductive region of the *central block* is not situated directly beneath the active Merapi volcano but shifted towards the north. The position of the *central block* does correlate with the maximum of a negative Bouguer anomaly measured by Hasegawa and Untung (1978) (see Fig. 14b). The Bouguer anomaly traces the Kendeng zone with a local minimum of about −60 mgal east of sites KAIB and SCHI (Hasegawa and Untung, 1978; Green et al., 1981). Hasegawa and Untung (1978) suggest that the anomaly might be the result of a blister of magma at a depth of less than 30 km or a flake of upper crust underthrust by the oceanic crust (Sano et al., 1978). These two scenarios should be different in terms of electrical conductivity, but the very high conductivity of the *central block* anomaly makes it very difficult

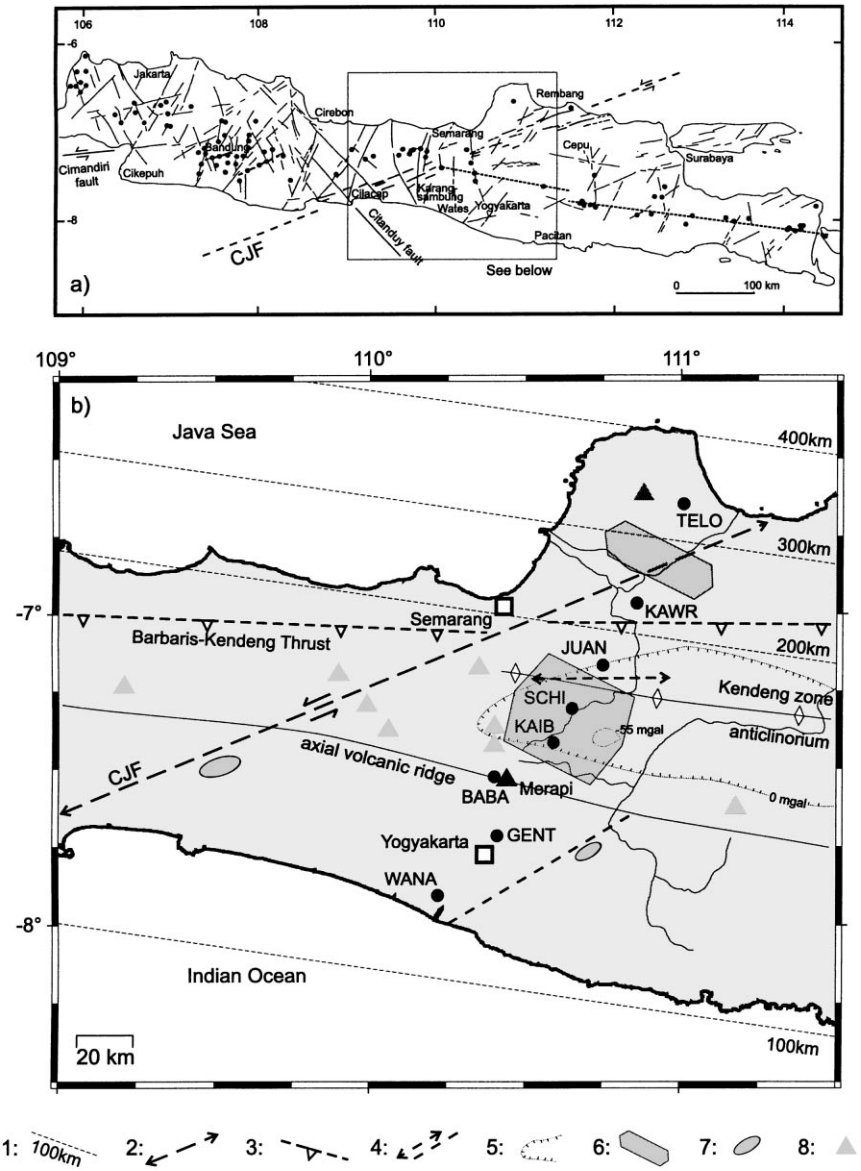

Fig. 14. (a) Tectonic lineaments on Java as inferred from satellite images (modified after Chotin et al., 1984b). Dots denote volcano summits; the short dashed line marks the volcanic axis in Central and East Java. Cimandiri fault according to Dardji et al. (1994), CJF: Central Java Fault zone. (b) Summary of the results of the magnetotelluric survey together with other geophysical and geological data. (1) Depth of Benioff zone according to Hamilton (1979). (2) CJF zone according to Chotin et al. (1984a,b). (3) Barbaris–Kendeng thrust according to Simandjuntak and Barber (1996). (4) Other faults according to Chotin et al. (1984a,b) and De Genevraye and Samuel (1973). (5) Region of negative Bouguer anomaly according to Hasegawa and Untung (1978). (6) Zones of high conductivity (South: *central block*; north: *northern block*. The lateral extensions, normal to the profile, are infinite in 2D models). (7) Ophiolitic mélanges: their positions relative to the faults are taken from Chotin et al. (1980). (8) Volcanoes: the black triangle denotes the Merapi volcano.

to resolve deeper structures with any confidence (see Section 3.3.2).

The localised character of the MT and GDS anomalies in the central and northern part of the profile suggest that the observed high conductivity could be related to tectonic structures like shear zones. Faults can cause electromagnetic anomalies because (i) two geologic units with different conductivity can be juxtaposed along a fault (Jones, 1998); (ii) the formation of a fractured, cataclastic zone along a fault can enhance the percolation of fluids and thereby cause higher conductivity (Unsworth et al., 1997); (iii) the shear planes of faults can be mineralised by a conducting phase of graphite, sulphide or iron oxide (ELEKTB Group, 1997). Any combination of the above options is possible. The important point is that it becomes possible to map fault zones at depth due to their increased conductivity. Central Java is covered with young volcanic and partly marine sediments which makes it very difficult to trace fault lines at the surface.

In the Late Pliocene a compressional stress regime developed which caused the formation of various E-W striking thrust faults in the northern half of Central Java (Simandjuntak and Barber, 1996; De Genevraye and Samuel, 1973). Two important upthrust zones are marked in Fig. 14b: the seismically active Barbaris–Kendeng thrust zone and a fault zone just south of site JUAN, supposedly originating from the basement with a vertical displacement of 1000 m (De Genevraye and Samuel, 1973). The position of this fault zone coincides with the northern boundary of the 0.2 Ω m core within the *centrol block*. This boundary was required to model northward-pointing real induction arrows at site JUAN in Section 3.3.2.

The position of the *northern block* anomaly between sites KAWR and TELO in Fig. 14b is in good agreement with the location of the CJF. The measured obliquely pointing induction arrows can be reproduced qualitatively with the three dimensional model in Fig. 13, which comprises a N70°E striking conductor. A likely candidate for the increased conductivity is in this case hot and saline fluids as hydrothermal springs and small mud volcanoes exist in the vicinity of site KAWR (e.g. Grobogan, Mrapen, Kuwu). The salinity of the Kuwu well is so high that it is used to produce salt. Serpent inites, which are contained within the ophiolitic mélanges (Hamilton, 1979), can cause low resistivity (Unsworth et al., 1997) but judging from the few outcrops in Central Java they are unlikely to form interconnected zones of increased conductivity. Graphitisation as the remnant of the shearing process can cause very high conductivity (Ritter et al., 1999). Organic carbon could be a source of this graphite, as it is abundant in the region in the form of coal measures and oil fields (e.g. near Cepu).

In view of the geodynamic development of Central Java we interpret our laterally extended conductivity anomalies as a broadly-fractured region in which faults provide conducting sites for fluid flow, mineralization or ascending melts. The setting of accretionary complexes between the old cratonized Sunda Land to the west and young oceanic crust in the east leads to this region of structural weakness. At the surface, this transition zone is expressed by (see Fig. 14a) a significant change in the pattern and density of faults and the spatial distribution of volcanoes; the latter are randomly distributed in the west and aligned along the volcanic axis in the east (Chotin et al., 1984a). The N70°E striking CJF system developed at least since the Miocene (Chotin et al., 1984b) within this transition zone and follows the Sunda Land margin.

5. Conclusion

We have modelled MT and GDS data along a profile across Central Java using 2D inversion and 2D/3D forward modelling approaches. The influences of the surrounding Indian Ocean and the Java Sea can be separated by hypothesis testing from conductivity anomalies inland. Within Java, several anomalies of extremely high conductivity can be distinguished from a generally very conductive shallow subsurface. Very deep structures that are directly related to the subduction process cannot be resolved.

We interpret the electrical anomalies as effects of a tectonic weak zone. Hot and saline fluids and/or partial melts are primary sources for high electrical conductivity in the vicinity of active volcanism. However, we could not find direct evidence for large magma accumulation in the immediate vicinity of the Merapi volcano. Present or historic tectonically active regions (under compression) are typically marked at the surface by strike-slip and thrust fault zones. On Java, their detection by geologic mapping methods is hampered since the whole island is covered by young volcanic

deposits. Our results show that electromagnetic sounding methods can help to locate such tectonic features if they become electrically conductive due to second order effects (fluid intrusions, mineralization).

Acknowledgements

This research project was supported by the German Science Foundation DFG (Ha1210/18) and by the Volcanological Survey of Indonesia. For their help during the field work we would like to thank E.M. Arsadi, S. Byrdma, S. Dwipa, F. Echternacht, A. Mahfi, A. Müller, and I. Nurnusanto. Reviews by Kathy Whaler, Sophie Hautot and Karsten Bahr are gratefully acknowledged.

References

Agarwal, A., Dosso, H.W., 1993. The characteristic periods of induction arrows for a conductive-resistive vertical interface — a numerical model study. Phys. Earth Planet. Interiors 76, 67–74.

Bahr, K., 1988. Interpretation of the magnetotelluric impedance tensor: regional induction and local telluric distortion. J. Geophys. 62, 119–127.

Bahr, K., 1991. Geological noise in magnetotelluric data: a classification of distortion types. Phys. Earth Planet. Inter. 66, 24–38.

Chamot-Rooke, N., Le Pichon, X., 1999. GPS determined eastward Sundaland motion with respect to Eurasia confirmed by earthquakes slip vectors at Sunda and Philippine trenches. Earth Planet. Sci. Lett. 173, 439–455.

Chotin, P., Giret, A., Rampnoux, J.P., 1980. Java island, a record of tectonic movements up a subduction zone (in French). Dull. Soc. Geol. France, Suppl. 22 (5), 175–177.

Chotin, P., Giret, A., Rampnoux, J.P., Rasplus, L., Suminta, S., Priyomarsono, S., 1984a. Scouting of fracturation in Java island, Indonesia (in French). Bull. Soc. Geol. France 6, 1325–1333.

Chotin, P., Rasplus, L., Rampnoux, J.P., Suminta, Nur Hasim, 1984b. Major strike slip fault zone and associated sedimentation in the central part of Java island (Indonesia) (in French). Bull. Soc. Geol. France 6, 1259–1268.

Daly, M.C., Cooper, M.A., Wilson, I., Smith, D.G., Hooper, B.D.G., 1991. Cenozoic plate tectonics and basin evolution in Indonesia. Mar. Pet. Geol. 8, 2–21.

Dardji, N., Villemin, T., Rampuoux, J.P., 1994. Paleostresses and strike-slip movement: the Cimandiri Fault Zone, West Java, Indonesia. J. Southeast Asian Earth Sci. 9 (1/2), 3–11.

De Genevraye, P., Samuel, L., 1973. Geology of the Kendeng zone (Central and East Java). In: Proceedings of the Annual Convention — Indonesian Petrol. Association, Vol. 1, Jakarta, pp. 17–30.

Elektb Group, 1997. KTB and the electrical conductivity of the crust. J. Geophys. Res. 102 (B8), 18289–18305.

Green, R., Adkins, J.S.Q., Harrington, H.J., Untung, M., 1981. Bouguer gravity map of Indonesia. Tectonophysics 72, 267–280.

Groom, R.W., Bailey, R.C., 1989. Decomposition of magnetotelluric impedance tensors in presence of local three-dimensional galvanic distortion. J. Geophys. Res. 94 (B2), 1913–1925.

Hamilton, W.B., 1978. Tectonic map of the Indonesion region. Scale 1:5 000 000. US Government Printing Office, Washington DC.

Hamilton, W.B., 1979. Tectonics of the Indonesian region, Vol. 1078 of Geol. Survey Prof. Paper. US Government Printing Office, Washington DC.

Hasegawa, H., Untung, M., 1978. Gravity — interpretation of results. In: Untung, M., Sato, Y. (Eds.), Gravity and Geological Studies in Java, Indonesia, Vol. 6 of Geological Surv. Indonesia (Geological Surv. Japan), Special Publication. Geol. Surv. Indonesia, pp. 46–70 (Chapter 2.4).

Hobbs, B.A., 1992. Terminology and symbols for use in studies of electromagnetic induction in the earth. Surv. Geophys. 13, 489–515.

Hutchison, C.S., 1989. Geological Evolution of Southeast Asia, Vol. 13 of Oxford Monographs on Geology and Geophysics. Clarendon Press, Oxford.

Jones, A.G., 1998. Waves of the future: superior inferences from collocated seismic and electromagnetic experiments. Tectonophysics 286, 273–298.

Jones, A.G., Dumas, I., 1993. Electromagnetic images of a volcanic zone. Phys. Earth. Planet. Inter. 81, 289–314.

Kieckhefer, R.M., Shor Jr., G.G., Curray, J.R., 1980. Seismic refraction studies of the Sunda trench and forearc basin. J. Geophys. Res. 85, 863–889.

Kurtz, R.D., DeLaurier, J.M., Gupta, J.C., 1986. A magnetotelluric sounding across Vancouver Island detects the subducting Juan de Fuca plate. Nature 321, 596–599.

Mackie, R.L., Smith, J.T., Madden, T.R., 1994. Three-dimensional electromagnetic modeling using finite difference equations: the magnetotelluric example. Radio Sci. 29 (4), 923–935.

Metcalfe, I., 1996. Pre-Cretaceous evolution of SE Asian terranes. In: Hall, R., Blundell, D. (Eds.), Tectonic Evolution of Southeast Asia, Vol. 106, Geological Soc. Special Publication, pp. 97–122.

Natori, H., 1978. Cenozoic sequence in Jawa and adjacent areas. In: Untung, M., Sato, Y. (Eds.), Gravity and Geological Studies in Jawa, Indonesia, Vol. 6 of Geological Surv. Indonesia (Geological Surv. Japan), Special Publication. Geological Surv. Indonesia, pp. 76–81 (Chapter 3.2).

Puspito, N.T., Shimazaki, K., 1995. Mantle structure and seismotectonics of Sunda and Banda arcs. Tectonophysics 251, 215–228.

Ritter, O., Haak, V., Rath, V., Stein, E., Stiller, M., 1999. Very high electrical conductivity beneath the Munchberg Gneiss area in Southern Germany: implications for horizontal transport along shear planes. Geophys. J. Int. 139 (2), 161–170.

Ritter, O., Hoffmann-Rothe, A., Müller, A., Dwipa, S., Arsadi, E.M., Mahfi, A., Nurnusanto, I., Byrdina, S., Echternach, F.,Haak, V., 1998a. A magnetotelluric profile across Central Java, Indonesia. Geophys. Res. Lett. 25 (23), 4265–4268.

Ritter, O., Junge, A., Dawes, G.J.K., 1998b. New equipment and processing for magnetotelluric remote reference observations. Geophys. J. Int. 132, 535–548.

Rodi, W., Mackie, R.L., 2001. Nonlinear conjugate gradients algorithm for 2-D magnetotelluric inversions.. Geophysics 66, 174–187.

Sano, S., Untung, M., Fuji, K., 1978. Some gravity features of island arcs of Jawa and Japan and their tectonic implications. In: Untung, M., Sato, Y. (Eds.), Gravity and Geological Studies in Jawa, Indonesia, Vol. 6 of Geological Surv. Indonesia (Geological Surv. Japan), Special Publication. Geol. Surv. Indonesia, pp. 183–207 (Chapter 5).

Simandjuntak, T.O., Barber, A.J., 1996. Contrasting tectonic styles in the Neogene orogenic belts of Indonesia. In: Hall, R., Blundell, D. (Eds.), Tectonic Evolution of Southeast Asia, Vol. 106. Geological Soc. Special Publication, pp. 185–201.

Simpson, F., 2000. A three-dimensional model of the southern Kenya Rift: departure from two dimensionality as a possible consequence of a rotating stress field. J. Geophys. Res. 105 (B8), 19321–19334.

Soeria-Atmadja, R., Surpaka, S., Dardji, N., 1998. Magmatism in western Indonesia, the trapping of the Sumba Block at the gateways to the east of Sundaland. J. Southeast Asian Earth Sci. 16 (2), 1–12.

Swift, C.M., 1967. A Magnetotelluric Investigation of an Electrical Conductivity Anomaly in the Southwestern United States. Ph.D. Thesis. MIT, Department of Geology and Geophysics, Cambridge, MA.

Unsworth, M.J., Malin, P.E., Egbert, G.D., Booker, J.R., 1997. Internal structure of the San Andreas fault at Parkfield, California. Geology 25 (4), 359–362.

Van Bemmelen, R.W., 1949a. The Geology of Indonesia — Vol. 1a: General Geology of Indonesia and Adjacent Archipelagos, 2nd Edition. Martinus Nijhoff, The Hague, 732 pp.

Van Bemmelen, R.W., 1949b. The Geology of Indonesia — Vol. 1b: Portfolio, 2nd Edition. Martinus Nijhoff, The Hague, 62 pp.

Widiyantoro, S., van der Hilst, R., 1997. Mantle structure beneath Indonesia inferred from high-resolution tomographic imaging. Geophys. J. Int. 130, 167–182.

Scientific Technical Report STR 05/10

GeoForschungsZentrum Potsdam

Geophys. J. Int. (2003) **153,** 548–568

A high-resolution magnetotelluric survey of the Iapetus Suture Zone in southwest Scotland

Sebastian Tauber,[1] Roger Banks,[1] Oliver Ritter[2] and Ute Weckmann[2,3]

[1] *Department of Geology & Geophysics, University of Edinburgh, Grant Institute, West Mains Road, Edinburgh* EH9 3JW, *UK. E-mail: Roger.Banks@ed.ac.uk*
[2] *GeoForschungsZentrum, Telegrafenberg, Potsdam,* D-14473 *Germany*
[3] *Universität Frankfurt, Institut für Meteorologie und Geophysik, Feldbergstrasse* 47, *Frankfurt,* D-60323 *Germany*

Accepted 2002 November 18. Received 2002 November 18; in original form 2001 November 6

SUMMARY

Magnetic variation (MV) surveys show a 40 km wide zone of high electrical conductivity in the middle crust extending across the Southern Uplands of Scotland from the North Sea to Galloway. A new magnetotelluric (MT) survey across the conductor in Galloway was designed to improve the resolution of structure in the depth range 1–15 km, and, at the same time, assess the improvement in resolution that could be achieved in a practical situation by optimizing data acquisition, processing, analysis and modelling. A 40 km long profile was measured, doubled for part of its length at a separation of 1 km, with a typical site spacing of 2 km or less. It was supplemented by shorter parallel and orthogonal lines, giving a total of 40 sites.

Galvanic distortion models involving regional 2-D structures gave poor fits to the impedance tensors both for the array as a whole and for individual sites, confirming the picture from induction arrow maps that many sites were influenced by 3-D structures on scales of a few kilometres and upwards. Other indicators of the electrical strike (regional and local MV measurements, the spatial structure of the Groom–Bailey regional impedance phase and of the rotated off-diagonal phase), gave values more in agreement with the geological strike of N52°E, which was adopted as the most appropriate coordinate system into which to resolve the data. The MT impedances were accordingly rotated into directions N38°W ('TM') and N52°E ('TE'), and inverted using the 2-D code of Rodi & Mackie. The investigation explored the sensitivity of the outcome to a wide range of starting model resistivities and roughness parameters, and to different data subsets. The 'TE' mode data were insensitive to structural detail, and the best fit achieved was unacceptable, suggesting the influence of structure outside the plane of the section. The 'TM' mode data could be fitted satisfactorily by varying the model roughness and gave the best control on the geometry of the conductive bodies. Forward modelling showed that the model generated from the 'TM' mode also fitted the MV data adequately.

The inversion resolved the conductive zone into distinct blocks, with edges matching faults mapped in the surface geology: the Leadhills, Fardingmullach and Orlock Bridge Faults, and the Moffat Valley lineament. In the resistivity image, the faults are vertical structures, disrupting other features to a depth of 15 km, which agrees with the view that, although they originated as thrusts, they were reactivated by strike-slip motion during oblique closure of the Iapetus Ocean. Within some of the blocks are highly conductive regions, no more than 4 km wide. The most likely explanation is graphite or other metallic mineralization, localized in shear zones.

Key words: continental crust, electrical conductivity, electromagnetic survey, magnetotellurics, magnetovariation, tectonics.

1 INTRODUCTION

The electrical conductivity of the crust beneath the Southern Uplands of Scotland has been investigated by repeated electromagnetic surveys, from Edwards *et al.* (1971) to Banks *et al.* (1996) (see the latter paper and Livelybrooks *et al.* 1993 for a list of references). Magnetic variation (MV) surveys at periods between 200 and 2000 s provide a regional-scale picture of conductive structures in the upper and middle crust. Fig. 1 is a hypothetical event map of the anomalous horizontal magnetic field at a period of 750 s. It has been computed from single-station transfer functions using the procedure described by Banks *et al.* (1993),

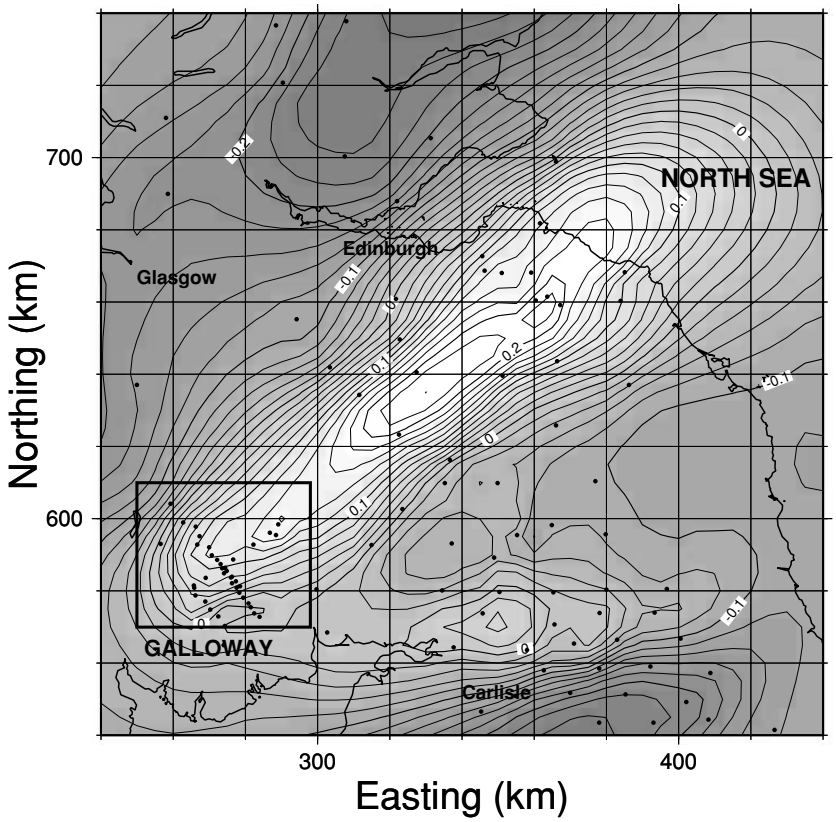

Figure 1. Magnetic variation anomalies in northern Britain. The map is a simulation of the horizontal magnetic field in the direction N45°W associated with a 1 nT horizontal magnetic field, direction N135°E at a reference site (Eskdalemuir magnetic observatory). The period of the electromagnetic field is 750 s. The direction of the horizontal field has been chosen to produce an undistorted image of the scattered currents created by a conductor aligned at N45°E. The anomaly maxima lie directly above the currents. Dots mark the positions of observations. The dense array of points surrounded by a box is the survey described in this paper. The box corresponds exactly to the area displayed in detail in Fig. 2.

but incorporating measurements from two new surveys, one by Junge (1995) extending coverage in the north and northeast, and one in the southwest, described in this paper. The parameters of the hypothetical event analysis have been chosen to optimize the spatial image of the conductor that runs northeast to southwest across the Southern Uplands, though they also provide a less optimal view of the conductor that runs east to west across northern England.

The new surveys confirm the continuity and horizontal extent of the conductor (at least 150 km), and precisely constrain its position in relation to the surface geology. It closely follows the trends of the major Caledonian faults and structural boundaries in the Southern Uplands (such as the Southern Uplands and Orlock Bridge Faults), changing orientation with them from N35°E in the northeast to N45°E in the southwest. The vertical magnetic field at the surface can be continued down to an equivalent current system in a thin sheet at a depth of 10 km (Banks 1979). The zone of enhanced currents, approximately 40 km wide, stretches from just southeast of the Southern Uplands Fault to 5 km southeast of the Orlock Bridge Fault, involving several of the crustal units into which the Southern Uplands is divided (see Fig. 2). Banks *et al.* (1996) suggested that the high conductivity was caused by graphite distributed throughout a block of meta-sedimentary rock that had been trapped at mid-crustal levels during the closure of the Iapetus Ocean. However, the high conductivity might instead be confined to a thin sheet marking the detachment zone where the Southern Uplands accretionary complex was thrust over the Avalonian basement rocks. The movement could have assisted conversion of the carbon-rich Moffat Shales to graphite (Jödicke 1992; ELEKTB group 1997).

Magnetic variation measurements are a valuable tool for mapping the lateral extent of conductors but provide only limited constraints on their depth. Magnetotelluric (MT) measurements are much more effective in this respect. Banks *et al.* (1996) compiled a database of the existing MT surveys of the Southern Uplands (referenced in Livelybrooks *et al.* 1993), and added new sites to create a composite profile that crossed both of the conductive structures shown in Fig. 1. Most of the new measurements were concentrated in the southern section, and the improved data quality led to a much more detailed image of the southern conductor. Because of the wider station separation and poorer quality TM mode data, the northern conductor was less well resolved. It appeared as a single feature in the electromagnetic image, continuous across strike, and of uncertain depth extent, and the 1996 survey was unable to determine its relationship to structures seen at the surface. A new survey was required, designed to resolve structure at depths between 1 and 15 km. It also provided the opportunity to assess the improvement in resolution that could be achieved *in a practical situation* by optimizing as many as possible of the different phases of MT data acquisition, processing, analysis and modelling.

2 THE SURVEY AREA AND ITS GEOLOGY

2.1 Choice of survey area

The area selected was in Galloway, in southwest Scotland. Previous MV surveys suggested that the conductive structure continues southwestwards from the profile investigated by Banks *et al.* (1996). A short MT line in the Thornhill basin (Beamish 1995) indicated that the crust below 8 km was moderately conductive. It also detected narrow conductive zones in the upper crust, possibly associated with the Caledonian faults. Galloway is largely rural, so that low levels of cultural noise could be anticipated. The area has been the target of detailed geological remapping by the British Geological Survey (Barnes *et al.* 1995; Phillips *et al.* 1995), and structures there are probably better known than in any other part of the Southern Uplands. With a single 40 km profile (see profile A in Fig. 2), it was possible to traverse a number of features, each of which (if associated with a mineral such as graphite) were potential conductors. They were: outcropping carbonaceous (black) shales repeating near the base of each thrust-bounded block of crust; a thrust that had been reactivated as a strike-slip fault during the closure of the Iapetus Ocean (the Orlock Bridge Fault); and a ductile shear zone (the Moniaive Shear Zone) which accommodated the strike-slip motion at a deeper level. A high-resolution MT survey might establish whether there were a physical connection between one or more of these structures and the region of high conductivity known to be present at depth. The existence of such a link would place important constraints on explanations for the high conductivity.

2.2 The geology of the survey area

It is thought that the Southern Uplands formed in Ordovician and Silurian times as an accretionary prism on the Laurentian margin of the Iapetus Ocean. Wedges of sediment were thrust over one another, creating a series of tracts bounded by thrust faults. Within each tract, the sediments were young to the northwest, but overall the tracts become progressively younger in a southeasterly direction. The sediments are predominantly greywackes, but carbonaceous shales (the Moffat shales) are present towards the base of each tract (Fig. 2). During the closure of the Iapetus Ocean, the entire accretionary wedge was thrust to the southeast over Avalonian basement. The detachment surface over which movement occurred is thought to be at a depth of 8–10 km (Leggett *et al.* 1983). The weakness of the shales may have assisted the movement. As the Iapetus ocean closed, Avalonia moved obliquely relative to Laurentia. Some of the NE–SW-aligned structures, such as the Orlock Bridge Fault, are believed to have been reactivated as sinistral strike-slip faults to accommodate the motion (Phillips *et al.* 1995). For over 100 km, the southern margin of the Orlock Bridge fault is formed by a ductile shear zone up to 5 km wide—the Moniaive Shear Zone. This zone probably represents a deeper and earlier expression of the sinistral deformation associated with the closure of Iapetus. During the Carboniferous period, vertical movement occurred along NW–SE faults. Consequently, the structural level exposed by erosion changes along strike, with the deepest levels exposed in the area between the Cairnsmore of Fleet granite and Moniaive (Stone *et al.* 1995). Although the main lithological and structural boundaries are aligned NE–SW, any associated conductive

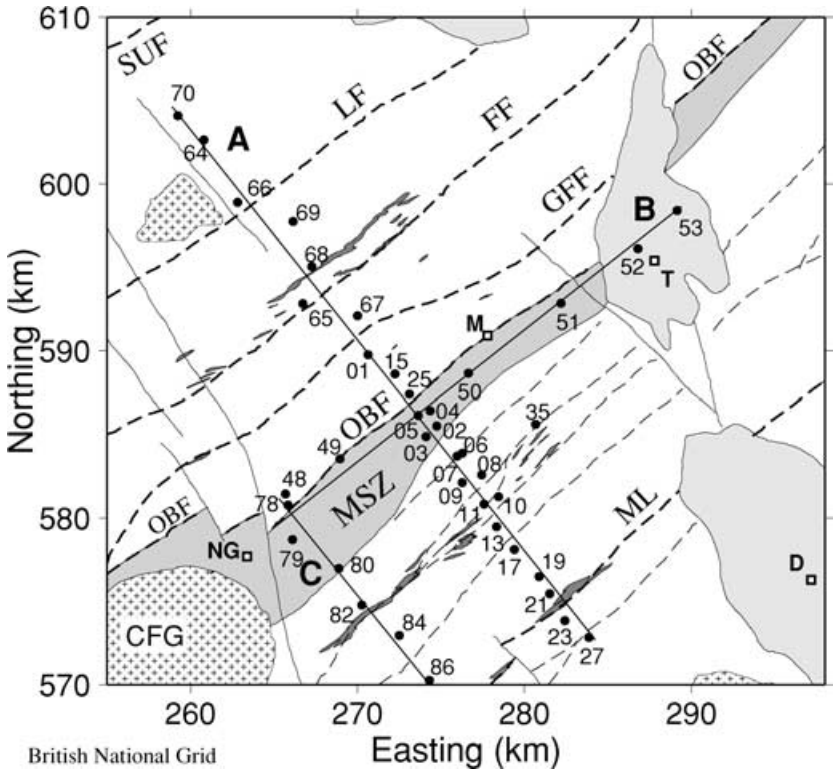

Figure 2. Location of MT sites (filled circles) in relation to Galloway geology (see Fig. 1 for the location of the map area). Black dashed lines, NE–SW tract-bounding faults (Caledonian); continuous lines, NW–SE normal faults (Carboniferous); unshaded areas, Ordovician and Silurian greywackes; light-shaded areas, Carboniferous/Permo-Triassic sediments; thin dark streaks, carbonaceous shales; broad dark zone (MSZ), Moniaive shear zone; + +, granite batholiths (CFG, Cairnsmore of Fleet). SUF, Southern Uplands Fault; LF, Leadhills Fault; FF, Fardingmullach Fault; GFF, Glen Foumart Fault; OBF, Orlock Bridge Fault; ML, Moffat Line. D, Dumfries; T, Thornhill; M, Moniaive; NG, New Galloway.

features may have been disrupted by the later faulting, creating 3-D structures.

3 FIELD MEASUREMENTS

3.1 General considerations in the design of the survey

An important element in the experimental design was the need to achieve a small station separation on the main MT profile (A in Fig. 2). Although the lithology of the surface rocks is relatively uniform, they are cut by faults, shear zones and black shales, and our aim was to try to detect and trace conductive zones associated with these narrow features as close to the surface as possible, so that they could be identified. Any spatial redundancy in the measured impedance would also help in the detection and correction of static shifts. In practice, a spacing of 1–2 km proved to be a reasonable compromise between what was logistically feasible and what was desirable for optimum resolution. The effect of small-scale heterogeneities and larger-scale 3-D structures outside the line of the main profile is often assessed by decomposing the impedance tensor at each site under the constraint of a limited 3-D model (Bahr 1988; Groom & Bailey 1989). We felt it was essential to support the results from such analysis by a limited form of 3-D survey. The SPAM III data acquisition system (Ritter *et al.* 1998), has the facility for recording data from a local base simultaneously with one or more remote sites, linked by up to a kilometre of digital cable. We made use of the capability to establish two parallel profiles on the main line, separated by the 800 m length of digital cable. By comparing the results, the consistency of the structure along strike could be assessed. Unfortunately, the transputer-based network proved to be vulnerable to interference from animals, etc., which caused the system and the recording to hang up. As a result, only part of the profile was duplicated. However, the main line was also supplemented by a shorter parallel profile a few kilometres away (C in Fig. 2), and by a number of separate sites forming a widely spaced profile parallel to the geological strike (B in Fig. 2). Recordings from independent systems were synchronized for remote reference processing by GPS timing.

3.2 Data acquisition

The main MT profile (profile A in Fig. 2) was aligned perpendicular to the strike of the principal Caledonian structures (N55°E). Its location was largely determined by access and communications. Two experiments were carried out, in 1997 October and 1998 October, each of 4 weeks duration. The first utilized a total of seven SPAM III data acquisition systems, two from the Natural Environment Research Council (NERC) Geophysical Equipment Pool, two from Edinburgh, two from the GeoForschungsZentrum (GFZ), Potsdam, and one from the University of Frankfurt. The bulk of the induction coils (Metronix MFS05) and silver/silver chloride electrodes were supplied by Potsdam; the NERC pool contributed CM11E coils. With this equipment, we were able to keep as many as six MT sites operational at any time, including one running continuously at a fixed location. The equipment at each site was programmed to the same pattern of data acquisition, synchronized by GPS. SPAM III is capable of continuous sampling at a rate of 512 Hz for all frequencies less than 128 Hz. However, to reduce the volume of stored high-frequency data, the two highest-frequency bands were recorded in a scheduled mode of hourly samples lasting 2 min (128–16 Hz) and 17 min (16–2 Hz). Frequencies less than 2 Hz were sampled continuously. At least two runs of 2.5 d were recorded at each site. The very highest-frequency band (1000–100 Hz) was acquired with daytime runs of a few hours duration.

The second experiment was on a smaller scale, aimed at filling in gaps left by the first and adding longer-period measurements at key locations. Unfortunately, problems with the prototype of the NERC long-period logging system prevented the acquisition of any long-period MT data. However, the bandwidth of the Metronix coils was such that the data they generated covered most of the frequency range required to penetrate the conductive middle crust. A further nine SPAM III sites were occupied.

One possible contribution to noise in the impedance data, relative to a 2-D interpretative model, is static shift caused by small-scale lateral variations in the resistivity of the surface layer. We intended to make use of the capability of the SPAM III system for multichannel input to detect and correct for local distortions in the electric field. At a number of sites electric field data were acquired with a range of different dipole lengths and geometries. These experiments showed that static shift effects were present on a scale of tens to hundreds of metres, and were related to topography of the bedrock surface beneath the cover of wet, peaty soil. However, the logistics of laying out complex networks of cable in forested areas proved difficult. Improving noise rejection using arrays of electrodes may only be feasible in much more open country. We relied instead on the close site spacing and the doubling of the profile to detect and correct for static shift effects. As it turned out, 3-D structures on a scale of kilometres rather than tens or hundreds of metres proved to be a more severe problem.

4 RESPONSE ESTIMATION

In all, 50 Gbytes of data were acquired at 40 sites, much of it of very high quality thanks to the low cultural noise levels. For most sites, robust remote reference processing (Egbert & Booker 1986) generated consistent, high-precision estimates of the MT impedance and MV transfer functions. The consistency of the resistivity and phase data was tested using the ρ^+ approach of Parker & Booker (1996), which also helped to identify suspect estimates in the dead band, and to establish an error floor of 3 per cent for the impedance values. Fig. 3 shows the impedances expressed in geographical coordinates (X, north; Y, east) at four representative sites distributed along the main profile. The dashed lines on each diagram show the ρ^+ response that best fits both the apparent resistivity and phase, together with the 68 per cent confidence limits on it. Values plotted as open circles were judged to be incompatible with the ρ^+ response, and were rejected. They are commonly in the period range from 0.1 to 10 s, which includes the 'dead band'. A different problem was identified at the most southerly locations on the profile, of which site 19 is representative. The data quality is good, but the phase of the impedance, ϕ_{YX}, exceeds 90° at periods beyond 100 s, suggesting strong 3-D effects. At site 10, the high phases across much of the measured frequency range signal the presence of a very strong conductivity anomaly.

5 STRIKE DETERMINATION

5.1 Induction arrow maps

A key step is to decide whether the data are compatible with a 2-D conductivity model, and to identify the electrical strike direction. One approach is to use the magnetic variation response. At periods

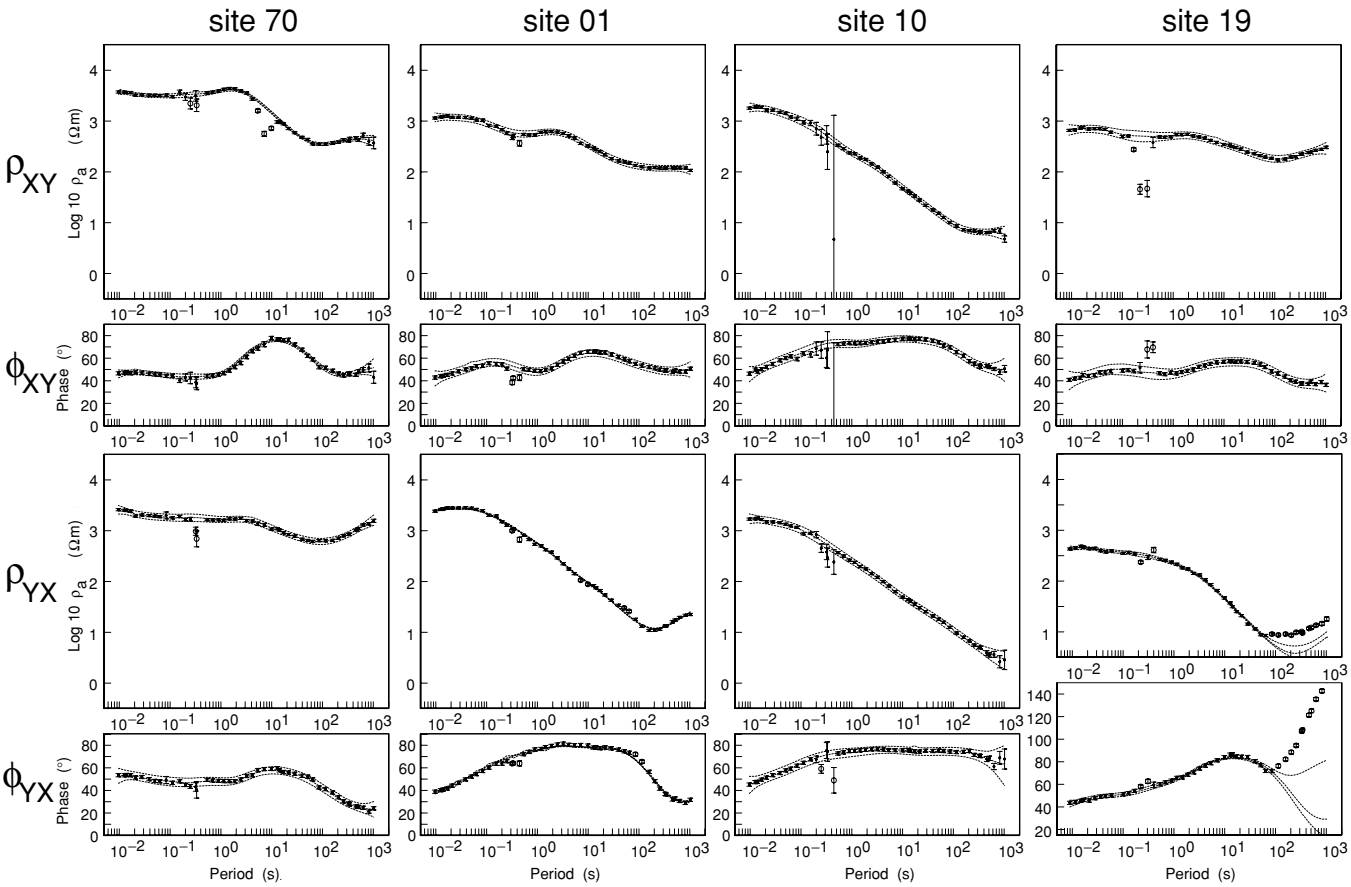

Figure 3. Apparent resistivity (ρ_{XY} and ρ_{YX}) and phase (ϕ_{XY} and ϕ_{YX}) responses measured in geographic coordinates (X, north; Y, east) at representative sites 70, 1, 10 and 19 on profile A (Fig. 2). The dashed lines show the best-fitting ρ^+ response and the 68 per cent confidence limits. The outliers in the dead band, marked by open circles, are subsequently excluded on the basis of the ρ^+ analysis.

greater than 100 s, the MV transfer functions for the Galloway sites are broadly consistent with the regional picture. The induction arrows (Fig. 4) indicate the presence of a 2-D conductor, aligned N45°E and concentrated beneath and to the south of the Orlock Bridge Fault. Even at 114 s, however, the real arrows at sites south of the Moniaive Shear Zone suggest the additional influence of a conductive structure to the east of the main profile. The arrows are tiny, but very consistent both in their magnitude and direction. The influence of the second conductor grows as the period decreases. The spatial pattern of arrows at 5 s period (and, less clearly, at 0.5 s) is suggestive of a conductive block running NE–SW and coinciding with one of the belts of black shale, but terminating east of profile A. The structure might be created by changes along-strike in the depth or thickness of the principal conductor. Vertical displacements on the NW–SE Carboniferous faults could cause such changes. Faults are marked immediately to the east of profile A, and also further east, associated with the Thornhill Basin. In the absence of more sites in the east of the area, we cannot say which is more likely to be responsible. What is clear from the MV data is that the overall 2-D regional structure (strike ∼N50°E) is disrupted by 3-D features with a spatial scale of a few kilometres, which most strongly influence the fields at periods less than 5 s.

5.2 Hypothetical event analysis of the MV response

When the size of 3-D inhomogeneities is small relative to the scale-length of the electromagnetic field, the scattered electric field is in-phase with the regional field. If the regional structure is 2-D, the impedance tensor and MV response simplify when the response is predicted for fields aligned with the regional strike. Ritter & Banks (1998) suggested using Argand diagrams of the vertical magnetic field generated by hypothetical event analysis, to detect the event direction that gave a consistent phase at sites in an array. Fig. 5 shows Argand diagrams of the Galloway response at a period of 750 s for a range of hypothetical event directions. The most consistent phase is generated when the horizontal field direction is N140°E, indicating a strike of N50°E. This is typical of the results for the period range for which the scattering model appears to be appropriate. At periods of less than a few tens of seconds the response is controlled by local induction effects.

5.3 Single-site Groom–Bailey analysis

Conventional (single-site and frequency-by-frequency) Groom–Bailey decomposition (Groom & Bailey 1989) and similar multifrequency, multisite analysis (McNeice & Jones 2001) also relies on a model in which the regional structure is assumed to be 2-D, with the local electric field at each site influenced by galvanic distortion. Application of the method generates correct values for the regional strike as long as the model itself is correct, but gives misleading answers when the actual structure is 3-D (Simpson 2000). Fig. 6 shows the Groom–Bailey parameters at site 1. The regional strike has a consistent orientation between 0° and −15° over three

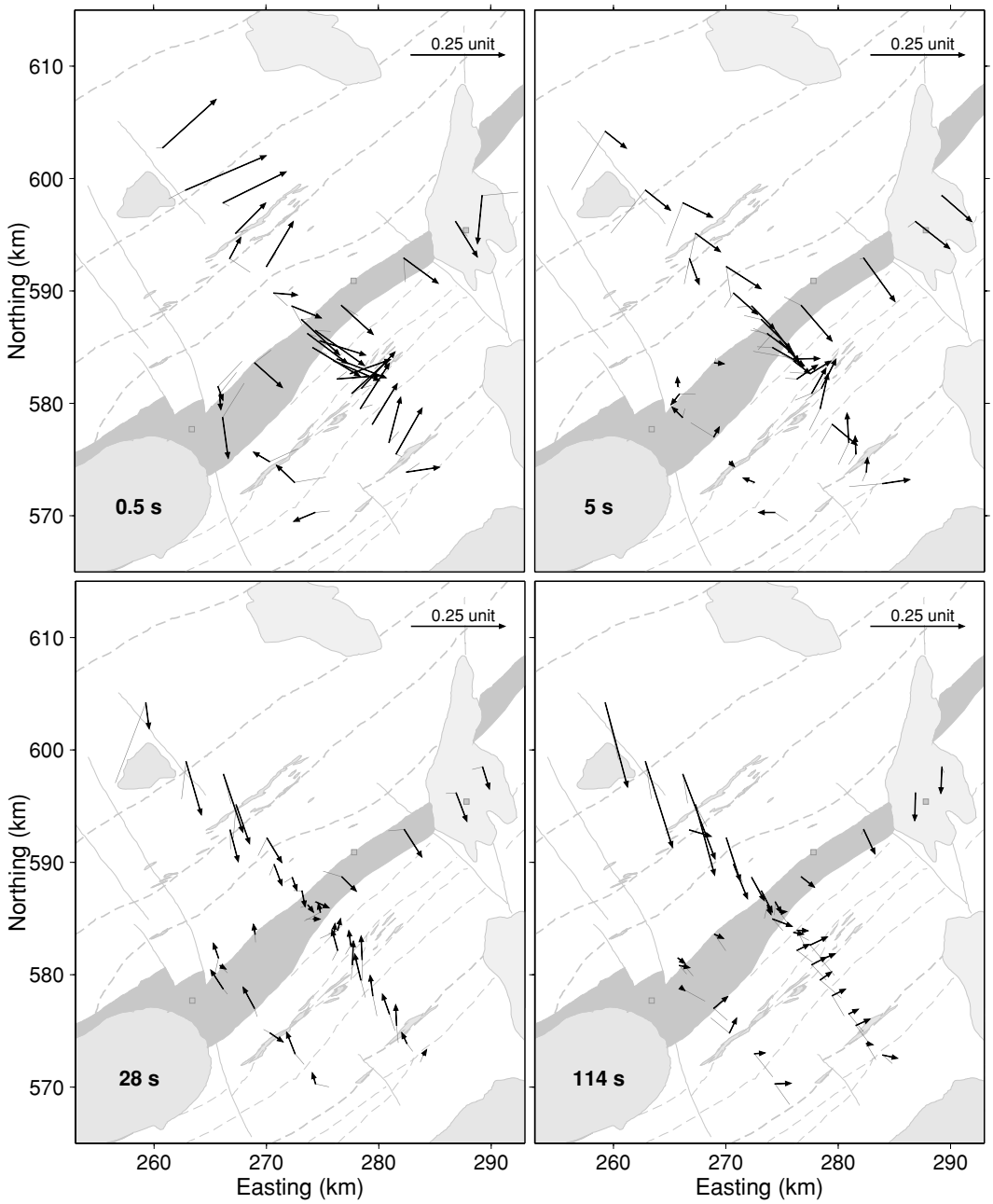

Figure 4. Maps showing the spatial variability of the induction arrows (Parkinson convention) at representative periods. Solid arrows are the real vectors; dotted lines the imaginary. The arrows are superimposed on a map of the main geological structures displayed in Fig. 2.

decades of period, but becomes unstable at periods shorter than a few seconds. Also, the fit of the model to the measured impedance is poor over most of the observed range of periods, and the same is true for many of the sites.

5.4 Multisite Groom–Bailey analysis

If an array of sites is influenced by the same 2-D regional structure, the measured impedances can be rotated to the same selected direction, the galvanic distortion model fitted to each, and the misfit summed over all the sites. The rotation angle is then varied to find the direction that gives the best overall fit to the observations (Smith 1995). Fig. 7 shows how the misfit varies with rotation angle for five periods that span the range investigated. At none of the periods (with the exception of the longest) does the model fit the data well. The difference at 750 s is that the error bounds on all the impedances are substantially wider. At most periods, the misfit is relatively insensitive to the rotation angle. However, the angle that minimizes the misfit does change systematically with period. At 0.05 s it is N55°E, in agreement with the geological strike. At 0.5 s, it has rotated to N70°E, at 5 s it is N85°E and at 50 s it is due east. At the longest period it rotates back to N80°E. Such behaviour could be interpreted as being the result of a change of electrical strike with effective depth of penetration. However, because of the poor performance of the model in describing the observations, and the likely importance of intersite variability, it would be unwise to give much weight to this result.

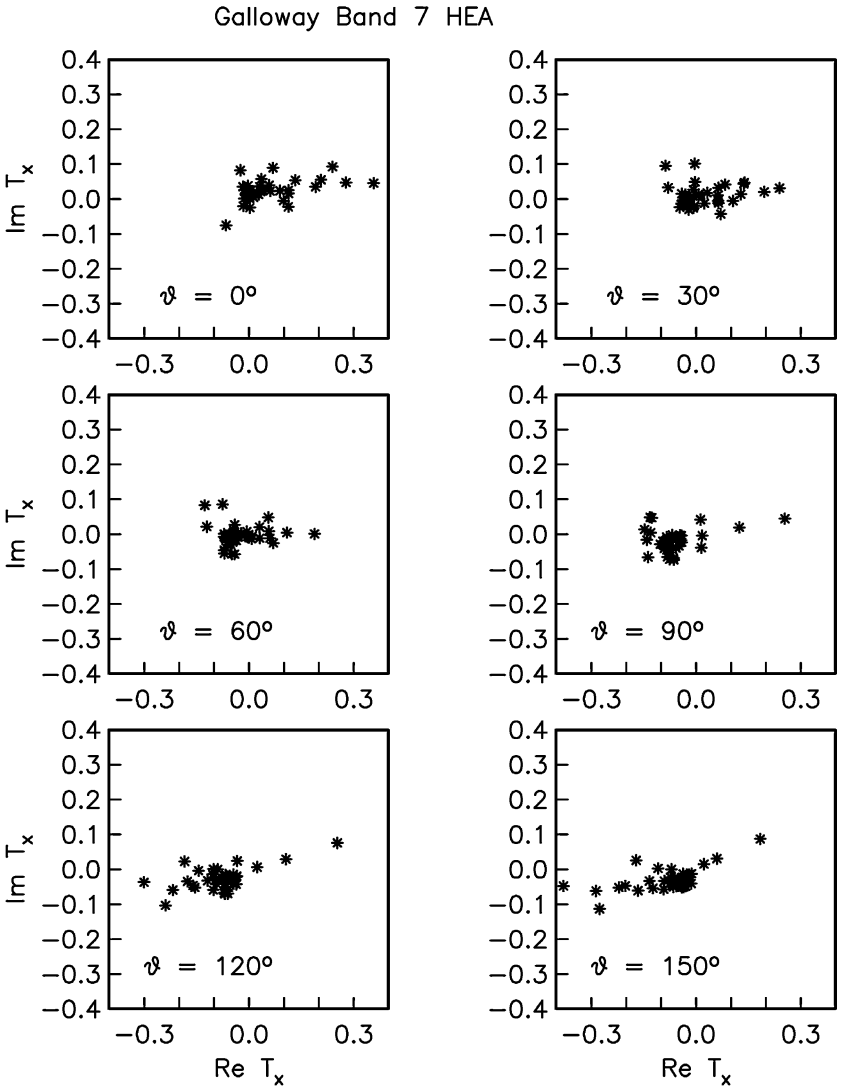

Figure 5. Hypothetical event analysis (Ritter & Banks 1998) of the Galloway MV data for a period of 750 s. θ is the direction (degrees E of N) of the hypothetical event in the horizontal magnetic field. The phase of the vertical magnetic field has a consistent value at all sites when θ lies between 120° and 150°. Further refinement suggests that the optimum value of θ is 140°, indicating a strike direction of N50°E.

5.5 Maps of the Groom–Bailey regional phases

Given the indications that the underlying assumption of the Groom–Bailey approach (that the regional structure is 2-D) is inappropriate, we decided to seek a method of quantifying the directionality of the electromagnetic field data that was not model-dependent. The information that is not used in the Groom–Bailey decomposition is the spatial organization of the measurement sites, and the spatial structure of the fields. One of the problems in quantifying the spatial structure is the impact of static shift and galvanic distortion in causing intersite variability on a scale smaller than the site separation. As a way of minimizing the aliasing of the structure, we took as our measure of the electromagnetic field the values of the regional TE and TM mode impedance phases extracted at each site using the Groom–Bailey approach. These parameters should possess spatial consistency not to be expected from the raw impedances because of the local distortion. Fig. 8 shows maps of the single-site Groom–Bailey rotation angle and TM and TE mode phases at three representative periods. Although the number and distribution of sites is limited, the spatial structure of the TM mode phase is reasonably well constrained by the two NW–SE profiles, and shows that, for periods between 3 and 300 s, the strike angle is around N45°E, and consistent with the geology.

5.6 Power spectra of phase maps

The use of the Groom–Bailey parameters is clearly unsatisfactory as a complete solution to the problem of quantifying the spatial structure of the field, because it still incorporates the assumption that the regional structure is 2-D. To avoid this element entirely, we have used the phase of the Z_{xy} element of the impedance tensor at a given period, rotated at all sites to the same selected azimuth. The geometry of the phase map can be characterized by the spatial covariance function or its Fourier transform, the 2-D spatial power spectrum. The power spectrum is most readily determined by computing the Fourier transform of the data, but this requires it to be interpolated on to a regular grid. Given the limited spatial coverage of our network, we can expect considerable uncertainty in the resultant spectrum. The algorithm we have used to grid the data is one that uses all the

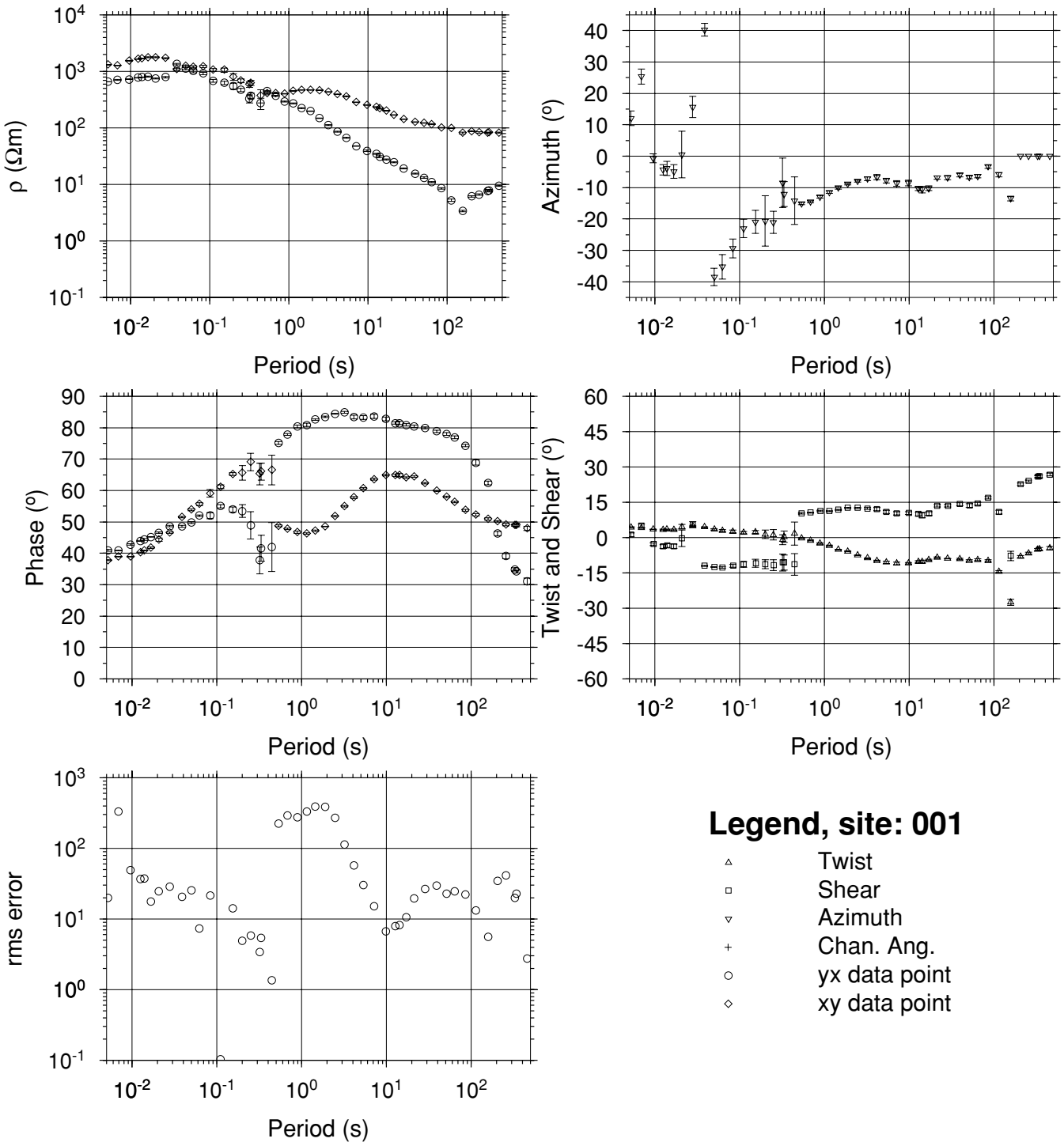

Figure 6. Groom–Bailey single-site parameters for site 1. A strike angle (azimuth) between 0° and −15° is indicated, but the fit of the model is poor.

measured data, weighted according to the distance of the sites from the required grid points. It deals relatively well with the problem of simulating data outside the measurement area, and also in avoiding short-wavelength features associated with closely spaced sites.

2-D features in the map appear as high-power structures along radial lines in the power spectrum, oriented at 90° to the anomalies. In order to quantify the directionality of the phase anomalies, we sum the power in pie slices in the wavenumber domain, each defining an equal angular range $\delta\phi$ ($\phi = \tan^{-1} k_y/k_x$, where k_x and k_y are the components of the wave vector in the x and y directions, respectively). A plot of the power against ϕ quantifies the relative importance and 2-D of anomalies with different directions. To investigate the change in the map as the excitation (direction of the horizontal magnetic field) is varied, we recompute $P(\phi)$ as the rotation angle (θ) of the impedance tensor is varied between 0° and 180°, and plot the power as a function of ϕ and θ. Fig. 9 shows the outcome for a period of 50 s. '2-D' structures should respond to excitation by a range of horizontal field directions, with maxima at

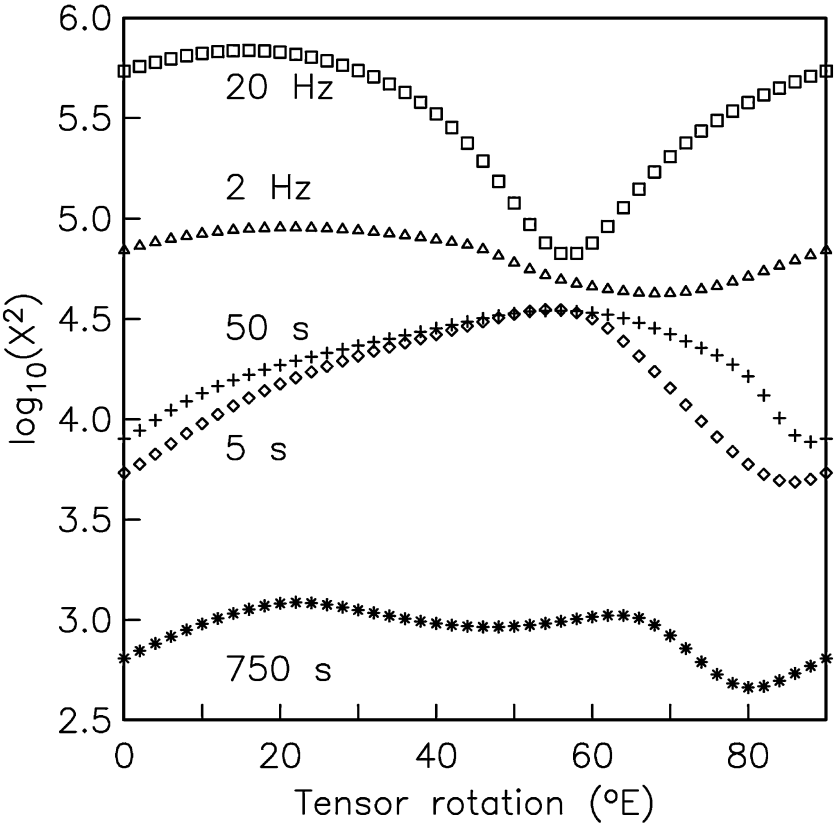

Figure 7. Dependence of misfit (summed over all sites) on the angle through which the impedance tensors at all sites are rotated. The model fitted is a 2-D regional structure with local galvanic distortion (Smith 1995). Except at 20 Hz, the misfit is relatively insensitive to the rotation angle. The suggested strike angles vary from N55°E to N90°E.

90° to the strike of the structure (the TE mode) and parallel to the structure (the TM mode). These maxima are likely to be different because of the difference in response of the structure to the two modes—the TE phase anomaly is distributed over the width of the conductor, while the TM phase anomalies are associated with the boundaries (see, e.g., Weidelt 1975). The maximum power at any excitation should correspond to the alignment of the structure. Two such features appear in Fig. 9, indicating structures aligned N5°W and N25°E. The latter feature changes with period and clearly relates to structures in the corresponding maps. The former is a fairly consistent feature at all periods, and may be an artefact generated by the site distribution and gridding procedure. Its presence suggests that we should be very cautious in drawing any firm conclusions concerning the strike using this method when the site distribution is restricted. However, we feel that the approach has many merits for analysing electromagnetic fields associated with complex 3-D structures, and will show its value in situations where the site distribution is more regular.

5.7 Interpredictability of TM mode apparent resistivities and phases

One further way of deciding whether the correct strike angle has been selected is to test the compatibility of the rotated TM mode apparent resistivities and phases (Parker & Booker 1996). For a 2-D structure, the TM mode phases should be predictable from apparent resistivities and vice versa, which suggests that the interpredictability could be used to test whether the chosen strike direction (and implied TM mode direction) is correct. The procedure adopted was to rotate the impedance tensor to a specified angle, and attempt to fit a D^+ model to the combined apparent resistivity and phase data. The misfit of the model is plotted as a function of the rotation angle. When the impedance tensors at the southern sites (already identified as showing unacceptable phases at the longest periods) are rotated in the quadrant from N45°W to N45°E, the misfit of the assumed TM mode does not show a strong dependence on the rotation angle. The misfit is marginally unacceptable for rotation angles in the range $-20°$ to $+20°$, but otherwise acceptable. We decided to follow the suggestion of Parker & Booker (1996), and also test the assumed TE mode. The misfit of the D^+ model to the combined data set (bottom panel in Fig. 10) strongly discriminates against rotation angles between $-20°$ and $+20°$, and the best fit is achieved for an angle between N35°W and N45°W. When the impedance tensor is rotated to N38°W, the TE phase lies in the correct quadrant and the apparent resistivity and phase are mutually compatible. On its own, this cannot be regarded as a 'strong' result, since it is not known under what conditions the TE response should pass the 1-D response test. However, the difference in sensitivity of the phase response of the two modes to 3-D effects is itself an indicator that they have been correctly identified. These pieces of evidence should be regarded as a small reinforcement of all the others assembled in support of the selected strike direction.

5.8 The choice of reference directions

It is unfortunate that analysis of the impedance tensor fails to give a clear answer to the question of whether a 2-D model is adequate,

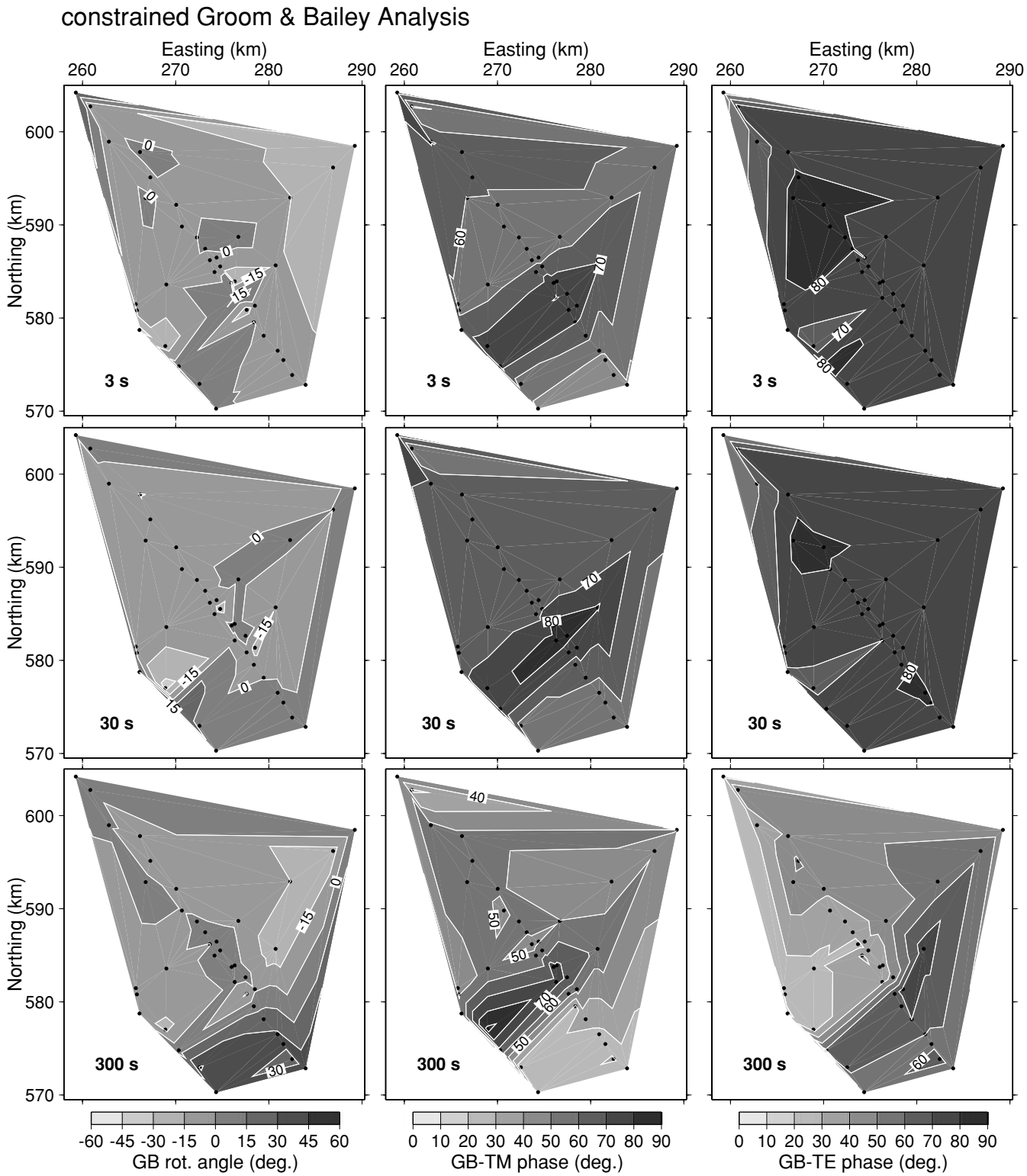

Figure 8. A comparison between the optimum Groom–Bailey angle and the spatial structure of the TM and TE mode phases. The preferred Groom–Bailey rotation angle is small (<15°) everywhere except in the extreme southeast. In contrast, the phases (particularly the TM mode) of the 'regional' impedance, independently determined at each site, follow the geological strike.

and if so which directions best represent the TE and TM modes. The tensor decomposition model fails to fit the observations adequately, either when the entire array is considered, or at the level of a single site. The electromagnetic environment of the majority of the sites must be influenced by electrical structures that are 3-D on a scale, which is significant when compared with the inductive scalelength, rather than being much smaller as the galvanic distortion model assumes. The cause of the 3-D effects may be structures on a scale

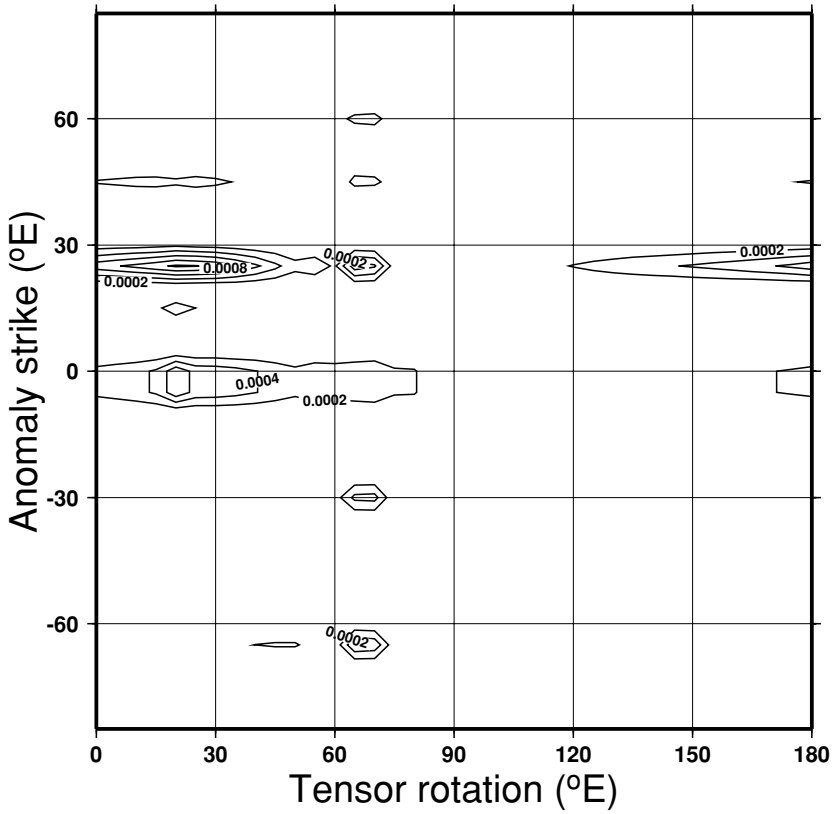

Figure 9. Distribution of power with azimuth in response to different rotation angles of the impedance tensor. The *y*-axis is the strike direction of 2-D features in maps of the phase of the Z_{xy} component of the impedance tensors. The tensors at all sites are rotated through the angle specified on the *x*-axis. This angle can be thought of as the direction of the regional electric field created in response to a uniform horizontal magnetic excitation at 90° to it. The period of the electromagnetic field is 50 s.

of kilometres or more, such as the changes along strike caused by the later cross-cutting faulting. Alternatively, they could be rock fabrics representing the response to changing patterns of deformation with depth, which could be treated numerically as a form of anisotropy (Heise & Pous 2001).

In this situation, we are driven back to those observations that directly relate to the spatial structure of the electromagnetic fields and the conductivity. The regional MV observations (Fig. 1) give the clearest image of the fields. That they also correctly identify the regional alignment of the conductive structures is shown by the models that have been derived from MT surveys that cross the MV anomaly at widely separated points along its length: at (347E, 666N) in East Lothian (Sule & Hutton 1986; Sule *et al.* 1993), at (314E, 634N) (Banks *et al.* 1996) and at (290E, 600N) (Beamish 1995). The agreement between the implied conductivity alignment, the geological structures and the orientation of other geophysical anomalies, particularly gravity, has convinced us that the directions to which we should rotate our electromagnetic observations in order to achieve the greatest simplicity are N38°W and N52°E. Because of the importance of the 3-D effects, these directions cannot be regarded as representing the TM and TE modes in the conventional sense. It is, however, convenient to label them as 'TM' and 'TE'. Because the decomposition model is invalid, we have not used it to extract 'regional' impedance values from the measured tensors, but have simply rotated them to our preferred directions. Note that, because the main profile was aligned on the basis of the geological strike, its direction coincides with that of the 'TM' axis.

6 MT PSEUDO-SECTIONS

Fig. 11 shows pseudo-sections of the 'TM' and 'TE' mode phases along the main profile (A in Fig. 2). Because of the 3-D effects discussed in Section 5, structures outside the line of the profile may contribute to some features in the pseudo-sections. In both the 'TE' and 'TM' mode sections the upper and middle crust can be loosely divided into three 'layers'. The resistivity of the surface layer is high (greater than 1000 Ω m) and uniform. It clearly corresponds to the Ordovician and Silurian meta-sedimentary rocks. At frequencies less than 10 Hz, the phase of both modes increases to values in the range 60°–70°, indicating the presence of an underlying conducting layer. Only at periods beyond 100 s does the phase fall again, showing that the deepest layer penetrated is resistive.

The 'TE' and 'TM' mode phases are noticeably different in their resolution of structure. The lateral variations in the 'TE' mode phase are generally smooth, with the exception of the high-frequency, high-phase feature immediately south of the Orlock Bridge fault (sites 6–9). Previous surveys of the Southern Uplands conductor (Livelybrooks *et al.* 1993; Banks *et al.* 1996) relied heavily on the TE mode data because its quality was higher than that of the TM mode. Features such as this were interpreted by models in which the conductive layer shallowed from 8 to 3 km depth. However, the 'TM' mode pseudo-section is able to resolve more complex structure across strike. It shows there are two principal conductive blocks separated by a more resistive unit. The high density of sites and the high quality of data give us confidence that the lateral changes in phase are really as abrupt as they appear. At least three of them match closely with

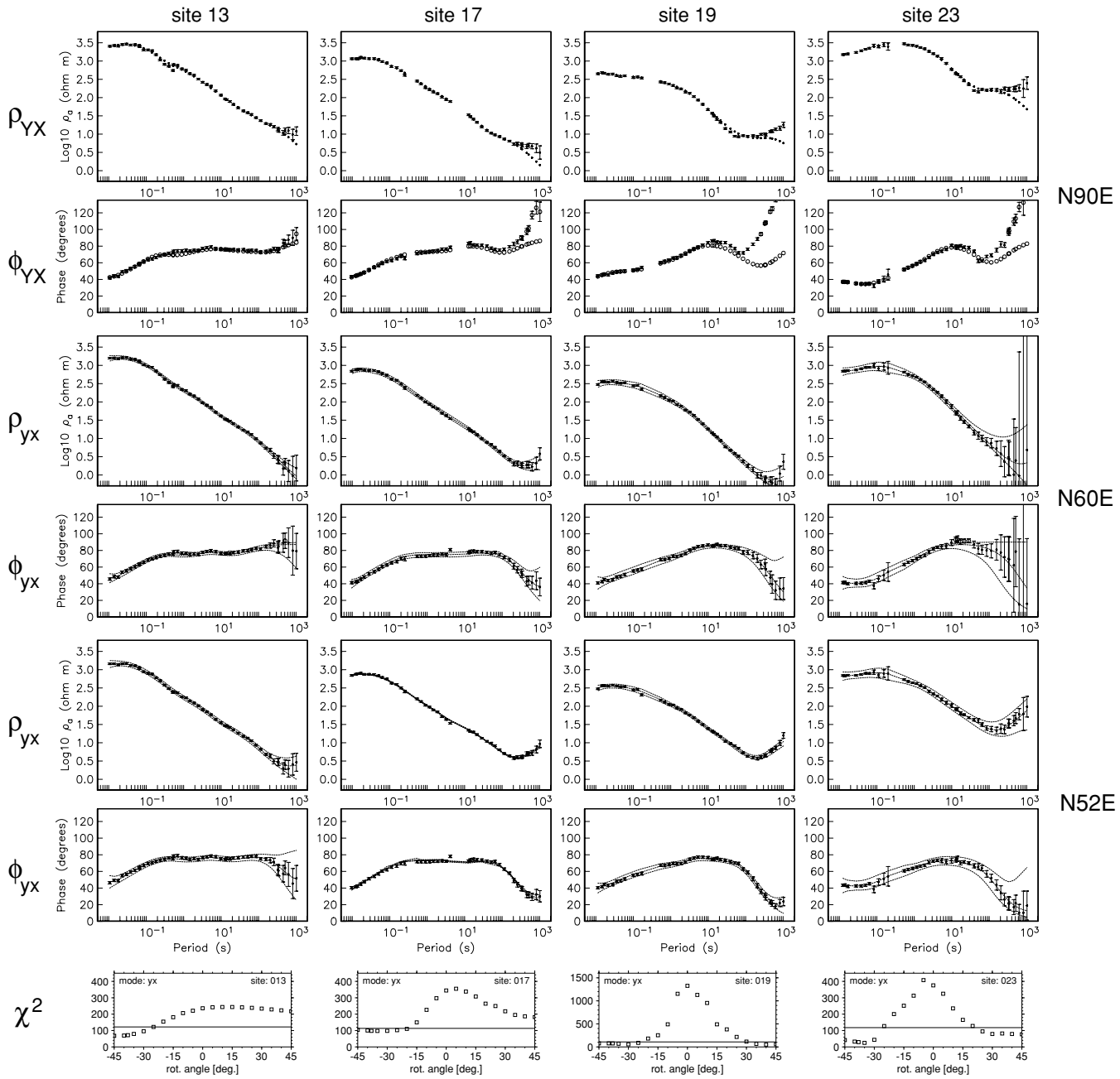

Figure 10. Apparent resistivity (ρ_{yx}) and phase (ϕ_{yx}) responses for sites on the main profile south of the Orlock Bridge fault. The impedance tensors have been rotated into directions that correspond to electric field alignments of N90°E, N60°E and N52°E. The lowest graphs display the χ^2 misfit of the ρ^+ analysis for individual sites as a function of the angle (relative to geographic north) through which the impedance has been rotated. The horizontal line marks the limiting value for an acceptable misfit.

the location of tract-bounding faults. Proceeding south along the profile, the southward conductive–resistive transition between sites 67 and 1 coincides with the Glen Foumart fault; the strongly marked resistive–conductive transition at sites 4 and 5 is immediately south of the Orlock Bridge fault, while the conductive–resistive change at site 17 marks the Moffat Valley lineament. Whatever is responsible for the conductive layer, its spatial geometry has been modified by movements on the tract-bounding faults. Perhaps this happened when they were first created as thrusts. More probably, it occurred later when they were reactivated as strike-slip or normal faults.

The highest-frequency parts of the phase pseudo-sections are relatively featureless, with only hints of the narrow structures we hoped to detect. Where such features are derived from observations at a single site they must be interpreted with caution. The high 'TM' mode phase at site 68 may be caused either by the nearby outcrop of black shale, or by a 3-D structure outside the line of the section. High 'TE' mode phases at sites 6–9 occur just to the north of another belt of black shale outcrops, but there is nothing to be seen at sites 21 and 23, which are similarly situated. If there is a relationship between the high conductivity and the occurrence of the black shales,

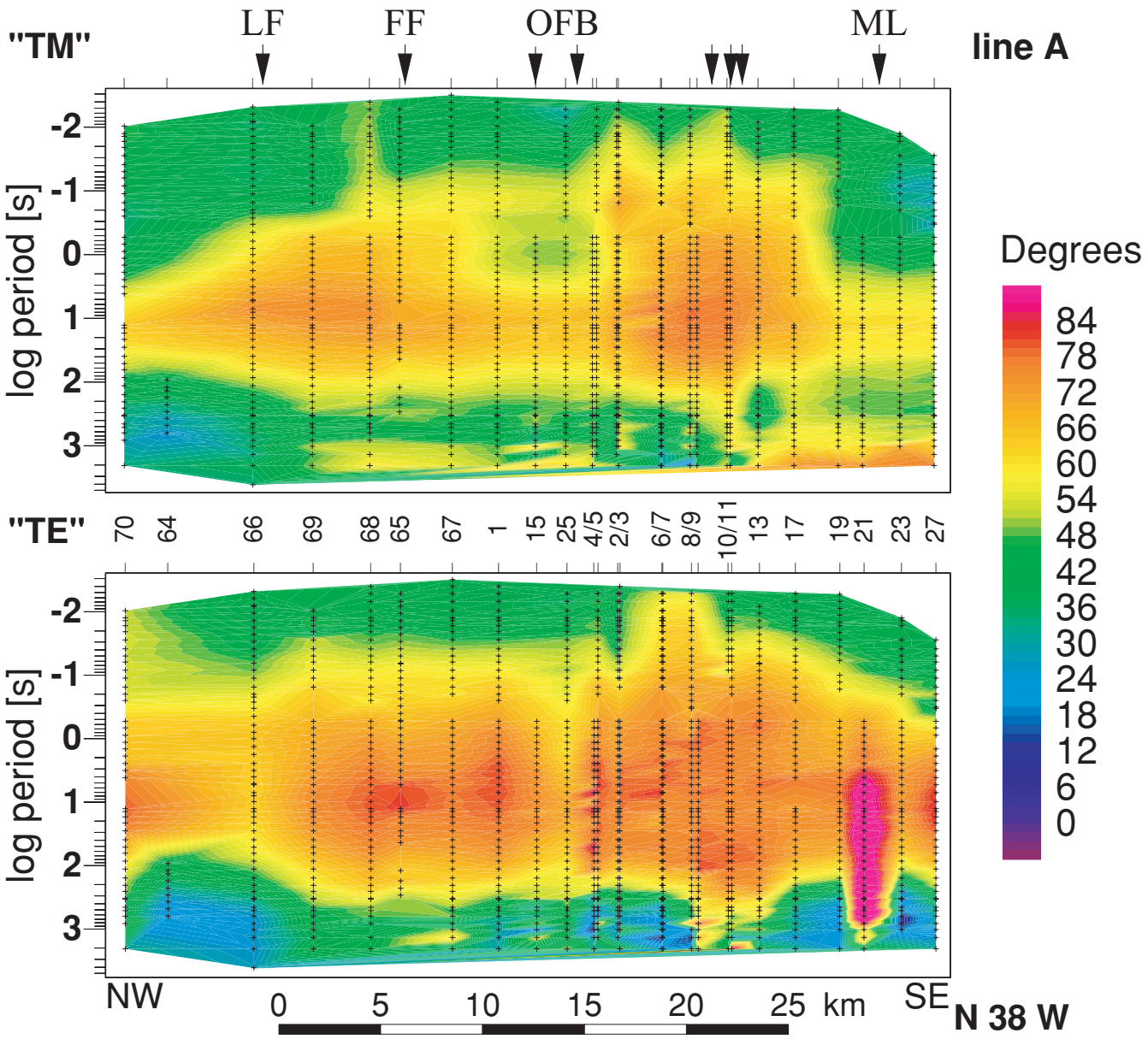

Figure 11. Pseudo-sections of the 'TM' and 'TE' mode phases along profile A in Fig. 2. The data were rotated into a direction N52°E. The 'TM' component is parallel to the profile, the 'TE' component along strike. The crosses show the coverage of the impedance estimates in space and frequency. LF, Leadhills Fault; FF, Fardingmullach Fault; OBF, Orlock Bridge Fault; ML, Moffat valley lineament.

it is not a simple one that can be readily detected in the near-surface environment.

7 2-D INVERSION

The MV data (Fig. 4) show that the electromagnetic fields at sites along profile A are influenced by 3-D fields outside the plane of the section, particularly at periods of 5 s and less. Ultimately, it will be necessary to assess the impact of the 3-D structures on the profile data by full 3-D modelling. However, 2-D modelling/inversion of the main profile is an essential first step towards constructing a model of the conductivity structure. Indeed, we hope that the first-order conductivity structures are 2-D. In order to extract them successfully, it is necessary to down-weight those features in the data that are most susceptible to the influence of the second-order 3-D structures. For instance, the effects of static shift can be minimized in initial inversions by giving greatest weight to the phase data. Its impact on the apparent resistivity pseudo-sections can be assessed and corrected for at a later stage. Larger-scale 3-D structures will affect the 'TE' mode data more than the 'TM', so initial model searches may be restricted to the latter.

'TM' and 'TE' mode response data for profile A were inverted using the 2-D code of Rodi & Mackie (2001). The starting model is a half-space of resistivity ρ_h. The aim of the inversion is to find the model that minimizes a penalty function made up from a combination of misfit to the observations and a measure of the model roughness, in proportions determined by a parameter τ. When τ is small, the emphasis is on achieving a good fit, which requires a rough structure. When τ is large, the emphasis is on finding a smooth model, which will necessarily fit the data less well.

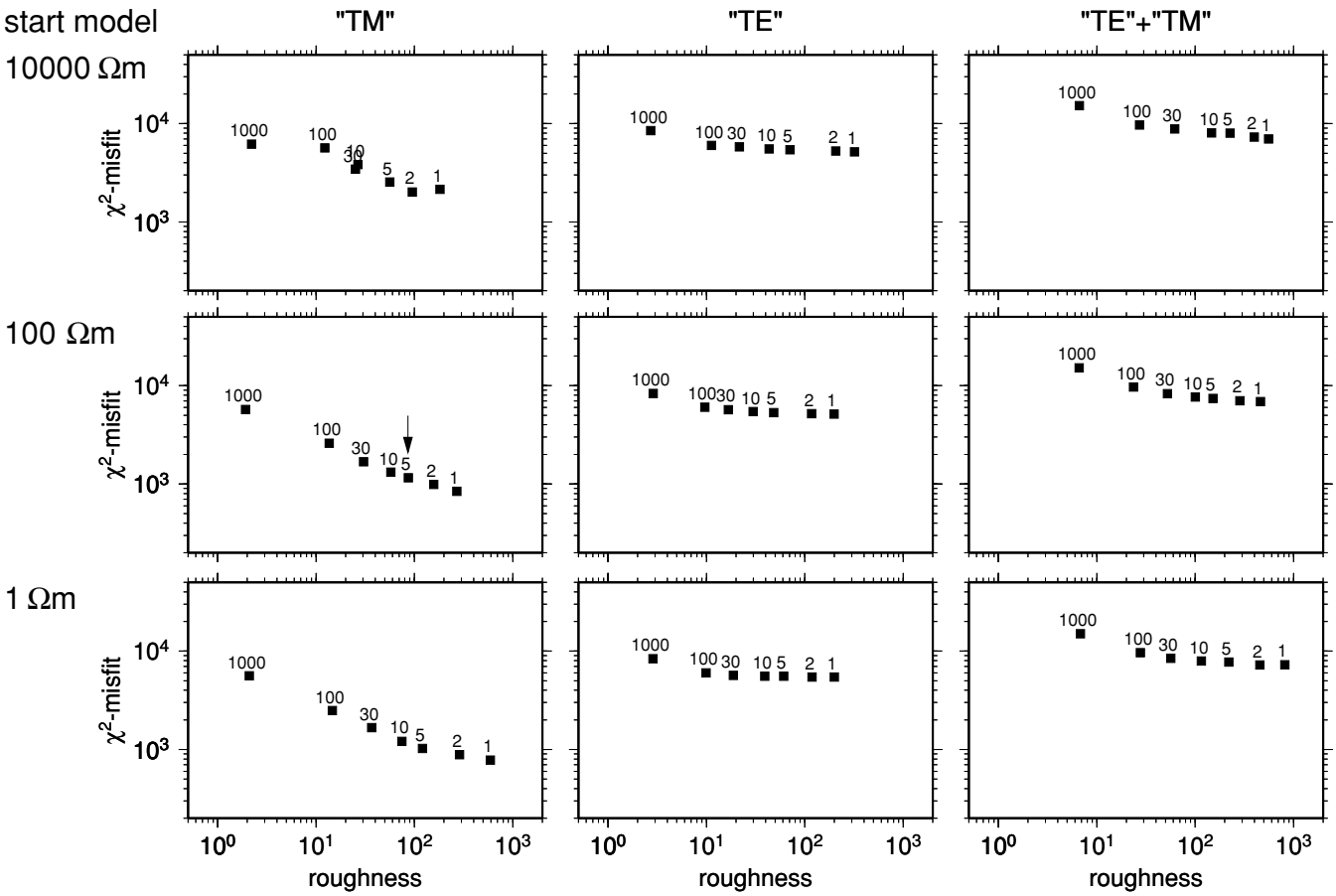

Figure 12. Interdependence of the data misfit (χ^2) and model roughness of 2-D models obtained by inverting the combined data set (right-hand column), 'TE' mode alone (centre column), and 'TM' mode alone (left-hand column). Each plotted point is labelled by the value of τ, which determines the weight of the model roughness relative to data misfit in the penalty function minimized. Each row corresponds to a different choice of the resistivity of the half-space that is the starting point of the inversion. The arrow points to the combination of τ and ρ_h selected for the model displayed in Fig. 16.

Considerable efforts were made to explore a wide range of the parameters and options (listed below in italics) which might influence the inversion. Their effects were judged by examining: (1) the overall data misfit of a given model as a function of its roughness (Fig. 12), and as a function of both τ and ρ_h (Fig. 14); (2) the distribution of rms site misfits with position along the profile (Fig. 13); and (3) the models themselves (Fig. 15).

(1) *The structure and size of the grid delimiting the resistivity model.* The size of the grid elements, particularly in the upper layers of the model, was refined until no further improvement in the misfit was achieved with all other parameters fixed.

(2) *Procedures for dealing with static shift.* The likely influence of static shift was handled by down-weighting the phase data relative to the apparent resistivity in the inversion. This was achieved by assigning an error floor of 1.72° to the phase (corresponding to a 3 per cent error in the impedance), and a higher error floor to the apparent resistivity. Inversions with error floors of 6 per cent (no static shift) and 25 per cent were compared. The models generated from the 'TM' mode data were relatively insensitive to the choice, but it made a substantial difference to those generated from the 'TE' mode. The 25 per cent error floor was adopted for the remaining experiments and the final inversions.

(3) *The subset of the data that were inverted—'TE', 'TM' or both.* Fig. 12 shows how the overall model misfit changes in response to the parameter τ for a range of starting model resistivities. The three columns display the behaviour when the two modes are inverted separately and together. When the 'TM' mode data are inverted on their own (left-hand column), the misfit decreases steadily and consistently as τ decreases and the roughness measure increases. The rougher models ($\tau \leq 10$) generate misfits that are distributed relatively uniformly among sites along the profile (Fig. 13a), with an rms misfit of 1 sd (standard deviation). When the 'TE' mode data are inverted on their own, however, there is much less improvement in fit either overall or at individual sites as τ is reduced (*cf.* Fig. 12). The rms misfit in the centre of the profile can be as low as 1 sd, but towards the northern and southern ends generally exceeds 2 sd (Fig. 13b). Irrespective of the choice of other parameters, no model can be found that fits the 'TE' mode data in a wholly acceptable way. Either the errors in the 'TE' response observations are systematically underestimated (which seems unlikely because of the similarity in level of misfit of the 'TE' and 'TM' modes in the ρ^+ analysis), or there is an inherent misfit in the 'TE' mode owing to the influence of structures outside the plane of the section. Whatever the cause, the choice of parameters and the resultant model should be more strongly influenced by the need to fit the 'TM' mode data rather than the 'TE' mode. As might be expected, when the combined 'TE' and 'TM' mode data set is inverted, it is the inability to find any model that fits the 'TE' mode that controls the response to changes in the roughness parameter and starting resistivity.

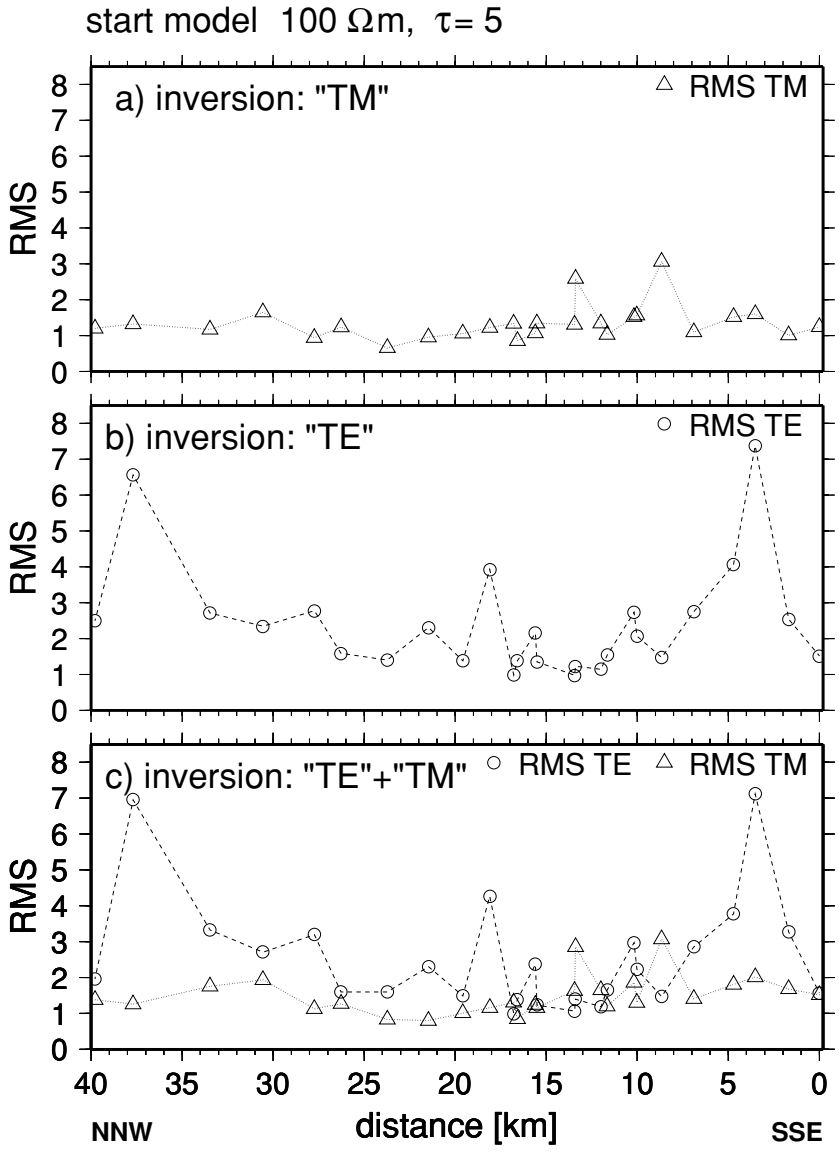

Figure 13. rms data misfits along profile A, fitting (a) the 'TM' mode alone, (b) the 'TE' mode alone, (c) both modes.

(4) *The parameters* τ *(which control the relative weights of data misfit and model roughness) and* ρ_h (*the resistivity of the half-space that is the starting point of the inversion*). Fig. 14 shows how the overall rms misfit changes in response to reducing τ (increasing roughness) from 1000 to 1, and to varying ρ_h between 10^{-1} and 10^4 Ω m. Improvements in the 'TM' mode fit as τ is reduced (Fig. 14a) are achieved for a wide range of starting models ($0.1 \leq \rho_h \leq 1000$ Ω m), indicating that the data definitely require the rougher structures corresponding to $1 \leq \tau \leq 5$. Acceptable misfits are generated when the resistivity of the initial half-space model is 100 Ω m or less. The behaviour of the 'TE' mode (Fig. 14b) is very different. Reducing τ does not significantly reduce the 'TE' mode misfit, irrespective of the starting model resistivity. However, the models that are generated by the inversion of the 'TE' mode are also insensitive to variations in ρ_h.

On the basis of these experiments, we focused our attention on models derived by inverting the data with $\tau \leq 30$, starting from a half-space with a resistivity of 1000 Ω m or less. Fig. 15 displays a representative sample of the results. The models generated by inverting the 'TM' mode alone (Fig. 15, left-hand column) all fit satisfactorily, with misfits in the range 1–1.2 sd. The essential geometrical features are a pair of shallow conductive blocks, linked at a depth of 12–15 km by a conductive layer. As ρ_h decreases, so does the average resistivity of the lowest part of the structure. Clearly, the data are insensitive to structure beneath the conductive layer, and the inversion procedure has insufficient information to navigate between misfit minima in very different regions of model space. Nonetheless, the geometry of the principal features above the 15 km level is stable with respect to changes in ρ_h. As τ is reduced, more complex features are superimposed on the basic block structure. These take the form of a thin horizontal conductor linking the tops of the conductive blocks, and protrusions from the shallow conductors into the uppermost resistive layer. Thin conductive features could be regarded as a sign of overfitting, if they resulted from 1-D inversion of a single site. Here, the layer is required by observations at a series of adjacent sites, and cannot be attributed to noise or static shift effects. The steeper features are less robust,

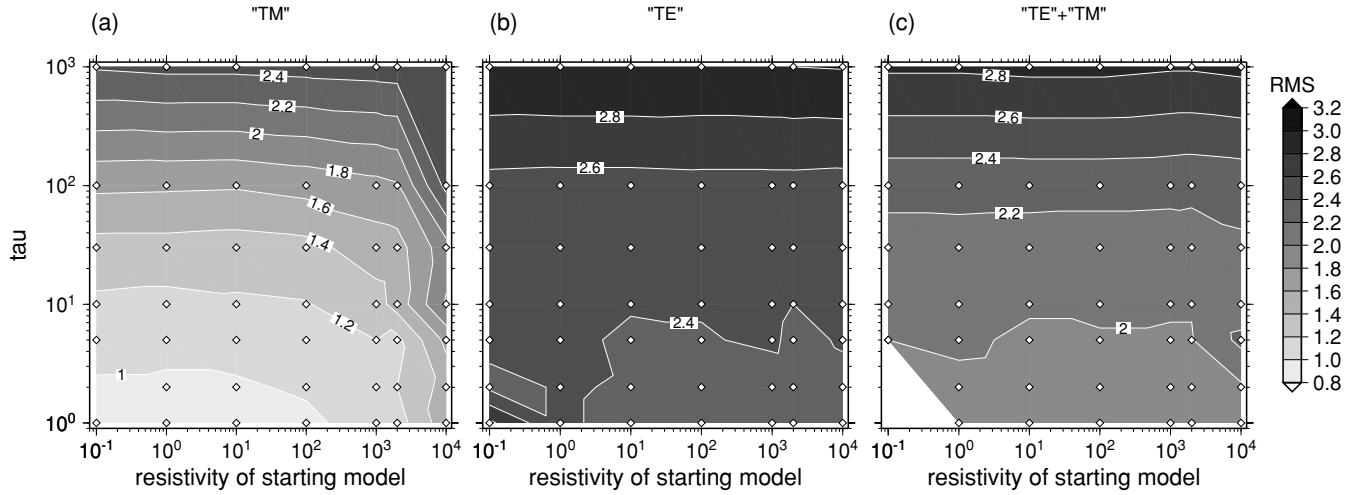

Figure 14. Dependence of the overall rms data misfits on the roughness weighting parameter τ and the resistivity ρ_h of the initial half-space. (a) Fitting the 'TM' mode alone; (b) fitting the 'TE' mode alone; (c) joint inversion of both modes.

since they do mostly derive from observations at no more than two adjacent sites.

Inversion of the 'TE' mode data alone (Fig. 15, centre column) generates models that remain smooth irrespective of the choice of parameters. They comprise two conductive blocks embedded in a two-layer background. The most noticeable difference in relation to the 'TM' mode inversions is the absolute level of the resistivity of the conductive features. The lowest resistivity in the model is 5 Ω m for the 'TM' mode but only 0.2 Ω m for the 'TE' mode. In general, it appears that the 'TE' mode data do not place strong constraints on the lateral boundaries of the conductors, while the 'TM' mode is less sensitive to the absolute level of their conductivity. The MV data were not incorporated into the inversion. Instead, we checked the success of the inversion of the MT data by forward modelling of the structure. Fig. 16 shows (and the fit of the MT response) the fit of the MV observations. It is clear that the models that incorporate 'TE' mode MT data, and that have higher absolute conductivities, fit the observations poorly, particularly at the longer periods (Fig. 16b), while the model derived solely from the 'TM' mode fits acceptably (Fig. 16a). The high values of conductivity generated by the 'TE' mode data must be the effects of higher real levels of conductivity along strike, out of the plane of the section, in agreement with the picture suggested by the induction arrows (Section 4), and the difficulty in fitting the 'TE' mode data.

8 GEOLOGICAL INTERPRETATION

Some issues remain to be resolved before a final analysis of the structural information contained in the MT profile can be extracted. These include the robustness of the smaller-scale features that appear when lower values of τ are selected, the style of the structural image generated by different starting model resistivities, and the decision as to whether to include the 'TE' mode data, which gives rise to significantly lower resistivities.

In view of these uncertainties, we have chosen to display and comment on a structure that does not emphasize the maximum possible amount of structural detail (we have selected $\tau = 5$), and to place it in a regional context, so as to emphasize the larger-scale features, which we do believe to be robust. The forward modelling of the MV data showed that the resistivities generated by incorporating the 'TE' mode into the MT inversion were unrealistically low, and probably arise from 3-D effects. We have therefore selected the model that is derived solely from the 'TM' mode impedances. This model (Fig. 17) has the further advantage that it clearly represents the same type of structure, and contains a similar level of structural detail, as the 'TM' mode phase pseudo-section (Fig. 11), which is the subset of the data least likely to be susceptible to 3-D effects. A model with such a direct relation to the data must represent a minimum input of prejudice on the part of modeller and/or software.

The inversion clearly incorporates some major structural features beyond the ends of the profile: deepening of the conductive layer beneath the Midland Valley at the northern end, and a conductive zone below 12 km beneath the southern end. These attributes are only controlled by one site at each end of the profile, and by the requirement to fit the 'TM' mode, which is influenced by the boundary conditions to north and south. Both aspects of the model may be real (the southern feature may represent the westward extension of the Northumberland Trough conductor see Fig. 1 and Banks *et al.* 1996), but they cannot be regarded as robust, and are not discussed further.

The very resistive surface layer is typically 4 km thick across most of the profile, and must correspond to the outcropping Ordovician and Silurian meta-sedimentary rocks (predominantly greywackes). Beneath the resistive layer, a 35 km wide conductive block is bounded by the Leadhills fault (LF) on the north and the Moffat Valley lineament (ML) on the south. It comprises three distinct units, the limits of which are marked by the Fardingmullach (FF) and Orlock Bridge (OBF) Faults. The northernmost and southernmost blocks are conductive from 4 km depth to at least 12 km. The block between them is resistive in this depth range. It coincides with a negative Bouguer gravity anomaly, which is a northeastwards continuation of the strong negative anomaly associated with the Cairnsmore of Fleet granite, and a southwestwards continuation of anomalies that have been interpreted as arising from a concealed granite batholith (Lagios & Hipkin 1979). Based on this link, it might be inferred that the resistive block is a concealed tongue of granite that has pushed northeast away from the main pluton. An alternative explanation is that the resistive meta-sedimentary rocks of the surface

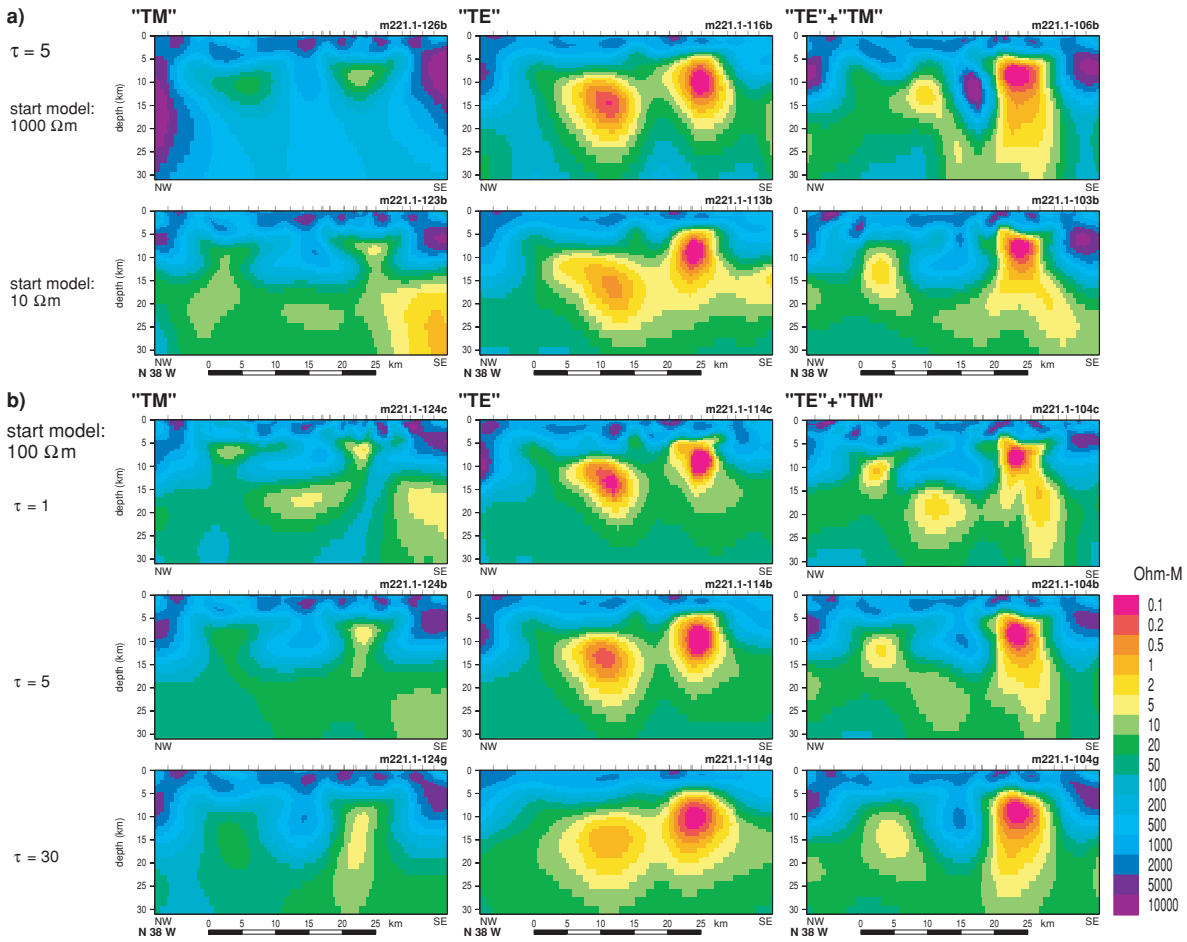

Figure 15. Resistivity models fitting the 'TM' mode (left-hand column) and 'TE' (centre column) modes alone, and both modes together (right-hand column). (a) Each row corresponds to a different choice of the resistivity of the half-space that is the starting point of the inversion. τ is set to 5. (b) Each row corresponds to a different value of τ. The starting point of the inversion is a half-space with a resistivity of 100 Ω m.

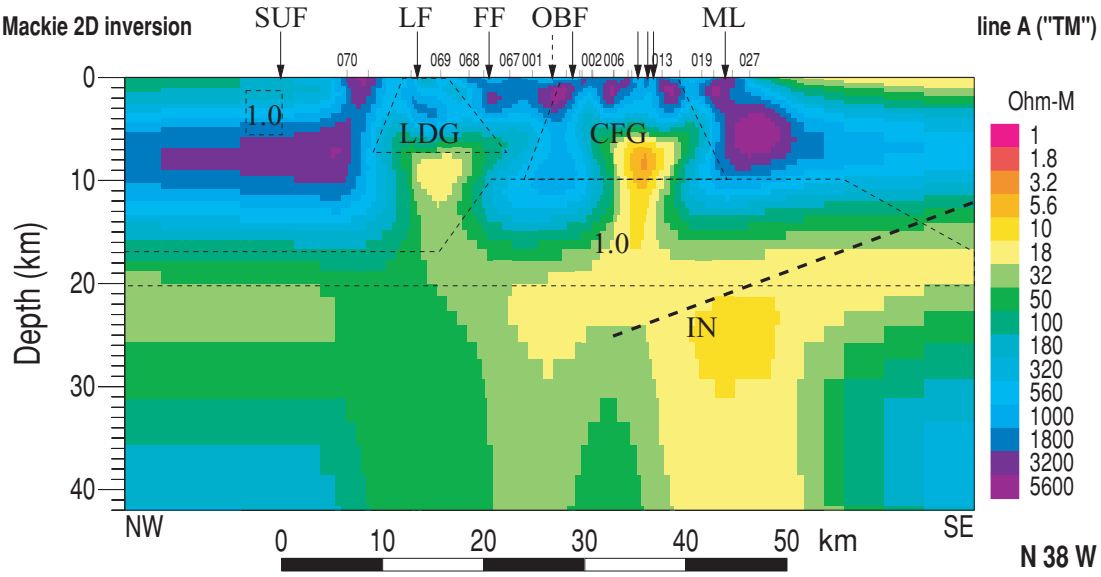

Figure 17. Resistivity model for line A derived by inverting only the 'TM' mode MT data. Note that the colour scale has been adjusted from that used in Fig. 15 to show the structures more clearly. The starting point for the inversion is a half-space with a resistivity of 100 Ω m, and the roughness parameter τ is 5. SUF, Southern Upland Fault; LF, Leadhills Fault; FF, Fardingmullach Fault; OBF, Orlock Bridge Fault; ML, Moffat Valley lineament. Other arrows mark outcrops of black shale. The dashed lines are features modelled from the aeromagnetic map by Kimbell & Stone (1995). They have been migrated along strike on to profile A. Nomenclature as in fig. 3(a) of Kimbell & Stone (1995): 1.0 is the magnetization in A m^{-1} of the Cairnsmore of Fleet granite; 1.0 is the magnetization in A m^{-1} of the magnetic block in the lower crust responsible for the Galloway magnetic high; IN, suggested position of the Iapetus Suture.

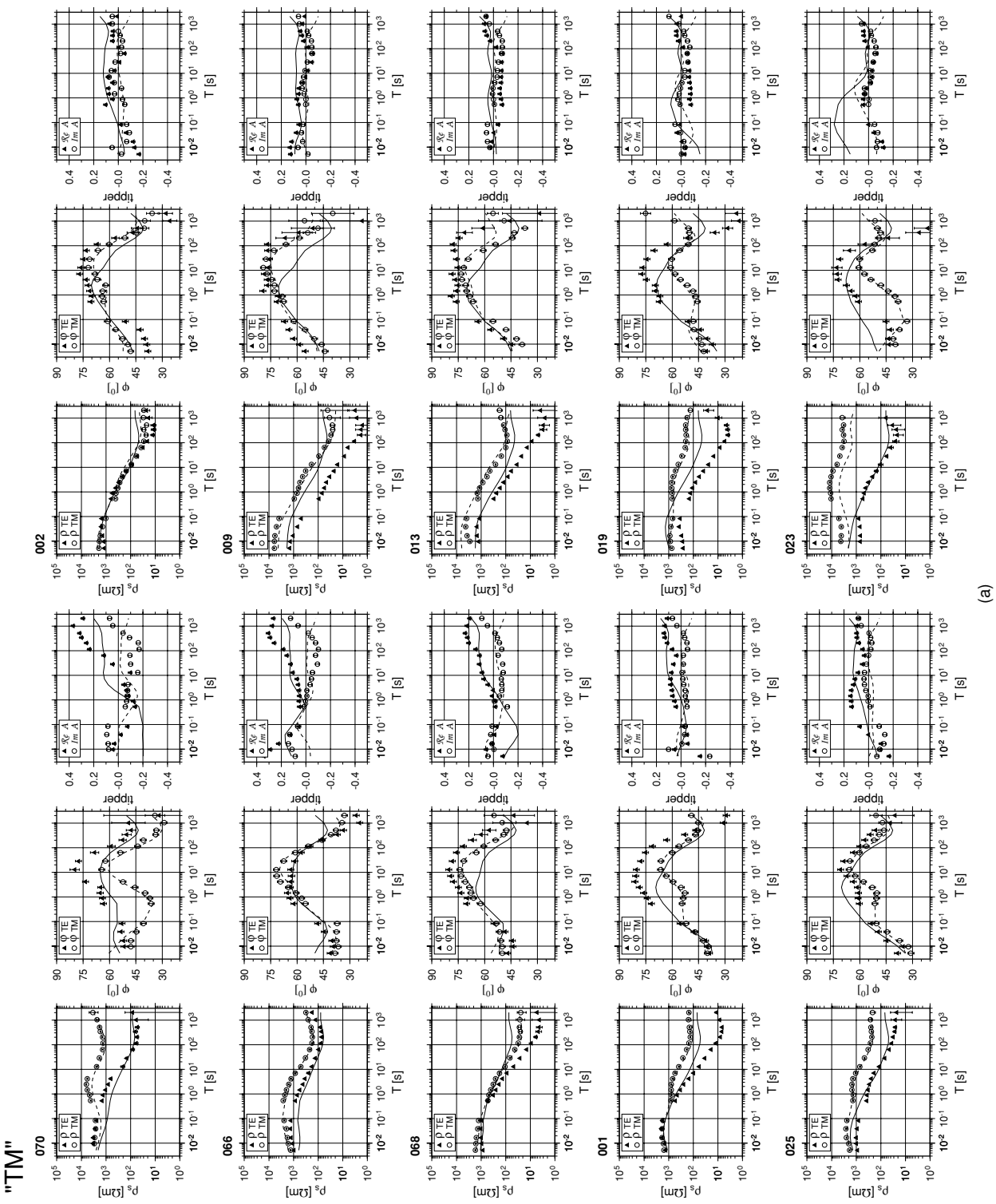

Figure 16. Fits of the observations on profile A to the models obtained using $\tau = 5$, half-space resistivity 100 Ω m in the inversion. For each site the three boxes show the observations and model response of (from left to right) the apparent resistivity ('TM' and 'TE' modes), the phases ('TM' and 'TE' modes), and the magnetic variation response for the 'TE' mode. (a) Fit of the model derived from inverting only the 'TM' mode MT data; (b) fit of the model derived from fitting both the 'TM' and 'TE' MT data.

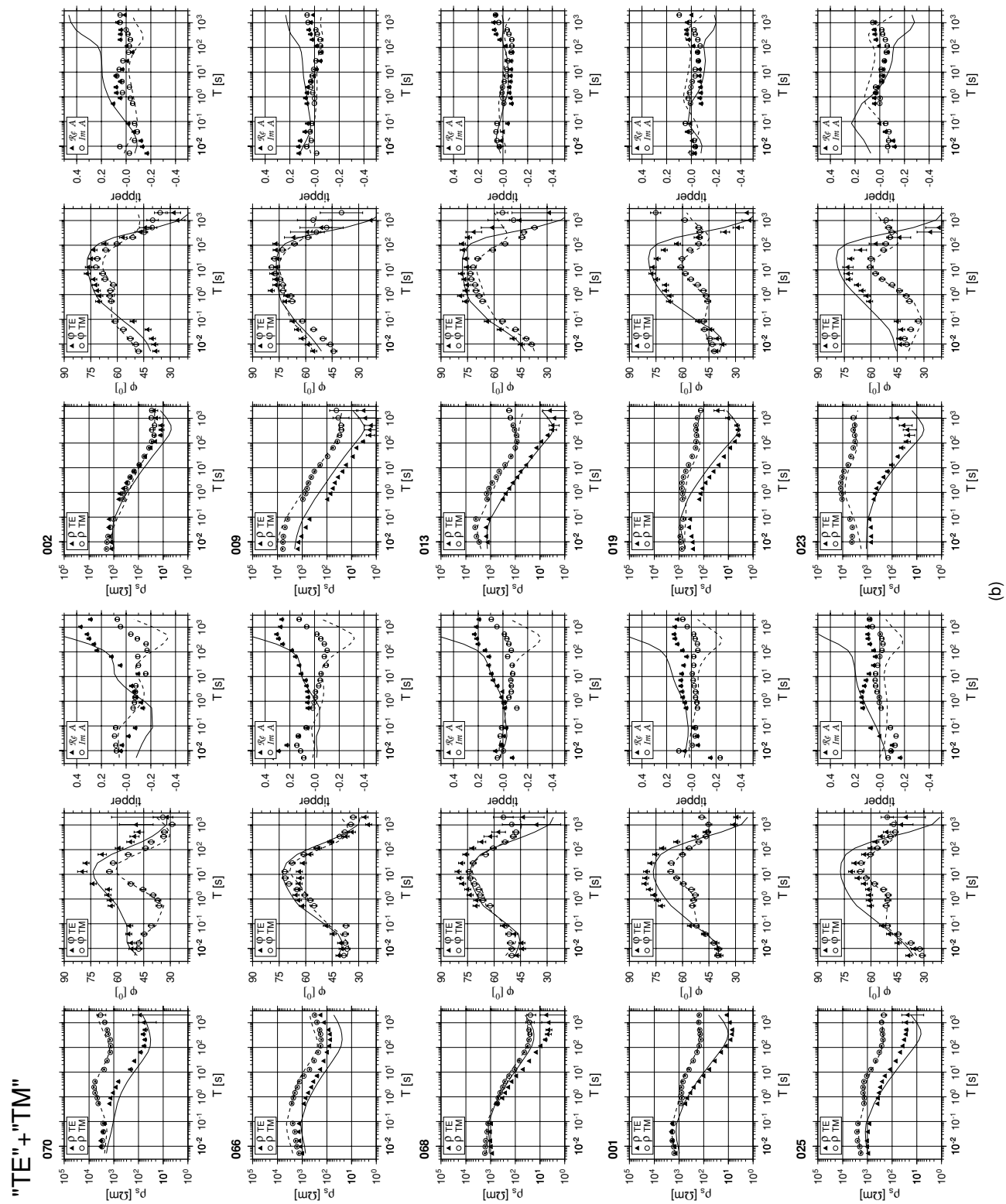

Figure 16. (*Continued.*)

layer have been juxtaposed with conductive rock by vertical and/or strike-slip movement along the bounding faults. This hypothesis is supported by a completely independent set of data. Merriman & Roberts (1999) have mapped changes in metamorphic grade across the faults, and used them to infer the directions of movement, which are in agreement with the resistivity model. However, it is unlikely that the vertical displacements are as large as 8 km, which is what the resistivity section suggests. Perhaps the displaced block is also underlain by a tongue of granite.

It is generally assumed that the tract-bounding faults were originally thrusts, listric at depth. However, there is little sign in Fig. 17 that structures become less steep at depth. Instead, the dominant impression from both the 'TM' mode phase pseudo-section and the resistivity model is that the major structural controls on the boundaries of resistive and conductive regions have been exerted by vertical or subvertical faults that extend to depths of more than 12 km. It is believed that the Orlock Bridge Fault, among others, was reactivated as a sinistral strike-slip fault during the final stages of closure of Iapetus. Judged from our image, it is the later phase of movement, predominantly concentrated on the Orlock Bridge and Fardingmullach Faults, which has left its mark on the distribution of resistivity.

The conductivity is greatest in two vertical blocks, each approximately 4 km wide, and extending from 4 to 12 km depth. The northernmost block is located between the Fardingmullach and Leadhills faults, on the northern side of an outcrop of the carbonaceous shale. It is linked by tenuous anomalies in the uppermost crust both to the shale outcrop and to the Leadhills fault. The centre of the southern block lies directly beneath a series of black shale outcrops, and is possibly linked both to them and to the surface expression of the Orlock Bridge fault and Moffat Valley lineament. The higher conductivity is restricted to depths in excess of 4 km, and at these depths the data are unable to resolve the width of the conductor to better than 4 km. The shallower features shift position with changes in the inversion parameters, and correlations between them and the surface geology must be treated with caution.

What conclusions can we draw from these observations concerning the cause of the high conductivity? If carbon is responsible, it is only when it has been buried below 4 km, and when the conditions for converting it to graphite and forming an interconnected network are in place. The conductivity of the blocks in the joint 'TE'/'TM' inversion is 5 S m^{-1}, but is less than 0.5 S m^{-1} if the 'TM' mode data alone are fitted. We are convinced (see the discussion above) that the high value generated by the 'TE' mode data is incorrect, and is the consequence of 3-D effects not allowed for in the inversion. Because our experiment cannot resolve conductors at 4 km any narrower than their depth, the 'conductive blocks' may represent a more complex conductive structure made up from several narrower bodies. If so, the 'blocks' may simply be normal crust that has been fractured by the tectonic processes related to the closure of Iapetus and injected with mineralizing fluids along a series of discrete planes. The source of such fluids could be the moderately conductive crust between 12 and 20 km depth that underlies the entire block. This unit coincides approximately with the source of the Galloway magnetic high, identified by Kimbell & Stone (1995). Fig. 17 shows the approximate position of the magnetized block, migrated along strike from Kimbell & Stone's profile to ours. They suggested the magnetic source could be a block of crust that was rifted from the northern margin of Avalonia, subsequently foundered, and was incorporated into the crust of the Southern Uplands during the final docking of the Avalonian and Laurentian plates.

9 COMMENTS ON THE RESOLUTION OF THE MT IMAGE

As well as providing new information concerning the structure of the Iapetus Suture Zone, an important aim of the project was to assess the improvement in structural resolution that could be achieved in a *practical situation* by optimizing as many as possible of the different phases of MT data acquisition, processing, analysis and modelling. The following comments summarize the experience generated by the experiment.

(1) The quality of individual MT impedance estimates is usually now very good, thanks to the reliability and flexibility of modern acquisition systems such as SPAM III. Artificial noise sources can still be a problem. In this case, the survey was planned in an area of low cultural noise levels. Even so, it was necessary to record for 4–5 d at each site to generate the data volumes required across the entire bandwidth. The introduction of GPS timing meant that robust remote reference processing could be applied to data from sites that were otherwise independent.

(2) The quality of the error estimates is just as important as that of the impedances. The ρ^+ approach to scrutinizing data quality suggested by Parker & Booker (1996) proved to be a valuable tool for the detection and elimination of inconsistent data, and for establishing a plausible error level. Judged by these criteria, we believe that 3 per cent is a realistic estimate of the error floor in the individual impedances.

(3) The MT profile was located in a region where the principal geological structures are 2-D, and where preliminary MV measurements indicated that the larger-scale conductivity structures were also 2-D. Nonetheless, we felt it was essential to supplement the main profile by a close parallel profile (less than 1 km away), a more distant parallel profile (8 km away) and a sparse profile in the expected strike direction. The magnetic variation transfer functions are of high quality, even though they are tiny over the conductor. At periods of less than a few tens of seconds they show consistent spatial patterns that are indicative of 3-D structures on a scale of several kilometres. We anticipate that, where similar high-quality MV measurements are made, 3-D structures on this scale will often be found.

(4) Because the larger-scale ('regional') structures were not 2-D, the galvanic distortion model did not fit the observations, and we could not use the strike values suggested either by single- or multisite analysis. In such a situation, even sparse observations of the spatial structure of quantities such as the impedance phase make a valuable contribution towards assessing the dimensionality and alignment of the conductivity structure. We feel our experience in Galloway confirms the importance of attempting a limited 3-D coverage, and further investigation of the spectral analysis method (Section 5.6) could help in choosing the form such coverage might take.

(5) Even though the superficial lithology was relatively uniform (except where the rocks were locally disrupted by faults and shear zones), we felt it was important to choose a station spacing on the main profile that oversampled potential structures. A spacing of between 1 and 2 km appeared to achieve this goal. The importance of a high site density was confirmed by the nature of the observed 'TM' mode phase pseudo-section, where the blocky structure could be linked to the faults bounding the tracts within the otherwise uniform meta-sedimentary rocks.

(6) The importance of data of equally high quality for both the 'TM' and 'TE' modes was emphasized by the experiments with 2-D inversion of the principal profile impedances. Much of the control on

the shapes of the conductors (more precisely, the spatial distribution of resistivity contrasts) was established by the 'TM' mode phase.

(7) Experiments to assess the potential effects of 3-D structures, such as those indicated by the MV data, must be the next step in the analysis of this data set.

ACKNOWLEDGMENTS

The research described in this paper was supported by grant GR3/10588 from the UK Natural Environment Research Council, and by loans of equipment from the NERC Geophysical Equipment Pool, the GeoForschungsZentrum Potsdam and the Johann Wolfgang Goethe University, Frankfurt. We are grateful to the many landowners who granted us permission to work on their land, and farmers who helped by turning off electrical machinery. David Bailey, Graham Dawes, Richard Holme, Rebecca Pique and David Wright gave invaluable assistance in the field, and Steve Constable, Gary Egbert, Alan Jones, Randall Mackie, Bob Parker and Volker Rath supplied us with software. Two anonymous referees made very helpful suggestions that contributed to a substantial improvement in the paper. To them all goes our sincere thanks.

REFERENCES

Bahr, K., 1988. Interpretation of the magnetotelluric impedance tensor: regional induction and local telluric distortion, *J. Geophys.,* **62,** 119–127.

Banks, R.J., 1979. The use of equivalent current systems in the interpretation of geomagnetic deep sounding data, *Geophys. J. R. astr. Soc.,* **56,** 139–157.

Banks, R.J., Irving, A.A.K. & Livelybrooks, D.W., 1993. The simulation of magnetic variation anomalies using single-station data, *Phys. Earth planet. Inter.,* **81,** 85–98.

Banks, R.J., Livelybrooks, D., Jones, P. & Longstaff, R., 1996. Causes of high crustal conductivity beneath the Iapetus suture zone in Great Britain, *Geophys. J. Int.,* **124,** 433–455.

Barnes, R.P., Phillips, E.R. & Boland, M.P., 1995. The Orlock Bridge Fault in the Southern Uplands of southwestern Scotland: a terrane boundary?, *Geol. Mag.,* **132,** 523–529.

Beamish, D., 1995. Deep resistivity imaging across the Northern and Central belts of the Southern Uplands, *Geol. Mag.,* **132,** 531–538.

Edwards, R.N., Law, L.K. & White, A., 1971. Geomagnetic variations in the British Isles and their relation to electrical currents in the ocean and shallow seas, *Phil. Trans. R. Soc. Lond.,* A, **270,** 289–323.

Egbert, G.D. & Booker, J.R., 1986. Robust estimation of geomagnetic transfer functions, *Geophys. J. R. astr. Soc.,* **87,** 173–194.

ELEKTB group, 1997. KTB and the electrical conductivity of the crust, *J. geophys. Res.,* **102,** 18 289–18 305.

Groom, R.W. & Bailey, R.C., 1989. Decomposition of magnetotelluric impedance tensor in the presence of local three-dimensional galvanic distortion, *J. geophys. Res.,* **94,** 1913–1925.

Heise, W. & Pous, J., 2001. Effects of the anisotropy on two-dimensional inversion procedure, *Geophys. J. Int.,* **147,** 610–621.

Jödicke, H., 1992. Water and graphite in the Earth's crust—an approach to interpretation of conductivity models, *Surveys Geophys.,* **13,** 381–407.

Junge, A., 1995. Magnetotellurics in the long period range, Final Report on EEC Human Capital and Mobility Contract No ERBCHBICT 93 0610.

Kimbell, G.S. & Stone, P., 1995. Crustal magnetization variations across the Iapetus Suture Zone, *Geol. Mag.,* **132,** 599–609.

Lagios, E. & Hipkin, R.G., 1979. The Tweeddale granite—a newly discovered batholith in the Southern Uplands, *Nature,* **280,** 672–675.

Leggett, J., McKerrow, W. & Soper, N., 1983. A model for the crustal evolution of southern Scotland, *Tectonics,* **2,** 187–210.

Livelybrooks, D., Banks, R.J., Parr, R.S. & Hutton, V.R.S., 1993. Inversion of electromagnetic induction data for the Iapetus Suture Zone in the UK, *Phys. Earth planet. Inter.,* **81,** 67–84.

McNeice, G.W. & Jones, A.G., 2001. Multisite, multifrequency tensor decomposition of magnetotelluric data, *Geophysics,* **66,** 158–173.

Merriman, R.J. & Roberts, B., 1999. Low-grade metamorphism in the Scottish Southern Uplands terrane: deciphering the patterns of accretionary burial, shearing and cryptic aureoles, *Trans. R. Soc. Edin. Earth Sc.,* **91,** 521–537.

Parker, R.L. & Booker, J.R., 1996. Optimal one-dimensional inversion and bounding of magnetotelluric apparent resistivity and phase measurements, *Phys. Earth planet. Inter.,* **98,** 269–282.

Phillips, E.R., Barnes, R.P., Boland, M.P., Fortey, N.J. & McMillan, A.A., 1995. The Moniaive Shear Zone: a major zone of sinistral strike-slip deformation in the Southern Uplands of Scotland, *Scott. J. Geol.,* **31,** 139–149.

Ritter, P. & Banks, R.J., 1998. Separation of local and regional information in distorted GDS response functions by hypothetical event analysis, *Geophys. J. Int.,* **135,** 923–942.

Ritter, O., Junge, A. & Dawes, G.J.K., 1998. New equipment and processing for magnetotelluric remote reference observations, *Geophys. J. Int.,* **132,** 535–548.

Rodi, W. & Mackie, R.L., 2001. Non-linear conjugate gradients algorithm for 2-D magnetotelluric inversion, *Geophysics,* **66,** 174–187.

Simpson, F., 2000. A three-dimensional electromagnetic model of the southern Kenya Rift: departure from two-dimensionality as a possible consequence of a rotating stress field, *J. geophys. Res.,* **105,** 19 321–19 334.

Smith, J.T., 1995. Understanding telluric distortion matrices, *Geophys. J. Int.,* **122,** 219–226.

Stone, P., Cook, J.M., McDermott, C., Robinson, J.J. & Simpson, P.R., 1995. Lithostratigraphic and structural controls on distribution of As and Au in southwest Southern Uplands, Scotland, *Trans. Instn. Min. Metall. (Sect. B: Appl. Earth Sci.),* **104,** 111–120.

Sule, P.O. & Hutton, V.R.S., 1986. A broad-band magnetotelluric study in south-eastern Scotland: data acquisition, analysis and one-dimensional modelling, *Ann. Geophysi.,* **4,** 145–156.

Sule, P.O., Hutton, V.R.S. & Dumitrescu, C., 1993. Subsurface structure of SE Scotland from broadband magnetotelluric measurements, *Phys. Earth planet. Inter.,* **81,** 9–24.

Weidelt, P., 1975. Electromagnetic induction in three-dimensional structures, *J. Geophys.,* **41,** 85–109.

Scientific Technical Report STR 05/10

GeoForschungsZentrum Potsdam

Available online at www.sciencedirect.com
SCIENCE DIRECT®
Physics of the Earth and Planetary Interiors 138 (2003) 71–90
PHYSICS OF THE EARTH AND PLANETARY INTERIORS
www.elsevier.com/locate/pepi

A magnetotelluric study of the Damara Belt in Namibia 1. Regional scale conductivity anomalies

Oliver Ritter[a,*], Ute Weckmann[a], Tim Vietor[a], Volker Haak[a]

[a] *GeoForschungsZentrum Potsdam, Telegrafenberg, D-14473 Potsdam, Germany*

Received 19 July 2002; received in revised form 5 March 2003; accepted 6 March 2003

Abstract

The Namibian margin is dominated by the late Proterozoic to early Cambrian fold belts of the Damara Orogen, which wrap around and separate the Congo and Kalahari Cratons. This mosaic of relatively 'soft' fold belts and 'hard' cratons apparently controlled the path for the opening of the South Atlantic in the early Cretaceous. The continents split along the coast-parallel fold belts of the Damara Orogen while the inland fold belt (Damara Belt) was effected by extension and widespread igneous intrusion but never developed to the rift stage. This paper is concerned with the interpretation of magnetotelluric (MT) data along a 200 km NW–SE profile across the Damara Belt in NW Namibia. The regional, two-dimensional electrical resistivity model and the induction vector data exhibit three distinctive zones: (i) a generally very resistive upper crust which is typical for the granites and metasediments of the Damara Belt, (ii) two subvertical conductors in upper to mid-crustal levels which correlate with major tectonic zone boundaries and (iii) a highly conductive middle to lower crust in the southern part of the profile. The geometry of the conductive structures could reflect a regional shear system in which upper crustal listric faults pass into a detachment zone in the middle crust. We interpret the high electrical conductivity in terms of graphite (or other forms of mineralization) enrichment along the shear planes. This zone of crustal weakness may have originated in Pre-Damara times and had probably experienced several episodes of crustal reactivation before the intrusion of basaltic dike swarms during the Cretaceous rifting and magmatism associated with the opening of the South Atlantic.

Keywords: Magnetotellurics; Damara mobile belt; Namibia; Shear zones

1. Introduction

Shear zones are linked with many dynamic processes on earth. The largest shear zones are hundreds of kilometres long and tens of kilometres thick, with displacements of tens to hundreds of kilometres. The characteristics of rock deformation vary, depending upon the conditions under which deformation occurred. Fault zones form under brittle conditions, while aseismic deformation accompanied by metamorphism is typical for shear zones which originated in a ductile regime.

Many regional lineaments in southern Africa are shear zones with large displacement, occurring both within and bounding orogenic belts (Coward and Daly, 1984). One of the largest of these is the Neoproterozoic to Paleozoic transcontinental Mwembeshi shear zone which extends across the African sub-continent from northern Namibia through Botswana, Zambia and Malawi (Daly, 1986, 1989). Linking the Pan-African orogens of southwest Africa with those

* Corresponding author. Tel.: +49-331-288-1257; fax: +49-331-288-1235.
E-mail address: oritter@gfz-potsdam.de (O. Ritter).
URL: http://www.gfz-potsdam.de/pb2/pb23/.

0031-9201/03/$ – see front matter
doi:10.1016/S0031-9201(03)00078-5

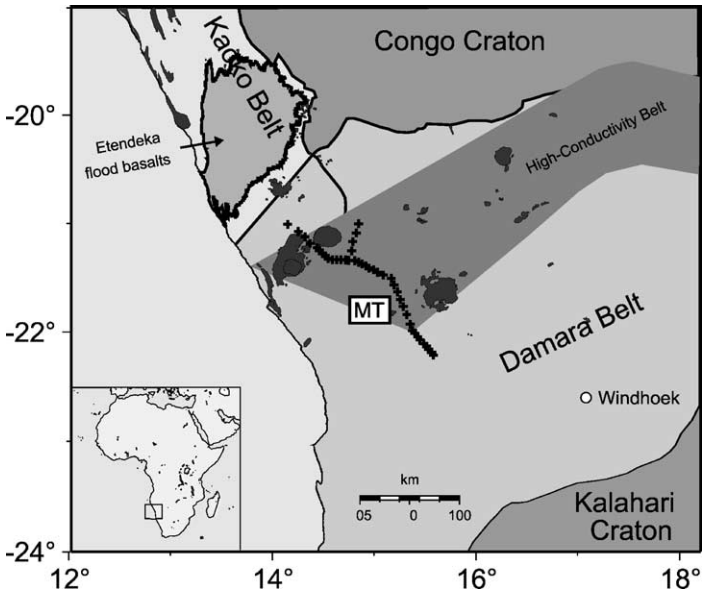

Fig. 1. Map of the continental margin of NW Namibia showing the location of the Damara Orogen sandwiched between the Congo and Kalahari Cratons. Also marked are the sites of the MT experiment (crosses) and the Van Zijl and De Beer conductivity belt (see text). Cretaceous igneous complexes are shown in dark grey.

of southeast Africa, it accumulated large amounts of shear during the amalgamation of South Gondwana (Porada, 1989). The location and regional trend of the Mwembeshi shear zone appears to correspond with an electrical *high conductivity belt* which was detected by magnetic variation data collected in the late 1960s and early 1970s by de Beer et al. (1982) and Van Zijl and de Beer (1983) (see Fig. 1). At that stage, these authors associated the anomaly with a zone of crustal weakness which provided a link between the Damara Belt and the Zambezi Belt to the east. Serpentinized lower crust was thought to be a likely cause for the high conductivity. However, the present state of knowledge and theory about crustal conductivity suggests that shear zones are a more plausible explanation, as they often exhibit anomalous conductivity due to higher contents of fluid, fault gouge, sulfides or graphite.

The German Continental deep drilling Program (KTB) was accompanied by surface observations, a large suite of borehole logs measuring physical and chemical properties, and laboratory studies on core samples (Haak and Jones, 1997). These experiments have revealed a quantitative relation between the shearing process, the formation of graphite and very high electrical conductivity (Elektb Group, 1997; Eisel et al., 2001). The essential observation was that conductive material becomes interconnected only through shearing. Thus, the mobility of shear zones—whether recent or fossil—creates the necessary conditions for crustal zones of high conductivity, which can be imaged with magnetotelluric (MT) experiments. The highly conductive material may be graphite, brines (saline water) or even melts. The important point is that large-scale interconnected zones of conducting material are created by the active motion in a shear zone.

Recent advances in the MT method provide a means to recognize the length and depth extent of shear zones. Particularly, Unsworth and colleagues (Unsworth et al., 1997, 1999, 2000; Bedrosian et al., 2002) imaged the internal structure of the San Andreas Fault (SAF) with magnetotelluric measurements. They attribute the high conductivity to brines in porous fractured rocks. A similar result was obtained for the West Fissure in Chile (Echternacht et al., 1997; Hoffmann-Rothe, 2002). Ledo et al. (2002) associated several high conductivity anomalies at different depth

scales with the Tintina Fault in Canada. Recent data from the Variscides in Iberia (Almeida et al., 2001; Santos et al., 2002) show a strong correlation of upper and lower lower crustal conductivity anomalies with regional fault and detachment zones. According to these authors, conductive features in the deep crust are caused by graphite. The role of graphite as a very good conductor and lubricant when distributed across shear planes is discussed in Ritter et al. (1999). Zones of high conductivity found in MT data from southern Scotland indicate that the Iapetus Suture was a whole crustal shear with a gently dipping ramp (Banks et al., 1996). Tauber et al. (2003) further found that the edges of conductive blocks match with faults mapped in the surface geology.

Other geophysical studies in Namibia have mainly involved offshore seismic reflection (MCS) profiling in connection with hydrocarbon exploration (Stewart et al., 2000; Gladczenko et al., 1997; Light et al., 1993) and have provided little information about deep crustal properties and depth to Moho. Bauer et al. (2000) reported on combined offshore–onshore wide-angle seismic and MCS profiles across the continental margin of NW Namibia, the results of which provide velocity–depth sections of the crust along two traverses across the ocean–continent boundary and onto the continental margin. Bailey et al. (2000) reported on MT work from the Zambezi Mobile Belt in northern Zimbabwe where a relatively conductive basement suggests chemical or tectonic alteration during rift formation due to metamorphic processes or tectonic disruption.

The regional MT experiment described in this paper focusses on major NE-oriented basement structures in the Damara fold belt. The 200 km-long MT profile crosses the Van Zijl and de Beer (1983) conductive belt, as well as several major tectonic and stratigraphic zone boundaries of the Damara fold belt. The new MT data show that the conductivity anomalies clearly correlate with regional tectonic features. The imaged zones of high conductivity probably outline a shear system in which upper crustal listric faults pass into a detachment zone in the middle crust. The distribution of sites limits the interpretation of the MT data to two dimensions. Two-dimensional modelling is adequate to image the most important regional features, but it cannot account for all of the complexity expressed in the data, and structural elements are not resolved in great detail. These issues, however, are at the centre of interest of a companion paper by Weckmann et al. (this issue; hereafter referred to as Part II) (Weckmann et al., 2003), which is concerned with a detailed MT investigation of one of the observed conductivity anomalies along the Waterberg Fault/Omaruru Lineament (WF/OL).

2. Geological background

The central Namibian Damara Belt is part of a system of many Pan-African convergent orogens that formed during the amalgamation of South Gondwana between 1000 and 450 Ma. In southwestern Africa the broadly synchronous closure of oceanic basins between the Kalahari, Congo and Sao Francisco Cratons led to the formation of the Damara/Ribeiro/Gariep Orogen (Miller, 1983; Prave, 1996; Seth et al., 1998; Frimmel and Frank, 1998). The NE striking Damara Belt represents remnants of the continental collision zone between the Congo and Kalahari Cratons to the north and south, respectively (see Fig. 1). It exhibits major changes of stratigraphic, structural and petrological evolution at distinct lineaments or shear zones oriented parallel to the suspected NE-strike of the suture zone. The polyphase history of these lineaments can be traced throughout the Pan-African evolution of the orogen, from the onset of extension to the last phases of continental collision.

The evolution of the Damara Orogen started with crustal extension and deposition of lacustrine to shallow marine rocks between 900 and 750 Ma in fault-bounded rift basins. During subsequent passive margin evolution, thick marine clastics intercalated with abundant biogenic carbonates were deposited and oceanic lithosphere formed in at least one of the rift structures. Northward subduction below the southern edge of the Congo Craton started around 650 Ma and led to continental collision in the early Cambrian (Miller, 1983; Prave, 1996; Germs, 1995). During continental collision the older extensional faults were partly reactivated as thrusts which now separate zones of different stratigraphic and structural evolutions, metamorphic grade, distribution of plutonic rocks and geochronology (Miller, 1983; Daly, 1986, 1989). Fig. 2 shows the location of the most prominent lineaments in plan view: the Autseib Fault (AF)–Otjohorongo

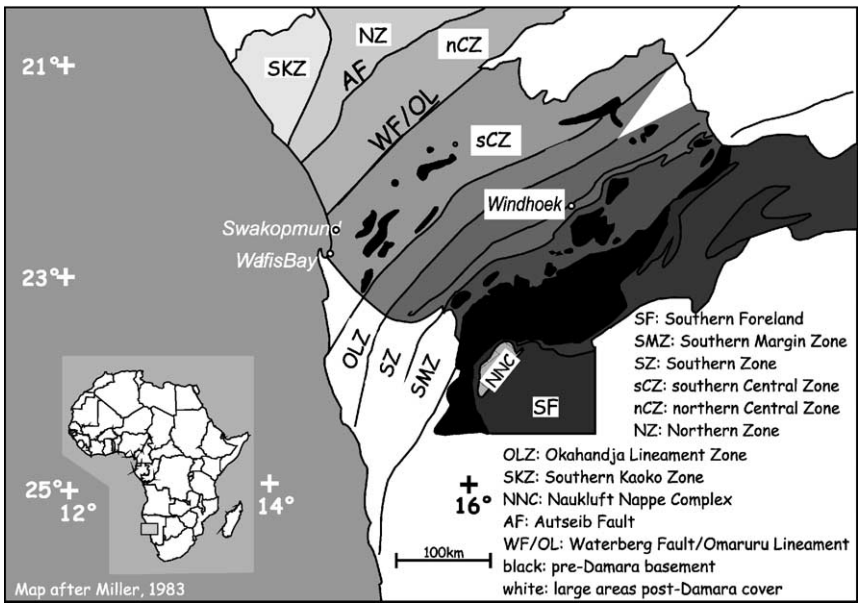

Fig. 2. Tectono-statigraphic zones of the Pan-African Damara Belt of central Namibia. The zonation according to Miller (1983) is based on stratigraphy, structure, grade of metamorphism, distribution of plutonic rocks, and geochronology. The lineaments form deep and steeply dipping ductile shear zones.

Thrust, the Waterberg Fault/Omaruru Lineament and the Okahandja Lineament. However, the geometry and interrelation of these lineaments at depth is unknown.

Subsequent erosion of the Damara Belt down to the present outcrop level was completed in the Permian when shallow marine sediments covered the high-grade metamorphic rocks of the internal zones of the orogen. However, the major tectono-stratigraphic lineaments of the Damara Orogen continued to control deformation of the Namibian crust. Mesozoic reactivation along the WF/OL is documented by offset of Triassic sedimentary rocks northeast of Omaruru and by offset or truncation of units in the Cretaceous Erongo complex (Holzförster et al., 1999). Raab et al. (2002) interpret differences in paleo-temperatures as evidence for late Cretaceous reactivation of WF/OL and estimate a net amount of vertical displacement across the WF/OL of approximately 2 km. The offshore sedimentary record also documents the Mesozoic reactivation of the fault (Clemson et al., 1997, 1999). Post-Damara reactivation is also recorded along the Autseib Fault as documented by offsets of Cretaceous intrusive rocks (Clemson et al., 1999).

In addition to these regional scale features, brittle deformation occurs on numerous faults localized in several swarms within the Damara Belt. The basement geology of the study area reflects the strong deformation during the continental collision. The topography cuts numerous dome and basin folds with subvertical limbs. The resulting map pattern (see Fig. 7 in Part II) is dominated by concentric stratigraphic contacts of the lower Damara sequence around the dome structures. The domes are frequently cored by syntectonic granites. The interleaving synclines are filled with rocks of the upper Damara sequence and host most of the post-tectonic granites (Miller, 1983).

3. Conductivity anomalies and crustal shear zones

Fig. 3 shows the locations of MT sites recorded in two field experiments in 1998 and 1999. At each site we collected five-component magnetotelluric data in the period range 0.001–1000 s. In 1998 we used 4 GPS synchronized S.P.A.M. MkIII real time instruments (Ritter et al., 1998) with Metronix MFS05 induction coils and Ag/AgCl electrodes. The instruments

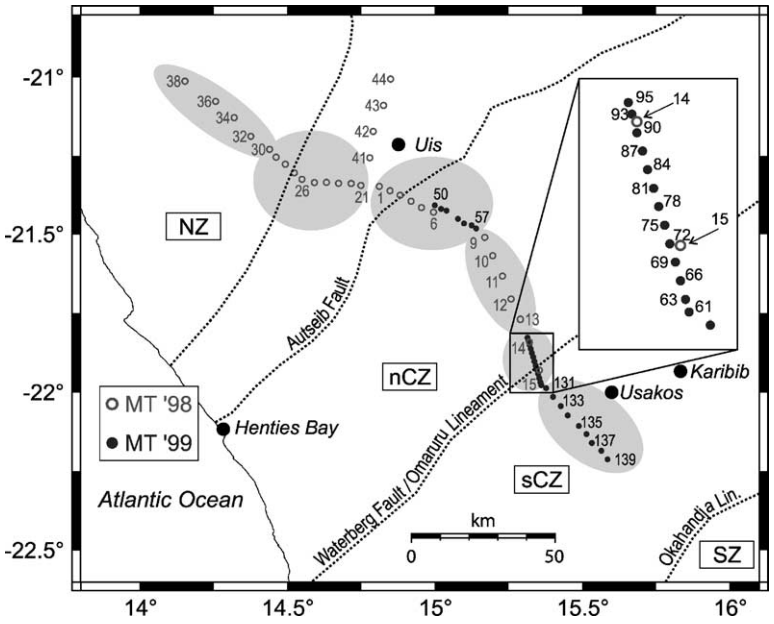

Fig. 3. Map of the magnetotelluric (MT) sites, recorded in NW Namibia during two field experiments in 1998 (open circles) and 1999 (filled circles). Plotted are the locations of those 54 sites (from a total of 110) used in the regional study. The 200 km long traverse crosses several tectono-stratigraphic zone boundaries of the Damara Belt (see Fig. 2). Shaded areas indicate the site-sets for which the McNeice/Jones tensor decomposition scheme was applied.

recorded continuously for 4 days at each of 33 locations with a site spacing between 4 and 12 km. In 1999 we collected data at 77 sites with 6 S.P.A.M. MkIII systems, with a typical recording time of 1–2 days per site. Most of these site were located near the WF/OL (Part II), but we also extended the regional profile of the previous year. All time series data were processed using the robust procedures described in Ritter et al. (1998). A single site processing was usually sufficient as signal to noise ratios were high at most sites.

The regional MT experiment was carried out along a profile designed to cross both the major NE trending tectonic structures and the Van Zijl and de Beer (1983) conductive belt. This experimental layout implies that we expect (mostly) two-dimensional lateral variations of associated conductivity anomalies with a geo-electric strike direction perpendicular to the profile. However, before inverting impedance tensor estimates using 2D models, it must be assessed whether a data set is consistent with two-dimensional structure, and if so, to make a best possible estimate of the regional strike direction. Geo-electric strike directions and estimates of the dimensionality of the subsurface can be derived from the MT impedance tensor which relates the horizontal components of the electric and magnetic fields. An independent determination of strike directions can be obtained from magnetic variation measurements, which relate horizontal to vertical magnetic fields. A convenient way to present vertical magnetic field response functions is in the form of induction vectors.

In this paper, induction vectors are plotted in the Wiese convention in which the real parts point away from the high conductivity side of a conductivity contrast. At shorter periods (high frequencies), the induction vectors are more influenced by shallow or local features, whereas long period variations are controlled by regional or deep structures (skin depth effect). The diagrams in Fig. 4a–c show the induction vectors of the Namibian data set at three different periods.

Towards the centre of Fig. 4a , the reversal of the real induction vector directions indicates a conductive region between the Autseib Fault and the Omaruru River. Sites located on or just north of the AF show

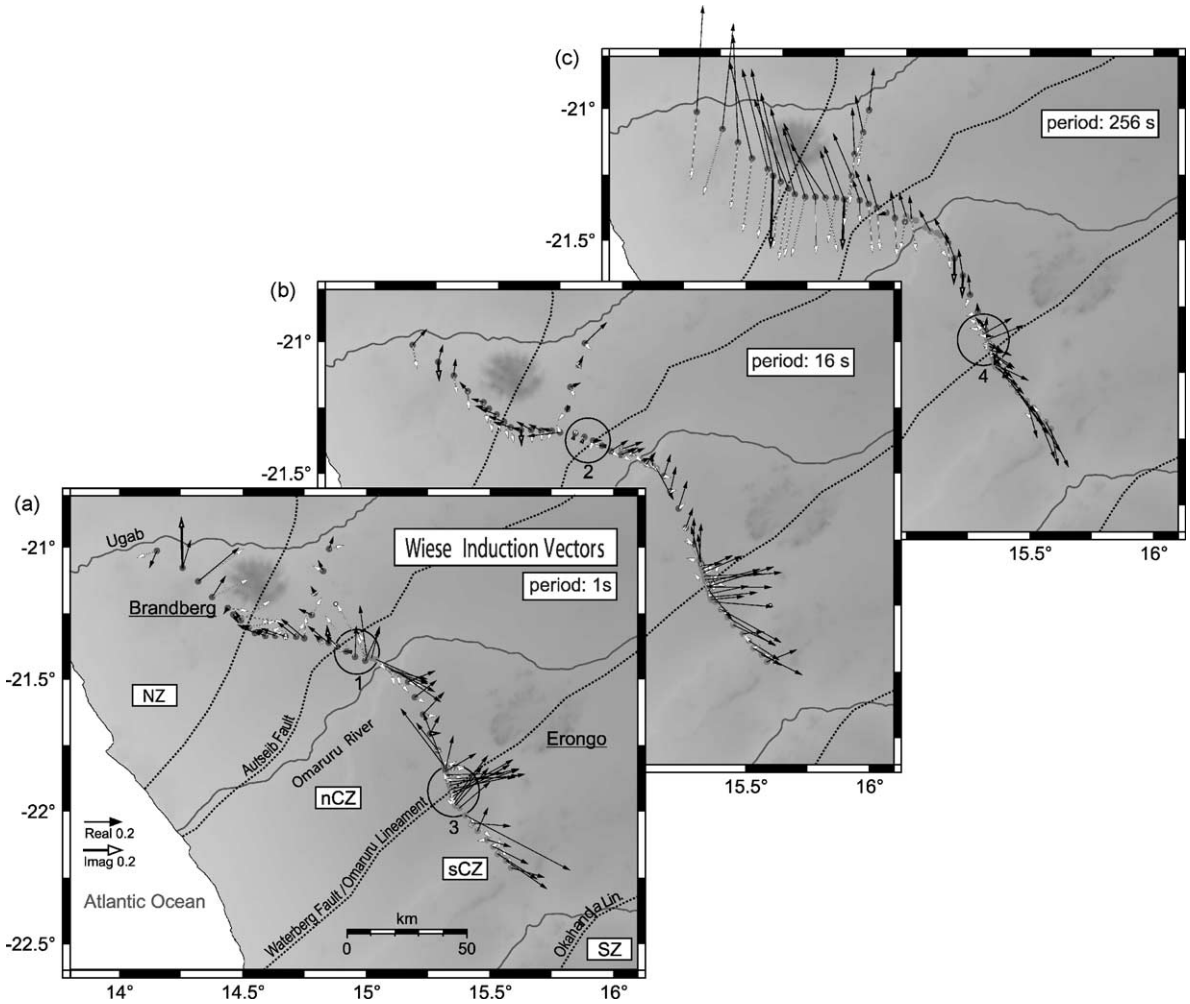

Fig. 4. The real (solid arrowhead) and imaginary (open arrowhead) induction vectors calculated from the 1, 16 and 256 s period data. Wiese convention: vectors point away from conductivity contrast. Reversals in the real induction vectors correlate with the position and orientation of major shear zones of the Damara Belt.

NW pointing vectors for 1 s period data, while they point SE at sites in the vicinity of the Omaruru River (zone 1 in Fig. 4a). This behaviour indicates an elongated conductive channel parallel to the AF. Interestingly though, we observe fairly large, obliquely pointing induction vectors at 1 s inside the conductive channel. From theory, we expect the largest real vectors—with opposite orientations—should appear along the transitions from conductive to resistive domains but the induction vectors should vanish towards the centre of the conductive channel. Such expectedly small real induction vectors are observed at a period of 16 s in Fig. 4b (zone 2).

The WF/OL is similarly marked as a conductive zone by the induction vectors (zone 3 in Fig. 4a). For sites at some distance from the fault, the real vectors point away from the WF/OL at both sides of the fault zone. At the WF/OL, the induction vector reversal can be observed over the whole period range, even at the longest period of 256 s (zone 4 in Fig. 4c). However, at shorter periods we again observe large fault-parallel induction vectors. Based on the

interpretation of many densely spaced and laterally distributed sites in the area of the WF/OL, we attribute these fault-parallel induction vectors to a superposition of an obliquely striking, elongated conductive body and electrical anisotropy in the fault zone (see Part II).

Despite these complications, there is a clear correlation between induction vector reversals and tectonic zone boundaries of the Damara Belt. Both the AF and the WF/OL, are identified as narrow zones of high electrical conductivity. At the longest period of 256 s, however, Fig. 4c indicates a different regional trend, as most sites in the Northern Zone (NZ) are now more in line with E–W oriented strike angles in the order of 70°N–80°E.

Traditionally, Swift's (1967) method was applied to derive an electric strike angle from the impedances by examining how the impedance tensor behaves under rotation. The skewness of the impedance tensor, i.e. the ratio of its diagonal to off-diagonal elements, was used as an indicator of the complexity of the subsurface. Swift's parameters can be misleading, however, as the measured electric field may be severely distorted in the presence of near-surface heterogeneities. Under these circumstances, tensor decomposition schemes can help resolve an undistorted regional 2D tensor and the regional strike angle from locally distorted data (Groom and Bailey, 1989; Bahr, 1988). Similarly, a phase-sensitive skew parameter can be found from the condition that in the coordinate system of the regional 2D structure the column elements of the impedance tensor must have the same phase (Bahr, 1991). Strike angles and skew values for all sites are plotted in Fig. 5 over the whole period range from 0.001 to 1000 s. The diagrams in the upper row of the figure show normal (Swift) and phase sensitive skew values (Bahr); the dotted lines indicate the empirically determined thresholds of 0.2 (Swift) and 0.3 (Bahr) above which the 2D assumption cannot be maintained (Bahr, 1991). There are a considerable number of skew values above 0.2, while most of the phase sensitive skews are below the 0.3 threshold. The most important result of tensor decomposition—if successful—is a consistent regional strike direction. If effects of local 3D galvanic distortion have been separated from the regional 2D MT tensor, one would expect a period-independent strike direction common to all sites. Inspection of Fig. 5, however, shows that a common strike angle cannot easily be identified in the data, as is evident by the roughly uniform distribution of strike angles. Similarly, no hint of a preferred direction emerges if the data are plotted as rose diagrams (bottom row of Fig. 5).

More advanced tensor decomposition algorithms were introduced by Smith (1995) and McNeice and Jones (2001). Smith's method comprises a different parametrisation of the distortion matrix and allows for the distortion model to either be fitted to individual periods or to a period band at each site. Fig. 6 shows strike angle estimates applying Smith's decomposition at four different period bands with each of the 54 sites being treated separately. For each period band we show diagrams of (i) strike angle versus period for a decomposition model fitting individual periods (ii) just below, the corresponding rose diagram, and (iii), at bottom, a rose diagram presentation of period-independent regional strike angles. Again, a clear regional strike direction is not easy to detect. But there is a tendency towards strike angles on the order of 60°N–90°E at longer periods, particularly for the band averaged estimates.

The method of McNeice and Jones (2001) is based on the Groom and Bailey decomposition scheme, but the transfer functions of several sites and frequency bands can be inverted jointly. The authors demonstrated with synthetic data that the multi-site multi-frequency decomposition can recover superior estimates of the regional impedances. Subsequent studies by Ledo et al. (2002) and Ledo and Jones (2002) suggest that it is advisable to divide the transect into subsets of sites and frequency bands rather than attempting to invert the whole data set. Fig. 7 shows the results of the tensor decomposition for six groups of sites (030-038, 021-030, 001-008/050-057, 009-013, 061-095/014/015 and 131-139, see Fig. 3). The figures show the regional strike as well as the twist and shear angles. The upper row of diagrams for each site-set gives the decomposition parameters for a joint inversion of two periods, while the second row of graphs shows the outcome if approximately one decade of data is inverted. If the tensor decomposition is successful, then strike, twist and shear angles should be period-independent (Echternacht et al., 1997). The first three subset of sites Fig. 7a–c reveal an approximately period-independent behaviour for periods longer than 1 s. The indicated regional strike

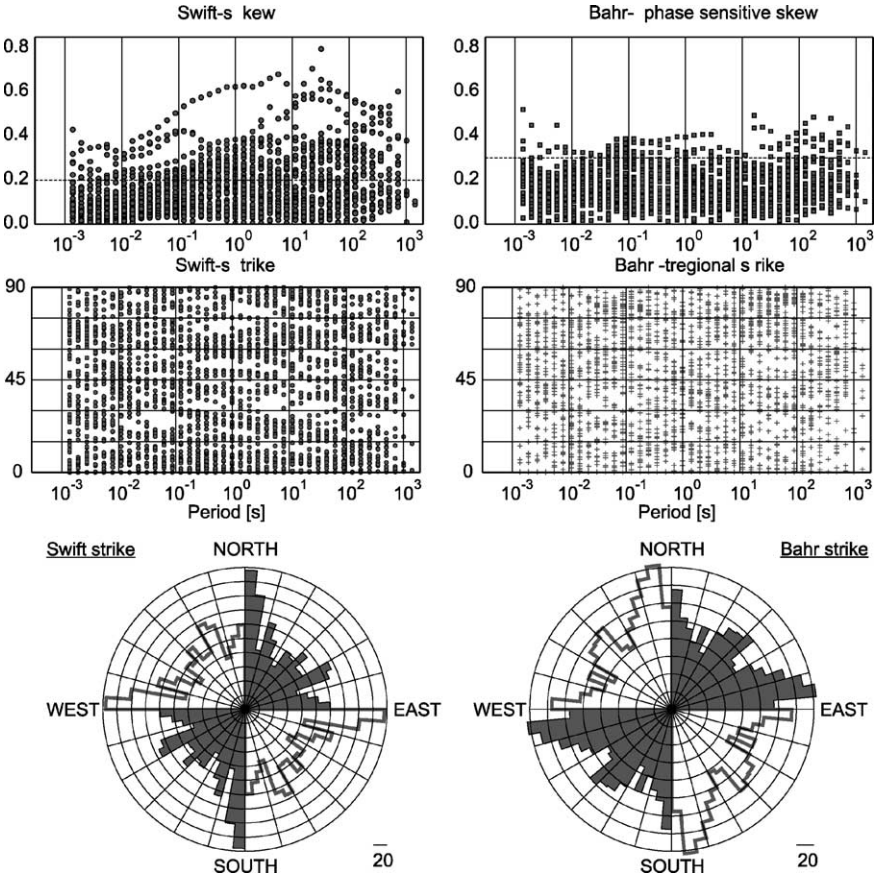

Fig. 5. Skewness of the impedance tensor and strike direction according to Swift's and Bahr's parametrisations. The strike directions calculated unconstrained, i.e. individually, at each period and site, show great variability.

angles vary in the range between 60°N–90°E; on average 65° ± 14°.

The situation is less clear in the southern Central Zone of the Damara Belt. Sites between the AF and WF/OL (013-009) and sites across the WF/OL (061-095, 014, 015) do not reveal any preferred regional strike direction, and both twist and shear angles are mostly scattered. It is possible that tensor decomposition methods fail for the site-set across the WF/OL because of strong local 3D effects and electrical anisotropy (see Part II). The responses from site-set 013-009 have a predominantly one-dimensional appearance (e.g. site 011 in Fig. 8) which would explain why a preferred strike direction cannot be found in the data. The southern most site-set (131-139), on the other hand, may reveal a similar regional strike as the northern sites of approx. N70°E, at least for the period band 10–100 s.

In summary, tensor decomposition methods indicate a regional strike on the order of N65°E in agreement with the orientation of the Van Zijl and de Beer conductivity belt and also with the induction vectors at long periods. At shorter periods, the induction vectors follow closely the trend of the large faults marking the Damara zone boundaries.

4. Two-dimensional modelling

In the previous section, we pointed out that both regional and local 3D features have an effect on this data set. Clearly, 2D modelling will not uncover all

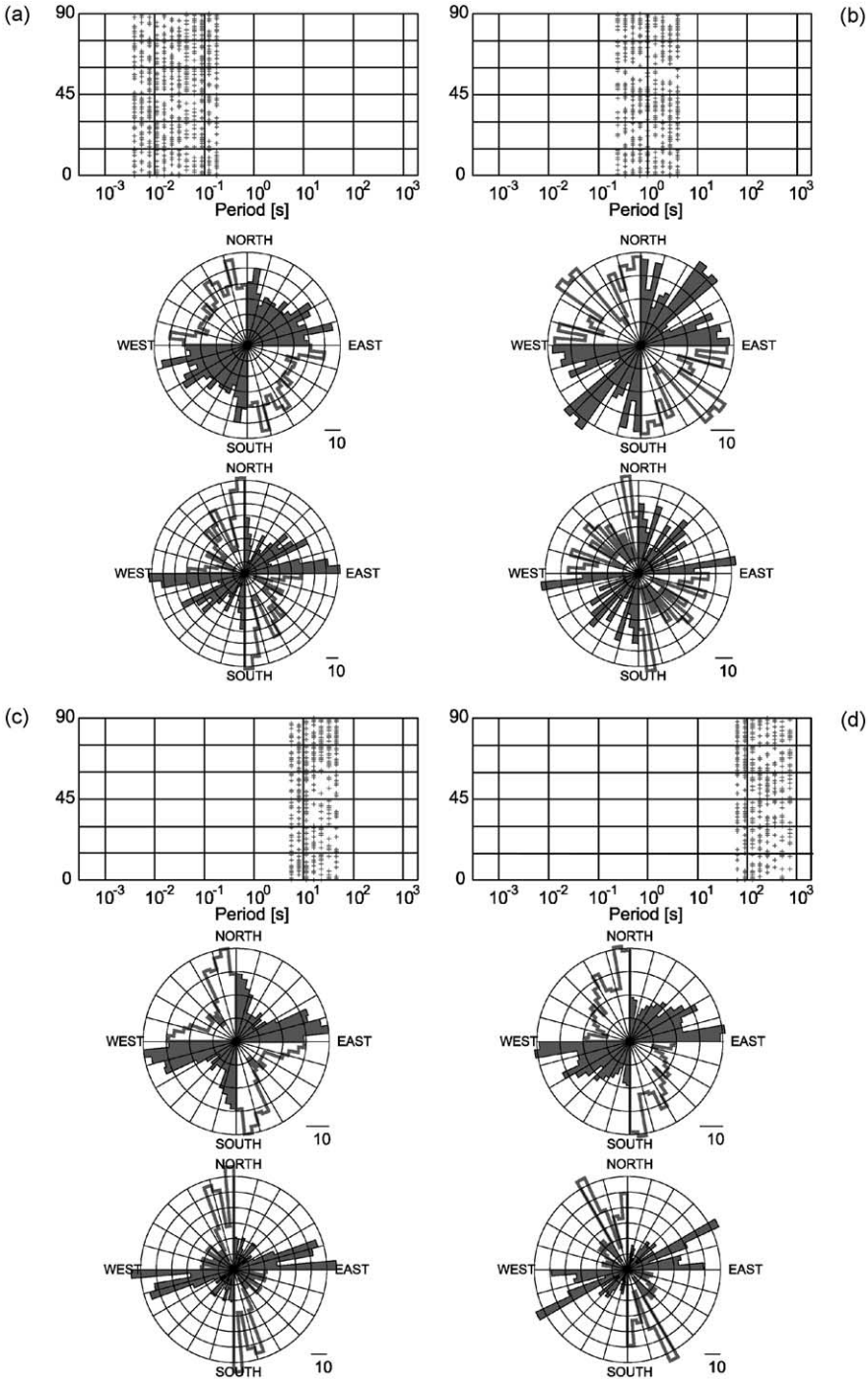

Fig. 6. Tensor decomposition using Smith's (1995) method. Four different period bands (a–d) of the impedances are examined for a common regional strike angle. Top diagrams: regional strike angles when fitting the data for individual periods. Middle diagrams: same data, but now plotted in a rose diagram. Bottom diagrams: rose diagram presentation of the best fitting strike angle for the whole period band. At longer periods, there is a preference for strike angles in the range 60°N–90°E.

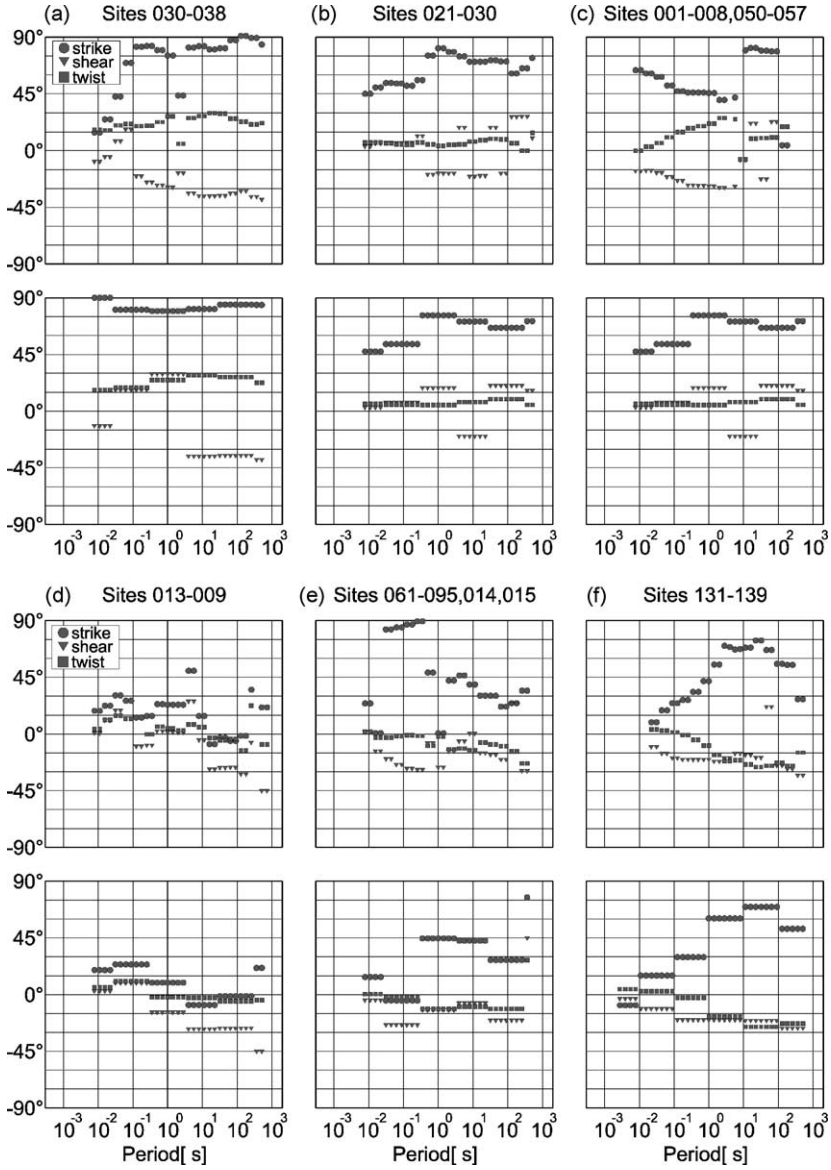

Fig. 7. Strike, shear and twist parameters of the McNeice and Jones tensor decomposition scheme. Six groups of sites (see Fig. 3) are analysed in an attempt to identify a common regional strike direction. The top diagrams show the results if two neighbouring periods are inverted; for the bottom row approximately one decade of data was inverted jointly.

aspects of such a complicated subsurface conductivity distribution. It is possible, however, to identify the most important regional features using a 2D approach. The presence or absence of structural elements in the 2D models are robust parameters, but the magnitude of conductivity anomalies may be biased by 3D effects (e.g. Unsworth et al., 1999).

The influence of 3D effects is most noticeable in the vicinity of the WF/OL, where we observe very high skew values, phases over 90°, and a strong coherency between parallel components of the electric

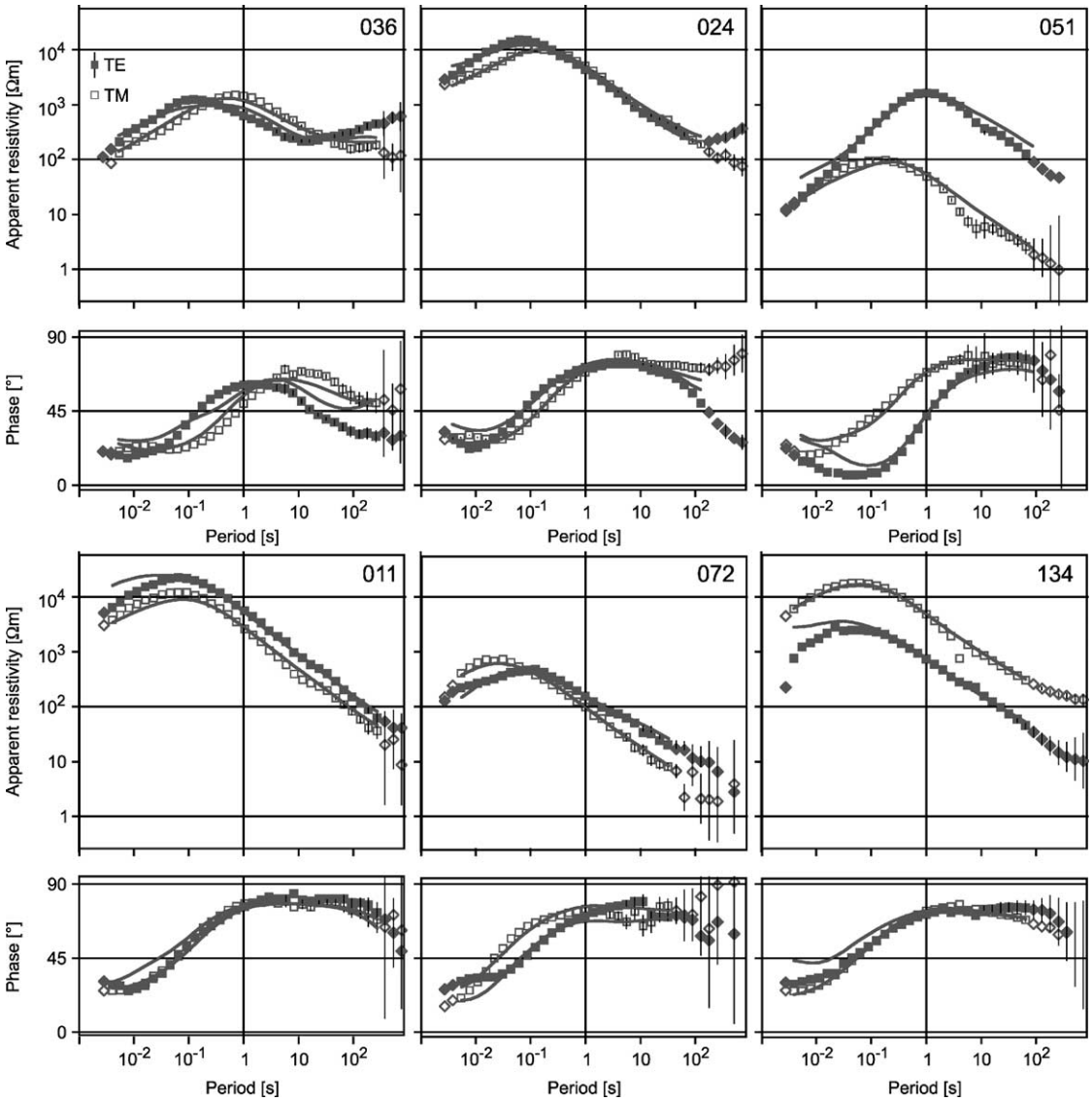

Fig. 8. Apparent resistivity and phase curves of sites representing different regions of the MT profile (compare Fig. 3). The data were rotated to N65°E. The solid lines indicate results of a combined TE + TM mode inversion of the complete data set (see Fig. 9). Diamond shaped symbols represent data points excluded from the inversions.

and magnetic fields. Most of the observed 3D effects can be explained through a combination of upper crustal bodies and anisotropic regions in the upper and lower crust (see Part II). For regional 2D modelling, we used only a few sites from the profile across the WF/OL (see inset in Fig. 3) such that the spacing between sites was 1.5 km. This was more consistent with the distribution of the remaining sites and kept the model grid at a manageable size. Furthermore, we removed all data showing phases above 90°; this occurred in the area north of the WF/OL, between sites 075 and 095 in the period band 10–1000 s.

The first step for 2D modelling is to identify the TE and TM mode impedances. TE mode impedances

correspond to electric currents flowing along the strike of a conductivity contrast, while TM mode data correspond to currents flowing normal to the strike. In the previous section, we discussed indications for a regional geo-electric strike direction of N65°E. Anisotropic 2D modelling of data from the vicinity of the WF/OL suggest N70°E for the direction of the enhanced conductivity (Part II), but the induction vectors at short periods (Fig. 4) and the surface expression of the fault zones appear to be more in line with a strike of approximately N45°E. In the end, we rotated the data to N65°E prior to 2D modelling.

Fig. 8 gives examples of apparent resistivity and phase curves of six sites, one from each of the subsets shown on Fig. 3. The data are rotated according to the direction of the geo-electric strike and in this sense are labelled as TE (solid squares) and TM (rectangles), respectively. Representative of the general situation of the Damara Belt are sites 024, 011, and 134. At short periods (shallow crust) we observe very high apparent resistivity values in the range of 5000–50,000 Ωm. Towards longer periods, the apparent resistivity curves decrease steeply and steadily while the phases rise above 60° indicative of a much more conductive deeper crust. Sites 051 and 072 are representative of site-sets from the vicinity of the large fault zones. They generally exhibit less resistive near surface structure but show similarly increasing conductivity with depth. The strong splitting of the TE (higher resistivity) and TM (lower resistivity) mode apparent resistivity curves at site 051 is typical for a site located on the conductive side of a nearby lateral conductivity contrast. Perhaps less clear is the situation for the northern most part of the profile, represented by site 036. However, the induction vectors in Fig. 4a indicate that these sites may be influenced by a more local, shallow zone of high conductivity.

In the following, we discuss the 2D inversion results. All two-dimensional resistivity models are derived from inversion of the MT data using the RLM2DI algorithm (Rodi and Mackie, 2001) which is part of the WinGLink[1] software package. RLM2DI finds regularized solutions (Tikhonov Regularization) to the two-dimensional inverse problem for MT data using the method of nonlinear conjugate gradients. The forward model simulations are computed using finite difference equations generated by network analogs to Maxwell's equations. The first step for the inversion is the design of a suitable finite-difference mesh, which depends largely on the site distribution and the frequency range of the observations. It must have at least one column for each station of the profile but grids preferably consist of a finer mesh where row thickness increases with depth based on the initial resistivity set for the model and the frequencies involved. After trials with different model sizes, we settled upon to a mesh of 131 horizontal by 84 vertical cells. All inversions started from a 100 Ωm homogeneous halfspace model.

The inversion algorithm attempts to minimize an objective function which is the sum of the normalized data misfits and the smoothness of the model. The trade-off between data misfits and model smoothness is controlled by the regularization parameter τ. The parameter τ is not automatically determined, but found through several runs of the inversion using different values of τ. The best value of τ will give the smoothest model and the target (smallest) misfit. In our case, a setting of $\tau = 3$ resulted in a good compromise between model roughness and data misfit. All inversion with a $\tau \geq 3$ reached convergence within a maximum number of 300 iterations.

Fig. 8 shows that most of the data <100 s have very small error bars, in fact many of them are too small to be plotted. However, some data points at very high frequencies and in the dead band, appear to be biased (offset from the curves) despite tiny error bars. Due to the limited recording time, many of the long period data (>100 s) are scattered and have larger error bars. Some of these data are incompatible with the 1D resistivity-phase relation. In the one-dimensional case and in most two-dimensional cases (if the data are in strike coordinates) apparent resistivity and phase can be predicted one from the other (Parker and Booker, 1996; Weidelt and Kaikkonen, 1994). Data points in violation of this relation cannot be fit by any inversion routine, and were thus marked inactive and excluded from the inversion. However, only pairs of TE and TM mode data can be marked inactive at individual periods; these are shown by diamond shaped symbols in Fig. 8. We furthermore decided to use pre-set error bounds instead of the statistically derived error bars in order to run the inversions with a higher emphasis

[1] http://www.geosystem.net/software.htm

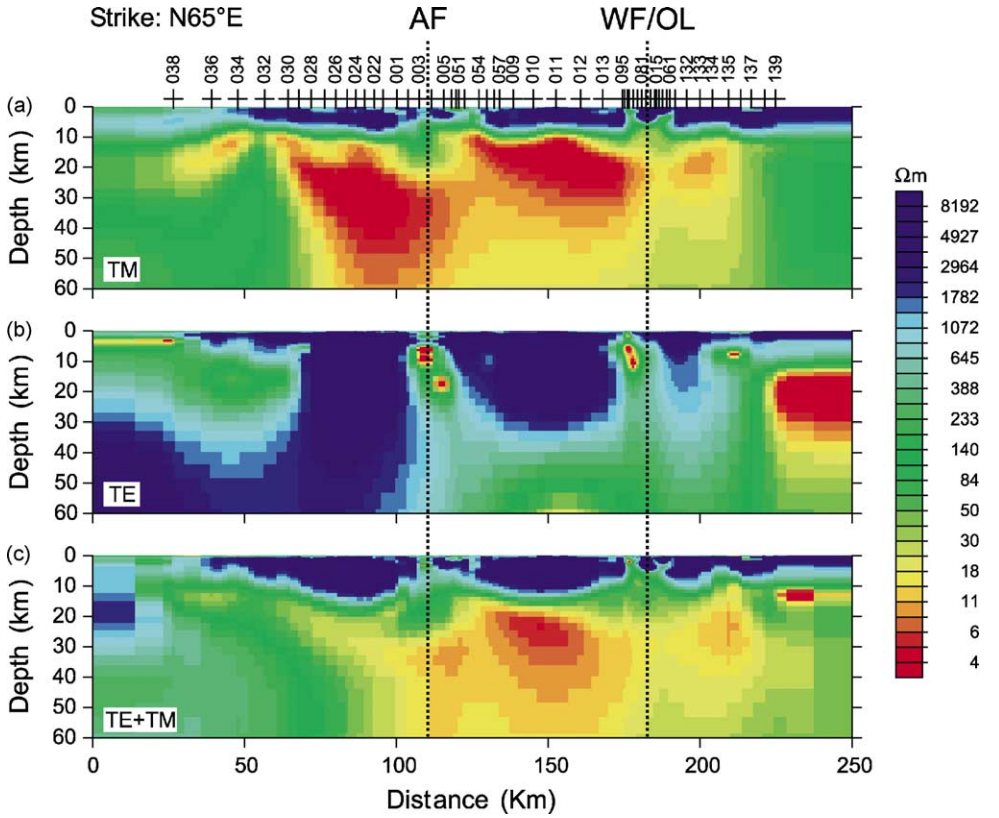

Fig. 9. Two-dimensional resistivity models of the crust derived from inversion of (a) TM, (b) TE, and (c) joint TM + TE mode magnetotelluric data using the RLM2DI algorithm. The main features of the resistivity models are the generally high conductivity of the mid-crust in the central part of the profile and the narrow, subvertical conductivity anomalies are attributed to basement shear zones (see text). AF: Autseib Fault, WF/OL: Waterberg Fault/Omaruru Lineament.

on fitting the phases as they are less sensitive to static shift effects.

Several authors have suggested basing the interpretation of MT data solely on the TM mode if the data show 3D effects because TM mode data are generally less influenced by off-profile features (e.g. Wannamaker et al., 1984). Unsworth et al. (1999) pointed out that the difficulty with this concept is that thin vertical conductors like fault zones are essentially invisible to TM mode electric currents. Electric charges accumulate on opposite sides of the conductor at depth but the effects are largely cancelled out at the surface. TE mode electric fields, on the other hand, are generated by currents flowing along the strike of the conductor and can be observed at the surface even if the conductive channel is narrow.

For comparison, we show results of inversions of the TM and TE mode data alone and a combined TM+TE mode inversion in Fig. 9. The individual TM/TE mode inversions were run with error bounds set to 10% for the apparent resistivity and to 0.6° for the phase data. Neither the TE nor the TM mode inversions included static shift as a free parameter. Fig. 9a shows the resistivity model if only the TM mode impedances are inverted. The data are well-fit to a normalized rms misfit of 1.7%. The resistivity section is dominated by two layers, a resistive upper crust and a conductive middle to lower crust. The upper crust at depths <10 km is very resistive (5000–15,000 Ωm), as expected for the high-grade metasediments and granites which constitute the local basement. Below about 15–20 km, the mid-crust appears heterogeneous, with much higher

conductivity in the central part of the profile than at either end.

As discussed before, a model which is more sensitive to thin vertical structures can be expected when only the TE mode data are inverted. The most prominent features in the TE-mode model in Fig. 9b are two sub-vertical zones of high conductivity near the AF and along the WF/OL. The model suggests that the faults dip steeply southward at approximately 65°and that these zones of high conductivity penetrate the whole crust. The best fitting TE mode model indicates a much thicker resistive upper crust and only a moderately conductive lower crust. All sections are truncated at a depth of 60 km because the imaged mid-crustal conductor results in an insensitivity to deeper structure. As usual for MT models, the thickness of the deep conductor is poorly constrained; it is possible that this 'layer' is thinner but more conductive. The TE mode model does fit the data although to a lesser degree, with a resulting rms error of 6.2%. However, closer inspection of the data reveals that this is generally due to relatively large misfits at the highest frequencies (compare Fig. 8) and also because of large static shifts at some sites (026, 002, 050, 136).

The resistivity section in Fig. 9c is obtained when the TE and TM mode data are fit simultaneously. The TM mode model of Fig. 9a was used as the starting model for the inversion and now, static shift was included as a free parameter. The algorithm assumes that the sum of the logarithms of the static shifts sum to zero. We set error bounds of 5% and 0.6° for TM mode apparent resistivity and phase curves and of 10% and 0.6° for TE mode. The error bound for the TE mode was set to a higher value when compared to the TM mode because the TE mode appeared to be more effected by static shift. The resulting rms misfit of the joint TE + TM mode inversion is 5.4% which can be further reduced to 3.7% if static shift at some sites is corrected manually. As expected, the combined TE + TM mode model exhibits some features from the inversion of individual modes. We recognize a generally resistive upper crust interrupted by sub-vertical conductors. The position of these conductors coincides with the location of induction vector reversals between the Omaruru River and AF and the WF/OL. The high conductivity in the lower crust is now more confined to the central part of the profile. The transition of the resistive upper crust to a conductive lower crust occurs at a depth between 13 and 17 km.

This marked difference between the results of modelling the two modes is similar to what Bailey et al. (2000) found for the Lower Zambesi and Mana Pools basins, respectively, and is discussed more generally in Berdichevsky et al. (1998).

Attempts to simultaneously fit the vertical magnetic field response functions with 2D inversion failed. This is not very surprising as the induction vectors at many sites in Fig. 4 show real vectors pointing obliquely to the profile and imaginary vectors which are not parallel to the real ones. We have already pointed out that the induction vectors appear to be particularly sensitive to electrical anisotropy in the fault zones.

5. Discussion

Our MT results generally support the existence of the conductivity belt proposed by Van Zijl and de Beer (1983) in Namibia. The layout of the MT profile and the dense station spacing allow for a much better definition of the crustal conductivity in this region. The locations of the upper crustal conductivity zones are sharply bounded by narrow, high-angle shear zones which correspond to major basement structures. Such laterally confined zones of crustal conductivity could not be resolved with the Van Zijl and de Beer (1983) magnetometer array study with a station separation on the order of 100–150 km and recording only at long periods (1000–10,000 s).

The cause of crustal conductivity anomalies can in general be fluids and/or conductive minerals (graphite, sulfides). Fluids cannot be ruled out in this case, but there is no supporting field evidence for hydrothermal alteration along the WF/OL or the AF. On the other hand, graphite-bearing marble units are widespread in both areas and graphite is more effective than saline fluids for increasing total conductivity. Sheared marble with schlieren of graphite along the shear planes occurs in the vicinity of the Omaruru Lineament and this type of rock could be responsible for the observed conductivity. The important point is that, regardless of what the conductive material in the rocks is, it must be interconnected over a distance of kilometres to produce the anomalies observed, and this can be best accomplished by movement along discrete fault zones.

Inspection of the fault zones in the field shows that they were initiated at or below the brittle–ductile transition thus the present erosional surface was at mid to lower crustal levels when the observed deformation began. Additionally, Liu et al. (1999) concluded from fabric analysis that the earliest deformation of the graphite bearing shear zones was semi-ductile. This suggests that they were formed during the late stages of the Pan-African collision as most of the overburden was removed during or soon after the orogeny, leaving the rocks under consideration in the brittle regime ever since (Miller, 1983). The emplacement of Mesozoic flood basalts did not alter this state as their maximum thickness did not exceed 5 km (Raab et al., 2002). Consequently, we propose a late Pan-African origin for the semi-ductile shear zones which may in turn be responsible for the accumulation of high conductivity material. Both the WF/OL and the AF lineaments were reactivated during the Mesozoic (Holzförster et al., 1999; Clemson et al., 1997, 1999), but it remains unclear how these events effected the evolution of the conductivity anomalies.

Further evidence for Cretaceous reactivation and for crustal weakness of the WF/OL zone comes from the large number of vertical dikes in this area. Geological mapping and Landsat imagery interpretation (Lord et al., 1996) reveal a major inland-trending dike swarm, which extends some 300 km NE from the Atlantic to the edge of the Congo Craton. The dike swarm parallels basement structures and is bounded by regional zone boundaries of the Damara fold belt. Limited geochemical and geochronologic work on the dikes indicates that they are early Cretaceous in age and they may represent feeders to now-eroded subaerial flood basalts of the Etendeka Group. Interestingly, both, the high conductivity zone and the area of the high dike density appear to be confined to the south by the WF/OL.

While we can positively link the sub-vertical conductors with surface observations, we have no such control on the identity of the deep crustal conductive 'layer'. It is has been suggested that the brittle–ductile transition may act as an impermeable barrier to the upward movement of brines trapped in the lower crust (e.g. Hyndman and Shearer, 1989). These trapped brines could form a thin but highly conductive layer in the middle crust. It is difficult, though, to imagine how the crust can retain fluids which originated from the collision of the Congo and Kalahari Cratons more than 500 Ma ago. This is even less plausible in the presence of deep reaching crustal fracture zones as suggested by both our MT models and regional intrusions of basaltic magmas in and through the crust in the Cretaceous. However, transport and circulation of fluids may have played an important role in the creation of these structures. In particular, these structures may have become good conductors through the deposition of phases such as graphite. Graphite in metamorphic rocks is either a result of the conversion of organic matter through metamorphism or of precipitation of solid carbon from natural carbon-bearing fluids (Luque et al., 1998). Laboratory measurements show that interconnected graphite flakes or graphite grain boundary coatings significantly enhance electrical conductivity (e.g. Nover et al., 1998). Once created, graphite can remain stable for very long time spans. Yardley and Valley (1997) also favour a dry lower crust for petrologic reasons, but it remains debatable as to how carbon contributes to the development of highly conductive layers in the middle and lower continental crust. Nevertheless, it appears to be the key issue for the interpretation of zones of high conductivity in old, deeply eroded orogenic belts generated by continental collision (e.g. Santos et al., 2002; Banks et al., 1996).

The MT results presented in this paper provide first insights into the deep structure of the Damara Belt. The geometry of the conductive zones suggests, that they represent the continuation of the WF/OL and the Autseib Fault at depth. Both structures appear to end in a common detachment. This finding is consistent with geodynamic models and deep seismic profiling studies of collisional orogeny which indicate that the major thrusts form a linked fault system rooted in the subduction zone (e.g. Willett et al., 1993; Beaumont and Quinlan, 1994). Such a system includes the major forelandward nappe thrusts that accrete lower plate material to form an orogenic wedge on the lower plate side of the orogen and the backthrusts that build up a wedge on the upper plate side. These thrust zones frequently follow inherited extensional structures (Beaumont et al., 2000).

Thrusting along these shear zones is reflected in the different stratigraphic levels exposed within the fault blocks. These offsets are observed along the OL, the

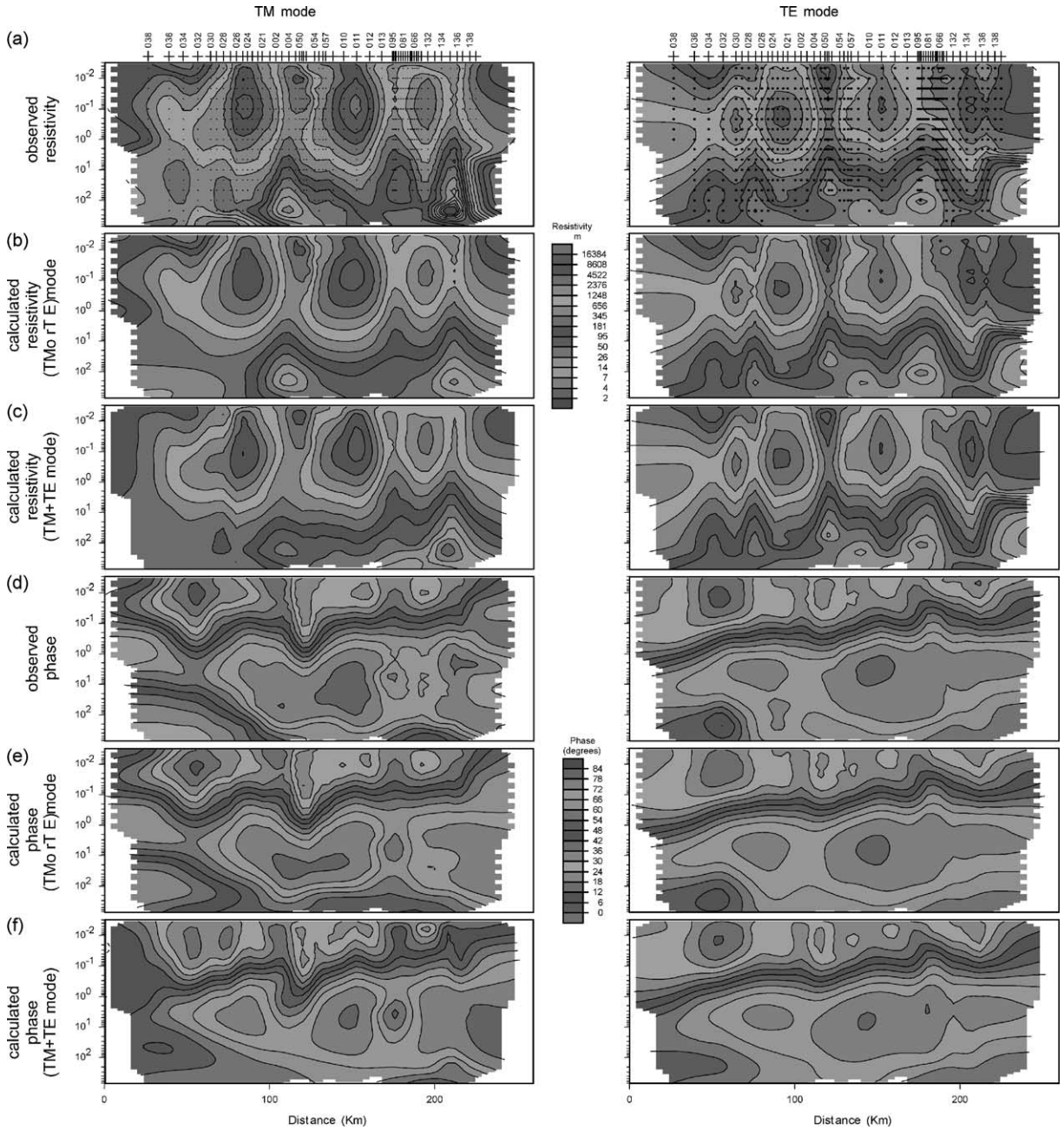

Fig. 10. Pseudosection comparison of observed data and modelling results. (a and d) Observed apparent resistivity/phase data; dots indicate data points. (b and e) Calculated apparent resistivity/phase data; left column: inversion of the TE mode data, right column: inversion of the TM mode data. (c and f) Calculated apparent resistivity/phase data for a combined TE + TM mode inversion. Note, the vertical scales of the graphs are period in seconds.

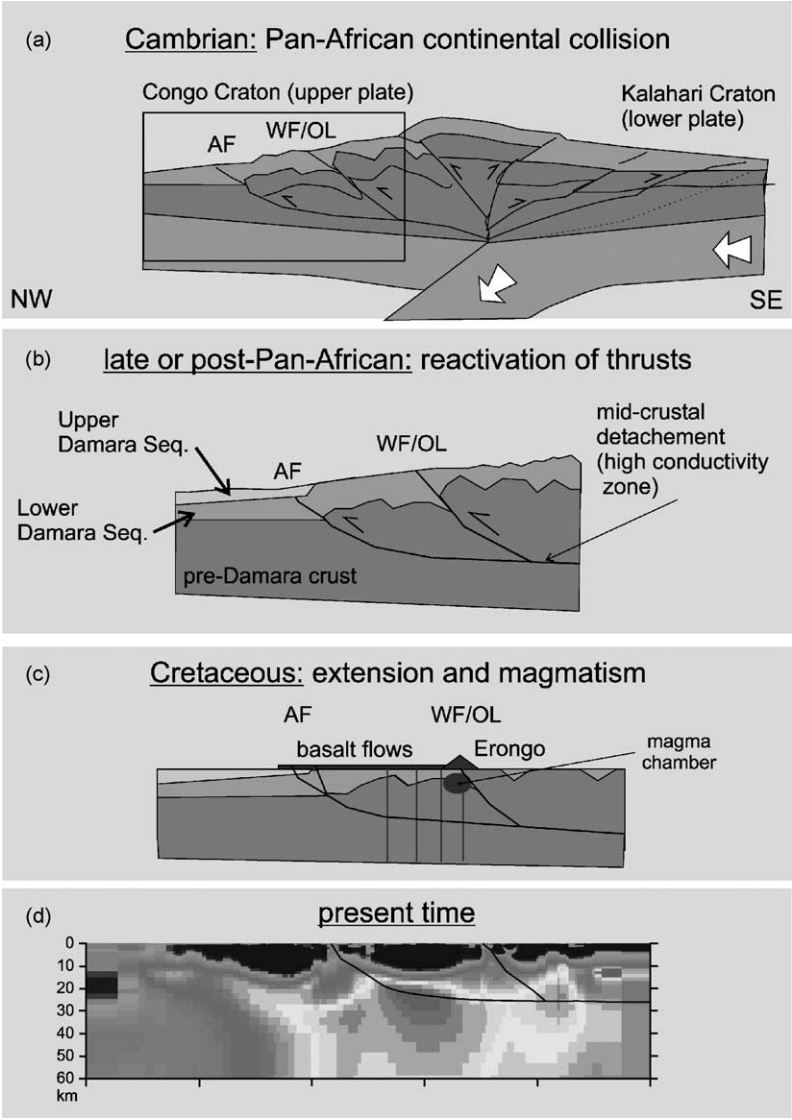

Fig. 11. Chronological cartoon of tectonic and magmatic events illustrating the connection between observed electrically conductivity anomalies and regional tectonism. (a) Pan-African continental collision: differential uplift on the southeast dipping ramps leads to a higher structural position of the sCZ (see Fig. 2). (b) Late orogenic reactivation of these ramps generates semi-ductile, graphite bearing shear zones. (c) Mobile shear zones control the spatial extent and direction of crustal deformation and magmatism in the Cretaceous. (d) The top of the high conductivity zone in the lower crust (compare Fig. 9c) is interpreted as a basement detachment zone.

WF/OL, and the AF in the Damara Belt. Multiple activations of these ramps during the orogeny are common and lead to semi-ductile or brittle overprinting of earlier ductile shear zones. Thus, we suggest that the electrical conductivity along the lineaments and in the mid-crust results from the reactivation of crustal scale shear zones during the late stages of the Pan-African orogeny (Fig. 10).

Summarizing the above ideas, Fig. 11 shows a schematic illustration of the proposed scenario: During

the Pan-African continental collision thick-skinned thrusting produced NW directed ductile shear zones. Accretion of foreland material in the footwall on the southeast dipping WF/OL brought the top of the Pre-Damara basement south of it into a higher structural position. In Fig. 11b, late tectonic or post-orogenic reactivation of these ramps leads to the generation of graphite by secondary enrichment or by deposition from fluids. Fig. 11c indicates how late to post-orogenic shear zones control the spatial extent and direction of crustal deformation and magmatism in the Cretaceous. The combined TE + TM mode MT model of Fig. 9c is reproduced in Fig. 11d and represents the present day situation: the basaltic flows at the surface are eroded, the sub-vertical dikes are remnants of the feeding channels. These dikes and a subsurface chamber of cold magma beneath the Erongo are now very resistive and therefore largely invisible to MT. The high conductivity is attributed to graphite enrichment within the fossilized shear zones.

Acknowledgements

The field campaigns in Namibia were funded by the GeoForschungsZentrum Potsdam. We thank the Geophysical Instrument Pool Potsdam, the University of Frankfurt, the Technical University of Berlin and the University of Edinburgh for providing the MT equipment. Without the support of the Geological Survey of Namibia (GSN), in particular of Gabi Schneider, Director of the GSN, and of Rainer Wackerle, in terms of logistic support, the experiment could not have been done. The success of this campaign also depended on the members of our field crew, Monika Korte, Guido Bengel, Svetlana Byrdina and Arne Hoffmann-Rothe, whom we would like to thank for their excellent work. We would also like to thank the team of the Brandberg Rest Camp in Uis where we stayed during both field experiments. Finally, we would like to acknowledge the work of the Namibia Working Group at the GFZ and particulary Bob Trumbull's contribution with many discussions and general help with the manuscripts. Critical and constructive comments from two anonymous referees helped clarify the manuscript.

References

Almeida, E., Pous, J., Santos, M.M., Fonesca, P., Marcuello, A., Queralt, P., Nolasco, R., Mendes-Victor, L., 2001. Electromagnetic imaging of transpressional tectonics in SW Iberia. Geophys. Res. Lett. 28 (3), 439–442.

Bahr, K., 1988. Interpretation of the magnetotelluric impedance tensor: regional induction and local telluric distortion. J. Geophys. 62, 119–127.

Bahr, K., 1991. Geological noise in magnetotelluric data: a classification of distortion types. Phys. Earth Planet. Inter. 66, 24–38.

Bailey, D., Whaler, K.A., Zengeni, T., Jones, P.C., Gwavava, O., 2000. A magnetotelluric model of the Mana Pools Basin, Northern Zimbabwe. J. Geophys. Res. 105 (5), 11185–11202.

Banks, R.J., Livelybrooks, D., Jones, P., Longstaff, R., 1996. Causes of high crustal conductivity beneath the Iapetus Suture Zone in Great Britain. Geophys. J. Int. 124, 433–455.

Bauer, K., Neben, S., Schreckenberger, B., Emmermann, R., Hinz, K., Fechner, N., Gohl, K., Schulze, A., Trumbull, R.B., Weber, K., 2000. Deep structure of the Namibia continental margin as derived from integrated geophysical studies: the MAMBA experiment. J. Geophys. Res. 105 (11), 25829–25853.

Beaumont, C., Quinlan, G., 1994. A geodynamic framework for interpreting crustal-scale seismic-reflectivity patterns in compressional orogens. Geophys. J. Int. 116, 754–783.

Beaumont, C., Munoz, J.A., Hamilton, J., Fullsack, P., 2000. Factors controlling the Alpine evolution of the central Pyrenees inferred from a comparison of observations and geodynamical models. J. Geophys. Res. 105, 8121–8145.

Bedrosian, P.A., Unsworth, M., Egbert, G., 2002. Magnetotelluric imaging of the creeping segment of the San Andreas Fault near Hollister. Geophys. Res. Lett. 29 (11), 10.1029/2001GL014119.

Berdichevsky, M.N., Dmitriev, V.I., Pozdnjakova, E.E., 1998. On two-dimensional interpretation of magnetotelluric soundings. Geophys. J. Int. 133, 585–606.

Clemson, J., Cartwright, J.A., Booth, J., 1997. Structural segmentation and the influence of basement structure on the Namibian passive margin. In: Roberts, A.M., Kusznir, N.J. (Eds.), Tectonic, Magmatic and Depositional Processes at Passive Continental Margins. J. Geol. Soc. London 154, 477–482.

Clemson, J., Cartwright, J., Swart, R., 1999. The Namib Rift; a rift system of possible Karoo age, offshore Namibia. In: Cameron, N.R., Bate, R.H., Clure, V.S. (Eds.), The oil and gas habitats of the South Atlantic. Geol. Soc. Specl. Publ. 153, 381–402.

Coward, M.P., Daly, M.C., 1984. Crustal lineaments and shear zones in Africa: their relationship to plate movements. Precambrian Res. 24, 27–45.

Daly, M.C., 1986. Crustal shear zones and thrust belts: their geometry and continuity in Central Africa. Phil. Trans. R. Soc. London 317 (A), 111–128.

Daly, M.C., 1989. Rift basin evolution in Africa: the influence of reactivated steep basement shear zones. In Cooper, G.D.W.M.A. (Ed.), Inversion Tectonics. Geol. Soc. Specl. Publ. 44(A), 309–334.

de Beer, J.H., Huyssen, R.M.J., Van Zijl, S.J.V., 1982. Magnetometer array studies and deep Schlumberger soundings in the Damara orogenic belt, South West Africa. Geophys. J. R. Astr. Soc. 70, 11–29.

Echternacht, F., Tauber, S., Eisel, M., Brasse, H., Schwarz, G., Haak, V., 1997. Electromagnetic study of the active continental margin in northern Chile. Phys. Earth Planet. Inter. 102, 69–87.

Eisel, M., Haak, V., Pek, J., Cerv, V., 2001. A magnetotelluric profile across the KTB surrounding: 2D and 3D modelling results. J. Geophys. Res. 106 (B8), 16061–16079.

Elektb Group, 1997. KTB and the electrical conductivity of the crust. J. Geophys. Res. 102 (B8), 18289–18305.

Frimmel, H.E., Frank, W., 1998. Neoproterozoic tectono-thermal evolution of the Gariep Belt and its basement, Namibia and South Africa. Precambrian Res. 90, 1–28.

Germs, G., 1995. The Neoproterozoic of southwestern Africa, with emphasis on platform stratigraphy and paleontology. Precambrian Res. 73, 137–151.

Gladczenko, T.P., Hinz, K., Eldholm, O., Meyer, H., Neben, S., Skogseid, J., 1997. South Atlantic volcanic margins. J. Geol. Soc. London 154, 465–470.

Groom, R.W., Bailey, R.C., 1989. Decomposition of magnetotelluric impedance tensors in presence of local three-dimensional galvanic distortion. J. Geophys. Res. 94 (B2), 1913–1925.

Haak, V., Jones, A.G., 1997. Introduction to special section: the KTB deep drill hole. J. Geophys. Res. 102 (B8), 18289–18305.

Hoffmann-Rothe, A., 2002. Combined structural and magnetotelluric investigation across the West Fault Zone in the Andes of Northern Chile. Ph.D. Thesis, Universität Potsdam.

Holzförster,, F., Stollhofen, H., Stanistreet, I.G., 1999. Lithostratigraphy and depositional environments in the Waterberg-Erongo area, central Namibia, and correlation with the main Karoo Basin, South Africa. J. Afr. Earth Sci. 29, 105–123.

Hyndman, R.D., Shearer, P.M., 1989. Water in the lower continental crust: modelling magnetotelluric and seismic reflection results. Geophys. J. Int. 98, 343–366.

Ledo, J., Jones, A.G., 2002. Regional electrical resistivity structure of the southern Canadian Cordillera and its physical interpreation. J. Geophys. Res. 106 (12), 30755–30769.

Ledo, J., Jones, A.G., Ferguson, I.F., 2002. Electromagnetic images of a strike-slip fault: the Tintina fault—Northern Canada. Geophys. Res. Lett. 29 (9), 10.1029/2001GL013408.

Light, M.P.R., Maslanyi, M.P., Greenwood, R.J., Banks, N.L., 1993. In: Williams, G.D., Dobb, A. (Eds.), Seismic Sequence Stratigraphy and Tectonics Offshore Namibia, Tectonics and Seismic Sequence Stratigraphy. Geol. Soc. Specl. Publ. 71, 163–191.

Liu, J., Yu, B., Weber, K., 1999. Coexisting brittle-ductile fracturing mechanisms in fault zones of the upper crust level. Chin. Sci. Bull. 44, 2107–2112.

Lord, J., Oliver, G.J.H., Soulsby, J.A., 1996. Landsat MSS imagery of a lower Cretaceous regional dyke swarm, Damaraland, Namibia: a precursor to the splitting of Western Gondwana. Int. J. Remote Sens. 17, 2945–2954.

Luque, F.J., Pasteris, J.D., Wopenka, B., Rodas, M., Barrenecha, J.F., 1998. Natural fluid-deposited graphite: mineralogical characteristics and mechanisms of formation. Am. J. Sci. 298, 471–498.

McNeice, G.W., Jones, A.G., 2001. Multisite, multifrequency tensor decomposition of magnetotelluric data. Geophysics 66, 158–173.

Miller, R.M., 1983. The Pan-African Damara Orogen of South West Africa/Namibia. Specl. Publ. Geol. Soc. S. Afr. 11, 431–515.

Nover, G., Heikamp, S., Meurer, H., Freund, D., 1998. In-situ electrical conductivity and permeability of mid-crustal rocks from the KTB drilling: consequences for high conductive layers in the earth crust. Surveys in Geophysics 19, 73–85.

Parker, R., Booker, J., 1996. Optimal one-dimensional inversion and bounding of magnetotelluric apparent resistivity and phase measurements. Phys. Earth Planet. Inter. 98, 269–282.

Porada, H., 1989. Pan-African rifting and orogenesis in southern to equatorial Africa and eastern Brazil. Precambrian Res. 44, 103–136.

Prave, A.R., 1996. Tale of three cratons: tectonostratigraphic anatomy of the Damara orogen in northwestern Namibia and the assembly of Gondwana. Geology 24, 1115–1118.

Raab, M.J., Brown, R.W., Gallagher, K., Carter, A., Weber, K., 2002. Late Cretaceous reactivation of major crustal shear zones in northern Namibia: constraints from apatite fission track analysis. Tectonophysics 349 (1–4), 75–92.

Ritter, O., Junge, A., Dawes, G.J.K., 1998. New equipment and processing for magnetotelluric remote reference observations. Geophys. J. Int. 132, 535–548.

Ritter, O., Haak, V., Rath, V., Stein, E., Stiller, M., 1999. Very high electrical conductivity beneath the Münchberg Gneiss area in Southern Germany: implications for horizontal transport along shear planes. Geophys. J. Int. 139 (2), 161–170.

Rodi, W., Mackie, R.L., 2001. Nonlinear conjugate gradients algorithm for 2D magnetotelluric inversion. Geophysics 66, 174–187.

Santos, F.A.M., Mateus, A., Almeida, E.P., Pous, J., Mendes-Victor, L.A., 2002. Are some of the deep crustal conductive features found in SW Iberia caused by graphite? Earth Planet. Sci. Lett. 201, 353–367.

Seth, B., Kroener, A., Mezger, K., Nemchin, A.A., Pidgeon, R.T., Okrusch, M., 1998. Archaean to neoproterozoic magmatic events in the Kaoko Belt of NW Namibia and their geodynamic significance. Precambrian Res. 92, 341–363.

Smith, J.T., 1995. Understanding telluric distortion matrices. Geophys. J. Int. 122, 219–226.

Stewart, J., Watts, A.B., Bagguley, J.G., 2000. Three-dimensional subsidence analysis and gravity modelling of the continental margin offshore Namibia. Geophys. J. Int. 141, 724–746.

Swift, C., 1967. A magnetotelluric investigation of an electrical conductivity anomaly in the southwestern United States. Ph.D. Thesis. MIT, Cambridge, Mass.

Tauber, S., Banks, R., Ritter, O., Weckmann, U., 2003. A high-resolution magnetotelluric survey of the Iapetus Suture Zone in south-west Scotland. Geophys. J. Int. 153 (3).

Unsworth, M.J., Malin, P.E., Egbert, G.D., Booker, J.R., 1997. Internal structure of the San Andreas fault at Parkfield, California. Geology 25 (4), 359–362.

Unsworth, M.J., Egbert, G., Booker, J., 1999. High-resolution electromagnetic imaging of the San Andreas fault in Central California. J. Geophys. Res. 105 (B1), 1131–1150.

Unsworth, M.J., Bedrosian, P., Eisel, M., Egbert, G., Siripunvaraporn, W., 2000. Along strike variations in the electrical structure of the San Andreas Fault at Parkfield, California. GRL 27 (18), 3021–3024.

Van Zijl, J.S., de Beer, J.H., 1983. Electrical structure of the Damara orogen and its tectonic significance. Geol. Soc. S. Afr. Specl. Publ. 11, 369–379.

Wannamaker, P.W., Hohmann, G.W., Ward, S., 1984. Magnetotelluric responses of three-dimensional bodies in layered earths. Geophysics 49, 1517–1533.

Weckmann, U., Ritter, O., Haak, V., 2003. A magnetotelluric study of the Damara Belt in Namibia 2. MT phases over 90° reveal the internal structure of the Waterberg Fault/Omaruru Lineament. Phys. Earth Planet. Inter., this issue.

Weidelt, P., Kaikkonen, P., 1994. Local 1-D interpretation of magnetotelluric B- polarization impedances. Geophys. J. Int. 117, 733–748.

Willett, S., Beaumont, C., Fullsack, P., 1993. Mechanical model for the tectonics of doubly vergent compressional orogens. Geology (Boulder) 21, 371–374.

Yardley, B.W.D., Valley, J.W., 1997. The petrologic case for a dry lower crust. J. Geophys. Res. 102, 12173–12185.

Available online at www.sciencedirect.com
SCIENCE DIRECT®
Physics of the Earth and Planetary Interiors 138 (2003) 91–112
PHYSICS OF THE EARTH AND PLANETARY INTERIORS
www.elsevier.com/locate/pepi

A magnetotelluric study of the Damara Belt in Namibia 2. MT phases over 90° reveal the internal structure of the Waterberg Fault/Omaruru Lineament

Ute Weckmann*, Oliver Ritter, Volker Haak

GeoForschungsZentrum Potsdam, Telegrafenberg, D-14473 Potsdam, Germany

Received 19 July 2002; received in revised form 5 March 2003; accepted 6 March 2003

Abstract

Magnetotelluric (MT) observations at some sites in the vicinity of the Waterberg Fault/Omaruru Lineament (WF/OL), a major tectono-stratigraphic zone boundary in the Central Zone of the Damara Belt, show evidence for strong three-dimensional (3D) effects. We observe very high skew values, phases over 90°, and a strong correlation of parallel components of the electric and magnetic fields at long periods. Because of the dense site spacing and good spatial coverage, we can positively attribute these effects to local geology and are able to resolve structural detail within the WF/OL. Mapping LaTorraca's electric characteristic vectors in form of ellipses proved particularly useful in identifying key elements of the conductivity structure for subsequent modelling. 3D and 2D anisotropic modelling can reproduce most of the observed 3D effects. The conductivity anomalies revealed in the area are: (i) a conductive ring structure in the shallow crust along the northern part of the profile; (ii) an anisotropic region in the upper crust with high conductivity parallel to the WF/OL; (iii) anisotropy in the lower crust with a different but undetermined strike direction; and (iv) a shallow elongated conductor sub-normal to the WF/OL. Modelling studies further suggest that the (anisotropic) fault zone is approximately 10 km wide and may reach down to a depth of 14 km or more.

Keywords: Magnetotellurics; Anisotropy; 3D effects; Namibia; Omaruru Lineament; Fossil shear zone

1. Introduction

The Waterberg Fault/Omaruru Lineament zone (WF/OL) in Namibia is a fossil shear zone which originated in Pre-Damara times more than 650 million years ago and which was reactivated several times in earth's history (Daly, 1989). It is well known that shear zones contain the most intensely deformed rocks and that the geometry and interaction of different structural elements within shear zones can be complicated. It is therefore not unexpected that the electrical response of the WF/OL is complex and difficult to interpret in terms of tectonic elements.

The ability of the magnetotelluric (MT) method to image the crust is often limited by data quality, by the distortion effects of small-scale near surface structures, or by imperfectly sampled three-dimensional (3D) features. Both, the distribution of sites along profiles and limited computing resources often confine our modelling to two dimensions. MT data can tell

* Corresponding author. Tel.: +49-331-288-1257; fax: +49-331-288-1235.
E-mail address: uweck@gfz-potsdam.de (U. Weckmann).
URL: http://www.gfz-potsdam.de/pb2/pb23/.

0031-9201/03/$ – see front matter © 2003 Elsevier Science B.V. All rights reserved.
doi:10.1016/S0031-9201(03)00079-7

us, however, if and to what extent three-dimensional distortion is present.

The derived impedance tensor $\underline{\underline{Z}}$ consists of four complex entries. In 1D and 2D environments (strike in x- or y-direction) the diagonal components, Z_{xx} and Z_{yy}, vanish. The 2×2 impedance tensor is only fully populated in a more general 3D case and in a 2D case rotated out of strike co-ordinates. In the latter case, a rotation into geo-electric strike direction is necessary to obtain an impedance tensor with ideal 2D appearance. In some situations tensor decomposition methods (e.g. Groom and Bailey, 1989; Groom and Bahr, 1992; Smith, 1995, 1997; McNeice and Jones, 2001) can help to separate local 3D galvanic distortion from regional 2D structures and to extract a regional geo-electric strike. The paper by Ritter et al. (this issue; hereafter referred to as Part I) is mainly concerned with the problem modelling the Damara Belt on a regional scale. The derived 2D models show a clear correlation between the observed conductivity anomalies and a regional shear system in which upper crustal listric faults pass into a mid-crustal detachment zone. However, it proved to be difficult to identify a clear regional geo-electric strike for this data set and the resulting models could not resolve details of the internal structure of the shear zones.

In a way, applying tensor decomposition methods is like walking on crutches. Crutches help us to get back our freedom of action when we are handicapped. But in the long term we like to get rid of them. The strategy behind tensor decomposition is to remove—as much as possible—the influence of local small-scale conductivity anomalies because they obscure our view of deeper and larger structures. However, we can never be certain about the correct definition of small or large and there is always a danger that we neglect important information contained in the data. The idea for the field work in 1999 was therefore to optimize the MT experiment in an attempt to maximize the resolution. The main aim of the study was to image the internal structure and the depth extent of the WF/OL. Good access to the area allowed us to set up the MT sites with a dense and regular spacing along two parallel profiles as well as an array of sites to provide lateral coverage of the fault zone (see Fig. 1(a)). The sparsely populated Namib desert provides excellent conditions to acquire high quality MT data.

The MT results from the experiment reveal strong 3D effects including an undetermined off-diagonal impedance tensor entry, phases over 90° and a strong coherency between parallel components of the electric and magnetic fields at long periods. Normally, phase values are bounded to a specific phase quadrant (Weidelt and Kaikkonen, 1994) and thus phase values out of quadrant often indicate problems with the instruments' response functions or with cultural noise. However, phases over 90° can also occur naturally in the presence of current deflection. In this paper, we show observations of such data and demonstrate that most of these effects can be explained by a combination of isolated high conductivity bodies in the upper crust and regions of electrical anisotropy in the upper and lower crust.

2. Field configuration and observed MT data

The magnetotelluric data were collected in 1999, using six GPS time synchronized S.P.A.M. MkIII instruments (Ritter et al., 1998). Metronix MFS05 induction coil magnetometers and Ag/AgCl electrodes of the Geophysical Instrument Pool Potsdam were deployed to record magnetic and electric field variations in the frequency range between 1000 and 0.001 Hz. Fig. 1(a) shows the target area together with the site locations (Fig. 1(a)). Forty-four of the MT sites are arranged along two dense profiles with a site spacing of 500 and 2000 m, respectively. Additional 16 sites, distributed to the east and west of the two profiles, provide good spatial coverage of the target area.

For the data processing, we used the robust remote reference processing procedures described in Ritter et al. (1998) but the application of the remote reference method or the source field coherency criterion did not alter the outcome of the data processing. Most of the impedance estimates are therefore obtained using a robust single site processing of the data. A data pre-selection scheme using a coherency criterion in the frequency domain was applied prior to a robust stacking which improved the data quality in the period band 5–50 s.

In Fig. 2, we show apparent resistivity and phase diagrams for three sites, which are representative of different areas of this data set. For this and all subsequent diagrams, the impedance tensor data is

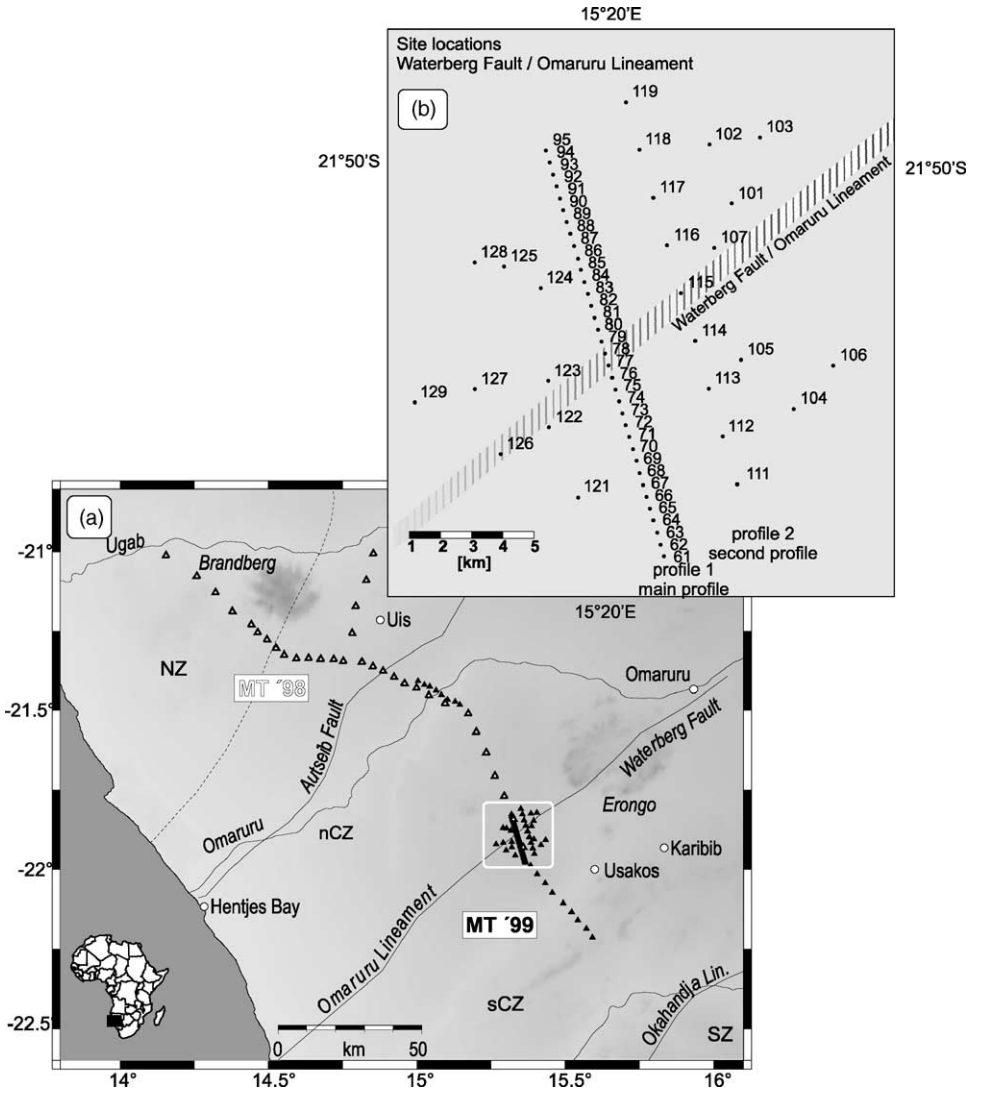

Fig. 1. (a) Map of all MT sites in the Damara Belt. The white rectangle outlines the area of the detailed study of the WF/OL relevant for this paper. The regional results are discussed in the companion paper (NZ: Northern Zone; nCZ: Northern Central Zone; sCZ: Southern Central Zone; SZ: Southern Zone). (b) Enlarged map of the sites across the WF/OL.

rotated to a geographic co-ordinate system ($x \hat{=}$ north, $y \hat{=}$ east).

The *xy*- and *yx*-components of the apparent resistivity and phase curves of site 063 in Fig. 2(a) vary smoothly and consistently with period. The general trend of the apparent resistivity curves indicates a change from resistive to more conductive structures with increasing period (depth). The phase values are in the expected quadrant between 0 and 90°. Site 063 is representative of the sites south of the WF/OL.

Site 085 (Fig. 1(b)) is located in the centre of the survey area. The apparent resistivity and phase curves are representative of the group of sites 073–090 (see Fig. 1). For the *yx*-component, we observe a similar behaviour of the apparent resistivity and phase curve as before. The *xy*-component, however, shows steeply decreasing apparent resistivity curves from

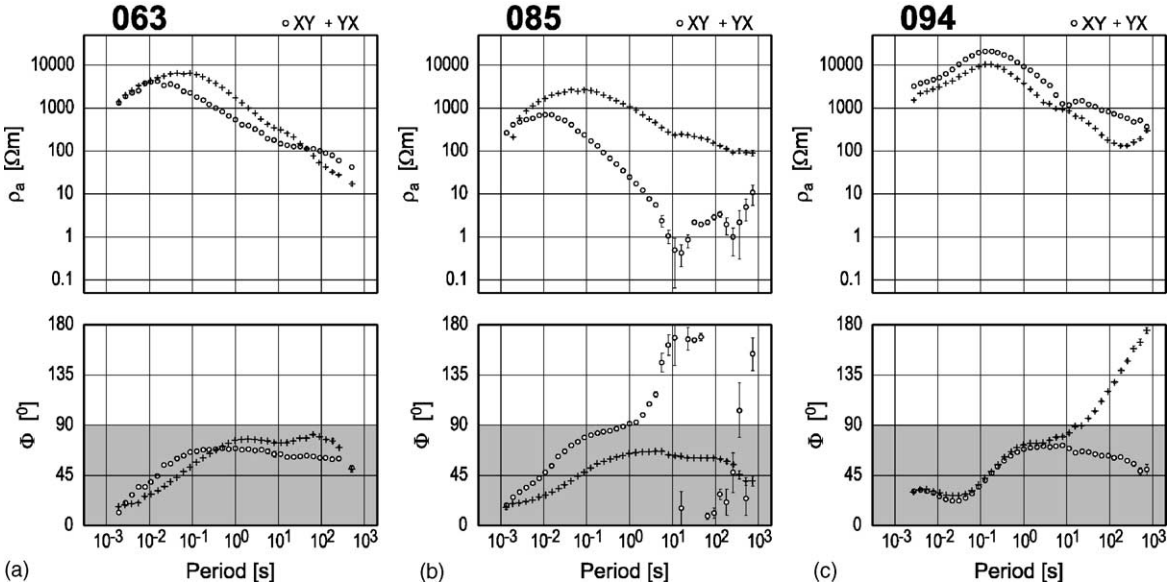

Fig. 2. Off-diagonal components of apparent resistivity and phase of three exemplary sites. (a) Site 063 is representative of the region south of the WF/OL. The curves appear to be undisturbed and smooth. (b) Site 085 is located north of the WF/OL and shows smooth curves for one off-diagonal component. The data of the *xy*-component scatter at periods >5 s and phases exceed 90°. (c) At site 094 situated in the northernmost part of the profiles, we observe phases of the *yx*-component leaving the quadrant at long periods.

approximately 1000 Ωm at 0.03 s period to 1 Ωm at 10 s period and an accompanying increase in the phase values. In the period band between 10 and 1000 s, the $\rho_{a,xy}$ curve scatters around a value of 1 Ωm. The corresponding phase curve leaves its expected quadrant at approximately 1 s but is mostly undetermined (scattered data points with large error bars) at periods >5 s. The general trend of the apparent resistivity curves, with a change from resistive to conductive, is comparable to site 063.

Phases above 90° are observed at several sites in the middle and northern part of the area, not only for the *xy*-component but also for the *yx*-component (e.g. Fig. 2(c)). A characteristic observation for most of the northern sites is one poorly resolved off-diagonal element of the impedance tensor at longer periods.

Site 094 in Fig. 2(c), which is situated approximately 10 km north of the fault zone, is an example of a station where the *yx*-component of the phase curve leaves its normal quadrant at periods >10 s. In this case, however, the phase data are not scattered, but cross the quadrant between 90 and 180° smoothly and continuously. The small bump in the apparent resistivity curves at around 10 s is found at many sites; it is most likely a bias effect caused by the small natural signal energy in this period band. Fortunately, this bias effect, which could not be reduced through remote reference processing, is rather irrelevant for the interpretation of the data.

Fig. 3 shows the apparent resistivity and phase curves of the same three sites calculated from the diagonal elements of the impedance tensor. Usually, we refrain from showing them as they are neglected when proceeding with a 2D interpretation. Additionally, they are commonly not well resolved due to the small size of the diagonal elements. We note, however, that in this case both diagonal tensor elements are for the most part well resolved. Around a period of 10 s we observe a small bias effect similar to the off-diagonal components, and at long periods >100 s the *yy*-component of sites 063 and 085 scatters. In general, the resulting apparent resistivity curves have similar magnitudes as the off-diagonal elements.

Polar diagrams provide a useful means to depict the magnitude of the impedance tensor elements for different co-ordinate systems (rotation angles). Fig. 4(a)

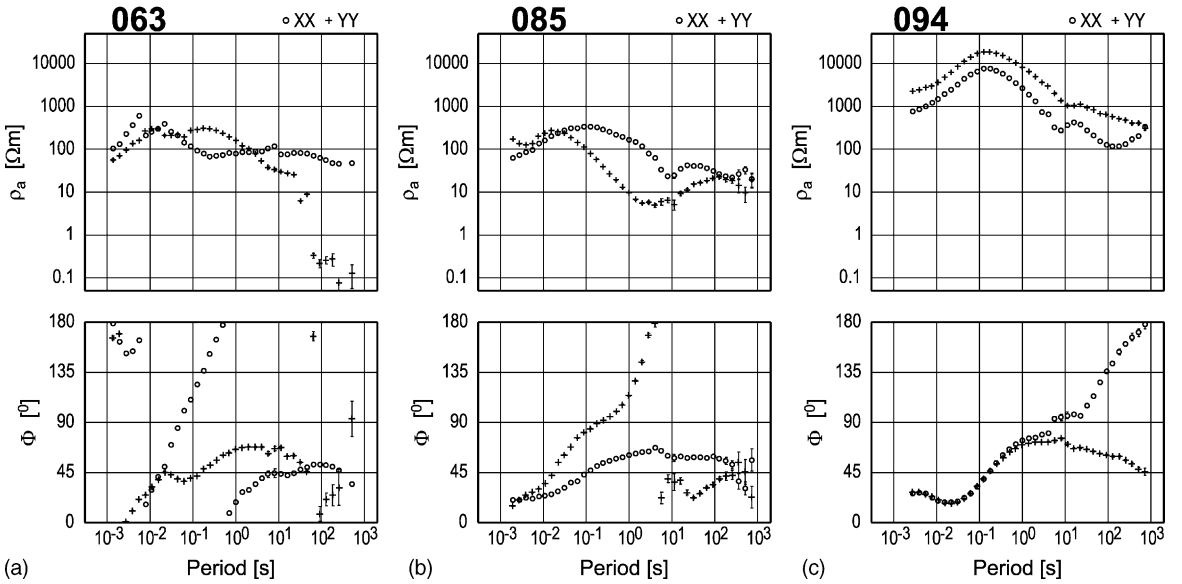

Fig. 3. The diagonal components of apparent resistivity and phase of the same three sites as shown in Fig. 2 are well resolved. In general, apparent resistivity values are of the same order of magnitude as those of the off-diagonal components.

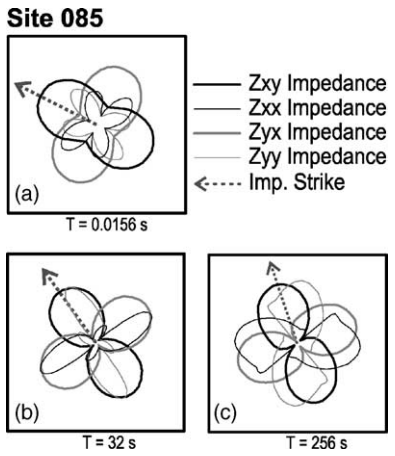

Fig. 4. Polar diagrams for all four impedance tensor elements. (a) At a period of 0.016 s, it is possible to minimize both diagonal entries (thin lines). The strike direction (with 90° ambiguity) indicated by an arrow coincides with the maximum of one off-diagonal component. (b and c) Polar diagrams at 32 and 256 s, respectively, show, that at best one diagonal element becomes small, but at the same time the other diagonal element is of the same order of magnitude as the large off-diagonal element (thick line). The impedance strike indicates the rotation angle (with 90° ambiguity) which minimizes the sum of the absolute values of both diagonal components (Swift strike angle).

shows polar diagrams for site 085 at three different frequencies. For clarity, we present all four tensor elements of the impedance. The impedance tensor at 64 Hz behaves as expected for the 2D case. We can identify a rotation angle for which both diagonal elements (thin lines) are small, while the off-diagonal entries (thick lines) become minimum and maximum, respectively. It is impossible though, to achieve this pattern at lower frequencies because at most rotation angles we obtain three large and one small tensor component or both elements of one row of the impedance tensor are large. Rotation by an angle of −18° in Fig. 4(c), for example, results in large *xy* and *yy* elements and small *yx*- and *xx*-components of the impedance tensor. The polar diagrams visually confirm that this is the best we can do at long periods as it is generally impossible to minimize both diagonal elements of the impedance tensor. Similarly, we could not find a co-ordinate system for which the phase values of the large components fall between 0 and 90°. This behaviour is unusual because a “normal” 1D or 2D setting—assuming that the data are in electric strike co-ordinates—results in much larger off-diagonal than diagonal tensor elements, and consequently, in much better determined off-diagonal than diagonal elements.

Fig. 5 shows pseudo sections of the off-diagonal components of ρ_a (top) and ϕ of all sites from the dense profile. The *xy*-component of the phase in Fig. 5 indicates rising phases, from approximately 30–70°, for the entire data set in the period range 0.01–1 s. For longer periods (1–1000 s), we observe a distinct change in the behaviour of the phases along the profile. In the northwestern part of the profile, the phases continue to rise at many sites (076–089), reaching values of 180°, while the phases of the southeastern sites remain below 75°. The pseudo section of the *yx*-polarisation of the phase in Fig. 5, on the other hand, indicates phases leaving the quadrant only at sites 094 and 095 at long periods (>100 s), while the rest of the sites show a fairly uniform pattern of a general decrease of phase values with period.

Fig. 6 displays pseudo sections of apparent resistivities and phases for the diagonal components. We observe a distinct change in $\rho_{a,xx}$ and ϕ_{xx} (top) across the WF/OL. Between 10^{-2} and 10^{0} s we find higher apparent resistivities north of the fault. Even more marked is the variation of the phase values. South of the fault we observe phase values between 0 and −180° at long periods, in contrast to phases values >90° in the north. In the *yy*-component of the apparent resistivity and phase (bottom) a lateral variation is less pronounced.

3. Geomagnetic results

So far, we have evaluated the data by studying the variation of the apparent resistivity and phase curves with period. This is useful because we know that the skin effect links electromagnetic fields at shorter periods with nearby, shallow structures while at the longer periods, they are dominated by more regional, deeper structures.

Fig. 7 shows the locations of the MT sites on a surface geological map. The profiles are centred upon the WF/OL, the boundary between the northern Central Zone and the southern Central Zone of the Damara Belt (see Part I). The metamorphic and meta-sedimentary rocks of the Damara sequences (Miller, 1983) appear to be structurally heterogeneous, but in terms of electrical conductivity they can be expected to be homogeneously resistive formations. Closer inspection of the map, however, reveals an oval structure in the northern part of the main profile. This ring structure consists of carbonate rocks, mostly graphite bearing marbles, which also occur in the southern part of the region. This is significant because such rocks can be very conductive if the graphite is inter-connected over large distances. Note also, that the 'anomalous' site 094 (see above) appears to be located exactly on the northern boundary of the marble ring.

The induction vector is a graphical representation of the vertical magnetic field transfer function which is non-zero only at lateral conductivity gradients and thus is a prime means of identifying boundaries. In Fig. 8 the induction vectors are shown for all sites at the three representative frequencies/periods of 128 Hz, 1 and 256 s (in the Wiese convention). At the highest frequency in Fig. 8(a), the induction vectors appear to point in random directions. This suggests the presence of local heterogeneities in the shallow crust. However, at the location of the WF/OL we can quite clearly identify a reversal of the real induction vectors (in black).

At a period of 1 s in Fig. 8(b), the induction vectors show a much more homogeneous behaviour. Interestingly though, the real parts at all sites suggest very consistently a lateral conductivity contrast further to the west with a strike almost parallel to the profiles. The imaginary vectors at most sites are neither parallel nor anti-parallel to the real vectors, indicating a more complex, three-dimensional conductivity structure. At the longest period of 256 s in Fig. 8(c), predominantly east pointing real induction vectors—with smaller lengths—are limited to an approximately 10 km wide region north of the WF/OL. To the north and south of this region the induction vectors tend to point in opposite directions. This behaviour becomes more distinct upon inclusion of some of the sites from the regional study (see Fig. 8(d) and Part I). This regional-scale reversal of the induction vectors can only be caused by a large-scale east–west striking conductive feature.

4. Evaluation of 3D parameters

In the following, we examine further physical properties of the data that are sensitive to 3D effects. In the course of trying to better understand this data set, we found that the univariate (or simple) coherency between individual components of the electric and

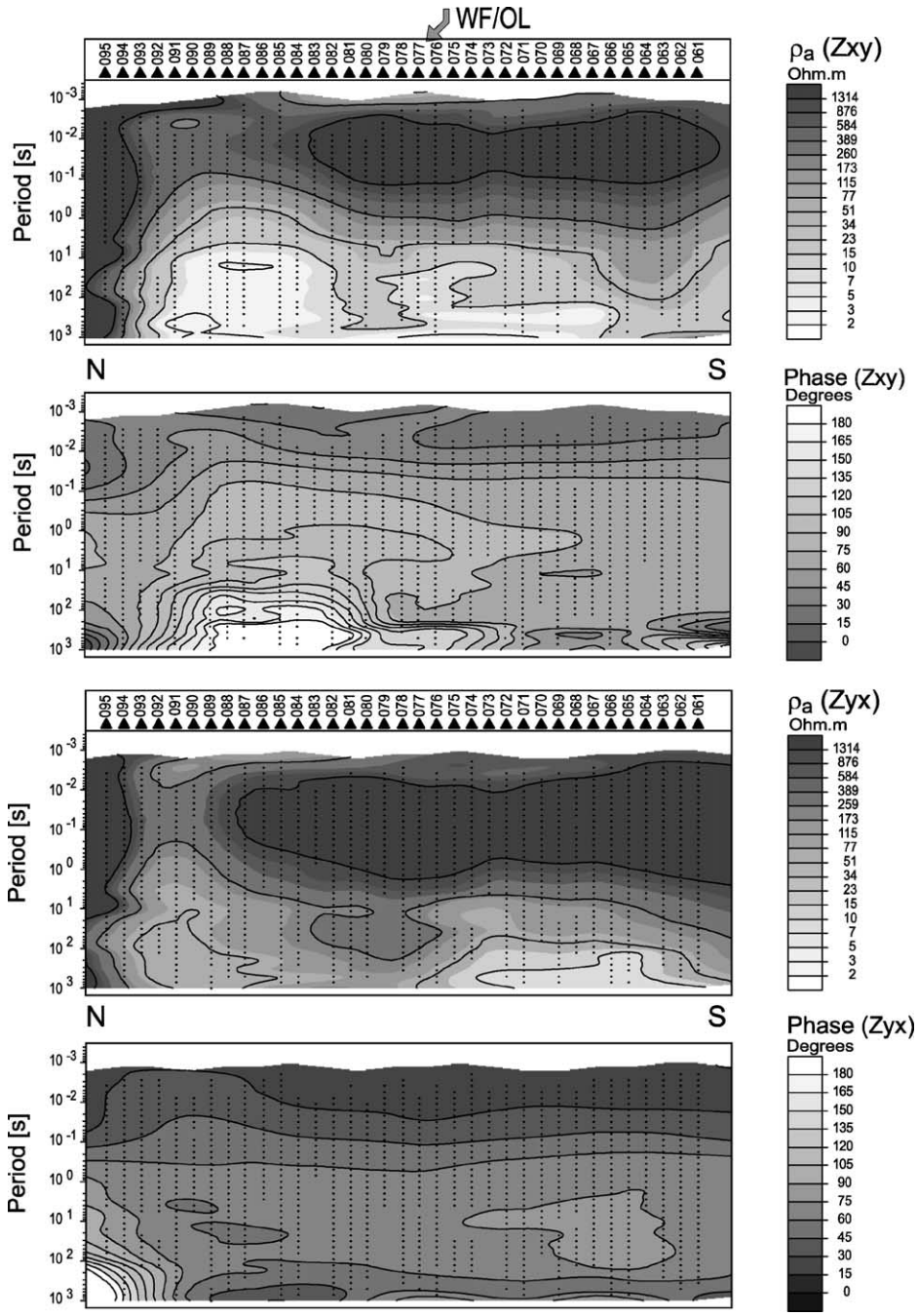

Fig. 5. The pseudo sections of apparent resistivity and phase along the dense profile illustrate that the 3D effects described by the exemplary sites in Figs. 2 and 3 are observable at several neighbouring sites. Whereas the apparent resistivities of the *xy*-component do not exhibit unusual behaviour, phases over 90° occur at sites north of the WF/OL. The apparent resistivities and phases of the *yx*-component do not change across the WF/OL, but the phases at the two northernmost sites are out of quadrant. The data points are marked with dots.

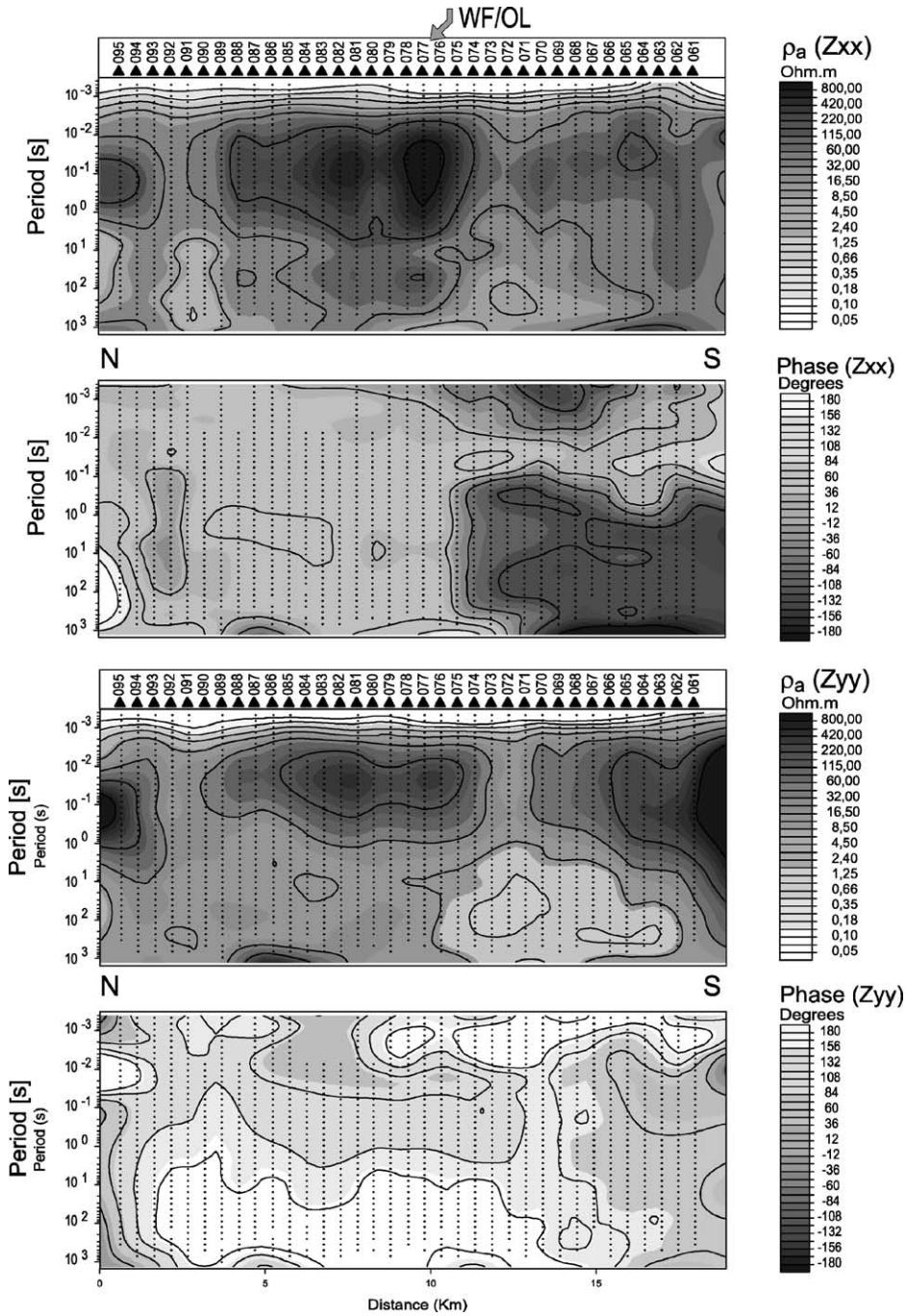

Fig. 6. The pseudo sections of apparent resistivity and phase of the it diagonal components along the dense profile. Between 10^{-2} and 10^{0} s $\rho_{a,xx}$ is characterized by generally higher values north of the WF/OL. South of the fault ϕ_{xx} values fall below 0°, whereas north of the WF/OL they fall within in the first quadrant.

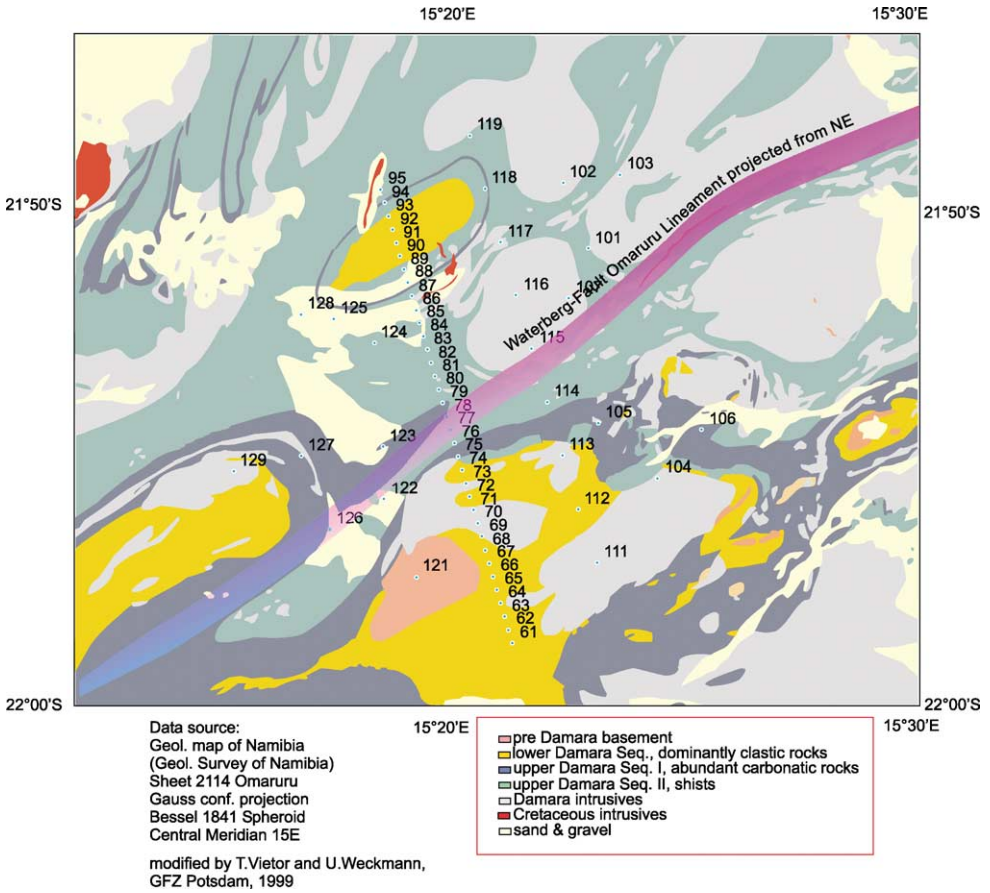

Fig. 7. MT sites locations overlain upon surface geology map. The position of the WF/OL is projected from satellite images. In the northern area, a ring structure consisting of carbonatic rocks is mapped. At this and other locations, where carbonatic rocks occur, graphite bearing marbles are found.

magnetic fields is a useful parameter for studying three-dimensionality in MT data. This is somewhat unconventional because coherency is normally used only at the data processing stages, as a statistic to measure the quality of the observations. The simple coherency is defined as:

$$\mathrm{coh}(XY) = \frac{|[XY^*]|^2}{[XX^*][YY^*]} \quad (1)$$

where X and Y represent frequency domain electric and magnetic field components, respectively. Y^* denotes the complex conjugate of Y and the terms enclosed in brackets define cross- and auto-spectra.

Based on Maxwell's theory and assuming uniform conductivity, we assume that the horizontal components of the magnetic field are associated with the respective orthogonal components of the electric field. Consequently, we expect a univariate coherency close to 1 between perpendicular components of the electric and magnetic field, while the coherency of parallel field components should be very small (≈0). Such expected behaviour of the univariate coherencies can be seen in Fig. 9(a) (right) with coh(EyBx) values mostly above 0.8 and coh(EyBy) values mostly below 0.25 for the whole period range. The univariate coherencies of the other two channels in Fig. 9(a) (left) show a similar pattern, however, only at shorter periods. For long periods (10–1000 s), we observe a rapid and continuous transition of coh(ExBy) from high to low values (≈0) while the univariate coherency

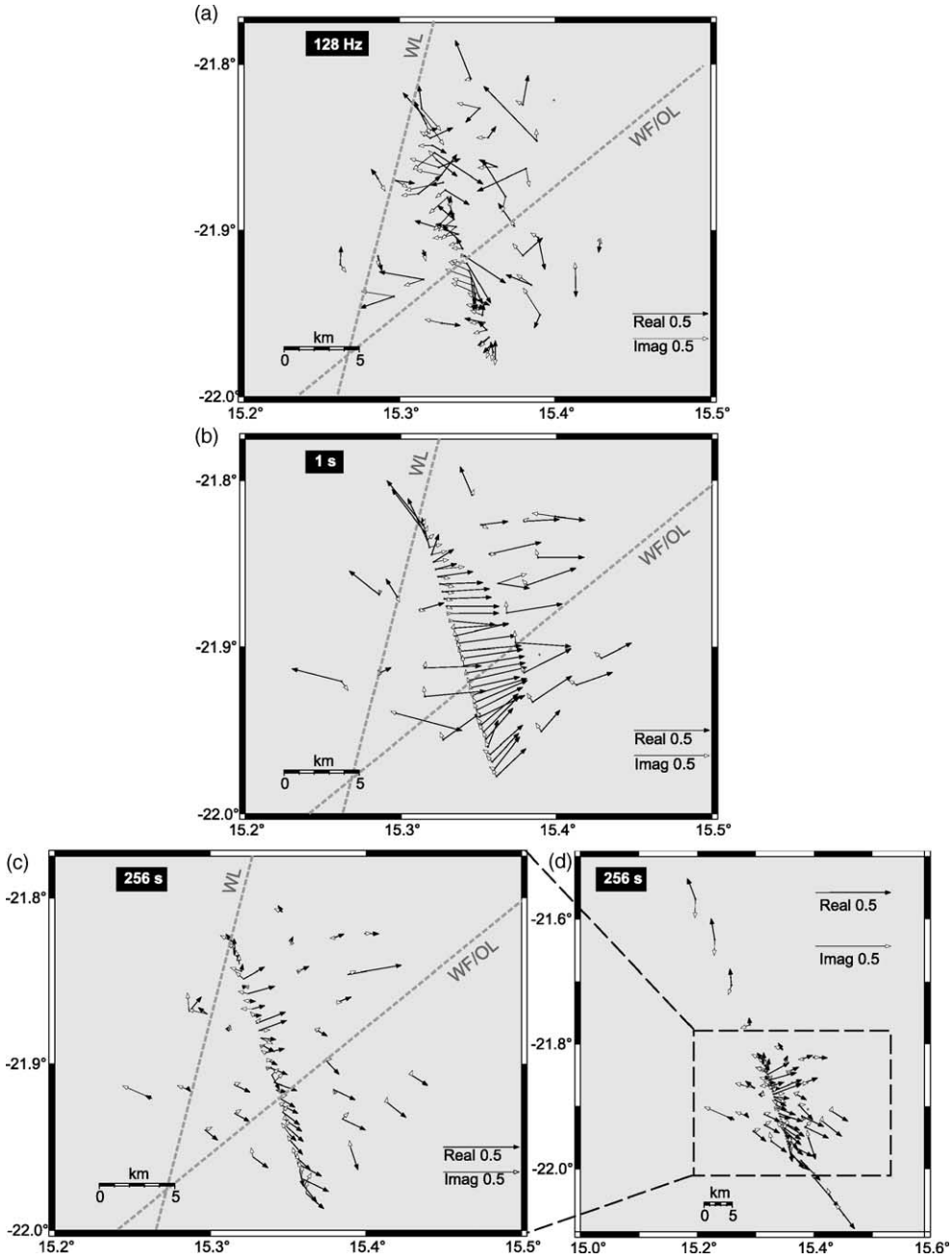

Fig. 8. Induction vectors across the WF/OL at three different periods. The locations of the WF/OL and the Welwitschia Lineament zone (WL) are displayed by grey dashed lines (see text). (a) At short periods the induction vectors scatter due to upper-crustal heterogeneities but a reversal clearly indicates the location of the WF/OL. (b) Surprisingly, most of the induction vectors at 1 s point eastwards. (c) At long periods, the induction vectors become smaller and indicate a smooth reversal from north pointing to southeast pointing real vectors. (d) The reversal is more obvious if we include additional sites to the north and south (see Part I).

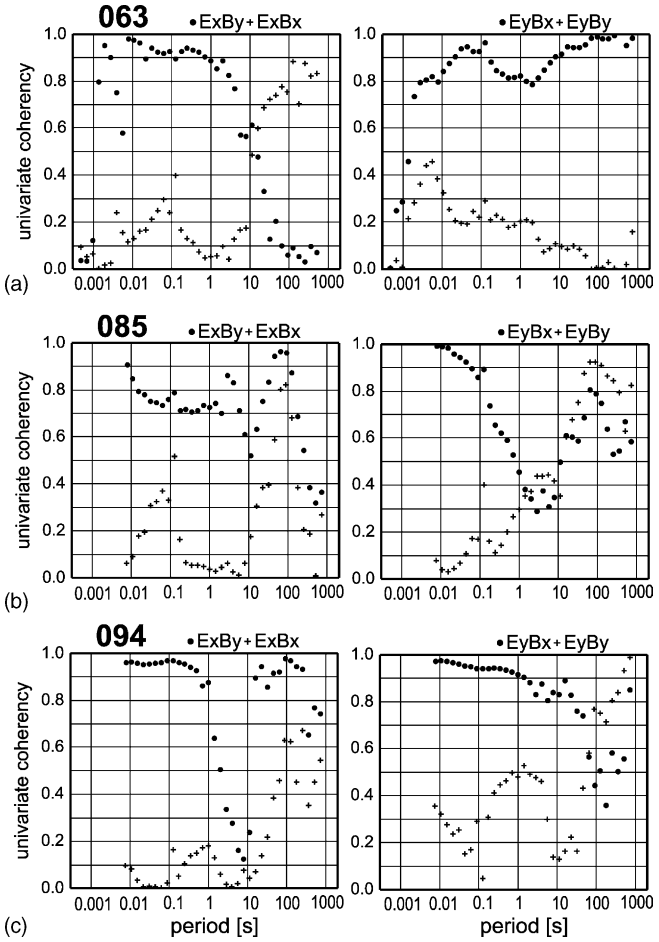

Fig. 9. The univariate coherencies EyBx and EyBy in diagram (a) expectedly show high values (∼1) for perpendicular and low values (∼0) for parallel components of electric and magnetic fields. However, the univariate coherencies ExBx and ExBy in diagram (a) indicate this behaviour for short periods only. At long periods, parallel electric and magnetic field components reveal a strong correlation. We observe similar behaviour at sites 085 and 094 (b and c).

between Ex and Bx increases to values of up to 0.9. The lack of correlation between Ex and By and the concomitant high correlation of Ex and Bx at long periods cannot be attributed to cultural noise and explains immediately why the Z_{xy} element of the impedance tensor is poorly resolved at many sites and why Z_{xx} is well determined (compare Figs. 2 and 3). Similar behaviour is seen at sites 085 and 094 in Fig. 9.

Usually, the skewness of the impedance tensor is evaluated to estimate the dimensionality of the data. Fig. 10 shows the normal (Swift, 1967) and the phase sensitive skew values (Bahr, 1991) for all sites shown in Fig. 1(b). Bahr's (1991)sensitive skew uses the fact that an impedance tensor in regional 2D strike direction results in tensor columns with equal phases in the case of small-scale local distortion. Most of the Bahr skew values at the shortest periods (<0.01 s) are smaller than the empirically determined thresholds of 0.3 (Bahr, 1991) for a 3D environment. The Swift skew values for the majority of the sites do not exceed the threshold of 0.2 (Swift, 1967). Large skews are found at longer periods, where they reach values of up to 1.0. Swift skews are even higher. Note that

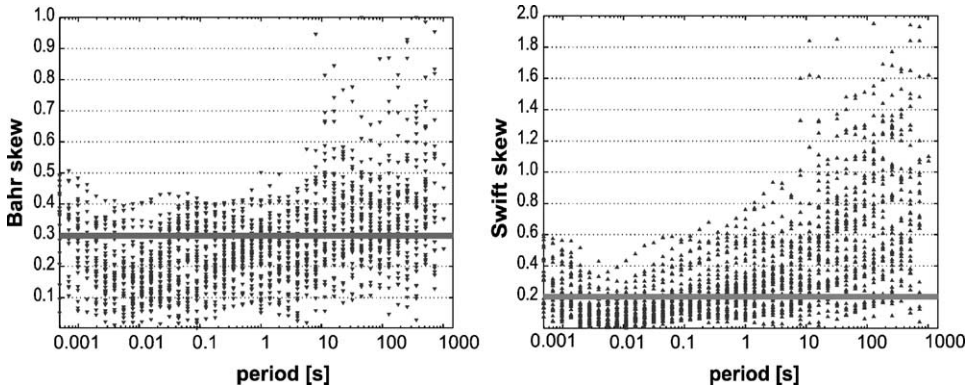

Fig. 10. Bahr and Swift skew values for sites shown in Fig. 1(b). Over almost the entire period range, and particularly at long periods, we observe skew values over the empirical thresholds of 0.3 (Bahr) and 0.2 (Swift). These high skew values are incompatible with a 1D or 2D environment.

in Part I we considered a different set of sites for the computation of 3D parameters.

Sometimes, 3D effects result from relatively small-scale heterogeneities in close vicinity to a particular site. Under these circumstances, tensor decomposition schemes (e.g. Bahr, 1988; Groom and Bailey, 1989) are commonly applied to resolve the undistorted regional 2D impedance tensor and the regional strike angle from locally distorted data. Fig. 11 shows the strike angles after Bahr decomposition of the data for all sites along the main profile. It is clear that this method does not provide a consistent strike angle for this data set.

With the method of McNeice and Jones (2001), the transfer functions of several sites and frequency bands can be inverted jointly as an extension of the Groom and Bailey decomposition algorithm (Groom and Bailey, 1989). To use the method, data from the main profile are separated into three sub-sets, containing sites 061–074, 075–084 and 085–095, respectively. Each frequency band consists of four adjacent frequencies. If the tensor decomposition is successful, a frequency-independent, regional strike direction is expected. Fig. 12 shows the parameters of regional strike as well as the so-called twist and shear angles (Groom and Bailey, 1989) versus period. The first sub-set of sites (see Fig. 12(a)) exhibit approximately frequency-independent behaviour for all three parameters at periods shorter than 1 s. The obtained strike angle varies around a mean value of approximately 0°. However, at longer periods the decomposition parameters scatter between 45 and −45°. This instability

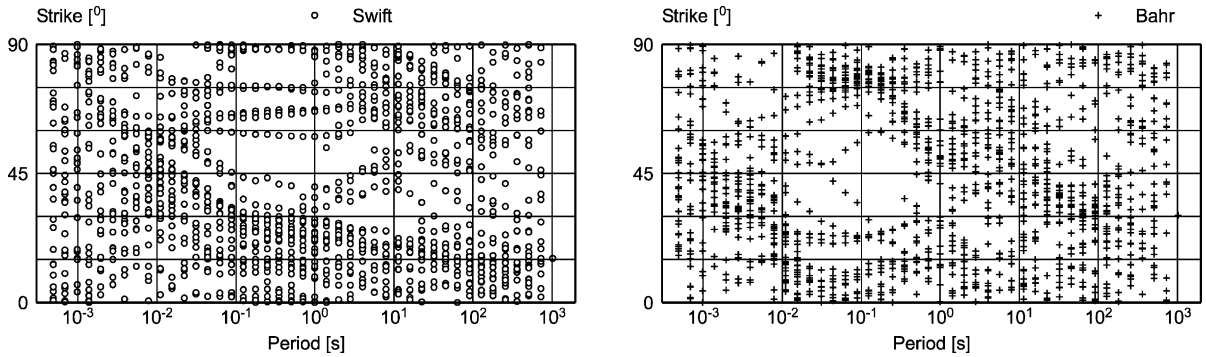

Fig. 11. Diagrams of the conventional and phase sensitive rotation angles of the sites across the WF/OL shown in Fig. 1(b) reveal that a distinct strike direction for this sub-set of the Namibian data set does not exist.

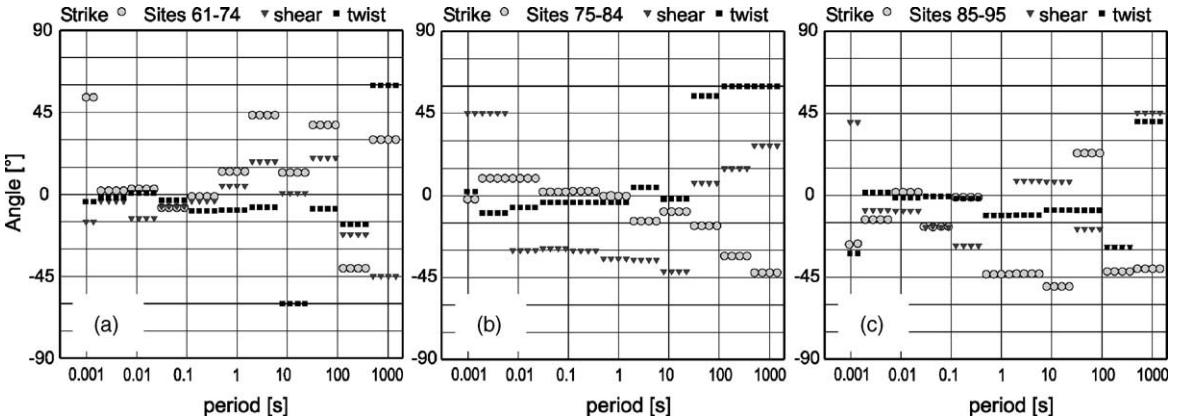

Fig. 12. Multisite, multifrequency GB decomposition of three sub-sets of sites: 061–074, 075–084 and 085–095. While at short periods (<1 s) the decomposition parameters are less frequency dependent, indicating a geo-electric strike direction around 0°, they strongly scatter at long periods.

indicates that the decomposition failed. Fig. 12(b) shows similar results for the sub-set of sites 075–084: frequency-dependent behaviour is observed at short periods, while at periods >10 s twist and shear angles scatter again. Decomposition parameters at the northernmost sites (Fig. 12(c)) do not exhibit any frequency independence; solely the twist angle appears to be stable at short periods.

A different approach of MT data decomposition was introduced by LaTorraca et al. (1986). Using a modified singular value decomposition (SVD), the complete MT impedance tensor is transformed into electric and magnetic characteristic vectors. As the principle axis of the magnetic and electric fields are not necessarily perpendicular, they introduced a skew angle, which is related to distortions of the electric current systems. With synthetic data LaTorraca et al. showed that the maximum-state polarisation ellipses are also suitable to map conductivity anomalies. Further modelling studies by LaTorraca et al. (1986) and Weckmann (2002) show that in the vicinity of a conductivity contrast the principle axes of the electric polarisation ellipses are sensitive to the conductivity boundary. On the resistive side of the boundary, electric polarisation ellipses are orientated perpendicular to the contrast while on the conductive side they are aligned parallel to the boundary.

The first set of LaTorraca polarisation ellipses is plotted in Fig. 13 at a frequency of 5.6 Hz. Note that the electric ellipses (E_1, in black colour) change their shape and orientation across the WF/OL whereas the magnetic ellipses (H_1, in grey) do not show significant variations. South of the WF/OL most of the electric ellipses are orientated approximately north/south. The ellipses are less elongated than those located on and to the north of the WF/OL, where we observe extremely elongated electric ellipses. This observation is not restricted to sites on the main profile, as most off-profile sites north of the WF/OL also show ellipses orientated parallel to the fault. This approximately 10 km broad zone of elongated ellipses coincides with the region of high conductivity indicated by the induction vectors at long periods and is consistent with the regional model in Part I.

Further north, at sites located above the conductive ring structure (sites 094, 118 and 088), extremely elongated electric polarisation ellipses appear to follow the structure. As expected for conductive material, they are aligned parallel to the ring. This observation is consistent with the induction arrows at short periods which also indicate this anomaly.

5. Interpretation of the MT data using 3D and anisotropic 2D modelling

From the previous section, we have indication of at least three conductive features: (i) a conductive ring in the northern part of the profile; (ii) an EW striking anomaly associated with the WF/OL effecting

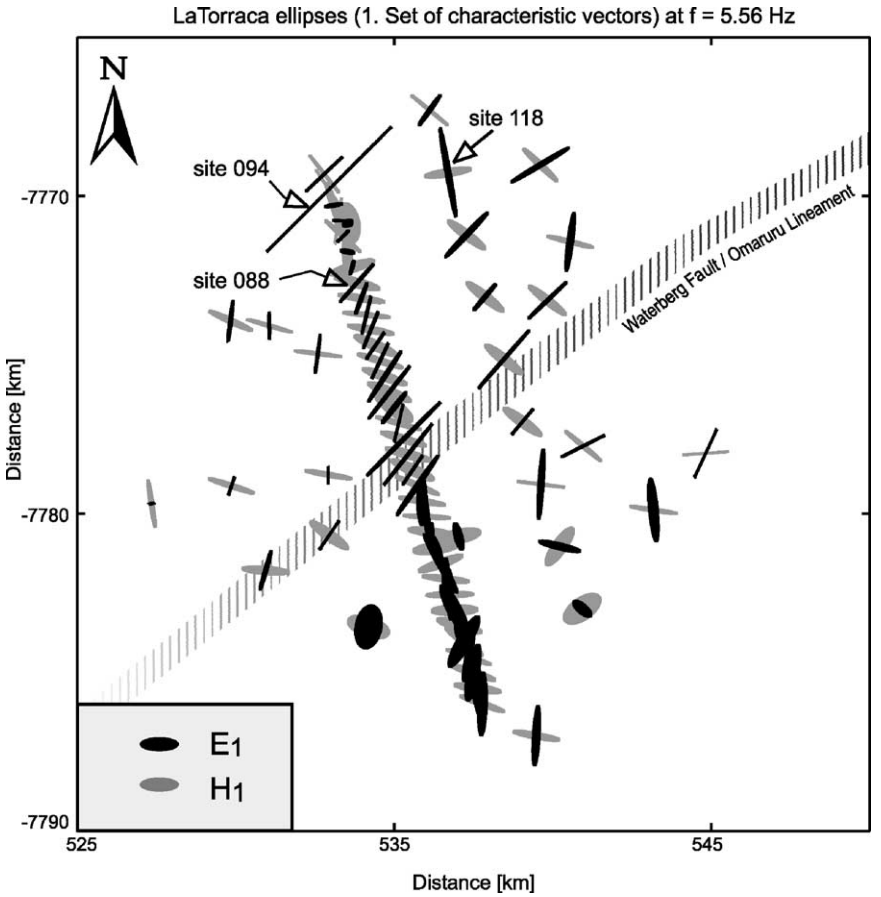

Fig. 13. First set of characteristic vectors obtained by LaTorraca SVD in the form of ellipses. In the southern part more circular, NS oriented electric ellipses (black) are observed, while north of the WF/OL ellipses orientated parallel to the fault predominate. Ellipses at sites 094, 118 and 088 image a conductivity anomaly associated with the carbonatic ring shown in Fig. 7.

both, the shortest and longest periods; and (iii) induction vectors at intermediate periods, indicating a NS orientated zone of high conductivity at some depth.

Inspired by the ring structure, we created a 3D model comprised of a conductive ring (1 Ωm) embedded within a resistive host (1000 Ωm) (see Fig. 14). The model results are computed using the 3D forward algorithm of Mackie et al. (1993). For better model convergence we substituted a square frame for the conductive ring; the modelling responses are similar to those of an oval body. The sides of the frame are 5 km in length and its depth extent is 3 km. The width of the conductive frame is 500 m. The frame is covered by a 300 m thick resistive layer (1000 Ωm).

Fig. 15 shows the phase diagrams of the off-diagonal components in plan view at a period of 100 s for the ring model. The *xy* phase values >90° are observed above the ring on sides parallel to the *x*-axis, while the *yx* phases leave the normal quadrant above sides parallel to the *y*-axis. This shallow and highly conductive ring structure thus acts to gather and deflect horizontal currents. This effect is confined to sites above the conductive ring. Fig. 16 shows the apparent resistivity and phase curves of three synthetic sites (labelled 1–3 in Fig. 14). Site 1, located outside the anomaly, shows normal ρ_a and phase curves in (Fig. 16(a)). At site 2, which is located above the conductive ring (Fig. 16(b)), we observe steeply decreasing apparent resistivity curves and phases leaving their assigned

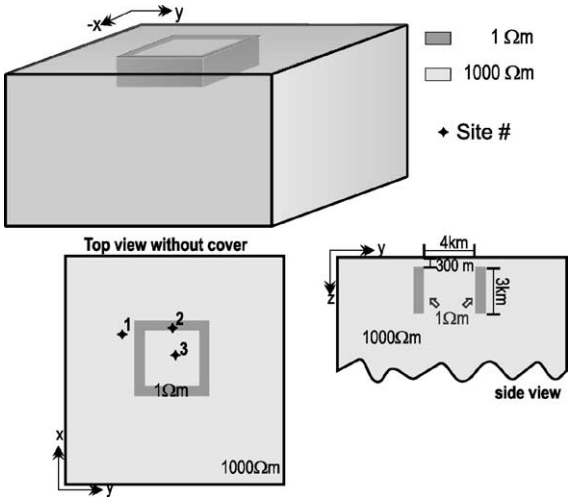

Fig. 14. 3D model of a high conductivity anomaly consisting of a conductive frame embedded in and filled with resistive material (1000 Ωm). The width of the frame is 5 km with a side thickness of 500 m and its depth extent amounts to 3 km. Synthetic sites 1–3 are marked by ✦ .

quadrant. Only the *yx*-component is effected in this way, while the *xy*-component is comparable with orthogonal sides of the frame. The apparent resistivity and phase curves at site 3 (Fig. 16(b)) which is situated inside the ring structure show an almost 1D behaviour. Although the transfer functions of sites 1 and 3 seem to reflect a 1D environment, they are deceptive. This modelling study demonstrates that even if the transfer functions look fairly simple and 1D, the environment is not necessarily 1D. It also shows that shallow anomalies can effect long period data. They can easily be misinterpreted as deep anomalies, if the site spacing is not dense enough (see also Park and Livelybrooks, 1989).

The general trend, particularly that of the *yx* phase curve of site 2, is comparable with site 094, located above the carbonate ring structure. Interestingly, phases over 90° could not be generated when the conductive frame was replaced by a conductive block or when we added a conductive bottom to the frame.

It is not possible to simulate univariate coherencies through numerical modelling. The LaTorraca skew, however, is a suitable alternative, as this property expresses the deviation from orthogonality of the electric and magnetic fields (LaTorraca et al., 1986). Fig. 17 compares the observed LaTorraca skew of site 094 with the synthetic data from site 2. The modelling results in Fig. 17 show no deviation from orthogonality between the electric and magnetic fields at periods <1 s. At longer periods, however, we observe deviation of -19°. The behaviour at site 094 is similar, but we observe a deviation from orthogonality at shorter periods and a maximum skew angle exceeding -30° (see Fig. 17).

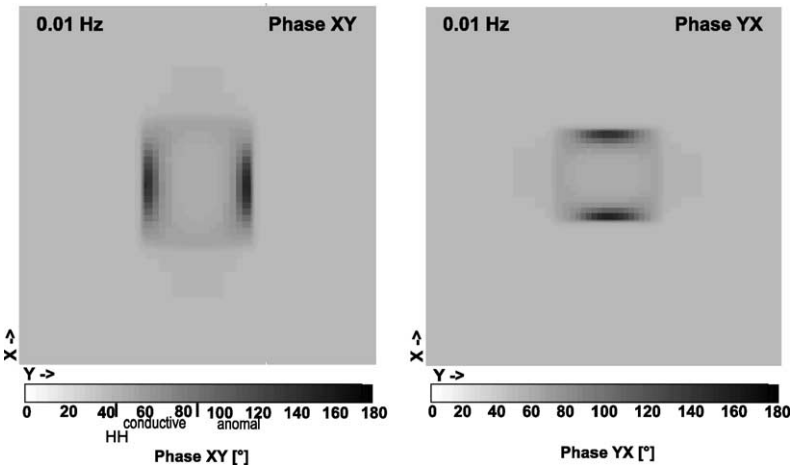

Fig. 15. Synthetic phase response of the model shown in Fig. 14. In some areas above the frame of the conductive ring structure the synthetic phase values of one off-diagonal component exceeds 90°. Inside and outside the anomaly we observe phase values of 45° reflecting the homogeneous half space (HH).

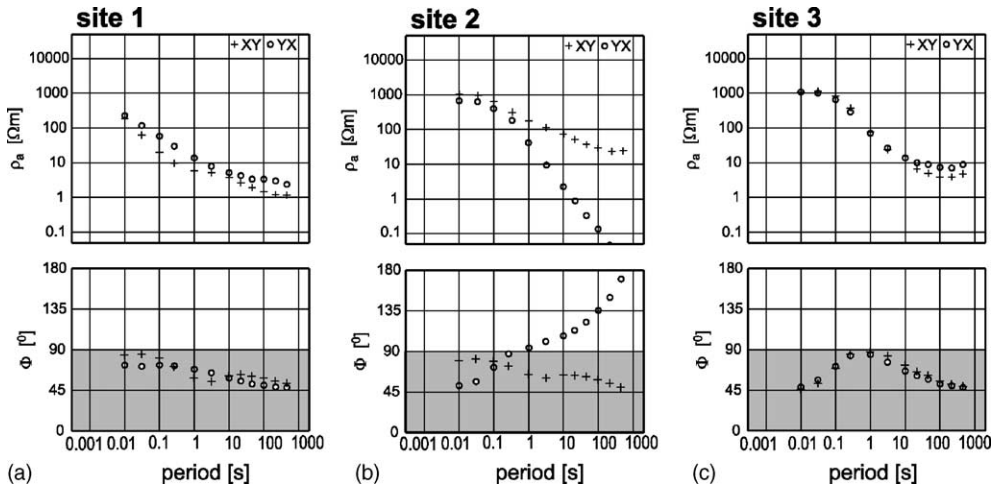

Fig. 16. Apparent resistivities and phases of the three synthetic sites of the 3D model in Fig. 14. At site 2, the conductive frame of the ring structure phases exceed 90° above 5 s. Sites inside (1) and outside the anomaly (3) do not show this behaviour, but rather indicate an approximately 1D environment.

Some of the observed effects in the northern part of the dense profiles can be explained with the ring model. However, the ring model also shows that effects such as phase values over 90° are restricted to a limited area in close proximity to the conductivity anomaly. A different explanation is required to explain *abnormal* phases over a region 10 km wide. The elongated La-Torraca polarisation ellipses in Fig. 13 and the induction vectors in Fig. 8(b) indicate that there may be a conductivity contrast parallel to the profiles. However, a similar effect could be produced by anisotropy with enhanced conductivity parallel to the WF/OL, which is very plausible in connection with a shear zone.

It would be desirable to calculate the model responses for all features in a single model. However, 3D (forward) modelling is currently limited to studies of relatively simple geometries. It is impossible to combine very small-scale and regional features in one 3D model due to numerical and computational limitations. In 3D grids, anisotropy can only be modelled as a macroscopic feature, in the form of parallel "dikes" of high or low conductivity. These in turn cause problems with grid generation. Particularly, if macro-anisotropy reaches the surface, synthetic sites above the "anisotropic" feature sit either on a conductive or a resistive dike. The shape of the resulting apparent resistivity and phase curves will thus differ at least at high frequencies depending strongly on its location. Especially the electric fields will strongly be effected by the conductivity of the cell the site sits on.

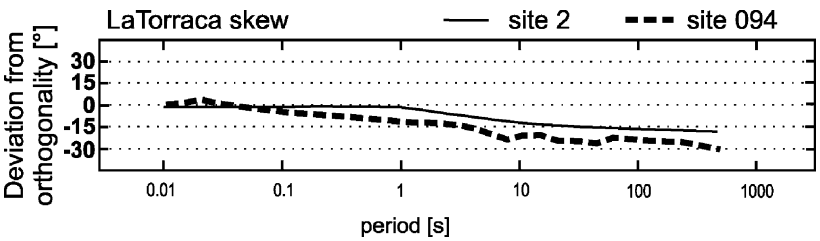

Fig. 17. LaTorraca skew values at synthetic site 2 above the conductive ring structure indicate that electric and magnetic fields deviate from orthogonality at long periods. The maximum deviation is −19° at long periods. At site 094 of the Namibian data set we observe similar behaviour, with a maximum deviation of −30°.

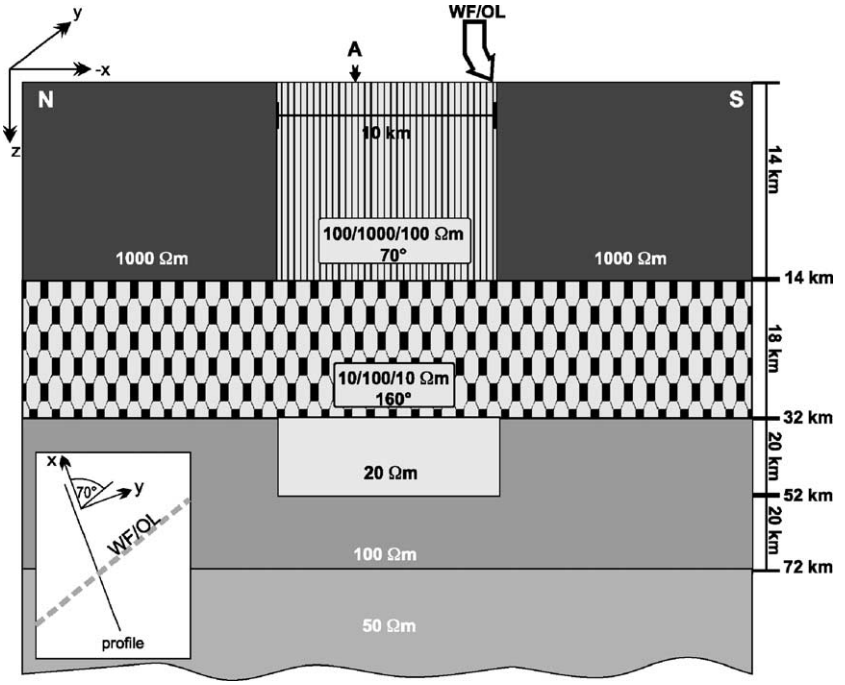

Fig. 18. 2D anisotropic model. In the upper layer a 10 km wide and 14 km deep anisotropic block is sandwiched between two resistive blocks. The anisotropy strike is parallel to the direction of the WF/OL. Attached underneath is a second anisotropic layer of 18 km thickness. The strike of its anisotropy is poorly resolved. The layered half space below 32 km includes an block of 20 Ωm to model the induction vectors at long periods.

Such problems can be avoided with micro-anisotropic modelling using Pek and Verner's code (1997). Here, the transfer functions at neighbouring sites above an anisotropic structure are identical.

The 2D anisotropic models for Pek and Verner's code (1997) consist of a finite system of homogeneous, but in general anisotropic, 2D blocks. Instead of a scalar conductivity σ, beeing assigned to a 2D block, the authors use a conductivity tensor $\underline{\underline{\sigma}}$, defined by its three principle values ($\sigma_{xx}, \sigma_{yy}, \sigma_{zz}$) and by three rotation angles. This means any orientation of the principle axes of the conductivity tensor in space can be achieved. The x-axis of our 2D model in Fig. 18 is in the direction of the main profile. The model was found by a trial-and-error approach. The main goal of this 2D anisotropic modelling study is to simulate the general behaviour of the sites to the north of the WF/OL, for which site 085 (Figs. 2 and 3) is representative. The most important characteristics of the observed curves at this site are: (i) steeply decreasing $\rho_{a,xy}$ curves; (ii) xy phases leaving the quadrant at $\approx$1 s; and (iii) diagonal elements of the impedance tensor which are of similar size to the off-diagonal elements. The last point is very significant, because with the inclusion of anisotropy, the diagonal components are no longer required to be zero as is the case with isotropic 2D modelling. Hence, with 2D anisotropic modelling we attempt to fit all four components of the impedance tensor. In particular, the period range of the transition of the xx-phase curve from the first into the following quadrants was a good indicator for fine tuning the models.

The regional 2D model of the Damara Belt (see Part I) indicates high resistivities for the upper crust. We therefore modelled the 10 km wide anisotropic zone sandwiched between two isotropic resistive blocks of 1000 Ωm. The principle resistivities of the anisotropic zone are $\rho_{xx}/\rho_{yy}/\rho_{zz} = 100/1000/100\,\Omega$m, and the anisotropy strikes with an angle of 70° with respect to the x-axis of the model. Beneath this layer, at a depth of approximately 14 km, the model in Fig. 18 contains another anisotropic layer of 18 km thickness

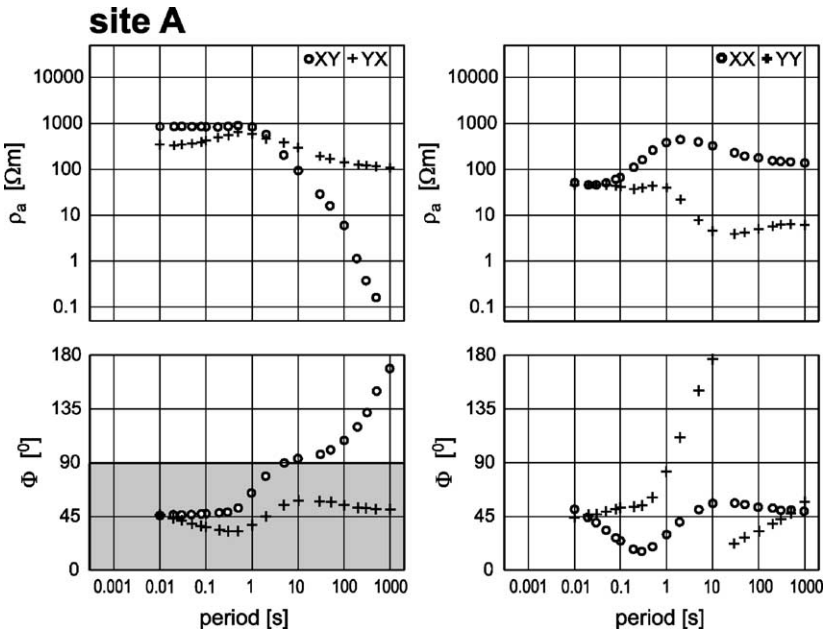

Fig. 19. Site A is exemplary of sites over the 10 km broad anisotropic block in Fig. 18. Similar to site 085 of the Namibia data set, we observe steeply decreasing apparent resistivities of the *xy*-component and corresponding phases over 90° at long periods. Note that the off-diagonal components *and* the diagonal components follow the observed data trends of site 085 in Figs. 2 and 3.

and $\rho_{xx}/\rho_{yy}/\rho_{zz} = 10/100/10\,\Omega$m with a strike direction of 160°. Below this second anisotropic layer, the model has another conductive region (20 Ωm) embedded in a layer of 100 Ωm. The bottom layer of the model, starting at a depth of 72 km, is a homogeneous half space of 50 Ωm.

We chose site A located at the centre of the anisotropic block in Fig. 18 for comparison with site 085. The apparent resistivity and phase curves of all four impedance entries are shown in Fig. 19. The *yx*-component of the resistivity curves, corresponding to the TM mode, shows high resistivities between 300 and 1000 Ωm at short periods. The *xy*-component, however, is strongly effected by the anisotropic layers, the apparent resistivities falling off rapidly to values below 1 Ωm at long periods. Like the behaviour of the corresponding data of site 085 in Fig. 2(b), the phases exceed 90° and cross the second quadrant steadily. As mentioned before, anisotropy with a strike different from the *x*–*y*-direction, generates non-zero diagonal elements which may be of significant size. The according apparent resistivity and phase curves must therefore also be compared with the data. The *xx* and *yy* ρ_a and phase curves of site A are plotted in the right column of Fig. 19. Comparison with Fig. 3(b) shows that the general trend of apparent resistivity curves for both components is reflected in the modelling results. Particularly at long periods, we observe more resistive ρ_a values for the *xx*-component than for the *xy*-component. Similar to the real data, the *xx* phase leaves the quadrant between 0 and 90° at a period of 1 s. The strike direction of the second anisotropic layer is poorly constrained, however, a difference in direction of less then 30° from that of the shallow anisotropic block results in identic resisivity and phase curves at long periods.

The 20 Ωm conductive zone at a depth of 32 km was added to the model in order to match the general behaviour of the observed induction vectors at long periods. Fig. 20 shows induction vectors for the anisotropic model at a period of 200 s. The real parts of the induction vectors show the expected reversal to the north and south of the 10 km wide zone and very small vectors within the conductive region.

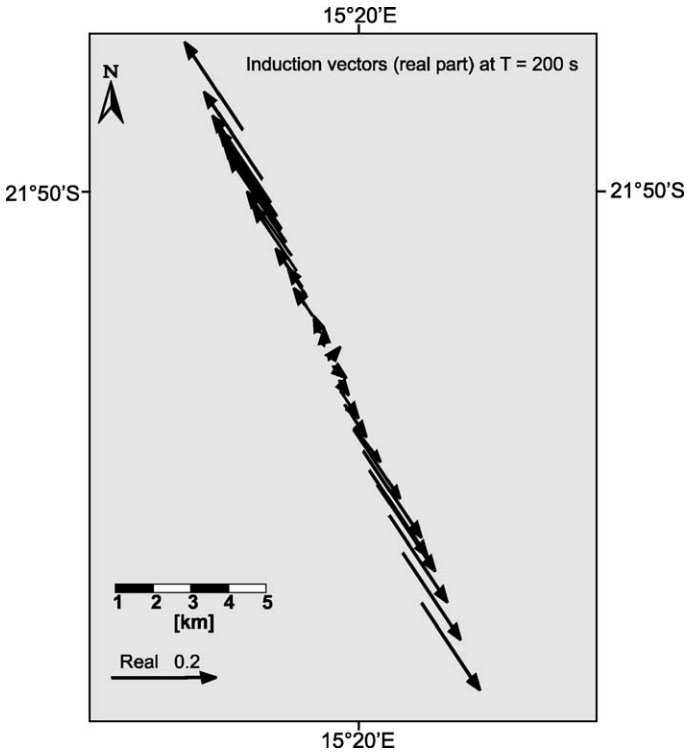

Fig. 20. Synthetic induction vector response of the model shown in Fig. 18. At long periods, the real induction vectors over the anisotropic model point away from the 10 km wide zone. Within this zone very small vectors are observed.

6. Discussion

The models presented here explain the most important aspects of the observations in the region under study. The three controlling conductivity features are summarized in Fig. 21. The cartoon shows: (i) a shallow conductive ring structure with a depth extent of 3 km in the northern part of the area; (ii) a 10 km wide anisotropic zone (reaching down to 14 km); and (iii) a conductive channel running NNE–SSW. The latter feature has not been discussed yet, but its inclusion seems necessary to explain the induction vectors at intermediate periods (≈1 s).

The compilation of these conductivity anomalies provides important insights into the internal structure of the WF/OL. The 2D anisotropic modelling suggests that the WF/OL is a 10 km wide zone with enhanced conductivity parallel to the fault. This zone reaches down to a depth of at least 14 km. This is in agreement with the regional model (see Part I), where isotropic 2D inversion model of a sub-set of the entire data shows the WF/OL and the Autseib Fault as steeply dipping conductive features. Both faults reach down into the mid-crust where they merge into a sub-horizontal conductive zone. According to Daly (1989), it is very reasonable to expect crustal-scale mechanical anisotropy to be associated with such large shear zones. Additionally, the importance of electrical anisotropy in connection with crustal-scale fault zones was also recognized in magnetotelluric studies of the KTB area (Eisel and Haak, 1999; Eisel et al., 2001), the Abitibi Subprovince in Canada (Tournerie and Chouteau, 1998) and the Southern Alps in New Zealand (Davey et al., 1998).

Our model of the WF/OL in Fig. 18 contains a second anisotropic layer in the lower crust. The inclusion of this layer is needed to generate phases over 90°. The absolute direction of the anisotropy cannot be resolved, but it is required to differ by at least 30° from the upper crustal anisotropy. The tectonic implications

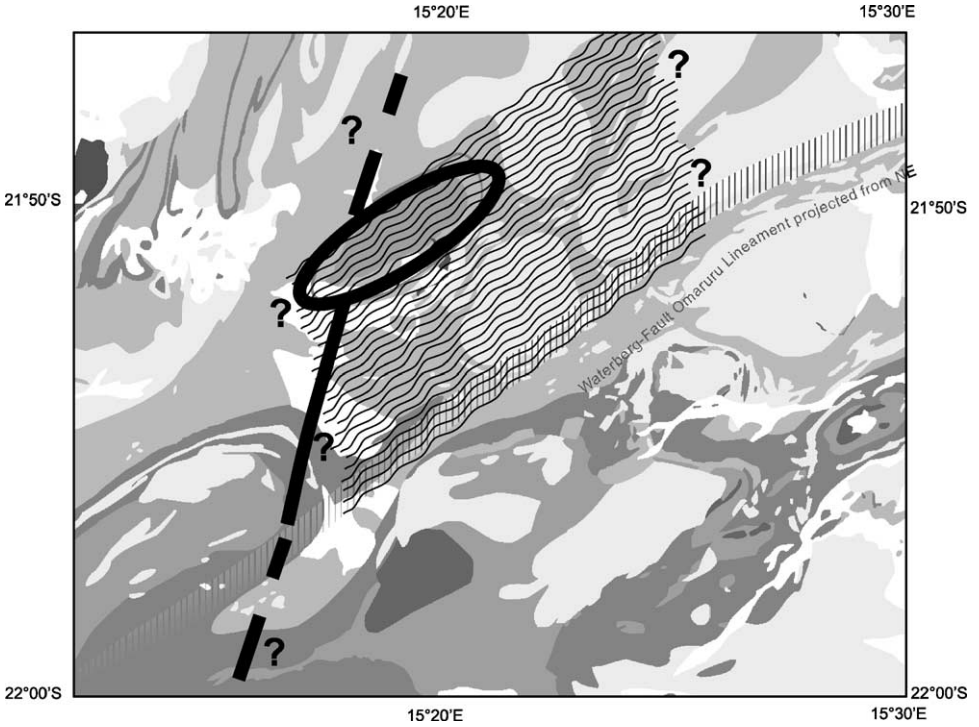

Fig. 21. Compilation of the three controlling conductivity anomalies overlain upon the surface geology (grey shades): (i) a shallow conductive ring structure attributed to graphite-bearing marbles in the northern area; (ii) a 10 km wide anisotropic zone north of the WF/OL with a depth extent of approximately 14 km; and (iii) a conductive channel running NNE–SSW which may coincide with the Welwitschia Lineament zone. From our observations we cannot tell whether the Welwitschia Lineament continues north of the ring structure or south of the WF/OL. For similar reasons, the continuation of this anisotropic zone to the west and east remains uncertain.

of the anisotropy remain unclear. It appears, however, that this layer coincides with the sub-horizontal detachment zone of the regional model.

The additional 20 Ωm conductivity anomaly in the upper mantle was required to model the reversal of the induction vectors at long periods with the same model. This feature is not required to fit the impedances, and its geological significance is uncertain.

The model in Fig. 18 cannot account for the eastward pointing induction vectors at 1 s. Further complications are indicated in the western part of the area. The reversing induction vectors (see Fig. 7) suggested the inclusion of the conductive channel in the sketch in Fig. 20. However, this anomaly alone cannot explain the direction and the lengths of the induction vectors along the main profile. Pek and Verner (1997) show that a 2D model comprised of a lateral conductivity contrast as well as anisotropy with a direction oblique to the model axis has a great impact on the induction vectors. Normally, induction vectors orient perpendicular to a lateral conductivity contrast, but the presence of anisotropy can distort the real vectors in a way that they point *parallel* to the direction of high conductivity.

It is plausible—but beyond our modelling capability—that the conductive channel labelled as WL in Fig. 8 causes eastward pointing induction arrows which are subsequently deflected by the anisotropic zone. The presence of anisotropy would also explain why the induction vectors have approximately constant lengths at sites in the eastern part of the measuring area. A compilation of all discussed conductive features would require a 3D anisotropic modelling code.

Interestingly though, there are indications for a the NNE–SSW trending tectonic feature. Corner (1983)

presented a simplified aeromagnetic map of the western Damara Belt in which he stressed the importance of the lineament zones on the tecto-genesis of the orogen. One of the most prominent features identified is the 200 km long, NNE trending Welwitschia Lineament zone. According to Corner (1983), the aeromagnetic data can resolve the strike of the lineament but not its exact location. The position of the WL in Fig. 17(b) is shifted from its original location by 2 km to the east which is well within the specified error margin of several kilometres. Unfortunately though, Corner does not discuss the role of the Welwitschia lineament nor do we have sufficient site coverage of this lineament zone to resolve its structure in detail. However, the MT data suggest that the high conductivity associated with the WL is limited to the shallow crust.

7. Conclusion

MT data collected across the WF/OL result in an electrical image of a fossil shear zone which shows much more complexity than comparable models from other fault zones (e.g. the San Andreas Fault). With this data set, it is not possible to remove strong 3D effects in the data using tensor decomposition methods. The presentation of electric and magnetic ellipses using LaTorraca's SVD method can reveal important information about the conductivity distribution of the subsurface. However, a meaningful image can only be obtained if the site spacing is sufficiently dense. Taking advantage of the good lateral distribution of sites across the WF/OL in Namibia we can be certain that: (i) conspicuous effects in MT data are caused by the geology; and (ii) that structural details of the WF/OL are resolved.

We are currently unable to develop a true 3D model reflecting all of the complexity. What we have are pieces of a puzzle: a conductive ring structure in the shallow crust, crustal-scale electrical anisotropy and an elongated conductor running sub-parallel to the WF/OL. The WF/OL is certainly not a lineament in a geometrical sense, but a 10 km wide and 14 km deep fault zone with enhanced conductivity parallel to the fault. This observation is in agreement with the regional Damara model (see Part I), where we concluded that the WF/OL probably merges into a detachment zone at mid-crustal depth.

The conductive ring in the northern part of the target area is a secondary structure superimposed on the 10 km wide anisotropic zone. We are not certain whether it is related to the WF/OL but our modelling studies clearly show that current gathering and deflection in the shallow crust can cause very strong 3D effects. The strongest effects from this shallow features appear at the longest periods in the MT data, which suggests caution when interpreting such data. Long period data are typically collected with a large site spacing and hence under-sampled upper crustal anomalies may easily be misinterpreted as deep structures.

Acknowledgements

The field campaigns in Namibia were funded by the GeoForschungsZentrum Potsdam. We thank the Geophysical Instrument Pool Potsdam, the University of Frankfurt, the Technical University of Berlin and the University of Edinburgh for providing the MT equipment. Without the support of the Geological Survey of Namibia (GSN), in particular of Gabi Schneider, Director of the GSN, and of Rainer Wackerle, in terms of logistic support, the experiment could not have been done. The success of this campaign also depended on the members of our field crew, Monika Korte, Guido Bengel, Svetlana Byrdina, Arne Hoffmann-Rothe and Tim Vietor, whom we would like to thank for their excellent work. We would also like to thank the team of the Brandberg Rest Camp in Uis where we stayed during both field experiments. Finally, we would like to acknowledge the work of the Namibia Working Group at the GFZ and particulary Bob Trumbull's contribution with many discussions and general help with the manuscripts. Critical and constructive comments from two anonymous referees helped clarify the manuscript.

References

Bahr, K., 1988. Interpretation of the magnetotelluric impedance tensor: regional induction and local telluric distortion. J. Geophys. 62, 119–127.

Bahr, K., 1991. Geological noise in magnetotelluric data: a classification of distortion types. Phys. Earth Planet. Inter. 66, 24–38.

Corner, B., 1983. An interpretation of the aeromagnetic data covering the western portion of the Damara Orogen in South

West Africa/Namibia. Spec. Publ. Geol. Soc. S. Afr. 11, 339–354.

Daly, M.C., 1989. Rift basin evolution in Africa: the influence of reactivated steep basement shear zones. Inversion tectonics. In: Cooper, G.D.W.M.A. (Ed.), Geological Society Special Publications, vol. 44, pp. 309–334.

Davey, F., Henyey, T., Holbrook, W., Okaya, D., Stern, T., Melhuish, A., Henrys, S., Anderson, H., Eberhart-Phillips, D., McEvilly, T., Uhrhammer, R., Wu, F., Jiracek, G., Wannamaker, P., Caldwell, G., Christenson, N., 1998. Preliminary results from a geophysical study across a modern continent–continent collisional plate boundary—the Southern Alps, New Zealand. Tectonophysics 288, 221–235.

Eisel, M., Haak, V., 1999. Macro-anisotropy of the electrical conductivity of the crust: a magnetotelluric study of the German Continental Deep Drilling Site (KTB). Geophys. J. Int. 136, 109–122.

Eisel, M., Haak, V., Pek, J., Ĉerv, V., 2001. A magnetotelluric profile across the German Deep Drilling Project (KTB) area: two- and three-dimensional modeling results. J. Geophys. Res. 106 (8), 16061–16073.

Groom, R.W., Bahr, K., 1992. Corrections for near surface effects: decomposition of the magnetotelluric impedance tensor and scaling corrections for regional resistivities: a tutorial. Surv. Geophys. 13, 341–379.

Groom, R.W., Bailey, R.C., 1989. Decomposition of magnetotelluric impedance tensors in presence of local three-dimensional galvanic distortion. J. Geophys. Res. 94 (B2), 1913–1925.

LaTorraca, G.A., Madden, T.R., Korringa, J., 1986. An analysis of the magnetotelluric impedance for three-dimensional conductivity structures. Geophysics 51, 1819–1829.

Mackie, R.L., Madden, T.R., Wannamaker, P.E., 1993. Three-dimensional magnetotelluric modelling using difference equations—theory and comparisons to integral equation solutions. Geophysics 58, 215–226.

McNeice, G.W., Jones, A.G., 2001. Multisite, multifrequency tensor decomposition of magnetotelluric data. Geophysics 66, 158–173.

Miller, R.M., 1983. The Pan-African Damara Orogen of South West Africa/Namibia. Spec. Publ. Geol. Soc. S. Afr. 11, 431–515.

Park, S.W., Livelybrooks, D.W., 1989. Quantitative interpretation of rotationally invariant parameters in magnetotellurics. Geophysics 54, 1483–1490.

Pek, J., Verner, T., 1997. Finite-difference modelling of magnetotelluric fields in two-dimensional anisotropic media. Geophys. J. Int. 128, 505–521.

Ritter, O., Junge, A., Dawes, G.J.K., 1998. New equipment and processing for magnetotelluric remote reference observations. Geophys. J. Int. 132, 535–548.

Ritter, O., Weckmann, U., Vietor, T., Haak, V., this issue. A magnetotelluric study of the Damara Belt in Namibia 1: Regional scale conductivity anomalies. Phys. Earth Planet. Inter., this issue.

Smith, J.T., 1995. Understanding telluric distortion matrices. Geophys. J. Int. 122, 219–226.

Smith, J.T., 1997. Estimating galvanic-distortion magnetic fields in magnetotellurics. Geophys. J. Int. 130, 65–72.

Swift, C., 1967. A magnetotelluric investigation of an electrical conductivity anomaly in the southwestern United States. Ph.D. Thesis, MIT Press. Cambridge, MA.

Tournerie, B., Chouteau, M., 1998. Deep conductivity structure in Abitibi, Canada, using long dipole magnetotelluric measurements. Geophys. Res. Lett. 25 (13), 2317–2320.

Weckmann, U., 2002. A new imaging method for crustal conductivity structures applied to magnetotelluric data from Namibia (in German). Ph.D. Thesis, Fachbereich Geowissenschaften, Freie Universität Berlin.

Weidelt, P., Kaikkonen, P., 1994. Local 1-D interpretation of magnetotelluric B-polarization impedances. Geophys. J. Int. 117, 733–748.

Correlation of electrical conductivity and structural damage at a major strike-slip fault in northern Chile

A. Hoffmann-Rothe
Department of Geodynamics, GeoForschungsZentrum Potsdam, Potsdam, Germany

O. Ritter
Department of Physics of the Earth, GeoForschungsZentrum Potsdam, Potsdam, Germany

C. Janssen
Department of Geodynamics, GeoForschungsZentrum Potsdam, Potsdam, Germany

Received 19 February 2004; revised 9 July 2004; accepted 19 July 2004; published 21 October 2004.

[1] Large-scale strike-slip fault zones are often imaged as electrically conductive structures in the brittle crust. However, the relationship of conductivity and internal architecture of the fault zone remains largely unclear. This paper presents results of a study designed to compare the record of structural deformation across a fault zone with its electrical conductivity image. Two high-resolution magnetotelluric profiles trend perpendicularly across the West fault, a branch of the Precordilleran fault system in northern Chile. The magnetotelluric and geomagnetic response functions in the frequency range from 1000 Hz to 0.1 Hz clearly image a fault zone conductor (FZC) about 350 m wide and 1500 m deep, trending along the surface trace of the fault. The position of the FZC and its geometric properties (width, dip) correlate with a region of intense fluid alteration and the orientation of fault-related damage elements (minor faults, fractures). According to estimates of fluid salinity and rock porosity, the conductivity anomaly results from meteoric water penetrating into a permeable zone. This suggests that the increase in electrical conductivity is causally related to a mesh of minor faults and fractures, acting as a pathway for fluids. The FZC reflects the central and most fractured part of the damage zone. In view of similar published magnetotelluric studies, we infer a dependency of a fault's state of activity and the characteristics of the FZC such as its conductance, width, and depth extent. Ongoing deformation is the controlling factor for maintaining a permeable and electrically conductive fracture network. *INDEX TERMS:* 1515 Geomagnetism and Paleomagnetism: Geomagnetic induction; 8010 Structural Geology: Fractures and faults; 8045 Structural Geology: Role of fluids; 9360 Information Related to Geographic Region: South America; 8150 Tectonophysics: Plate boundary—general (3040); *KEYWORDS:* magnetotellurics, fault architecture, fault zone conductor, Chilean Andes, fracture network, electrical conductivity

Citation: Hoffmann-Rothe, A., O. Ritter, and C. Janssen (2004), Correlation of electrical conductivity and structural damage at a major strike-slip fault in northern Chile, *J. Geophys. Res.*, *109*, B10101, doi:10.1029/2004JB003030.

1. Introduction

[2] Upper-crustal fault zones are structurally complex and lithologically heterogeneous zones of brittle deformation. Their appearance (internal architecture) is subject to an interplay of hydraulic and mechanical properties. Fault zones control subsurface fluid flow (meteoric waters, brines, melts) either by localizing flow in the fault zone or by impeding cross fault fluid mobility [*Caine et al.*, 1996]. They may form vertical flow conduits [*Rice*, 1992] or control groundwater flow along the fault's strike [*Gudmundsson*, 2000]. The presence of high-pressure fluids within faults is held liable for the inherent weakness of many crustal-scale faults [*Faulkner and Rutter*, 2001; *Hickman et al.*, 1995] and likely relates to the earthquake cycle [*Blanpied et al.*, 1992; *Byerlee*, 1993].

[3] The internal architecture of a fault both influences and depends on the fluid involvement in the fault zone. Recently, we have achieved a better understanding of the internal structure of brittle fault zones and discrete fractures from field work in many different settings [e.g., *Faulkner et al.*, 2003; *Janssen et al.*, 2002; *Sculz and Evans*, 2000, 1998; *Cello et al.*, 2000; *Unsworth et al.*, 1997; *Chester et al.*, 1993]. Commonly, three architectural elements are discriminated for brittle fault zones in low-porosity rocks [e.g., *Chester and Logan*, 1986; *Caine et al.*, 1996; *Rawling et al.*, 2001]: (1) the host rock (country rock) or protolith, which is the unfaulted rock volume bounding fault-related structures; (2) the damage zone, which comprises minor faults, fractures, fracture

0148-0227/04/2004JB003030$09.00

networks, veins, cleavages or other subsidiary structures all related to the main fault growth processes; (3) the fault core, where most of the fault displacement is localized. The fault core is rarely developed as a discrete slip surface, but commonly found to be composed of cataclastic rocks like breccias, clay-rich gouges of variable degree of induration/consolidation, or geochemically altered zones. It may also be developed as a wide region of several anastomosing strands of fault gouge, as observed for phyllosilicate rich fault zone material [*Faulkner et al.*, 2003]. The width of the damage zone is structurally defined as the regions that bound the fault core on both sides and in which fracture density is above a certain threshold value [e.g., *Schulz and Evans*, 1998, 2000; *Cello et al.*, 2000].

[4] Usually, structural geology investigations of large-scale strike-slip fault zones are restricted to surface exposures of the fault and little is known about their subsurface continuation. Images of the subsurface electrical conductivity structure of fault zones can be used to overcome this problem. Several published results demonstrate the successful application of the magnetotelluric (MT) method for studying fault-related structures and their geometry at depth [e.g., *Ritter et al.*, 2004, 2003; *Bedrosian et al.*, 2002; *Wannamaker et al.*, 2002; *Hoffmann-Rothe et al.*, 2001; *Unsworth and Bedrosian*, 2004; *Unsworth et al.*, 2000, 1999, 1997; *Jones*, 1998; *Mackie et al.*, 1997]. Particularly, the work on the conductivity structure of segments of the San Andreas Fault in California exemplifies the existence of fault-related subsurface anomalies of high conductivity, so-called fault zone conductors (FZC).

[5] How can faults alter the subsurface electrical conductivity? The conductivity of a rock depends strongly on the percentage, connectivity and contents of the pore volume between the minerals, while the rock matrix is usually very resistive [*Haak and Hutton*, 1986]. Small amounts of an interconnected fluid phase can increase the conductivity of a material by several orders of magnitude. Hence the MT method is primarily sensitive to the structural characteristics of a rock (matrix discontinuities/fractures, porosity/permeability) and subordinately to the rock composition. This makes the method valuable in resolving the structural damage related to brittle faulting.

[6] Faults can alter the subsurface electric conductivity in several ways: (1) by juxtaposing two geologic units with differing electrical conductivities via lateral or vertical displacement; (2) by creating permeable pathways for saline fluids within fractured parts of the fault zone; (3) by developing clay-rich fault zone materials (clay gouges), which are by themselves conductive; (4) by precipitation or concentration of an electronic conductive phase (graphite, sulfides, ores) that forms an interconnected network or film [*EleKTB Group*, 1997; *Jödicke et al.*, 2004].

[7] High conductivities in upper crustal fault studies appear to be mainly related to the presence of fluids in the fault zone. Imaging fault zone fluids is therefore most promising for deciphering hydraulic properties and structural units of a fault zone. What can we learn about the internal architecture of faults and their mechanical and hydraulic properties from MT? The target of this study is a segment of the strike-slip dominated West fault in northern Chile, where structural and electromagnetic studies can be combined in an almost ideal manner. We show that the subsurface electric current flow in the vicinity of the fault zone is a consequence of the deformational processes. Hypothesis testing is used to evaluate the resolution and robustness of the observed conductivity anomalies, in particular of the imaged fault zone conductor. With respect to the above posed question we then synoptically interpret the subsurface conductivity image and the structural damage record of the fault at the surface.

2. Geological Setting

[8] The Precordilleran fault system (PFS) is a broad shear system of more than 2000 km length [*Lindsay et al.*, 1995] (Figure 1a). The northern part of the PFS between 23°S and 20°S is referred to as West fault zone (WFZ), adopting the terminology of *Tomlinson and Blanco* [1997a]. Its main branch is the West fault (WF; also: West Fissure/Falla Oeste), which can be traced for 170 km almost continuously from Calama to Quebrada Blanca [*Dilles et al.*, 1997] (Figure 1a). Regional magnetotelluric surveys (PICA and ANCORP profiles, Figure 1a) have identified the PFS as a first-order feature that most likely transects the entire forearc lithosphere [*Brasse et al.*, 2002; *Echternacht et al.*, 1997].

[9] The PFS was initiated as dextral trench-linked strike-slip fault within the Eocene-Oligocene magmatic arc [*Reutter et al.*, 1996]. Shallow silicic plutons were emplaced in the late Eocene/early Oligocene, several of which are N–S elongated and aligned along the present trace of the West fault, suggesting that the fault controlled at least locally the emplacement of intrusives [*Ossandón et al.*, 2001].

[10] The major movements along the WFZ in the Oligocene to early Miocene have been sinistral with a displacement between 35 to 37 km [*Tomlinson and Blanco*, 1997b; *Dilles et al.*, 1997]. Hypogene enrichment processes (mineralization due to ascending hydrothermal solutions) led to the formation of economically important porphyry copper deposits of the Precordillera [*Reynolds et al.*, 1998] and were largely controlled by the PFS/WFZ. The fracture permeability of the WFZ also imposed a structural control on the mineralization and alteration of the deposits in the middle Miocene supergene stage (oxidation and enrichment due to descending groundwater after exhumation of the deposit [*Lindsay et al.*, 1996, 1995; *Sillitoe and McKee*, 1996]).

[11] In the Middle Miocene the WFZ was reactivated as dextral system with offsets in the range of $\sim 0.5 \pm 0.5$ km and minor movements have lasted until the late Pliocene [*Dilles et al.*, 1997; *Tomlinson and Blanco*, 1997b]. Evidence for recent activity along the WF is neither supported from field work nor by recent seismicity [*Belmonte*, 2002] (see http://www.diss.fu-berlin.de/2002/202).

[12] The study area is situated north of Chuquicamata between the copper districts of Radomiro Tomic (22°8′S) and El Abra (21°54′S). The region represents a westward inclined plain of Quaternary alluvial deposits, cut by E–W trending drainage valleys, which are less than 30 m deep. These valleys allow a detailed investigation of fault-related deformation in an area of 2.5 × 2 km, subsequently called the "Gorila region."

[13] The basement in the study area consists of upper Carboniferous to lower Triassic volcanics. It is overlain by a thin sequence of Triassic/Jurassic, mainly marine, sedimen-

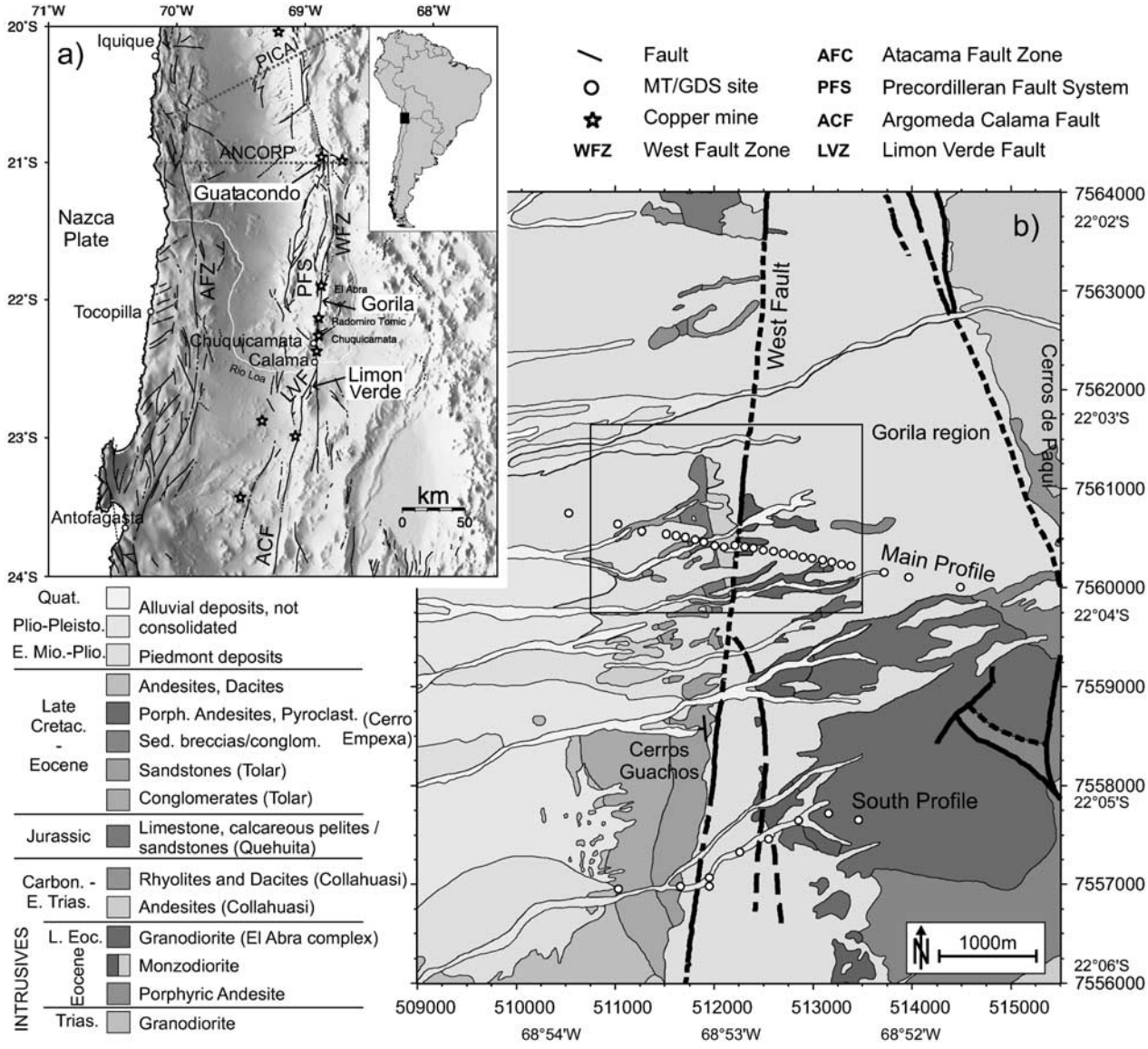

Figure 1. (a) Faults and lineaments in northern Chile according to *Reutter et al.* [1996]. Gorila is the study area presented in this paper. Studies of two other segments of the West fault zone are published by *Janssen et al.* [2002, 2004]. Dotted lines are transects of two regional magnetotelluric studies [*Brasse et al.*, 2002]. (b) Geology of the study area [modified after *Maksaev et al.*, 1999]. White dots indicate magnetotelluric sites, and the rectangle outlines the area of the structural geology investigation (Gorila region). See color version of this figure at back of this issue.

tary rocks, Cretaceous andesitic volcanics and a thick continental succession of conglomerates and sandstones. In the Gorila region, the WF separates a quartziferous monzodiorite of the Eocene from Triassic andesites and dacites. Rocks adjacent to the fault show intense alteration being part of the quartz-sericite suite of the nearby porphyry copper deposits [*Ossandón et al.*, 2001]. Laminated calcareous sinter deposits (travertine) north of the study area indicate hydrothermal spring activity in late Miocene to Pliocene time [*Maksaev et al.*, 1999].

3. Electrical Conductivity Image

[14] The magnetotelluric method (MT) is based on the observation of orthogonal components of time-varying horizontal electric (**E** in mV/km) and magnetic fields (**B** in nT) at the Earth's surface:

$$\begin{pmatrix} E_x \\ E_y \end{pmatrix} = \begin{pmatrix} Z_{xx} & Z_{xy} \\ Z_{yx} & Z_{yy} \end{pmatrix} \begin{pmatrix} B_x \\ B_y \end{pmatrix}. \quad (1)$$

The impedance tensor $\hat{\mathbf{Z}}$ contains the information on the subsurface conductivity structure, from which frequency-dependent sounding curves of apparent resistivity ρ_a and phase ϕ are derived. Lateral conductivity contrasts, for instance caused by highly conductive fault zones, generate a vertical magnetic field B_z. The respective response functions T_x and T_y are defined similarly to equation (1),

$B_z = T_x B_x + T_y B_y$, and are commonly represented in the form of induction arrows to map lateral variations of the subsurface conductivity pattern [*Wiese*, 1962].

3.1. Data Acquisition and Processing

[15] The Main profile is 4 km long, consists of 26 recording sites and trends N110°E, perpendicular to the strike of the West fault (Figure 1b). The central 20 sites of the profile are 100 m apart from each other while the spacing of the remaining stations increases toward both ends of the profile. A second 2.5 km long profile (South profile) comprises 9 sites with a spacing of 300 m; it is roughly three kilometers further to the south. We recorded broadband magnetotelluric data in the frequency range from 1000 Hz to 0.001 Hz with the real time instrument S.P.A.M. MkIII [*Ritter et al.*, 1998]. Magnetic fields were recorded with three orthogonal induction coil magnetometers per site and the electric fields were acquired along orthogonal dipoles with nonpolarizing Ag-AgCl electrodes. Where possible, the GPS synchronized instruments were left in the field for two days of continuous recording. For the analysis of the data set we used an iterative robust processing algorithm described in *Ritter et al.* [1998].

[16] Figure 2 shows the processed MT data, as used for the subsequent resistivity modeling, for several representative sites. The overall data quality is high, as indicated by smoothly varying curves over period T and consistent trends of ρ_a and ϕ curves. Data of periods around 10 s, where the source field energy has a natural low (dead-band), could be improved significantly by attempting to identify and reject unphysical data prior to the robust processing, based on parameters such as coherency, spectral power, polarization and the distribution of the significant impedance estimates (EMSEL/SEL4ROB code by *Weckmann* [2002] (see http://www.gfz-potsdam.de/bib/zbstr.htm and http://www.diss.fu-berlin.de/2002/24/indexe.html).

3.2. Dimensionality and Geoelectric Strike

[17] If the central parts of a fault are electrically conductive they represent an elongated feature with subsurface current flow parallel to the strike of the fault (geoelectric strike). This assumption is crucial for an interpretation of the data set on a two-dimensional (2-D) basis and its validity needs to be tested thoroughly beforehand.

[18] Geoelectric strike angles can be derived from the impedance tensor $\hat{\mathbf{Z}}$ by minimizing the sum of its diagonal elements [*Swift*, 1967]. Local distortion of the regional electromagnetic field caused by small-scale inhomogeneities can be removed by fitting a decomposition model [*Bahr*, 1988, 1991; *Smith*, 1995]. The upper two rows of Figure 3 show results of the geoelectric strike using the conventional and phase-sensitive method. Although the strike exhibits some variation (Figures 3a–3c), the angles are noticeably close to the WF strike. Application of the Bahr decomposition to the data (Figures 3e–3g) results in less scattering and a relatively uniform "regional" strike direction (note, that in the absence of local heterogeneities Swift strike is equal to Bahr strike). In the higher frequency bands (Figures 3e and 3f) the angles are in accordance with the orientation of the WF, while in the band between 10 and 1000 s (Figure 3g), the geoelectric strike indicates more westerly directions when compared with the WF strike.

[19] The orientation of induction arrows in the frequency range between 1000 and 0.1 Hz (Figure 3i) reveals a consistent picture, for which Figure 4 shows a representative example at f = 11Hz. The westward and eastward pointing arrows of the resistive zones 1 and 3, respectively, indicate a zone of low resistivity that trends parallel to fault strike and is located to its east (real arrows are oriented perpendicular to the electric strike). As expected, within this conductive zone 2, the real arrows change their orientation from pointing to the west in zone 1 to an eastward orientation in zone 3 and with increasing distance from the conductive zone the real arrows of zone 3 become smaller. This result is even clearer for the South profile where a conductive region (zone 2) can easily be identified by a reversal of the induction arrows and a small arrow located in its center. A subparallel alignment of the real arrows to their imaginary parts is another indication for a two dimensional geometry.

[20] Contrary to that, real induction arrows between 10 and 1000 s point to a southerly direction, hinting at a feature with an E–W oriented lateral conductivity contrast. Thus the electric strike angles of Figure 3j can not be unequivocally attributed to the ±NNE trending WF structure. Most likely, a regional-scale feature is sensed in the long period range that causes electric currents to flow in an E–W direction.

[21] *Smith* [1995] suggested to calculate a single best fitting strike angle for the whole period range at each site (Figure 3k): For a majority of sites, the derived strike angle matches the WF strike. A final analysis of the data is based on the multisite-multifrequency approach by *McNeice and Jones* [2001], in which the data of all sites are decomposed within predefined frequency ranges (bandwidth of half a decade). This method again matches the strike of the West fault very well for frequencies below 5 Hz (not shown [*Hoffmann-Rothe*, 2002] (see http://www.gfz-potsdam.de/bib/zbstr.htm and http://pub.ub.uni-potsdam.de/mathnat.htm)).

[22] The ratio of the diagonal elements (Z_{xx}, Z_{yy}) to the off-diagonal elements (Z_{xy}, Z_{yx}), the skew, is a simple analytical measure of the dimensionality of the impedance tensor [*Swift*, 1967]. There is mutual agreement among MT practitioners that values of $S_{Swift} > 0.3$ are incompatible with a 1-D or 2-D interpretation. Skew values below 0.3 are observed in the Gorila data set for periods below 10 s (Figure 5a). The phase-sensitive skew value S_{Bahr} [*Bahr*, 1988, 1991] in Figure 5b is similar to Swifts skew but accounts for a tensor decomposition model. Again, a more complex 3D regional conductivity structure is indicated for longer periods (T > 10 s), i.e., with increasing induction range.

[23] To conclude, the dimensionality/directionality analysis results in a consistent pattern for the frequency range between 1000 Hz to 0.1 Hz, for which a two dimensional model approximation of the data is justified. Consequently, the data set is interpreted in a coordinate system oriented parallel to the West fault strike of N10°E and impedance tensors of all sites are rotated accordingly. In this coordinate system the recorded XY component is equal to the TE mode (current flow along the x coordinate axis, i.e., parallel to the

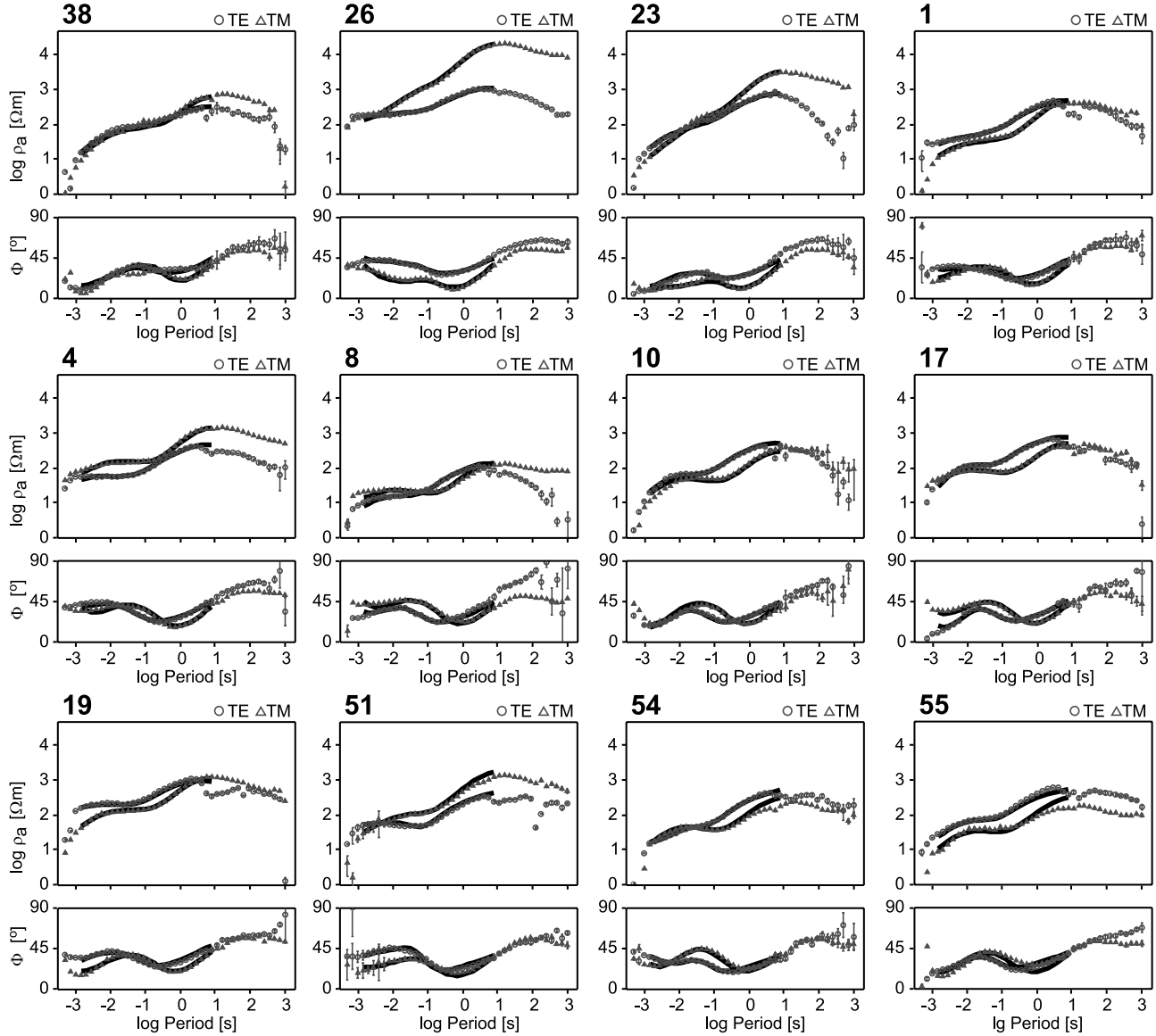

Figure 2. Apparent resistivity ρ_a and phase ϕ curves rotated to the coordinate system of the geoelectric strike (N10°E) at several representative sites. Solid curves are the model responses of the joint inversion (Figure 6).

strike of the WF) and the YX component equals the TM mode.

3.3. Inversion Models

[24] The TE and TM mode data are jointly inverted using a 2-D finite difference inversion module of the WinGLink software package (http://www.geosystem.net) based on the code of *Mackie et al.* [1997] and *Rodi and Mackie* [2001]. Starting from an a priori model the algorithm seeks a ''minimum structure'' model that minimizes the least squares misfit between observed and modeled data for each iteration. A regularization parameter τ controls the tradeoff between fitting the data and deviations from the model constraint, i.e., the model solution of the previous iteration. The larger the values of τ, the ''smoother'' the model result at the expense of a worse data fit [*Mackie et al.*, 1997].

[25] The inversion starts with a homogeneous half-space resistivity of 100 Ωm, a value close to the average bulk apparent resistivity of the sounding curves of all sites within the inverted frequency range (~150 Ωm). The data errors are set to 10% for apparent resistivities and 2° for the phases. Larger error bounds for ρ_a are chosen in order to down-weight static shift effects. Running several inversions with τ varying in a range form 0.1 to 1000 resulted in a τ value of 3 as the best compromise of RMS misfit, resolution of shallow structures, smoothness of the model and computational time expense [*Hoffmann-Rothe*, 2002].

[26] Figure 6 shows the resulting inversion models for the two profiles. The most robustly imaged feature of both profiles is the central conductive structure numbered 1 and 9, respectively (fault zone conductor: FZC). It reaches to a depth of approximately 1300 m on the main profile and dips steeply toward the east. Another conductive region 7 is separated from the FZC by a resistive structure 6. The eastern edge of the model is composed of a resistive block 8 that becomes less resistive at 1000 m depth. A broad and

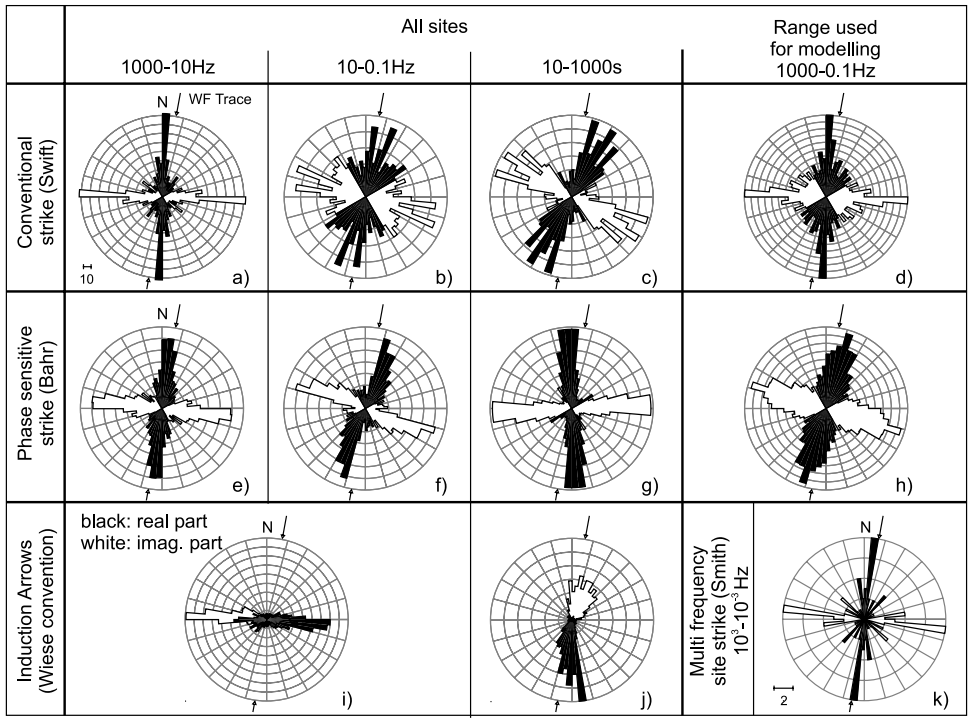

Figure 3. (a–d) Circular histograms of conventional strike [*Swift*, 1967] and (e–h) phase-sensitive strike [*Bahr*, 1988] for various frequency ranges. (k) Multifrequency strike angles for whole sites according to *Smith* [1995]. In all histograms, except for Figure 3k, a circle represents 10 data points. The black bars plot in the azimuth range between N30°W and N60°E, which is the quadrant containing the West fault's strike (indicated by black arrows). The white bars represent a 90° ambiguity of the calculated strike angle. Figures 3d and 3h summarize strike angles for the whole frequency range used for modeling. The directional information of the induction arrows (Wiese convention) is shown in Figures 3i and 3j. Here, black bars denote the real induction arrows and white bars the imaginary parts. Note that induction arrows are oriented perpendicular to the conductivity contrast (see Figure 4). The magnetic declination of approximately −2.3° at the time of the experiment is taken into account in all calculations. See text for discussion.

deeply reaching resistive structure 3 lies to the west of the WF trace in direct contact with the FZC. The shallow part of this block is disrupted by a U-shaped zone of high conductivity 4, where the profile crosses a little valley and its sedimentary filling (sites 26 and 27 are located in the valley). The western boundary of the model seems to indicate a westward inclined structure of high conductivity 5. The South model with greater site spacing generally exhibits less complexity. The FZC reaches to a depth of approximately 1500 m, but its dip is not resolved. A resistive block, comparable to 3 of the Main profile, is missing, as is a conductive structure comparable to 7. The resistive block 10 could be an extension of anomaly 8 of the Main profile.

[27] The model response generally fits the data very well (Figure 7a). Inspection of the individual data fit curves in Figure 2 shows that most of the misfit is within the very high frequency data between 1000 Hz and 500 Hz, corresponding to an induction range of the uppermost tens of meters. The static shift factors estimated for each site are shown in Figure 7b.

3.4. Sensitivity Studies

[28] To test the robustness and resolution of the imaged conductivity anomalies we ran a series of parameter studies for the Main profile. The annotations in Figure 6 summarize the results of the sensitivity tests.

3.4.1. Fault Zone Conductor (FZC)

[29] The FZC is a very robust feature in both profiles, as the following two tests with 100 Ωm half-space a priori models show.

[30] 1. Setting τ to 100 results in models in which all small-scale features disappear in favor of a very smooth model (Figure 8b). Only the FZC remains as a pronounced feature.

[31] 2. Because of the dense site spacing there is a significant overlap in the induction ranges between sites. Hence the FZC reappears in the inversion model even if the four sites located on top of it are omitted (Figure 8c). However, the information on the dip angle is now mostly lost.

3.4.2. Eastward Dip of the FZC

[32] Is the dip of the FZC a required feature of the model or could a subvertical anomaly also explain the data? The FZC of the reference model was altered to represent a vertical anomaly with straight boundaries to the resistive vicinity (eastern and western conductive anomalies removed; Figure 9a). Subsequently, this model was used as starting model for the inversion. The inversion algorithm now attempts to find a smooth solution close to the a priori

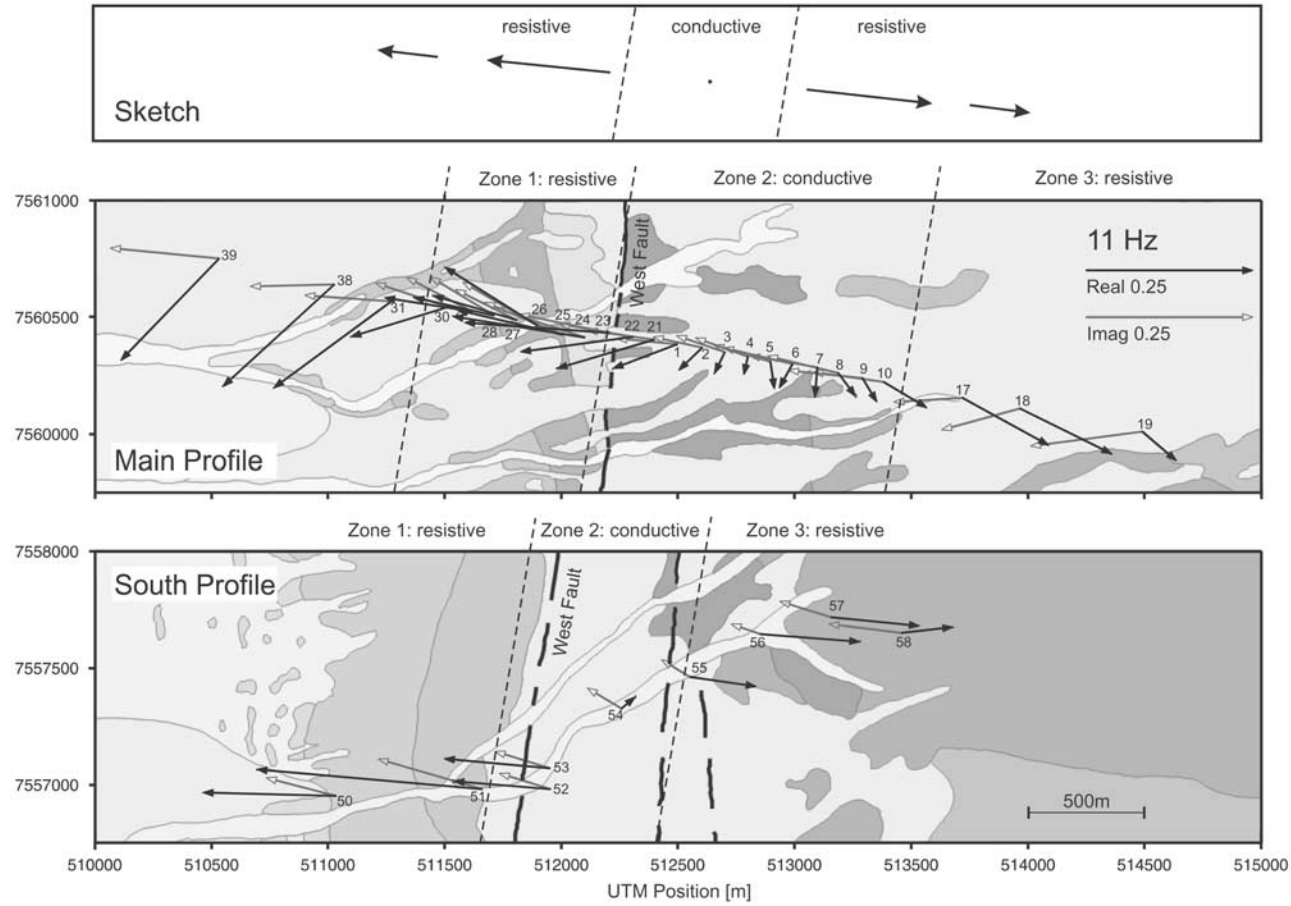

Figure 4. (top) Sketch of expected induction arrow orientation for a profile crossing a conductive zone. (bottom) Induction arrow data for the Main and South profiles at a frequency of 11 Hz. Real arrows point away from conductive regions (convention of *Wiese* [1962]), and the length is a measure of the conductivity contrast. Real parts are marked in black, and imaginary parts are marked in gray with hollow arrow heads. The subdivision into conductive and resistive zones is arbitrary and meant to sketch the location of lateral conductivity boundaries. The background shows geologic units. See text for discussion.

model. The inversion result in Figure 9b reveals a FZC which remains vertically oriented. However, the conductivities of cells within the FZC rearrange to an eastward dipping distribution of cells with higher conductivity. This effect is small but clearly identifiable in all tested models.

3.4.3. Minimum Depth Extent of the FZC

[33] Lower boundaries of conductive structures are difficult to resolve with MT [*Weidelt*, 1985]. In order to obtain an estimate of the minimum depth extent of the FZC, we first calculated a series of forward models. On the basis of the reference model the depth of the FZC conductor is modified in each of the forward models, while leaving the surrounding conductivity structures unchanged. The curve in Figure 10 shows the resulting RMS misfits of each forward solution against the depth of the FZC. The significant increase of RMS errors for a FZC depth of less than 1100 m indicates the minimum depth for the FZC required to fit the data satisfactorily, suggesting that an eastward dipping conductor is favored by the MT data.

[34] However, a deeper FZC can not be excluded. To further test if the anomaly could be deep reaching, we also ran a constrained inversion with a FZC reaching down to ~3000 m as the a priori starting model (Figure 8e). The RMS error of the converged inversion (Figure 8f) is of the order of the reference model misfit, but in comparison with the starting model the resistivities of the FZC are higher by a factor of two below a depth of about 800 m. This may indicate that a shallower FZC is more consistent with the data. The question, how deep the FZC reaches, is difficult to resolve. Inversions of the Main and South profile data, starting from a homogeneous half-space, result in a depth extent of the FZC between 1300 m and 1500 m which may be a good compromise.

3.4.4. Width of the FZC

[35] The width of the FZC is that portion of the FZC which has resistivities below the bulk apparent resistivity of all recorded sites (see Figure 6, dashed line). This width is measured at the depth where the conductivity of the anomaly is highest, resulting in values of 300 m for the Main profile and 800 m for the South profile. What significance have these estimates?

[36] The lateral resolution of the MT survey is limited by the site spacing as well as the electrode spacing perpendicular to the fault trace, which are both 100 m for the central

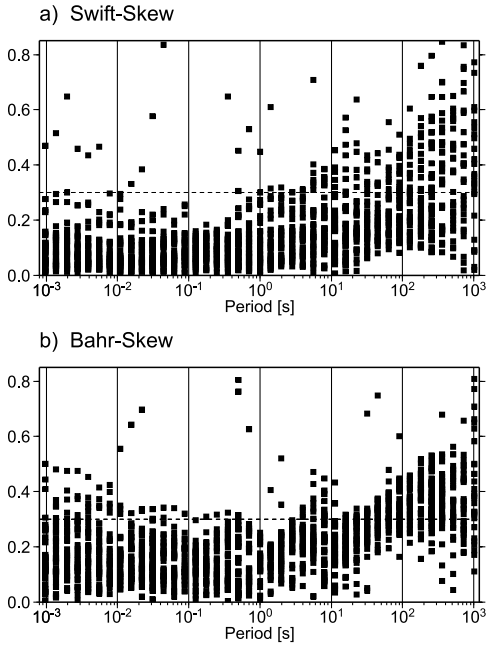

Figure 5. (a) Swift skews and (b) Bahr skews for all sites. Values above 0.3 are inconsistent with 2-D or 1-D subsurface resistivity distributions.

part of the Main profile. Electric fields are deduced from the potential difference between the electrodes, whereas the inversion treats electric fields as point information [*Poll et al.*, 1989]. That means, lateral resolution can not be better than the distance between the electrodes. This limitation is acceptable for two reasons: (1) averaging electric fields over that distance also averages small-scale inhomogeneities that causes static shift; (2) the regularization parameter τ itself coarsens lateral resolution. Owing to the broader site spacing along the South profile, the imaged width of the FZC most likely overestimates the true width.

3.4.5. Anomalies East and West of the FZC

[37] The modeling studies reveal some features east and west of the FZC that are less certain. In the western part of the Main profile feature 5 is conspicuous, suggesting a westward inclined conductive anomaly. The resolution of this anomaly 5 is problematic because of the increased site spacing and the anomaly's position at the edge of the model space. Inverting without sites 38 and 31 results in a very similar conductivity image (Figure 8d). The resistive region at a depth between 100 m and 500 m beneath sites 39 and 38 seems to be a stable feature. Whether the conductive regions beneath sites 39 to 30 are really connected could not be decided due to the larger station spacing.

[38] East of the FZC, the sequence of conductive region 2, resistive region 6, conductive region 7, and resistive block 8 is a stable feature in all tested models (Figure 8a). Ambiguities in the position of these features seem to be closely related to site 8. If site 8 is omitted from the

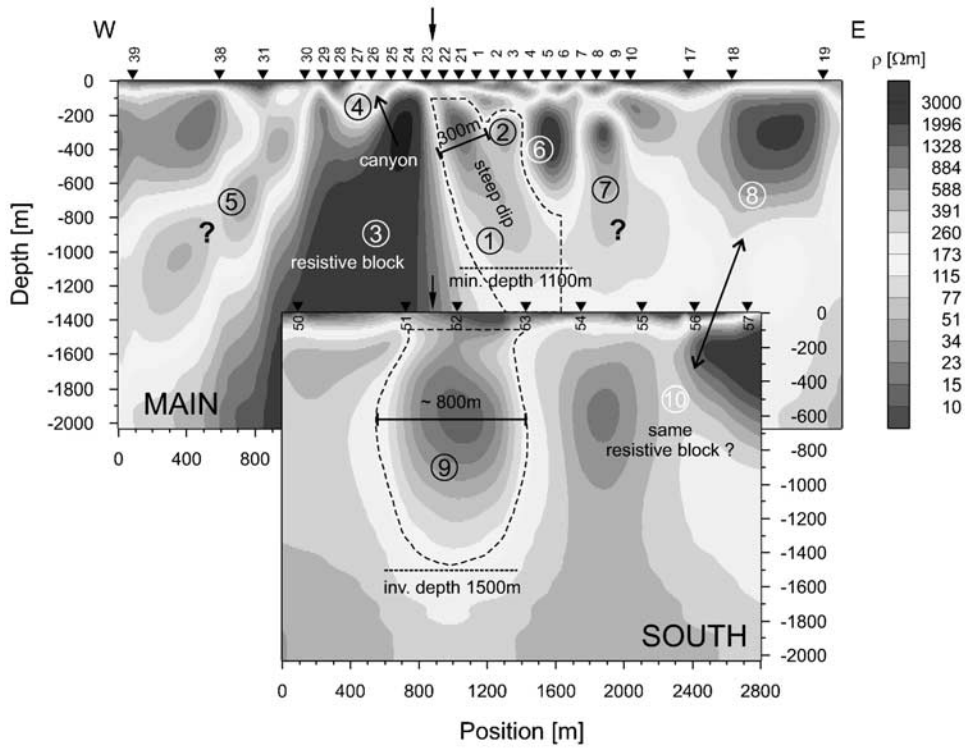

Figure 6. 2-D inversion models of the Main and South profiles. Black arrows mark the position of the West fault surface trace. Numbers denote features discussed in the text. Some estimates of the parameter/sensitivity studies are included. The long dashed lines mark the boundaries of the fault zone conductors (FZC = anomalies 1 and 9, average conductivity 79 Ωm). The minimum depth is a result from sensitivity tests shown in Figure 10. See color version of this figure at back of this issue.

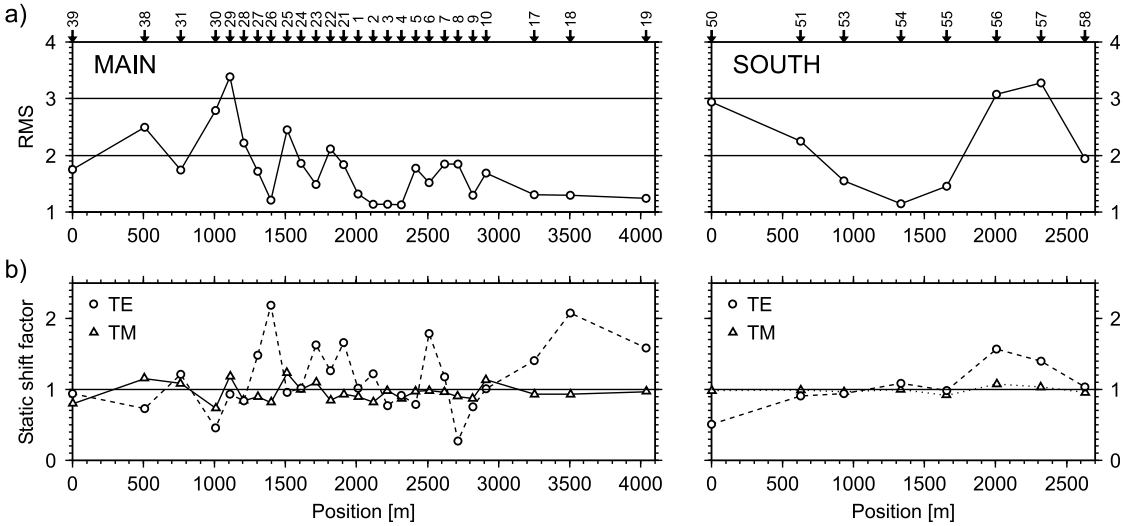

Figure 7. (a) RMS error and (b) static shift factors for each site of the models shown in Figure 6 (error floors, ρ = 10%, ϕ = 2°). Shift factors >1 denote that the recorded data are linearly shifted to higher resistivities and vice versa.

inversion the conductive anomaly 7 shifts to the east (Figure 8d). The data of site 8 are consistent with the curves of the neighboring sites but apparently exhibit a different geoelectric strike angle [*Hoffmann-Rothe*, 2002]. However, the position and geometry of the FZC 1 is not affected by site 8 (e.g., Figure 8d).

4. Fault Damage Characteristics

[39] In order to compare the subsurface conductivity image of the fault with the record of structural damage at the surface we mapped fault-related damage on outcrop scale in the study area. The data were then used to construct a damage element density profile trending perpendicular to the West fault and parallel to the Main profile (Figure 11b).

[40] The majority of the data set comprises orientation data of fault-related rock surfaces that were measured within one meter above and below the reaches of a horizontal scan line along the outcrop wall faces. Planes considered have an exposed surface of at least dinA5 size except for surfaces having clear striations. Slicken lines were identified on most of the surfaces indicating that slip occurred on them [*Hoffmann-Rothe*, 2002]. Minor subsidiary faults cutting the entire face of an exposure were mapped separately. Some of these faults have centimeter wide white gouges, implying significant localization of slip.

[41] According to the histogram of damage element frequency in Figure 11b, the WF is characterized by an ~1000 m wide zone of increased deformation intensity compared to the surrounding host rock, defining the structural damage zone. A fault core of the type visible for the WF in the copper pit mine of Chuquicamata, with a black argillitic fault gouge up to 5 m thick [*Ossandón et al.*, 2001], is not exposed (or preserved) in the Gorila region. Instead, a ~400 m wide fluid alteration zone of intense material comminution is discernible, in which almost no damage elements can be identified [*Janssen et al.*, 2004; *Hoffmann-Rothe*, 2002] (compare photo in Figure 4d of *Janssen et al.* [2004]). Only larger blocks that are less affected by alteration, contribute to the fault damage data. As the constituents (fluids) driving alteration processes need pathways and surfaces to react on, it is reasonable to conclude that the altered part was intensely fractured, too. The granular and unconsolidated alteration zone material exhibits subvertical bands of red, yellow or brownish color. Some of these are narrow (~10–20 cm) and consolidated but irregularly bounded ribs or sheets that run parallel to the WF trace for several meters. Mineral enrichment processes, mostly of iron oxides (hematite), along faults or fault/fracture systems during active stages of faulting and mineralization are held liable for the formation of this banding ("lithified" subsidiary faults). The rock material progressively consolidates toward the eastern edge of the alteration zone and damage element density fades out to background level (Figure 11b). Alternatively, the increase of damage elements between 500 and 800 m east of the fault trace in Figure 11b may be interpreted as a second principal fault branch. However, we could not identify a distinct larger fault in this position. In contrast to the eastern edge of the alteration zone, the western margin is marked by an abrupt change in cohesiveness of the rocks, due to the lithological transition from volcanic (andesites) to plutonic rocks (monzodiorites).

[42] A kinematic analysis of the data proves the prevalence of strike-slip deformation of the investigated section of the WF [*Hoffmann-Rothe*, 2002]. Particularly, minor faults in close vicinity to the WF trace (compare Figure 4c in *Janssen et al.* [2004] for a photo) and structures of the alteration zone dip steeply (~75°; Figure 11d), as expected for strike-slip dominated faults. The mean fault plane orientation also fits very well to the strike of the WF trace (Figure 11a). In summary, a steeply eastward dipping and about 400 m wide fault/fracture mesh runs parallel to the WF fault.

5. Discussion

5.1. Correlation of MT and Fault Damage

[43] Figure 12 shows a synopsis of the local geology of the study area, including the inversion models for the Main

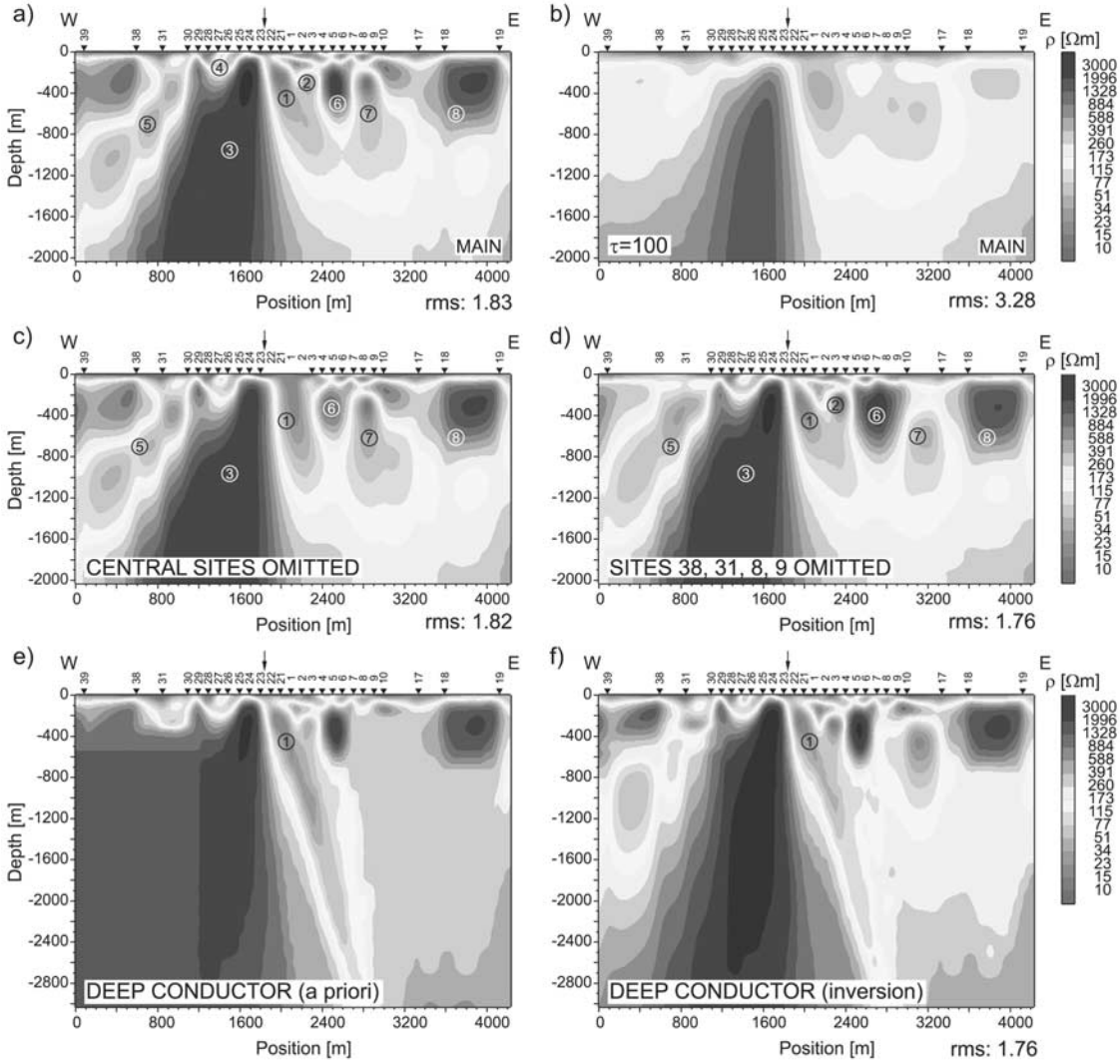

Figure 8. Resolution tests of conductive structures of the Main profile. (a) Reference model of Figure 6. (b) τ set to 100. (c, d) Some sites omitted. Other parameters, in particular the mesh dimensions, remain identical to the reference model. (e) Depth extent of the inclined conductor tested using an a priori model with a deeper-reaching FZC. The inversion result shown in Figure 8f is obtained by forcing the inversion algorithm to solve for a smooth variation close to the a priori model. See color version of this figure at back of this issue.

and South MT profiles and the results of the structural investigation along the Main profile. Is there a correlation of geology, fault-related structures and conductivity anomalies?

[44] 1. The spatial coincidence of the FZCs with the mapped surface trace of the West fault is a first-order concurrence (Figure 12). Along the Main profile, the FZC lies directly to the east of the fault trace and matches the lateral extent of the 400 m wide heavily altered fluid alteration zone (Figure 11). The FZC of the South profile also exhibits highest conductivities beneath the site east of the fault trace (Figure 6). It is reasonable to assume that the FZC runs parallel to the WF segment under investigation.

[45] 2. On the Main profile we image lowest conductivities west of the trace beneath the Early Triassic andesitic and Jurassic calcareous series. Consistently, such a resistive block is missing at the South profile, where these Jurassic/Triassic formations are not exposed.

[46] 3. The dip of damage elements in the vicinity of the fault (subsidiary faults and relic structures of the alteration zone) and the dip of the FZC of the Main profile are conspicuously similar. Both range between 70° and 80° (Figures 11c and 11d). This suggests that the increase of electrical conductivity is causally related to a present or relict mesh of faults and fractures, which may serve as pathway for fluid migration [*Sibson*, 1996].

[47] 44. The correlation of deformation element density and conductivity image in Figure 11 suggest that the eastern rise of densities correlates with a resistive region. It shall be noted, however, that the position of this resistive block beneath sites 4–7 is not as reliably resolved as the fault zone conductor (see section 3.4.5).

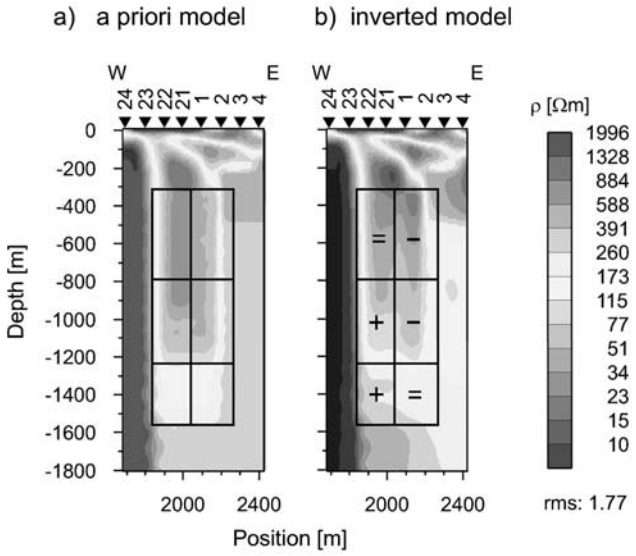

Figure 9. (a) Starting model with a modified FZC having vertical boundaries as constraint for the inversion. (b) Converged inversion result. Boundaries of the FZC and the more resistive vicinity remain vertical. Internally, the resistivities are rearranged in such a way that the upper right rectangle becomes more conductive and the lower left rectangle more resistive, suggesting that an eastward dipping conductive anomaly is favored by the data. See color version of this figure at back of this issue.

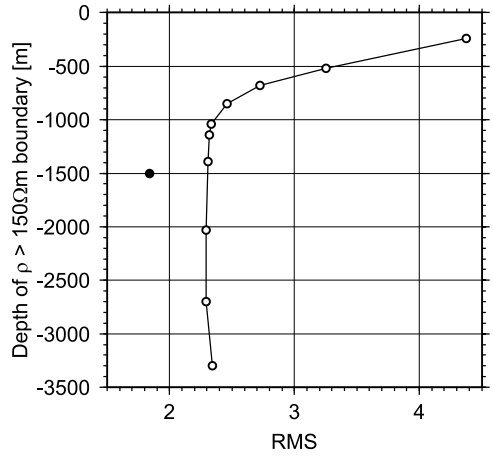

Figure 10. RMS misfit evolution of forward models with modification of the depth extent of the FZC based on the reference model. The values shown refer to the depth at which the resistivities of the FZC exceed 150 Ωm (bulk resistivity of all recorded sites). The black dot denotes the respective value for the reference model.

[48] 5. A structural surface expression of the conductive anomaly at the western edge of the Main profile (anomaly 5) was not found. The sedimentary succession in this part of the study area dips to the west, but an interrelation with the poorly resolved anomaly remains speculative.

5.2. Conductive Constituent

[49] Are fluids sufficient to explain the observed high electrical conductivity of the FZC? Saline fluids in a fault fracture mesh can increase electrical conductivity due to ionic conduction if the mesh (or the material pore space) is sufficiently interconnected to allow for electric current flow. Additionally, the fluid contained in the rock mass must be saline enough to provide the electrolyte. The spring emanating on the West fault trace proves the availability of surface water in the study area. Furthermore, the presence of fluids of primarily meteoric origin in the younger geologic past is supported by fluid-rock chemistry of the alteration zone material [*Janssen et al.*, 2004].

[50] Table 1 lists fluid salinities and inferred fluid resistivities of water samples from the spring in the study area and from samples taken in the copper mining district of Radomiro Tomic (15 km south of the Gorila region

Table 1. Specific Fluid Resistivity (ρ_f) Calculation for Several Groundwater Samples From Different Depth Below Surface Level[a]

	Sample Water Source		
	Radomiro Tomic Exploration Shaft (200 m Below Surface Level)	Radomiro Tomic Open Pit (Beneath Water Table)	Gorila Surface Spring
Main ions, mg/L			
Cl^-	7170	1680	60.4
SO_4^{2-}	<0.5	<0.25	179
Ca^{2+}	647	465	102.2
Mg^{2+}	57.5	42	12.2
Na^+	128	69	39.1
K^+	4880	1910	10
Equiv. *B*, mequ/L	184.83	62.95	6.58
Fluid res. ρ_f, Ωm	0.6[b]	1.7[b]	16.7[c]
With Bulk Rock Resistivity ρ_r = 79 Ωm and Porosity $\Phi^m = \rho_f/\rho_r$ (Archie's Law)			
Φ for m = 1, %	0.8	2.2	21
Φ for m = 1.5, %	3.9	7.7	35
Φ for m = 2, %	8.7	14.7	46

[a]The determinant ion constituents for the physical properties of the water are chosen according to *Berktold* [1982]. *B* is the equivalent concentration of electrolyte. Fluid resistivities ρ_f are calculated from empirical relations described by *Berktold* [1982]. Data for Radomiro Tomic copper mine are taken from *Cuadra and Rojas* [2001], and the spring water was analyzed by G. Schettler (GFZ). The average rock resistivity ρ_r of the central conductors of the Main and South MT profiles is 79 Ωm. The interconnected porosity Φ, filled with fluids of resistivity ρ_f, that is needed to explain the bulk resistivity ρ_r exclusively from the fluid contents is calculated with Archie's empirical law.

[b]For Cl-dominated water, $\rho_f = 1/123\ B^{0.9388}$.

[c]For $1 < B < 10$, $\rho_f = 1/B(95.5 - 5.54 \log B)$.

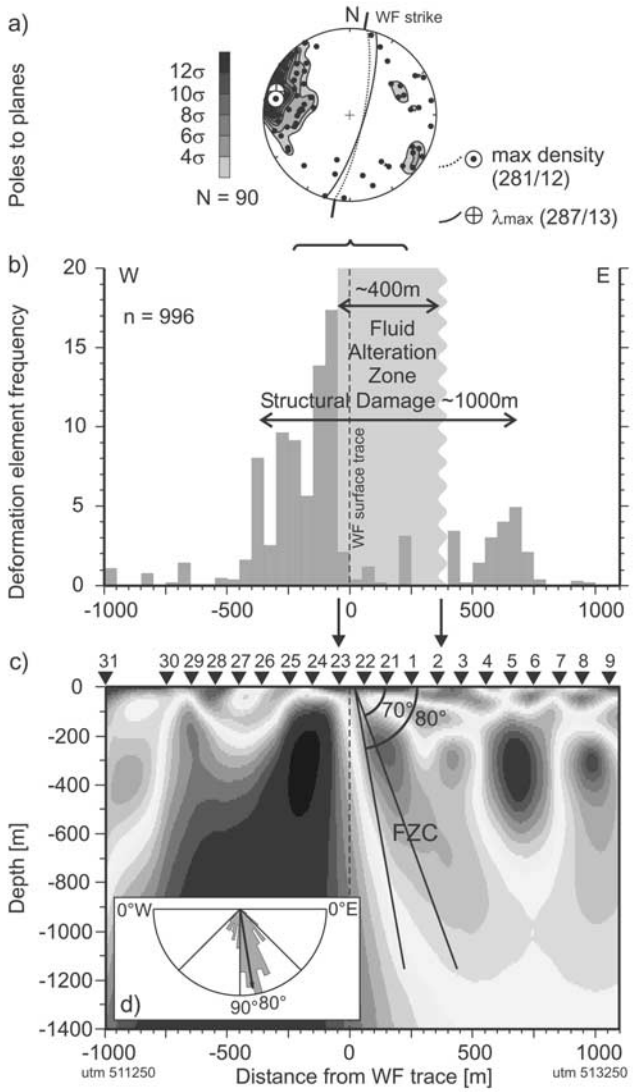

Figure 11. Correlation of fault-related damage and subsurface conductivity structure along the Main MT profile. (a) Orientation of minor faults/alteration bands around the fault trace (contour plot: equal area, lower hemisphere projection; density contours based on smoothed 1% area counting on a sphere, grouped in multiples of standard deviation relative to uniform population; cluster and eigenvalue distribution with directional maximum and corresponding great circles are shown). (b) Deformation element density profile and alteration zone. (c) Central part of the inversion result of the Main profile. Solid lines mark a dip range from 70° to 80°. (d) Dip of minor faults/alteration bands (arrow is the mean dip and mean resultant length). The fluid alteration zone correlates spatially with the FZC, and the dip of the anomaly coincides with the eastward dip of minor faults surrounding the WF trace.

and directly to the east of the WF [*Cuadra and Rojas* [2001]). Assuming the samples are characteristic for regional groundwaters in the alteration zones, they represent qualitatively the salinity and conductivity variation with depth. The spring water with a characteristic meteoric stable isotope signature [*Janssen et al.*, 2004] is the most juvenile water and the most resistive (17 Ωm, Table 1). The open pit mine water sample drains from deep subsurface levels of ~200 m, causing higher ion content and lower fluid resistivity of 1.7 Ωm. The underground water sample with the longest exposure to fluid-rock interactions is the most conductive (0.6 Ωm).

[51] Using a simplified version of *Archie*'s [1942] empirical law, we can now relate the calculated fluid resistivities ρ_f to the interconnected porosity Φ required to explain the measured bulk rock resistivity (79 Ωm): $\rho_r = \rho_f \Phi^{-m}$. This relation is applicable to correlate porosity and resistivity of rocks at shallow depth and under low-temperature conditions [*Glover et al.*, 2000]. The cementation exponent m is related to the connectivity of the pore space containing the conductive fluid. Full connectivity is implied for $m = 1$, while m rises with increasing compaction and cementation of the rock mass [*Schopper*, 1982]. *Unsworth et al.* [1997] suggest using the lower bound of m to apply to porosity in fault zones with open crack textures.

[52] The bottom part of Table 1 lists the results of the porosity estimates; lower bound porosity values are highlighted. The subsurface water samples have relatively low inferred porosities ranging between 0.8% and 7.7%. For comparison, porosity measurements on granitic fault rock samples from the Limon Verde branch of the WFZ have resulted in values of about 8% compared to the protolith with 0.8–1.5% porosity [*Janssen et al.*, 2002]. The low-saline spring water yields an inferred porosity up to 21–35%, a reasonable value, regarding the unconsolidated alteration zone material at the surface. However, the porosity estimates have to be interpreted with care, where pore space is not saturated with water. Also note, that this estimation ignores effects of electrochemical interaction of the fluid with the solid material along surfaces of pores or cracks that may also significantly contribute to conductivity, particularly where water rich alteration products (e.g., clay minerals) are involved [*Schopper*, 1982; *Wildenschild et al.*, 2000]. A little amount of clay minerals may therefore decrease the amount of porosity (fluid, salinity) required to explain the observed conductive anomalies.

[53] Two other possible mechanisms could be responsible for the conductivity anomaly: (1) Solutes, such as metallic oxides or sulfide ores, could have precipitated on the mesh surfaces as interconnected electronically conductive phase. Although this is likely in areas of extreme copper enrichment, ore coatings on slip surfaces were not observed in the Gorila region. Moreover, an interconnected mesh of an electronically conductive phase is difficult to conceive regarding the degree of comminution in the alteration zone. (2) Fault-related clay gouges resulting from shear comminution and geochemical alteration driven by the fluid phase may have low electrical resistivity, typically ranging between 3 and 10 Ωm [*Palacky*, 1987; *Eberhart-Phillips et al.*, 1995]. The field record exhibits no intact gouges within the alteration zone and the little gouges in the resistive Jurassic and Triassic series are dominated by quartz/feldspar or calcite minerals. We conclude that fluids of meteoric origin that penetrate the intensely damaged and fractured part of

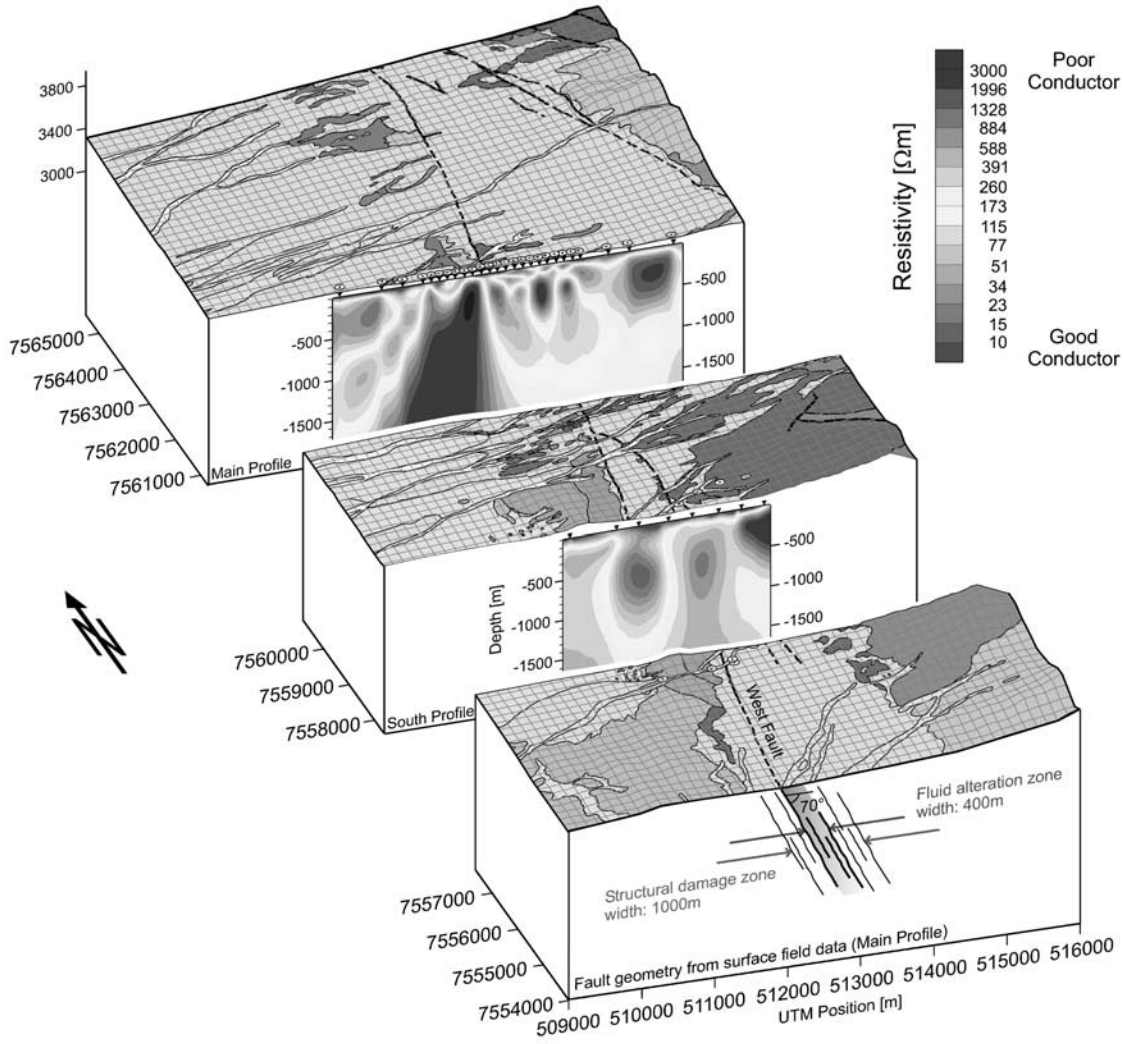

Figure 12. Block diagram with geology (compare map in Figure 1 for legend) summarizing the magnetotelluric inversion models of both profiles and the results of the structural investigation along the Main profile. The latter are schematically drawn on the front panel of the block diagram and extrapolated to greater depth. Magnetotelluric inversion models are not vertically exaggerated; morphology is exaggerated by factor 2. See color version of this figure at back of this issue.

the fault zone are sufficient to explain the observed high conductivity.

5.3. West Fault as Fluid Conduit

[54] In a predominant strike-slip regime, the damage elements (shear fractures, reactivated shear planes, extension fractures) interlink parallel to the subvertically oriented intermediate stress axis σ_2 and thereby form a "tubular component," which enhances vertical permeability [*Sibson*, 1996; *Caine and Forster*, 1999]. As the FZC of the WF is confined to shallow depth and fluids involved in the alteration processes are of meteoric origin, it is reasonable to expect the WF to act as a sink for fluids (Figure 13). Given the morphology of the Gorila region, gravity drives surface water toward the fault that penetrates the damage/alteration zone. Permeability contrasts resulting from juxtaposition of country rocks of different composition and texture (alteration zone vs. Triassic andesites/Jurassic limestones) prevents westward fluid flow across the fault (juxtaposition seal) and may even force the water to flow out in cold springs located on the fault trace.

[55] The scenario depicted in Figure 13 implies that a fair amount of interconnected porosity must have remained within the alteration zone even after apparent cessation of faulting activity in the late Pliocene. However, the depth extent of the FZCs appears to be restricted to about 1500 m, suggesting that healing and cementation processes plug the fault fracture mesh at greater depth. A mesh constitutes an effective conduit for fluids while ongoing deformation, whether seismically or aseismically, keeps the cracks permeable [*Sibson*, 1994, 1996]. Otherwise, solutes carried in the fluid precipitate in the mesh and may eventually seal fluid pathways. The deposited seal depends mainly on the rock composition, which controls the solute in the fluid phase, and the temperature conditions [*Parry*, 1998]. Quartz sealed structures are typical at greater depth since the kinetics of dissolution

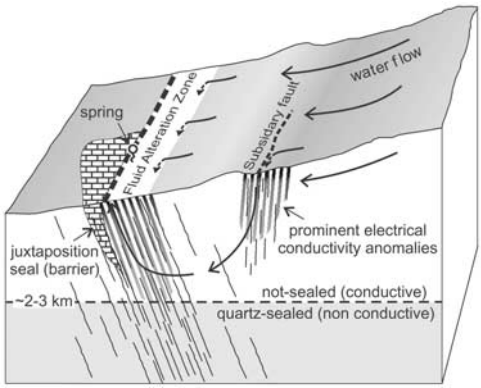

Figure 13. Conceptual sketch showing water inflow into the alteration zone and possible larger subsidiary faults. Electrically conductive anomalies result where permeability in the fault fracture mesh remains unsealed at shallow depth. Horizontal fluid flow across the fault may be barred by a juxtaposition seal resulting from rocks with different permeability and healing properties. Waters are forced back to the surface and form springs within the alteration zone.

and precipitation of silica start to be efficient at temperatures in excess of 70°–90°C. Carbonate precipitation occurs at lower temperatures (<80°C) and depth [*Renard et al.*, 2000; *Labaume et al.*, 2001]. The alteration products exposed at the surface indicate low-temperature alteration conditions (<100°C) and no SiO_2 dissolution processes [*Janssen et al.*, 2004]. The fault fracture mesh is (and was) not sealed at shallow depth, but permeability reduction due to quartz seals likely prevents fluid flow to greater depth (Figure 13). The calcareous Jurassic series are particularly prone to calcite precipitation. This, in combination with the generally lower bulk porosity of limestones, may explain the high resistivities observed west of the fault trace at the Main profile.

[56] The fault zone conductors discussed here mirror present day upper crustal fluid penetration into the structurally damaged fault zone. However, the WFZ has played a major role as crustal-scale fluid conduit throughout its existence, when fracture permeability structurally controlled fluid flow in the hypogene and supergene ore enrichment processes [*Ossandón et al.*, 2001; *Lindsay et al.*, 1995, 1996; *Cuadra and Rojas*, 2001]. Note, that these past fluid-conduit systems are not responsible for the observed shallow conductor and apparently have not created a permanent conductive anomaly. Whether fracture permeability also causes the midcrustal conductor imaged in position of the Precordilleran fault system [*Brasse et al.*, 2002] remains speculative.

[57] The local copper ore bodies (Chuquicamata, Radomiro Tomic and El Abra) are all located to the east of the West fault trace. At Chuquicamata the copper bearing porphyries are clearly cut off by the fault and there is an economical interest in finding the corresponding western parts, assuming they exist. In the case that the imaged eastward dip of the FZC is maintained at greater depth and was similar in periods of extensive fluid flow, fluids using the fault as pathway may preferentially escape into the hanging wall, causing mineralization and alteration on one side (the eastern side) of the fault only.

5.4. Internal Fault Architecture and Conductivity Image of the West Fault

[58] In view of the discussion above, the internal architecture of the WF in the Gorila region can be summarized as follows.

[59] 1. The frequency distribution of the damage elements on a profile perpendicular to the WF (Figure 11) is rather typical, showing an increasing number with proximity to the fault trace. This delineates a damage zone 1000 m wide along the Main profile. Consequently, the 300 m wide FZC does not image the damage zone as a whole.

[60] 2. The central 400 m of the damage zone comprise strongly comminuted and altered granitoid rocks. Prior to alteration this zone likely exhibited the locus of fault-related deformation and provided an increased surface area for alteration processes to be effective. This part of the fault zone is electrically conductive for it is sufficiently permeable to allow water to enter. Cross fault fluid flow is hampered by a juxtaposition seal.

[61] 3. Adopting the classification of architectural styles and permeability structures of fault zones proposed by *Caine et al.* [1996] and *Caine and Forster* [1999] this segment of the West fault is best described as a "distributed deformation zone," which is characterized by "well-developed discrete slip surfaces and associated fracture networks," while a well-developed fault core cataclasite is missing.

5.5. Comparison of Upper Crustal Fault Zone Studies

[62] Many authors have emphasized that structural and fluid flow properties of a developing large fault system not only vary with time but also in space, in particular along the length of a strike-slip fault [e.g., *Evans et al.*, 1997; *Caine et al.*, 1996]. This is also true for electrical conductivity images obtained at different segments of a fault system. Figure 14 summarizes the results of MT profiles crossing segments of the West fault zone and the San Andreas Fault (SAF), representing the best studied fault system to date. The most important difference between these two fault systems is their present state of activity.

[63] The Guatacondo and Limon Verde Segments of the WFZ are devoid of present faulting activity (see Figure 1a for locations). Electrically conductive zones have been imaged in position of the fault traces, but the depth extent is no more than 200 m (Figure 14) [*Janssen et al.*, 2002]. Sealing and cementation of the fault fracture mesh and associated permeability has progressed much further on these segments than in the Gorila region.

[64] The MT surveys crossing the SAF segments have an experimental layout comparable to the study presented in this paper; that is, site spacing is dense across the surface fault trace. A FZC is imaged at all segments and hydrogeologic interpretations of the FZCs are favored (see figure caption for references). These studies in conjunction with the results from the West fault segments support the assumption that the properties of FZCs are linked to the state of activity of a fault [e.g., *Mogi et al.*, 1991; *Bedrosian et al.*, 2002]. The greater the activity of a fault segment, the more pronounced the conductivity increase of the FZC

Property	West Fault System			San Andreas Fault		
	Guatacondo[1]	Limon Verde[1]	Gorila region[2]	Carrizo Plain[3]	Parkfield[4]	Hollister[5]
Recent activity	inactive	inactive	inactive	locked since 1857	extensive micro-seismicity, creeping	continuous creep 15mm/a
Width of FZC	< 100 m	–	300-400 m	< 300 m	750 m	750 m
Depth of FZC	50 m	200 m	1500 m	3000 m	2000-5000m	8000 m
Conductance	–	< 5 S	5 S	20 S	250 S	600 S
high low						
Porosity estim.	–	–	1-14%	–[6]	10-30%	10-35%
Cause of low ρ	Surface penetration of meteoric fuids			Saline fuids of meteoric origin		

[1] Janssen et al. (2002), [2] This study, [3] Unsworth et al. (1999), [4] Unsworth et al. (1997, 1999, 2000, 2004), [5] Bedrosian et al. (2002), [6] 'lower porosity than Parkfield', Unsworth et al. (1999)

Figure 14. Comparison of high-resolution MT studies across the West fault system and the San Andreas Fault. Recent activity denotes the current state of deformation at the fault segments. Porosities are estimated with Archie's law using fluid conductivities of water samples (drill hole and spring data) that have been collected in the vicinity of the respective fault segments. The porosity ranges correspond to *m* exponents in Archie's law of one and two. Gray shaded sketches represent depth range, width, and conductance of the FZCs.

(sketches Figure 14; conductance is the product of width and average conductivity of the FZC). Compared to the presently deforming Parkfield and Hollister segments, the Carrizo Plain segment exhibits a conductance an order of magnitude smaller. The conductance of the WF segment in the Gorila region, without evident sign of activity is yet another order of magnitude smaller, while the anomalies of the inactive segments (Limon Verde, Guatacondo) merely trace the former locus of deformation at the surface. This fits well in the concept of fault fracture meshes only being permeable for conductive fluids while they are under deformation [*Sibson*, 1994]. Sealing of the fluid pathways reduces permeability after cessation of faulting activity.

[65] Even though fault activity and conductivity image appear to be directly linked, we actually have to consider a complex interplay of properties and feedback mechanisms (Figure 15): The electromagnetic image of a brittle fault zone will primarily be governed by the fluid supply, either from the surrounding lithologies or from deeply rooted fluid sources. Strength (competence) of adjacent rock masses influences where structural damage will localize and thereby the position of a potential FZC relative to the fault trace. The availability of (overpressurized) fluids in the fault zone affects strength of the fault material and consequently the fault's activity. Often, seismicity seems to be confined along one edge of a FZC, indicating that the conductive region is too weak for brittle faulting [*Unsworth et al.*, 1999; *Bedrosian et al.*, 2002]. Alternatively, the seismicity may be a result of seepage/migration of fluids from the fluid-filled conductive zones to less permeable regions of the crust, where they trigger an earthquake [*Mitsuhata et al.*, 2001]. Finally, fluids transport solutes and have control on sealing mechanisms of the fault fracture mesh, which may lead to strength recovery of the fault system.

[66] The detection of a FZC helps to understand the internal architecture of a fault. Zones of intense structural damage can be identified, as well as the location of impermeable portions and/or barriers for fluid flow. In conjunction with additional information on lithology and fluid sources it may be possible to determine the current state of faulting activity.

5.6. Conclusion

[67] In this paper, the upper crustal electrical conductivity image of a profile crossing a fault zone is calibrated against the record of fault-related structural damage. The findings of the respective methods show strong correlation.

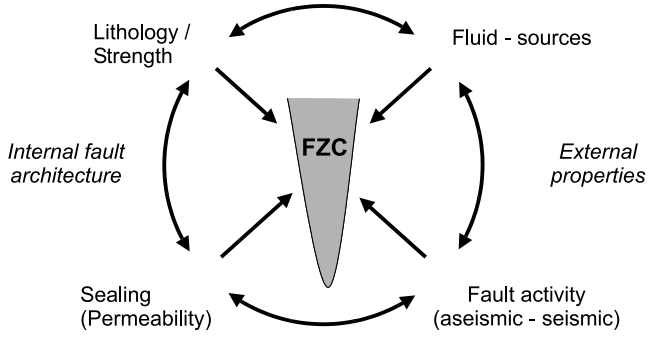

Figure 15. Existence and formation of an electrical conductivity anomaly along a fault (FZC) depending on a complex interplay of properties. For example, fluid sources and solutes have control on sealing mechanisms of the fault/fracture mesh, the permeability of the fault zone material, and thus also on strength recovery of the fault system.

[68] 1. The dimensionality and directionality analysis of the MT data shows that the WF fault represents a conduit for electric current flow parallel to the fault. A two-dimensional interpretation of the data is justified in the high-frequency range (1000 Hz to 0.1 Hz). The investigated WF segment is characterized by a steeply dipping fault zone conductor (FZC) confined to the uppermost 2 km of the crust.

[69] 2. The FZC spatially coincides with a 400 m wide, intensely comminuted fluid alteration zone, which is more or less centered in a 1000 m wide damage zone, based on outcrop-scale structural mapping. The dip of the FZC matches the orientation of subsidiary faults in the vicinity of the fault trace and the alteration zone, suggesting that the high conductivity is causally related to a conserved mesh of minor faults and fractures. Fluids of meteoric origin entering the damaged zone from the surface suffice to create the observed conductivity anomaly. Most likely, the present inactivity of the fault caused sealing of the fault fracture mesh at depth, where dissolution and precipitation of minerals is effective and consequently limits the depth extent of the FZC.

[70] The fault damage zone is commonly viewed as the most permeable fault unit [e.g., *Caine et al.*, 1996]. This may lead to the assumption that a FZC images the damage zone of a fault. As the WF example demonstrates, this must not be the case. Firstly, the state of activity will control the extent of healing of damage elements and narrow the potentially "conductive width" of the damage zone down to the most intensely fractured portion. Secondly, barriers for cross fault fluid flow, may they result from juxtaposition of different rock masses or the creation of impermeable fault gouges, can govern the location of the FZC.

[71] With regard to other published MT surveys across fault zones, especially the San Andreas Fault, the conductivity image of the West fault supports the assumption that the depth extent and conductivity of a FZC is correlated with youthfulness of fault activity. Ongoing deformation will keep the fault fracture mesh permeable for fluids and impede cementation and sealing of fluid pathways.

[72] **Acknowledgments.** This study was funded by the Deutsche Forschungsgemeinschaft (DFG) within the framework of the Collaborative Research Project SFB 267 "Deformation Processes in the Andes." We wish to thank many colleagues for their cooperation while organizing and accomplishing the fieldwork, namely H. Wilke (Universidad Católica del Norte, Antofagasta), L. Baeza, the late G. Behn (both Codelco Chile), W. Soyer, H. Brasse, E. Cisternas, P. Salazar, and L. Wong. We are grateful for valuable discussions with G. Dresen and V. Haak. We also thank J. P. Evans, P. Wannamaker, and one anonymous reviewer for helpful comments and improvement of the manuscript. The MT instruments were provided by the Geophysical Instrument Pool of the GeoForschungsZentrum (GFZ) Potsdam. Most of the diagrams were generated using the public domain software GMT [*Wessel and Smith*, 1998].

References

Archie, G. E. (1942), The electrical resistivity log as an aid in determining some reservoir characteristics, *Trans. Am. Inst. Min. Metall. Pet. Eng.*, *146*, 54–62.

Bahr, K. (1988), Interpretation of the magnetotelluric impedance tensor: Regional induction and local telluric distortion, *J. Geophys.*, *62*, 119–127.

Bahr, K. (1991), Geological noise in magnetotelluric data: A classification of distortion types, *Phys. Earth Planet. Inter.*, *66*, 24–38.

Bedrosian, P. A., M. J. Unsworth, and G. Egbert (2002), Magnetotelluric imaging of the creeping segment of the San Andreas Fault near Hollister, *Geophys. Res. Lett.*, *29*(11), 1506, doi:10.1029/2001GL014119.

Belmonte, A. (2002), Crustal seismicity, structure and rheology of the upper plate between the Pre-Cordillere and the volcanic arc in northern Chile (22°S–24°S), Ph.D. thesis, Free Univ. Berlin.

Berktold, A. (1982), Electrical conductivity of moisture containing rocks, in *Physical Properties of Rocks, Numerical Data and Functional Relationships in Science and Technology*, vol. 1b, edited by G. Angenheister, pp. 262–275, Springer-Verlag, New York.

Blanpied, M. L., D. A. Lockner, and J. D. Byerlee (1992), An earthquake mechanism based on rapid sealing of faults, *Nature*, *358*, 574–576.

Brasse, H., P. Lezaeta, K. Schwalenberg, W. Soyer, and V. Haak (2002), The Bolivian Altiplano Conductivity Anomaly, *J. Geophys. Res.*, *107*(B5), 2096, doi:10.1029/2001JB000391.

Byerlee, J. (1993), Model for episodic flow of high-pressure water in fault zones before earthquakes, *Geology*, *21*, 303–306.

Caine, J. S., and C. P. Forster (1999), Fault zone architecture and fluid flow: Insights from field data and numerical modeling, in *Faults and Subsurface Fluid Flow in the Shallow Crust*, *Geophys. Monogr. Ser.*, vol. 113, edited by W. C. Haneberg, pp. 101–127, AGU, Washington, D. C.

Caine, J. S., J. P. Evans, and C. P. Forster (1996), Fault zone architecture and permeability structure, *Geology*, *24*, 1125–1128.

Cello, G., R. Gambini, S. Mazzoli, A. Read, E. Tondi, and V. Zucconi (2000), Fault zone characteristics and scaling properties of the Val d'Agri Fault System (Southern Apennines, Italy), *J. Geodyn.*, *29*, 293–307.

Chester, F. M., and J. M. Logan (1986), Implications for mechanical properties of brittle faults from observations of the Punchbowl Fault Zone, California, *Pure Appl. Geophys.*, *124*, 79–106.

Chester, F. M., J. P. Evans, and R. L. Biegel (1993), Internal structure and weakening mechanisms of the San Andreas Fault, *J. Geophys. Res.*, *98*, 771–786.

Cuadra, P., and G. Rojas (2001), Oxide mineralisation at the Radomiro Tomic porphyry copper deposit, Northern Chile, *Econ. Geol.*, *96*, 387–400.

Dilles, J., A. J. Tomlinson, M. Martin, and N. Blanco (1997), The El Abra and Fortuna complexes: A porphyry copper batholith sinistrally displaced by the Falla Oeste, in *VIII Congresso Geológico Chileno*, ACTAS vol. 3, *Nuevos Antecedentes de la Geología del Distrio de Chuquicamata, Periodo 1994–1995—Sesión 1: Geología Regional*, Dep. de Ciencias Geol., Univ. Catolica del Norte, Antofagasta, Chile.

Eberhart-Phillips, D., W. D. Stanley, B. D. Rodriguez, and W. J. Lutter (1995), Surface seismic and electrical methods to detect fluids related to faulting, *J. Geophys. Res.*, *100*, 12,919–12,936.

Echternacht, F., S. Tauber, M. Eisel, H. Brasse, G. Schwarz, and V. Haak (1997), Electromagnetic study of the active continental margin in northern Chile, *Phys. Earth Planet. Inter.*, *102*, 69–87.

EleKTB Group (1997), KTB and the electrical conductivity of the crust, *J. Geophys. Res.*, *102*, 18,289–18,305.

Evans, J. P., C. B. Forster, and J. V. Goddard (1997), Permeability of fault-related rocks, and implications for hydraulic structure of fault zones, *J. Struct. Geol.*, *19*, 1393–1404.

Faulkner, D. R., and E. H. Rutter (2001), Can the maintenance of overpressured fluids in large strike-slip fault zones explain their apparent weakness?, *Geology*, *29*, 503–506.

Faulkner, D. R., A. C. Lewis, and E. H. Rutter (2003), On the internal structure and mechanism of large strike-slip fault zones: Field observations of the Caboneras fault in southeasten Spain, *Tectonophysics*, *367*, 235–251.

Glover, P., M. J. Hole, and J. Pous (2000), A modified Archie's law for two conducting phases, *Earth Planet. Sci. Lett.*, *180*, 369–383.

Gudmundsson, A. (2000), Active fault zones and groundwater flow, *Geophys. Res. Lett.*, *27*, 2993–2996.

Haak, V., and V. R. S. Hutton (1986), Electrical resistivity in continental lower crust, in *The Nature of the Lower Continental Crust*, *Spec. Publ.*, vol. 24, edited by J. B. Dawson, pp. 35–49, Geol. Soc. London, U. K.

Hickman, S. H., R. Sibson, and R. Bruhn (1995), Mechanical involvement of fluids in faulting, *J. Geophys. Res.*, *100*, 12,831–12,840.

Hoffmann-Rothe, A. (2002), Combined structural and magnetotelluric investigation across the West Fault Zone in northern Chile, *Sci. Tech. Rep. STR02/12*, 110 pp., GeoForschungsZentrum, Potsdam, Germany.

Hoffmann-Rothe, A., O. Ritter, and V. Haak (2001), Magnetotelluric and geomagnetic modelling reveals zones of very high electrical conductivity in the upper crust of Central Java, *Phys. Earth Planet. Inter.*, *124*, 131–151.

Janssen, C., A. Hoffmann-Rothe, S. Tauber, and H. Wilke (2002), Internal structure of the Precordilleran fault system (Chile)—Insights from structural and geophysical observations, *J. Struct. Geol.*, *24*, 123–143.

Janssen, C., V. Lüders, and A. Hoffmann-Rothe (2004), Contrasting styles of fluid-rock interaction within the West Fissure Zone in northern Chile, in *Flow Processes in Faults and Shear Zones*, *Spec. Publ.*, vol. 224, pp. 141–160, Geol. Soc. London, U. K.

Jödicke, H., J. H. Kruhl, C. Ballhaus, P. Giese, and J. Untiedt (2004), Syngenetic, thin graphite-rich horizons in lower crustal rocks from the Serre San Bruno, Calabria (Italy), and implications for the nature of high-conducting deep crustal layers, *Phys. Earth Planet. Inter.*, *141*, 37–58.

Jones, A. G. (1998), Waves of the future: Superior inferences from collocated seismic and electromagnetic experiments, *Tectonics*, *286*, 273–298.

Labaume, P., S. M. F. Sheppard, and I. Moretti (2001), Fluid flow in cataclastic thrust fault zones in sandstones, Sub-Andean Zone, southern Bolivia, *Tectonophysics*, *340*, 141–172.

Lindsay, D., M. Zentilli, and J. Rojas de la Rivera (1995), Evolution of an active ductile to brittle shear system controlling mineralization at the Chuquicamata porphyry copper deposit, Chile, *Int. Geol. Rev.*, *37*, 945–958.

Lindsay, D., M. Zentilli, and G. Ossandon (1996), Falla Oeste fault system: Record of its regional significance as exposed in the Chuquicamata open pit, northern Chile, paper presented at the 3rd International Symposium on Andean Geodynamics, St. Malo, France.

Mackie, R. L., D. W. Livelybrooks, T. R. Madden, and J. C. Larsen (1997), A magnetotelluric investigation of the San Andreas fault at Carrizo Plain, California, *Geophys. Res. Lett.*, *24*, 1847–1850.

Maksaev, V., H. H. Dilles, and A. J. Tomlinson (1999), Mapa geológico del Cuadrángulo Cerros de Paqui, Región de Antofagasta, scale 1:50,000, Serv. Nac. de Geol. y Min. y Coop. Nac. del Cobre, Santiago.

McNeice, G. W., and A. G. Jones (2001), Multisite, multifrequency tensor decomposition of magnetotelluric data, *Geophysics*, *66*, 158–173.

Mitsuhata, Y., Y. Ogawa, M. Mishina, T. Kono, T. Yokokura, and T. Uchida (2001), Electromagnetic heterogeneity of the seismogenic region 1962 M6.5 Northern Miyagi Earthquake northeastern Japan, *Geophys. Res. Lett.*, *28*, 4371–4374.

Mogi, T., I. Katsura, and S. Nishimura (1991), Magnetotelluric survey of an active fault system in the northern part of Kinki District, southwest Japan, *J. Struct. Geol.*, *13*, 235–240.

Ossandón, G., R. Fréraut, L. B. Gustafson, D. D. Lindsay, and M. Zentilli (2001), Geology of the Chuquicamata mine: A progress report, *Econ. Geol.*, *96*, 249–270.

Palacky, G. J. (1987), Resistivity characteristics of geologic targets, in *Electromagnetic Methods in Applied Geophysics—Theory*, vol. 1, edited by M. N. Nabighian, pp. 53–129, Soc. Explor. Geophys., Tulsa, Okla.

Parry, W. T. (1998), Fault-fluid compositions from fluid-inclusion observation and solubilities of fracture-sealing minerals, *Tectonophysics*, *290*, 1–26.

Poll, H. E., J. T. Weaver, and A. G. Jones (1989), Calculations of voltages for magnetotelluric modelling of a region with near-surface inhomogeneities, *Phys. Earth Planet. Inter.*, *53*, 287–297.

Rawling, G. C., L. B. Goodwin, and J. L. Wilson (2001), Internal architecture, permeability structure, and hydrologic significance of contrasting fault-zone types, *Geology*, *29*, 43–46.

Renard, F., J.-P. Gratier, and B. Jamtveit (2000), Kinetics of crack-sealing, intergranular pressure solution, and compaction around active faults, *J. Struct. Geol.*, *22*, 1395–1407.

Reutter, K.-J., E. Scheuber, and G. Chong (1996), The Precordilleran fault system of Chuquicamata, northern Chile: Evidence for reverasals along arc-parallel strike-slip faults, *Tectonophysics*, *259*, 213–228.

Reynolds, P., C. Ravenhurst, M. Zentilli, and D. Lindsay (1998), High-precision $^{40}ar/^{39}ar$ dating of two consecutive hydrothermal events in the chuquicamata porphyry copper system, chile, *Chem. Geol.*, *148*, 45–60.

Rice, J. R. (1992), Fault stress states, pore pressure distributions, and the weakness of the San Andreas Fault, in *Fault Mechanics and Transport Properties of Rocks*, edited by B. Evans and T.-F. Wong, pp. 474–503, Academic, San Diego, Calif.

Ritter, O., A. Junge, and G. J. K. Dawes (1998), New equipment and processing for magnetotelluric remote reference observations, *Geophys. J. Int.*, *132*, 535–548.

Ritter, O., T. Ryberg, U. Weckmann, A. Hoffmann-Rothe, A. Abueladas, Z. Garfunkel, and DESERT Research Group (2003), Geophysical images of the Dead Sea Transform in Jordan reveal an impermeable barrier for fluid flow, *Geophys. Res. Lett.*, *30*(14), 1741, doi:10.1029/2003GL017541.

Ritter, O., A. Hoffmann-Rothe, P. A. Bedrosian, U. Weckmann, and V. Haak (2004), Electrical conductivity images of active and fossil fault zones, in *Microstructural Evolution and Physical Properties in High-Strain Zones*, edited by D. Bruhn and L. Burlini, Geol. Soc. London Spec. Publ., in press.

Rodi, W., and R. L. Mackie (2001), Nonlinear conjugate gradients algorithm for 2-D magnetotelluric inversion, *Geophysics*, *66*, 174–187.

Schopper, J. R. (1982), Electrical conductivity of rocks containing electrolytes, in *Physical Properties of Rocks, Landolt-Börnstein, Numerical Data and Functional Relationships in Science and Technology*, vol. 1b, edited by G. Angenheister, pp. 276–291, Springer Verlag, New York.

Schulz, S. E., and J. P. Evans (1998), Spatial variability in microscopic deformation and composition of the Punchbowl fault, southern California: Implications for mechanisms, fluid-rock interaction, and fault morphology, *Tectonophysics*, *295*, 223–244.

Schulz, S. E., and J. P. Evans (2000), Mesoscopic structure of the Punchbowl fault, southern California and the geologic and geophysical structure of active strike-slip faults, *J. Struct. Geol.*, *22*, 913–930.

Sibson, R. H. (1994), Crustal stress, faulting and fluid flow, in *Geofluids: Origin, Migration and Evolution of Fluids in Sedimentary Basins*, *Geol. Soc. London Spec. Publ.*, *78*, 69–84.

Sibson, R. H. (1996), Structural permeability of fluid-driven fault-fracture meshes, *J. Struct. Geol.*, *18*, 1031–1042.

Sillitoe, R. H., and E. H. McKee (1996), Age of supergene oxidation and enrichment in the Chilean porphyry copper province, *Econ. Geol.*, *91*, 164–179.

Smith, J. T. (1995), Understanding telluric distortion matrices, *Geophys. J. Int.*, *122*, 219–226.

Swift, C. M. (1967), A magnetotelluric investigation of an electrical conductivity anomaly in the southwestern United States, Ph.D. thesis, Dept. of Geol. and Geophys., Mass. Inst. of Technol., Cambridge.

Tomlinson, A. J., and N. Blanco (1997a), Structural evolution and displacement history of the West Fault system, Precordillera, Chile: part I, Syn-mineral history, in *VIII Congresso Geológico Chileno*, ACTAS vol. 3, *Nuevos Antecedentes de la Geología del Distrio de Chuquicamata, Periodo 1994–1995—Sessión 1: Geología Regional*, pp. 1873–1877, Dep. de Ciencias Geol. Univ. Catolica del Norte, Antofagasta, Chile.

Tomlinson, A. J., and N. Blanco (1997b), Structural evolution and displacement history of the West Fault system, Precordillera, Chile: Part II, Post-mineral history, in *VIII Congresso Geológico Chileno*, ACTAS vol. 3, *Nuevos Antecedentes de la Geología del Distrio de Chuquicamata, Periodo 1994–1995—Sessión 1: Geología Regional*, pp. 1878–1882, Dep. de Ciencias Geol. Univ. Catolica del Norte, Antofagasta, Chile.

Unsworth, M. J., and P. Bedrosian (2004), Electrical resistivity structure at the SAFOD site from magnetotelluric exploration, *Geophys. Res. Lett.*, *31*, L12S05, doi:10.1029/2003GL019405.

Unsworth, M. J., P. E. Malin, G. D. Egbert, and J. R. Booker (1997), Internal structure of the San Andreas fault at Parkfield, California, *Geology*, *25*, 359–362.

Unsworth, M. J., G. D. Egbert, and J. R. Booker (1999), High resolution electromagnetic imaging of the San Andreas fault in Central California, *J. Geophys. Res.*, *104*, 1131–1150.

Unsworth, M. J., P. Bedrosian, M. Eisel, G. D. Egbert, and W. Siripunvaraporn (2000), Along strike variations in the electrical structure of the San Andreas fault at Parkfield, California, *Geophys. Res. Lett.*, *27*, 3021–3024.

Wannamaker, P. E., G. R. Jiracek, J. A. Stodt, T. G. Caldwell, V. M. Gonzales, J. D. McKnight, and A. D. Porter (2002), Fluid generation and pathways beneath an active compressional orogen, the New Zealand Alps, inferred from magnetotelluric data, *J. Geophys. Res.*, *107*(B6), 2117, doi:10.1029/2001JB000186.

Weckmann, U. (2002), A new method to image crustal conductivity structures using magnetotelluric data from Namibia, *Rep. STR02/08*, 133 pp., GeoForschungsZentrum, Potsdam, Germany.

Weidelt, P. (1985), Construction of conductance bounds from magnetotelluric impedances, *J. Geophys.*, *57*, 191–206.

Wessel, P., and W. H. F. Smith (1998), New, improved version of the Generic Mapping Tools released, *Eos Trans. AGU*, *79*(47), 579. [version 3.1]

Wiese, H. (1962), Die Streichrichtung der Untergrundstrukturen des elektrischen Widerstandes, erschlossen aus geomagnetischen Variationen, *Pure Appl. Geophys.*, *52*, 83–103.

Wildenschild, D., J. J. Roberts, and E. D. Carlberg (2000), On the relationship between microstructure and electric and hydraulic properties of sand-clay mixtures, *Geophys. Res. Lett.*, *27*, 3085–3088.

A. Hoffmann-Rothe and C. Janssen, Department of Geodynamics, GeoForschungsZentrum Potsdam, Telegrafenberg, D-14473 Potsdam, Germany. (ahoro@gfz-potsdam.de; jans@gfz-potsdam.de)

O. Ritter, Department of Physics of the Earth, GeoForschungsZentrum Potsdam, Telegrafenberg, D-14473 Potsdam, Germany. (oritter@gfz-potsdam.de)

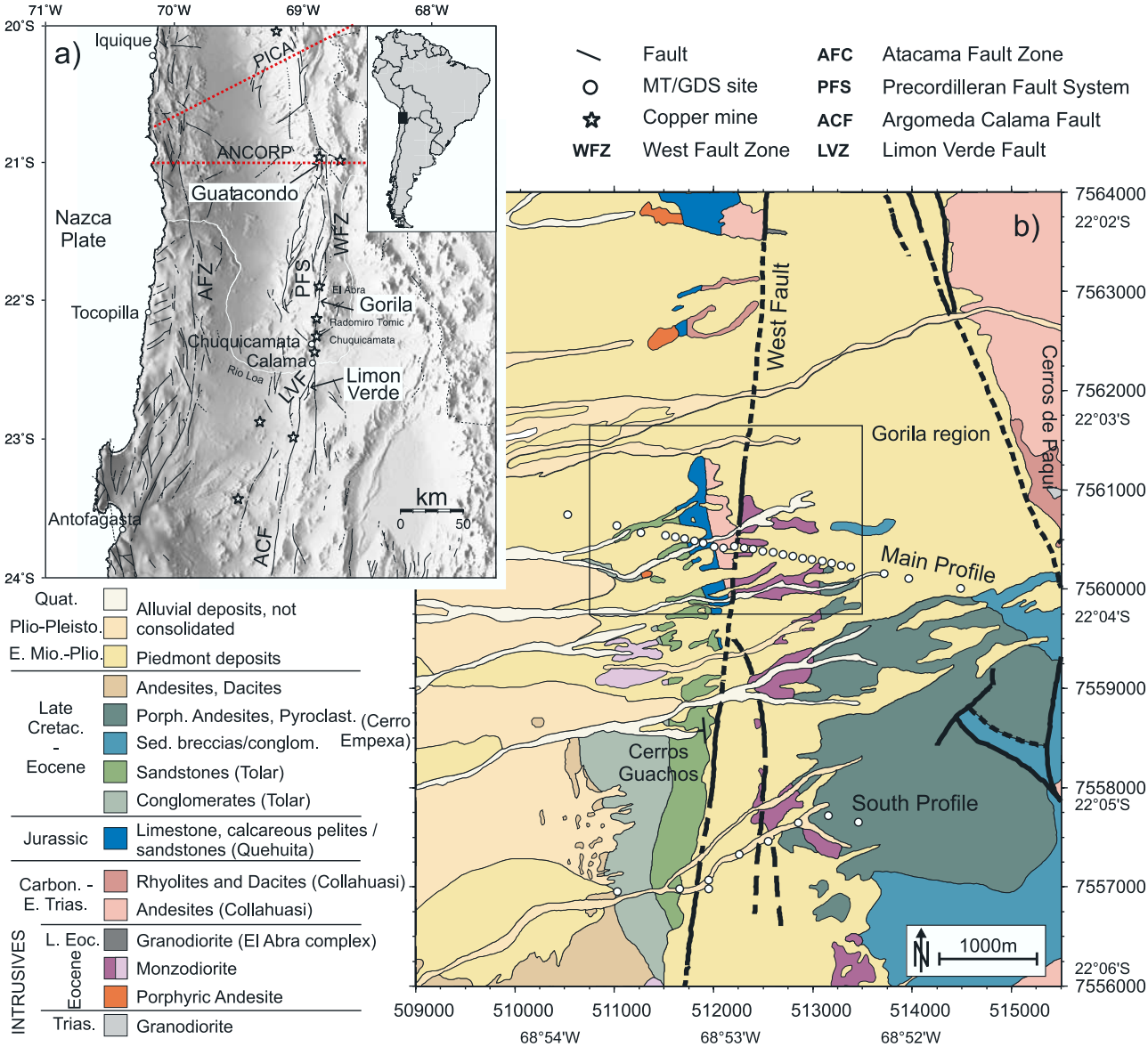

Figure 1. (a) Faults and lineaments in northern Chile according to *Reutter et al.* [1996]. Gorila is the study area presented in this paper. Studies of two other segments of the West fault zone are published by *Janssen et al.* [2002, 2004]. Dotted lines are transects of two regional magnetotelluric studies [*Brasse et al.*, 2002]. (b) Geology of the study area [modified after *Maksaev et al.*, 1999]. White dots indicate magnetotelluric sites, and the rectangle outlines the area of the structural geology investigation (Gorila region).

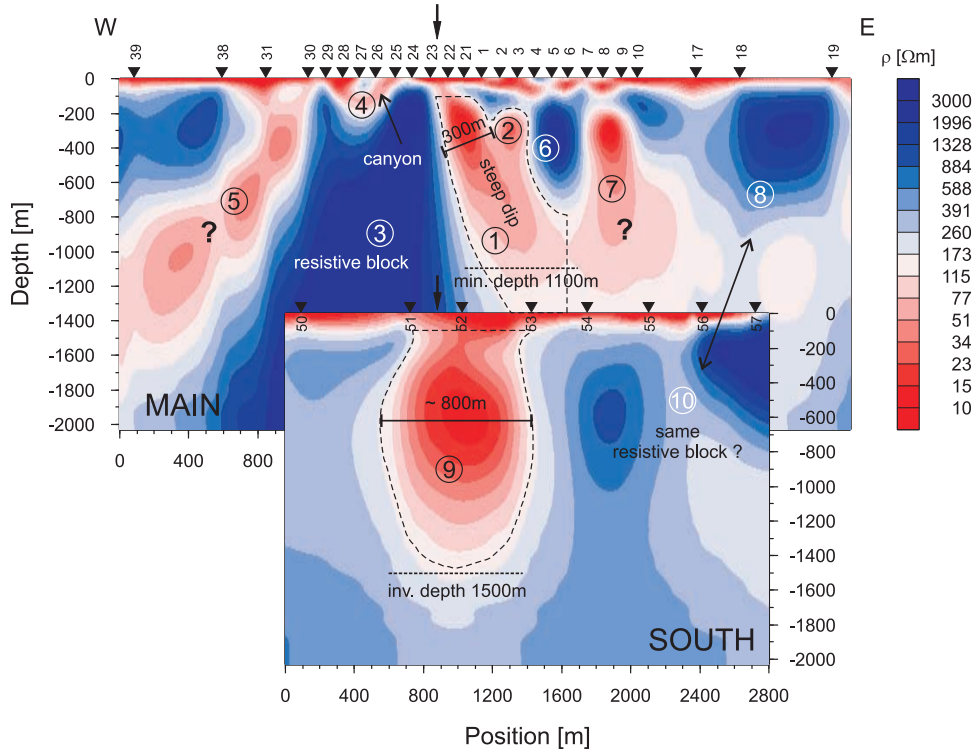

Figure 6. 2-D inversion models of the Main and South profiles. Black arrows mark the position of the West fault surface trace. Numbers denote features discussed in the text. Some estimates of the parameter/sensitivity studies are included. The long dashed lines mark the boundaries of the fault zone conductors (FZC = anomalies 1 and 9, average conductivity 79 Ωm). The minimum depth is a result from sensitivity tests shown in Figure 10.

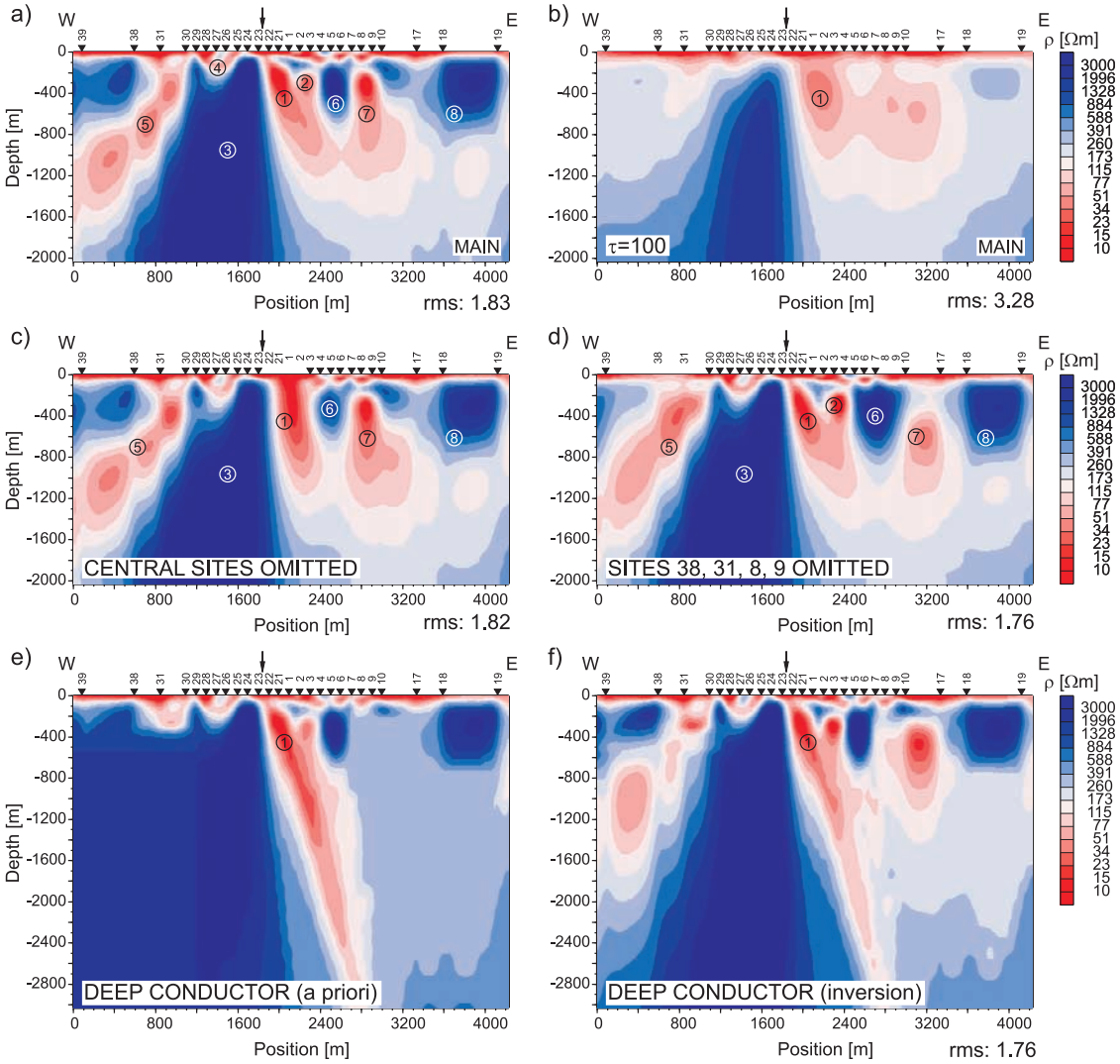

Figure 8. Resolution tests of conductive structures of the Main profile. (a) Reference model of Figure 6. (b) τ set to 100. (c, d) Some sites omitted. Other parameters, in particular the mesh dimensions, remain identical to the reference model. (e) Depth extent of the inclined conductor tested using an a priori model with a deeper-reaching FZC. The inversion result shown in Figure 8f is obtained by forcing the inversion algorithm to solve for a smooth variation close to the a priori model.

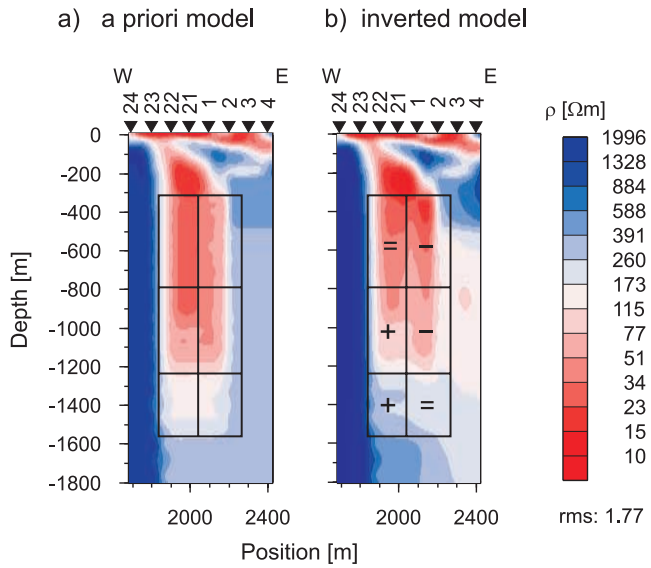

Figure 9. (a) Starting model with a modified FZC having vertical boundaries as constraint for the inversion. (b) Converged inversion result. Boundaries of the FZC and the more resistive vicinity remain vertical. Internally, the resistivities are rearranged in such a way that the upper right rectangle becomes more conductive and the lower left rectangle more resistive, suggesting that an eastward dipping conductive anomaly is favored by the data.

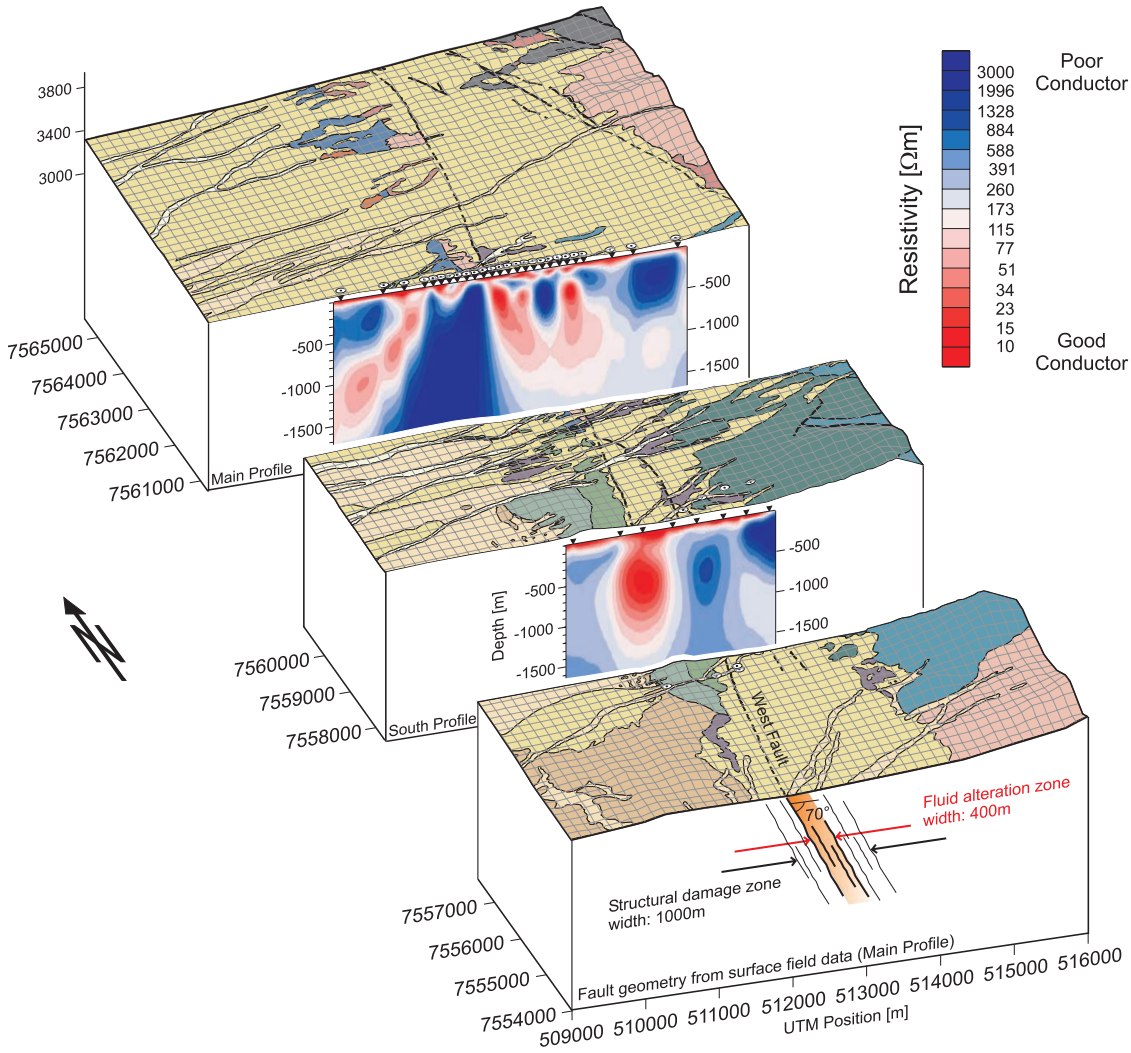

Figure 12. Block diagram with geology (compare map in Figure 1 for legend) summarizing the magnetotelluric inversion models of both profiles and the results of the structural investigation along the Main profile. The latter are schematically drawn on the front panel of the block diagram and extrapolated to greater depth. Magnetotelluric inversion models are not vertically exaggerated; morphology is exaggerated by factor 2.

Geophysical images of the Dead Sea Transform in Jordan reveal an impermeable barrier for fluid flow

O. Ritter,[1] T. Ryberg,[1] U. Weckmann,[1] A. Hoffmann-Rothe,[1] A. Abueladas,[2]
Z. Garfunkel,[3] and DESERT Research Group

Received 16 April 2003; accepted 16 June 2003; published 22 July 2003.

[1] High-resolutionseismictomography and magnetotelluric (MT) soundings of the shallow crust show strong changes in material properties across the Dead Sea Transform Fault (DST) in the Arava valley in Jordan. 2D inversion results of the MT data indicate that the DST is associated with a strong lateral conductivity contrast of a highly conductive layer at a depth of approximately 1.5 km cut-off at a position coinciding with the surface trace of the DST. At the same location, we observe a sharp increase of P wave velocities from <4 km/s west of the fault to >5 km/s to the east. The high velocities in the east probably reflect Precambrian rocks while the high electrical conductivity west of the DST is attributed to saline fluids within the sedimentary filling. In this sense, the DST appears to act as an impermeable barrier between two different rock formations. Such a localized fluid barrier is consistent with models of fault zone evolution but has so far not been imaged by geophysical methods. The situation at the DST is remarkably different from active segments of the San Andreas Fault which typically show a conductive fault core acting as a fluid conduit. *INDEX TERMS:* 1515 Geomagnetism and Paleomagnetism: Geomagnetic induction; 7205 Seismology: Continental crust (1242); 8005 Structural Geology: Folds and folding; 8180 Tectonophysics: Tomography. **Citation:** Ritter, O., T. Ryberg, U. Weckmann, A. Hoffmann-Rothe, A. Abueladas, Z. Garfunkel, and DESERT Research Group, Geophysical images of the Dead Sea Transform in Jordan reveal an impermeable barrier for fluid flow, *Geophys. Res. Lett.*, *30*(14), 1741, doi:10.1029/2003GL017541, 2003.

1. Introduction

[2] The Dead Sea Transform (DST) fault is a major strike slip fault in the continental lithosphere. It forms the boundary between the African and Arabian plates (see Figure 1) and joins the divergent plate boundaries along the Red Sea rift in the south with the Alpine orogenic belt to the north along a length of more than 1000 km with a total left lateral motion of 105 km [*Freund et al.*, 1970]. The regional style of tectonism has been described as rifting, (leaky) transform, or some combination of the two [*Garfunkel*, 1970, *Garfunkel and Ben-Avraham*, 1996].

[3] In this letter, we report on geophysical experiments carried out as part of the multi-disciplinary DESERT (DEad SEa Rift Transect) project, a 300 km long transect traversing Israel, Jordan and the Palestine territories [*DESERT Research Group*, 2000]. The location in the Arava valley was chosen in order to study the DST (locally the Arava Fault, AF - the dominant fault of the DST between the Dead Sea and the Gulf of Elat-Aqaba) and the tectonic processes controlling it in their simplest expression, far from the Dead Sea pull-apart basin and the active rifting of the Red Sea. The relative simplicity of the DST in the Arava Valley puts it in marked contrast to other large fault systems such as the San Andreas Fault (SAF) system which originated from complicated interaction between oceanic sub-plates and an accreted continental margin [*Atwater*, 1970, *Fuis*, 1998].

2. Seismic Data

[4] Tomographic inversion techniques were applied to first arrival times of direct P waves to study the shallow part (<10 km) of the crust. Vibroseis trucks have been used as seismic sources. The total length of this near-vertical reflection line (NVR) was 100 km. The line is centered on the AF and oriented approximately perpendicular to the DST. The recording spread consisted of 180 seismic receivers over a distance of 18 km. In addition to this movable spread, 86 seismic stations were permanently deployed along the line to record wide-angle data. From this combined data set 280335 P wave first arrival times from 1734 shots at 266 receivers were manually picked. These picks were then inverted using the FAST code [*Zelt and Barton*, 1998] in its two-dimensional version. Given the crooked geometry of the line, we projected source and receiver locations onto a straight line using a regression fit in a manner similar to the technique of *Zelt* [1999]. The velocity model grid consists of 1000 horizontal by 240 vertical blocks, each 100 m by 50 m in size, resulting in a model extending 100 km in length and 10 km in depth. Only the shallow part of the model, however, is penetrated by rays and therefore constrained by data. The highest ray density (>100 per block) and thus the best model resolution is obtained for the top ~3 km of the crust. Deeper parts of the model are less well resolved. The stability and robustness of the final model was confirmed by testing various inversion parameters (shifted and sparser grids, smoothness constraints, regularization parameters) and checker-board tests were carried out to evaluate the resolution of structural details in the model. The horizontal and vertical resolutions are better than 200 and 100 m to a depth of 1 km and 500 and 300 m at 2 km depth, respectively. Resolution decreases quickly with increasing depth. We reached a final RMS travel time misfit of 0.05 s.

[1]GeoForschungsZentrum, Potsdam, Germany.
[2]Natural Resources Authority, Amman, Jordan.
[3]Hebrew University, Jerusalem, Israel.

0094-8276/03/2003GL017541$05.00

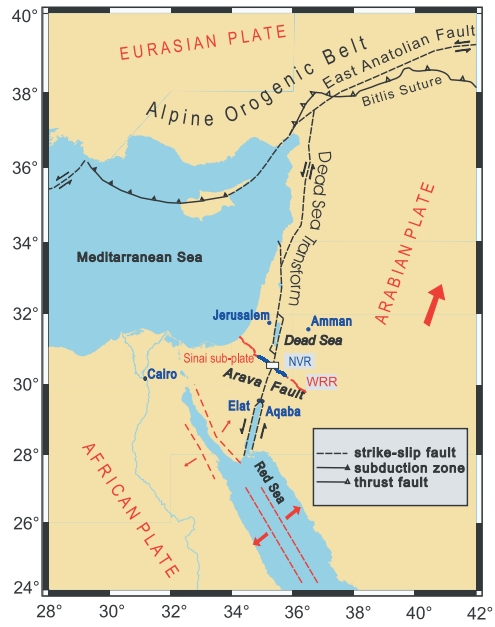

Figure 1. Plate tectonic setting of the Dead Sea Rift. The measuring area (white rectangle) is located in the Arava valley, which extends for 200 km between the Dead Sea and the Red Sea (Gulf of Aqaba/Elat). Also shown are locations of the seismic wide angle reflection/refraction (WRR) and near vertical reflection (NVR) experiments. The Arava valley is a topographic low formed by shearing along the transform that separates the Arabian plate from the Sinai sub-plate.

The velocity features we discuss are stable through all of these tests and are above the uncertainty level in the final model.

[5] The final model in Figure 2a shows a 30 km wide section of the NVR line centered on the AF. It reveals a complex velocity distribution which generally correlates with surface geology. The uppermost crust (to a depth of ~0.5–1 km) is generally characterized by the low velocities (<3 km/s) of the sedimentary fill. In the vicinity of the AF this layer is reduced to a thickness of 200 m. At greater depth (down to 2 km), however, we notice a clear change of material properties across the fault with low velocities of ~4 km/s west of the fault and a significant increase to velocities above 4.8 km/s on the eastern side. The Zofar Fault is imaged as several thin high velocity (4.7 km/s) blocks. On the eastern side of the Zofar Fault and on the western flank of the Dead Sea Rift the sedimentary filling increases to a depth of 1.5 km. At the eastern flank of the Dead Sea Rift outcrops of higher velocity material occur which could be related to the Precambrian Arava complex.

[6] The basis for the structural interpretation that overlies the seismic velocity west of the AF is interpolated from data of several deep drill holes, surface geological sections, and detailed seismic reflection data [*Bartov et al.*, 1998]. The structural information east of the AF is primarily based on outcrops.

[7] In summary, the shallow seismic P wave velocity structure of the rift valley reveals fault blocks along the eastern and western bounding normal faults (Zofar and Al Quwayra Faults) and a significant change in material

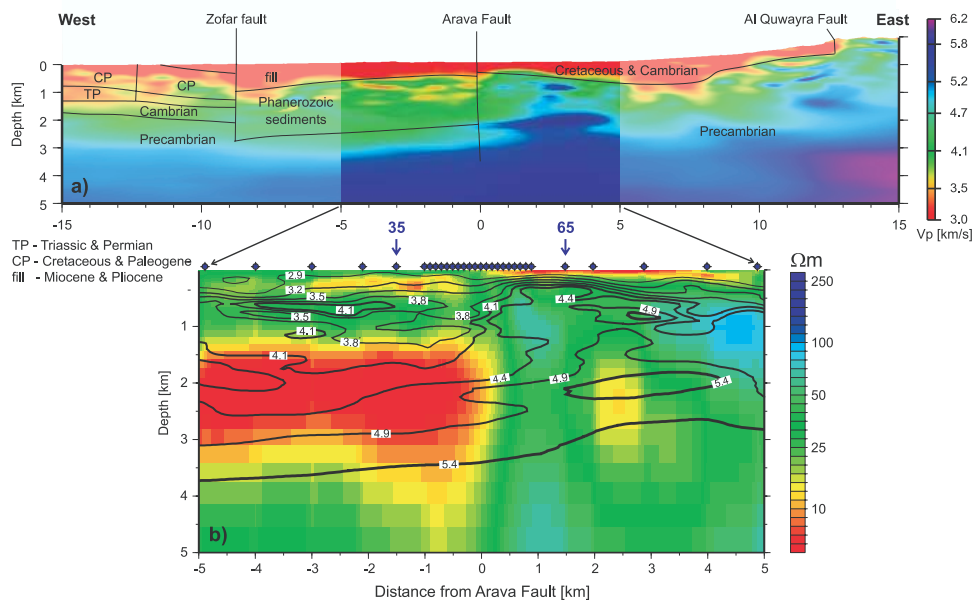

Figure 2. a) Part of the tomographic P wave velocity model, centered on the Arava Fault (AF) zone. With a receiver spacing of 100 m and 500 shot points, the resolution at depth is good down to 3 km (the ray hit count generally exceeds 100 per block). Main geological units are also indicated. b) Blowup of superimposed magnetotelluric (color-coded) and seismic P wave velocity results (contour lines derived from a) in the vicinity of the AF. The 30 MT recording sites are shown as diamonds at the top. Red and yellow colors indicate high conductivity. Only the top 5 km of the crust are shown, as resolution degrades at larger depths due to the finite length of the MT profile (10 km). Both the MT and seismic data indicate significant lateral changes in physical properties across the AF.

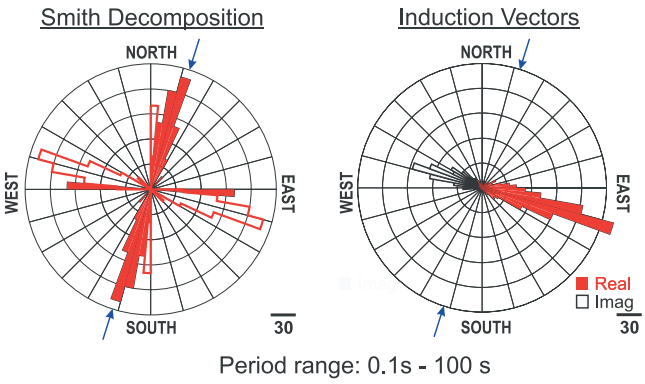

Figure 3. Left: Regional strike angles calculated from the data of all sites in the period range 0.1 s to 100 s using *Smith*'s [1995] tensor decomposition method. Hollow vectors indicate that strike angles have a 90° ambiguity. Right: Rose diagram for real (solid) and imaginary (hollow) induction vector directions. The data represent a typical 2D structure with a geo-electric strike direction of N17°E (blue arrows). This direction coincides with the surface expression of the DST.

properties across the AF, with a buried basement high east of the fault.

3. Magnetotelluric Data

[8] The MT data were recorded in 2000 along a 10 km long segment, centered on the AF and coincident with the NVR profile. A dense site spacing of 100 m in the center of the profile was supplemented by more widely spaced sites near the profile ends. In total, measurements at 30 sites were made with GPS synchronized S.P.A.M. MkIII broadband instruments [*Ritter et al.*, 1998], Metronix MFS05 induction coil magnetometers and non-polarizable Ag/AgCl telluric electrodes. Data were recorded in the frequency range from 1 kHz to 1 mHz and processed according to *Ritter et al.* [1998].

[9] Working along profiles implies that the subsurface conductivity structure is expected to vary only in two dimensions (with depth and along the profile) with a geo-electric strike direction perpendicular to the profile. Before inverting the data with 2D models, it is necessary to first assess if the MT data are consistent with 2D assumptions, and if so, to make a best possible estimate of the regional strike direction. Geo-electric strike directions and estimates of the dimensionality of the subsurface can be derived from the measured MT impedance tensor and from magnetic variation data (induction vectors). Typically, impedance tensor decomposition schemes are applied to ensure that a regional structure and its strike are not obscured by small scale heterogeneities. The rose diagram on the left hand side of Figure 3 shows regional strike angles using the method of *Smith* [1995] with a clearly preferred orientation of N17°E. This strike is confirmed by the induction vector directions on the right hand side of Figure 3. The diagram reflects the typical situation for a 2D environment in which real and imaginary induction vectors point parallel to each other and orthogonal to the strike of a lateral conductivity contrast.

[10] The resistivity section in Figure 2b is the result of a 2D inversion of the MT data using the RLM2DI algorithm [*Rodi and Mackie*, 2001] (http://www.scientificetechnical.com/cgg/cgg-software.htm). Examples of data and model responses for a site west (35) and east of the AF (65) are given in Figure 4. The inversion started from a 100 Ωm homogeneous half-space model with a mesh of 163 horizontal by 96 vertical cells. The trade-off between data misfit and model smoothness is controlled by the regularization parameter τ which must be determined iteratively. In our case, a setting of $\tau = 10$ resulted in a good compromise between model roughness and data misfit. The inversion fitted the TE and TM mode data as well as the vertical magnetic field response functions. Static shift was included as a free parameter. The inversion reached convergence to a normalized rms misfit of 1.4 using pre-set error bounds of 5% in apparent resistivity, 0.6° in phase and 0.01 for the vertical magnetic fields.

[11] For the shallow crust, the inversion model in Figure 2b reveals a highly electrically conductive layer (red and yellow colors) from the surface to a depth of ~100 m on the eastern side of the profile. This layer appears to be interrupted at the AF (0 km) and possibly continues west of the fault at a deeper level (~150 m–250 m). The most prominent features, however, in the resistivity model are firstly the sharp lateral contrast under the surface trace of the AF, and secondly the conductive half-layer west of the AF starting at a depth of ~1.3 km. The high conductivity of the half-layer is probably caused by brines within the Phanerozoic sediments. In the Zofar-20 well, ~14 km west of the AF, saline waters have been found in a lower Cretaceous aquifer (depth: ~1000 m, temperature: 53° C, salinity: 6.5 g/l; pers. comm. Th. Wiersberg, K. Erbas, GFZ Potsdam), which may continue along-profile to the location in the Arava Valley, where it is cut by the AF. East of the AF, higher P wave velocities (4.8 km/s) could reflect the Precambrian basement, however the intermediate resistivities (20 to 80 Ωm) observed are lower than expected. It is possible that fractured Precambrian magmatic rocks containing interconnected fluid bearing veins may explain both the high seismic velocities and the lower than expected resistivities.

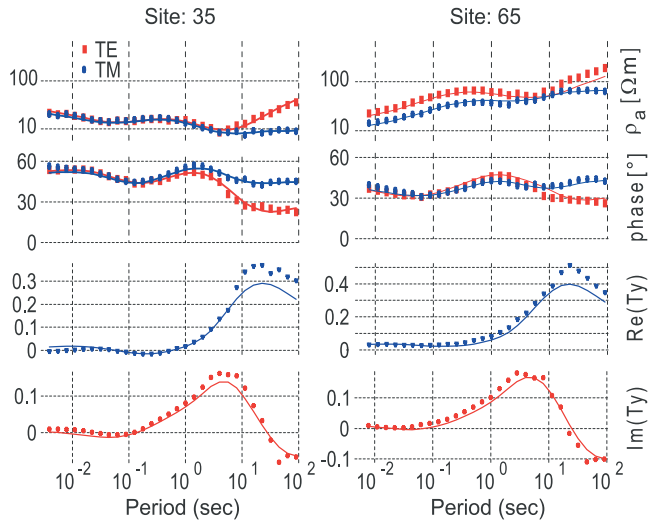

Figure 4. Data (markers) and model responses (solid lines) of two MT sites located west (35) and east (65) of the fault. The top two diagrams show TE and TM mode (ie. rotated to geo-electric strike coordinates) apparent resistivity and phase curves. Bottom panels illustrate real and imaginary parts of the vertical magnetic field response function T_y, calculated from the ratio of vertical to horizontal field components.

4. Discussion

[12] The MT conductivity model of the AF shows important differences when compared with corresponding images of the SAF. The results of several short MT profiles across the SAF near Parkfield [*Unsworth et al.*, 2000], a location described as transitional between locked and creeping, indicate a strong correlation of the fault core with zones of high conductivity to a maximum depth of ~3 km. This fault zone conductor at the SAF is attributed to the circulation of saline fluids within the fault zone. The width of the conductive zone (0.5 km) is in the same order of magnitude as the width of a seismic low-velocity zone inferred from fault-zone-guided wave observations [*Li et al.*, 1990], while its depth extent (3 km) coincides with the occurrence of a cluster of small earthquakes. Recent tomographic velocity images of the SAF [*Thurber et al.*, 2003] show a block-like structure of high and low velocity blocks on both sides of the fault; very similar to the situation at the DST (Figure 2a). In contrast, no significant conductivity anomaly is associated along a locked and seismically quiet segment near Carrizo Plain [*Mackie et al.*, 1997; *Unsworth et al.*, 1999].

[13] THE Arava Fault, on the other hand, appears to act as an impermeable barrier between two different rock formations (Figure 2b). The high electrical conductivity west of the AF is attributed to the sedimentary filling rather than a narrow conductive fault core, which is typical for active segments of the SAF [*Bedrosian et al.*, 2002]. It is possible though, that the damage zone of the AF is so narrow that it cannot be resolved even with the dense site spacing of the MT experiment. This assumption is supported by preliminary results from geological mapping and an independent study using fault-guided waves [*Haberland et al.*, 2003] that suggest a very narrow low-velocity waveguide of 3 to 10 m width exists (with 40 to 50% velocity reduction) at the AF. This width is too narrow to be resolved by seismic tomography or MT. The reason for this difference between the AF (very narrow fault zone) and the SAF (wide gouge zone) is not yet clear, but seems to coincide with generally lower slip rates and the relatively low recent seismicity associated with this segment of the AF.

[14] The fault core and damage zone are distinct structural and hydrogeologic units that reflect the material properties and deformation conditions within a fault zone. A fault can act as a conduit, barrier or combined conduit-barrier system depending on the relative size of the fault's core and damage zone and the inherent variability of fracture permeability [*Caine et al.*, 1996]. A wide fault core can be generated by cycles of fault healing and strength build-up with subsequent formation of new faults at locations where strength contrasts are greatest [e.g. *Mitra and Ismat*, 2001]. In contrast, the very narrow fault gouge and non-existing damage zone could therefore indicate that the DST has experienced continuous deformation concentrated upon a single, very narrow shear zone. As a consequence, the existence or non-existence of high electrical conductivity in the central part of large-scale strike-slip fault zones may be an indicator for the degree of strain localization during faulting.

[15] **Acknowledgments.** We thank the National Ministry of Infrastructure of Israel, the Natural Resources Authority of Jordan and the An-Najah University in Nablus, Palestine Territories for their support throughout this project. The seismic and MT instruments were provided by the Geophysical Instrument Pool of the GeoForschungsZentrum (GFZ) Potsdam. The seismic experiment was funded by the Deutsche Forschungsgemeinschaft, the GFZ, and the Minerva Dead Sea Research Center; the MT pilot study was funded by the GFZ. Finally, we would like to acknowledge the work of the DESERT Working Group at the GFZ and particulary Paul Bedrosian's contribution with many discussions and general help with the manuscript. Critical and constructive comments from Martyn Unsworth and an anonymous referee helped clarify the manuscript.

References

Atwater, T., Implications of plate tectonics for the Cenozoic tectonic evolution of western North America, *Bull. Geol. Soc. Am.*, *81*, 3513–3536, 1970.

Bartov, Y., Y. Avni, R. Calvo, and U. Frieslander, The Zofar Fault - a major intra-rift feature in the Arava rift valley, *Geol. Survey of Israel, current research*, *11*, 27–32, 1998.

Bedrosian, P. A., M. Unsworth, and G. Egbert, Magnetotelluric imaging of the creeping segment of the San Andreas Fault near Hollister, *Geophys. Res. Lett.*, *29*, doi:10.1029/2001GL014119, 2002.

Caine, J. S., J. P. Evans, and C. B. Forster, Fault zone architecture and permeability structure, *Geology*, *24*, 1025–1028, 1996.

DESERT Reseach Group, Multinational geoscientific research effort kicks off in the middle east, *Eos, Transactions, American Geophysical Union, No.50, December 12*, *81*, 609, 616–617, 2000.

Freund, R., Z. Garfunkel, I. Zak, M. Goldberg, T. Weissbrod, and B. Derin, The shear along the Dead Sea rift, *Philos. Transaction of the Royal Society of London*, *267*, 117–126, 1970.

Fuis, G. S., West Margin North America - a synthesis of recent seismic transects, *Tectonophysics*, *288*, 265–292, 1998.

Garfunkel, Z., Active faulting in the Dead Sea rift, *Tectonophysics*, *80*, 1–26, 1970.

Garfunkel, Z., and Z. Ben-Avraham, The structure of the dead sea basin, *Tectonophysics*, *266*, 155–176, 1996.

Haberland, C., A. Agnon, R. El-Kelani, N. Maercklin, I. Qabbani, G. Rümpker, T. Ryberg, F. Scherbaum, and M. Weber, Modeling of seismic guided waves at the Dead Sea Transform, *J. Geophys. Res*, p. in press, 2003.

Li, Y.-L., P. Leary, K. Aki, and P. Malin, Seismic trapped modes in the Oroville and San Andreas fault zones, *Science*, *249*, 763–765, 1990.

Mackie, R. L., D. W. Livelybrooks, T. R. Madden, and J. C. Larsen, A magnetotelluric investigation of the San Andreas fault at Carrizo Plain, California, *Geophys. Res. Lett.*, *24*, 1847–1850, 1997.

Mitra, G., and Z. Ismat, Microfracturing associated with reactivated fault zones and shear zones: what can it tell us about deformation history?, in *The Nature and Tectonic Significance of Fault Zone Weakening*, edited by R. E. Holdsworth, R. A. Strachan, J. F. Magloughlin, and R. J. Knipe, vol. 186 of *Geological Society*, *Special Publications*, pp. 113–140, London, 2001.

Ritter, O., A. Junge, and G. J. K. Dawes, New equipment and processing for magnetotelluric remote reference observations, *Geophys. J. Int.*, *132*, 535–548, 1998.

Rodi, W., and R. L. Mackie, Nonlinear conjugate gradients algorithm for 2D magnetotelluric inversion, *Geophysics*, *66*, 174–187, 2001.

Smith, J. T., Understanding telluric distortion matrices, *Geophys. J. Int.*, *122*, 219–226, 1995.

Thurber, C. H., S. Roecker, K. Roberts, M. Gold, L. Powell, and K. Rittger, Earthquake locations and three-dimensional fault zone structure along the creeping section of the San Andreas fault near Parkfield, CA: Preparing for SAFOD, *Geophys. Res. Lett.*, *30*, doi:10.1029/2002GL016004, 2003.

Unsworth, M. J., G. Egbert, and J. Booker, High-resolution electromagnetic imaging of the San Andreas fault in Central California, *J. Geophys. Res.*, *105*, 1131–1150, 1999.

Unsworth, M. J., P. Bedrosian, M. Eisel, G. Egbert, and W. Siripunvaraporn, Along strike variations in the electrical structure of the San Andreas Fault at Parkfield, California, *Geophys. Res. Lett.*, *27*, 3021–3024, 2000.

Zelt, C. A., Modelling strategies and model assessment for wide-angle seismic traveltime data, *Geophys. J. Int.*, *139*, 183–204, 1999.

Zelt, C. A., and P. J. Barton, 3D seismic refraction tomography: A comparison of two methods applied to data from the Faeroe Basin, *J. Geophys. Res.*, *103*, 7187–7210, 1998.

A. Abueladas, Natural Resources Authority, Amman, Jordan.

Z. Garfunkel, Hebrew University, Jerusalem, Israel.

O. Ritter, GeoForschungsZentrum, Telegrafenberg, D-14473 Potsdam, Germany. (oritter@gfz-potsdam.de)

A. Hoffmann-Rothe, T. Ryberg, and U. Weckmann, GeoForschungsZentrum Potsdam, Germany.

DESERT Research Group.

Electrical conductivity images of active and fossil fault zones*

O. Ritter, A. Hoffmann-Rothe, P.A. Bedrosian, U. Weckmann, V. Haak

GeoForschungsZentrum Potsdam, Telegrafenberg, D-14473 Potsdam, Germany (email: oritter@gfz-potsdam.de)

Abstract

We compare recent magnetotelluric investigations of four large fault systems: (i) the actively deforming, ocean-continent interplate San Andreas Fault (SAF), (ii) the actively deforming, continent-continent interplate Dead Sea Transform (DST), (iii) the currently inactive, trench-linked intraplate West Fault (WF) in northern Chile, and (iv) the Waterberg Fault/Omaruru Lineament (WF/OL) in Namibia, a fossilized intraplate shear zone formed during early Proterozoic continental collision. These fault zones show both similarities and marked differences in their electrical subsurface structure. The central segment of the SAF is characterized by a zone of high conductivity extending to several kilometres depth and attributed to fluids within a highly fractured damage zone. The WF exhibits a less pronounced but similar fault zone conductor (FZC) which can be explained by meteoric waters entering the fault zone. The DST appears different as it shows a distinct lack of a FZC and seems to act primarily as an impermeable barrier to cross-fault fluid transport. Differences in the electrical structure of these faults within the upper crust may be linked to the degree of deformation localization within the fault zone. At the DST, with no observable fault zone conductor, strain may have been localized for a considerable time span along a narrow, meter-scale damage zone with a sustained strength difference between the shear plane and the surrounding host rock. In the case of the SAF, a positive correlation of conductance and fault activity is observed, with more active fault segments associated with wider, deeper, and more conductive fault zone anomalies. Fault zone conductors, however, do not uniquely identify specific architectural or hydrological units of a fault. A more comprehensive whole-fault picture for the brittle crust can be developed in combination with seismicity and structural information. Giving a window into lower-crustal shear zones, the fossil WF/OL in Namibia is imaged as a sub vertical, 14 km deep, 10 km wide zone of high and anisotropic conductivity. The present level of exhumation suggests that the WF/OL penetrated the entire crust as a relatively narrow shear zone. Contrary to the fluid driven conductivity anomalies of active faults, the anomaly here is attributed to graphitic enrichment along former shear planes. Once created, graphite is stable over very long time spans and thus fault/shear zones may remain conductive long after activity ceases.

*pre-print of: Bruhn, D. & Burlini, L. (eds.) 2005. High-Strain Zones: Structure and Physical Properties. Geological Society, London, Special Publications, 245, 165-185.

1 Introduction

The San Andreas Fault in California, the North Anatolian Fault in Turkey, the Altyn Tagh Fault in China, and the Dead Sea Transform in Jordan are prominent examples of high strain zones and expressions of dynamic processes in the earth's lithosphere. Such large-scale faults can be traced for hundreds to thousands of kilometres on the earth's surface. There is growing evidence that some of them penetrate the mantle lithosphere, leaving in their wake a region of lithospheric-scale weakness (Herquel et al., 1999; Henstock et al., 1997; Rümpker et al., 2003) while complex zones of localized brittle deformation characterize shearing in the upper (seismogenic) crust. Information about the structure (and dynamics) of these zones derive primarily from surface investigations of active and exhumed fault zones, as well as geophysical images of the subsurface.

A considerable amount of research has focussed on the internal structure of crustal fault zones and the mechanics of faulting (Chester et al., 1993; Holdsworth et al., 2001; Ben-Zion & Sammis, 2003; Faulkner et al., 2003). It is well established that the structural and compositional evolution of fault zones is intimately linked to fluids; they may also control the nucleation, propagation, arrest, and recurrence of brittle failure (Hickman et al., 1995). Fluids can induce fracturing by modifying the strength and constitution of the host rocks. Subsequent deformation creates further pathways for fluids to enter the fault zone, creating a highly permeable conduit for fluid flow (leading to a feedback mechanism). A lithological contrast resulting from the fault's displacement or the formation of gouge due to shearing processes may further create a barrier impeding cross-fault fluid flow (Caine et al., 1996).

Surface-based geophysical methods provide invaluable information concerning the nature and distribution of fluids at seismogenic depths (Eberhart-Phillips et al., 1995). The most intensively studied example of any fault is the San Andreas Fault, separating the oceanic Pacific plate from the continental North American plate. Unsworth et al. (1997) demonstrated that its internal structure can be imaged with magnetotelluric (MT) measurements. Several short profiles across the San Andreas Fault image a highly conductive structure down to several kilometres depth, attributed to the circulation of saline fluids within the damage zone of the fault. In this situation, bulk conductivity is dominated by ion transport within the pore space. Fluid transport within the rock opens pores and cracks, increasing the mobility of solutes such as salts, calcite, or quartz, thereby increasing the bulk conductivity. Precipitation from hydrothermal fluids, on the other hand, may cement open fractures within the rock and, in turn, lower bulk conductivity.

Exhumed fossil shear zones, in contrast to upper-crustal faults, commonly expose structures which originated below the depth of predominantly brittle deformation (though they may have experienced brittle deformation during reactivation). These shear zones can be similarly conductive, but in these cases, bulk conductivity may be dominated by electron transport, for example in an interconnected graphite network. Data from the KTB deep drill hole and its accompanying experiments revealed a quantitative relation between the shearing process along faults, the formation of graphite, and high electrical conductivity (ELEKTB Group, 1997). The critical observation is that the shearing process itself can lead to the interconnection of conductive material (Jödicke et al., 2004).

Images of electrical conductivity can help decipher the internal architecture of crustal-scale fault zones and the magnetotelluric method is one of the few tools capable of imaging from the earth's surface through to the mantle. We start with a short

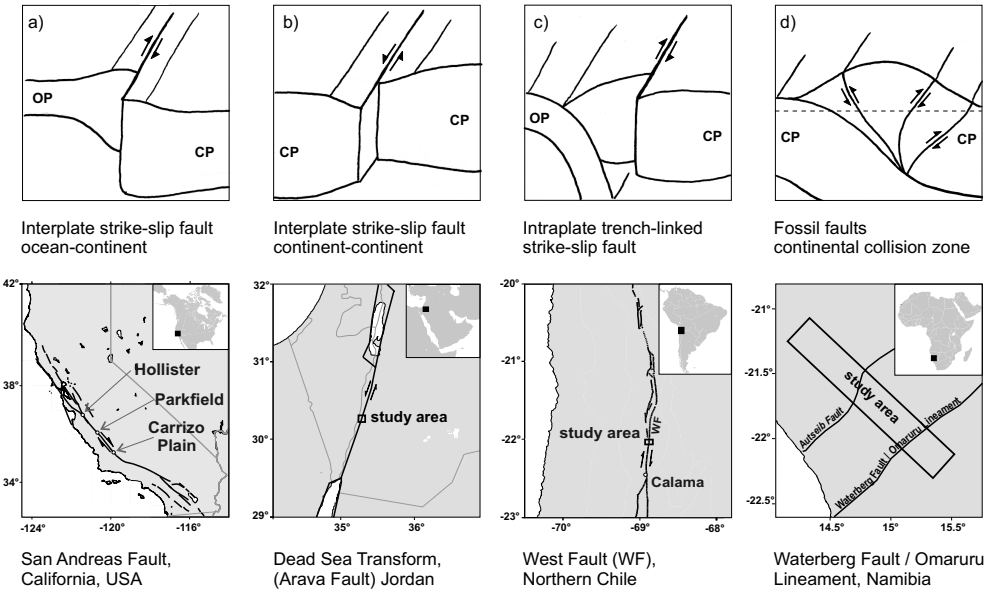

Figure 1: Geodynamic settings of case studies discussed in this paper. (a),(b),(c) The brittle upper crustal part of these active margins is accessible for investigation. Ductile deformation, operating at greater depth is not easily imaged. (d) Fossil shear zones exhumed at the surface (dashed line indicating present surface level) serve as a proxy for lower crustal shearing processes at currently active faults. (OP: oceanic plate, CP: continental plate)

description of MT and its resolution characteristics. The main part of this paper presents MT studies of four crustal-scale fault zones in the geodynamic settings shown in Figure 1, and is not intended to be an exhaustive review. Actively deforming faults are represented by the ocean-continent interplate San Andreas Fault (SAF) in California and the continent-continent interplate Dead Sea Transform (DST) in Jordan. These fault zones exhibit markedly different conductivity structure. The currently inactive West Fault (WF) in northern Chile is a trench-linked intraplate strike-slip fault associated with the Andean subducting margin. Exposure of the fault's damage zone illuminates how structural damage is linked to electrical conductivity. A fossil representative of a lower-crustal shear zone is the Waterberg Fault/Omaruru Lineament (WF/OL) in Namibia, part of a broad Paleozoic suture. Having experienced several episodes of reactivation, this mechanically weak zone, formerly within the lower crust, exhibits strong electrical anisotropy. Following the presentation of these case studies, both upper and lower crustal structure are discussed, with attention to the hydrological and structural implications these conductivity images provide.

1.1 Some background on the magnetotelluric method

1.1.1 The electrical conductivity of rocks

The electrical resistivity (ρ) and its inverse the electrical conductivity (σ) characterize charge transport within materials. They are intrinsic material properties, independent of sample size. Rocks and rock forming minerals vary in their electrical properties, with conductivities ranging from 10^6 to $10^{-14} S/m$ (Guéguen & Palciauskas, 1994). A summary of important crustal constituents and their conductivities is given in Figure 2.

In most sedimentary rocks, currents are propagated primarily by ions within pore fluids. Bulk conductivity is thus strongly dependent on the volume of included fluid and its conductivity, in addition to the size and arrangement of pores. Fluid conductivity itself is temperature dependent, and further varies with the concentration, mobility, and charge of the ions. The relationship between fluid conductivity (σ_{fluid}) and bulk conductivity (σ_{rock}) can be described by the empirical Archie's law (Archie, 1942), given in its simplified form:

$$\frac{\sigma_{fluid}}{\sigma_{rock}} = \phi^{-m}. \tag{1}$$

ϕ is the porosity of the rock raised to the cementation or compaction exponent (m), which typically varies with pore geometry from 1 for spheres to 2 for cracks.

Rocks containing a high concentration of minerals such as sulfides, magnetite, and graphite may exhibit high conductivity if these electronically-conducting minerals are interconnected. Even small concentrations of graphite can significantly increase conductivity due to its tendency to form thin continuous films along grain boundaries (Guéguen & Palciauskas, 1994). Graphite in metamorphic rocks typically results from the conversion of organic matter through metamorphism or precipitation from natural, carbon-bearing fluids (Luque et al., 1998; Wannamaker, 2000). Conductivity will increase if shearing processes smear isolated graphite grains into continuous films or press them into interconnected crack systems (Jödicke et al., 2004). Additionally, graphite coatings lower shear friction and hence add to the mobility of faults. Once created, graphite is stable over very long time spans allowing shear zones to remain conductive long after activity ceases. A good example is the Münchberg Gneiss complex in southern Germany, where graphitic remnants along horizontal shear planes

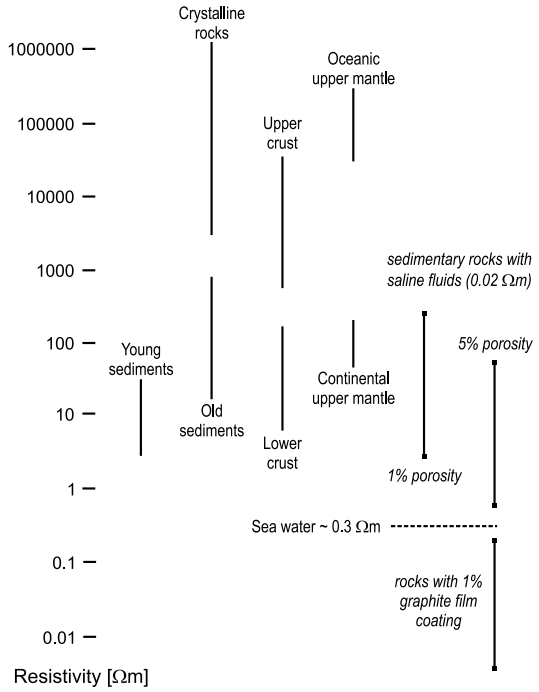

Figure 2: The range of electrical resistivity in earth materials. Resistivities of fluid-bearing rocks are largely independent of rock type and calculated based upon a fluid resistivity of $0.02\,\Omega m$. Upper and lower resistivity bounds correspond to fluids contained in spherical pores and cracks, respectively. In the case of graphite films, bulk resistivity scales with the grain size of the host rock (after Haak & Hutton (1986).)

likely cause the observed high conductivity anomalies (Ritter et al., 1999). Quantifying the effect of graphite or other conductive minerals on bulk conductivity requires mixing laws (Doyen, 1988) or network and percolation theories.

1.1.2 The magnetotelluric impedance tensor

The magnetotelluric method is based on the induction of electromagnetic fields in the earth. Its ultimate aim is to determine the electrical conductivity structure of the subsurface. Observations of orthogonal components of time-varying horizontal electric $\mathbf{E}\,[mV/km]$ and magnetic fields $\mathbf{B}\,[nT]$ at the surface of the earth are related via the components of the impedance tensor $\mathbf{Z}$:

$$\begin{pmatrix} E_x \\ E_y \end{pmatrix} = \begin{pmatrix} Z_{xx} & Z_{xy} \\ Z_{yx} & Z_{yy} \end{pmatrix} \begin{pmatrix} B_x \\ B_y \end{pmatrix} . \tag{2}$$

The impedance tensor $\mathbf{Z}$ is a frequency-dependent, complex quantity. At a particular frequency (ω), it can be converted into an amplitude (apparent resistivity $\rho_a(\omega)$) and phase ($\phi(\omega)$) relation. In magnetotellurics, frequency ω can be viewed as a rough (non-linear) proxy for depth, as lower frequencies penetrate deeper into the subsurface (skin depth effect). Only in the special case of a homogeneous conductivity structure is the apparent resistivity frequency independent and equal to the earth resistivity.

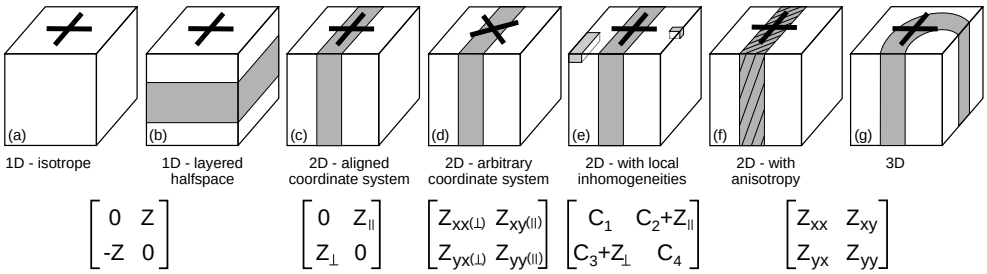

Figure 3: Symmetries in earth conductivity structure reflected in the MT impedance tensor (**Z**): (a),(b) a homogeneous or 1D earth structure gives rise to **Z** with off-diagonal elements of opposite sign. (c) measurements made over 2D earth structure giving rise to **Z** with unequal off-diagonal elements. The measurements are aligned with earth structure. (d) general case of (c) with a fully occupied tensor, i.e. all elements of **Z** are non-zero. Case (d) can be mathematically rotated into case (c). (e) 2D earth structure with localized 3D distortion. Frequency-independent real constants C_1-C_4 represent effects of 3D galvanic distortion and can to some degree be determined through tensor decomposition. (f),(g) 2D anisotropic and 3D earth structure generate fully occupied **Z** except in special cases.

If lateral conductivity variations exist within the subsurface on length scales equal to or greater than the penetration depth of the induced horizontal magnetic fields, a vertical magnetic field component is generated. The geomagnetic response functions $T_x(\omega), T_y(\omega)$ are defined as:

$$B_z = T_x\, B_x + T_y\, B_y\,. \tag{3}$$

The form of the impedance tensor and the existence of vertical magnetic fields are directly linked to the electric and magnetic field distributions at the earth's surface, and in turn the (electrical) complexity of the subsurface. Over a 1D earth (conductivity varying only with depth) vertical magnetic fields and the diagonal entries of the impedance tensor vanish and the off-diagonal elements carry the same impedance information Z (Figure 3(a),(b)). The measured impedance tensors over a 2D earth (conductivity varying with depth and in one lateral direction) have vanishing diagonal elements only if the electromagnetic fields are either recorded or mathematically rotated into a coordinate system aligned with geoelectric strike (Figure 3(c),(d)). The impedance tensor is fully occupied over a 3D conductivity distribution (Figure 3(g)) except at particular locations where, due to symmetry, the field distributions and therefore the impedance tensor may appear 1D or 2D. In the presence of electrical anisotropy a fully occupied impedance tensor is observed even if the regional structure is 2D. Only in the rare case of anisotropy striking parallel to the regional strike will the impedance tensor reduce to its 2D form (Figure 3(f)).

1.1.3 Tensor rotation and induction arrows

Traditionally, Swift's (1967) method was applied to derive a geoelectric strike angle from the measured impedance tensor by searching for a rotation angle which maximizes the off-diagonal components (see 2D aligned coordinate system in Figure 3(c)). Swift's parameter can be misleading, however, as the measured electric

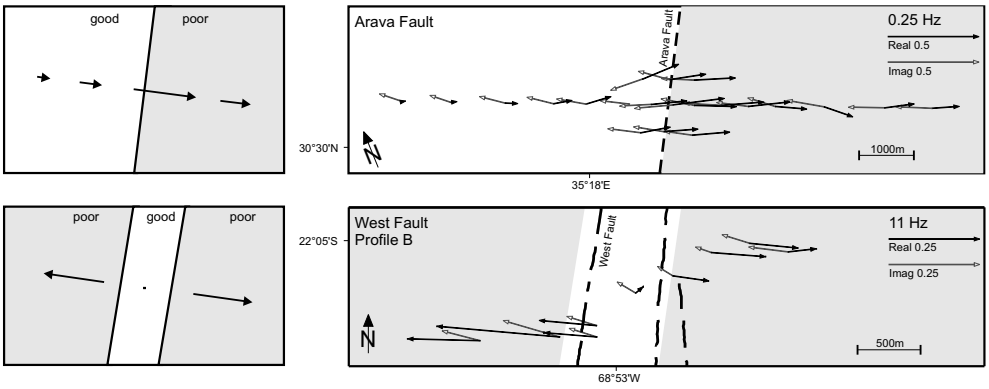

Figure 4: Expected and observed behaviour of induction vectors (IV) for two different fault structures. In Wiese convention real (black) arrows point away from good conductors; imaginary (grey) arrows are parallel or antiparallel to the real arrows, given 2D earth structure. Across a conductivity contrast (top panel) real IVs point away from the more conductive side and are largest over the less conductive side. The DST, locally the Arava Fault, is representative of this type of fault structure. A conductive fault zone sandwiched between more resistive units is characterized by IVs pointing away from the fault on both sides and small IVs over the fault zone conductor. The West Fault is representative of this type of fault structure.

field may be severely distorted in the presence of near-surface heterogeneities (compare Figure 3(e)). Under these circumstances, tensor decomposition methods can help recover an (undistorted) regional 2D impedance tensor from the measured impedance tensor (Smith, 1995; McNeice & Jones, 2001, and references therein). These methods assume that local 3D bodies (distorters) accumulate charges at their edges giving rise to a frequency-independent response intertwined with the (desired) regional 2D impedance tensor. Tensor decomposition thus attempts to separate a real distortion matrix from the measured impedance tensor which contains, among other distortion parameters, information on the strike direction. A consistent frequency-independent strike direction must exist if the 2D assumptions are fulfilled.

An independent determination of strike directions is obtained from geomagnetic response functions, relating horizontal and vertical magnetic fields (see equation 3). The induction vector is a graphical representation of the vertical magnetic field transfer function in which T_x and T_y are viewed as components of a vector and plotted in map view. Induction vectors vanish in the absence of lateral resistivity gradients and thus provide an important means of identifying conductivity contrasts that may be expected across a fault. In the two-dimensional case, real and imaginary induction arrows are parallel or anti-parallel to each other, and parallel to geoelectric strike (see Figure 4). In this paper, induction vectors are plotted in the Wiese (1962) convention, in which the real parts point away from regions of high conductivity.

1.1.4 2D Modelling and Inversion

In order to determine the two-dimensional conductivity distribution of the subsurface either forward modelling or inversion is applied to apparent resistivity and phase curves. It is at this point that an accurate assessment of the dimensionality of MT

data is important. In the case of 2D isotropic earth structure, the MT equations reduce to fitting two elements of the impedance tensor. While real MT data are seldom purely 2D, methodologies have been established for the analysis of weakly 3D data sets using 2D inversion methods (e.g. Ledo et al., 2002). The alternative, a 3D inversion, is in most cases not feasible due both to computational requirements and the areal data coverage required to constrain such an inversion.

All 2D resistivity models, save the anisotropic models, presented in this paper derive from inversion of MT data using the iterative RLM2DI algorithm (Rodi & Mackie, 2001), part of the WinGLink[1] software package. RLM2DI finds regularized solutions (Tikhonov Regularization) to the 2D MT inverse problem using the method of nonlinear conjugate gradients. Prior to inversion, a finite-difference mesh is created, where row thickness increases with depth (dependent on the frequency range of the data) and column width scales with site spacing. A homogeneous resistivity model is commonly employed as a starting model. Alternatively, geological or geophysical constraints may be introduced into the starting resistivity model *a priori*. The inversion algorithm attempts to minimize an objective function expressed as the sum of the normalized data misfit and the smoothness of the model. The trade-off between data misfit and model smoothness is controlled by the regularization parameter τ, determined via several inversion runs. The best value of τ gives rise to monotonic decreases in both data misfit and model smoothness as the inversion proceeds.

The smoothness (Laplacian) regularization described above is but one way to constrain the inherently non-unique MT problem. Regularization can be chosen, for example, to minimize the flatness (gradient) of the model or its deviation from an *a priori* model. Each regularization has its strengths and weaknesses, which must be taken into account when assessing the fit of the inversion model. For the studies presented in this paper, the smoothness regularization produces minimum structure models, in which only structures required by the data are presented. A disadvantage of this approach is that sharp boundaries are sometimes not well recovered during inversion, resulting in a smearing of structures at depth. The assessment of any MT inversion model hinges not only on the r.m.s. data misfit, but also on a careful examination of the existence, geometry, and resistivity of individual features of the model.

Forward modelling is often used to assess the sensitivity of measured data to modification of part of an inversion model. It is also commonly employed to determine the resolution depth, that is, the depth below which changes in conductivity are invisible to measured data. Constrained inversion, in which part of a model is modified and held fixed during subsequent inversion is further used to constrain the geometry and strength of anomalous structure.

In the case of a one-dimensional earth, the conductance, $s\,[S]$, of a layer of thickness, $h\,[m]$, is the most robust parameter determined by magnetotellurics, and is used to quantitatively compare conductivity anomalies (e.g. Li et al., 2003):

$$s = \sigma h\,. \tag{4}$$

In the case of two- and three-dimensional earth structure, conductance can still be calculated, but will vary with location (Bedrosian et al., 2004). For the purpose of this paper, we wish to compare the conductivity anomalies associated with various fault zones. We thus introduce the lateral conductance, a quantity we define as the product of the average width and conductivity of an imaged conductor. In a 1D case,

[1] http://www.geosystem.net/software.htm

lateral conductance is meaningless, while in a 3D case, it is direction dependent. It is important to note that while lateral conductance can be used for comparison of fault zones, it is not subject to a conductivity/thickness trade-off. The studies presented herein, for example, can distinguish between a $500\,m$ wide, $1\,S/m$ zone and a $1\,km$ wide, $0.5\,S/m$ zone.

2D inversion is limited to fitting only two elements of the measured impedance tensor (see Fig. 3c). For data sets exhibiting significant diagonal impedance elements, the 2D anisotropic forward modelling code of Pek & Verner (1997) can be used to model a 3D conductivity tensor if an anisotropic subsurface is a reasonable assumption. By defining a set of three conductivity values and their associated rotation angles, the surface response of any physically possible electrical anisotropy can be calculated. Defining conductivities in different directions primarily reflects the intrinsic or microscopic anisotropy of rocks. However, Eisel & Haak (1999) point out that MT results over a microscopically anisotropic subsurface are indistinguishable from those over structural or macroscopic anisotropy in the form of conductive lamellae. Intrinsic electrical anisotropy may arise from a crystallographic preferred orientation (CPO) in the subsurface, while structural anisotropy is commonly of tectonic or volcanic origin.

2 Case studies

2.1 The San Andreas Fault in California, USA

Formed around 30 Ma ago as the Pacific plate impinged upon the North American plate, the San Andreas Fault (SAF) continues to lengthen as the Mendocino and Rivera triple junctions migrate apart. The SAF exhibits a right-lateral offset of $\sim 300\,km$ and currently accommodates $\sim 35\,mm/yr$ of strain across its multiple strands (Irwin, 1990; Bennett et al., 1999; Argus & Gordon, 2001). There is marked seismic variability along the SAF, with some segments characterized by infrequent, large-magnitude earthquakes while others exhibit abundant microseismicity and aseismic creep (Allen, 1968).

Throughout central California, the SAF juxtaposes granitic rocks of the Salinian block against the Franciscan complex, a Mesozoic subduction complex. MT profiles ($\sim 20\,km$ length) acquired near Hollister (in 1999) and Parkfield (in 1997) are considered here (see Figure 1(a) for locations). The SAF near Hollister creeps, while at Parkfield it is in transition between a creeping segment to the north and a locked segment to the south. MT data were recorded in the frequency range $100 - 0.001\,Hz$ at 80 (50) sites at Hollister (Parkfield). Calculation of geoelectric strike is consistently within 5° of geological strike at all but the lowest frequencies (Unsworth et al., 1999; Bedrosian et al., 2004).

2D resistivity models, derived via inversion of MT and vertical magnetic field data, are shown in Figure 5. At both locations, a strong resistivity contrast is imaged between the Salinian granites southwest of the fault and a highly conductive zone to the northeast. This boundary is further delineated by seismicity between 2 and $7\,km$ depth. At Hollister, the prominent zone of high conductivity is loosely bound between the San Andreas and Calaveras faults, extending to mid-crustal depths beneath the SAF (Bedrosian et al., 2004). At Parkfield, anomalous conductivity is confined to a zone centred on the SAF and extending from the surface to $2 - 5\,km$ depth, based on constrained inversion studies by Unsworth & Bedrosian (2004). To the northeast, a

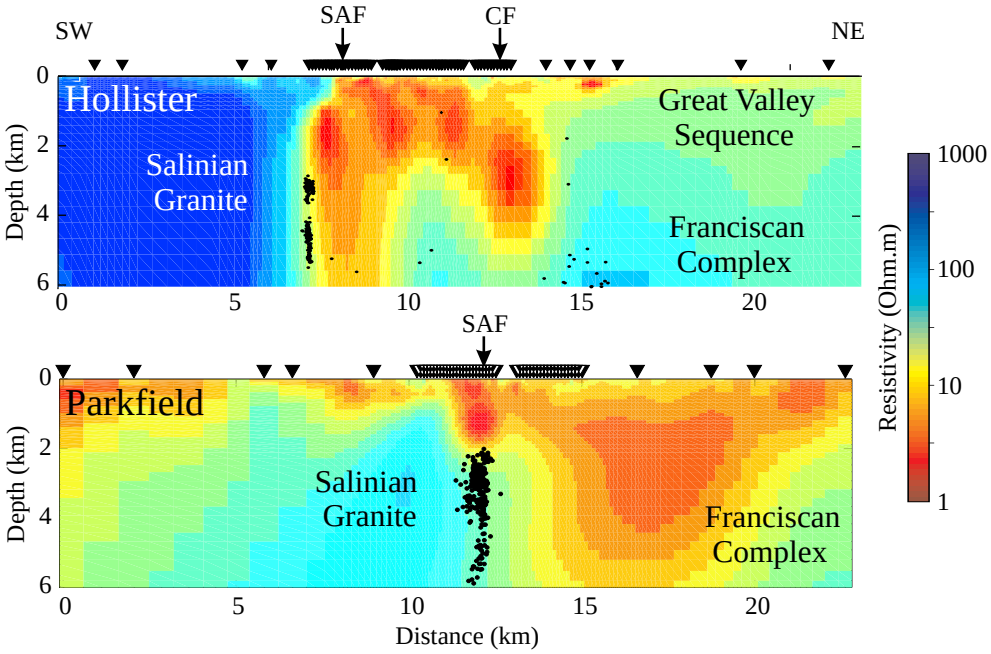

Figure 5: Hollister and Parkfield resistivity models after Bedrosian et al. (2002) and Unsworth & Bedrosian (2004), respectively. Black dots indicate earthquake hypocentres within 1km of each profile. Inverted triangles indicate site locations, while arrows denote surface traces of the San Andreas (SAF) and Calaveras (CF) faults. Hypocentres are from the Northern California Seismic Network, UC Berkeley High Resolution Seismic Network and the Parkfield Area Seismic Observatory.

diffuse zone of high conductivity is imaged.

The prominent fault zone conductors (FZC) imaged at Hollister and Parkfield coincide with zones of reduced seismic velocity and enhanced Vp/Vs (Thurber et al., 1997, 2003; Catchings et al., 2002). Furthermore, the depths and geometries of the low velocity zones are similar to those of the imaged FZCs.

The most plausible explanation for the anomalously high conductivity at both locations is saline fluids within a fractured region surrounding the fault (Unsworth et al., 1997; Bedrosian et al., 2004). However, Park et al. (2003) alternatively propose that the sediments of the Parkfield syncline may explain the observed FZC at Parkfield, however an additional MT profile $6\,km$ to the south imaged both a FZC and the Parkfield syncline (Unsworth et al., 2000), suggesting the syncline cannot solely explain the high conductivity of the fault zone. The case for fluids is supported by high salinities measured in wells close to the fault. Using Archie's law (equation 1), porosities of $9-30\,\%$ and $15-35\,\%$ have been estimated for Parkfield and Hollister, respectively (Unsworth et al., 1997; Bedrosian et al., 2002).

2.2 The Dead Sea Transform in the Arava Valley, Jordan

The Dead Sea Transform (DST) is a left-lateral transform fault separating the continental African and Arabian plates (Garfunkel & Avraham, 1996). It extends over $1000\,km$ from the Red Sea in the south to the Taurus collision zone in the north (Figure 1(b)). The fault has been active, more or less continuously, since its origin in the Miocene with a total left-lateral motion of $105\,km$ (Freund et al., 1970) and a present-day slip rate of $4\pm2\,mm/year$ (Klinger et al., 2000a; Wdowinski et al., 2004). MT studies were part of the multi-disciplinary DESERT (DEad SEa Rift Transect) project, a $300\,km$ long profile traversing Israel, Jordan and the Palestinian territories.

Figure 6 shows images obtained from magnetotelluric modelling (a) and seismic tomography (b) across the Arava Fault (AF), a local expression of the DST (Ritter et al., 2003a). The total length of the near-vertical seismic reflection line was $100\,km$; MT data were recorded along the innermost $10\,km$ of this profile, centred on the AF. A dense site spacing of $100\,m$ in the centre of the MT profile was supplemented by more widely spaced sites near the profile ends. Strike angle analysis using the method of Smith (1995) reveals a geoelectric strike of N17°E, in close agreement with the surface strike of the AF (N15°E). This strike angle is further confirmed by induction vectors as shown in the upper panel of Figure 4.

For the shallow crust, the inversion model reveals a highly conductive layer from the surface to a depth of $\sim100\,m$ on the eastern side of the profile. However, the most prominent feature on the MT image is a conductive half-layer confined to west of the fault and beginning at a depth of approximately $1.5\,km$. The surface trace of the AF correlates with a sharp vertical conductivity boundary at the eastern edge of this feature. The high conductivity may be due to brines in porous sedimentary rocks; saline waters have been found in a lower Cretaceous aquifer at a depth of $\sim1000\,m$ in a drill hole $\sim14\,km$ west of the AF (Ritter et al., 2003a). The seismic image reveals a strong increase in P-wave velocities (to values exceeding $5\,km/s$) east of the AF, where the MT model indicates higher resistivities. The seismic velocities are consistent with crystalline basement rocks; however the observed resistivities ($50-250\,\Omega m$) are unusually low for unfractured crystalline rocks. Both the seismic and MT observations may be explained by fractured crystalline rocks with interconnected fluid bearing veins.

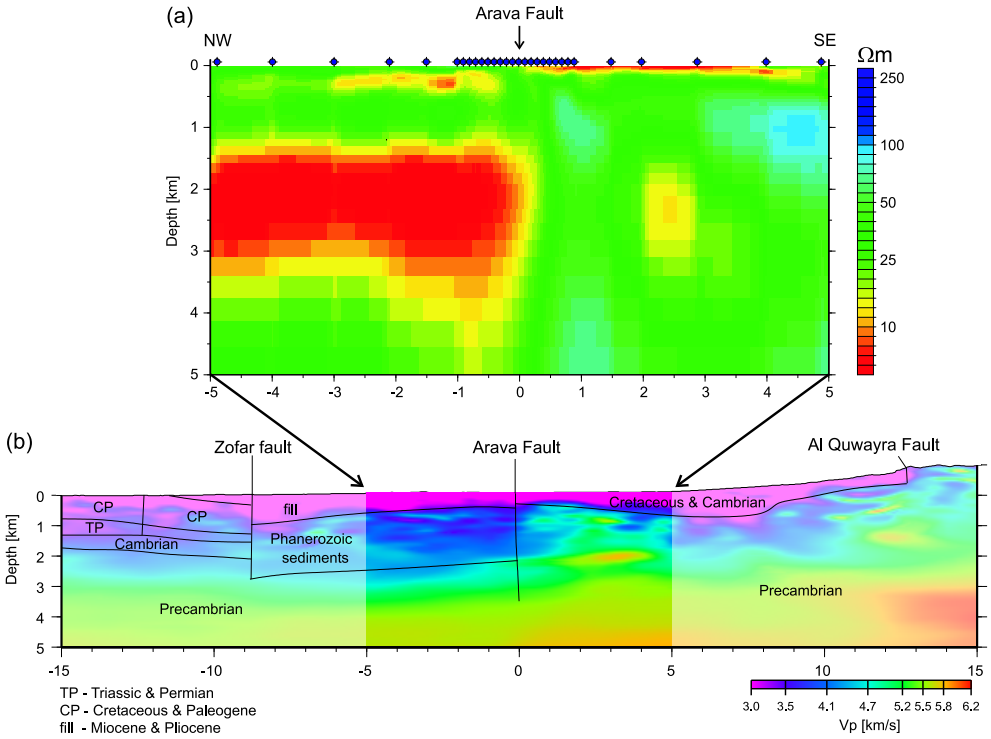

Figure 6: Coincident magnetotelluric and seismic tomography sections crossing the Arava Fault (AF) modified after Ritter et al. (2003a). (a) Resistivity model surrounding the AF. Diamonds depict MT site locations. (b) Seismic tomography section with overlain structural interpretation taken from Ritter et al. (2003a). Only the upper $5\,km$ of the crust are shown, as resolution degrades at larger depths due to limited profile length (MT) and diminished ray coverage (seismics). Both model sections indicate significant lateral changes of physical properties across the AF.

2.3 The West Fault in northern Chile

The Precordilleran Fault System (PFS), classified as a trench-linked strike-slip fault, trends subparallel to the northern Chilean margin for more than $2000\,km$ (Figure 1(c)). It was initiated in an Eocene magmatic arc in response to oblique convergence of the Nazca and South American plates. The West Fault (WF) forms the main branch of the northern PFS. It records $\sim$40 km of left-lateral displacement, although the sense of slip has seen several reversals throughout the fault's evolution. Belmonte (2002) reports little seismicity in recent times.

MT profiles (2.5 and $4\,km$ long) were recorded where the fault cuts an inclined plain of Quaternary alluvial deposits (Hoffmann-Rothe, 2002; Hoffmann-Rothe et al., 2004). The profiles are separated along strike by $3.5\,km$ and have site spacings between 100 and $300\,m$. Data were recorded in the frequency range from $1000-0.001\,Hz$. Dimensionality and distortion analysis reveal a geoelectric strike direction of N10°E for the frequency range from $1000-0.1\,Hz$, consistent with the strike of the surface trace. This strike direction is supported by the induction vectors shown in the lower panel of Figure 4. At greater skin depths (frequencies $<0.1\,Hz$) the conductivity

structure becomes more complex, as different strike directions begin to effect the data; modelling and inversion are thus limited to frequencies above 0.1 Hz.

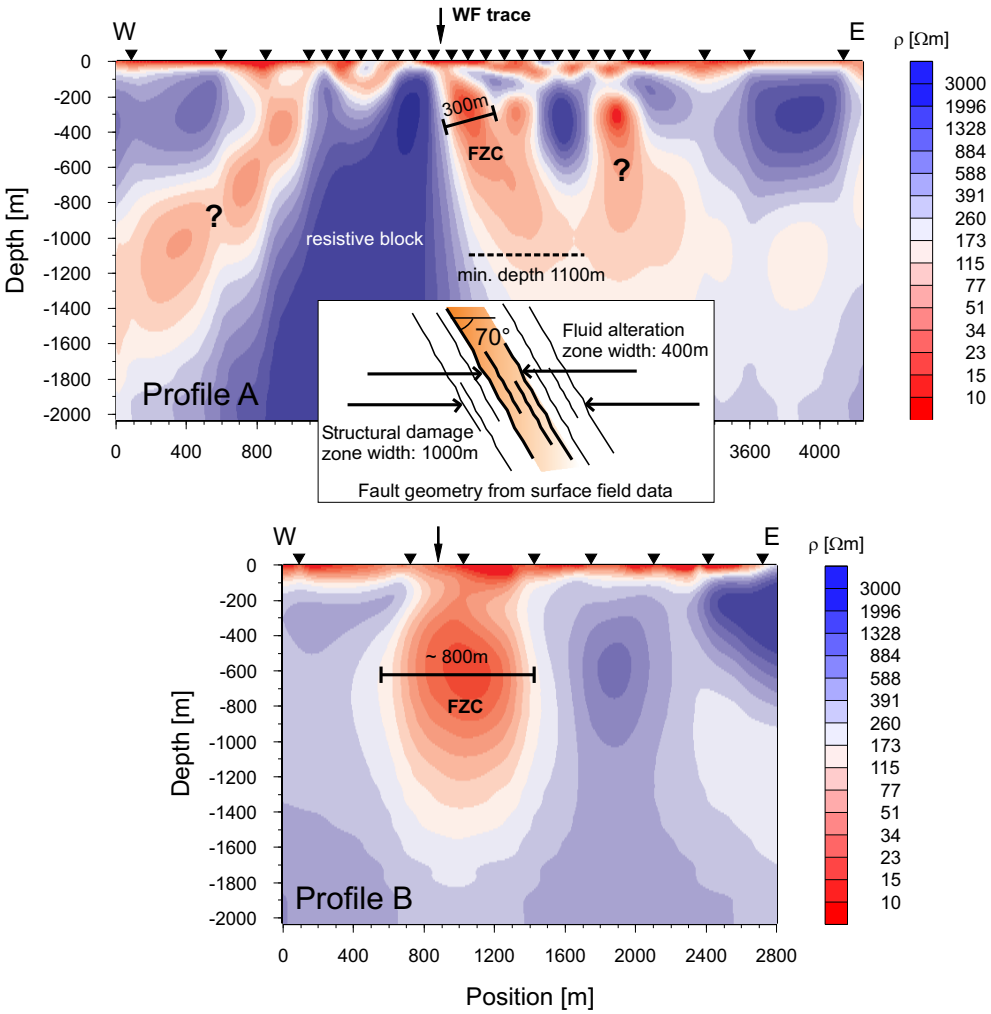

Figure 7: Resistivity models of the West Fault modified after Hoffmann-Rothe et al. (2004). Sites are depicted by inverted triangles. The most prominent feature on both profiles is a zone of high conductivity adjacent to the fault (labelled FZC). The inset depicts results from structural mapping along profile A, extrapolated to greater depth. The correlation of dip angles of the FZC and the fault/fracture mesh suggests that high conductivity arises from fluids within the fault/fracture mesh. Question marks indicate poorly constrained model features. Profile B is located 3.5 km further south of profile A

2D inversion models for both profiles are shown in Figure 7 (Hoffmann-Rothe et al., 2004). The most prominent and robustly imaged structure is a sub-vertical zone of high conductivity located east of the surface trace. Hypothesis testing using forward modelling and inversion confine the depth of the FZC to about 1500 m. Independent evidence from fracture density mapping reveals a ∼1000 m wide damage

zone. Comparison of structural and MT results (inset in Figure 7) shows a good spatial correlation of the FZC with a $\sim 400\,m$ wide zone of intensely comminuted material that has undergone pronounced fluid alteration (Janssen et al., 2002, 2004). Along profile A (see Figure 7) the FZC is about $300\,m$ wide and bounded to the west by a resistive block. This resistive block corresponds to Jurassic limestones and Triassic andesites which outcrop at locations west of the fault and are not present along the southern profile (B). Subsidiary faults and fractures preserved in the alteration zone of profile A are steeply inclined $\sim 70^\circ$ to the east; a similar dip angle is required for the FZC of profile A based on constrained inversion studies. Together this suggests that fluids within the fault/fracture mesh give rise to the high conductivity. This scenario is further supported by the presence of a spring which surfaces along the trace of the fault. Groundwater salinity measured in adjacent boreholes and mines, in conjunction with the observed conductivity of the FZC results in porosity estimates of 20% at the surface reducing to 1% at $200\,m$ depth (Archie's law).

2.4 The Waterberg Fault / Omaruru Lineament in Namibia

The Namibian Damara Belt is part of a system of convergent orogens formed during the amalgamation of South Gondwana. It is the remnant of continental collision between the Kongo and Kalahari cratons in the early Cambrian (Miller, 1983). During this orogeny, older extensional faults were reactivated as thrusts which now separate zones of different stratigraphic and structural evolution, metamorphic grade, distribution of plutonic rocks and geochronology (Daly, 1986, 1989). Subsequently, the Damara Belt was eroded down to form a new basement on which Permian marine sediments were deposited. The major tectono-stratigraphic lineaments, including the Autseib Fault (AuF) and the Waterberg Fault/Omaruru Lineament (WF/OL), can be traced for hundreds of kilometres, and subsequently continued to control deformation of the Namibian crust in the Cretaceous (Holzförster et al., 1999; Raab et al., 2002)(Figure 1(d)).

This fossil fault zone, though quite dissimilar to the previous examples of active regimes, illustrates a high strain zone that is also marked by high conductivity. MT data were collected on both regional ($200\,km$) and local ($20\,km$) scales, with the majority of the 110 sites focused on the local profiles, where site spacings ranged from $500 - 2000\,m$.

The regional scale MT model, shown in Figure 8(a), provides insight into the deep structure of the Damara Belt (Ritter et al., 2003b). A generally resistive upper crust is imaged which at depths of $15 \pm 2\,km$ transitions to a conductive lower crust confined to the central part of the profile. The resistive upper crust is furthermore pierced by two sub-vertical conductors, whose locations coincide with the surface expression of the AuF and WF/OL, suggesting they represent the continuation of these shear zones at depth. Both structures appear to terminate at the lower-crustal conductor, the top of which is interpreted as a lower-crustal detachment.

The local MT study consisted of two dense profiles crossing the WF/OL with additional off-profile sites to provide areal coverage of the lineament zone (Weckmann et al., 2003a). The acquired data show fully occupied 3D impedance tensors which originate from a more complicated earth structure than the 2D lineament structure observed at the surface. Based on a new imaging method (Weckmann et al., 2003b) which transforms the entire impedance tensor into resistivity ellipses, 3D effects can be attributed to a $10\,km$ wide zone of anisotropic conductivity in the shallow crust. Figure 8(b) illustrates a simplified 2D anisotropic model of the WF/OL and its close

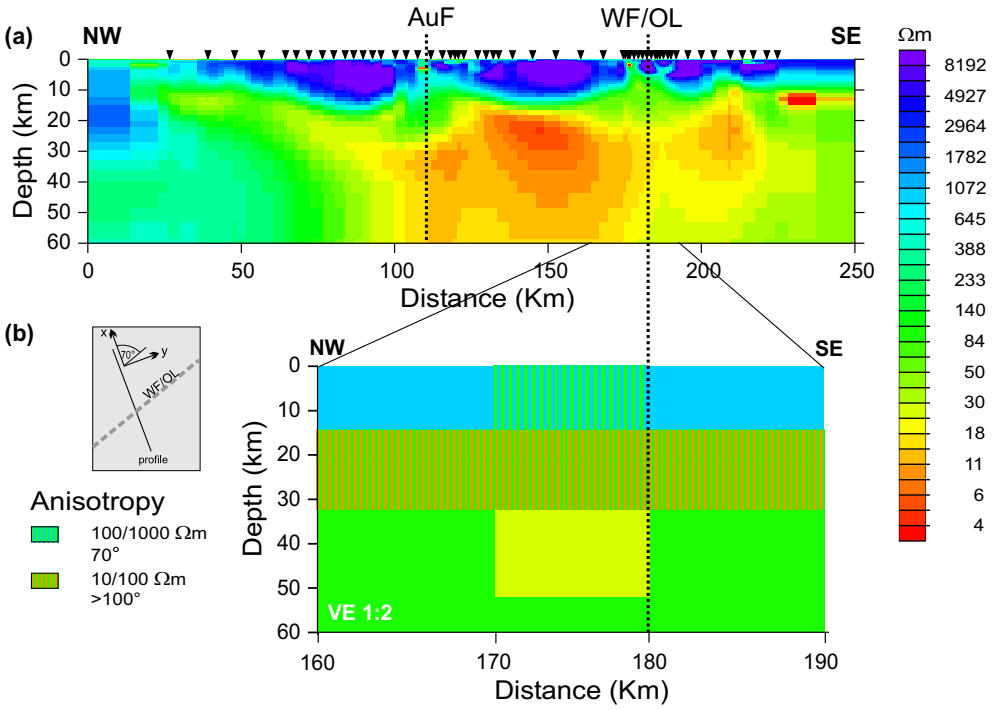

Figure 8: Resistivity models of the Damara belt, Namibia modified after Ritter et al. (2003b) and Weckmann et al. (2003a) using the same colour scale. (a) 2D regional model of the lithosphere. Main features of the resistivity model include the general high conductivity of the mid-crust in the central part of the profile and the narrow, sub-vertical conductivity anomalies attributed to basement shear zones. AuF=Autseib Fault, WF/OL=Waterberg Fault/Omaruru Lineament. (b) 2D anisotropic model of the WF/OL: In the upper layer, a 10 km wide and 14 km deep anisotropic block (anisotropy striking subparallel to the strike of the WF/OL) is sandwiched between two resistive blocks. Beneath is a second anisotropic layer with a poorly defined strike. A 20 Ωm block embedded within the bottom half space is required to model the low-frequency induction vectors.

surroundings which reproduces the general characteristics of the data (Weckmann et al., 2003a). Despite its simple block structure, the model can resolve the internal structure and minimal depth extent of the fault, as the unusual shape of the observed MT responses considerably reduces the number of equivalent models. The data can only be fit if the anisotropic zone reaches to at least 14 km depth. The ratio of orthogonal to fault parallel conductivity is 1:10, with a strike direction of N70°E, subparallel to the WF/OL. An anisotropic lower-crustal layer is also necessary, with an anisotropy direction differing by at least 30° from that of the upper crustal layer. The tectonic significance of this layer is unknown. A 20 Ωm block is further embedded within the bottom half space and is required to model the induction vectors at long periods.

The regional and the local models of the WF/OL look quite dissimilar, however, this is primarily due to the disparate resolving power of the applied techniques. Isotropic 2D inversion tries to fit two components (see Fig. 3(c)) of the impedance

tensor at all sites over the entire frequency range, but cannot explain the observed diagonal components of the impedance tensor. 2D anisotropic forward modelling, on the other hand, can model the entire 3D impedance tensor, but is limited to finding generalized models which reproduce the basic characteristics of the data. The lateral and depth extents of the anisotropic block coincide very well with the width of the sub-vertical conductor(s) in the regional model. Additionally, the depth of the lower-crustal conductor in the regional model agrees with the depth to the lower anisotropic layer in the local model. The resistivities of both models are also comparable; in the regional model they represent an azimuthal average of the anisotropic resistivity of the local model.

Fluids cannot be ruled out as a cause of the observed crustal conductivity, however there is no supporting field evidence for hydrothermal alteration along the WF/OL. In contrast, graphite bearing marbles are widespread in the area and suggest that shearing could create an interconnected graphite network on kilometre length scales (Liu et al., 2002).

3 Discussion

3.1 The shallow picture

Images of fault zone conductors (FZC) are characteristic of a number of faults throughout the world. Examples include the San Andreas Fault at Parkfield (Unsworth et al., 2000) and Hollister (Bedrosian et al., 2002), the West Fault in Chile (Hoffmann-Rothe et al., 2004), and the Yamasaki fault in Japan (Electromagnetic Research Group for the Active Fault, 1982). A FZC is absent, however, along the active Arava Fault in Jordan (Ritter et al., 2003a) and only weakly expressed along the San Andreas Fault at Carrizo Plain (Unsworth et al., 1999). What are the major controls for the extent of enhanced conductivity within and surrounding the damage zone of a fault? In order to address this question we must consider the complex interplay between electrical conductivity, lithology, fluid supply, permeability, and fault geometry as related to the faults described in this paper (see Table 1).

	Arava Fault	West Fault	San Andreas Fault		
			Hollister	Parkfield	Carrizo Plain
FZC imaged?	no	yes	yes	yes	yes
Recent activity	active	currently inactive	creeping	small earthq., creeping	locked since 1875
Width of FZC	not resolved	300-400m	750m	750m	<300m
Depth of FZC	not resolved	~1.5km	~8km	2-5km	~3km
Lateral conductance	not resolved	~5S	~600S	~250S	~20S

Table 1: Comparison of fault zone conductivity structure (mod. after Hoffmann-Rothe et al., 2004). Findings from Carrizo Plain (Unsworth et al., 1999) are listed in addition to studies discussed in this paper.

The San Andreas and West faults are characterized by fault zone conductors with widths of hundreds of meters and depths ranging from 1.5 to over 8 km (Table 1). The spatial extents of these FZCs are in rough accordance with other studies. At the West Fault, fracture density mapping shows strain distributed over a broad zone, with a region of intense shearing whose width is on the order of the FZC width (Hoffmann-Rothe et al., 2004). Along the SAF, seismic tomography studies (Thurber et al., 2003, 1997; Catchings et al., 2002) image zones of reduced Vp and enhanced Vp/Vs coincident with the imaged FZCs and of similar scale and geometry. Additionally, fault zone trapped wave studies estimate a damage zone of $\sim$150 m width at a location $\sim$15 km southeast of the Parkfield MT study (Li et al., 2004).

The fault zones under consideration can also be examined in light of their lateral conductances (see section 1.1.4). Bedrosian et al. (2002) note a FZC with $\sim$600 S lateral conductance at Hollister. A more modest conductance of $\sim$250 S exists at Parkfield, whereas at Carrizo Plain, a mere 20 S is observed (Unsworth et al., 1999). As discussed in section 2.1, the high lateral conductances at Hollister and Parkfield are best explained by saline fluids within and surrounding the damage zone of the fault. In contrast, the lateral conductance at Carrizo Plain can be adequately explained by a narrow zone of deformation with only small quantities of fluids present (Unsworth et al., 1999). Meteoric waters, transported towards the fault zone by topography sufficiently explain the observed lateral conductance of 5 S at the West Fault.

The lack of an imaged FZC at the AF only shows that a SAF-type FZC is not required to fit the data. Constrained inversion can be used to provide limits on the maximum conductance that can be added to the model in Figure 6. Within 200 m of the fault trace and from the surface to 1500 m depth, the average resistivity is on the order of 20 Ωm, giving rise to a 'background' conductance of 20 S for this 400 m wide zone. How much additional conductance can be added to this model and still fit the data? 2D inversions based on this model, but with the *a priori* inclusion of a vertical FZC show that at most 20 S can be added between the surface and 400 m depth, 40 S between 400 m and 1000 m depth, and 80 S between 1000 m and 1500 m depth. Anything greater is incompatible with the measured data, meaning that a FZC of any significance could only be 'hidden' beneath the fault at depths below 1500 m. At these depths, however, a FZC would effectively merge with the prominent conductive half-layer and could not be resolved.

Seismicity provides another means by which to compare the faults under consideration. On a regional scale, the distribution of seismicity along the SAF correlates well with the lateral conductance and spatial extent of the FZC (see Table 1). Hollister exhibits abundant microseismicity, pronounced aseismic creep, a distinct absence of earthquakes with magnitude greater than 5, and the area of highest lateral conductance (of six published MT profiles along ths SAF). Carrizo Plain, in contrast, with its modest lateral conductance, has no creep and suffers large, damaging earthquakes such as the 1857 Fort Tejon quake (M=7.8, (Ellsworth, 1990)). Parkfield lies in transition between the active, creeping segment to the north and the locked segment to the south and, consequently, the imaged FZC is intermediate between Hollister and Carrizo Plain with respect to lateral conductance and spatial extent. The West Fault, believed to be currently inactive, is characterized by a low lateral conductance. The few seismic events which have been located at depths between 5 and 18 km cannot clearly be attributed to the Precordilleran Fault System (Belmonte, 2002).

The DST within the Arava Valley is nearly devoid of recent seismicity (Ambraseys & Jackson, 1998). This conclusion must be tempered, however, by the fact that regional seismic networks have only been in operation since the 1980s, and even then

have a detection threshold of magnitude 2.5 (Klinger et al., 2000b). Nevertheless, several magnitude 7 events can be confidently attributed to this segment of the fault within the last millennia and suggest a recurrence interval of ∼250 years (Klinger et al., 2000b). Based on this incomplete catalogue, we infer that seismic behaviour along the DST most closely resembles the SAF at Carrizo Plain. The fact that a FZC of modest conductance is imaged at Carrizo Plain while none is seen along the DST may be related to the lower strain rates ($2-6\,mm/yr$ versus $33-39\,mm/yr$) and cumulative slip ($105\,km$ versus $\sim 300\,km$) attributed to the DST within the Arava Valley (Irwin, 1990; Bennett et al., 1999; Argus & Gordon, 2001).

3.1.1 Structural and hydrogeological implications

At the SAF, DST, and WF, fluids are proposed to explain the upper-crustal zones of high conductivity within or surrounding the fault zones. In conceptual fault zone models, large-scale faults can be broken down into three structural, mechanical, and hydrologic units (see Figure 9): (i) the protolith, or undeformed country rock, (ii) the damage zone, a broad (up to hundreds of meters) highly permeable zone with an increased concentration of fractures, faults and veins, and (iii) the fault core, a narrow (centimeters to meters), often impermeable zone of highly deformed rock where the majority of slip is accommodated (Chester & Logan, 1986; Caine et al., 1996; Evans et al., 1997). The fluid transport properties of faults are primarily controlled by fault geometry and permeability contrasts. Fluid transport in faults can be classified as localized conduit, distributed conduit, localized barrier or a combined conduit barrier (Caine et al., 1996).

In what way are the observed conductivity structures related to the above mentioned hydrogeological classes or architectural units of fault zones? The FZCs imaged on three parallel profiles at Parkfield (Unsworth et al., 2000) suggest that, at least locally, they form a continuous along-strike feature and a possible conduit for fluid flows (Gudmundsson, 2000). Studies of fault gouge from $400\,m$ depth support this possibility, concluding that the SAF near Hollister is permeable to fluids at shallow depths (O'Neil, 1984). The MT results from Hollister, where two profiles spaced $20\,km$ apart image similar FZCs, further suggest that the FZC, though varying in strength and extent, may be a continuous feature throughout much of central California.

The sharp resistivity contrast along the western edge of the FZCs (Figure 5) additionally suggests that the SAF acts as a barrier to cross-fault fluid flow transport (Bedrosian et al., 2002). A strong lithological contrast clearly exists across the fault and there is little geochemical evidence of fluid mixing. Irwin & Barnes (1975) noticed an abundance of chloride-rich springs on the eastern (Franciscan) side of the SAF in contrast to the western (Salinian) side. If these saline waters had infiltrated the granites southwest of the fault, one would expect significantly lower resistivities than the $200-1000\,\Omega m$ observed west of the fault. Whether the fluid barrier is due to the lithology contrast, a mineralized fault seal or a combination of the two cannot be resolved from the conductivity models.

The West Fault paints a similar picture to that of the SAF. The FZC appears continuous along strike and is sharply terminated along its western edge. A zone of alteration acts as a sink for surficially derived meteoric water. The continuity of the FZC as seen on the two profiles, suggests a potential along-strike fluid conduit. Springs emanating along the fault trace indicate that cross-fault fluid flow transport is hampered.

The conductivity model along the Arava Fault (Figure 6) reveals two highly con-

ductive zones cut abruptly by the AF, including the prominent conductor between 1.5 and 3 km depth west of the fault. These truncated conductors are also imaged on parallel profiles, and can be traced for more than 10 km along strike (not shown). A lithological change (across the fault) from Phanerozoic sequences (limestones/sandstones) to Precambrian metamorphic basement may be the cause of the deeper conductivity contrast, however the near surface conductors, on opposite sides of the fault, are in similar lithology (alluvial fan deposits). This suggests that an impermeable fault-seal may be arresting cross-fault fluid flow transport at shallow depths. Additionally, the interconnected fluid-bearing veins, posited to exist within the Precambrian basement (see section 2.2), do not appear linked to the deep conductor west of the fault. Thus, a fault-seal may be restricting fluid transport at greater depths as well.

The distinct lack of a FZC associated with the Arava Fault may imply that a broad damage zone does not exist. According to fault scaling laws, however, it is reasonable to expect a damage zone up to 1 km wide for the Arava Fault, based on its displacement of $\sim$105 km (Scholz, 1987; Scholz et al., 1993). What could give rise to this apparent discrepancy?

(i) The alluvial fan deposits at the surface record only a short time span of faulting and hence little displacement has accumulated. In this case, we would expect a FZC at greater depths (below 1 km), where basement rocks are cut. Constrained inversions indicate that a FZC at that depth cannot be ruled out, though we can exclude the existence of a shallow FZC (above 1.5 km).

(ii) Deformation is partitioned among parallel, yet undetected fault strands. Seismic sections suggest the existence of parallel faults but neither seismic profiles nor surface observations support a substantial strike-slip component.

(iii) There is no FZC or it is too narrow to be resolved with MT, i.e. it has a width of less than 50 m. This conclusion is supported by the fault zone trapped wave study of Haberland et al. (2003) which argues for a low-velocity fault zone of 3 to 10 m width (with 40 to 50% velocity reduction relative to the country rock). Furthermore, the field record of deformation along the fault trace, where accessible, does not exhibit a broad or intensively fractured damage zone.

The last suggestion is our preferred interpretation. It implies that strain is extremely localized along shear planes within a very narrow damage zone. Processes of fault hardening and weakening within fault zones control whether they grow in width or remain localized throughout time (Mitra & Ismat, 2001). It is therefore conceivable that the AF has not experienced episodes of complete strength recovery, whereas the WF and the SAF have gone through repeated cycles of healing, strength reloading and subsequent failure, causing the formation of broad zones of structural deformation. Alternatively, where a prominent strength contrast exists across the fault, structural deformation predominantly effects the weaker block and is distributed over a wider range (for example, the SAF at Hollister). Hence, the lack of a FZC at the AF may indicate that there exists little strength contrast between the eastern and western side of the fault. In summary, the spatial extent of the FZC, where present, appears to reflect the size of the zone of intense structural deformation, and as such may be indicative of the degree of strain localization within the fault.

The relationship between seismicity and the imaged FZCs offers some insight into the dynamics of faulting. Along the San Andreas Fault, seismicity is confined to the edge (base) of the imaged FZCs at Hollister (Parkfield) (Figure 5). This spatial

separation between seismicity and the FZC suggests that fluids may inhibit seismicity in the upper crust. Unsworth et al. (2000) proposed that FZCs composed of fluid-saturated fault breccia are too weak to accumulate the shear stresses necessary to undergo brittle failure. This hypothesis, however, requires that fluids within the fault zone are hydraulically conductive (at hydrostatic pressure), as overpressured fluids tend to induce rather than inhibit seismicity. Studies by Townend & Zoback (2000) find this to be the case, and infer that interconnected faults and fractures help to maintain hydrostatic pressure.

Based on the discussion until now, is it possible to relate the imaged conductivity anomalies to fault zone architecture? Magnetotellurics provides one piece of the puzzle, imaging some or all of a fault's damage zone while remaining blind to the narrow fault core. Of the faults studied, the imaged FZCs are best explained by fluid-filled fractures, and thus the MT images also provide indirect information on fluid supply and fault zone permeability. Seismicity, on the other hand, can pinpoint the core of a fault, but provides no information about the damage zone of a fault. It is the spatial relationship between the active shear plane (defined by seismicity and/or the fault trace) and the imaged FZC that can be used to shed light upon the extent, symmetry, and hydrogeology of a fault. Figure 9, based on this idea, presents a classification of fault zone architecture within the framework of this study.

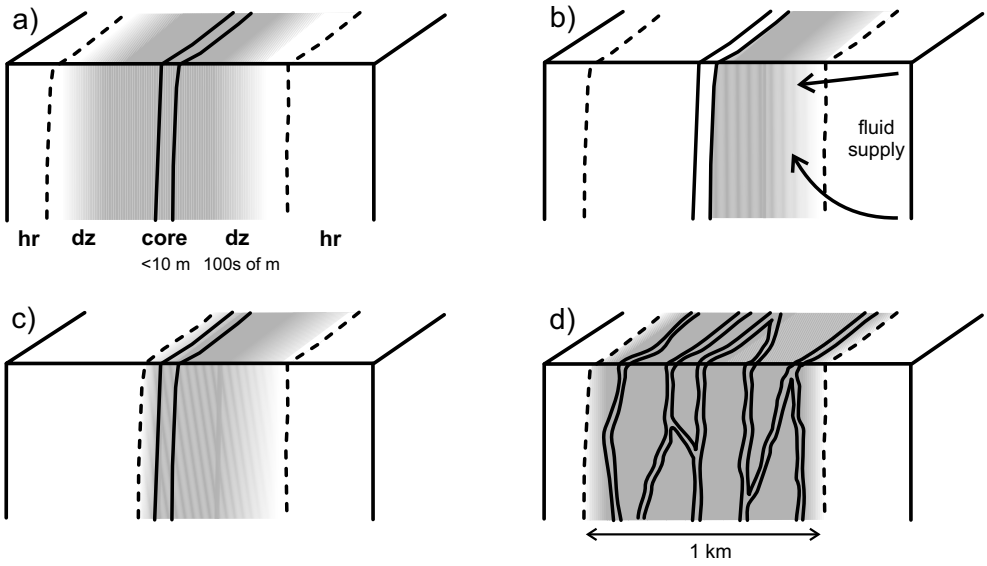

Figure 9: Interrelation of the conceptual model of large-scale strike-slip fault zones with electrical conductivity images. The FZCs are shaded in grey, arrows indicate fluid flow. hr: undeformed host rock (protolith); dz: damage zone. Dashed lines indicate the gradual transition from damage zone to host rock. See text for discussion.

(i) 'Classical' symmetric fault zone (Figure 9(a)). Given a symmetric deformation zone, seismicity and the surface trace would align with the centre of the FZC. The FZC thus reflects the entire permeable damage zone. Fracture density mapping would further reveal a symmetric damage profile peaked over the fault core. This scenario is similar to what is seen at Parkfield, though structural confirmation is unavailable due to a lack of outcrop.

(ii) Symmetric damage zone with an impermeable fault seal (Figure 9(b)). Seismicity and the surface trace will in this case be aligned with one edge of the FZC, rather than the centre. As in the previous case, however, structural mapping would reveal a symmetric fracture distribution. Due to an impermeable fault core, only the side of the damage zone penetrated by fluids is imaged with MT. The existence and location of the FZC can thus be directly linked to local fluid supply. This type of image is relevant to a number of the locations discussed in this paper. Along the West Fault, the surface trace locates at the edge of the imaged FZC, a symmetric fracture distribution is found, and fluid supply is clearly one-sided (controlled by topography). A similar conductivity image is found at the Arava Fault, where an impermeable seal is also believed to be in place. In contrast, however, the associated layer of high conductivity is not related to a damage zone. The San Andreas Fault at Hollister is, similar to the West Fault, characterized by a fault core aligned with the edge of the FZC. There is further evidence that fluids are supplied from the east side of the fault plane, where the FZC is imaged. Unlike at the WF, however, the absence of structural mapping precludes us from attributing these observations to an impermeable fault seal.

(iii) Asymmetric fault zone (Figure 9(c)). An asymmetric fault zone, in which damage is concentrated largely on one side of the fault, is plausible where a pronounced strength contrast exists across the fault. Though not common in the literature, an asymmetric damage zone has been suggested for the Punchbowl fault in southern California (Schulz & Evans, 2000). Concerning our observations, the spatial relation between seismicity and the FZC would be similar to the previous case shown in Figure 9(b). The FZC would correlate with the mechanically weaker, and probably more permeable lithology. Structural mapping would provide a clear means of differentiating between this and the previous case. The San Andreas Fault at Hollister may fall into this class of fault zone. There is a known lithology contrast between the Salinian granite and the highly deformed Franciscan Complex, within which the FZC is imaged. In the absence of further information, however, it is not possible to attribute the observations at Hollister to this or the previous class.

(iv) Anastomosing fault zone (Figure 9(d)). Faulkner et al. (2003) expand upon the conceptual model of large strike slip fault zones, drawing attention to fault zones in phyllosilicate-rich material which exhibit broad damage zones composed of anastomosing strands of fault gouge bands (Figure 9(d)). The MT image in this case is difficult to predict, and will depend on both the relative permeability within the fault zone and the spacing and lateral extent of gouge bands. It is, however, possible that such a fault zone could exhibit strong electrical anisotropy, similar to what we observe at the WF/OL in Namibia.

3.2 The deeper picture

The discussion has until now focused on the upper-crustal structure of active fault zones, such as the SAF and DST, and the currently inactive WF. In order to understand better the dynamics of faulting and its relation to lithospheric driving forces, a whole-fault picture is needed. Figure 10 presents an adaptation of *Sibson's* (1983) view on the downward continuation of major fault zones together with a range of models inferred from published regional studies. An open question centres on whether shear zones remain localized in the ductile regime and retain a constant width (Figure 10(a))

or broaden with increasing depth (Figure 10(c)), consistent with the increased role of dislocation creep at elevated temperatures. Molnar et al. (1999) suggest that continuous deformation may occur within the ductile regime, implying a vertical decoupling around the brittle-ductile transition (Figure 10(d)).

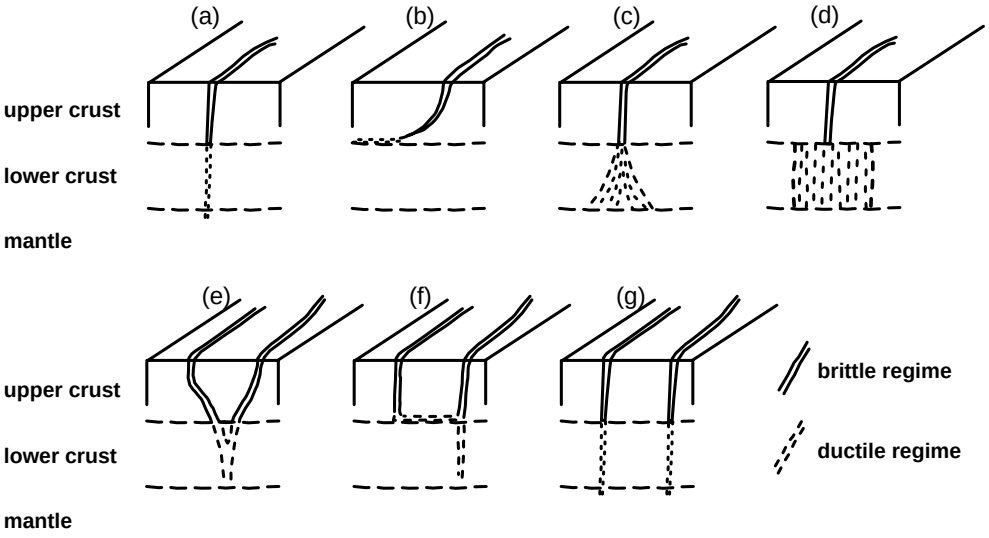

Figure 10: A range of end-member models for ductile shearing in the lower crust and upper mantle: (a) localized deformation cutting the lithosphere (e.g. Norris & Cooper, 2003), (b) listric fault soling into lower crustal detachment, (c) broadening deformation governed by lower crustal rheology and temperature (e.g. Hanmer (1988)), (d) continuous instead of localized deformation of lower crust and mantle lithosphere (e.g. Molnar et al., 1999). Models discussed for the SAF system of parallel upper crustal fault strands: (e) distributed upper-crustal strain with a common ductile root (Parsons & Hart, 1999), (f) upper crustal faults connected via décollement (Brocher et al., 1994), (g) singular through-going faults (Henstock et al., 1997).

Seismology provides the only other means to image *in situ* lower-crustal shear zones, however these images are not always in strict accordance with one another. A case in point is the linkage of subparallel strands of the SAF at depth. Studies within and north of the San Francisco Bay area argue for faults merging in the lower crust (10(e)), connected by a mid-crustal detachment (10(f)), and remaining parallel and separate throughout the entire crust (10(g)) (Parsons & Hart, 1999; Brocher et al., 1994; Henstock et al., 1997).

To assess the structure of lower-crustal shear zones with MT we face the difficulty of decreasing resolution with increasing depth, as well as the masking effect of upper-crustal conductivity. Electromagnetic studies across the Alpine Fault in New Zealand Southern Alps (Ingham & Brown, 1998; Wannamaker et al., 2002) show quite clearly that observed conductivity anomalies coincide with fault zones in the upper crust. However, the deeper structures of the Alpine Fault are clouded, and the lower crust as imaged appears generally conductive but unstructured. A way to overcome this resolution obstacle is to study exhumed fossil shear zones as analogues for the ductile roots of modern fault zones. This is of course a well-known strategy among structural geologists, the investigation the Ivrea-Verbano zone in the Italian Southern

Alps (Rutter et al., 1995) serving as a representative example.

The WF/OL, one of the major fault zones within the Damara orogen, originated in a collisional setting and has been reactivated several times. Metamorphic facies indicate the area surrounding the WF/OL was once at mid-crustal depths. The conductivity model in Figure 8(b) indicates that the WF/OL is not a single, narrow fault but rather a 10 km wide anisotropic fault zone with high conductivity parallel to strike. In general, MT cannot distinguish between intrinsic and structural anisotropy (see section 1.1.4), however, graphite-bearing marbles in the vicinity suggest that graphite films or lamellae may exist along shear planes within the lineament. Causes for high conductivity in lower-crustal shear zones are discussed in some detail in Wannamaker et al. (2002) for the Alpine Fault - a modern analogue of the WF/OL. It is the stability of graphite over long time spans combined with its high conductivity (when connected by shearing) which makes graphite an ideal contrast medium for studying the structure of fault zones at depth (Boerner et al., 1996; Wannamaker, 2000).

The depth of the modelled anisotropic zone in Figure 8(b) must be at least 14 km. Considering that the upper crust has already been eroded, this suggests the fault zone penetrated throughout the entire crust. The conductivity structure of the WF/OL thus supports a model with strain localized within a zone of moderate width in the lower crust and falls somewhere between the models depicted by Figures 10(c) and 10(d). The width of 10 km of this zone is in the range of observed and imaged mylonitic shear zones (Herquel et al., 1999; Henstock et al., 1997; Norris & Cooper, 2003, and references therein) and suggests localized strain compared to the discontinuous deformation model in Figure 10(d). The anisotropy in electrical conductivity implies that within this zone strain remains concentrated on sub-vertical anastomosing shear zones of relatively narrow width (semi-continuous deformation of the middle and lower crust).

Sutures and their investigations can thus provide insights into the former ductile lower crust (e.g. Banks et al., 1996; Eisel & Haak, 1999; Eisel et al., 2001; Santos et al., 1999, 2002; Almeida et al., 2001; Tauber et al., 2003). However, to unravel the lower-crustal structure of former times requires high resolution images of the present upper crust, and only with a sufficiently high areal site coverage can we constrain the presence and nature of electrical anisotropy. Often MT studies in basement complexes, such as the Canadian shield (Jones, 1999; Jones et al., 2001, 2003) focus on the regional conductivity distribution. While these experiments resolve deep lithospheric anomalies, the structure of fossil shear zones in the upper crust remains poorly resolved.

4 Conclusions

Electrical images from the San Andreas Fault in California, the West Fault in Chile and the Arava Fault in Jordan show both similarities and differences in their subsurface structure of the upper crust.

Typical of many of the young (as compared to fossil) faults investigated in this paper are sub-vertical regions of high conductivity, associated with the faults' damage zones. Fluids distributed within the fracture network of the damage zone generally explain the observed high conductivity. At least for the SAF, the MT images reveal a correlation between FZC magnitude (lateral conductance) and seismicity. The creeping segment of the SAF at Hollister, associated with the highest fault zone conduc-

tance, is characterized by abundant microseismicity and a lack of strong earthquakes. In contrast, the locked segment near Carrizo Plain, where a low-conductance fault zone is imaged, suffers large and damaging earthquakes. Within this framework, the shallow and weak FZCs of the currently inactive WF and the locked SAF at Carrizo Plain may be imaging a closing fracture network across the entire fault zone, i.e. cementation and sealing processes are in operation.

The image of the AF in Jordan appears to be an exception, as it shows a distinct lack of an electrically conducting deformation zone at its centre. The lack of a FZC in the brittle crust is coupled with the fault acting as a barrier to cross-fault fluid transport due to an impermeable fault seal, a lithological contrast across the fault, or some combination of the two. At the SAF and WF, the widths of the FZCs are on the order of a few hundred meters, in agreement with independent estimates of damage-zone width. According to Mitra & Ismat (2001), fault zones can grow in width due to repeated cycles of healing and reloading with successive rupturing. In contrast, the narrow, meter-scale damage zone at the AF is the result of a faulting mechanism where strain is extremely localized, apparently over long periods of time.

Care must be taken when interpreting electrical images of fault zones as conductivity structures are not invariably linked to specific architectural units within the fault. A reasonably comprehensive whole-fault picture is best obtained by combining MT images (fluids in fracture nets) with information from seismology (fault core or active slip plane) and structural geology (fracture density). A FZC may image either the entire damage zone including the fault's core (e.g. the SAF at Parkfield) or some part of it (e.g. the WF in Chile or the SAF at Hollister). The narrow core of a fault is beyond the resolution power of MT. However, taking into account the sealing potential of fault gouge, the position of a fault core can be inferred for at least some of the examined faults.

Fossil shear zones, often exhumed from mid-crustal depths, can provide insight into former lower-crustal shear zones. In the absence of large volumes of fluids, as suggested for the other fault systems, graphite films, interconnected through shearing, can cause the observed high electrical conductivity. To resolve structural details of fossil shear zones, however, requires high resolution images of today's upper crust. The fossil Waterberg Fault/Omaruru Lineament in Namibia is imaged as a 10 km wide and 14 km deep zone of anisotropic conductivity. The present level of exhumation suggests that the WF/OL penetrated the entire crust as a relatively narrow shear zone.

The examples presented in this paper illustrate the utility of the magnetotelluric method in imaging fault zone structure within the brittle crust. High resolution images are obtained if data are gathered with a dense site spacing on the order of one-hundred meters, ideally with detailed areal coverage of the target region. The conductivity structures associated with fault zones in the brittle crust reflect a complex interplay between lithology, fluid supply, permeability, and fault geometry. This combination can best be untangled for an individual fault zone using additional information from structural geology and seismology.

Acknowledgements

We thank Dan Faulkner, Phil Wannamaker, and an anonymous reviewer for their critical and constructive comments, which have helped to clarify this manuscript. The existence of the Geophysical Instrument Pool Potsdam and Electromagnetic Consor-

tium for Studies of the Continents made possible the high-resolution studies discussed herein. One of the authors (PB) was funded by the Alexander von Humboldt Foundation.

References

Allen, C., 1968. The tectonic environments of seismically active and inactive areas along the San Andreas fault system, in *Proceedings of conference on geologic problems of the San Andreas fault system*, edited by W. Dickinson & A. Grantz, pp. 70–82, Stanford University Publications.

Almeida, E., Pous, J., Monteiro-Santos, M., Fonesca, P., Marcuello, A., Queralt, P., Nolasco, R., & Mendes-Victor, L., 2001. Electromagnetic imaging of transpressional tectonics in SW Iberia, *Geophysical Research Letters*, **28**(3), 439–442.

Ambraseys, N. N. & Jackson, J. A., 1998. Faulting associated with historical and recent earthquakes in the Eastern Meaditerranean region, *Geophysical Journal International*, **133**, 390–406.

Archie, G. E., 1942. The electrical resistivity log as an aid in determining some reservoir characteristics, *Transactions of the American Institute of Mining, Metallurgical and Petroleum Engeneers*, **146**, 54–62.

Argus, D. & Gordon, R., 2001. Present day motion across the Coast Ranges and San Andreas fault system in central California, *Geological Society of America Bulletin*, **113**, 1580–1592.

Banks, R. J., Livelybrooks, D., Jones, P., & Longstaff, R., 1996. Causes of high crustal conductivity beneath the Iapetus Suture Zone in Great Britain, *Geophysical Journal International*, **124**, 433–455.

Bedrosian, P., Unsworth, M., Egbert, G., & Thurber, C., 2004. Geophysical images of the creeping segment of the San Andreas Fault: Implications for the role of crustal fluids in the earthquake process, *Tectonophysics*, **385**, 137–158.

Bedrosian, P. A., Unsworth, M. J., & Egbert, G., 2002. Magnetotelluric imaging of the creeping segment of the San Andreas Fault near Hollister, *Geophysical Research Letters*, **29**(11), 10.1029/2001GL014119.

Belmonte, A., 2002. *Crustal seismicity, structure and rheology of the upper plate between the Pre-Cordillere and the volcanic arc in northern Chile (22° S-24° S)*, Ph.D. thesis, Free University Berlin, http://www.diss.fu-berlin.de/2002/202/.

Ben-Zion, Y. & Sammis, C. G., 2003. Characterization of fault zones, *Pure and Applied Geophysics*, **160**, 677–715.

Bennett, R., Davis, J., & Wernicke, B., 1999. Present-day pattern of Cordilleran deformation in the western United States, *Geology*, **27**, 371–374.

Boerner, D., Kurtz, R., & Craven, J., 1996. Electrical conductivity and paleoproterozoic foredeeps, *Journal of Geophysical Research*, **101**(B6), 13775–13791.

Brocher, T. M., McCarthy, J., Hart, P. E., Holbrook, W. S., Furlong, K. P., McEvilly, T. V., Hole, J. A., & Klemperer, S. L., 1994. Seismic evidence for a lower-crustal detachment beneath San Francisco Bay, California, *Science*, **265**, 1436–1439.

Caine, J. S., Evans, J. P., & Forster, C. P., 1996. Fault zone architecture and permeability structure, *Geology*, **24**(11), 1125–1128.

Catchings, R., Rymer, M., Goldman, M., Hole, J., Huggins, R., & Lippus, C., 2002. High-resolution seismic velocities and shallow structure of the San Andreas fault zone at Middle Mountain, Parkfield, California, *Bulletin of the Seismological Society of America*, **92**, 2493–2503.

Chester, F. M. & Logan, J. M., 1986. Implications for mechanical properties of brittle faults from observations of the Punchbowl fault zone, California, *Pure and Applied Geophysics*, **124**(1/2), 79–106.

Chester, F. M., Evans, J. P., & Biegel, R. L., 1993. Internal structure and weakening mechanisms of the San Andreas Fault, *Journal of Geophysical Research*, **98**, 771–786.

Daly, M., 1989. Rift basin evolution in africa: the influence of reactivated steep basement shear zones, in *Inversion Tectonics*, edited by G. Cooper, vol. 44 of **The Geological Society Special Publications**, pp. 309–334, London.

Daly, M. C., 1986. Crustal shear zones and thrust belts: their geometry and continuity in Central Africa, *Philosophical Transactions Royal Society of London*, **317**(A), 111–128.

Doyen, P., 1988. Permeability, conductivity, and pore geometry of sandstone, *Journal of Geophysical Research*, **93**, 7729–7740.

Eberhart-Phillips, D., Stanley, W. D., Rodriguez, B. D., & Lutter, W. J., 1995. Surface seismic and electrical methods to detect fluids related to faulting, *Journal of Geophysical Research*, **100**(B7), 12919–12936.

Eisel, M. & Haak, V., 1999. Macro-anisotropy of the electrical conductivity of the crust: a magnetotelluric study of the German Continental Deep Drilling Site (KTB), *Geophysical Journal International*, **136**, 109–122.

Eisel, M., Haak, V., Pek, J., & Cerv, V., 2001. A magnetotelluric profile across the KTB surrounding: 2D and 3D modelling results, *Journal of Geophysical Research*, **106**(B8), 16061–16079.

Electromagnetic Research Group for the Active Fault, 1982. Low electrical resistivity along an active fault, *Journal of Geomagnetism and Geoelectricity*, **34**, 103–127.

ELEKTB Group, 1997. KTB and the electrical conductivity of the crust, *Journal of Geophysical Research*, **102**(B8), 18289–18305.

Ellsworth, W. L., 1990. Earthquake history, 1769-1989, in The San Andreas Fault System, California, *edited by R. Wallace, United States Geological Survey, Professional Paper 1515, Reston, VA*, pp. 153–188.

Evans, J. P., Forster, C. B., & Goddard, J. V., 1997. Permeability of fault-related rocks and implications for hydraulic structure of fault zones, *Journal of Structural Geology*, **19**(11), 1393–1404.

Faulkner, D. R., Lewis, A. C., & Rutter, E. H., 2003. On the internal structure and mechanism of large strike-slip fault zones: field observations of the Caboneras fault in southeasten Spain, *Tectonophysics*, **367**, 235–251.

Freund, R., Garfunkel, Z., Zak, I., Goldberg, M., Weissbrod, T., & Derin, B., 1970. The shear along the Dead Sea rift, *Philosophical Transactions Royal Society of London*, **267**, 117–126.

Garfunkel, Z. & Avraham, Z.-B., 1996. The structure of the Dead Sea basin, *Tectonophysics*, **266**, 155–176.

Gudmundsson, A., 2000. Active fault zones and groundwater flow, *Geophysical Research Letters*, **27**(18), 2993–2996.

Guéguen, Y. & Palciauskas, V., 1994. *Introduction to the Physics of Rocks*, Princeton University Press, UK.

Haak, V. & Hutton, V. R. S., 1986. Electrical resistivity in continental lower crust, in *The Nature of the Lower Continental Crust*, edited by J. B. Dawson, vol. 24 of **The Geological Society Special Publications**, pp. 35–49, London.

Haberland, C., Agnon, A., El-Kelani, R., Maercklin, N., Qabbani, I., Rümpker, G., Ryberg, T., Scherbaum, F., & Weber, M., 2003. Modeling of seismic guided waves at the Dead Sea Transform, *Journal of Geophysical Research*, 10.1029/2002JB002309.

Hanmer, S., 1988. Great Slave Lake shear zone, Canadian Shield: reconstructed vertical profile of a crustal-scale fault zone, *Tectonophysics*, **149**, 245–264.

Henstock, T., Levander, A., & Hole, J., 1997. Deformation in the lower crust of the San Andreas Fault system in northern California, *Science*, **278**, 650–653.

Herquel, G., Tapponnier, P., Wittlinger, G., Mei, J., & Danian, S., 1999. Teleseismic shear wave splitting and lithospheric anisotropy beneath and across the Altyn Tagh fault, *Geophysical Research Letters*, **26**, 3225–3228.

Hickman, S. H., Sibson, R., & Bruhn, R., 1995. Mechanical involvment of fluids in faulting, *Journal of Geophysical Research*, **100**, 12831–12840.

Hoffmann-Rothe, A., 2002. *Combined structural and magnetotelluric investigation across the West Fault zone in the Andes of northern Chile*, Ph.D. thesis, University of Potsdam, http://www.gfz-potsdam.de/bib/pub/str0212/0212.htm.

Hoffmann-Rothe, A., Ritter, O., & Janssen, C., 2004. Correlation of Electrical Conductivity and Structural Damage at a Major Strike- Slip Fault in Northern Chile, *Journal of Geophysical Research*, in press.

Holdsworth, R. E., Hand, M., Miller, J. A., & Buick, I. S., 2001. Continental reactivation and reworking: an introduction, in *Continental Reactivation and Reworking*, edited by J. A. Miller, R. E. Holdsworth, I. S. Buick, & M. Hand, vol. 184 of **The Geological Society Special Publications**, pp. 1–12, London.

Holzförster, F., Stollhofen, H., & Stanistreet, I. G., 1999. Lithostratigraphy and depositional environments in the Waterberg-Erongo area, central Namibia, and correlation with the main Karoo Basin, South Africa, *Journal of African Earth Sciences*, **29**, 105–123.

Ingham, M. & Brown, C., 1998. A magnetotelluric study of the Alpine Fault, New Zealand, *Geophysical Journal International*, **135**(2), 542–552.

Irwin, W., 1990. Geology and plate-tectonic development, in *The San Andreas Fault System, California*, edited by R. Wallace, pp. 61–80, United States Geological Survey, Professional Paper 1515, Reston, VA.

Irwin, W. & Barnes, I., 1975. Effect of geologic structure and metamorphic fluids on seismic behavior of the San Andreas fault system in central and northern California, *Geology*, **3**, 713–716.

Janssen, C., Hoffmann-Rothe, A., Tauber, S., & Wilke, H., 2002. Internal structure of the Precordilleran fault system (Chile) - insights from structural and geophysical observations, *Journal of Structural Geology*, **24**, 123–143.

Janssen, C., Lüders, V., & Hoffmann-Rothe, A., 2004. Contrasting styles of fluid-rock interaction within the West Fissure Zone in northern Chile, in *Flow processes in Faults and Shear Zones*, vol. 224, pp. 141–160.

Jödicke, H., Kruhl, J. H., Ballhaus, C., Giese, P., & Untiedt, J., 2004. Syngenetic, thin graphite-rich horizons in lower crustal rocks from the Serre San Bruno, Calabria (Italy), and implications for the nature of high-conducting deep crustal layers, *Physics of the Earth and Planetary Interior*, **141**, 37–58.

Jones, A. G., 1999. Imaging the continental upper mantle using electromagnetic methods, *Lithos*, **48**, 57–80.

Jones, A. G., Ferguson, I. J., Chave, A., Evans, R., & McNeice, G., 2001. Electrical lithosphere of the Slave craton, *Geology*, **29**(5), 423–426.

Jones, A. G., Lezaeta, P., Ferguson, I. J., Chave, A. D., Evans, R. L., Garcia, X., & Spratt, J., 2003. The electrical structure of the Slave craton, *Lithos*, **71**(2-4), 505–527.

Klinger, Y., Avouac, J. P., Karaki, N. A., Dorbath, L., Bourles, D., & Reyss, J. L., 2000. Slip rate on the Dead Sea transform fault in northern Araba valley (Jordan), *Geophysical Journal International*, **142**, 755–768.

Klinger, Y., Avouac, J. P., Karaki, N. A., Dorbath, L., & Tisnerat, N., 2000. Seismic behaviour of the Dead Sea fault along Araba valley, Jordan, *Geophysical Journal International*, **142**, 769–782.

Ledo, J., Queralt, P., Marti, A., & Jones, A., 2002. Two-dimensional interpretation of three-dimensional magnetotelluric data; an example of limitations and resolution, *Geophysical Journal International*, **150**, 127–139.

Li, S., Unsworth, M. J., Booker, J., Wei, W., Tan, H., & Jones, A., 2003. Partial melt or aqueous fluid in the mid-crust of southern Tibet? Constraints from INDEPTH magnetotelluric data, *Geophysical Journal International*, **153**, 289–304.

Li, Y. G., Vidale, J., & Cochran, E., 2004. Low-velocity damaged structure of the San Andreas fault at Parkfield from fault-zone trapped waves, *Geophysical Research Letters*, **31**, doi:10.1029/2003GL019044.

Liu, J., Walter, J., & Weber, K., 2002. Fluid-enhanced low-temperature plasticity of calcite marble: Microstructures and mechanisms, *Geology*, **30**, 787–790.

Luque, F. J., Pasteris, J. D., Wopenka, B., Rodas, M., & Barrenecha, J. F., 1998. Natural fluid-deposited graphite: mineralogical characteristics and mechanisms of formation, *American Journal of Science*, **298**, 471–498.

McNeice, G. W. & Jones, A. G., 2001. Multisite, multifrequency tensor decomposition of magnetotelluric data, *Geophysics*, **66**, 158–173.

Miller, R., 1983. The Pan-African Damara Orogen of the South West Africa / Namibia, *Special Publication of the Geological Society of South Africa*, **11**, 431–515.

Mitra, G. & Ismat, Z., 2001. Microfracturing associated with reactivated fault zones and shear zones: what can it tell us about deformation history?, in *The Nature and Tectonic Significance of Fault Zone Weakening*, edited by R. E. Holdsworth, R. A. Strachan, J. F. Magloughlin, & R. J. Knipe, vol. 186 of **The Geological Society Special Publications**, pp. 113–140, London.

Molnar, P., Anderson, H. J., Audoine, E., Eberhart-Philips, D., Gledhill, K. R., Klosko, E. R., McEvilly, T. V., Okaya, D., Savage, M. K., Stern, T., & Wu, F. T., 1999. Continuous Deformation versus faulting through the continental lithosphere of New Zealand, *Science*, **286**, 516–519.

Norris, R. J. & Cooper, A. F., 2003. Very high strains recorded in mylonites along the Alpine Fault, New Zealand: implications for the deep structure of plate boundary faults, *Journal of Structural Geology*, **25**, 2141–2157.

O'Neil, J., 1984. Water-rock interactions in fault gouge, *Pure and Applied Geophysics*, **122**, 440–446.

Park, S. K., Thompson, S. C., Rybin, A., Batalev, V., & Bielinski, R., 2003. Structural constraints in neotectonic studies of thrust faults from the magnetotelluric method, *Tectonics*, **22**(2), 10.1029/2001TC001318.

Parsons, T. & Hart, P. E., 1999. Dipping San Andreas and Hayward faults revealed beneath San Francisco Bay, California, *Geology*, **27**(9), 839–842.

Pek, J. & Verner, T., 1997. Finite-difference modelling of magnetotelluric fields in two-dimensional anisotropic media, *Geophysical Journal International*, **132**, 535–548.

Raab, M. J., Brown, R. W., Gallagher, K., Carter, A., & Weber, K., 2002. Late Cretaceous reactivation of major crustal shear zones in northern Namibia: constraints from apatite fission track analysis, *Tectonophysics*, **349**(1-4), 75–92.

Ritter, O., Haak, V., Rath, V., Stein, E., & Stiller, M., 1999. Very high electrical conductivity beneath the Münchberg Gneiss area in southern Germany: Implications for horizontal transport along shear planes, *Geophysical Journal International*, **139:2**, 161–170.

Ritter, O., Ryberg, T., Weckmann, U., Hoffmann-Rothe, A., Abueladas, A., Garfunkel, Z., & DESERT Research group, 2003. Geophysical images of the Dead Sea Transform in Jordan reveal an impermeable barrier for fluid flow, *Geophysical Research Letters*, **30**(14), 1741, doi:10.1029/2003GL017541.

Ritter, O., Weckmann, U., Vietor, T., & Haak, V., 2003. A magnetotelluric study of the Damara Belt in Namibia 1. regional scale conductivity anomalies, *Physics of the Earth and Planetary Interior*, **138**, 71–90, doi:10.1016/S0031–9201(03)00078–5.

Rodi, W. & Mackie, R. L., 2001. Nonlinear conjugate gradients algorithm for 2D magnetotelluric inversion, *Geophysics*, **66**, 174–187.

Rümpker, G., Ryberg, T., Bock, G., & DESERT Seismology Group, 2003. Boundary-layer mantle flow under the Dead Sea transform fault inferred from seismic anisotropy, *Nature*, **425**, 497 – 501.

Rutter, E., Brodie, K., & Evans, P., 1995. Structural geometry, lower crustal magmatic underplating and lithospheric stretching in the Ivrea-Verbano zone, northern Italy, *Journal of Structural Geology*, **15**(3-5), 647–662.

Santos, F., Pous, J., Almeida, E., Queralt, P., Marcuello, A., Matias, H., & Victor, L., 1999. Magnetotelluric survey of the electrical conductivity of the crust across the Ossa Morena zone and South Portugese zone suture, *Tectonophysics*, **313**, 449–462.

Santos, F. A. M., Mateus, A., Almeida, E. P., Pous, J., & Mendes-Victor, L. A., 2002. Are some of the deep crustal conductive features found in SW Iberia caused by graphite?, *Earth and Planetary Science Letters*, **201**, 353–367.

Scholz, C. H., 1987. Wear and gouge formation in brittle faulting, *Geology*, **15**, 493–495.

Scholz, C. H., Dawers, N. H., Yu, J.-Z., Anders, M. H., & Cowie, P. A., 1993. Fault growth and fault scaling laws: preliminary results, *Journal of Geophysical Research*, **98**(B12), 21951–21961.

Schulz, S. E. & Evans, J. P., 2000. Mesoscopic structure of the Punchbowl fault, southern California and the geologic and geophysical structure of active strike-slip faults, *Journal of Structural Geology*, **22**, 913–930.

Sibson, R. H., 1983. Continental fault structure and the shallow earthquake source, *Journal of the Geological Society*, **140**, 741–767.

Smith, J., 1995. Understanding telluric distortion matrices, *Geophysical Journal International*, **122**, 219–226.

Swift, C., 1967. *A magnetotelluric investigation of an electrical conductivity anomaly in the southwestern United States*, Ph.D. Thesis, M.I.T. Cambridge, Mass.

Tauber, S., Banks, R., Ritter, O., & Weckmann, U., 2003. A high-resolution magnetotelluric survey of the Iapetus Suture Zone in southwest Scotland, *Geophysical Journal International*, **153**, 548–568.

Thurber, C., Roecker, S., Ellsworth, W., Chen, Y., Lutter, W., & Sessions, R., 1997. Two-dimensional seismic image of the San Andreas fault in the northern Gabilan Range, central California: evidence for fluids in the fault zone, *Geophysical Research Letters*, **24**, 1591–1594.

Thurber, C. H., Roecker, S., Roberts, K., Gold, M., Powell, L., & Rittger, K., 2003. Earthquake locations and three-dimensional fault zone structure along the creeping section of the San Andreas fault near Parkfield, CA: preparing for SAFOD, *Geophysical Research Letters*, **30**, doi:10.1029/2002GL016004.

Townend, J. & Zoback, M. D., 2000. How faulting keeps the crust strong, *Geology*, **28**(5), 399–402.

Unsworth, M. & Bedrosian, P. A., 2004. Electrical resistivity structure at the SAFOD site from magnetotelluric exploration, *Geophysical Research Letters*, **31**(12), 10.1029/2003GL019405.

Unsworth, M. J., Malin, P. E., Egbert, G. D., & Booker, J. R., 1997. Internal structure of the San Andreas fault at Parkfield, California, *Geology*, **25**(4), 359–362.

Unsworth, M. J., Egbert, G. D., & Booker, J. R., 1999. High resolution electromagnetic imaging of the San Andreas fault in central California, *Journal of Geophysical Research*, **104**, 1131–1150.

Unsworth, M. J., Bedrosian, P., Eisel, M., Egbert, G. D., & Siripunvaraporn, W., 2000. Along strike variations in the electrical structure of the San Andreas fault at Parkfield, California, *Geophysical Research Letters*, **27**(18), 3021–3024.

Wannamaker, P. E., 2000. Comment on The petrologic case for a dry lower crust by Bruce W. D. Yardley and John W. Valley, *Journal of Geophysical Research*, **105**, 6057 (1999JB900324).

Wannamaker, P. E., Jiracek, G. R., Todt, J. A., Caldwell, T. G., Gonzales, V. M., McKnight, J. D., & Porter, A. D., 2002. Fluid generation and pathways beneath an active compressional orogen, the New Zealand Alps, inferred from magnetotelluric data, *Journal of Geophysical Research*, **107**, 10.1029/2001JB000186.

Wdowinski, S., Bock, Y., Baer, G., Prawirodirdju, L., Bechor, N., Naaman, S., Knafo, R., Forrai, Y., & Melzer, Y., 2004. GPS measurements of current crustal-movements along the Dead Sea Fault, *Journal of Geophysical Research*, **109**, 10.1029/2003JB002640.

Weckmann, U., Ritter, O., & Haak, V., 2003. A Magnetotelluric study of the Damara Belt in Namibia 2. internal structure of the Waterberg Fault / Omaruru Lineament, *Physics of the Earth and Planetary Interior*, **138**, 91–112, doi:10.1016/S0031–9201(03)00079–7.

Weckmann, U., Ritter, O., & Haak, V., 2003. Images of the magnetotelluric apparent resistivity tensor, *Geophysical Journal International*, **155**, 456–468.

Wiese, H., 1962. Geomagnetische Tiefentellurik Teil II: die Streichrichtung der Untergrundstrukturen des elektrischen Widerstandes, erschlossen aus geomagnetischen Variationen, *Geofisica pura e applicata*, **52**, 83–103.

Scientific Technical Report STR 05/10

GeoForschungsZentrum Potsdam

Geophys. J. Int. (1998) **132,** 535–548

New equipment and processing for magnetotelluric remote reference observations

Oliver Ritter,[1] Andreas Junge[2] and Graham J. K. Dawes[3]

[1] *GeoForschungsZentrum Potsdam, Telegrafenberg,* D-14473 *Potsdam, Germany. E-mail: oritter@gfz.potsdam.de*
[2] *Institut für Meteorologie und Geophysik, Universität Frankfurt, Feldbergstrasse* 47, D-60323 *Frankfurt, Germany*
[3] *Department of Geology and Geophysics, University of Edinburgh, Grant Institute, West Mains Road, Edinburgh* EH9 3JW, *UK*

Accepted 1997 August 29. Received 1997 August 28; in original form 1997 January 24

SUMMARY

Robust estimates of magnetotelluric and geomagnetic response functions are determined using the coherency and expected uniformity of the magnetic source field as quality criteria. The method is applied on data sets of three simultaneously recording sites. For the data acquisition we used a new generation of geophysical equipment (S.P.A.M. MkIII), which comprises novel concepts of parallel computing and networked, digital data transmission. The data-processing results show that the amount of noise on the horizontal components of the magnetic field varies considerably in time, between sites and over the frequency range. The removal of such contaminated data beforehand is essential for most data-processing schemes, as the magnetic channels are usually assumed to be free of noise. The standard remote reference method is aimed at reducing bias in response function estimates. However, this does not necessarily improve their precision as our results clearly show. With our method, on the other hand, we can filter out source field irregularities, thereby providing suitable working conditions for the robust algorithm, and eventually obtain considerably improved results. Contrary to previous concepts, we suggest rejecting as much data as feasible in order to concentrate on the remaining parts of high-quality observations.

Key words: data processing, electromagnetic instrumentation, magnetotellurics.

1 INTRODUCTION

The magnetotelluric (MT) method is applied to determine the electrical conductivity distribution beneath the Earth's surface. Electric currents in the atmosphere give rise to magnetic field variations which induce electric currents in the Earth. For MT measurements, orthogonal components of the electric and magnetic fields are recorded as time variations at the surface of the Earth. In the frequency-domain representation, the electric and horizontal magnetic field components are linearly related by the impedance tensor $\boldsymbol{Z}$, a so-called response function of the Earth. The aim of electromagnetic data-processing procedures is to estimate these response functions as accurately as possible.

It is often rather difficult to acquire high-quality MT data because the measurements rely on a highly variable strength of the natural electromagnetic excitation. The signal amplitudes of the vertical variation field, for instance, are of the order of 10 000 times smaller than the static main field. More severe problems are caused by civilization, which produces all kinds of electromagnetic signals, for example from mains power supplies, electric railways, electric fences, radar and radio transmitters, etc. (Szarka 1988). These sources generate very coherent large-amplitude electromagnetic signals which are superimposed on the natural variation field. Such artificially produced events are therefore not electromagnetic noise, although they are considered noise by magnetotelluric practitioners. In practice, it is very difficult to distinguish coherent cultural signals from the natural electromagnetic fields in which we are interested. We aim to separate signal from noise at the data-processing stage by analysing data from frequently repeated experiments (long recording times) using modern statistical methods. However, to tackle the problems we require not only sophisticated data-processing procedures but also highly specialized geophysical instrumentation. Good equipment is particularly important, as it is usually impossible to recover erroneous field recordings by data-analysis methods.

There has been an enormous progress in MT data-processing algorithms over the past two decades; a review is given by Junge (1996). Progress has mainly come about through two developments—robust statistics and the remote reference method. Robust algorithms are based on data-adaptive weighting schemes, which aim to detect and reject outliers from a majority of *well-behaved* samples (e.g. Egbert & Booker 1986; Chave, Thomson & Ander 1987). The remote reference method requires simultaneously recorded horizontal

GJI000 18/2/98 09:07:37 3B2 version 5.20
The Charlesworth Group, Huddersfield 01484 517077

magnetic fields from two sites which ideally have only components of correlated signal and uncorrelated noise (Goubau, Gamble & Clarke 1978; Gamble, Goubau & Clarke 1979). The most promising results are achieved by a combination of both methods—a robust remote reference processing (e.g. Larsen 1989; Jones *et al.* 1989).

However, a robust remote reference processing is still a bivariate data-analysis tool, as a consequence of which the measured electromagnetic signals must be divided into noise-free dependent and noisy independent channels. This division is introduced for theoretical reasons, while we know of course that in practice all channels are affected by noise. Data-processing methods which allow noise in all channels have been introduced by Park & Chave (1984) and Chave & Thomson (1989), and more recently by Larsen *et al.* (1996) and Egbert (1997). It is extremely difficult, though, to estimate reliably the covariance matrix of the noise, which is necessary for a multivariate approach. A multivariate data processing will be superior to all other methods if the nature of the noise can be recognized correctly. However, its numerical application is rather costly and it might sometimes lead to incorrect results (Larsen 1989; Egbert 1997).

A new method is thus proposed in this paper. This method uses physical properties of the magnetic source field—its homogeneity and spatial coherence—to simplify the processing problem. Its application is demonstrated on noisy field data from southern Scotland, in which some apparently useless response function results are converted into interpretable curves. For the fieldwork, we used a new generation of geophysical instruments (S.P.A.M. MkIII), which facilitate simultaneous recordings of electromagnetic field data from many stations at high frequencies.

2 RESPONSE FUNCTION ESTIMATION

In the frequency domain, the complex relation between the electromagnetic signals can be written

$$\begin{pmatrix} E_x \\ E_y \end{pmatrix} = \begin{pmatrix} Z_{xx} & Z_{xy} \\ Z_{yx} & Z_{yy} \end{pmatrix} \begin{pmatrix} B_x \\ B_y \end{pmatrix}, \tag{1}$$

where $\mathbf{E}$ is the electric field in mV km^{-1}, $\mathbf{B}$ is the magnetic field in nT and Z_{ij} are the components of $\boldsymbol{Z}$. We assume plane-wave sources, dependence on frequency and Cartesian coordinate systems. x, y and z are defined to be positive when pointing towards the north, the east and downwards, respectively. A non-zero vertical magnetic field component is generated if lateral conductivity variations are of the order of the induction range of the observations. The geomagnetic response functions $\mathscr{A}$, $\mathscr{B}$ are defined in a similar manner to eq. (1):

$$B_z = \mathscr{A} B_x + \mathscr{B} B_y . \tag{2}$$

In practice, the response functions are estimated from imperfect data. From different samples we aim to choose our parameters so that the misfit to the data is minimized by some norm, e.g. L_1 or L_2. Generally, we must solve linear equations of the type

$$Z = aX + bY + \delta Z . \tag{3}$$

Z is the output channel of the linear system, which is normally associated with E_x, E_y or B_z, while X and Y are the input channels, associated with the horizontal magnetic fields B_x and B_y. The noise term δZ is assumed to affect only the output channel Z. Then, the solution for the response function a (and similarly for b) using the least-squares (LS) method is

$$a = \frac{\langle ZX^* \rangle \langle YY^* \rangle - \langle ZY^* \rangle \langle YX^* \rangle}{\langle XX^* \rangle \langle YY^* \rangle - \langle XY^* \rangle \langle YX^* \rangle} . \tag{4}$$

The bracketed terms indicate cross- or auto-spectra, calculated and stacked from individual time segments and averaged over a certain frequency band; the asterisk denotes a complex conjugate.

2.1 The remote reference method

Consider now all channels to be combinations of signal and noise, indicated by the indices S and N, e.g. $X := X_S + X_N$, etc. By definition, statistical noise is uncorrelated with the signal. If, additionally, noise between different channels is assumed to be uncorrelated and the signal is correlated, only the first term on the right-hand side of eq. (5) is non-zero:

$$\langle XY^* \rangle = \langle X_S Y_S^* \rangle + \langle X_S Y_N^* \rangle + \langle X_N Y_S^* \rangle + \langle X_N Y_N^* \rangle . \tag{5}$$

Auto-spectra, on the other hand, will always be contaminated:

$$\langle XX^* \rangle = \langle X_S X_S^* \rangle + \underbrace{\langle X_N X_N^* \rangle}_{=\text{bias}} , \tag{6}$$

and eventually cause biased response function estimates. Being based on the idea that magnetic fields recorded at two different sites have only uncorrelated noise components, the classical remote reference technique reduces the effects of bias (Goubau *et al.* 1978; Gamble *et al.* 1979). Using the input components from two sites, the impedance tensor can be rewritten as

$$\boldsymbol{Z}_r = (\mathbf{E}\mathbf{B}_r^*)(\mathbf{B}\mathbf{B}_r^*)^{-1} ; \qquad \mathbf{E}\mathbf{B}^* := \begin{pmatrix} \langle E_x B_x^* \rangle & \langle E_x B_y^* \rangle \\ \langle E_y B_x^* \rangle & \langle E_y B_y^* \rangle \end{pmatrix}, \tag{7}$$

where the subscript r denotes the fields of a remote site. Now, only cross-spectra of horizontal magnetic field components of local and remote sites appear in the solution of $\boldsymbol{Z}_r$. The estimation of $\boldsymbol{Z}_r$ is unbiased if the noise between the two sites is uncorrelated.

2.2 The source-field criterion

For magnetotelluric measurements in mid-latitudes in the period range below 10 000 s, the wavelengths of the inducing electromagnetic fields are generally large compared to their penetration depth in the Earth. Then, the influence of the source geometry on the response functions can be neglected; the source field is called *quasi-uniform*. For any two sites under these constraints, the horizontal magnetic field variations are connected by magnetic response functions (MRF) which are time-independent:

$$\mathbf{T} = (\mathbf{B}\mathbf{B}_r^*)(\mathbf{B}_r\mathbf{B}_r^*)^{-1} ; \qquad \mathbf{T} := \begin{pmatrix} T_{xx} & T_{xy} \\ T_{yx} & T_{yy} \end{pmatrix} . \tag{8}$$

For exactly uniform source fields and for a horizontally layered earth, $\mathbf{T} = \mathbf{I}$ for all frequencies. Lateral conductivity anomalies, however, also give rise to anomalous horizontal magnetic fields which are superimposed on the source fields. For the general case, the MRFs are therefore frequency-dependent, complex valued and different from unity (Larsen

et al. 1996). The gradient of the anomalous component is largest close to the edges of a lateral conductivity contrast, but decreases rapidly with increasing distance from the boundary (Banks, Irving & Livelybrooks 1993; Weaver 1994). Thus, the observed MRFs of densely spaced sites should, in general, be close to unity.

The ratio of predicted to measured signal energy between output and input channels is given by the multiple quadratic coherencies r_x^2 and r_y^2, where r_x refers to B_x and r_y to B_y as output channels:

$$r_x^2 = \frac{T_{xx}\langle B_x B_{xr}^* \rangle + T_{xy}\langle B_x B_{yr}^* \rangle}{\langle B_{xr} B_{xr}^* \rangle} . \tag{9}$$

The results for the multiple coherency can be biased due to noise in the auto-spectra in the denominator and in the response functions. The coherency will be close to 1, however, if local and remote sites are only little affected by noise. Processing results for single site and remote reference are the same if $r_{x,y}^2 = 1$.

The proposed source-field criterion causes data rejection based on two aspects: (1) if horizontal magnetic field components between two sites have low coherencies (coherency criterion) and (2) if the response functions are considerably different from unity (target criterion). The method is applied iteratively by comparison of both horizontal magnetic fields of the local site with all or some combinations of the reference site(s). Events with inconsistent horizontal magnetic field data are thereby removed step by step, leaving a reduced but cleaned data set for the final robust stacking. A more detailed discussion of the method is given in Section 4.

The appropriateness of the target criterion depends on the data set as the frequency range of the observations, the geological complexity and the distance between the sites have to be considered. From our experience, however, the target criterion can be used in general.

2.3 The iterative robust algorithm

Generally, the true noise distribution in our observations is unknown; however, applying least-square methods the noise has to be normally distributed to obtain maximum-likelihood estimates. Robust methods aim to single out moderate number of data that are not normally distributed. In that respect, response functions estimated with robust methods are less sensitive to a moderate amount of *bad* data or to an inadequately chosen statistical model. Robust processing of AMT data by automatic weighting algorithms has been widely used, for example by dividing the time-series into segments of equal length, estimating auto- and cross-spectra from each segment and stacking the weighted spectra after applying a smoothing window in the frequency domain.

As weighting of data can cause downward-biased estimation of variance, a better estimate is obtained using Huber's (1981) expression for asymptotic variances (*cf*. Egbert & Booker 1986, Appendix). However, the estimation of the number of degrees of freedom ν depends on the number of stacked spectra and the smoothing window for which the equivalent bandwidth may be used to estimate ν under the assumption that adjacent raw spectral values are statistically independent. As this assumption seems to be often violated, an attempt is made to estimate the true value of ν.

With the assumption that the weighted residuals are normally distributed with variance σ^2, the variance of the single-time-segment residuals obeys approximately a χ_ν^2 distribution with ν degrees of freedom. An estimate of ν is obtained directly from the distribution of σ. A property of the χ_ν^2 distribution is that its expectation is $E\{\sigma^2\} = \nu\sigma^2$ and its variance is $\mathrm{var}\{\sigma^2\} = 2\nu(\sigma^2)^2$. It follows that

$$\hat{\nu} = \frac{2(E\{\sigma^2\})}{\mathrm{var}\{\sigma^2\}} . \tag{10}$$

However, application of eq. (10) shows that the hypothetical estimate of ν from the shape of the spectral window is often severely overestimated.

In this context we describe a method developed by Junge (1990, 1992, 1994) which has been tested extensively on a huge volume of data from various regions. The algorithm has proven to be fast, reliable and efficient. The method combines two parts: (1) the χ^2 criterion and (2) the consistency criterion. (1) The χ^2 criterion examines whether a single-event spectrum fits into the global view of the majority of all data. Accordingly, the influence of a single-event spectrum is increased or decreased by a robust weighting scheme. (2) The consistency criterion reduces non-stationary contributions in the response functions by iteratively replacing a certain amount of the *bad* data with predicted values. A more detailed description of the algorithm is given in Appendix A.

In the present form, the estimation of confidence limits for the response functions is still based on a parametric model for the distribution of the noise. Chave *et al.* (1987) and Larsen *et al.* (1996) have suggested using the non-parametric jackknife method instead, as it will generally be more robust against deviations from the expected model.

3 S.P.A.M. MKIII

Before we concentrate further on aspects of the data processing, we would like to introduce the newly developed S.P.A.M. MkIII instrument which was used to collect our remote-referenced audiomagnetotelluric data sets.

S.P.A.M. systems are short-period automatic magnetotelluric instruments developed since 1980 by Graham Dawes at the University of Edinburgh; work on the new generation of instruments started in 1990 (Dawes 1990). Today, S.P.A.M. MkIII systems are successfully used by a number of research institutions across Europe, including the geophysical equipment pools of NERC and GeoForschungsZentrum Potsdam and the geophysics departments of the universities in Edinburgh, Frankfurt and TU Berlin. An early summary of the ideas behind the instrument can be found in Ritter & Dawes (1992); more up-to-date summaries are given by Ritter (1995) and Nascimento (1997).

S.P.A.M. MkIII operates as a networked instrument. This network consists of geophysical sensors with distributed analogue and digital processing and control units. Networks can be very simple, for example a standard five-component MT configuration, or they can be complex systems, where many compatible S.P.A.M. MkIII modules (for example from different research institutions) are interconnected.

The network communication is based on bi-directional digital data transfer, and all devices on the network are synchronized. The timing of S.P.A.M. MkIII can also be

controlled by GPS clocks in order to synchronize recordings of separated networks over large distances. Because digitally transmitted signals do not deteriorate with distance, reference fields from remote sites can be collected together with signals from local sites. Furthermore, the instrument is not restricted to recording electromagnetic data only, but can be used more generally for geophysical data acquisition, for example a combination of seismic and electromagnetic recordings. Improved computational power allows parts of the analogue signal conditioning to be replaced by digital signal processing. Consequently, the design of the analogue sections has become simpler, which means improved reliability and better noise figures. The computational heart of S.P.A.M. MkIII is the *transputer*, a microprocessor with built-in parallel processing and network support. Parallel execution of processes enables a digital and concurrent generation of the frequency bands used for the data processing. This is an important improvement over existing instruments as it results in shorter recording times. Until now, different frequency bands had to be recorded sequentially.

All parts of the instrument are built in a highly modular fashion to allow test facilities, modifications, replacements or enhancements of parts of the system without having to change everything. The overall power consumption is greatly improved over older generations of S.P.A.M. (and comparable instruments) because new low-power devices can be used throughout the system.

A S.P.A.M. MkIII network consists of four major nodes (see Fig. 1).

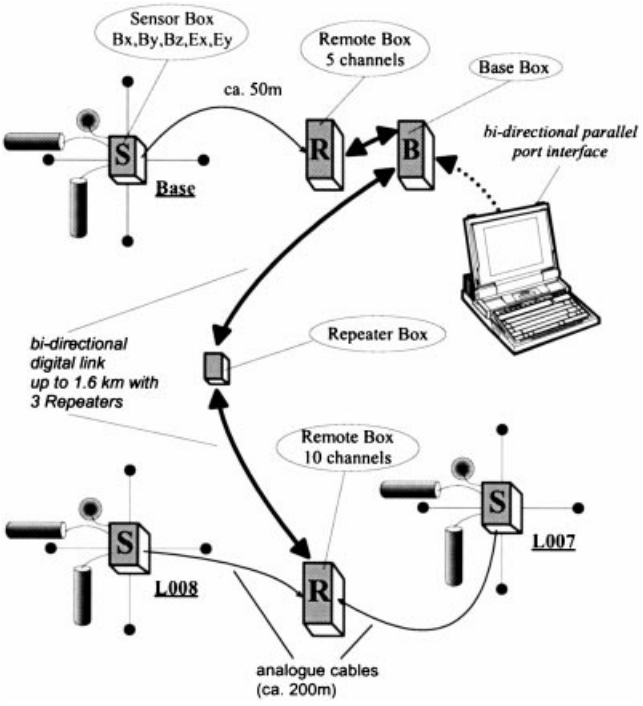

Figure 1. S.P.A.M. MkIII is a networked geophysical instrument. Analogue signals from geophysical sensors are preconditioned at the sensor nodes S and then transferred to the remote node(s) R. In remote boxes, analogue and digital signal processing is performed and the data are forwarded to the base node B in digital form, as time-series and/or frequency spectra. The base node controls the entire network and analyses all incoming data streams. Repeater nodes are necessary to drive long cables.

(1) The *sensor node*: this is used to connect various geophysical sensors (for example induction coil magnetometers, electrodes, seismometers, etc.). All necessary signal preconditioning and power supplies are included. The sensor node provides one channel board of the correct type for each sensor.

(2) The *remote node*: analogue signals from the sensor node(s) in the frequency range 2kHz–DC are captured, further bandpass filtered, optionally notch filtered, and amplified using automatic, software-controlled gain ranging. All parts of the analogue signal path can be monitored in real-time. Eventually, analogue signals are converted to digital data and subsequently digital data processing is performed.

Fig. 2 shows a diagram of S.P.A.M. MkIII's binary decimation and processing scheme to generate (narrow) frequency bands for the data analysis. The raw time-series data are low-pass filtered and decimated in octave steps. Low-pass-filtered time-series data can subsequently be high-pass filtered, to create bandpass-filtered data streams. Low- and high-pass corner frequency settings are variable in octave steps ('power of two'). Adjacent or overlapping time segments can be chosen for the FFT. All data can be forwarded to the base node—via high-speed serial data transmission—as the original time-series, as decimated and low-pass-filtered time-series, as bandpass-filtered time-series or as calibrated frequency spectra. Any mixture is possible and all time-series are continuous streams of data which can be stored and/or further processed at the base node.

(3) The *base-node*: this receives GPS signals and controls the entire network. Only one base node per network is permitted. All control registers (switches, gains, filters, multiplexers, overload detectors, etc.) in all attached remote and sensor nodes are set and/or read from the base node. The base node collects all time- and/or frequency-domain data sent over the network from the remote nodes and performs real-time data processing. The time-series data and the stacked results can be stored on an internal hard disk and/or be transferred to a laptop personal computer (PC).

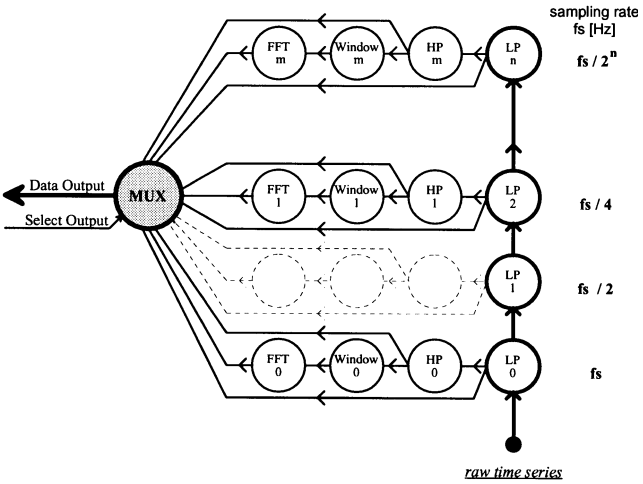

Figure 2. S.P.A.M. MkIII's digital data filtering and decimation scheme. Low-pass and high-pass corner frequency settings are variable in octave steps. All data can be transmitted as original time-series, as decimated and low-pass-filtered time-series, as bandpass filtered time-series or as calibrated frequency spectra. Any mixture is possible and all time-series are continuous streams of data. (MUX is a software multiplexer.)

The PC serves as the front-end for user interaction and as a graphics terminal during normal operation. However, it can be disconnected (and re-connected later) if S.P.A.M. MkIII is configured to run unattended, for example to collect and process data in an overnight run. The PC is also used to boot the whole transputer network, as all necessary data and program files can be sent from the PC to all transputers in the network.

(4) The *repeater node*: this is used to refresh digital signals if they are attenuated or otherwise weakened by the communication media (e.g. long copper cables).

4 EXAMPLES USING FIELD DATA

The field data were recorded at a location in southeastern Scotland in the vicinity of the Southern Upland Fault complex, approximately 35 km southeast of Edinburgh. In total, we measured electromagnetic data at seven sites with five-component MT configurations. Using the new facilities of S.P.A.M. MkIII, three sites were always recorded simultaneously. During the survey, the location of the BASE site remained fixed while the other sites were recorded in pairs, at varying distances from the reference point. To discuss the application of the methods described in this paper we concentrate on the spread of sites with the widest extensions: sites BASE, L007 and L008. The distance between site BASE and the travelling sites is 1600 m; the distance between L007 and L008 is 350 m (see Fig. 1). For clarity, we focus on the processing results of the geomagnetic response functions, although the algorithms work equally well for the estimation of the impedance tensor.

For the data processing, the continuously recorded time-series are divided into adjacent segments of fixed lengths (see Table 1). All data segments are cosine tapered and Fourier transformed. The frequency-domain data are corrected for the influence of the instrument response functions, and the calibrated Fourier coefficients are divided into sub-bands, with centre frequencies equally distributed on a logarithmic scale. For each band and all channels, smoothed auto- and cross-spectra estimates are computed. Final response functions are calculated by stacking the single-event spectra from all frequency bands with the iterative robust algorithm from Section 2.3.

Table 1. The data are recorded in six adjacent and one overlapping frequency band; the second and third columns give the actual low-pass and high-pass settings of the digital bandpass filters. For the highest frequency band, the length of a time segment was set to 512 samples; for all other frequency bands a length of 256 samples was chosen. The fifth column lists the overall amount of events for a given segment length. The sampling rate is four times the low-pass corner frequency. The overlapping band 6 is activated to improve the resolution for the longest-period recordings at approximately 100 s.

	low pass	high pass	samples	total events
Band 0	128 Hz	16 Hz	512	1267
Band 1	16 Hz	4 Hz	256	2902
Band 2	4 Hz	1 Hz	256	2441
Band 3	1 s	4 s	256	509
Band 4	4 s	16 s	256	151
Band 5	16 s	128 s	256	35
Band 6	32 s	128 s	256	16

Fig. 3 shows the results of an automatic, robust, single site processing of all available data sets. The geomagnetic response functions for site L008 show a substantial vertical magnetic field anomaly varying smoothly and consistently over most parts of the frequency range. The type of curve is also in good agreement with results from other sites in the area and fits nicely onto a set of long-period data (not shown). The results of sites L007 and BASE, however, look very different from L008,

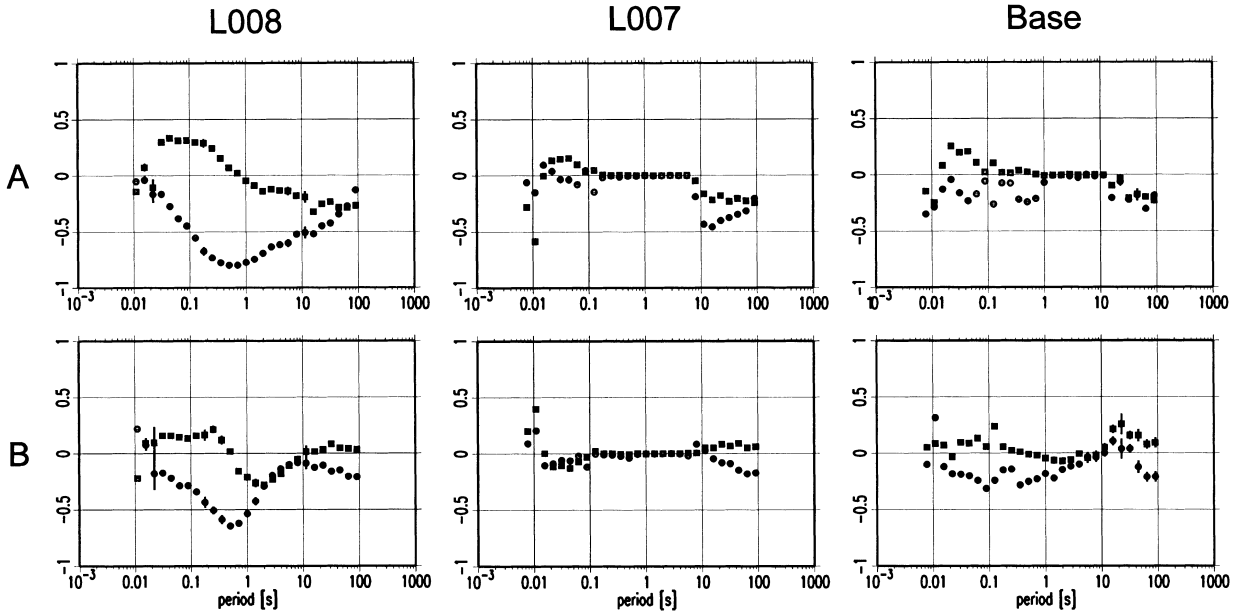

Figure 3. Robust single-site processing of sites L008, L007 and BASE (from left to right) using all available data. The $\mathscr{A}$ and $\mathscr{B}$ response functions [in real (circles) and imaginary (squares) parts] are plotted in the upper and lower sections of the graphs. Clearly, the results for sites L007 and BASE are severely damaged by noise.

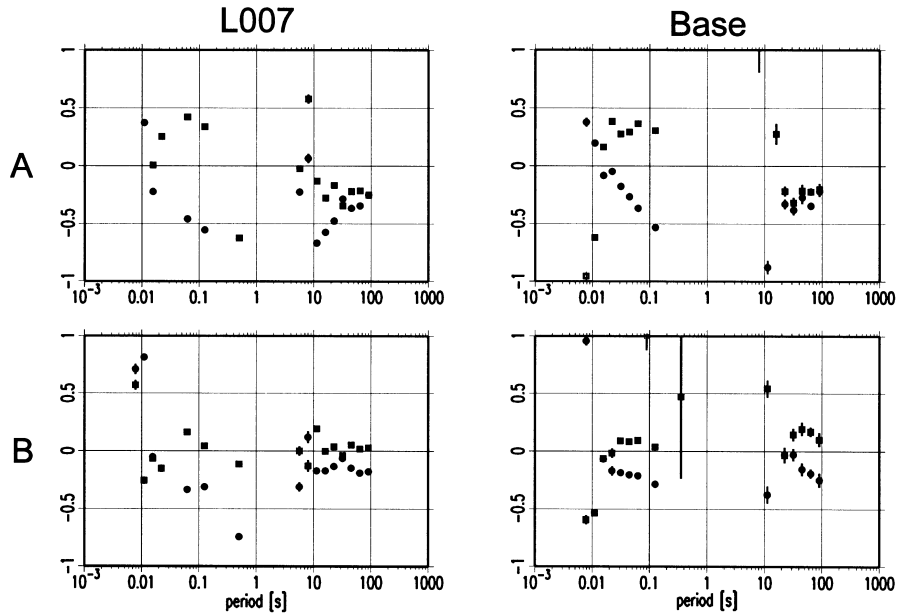

Figure 4. Robust remote reference processing of sites L007 and BASE using all available data. L008 serves as the reference site. The effects of noise are so strong that the remote reference method becomes unstable.

although one would expect similar response functions, considering the relatively small extensions of the station array. The data of these two sites are obviously severely disturbed, the curves look non-physical, and furthermore, the coherencies between vertical and horizontal magnetic components are very low. The error bars are small, but only because the number of estimates is large (see Table 1).

Fig. 4 shows no improvement if we simply apply the remote reference method to sites L007 and BASE using L008 as the reference site. The method depends on both local and remote fields and it appears that noise on the local fields is so strong that the response function estimates become unstable. If we simply replace the horizontal magnetic fields of the local sites with those from the remote site, we obtain the results shown in Fig. 5. Clearly, these *pseudo*-remote reference curves are considerably improved over those of Fig. 4. Now, most of the expected structures can be recognized. Obviously, the outcome is still prone to bias, possibly due to lateral conductivity changes and because the response function estimates rely on auto-spectra. In any case, the pseudo-remote reference results indicate that the problem is connected with poor horizontal magnetic fields at both local sites. For the remote reference

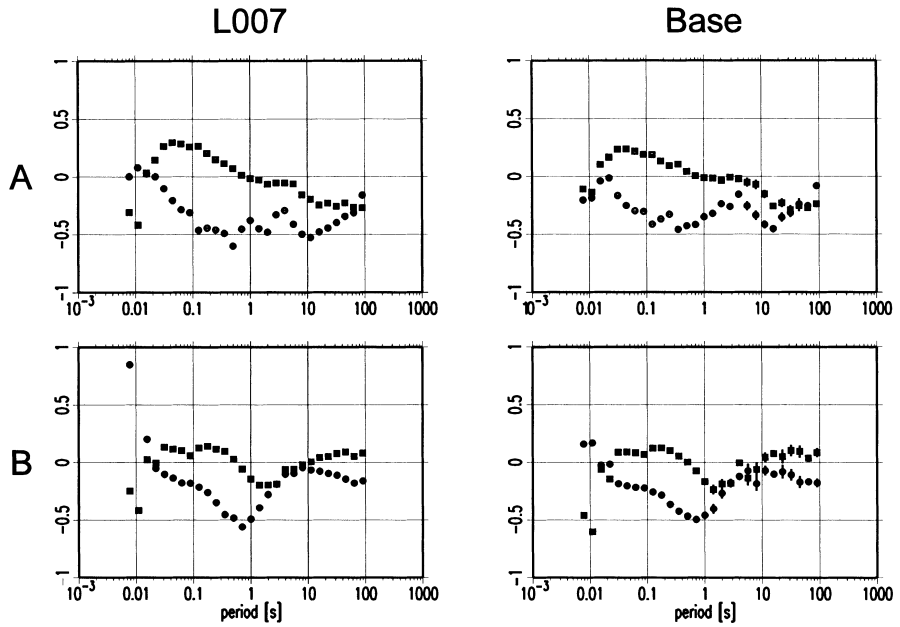

Figure 5. Robust pseudo-remote reference processing of sites L007 and Base using all available data. The local horizontal magnetic fields are replaced by those from site L008. The response function results for the local sites are improved compared to those from Figs 3 and 4. This means that (1) the horizontal fields are strongly disturbed at both local sites and (2) the remote reference method is extremely sensitive to noise in the local fields.

method to function properly we must ensure that noise at local and remote sites is uncorrelated, and—just as important—that the signal is spatially coherent. While it is extremely difficult to detect and separate coherent noise, it is straightforward to examine the coherency of the source field between the sites.

The robust algorithm can generally be applied to solve linear, bivariate problems, for example to obtain robust estimates of the MRFs of eq. (8). The MRF curves between L008 and the local sites L007 and BASE are shown in Figs 6(a) and (b), respectively. We observe mostly a close-to-unity response for T_{xx} and T_{yy}, as is expected for densely spaced sites. However, the effects of noise are also visible, for example in the period range 0.1–10 s in $\mathscr{R}eT_{xx}$(L007) and between 0.01 and 0.1 s in $\mathscr{R}eT_{xx}$(BASE). In particular, the abrupt transition from 0.5 to 1 of $\mathscr{R}eT_{xx}$(L007) at 10 s cannot be explained by a geological feature. It is most likely that the whole effect of continuously decreasing values in the period range 0.1–10 s is caused by some strong local noise source in combination with little natural signal energy. Also conspicuous are the deviations from zero in the imaginary parts at the highest frequencies at L007. We cannot distinguish between phase shifts caused by anomalous fields and those from near-field source effects if they are coherent, but the period range coincides with the strongly scattered part of the otherwise very smooth response function curves of L008 in Fig. 3. For the remaining parts, however, T_{xx} and T_{yy} in Figs 6(a) and (b) are—within reasonable bounds—close to unity. T_{xy} and T_{yx}, which are not shown, are zero within their error bars.

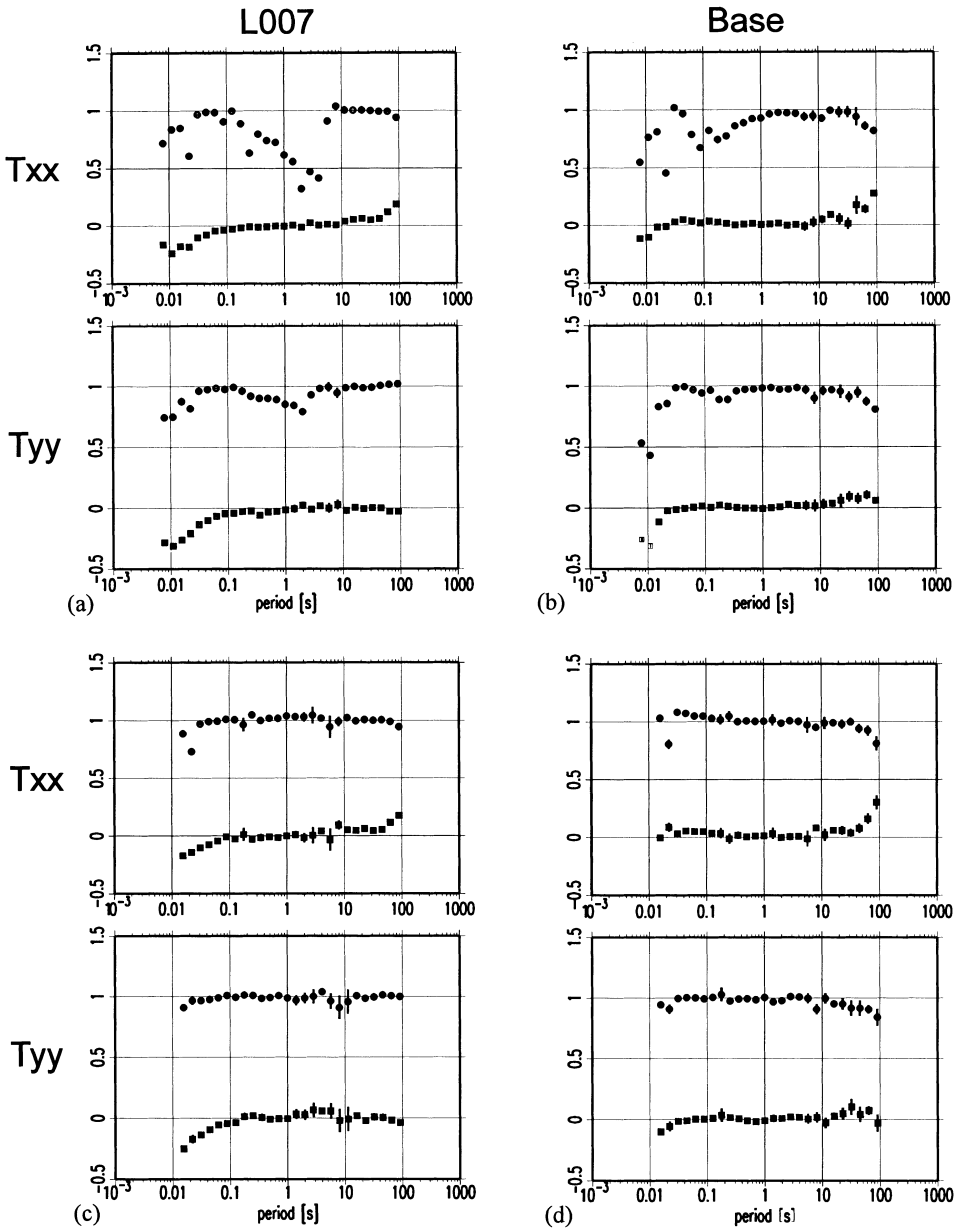

Figure 6. Robust estimation of the MRFs between local sites L007 and BASE using L008 as the reference: (a) and (b) using all available data; (c) and (d) using the reduced data set after application of the source-field criterion. The MRFs in (a) and (b) show at some periods deviations from the expected close-to-unity response and have poor statistical properties. With the reduced data set in (c) and (d), we observe the expected close-to-unity response over the whole frequency range. The deviation of the imaginary parts at the highest frequencies is preserved by the target criterion.

Hence, the source field criterion from Section 2.2 is applied for a reprocessing of the data. The coherency threshold is set to 0.8 and the MRFs are allowed to vary within a radius of 0.2 around unity in the complex plane. Both limits have been determined empirically. They depend on the amount and quality of the data and are adjusted accordingly. The data set contains six synchronously recorded horizontal magnetic field components of three sites, which leaves various possible channel combinations. In the example, the source field criterion is applied step by step to the following eight channel combinations:

$$B_x(\mathrm{L008}) = T_{xx}B_x(\mathrm{BASE}) + T_{xy}B_y(\mathrm{BASE}),$$

$$B_x(\mathrm{L008}) = T_{xx}B_x(\mathrm{L007}) + T_{xy}B_y(\mathrm{L007}),$$

$$B_y(\mathrm{L008}) = T_{yx}B_x(\mathrm{BASE}) + T_{yy}B_y(\mathrm{BASE}),$$

$$B_y(\mathrm{L008}) = T_{yx}B_x(\mathrm{L007}) + T_{yy}B_y(\mathrm{L007}),$$

$$B_x(\mathrm{L008}) = T_{xx}B_x(\mathrm{BASE}) + T_{xy}B_y(\mathrm{L007}),$$

$$B_x(\mathrm{L008}) = T_{xx}B_x(\mathrm{L007}) + T_{xy}B_y(\mathrm{BASE}),$$

$$B_y(\mathrm{L008}) = T_{yx}B_x(\mathrm{BASE}) + T_{yy}B_y(\mathrm{L007}),$$

$$B_y(\mathrm{L008}) = T_{yx}B_x(\mathrm{L007}) + T_{yy}B_y(\mathrm{BASE}).$$

Putting the assumed noise-free component on the left side of the equation amplifies the bias of the response functions. Thus, the noisy segments of the time-series automatically yield deviations from unity and, consequently, will be removed from the data set. The effects on the data selection process are demonstrated in Figs 7 and 8. Fig. 7(a) examines coherencies and MRFs between B_x(L008) and $B_{x,y}$(BASE) at a frequency of 16 Hz. The top diagram shows the multiple coherency, plotted for each event; the solid line indicates the threshold of 0.8. The estimates are derived from 1267 time-series segments (events) of 512 samples each (see Table 1). All those events with coherencies below 0.8 are rejected; 203 out of 1267 in the example. Plotted in the diagram just below the coherencies are the magnitudes of the single-event MRFs. Note that the events are ordered in time. The two smaller diagrams at the bottom left, on the other hand, concentrate on the stationarity of the MRFs. The MRFs are plotted in the complex plane and the circles indicate the areas of acceptance: 470 events of a total of 1064 with coherencies better than 0.8 fail to lie within a distance of 0.2 of the target response functions (1, 0) and (0, 0). Overall, 673 events are rejected and 594 are promoted to the next step which compares B_x(L008) with $B_{x,y}$(L007). At this stage, which is not shown, 397 events are accepted. Fig. 7(b) shows the third step, in which B_y(L008) is examined with respect to $B_{x,y}$(BASE). Now the data appear cleaned, because only 33 events out of 397 are rejected. Most of the coherencies are very close to 1 and most of the data are within the target, that is they are arranged as expected within close bounds to a unity response. After all eight decimation steps, 308 events are accepted.

The situation changes completely in Fig. 8, where the data are examined at 45 Hz, close to the frequency of mains power supplies (50 Hz) which generate near-field signals with much higher amplitudes than the natural signals. The main part of that signal is already filtered by S.P.A.M. MkIII but there is always leakage to the neighbouring frequencies. Thus, more than 1000 events out of 1267 fail to reach the required coherency of 0.8 at the first hurdle. The data section between events 350 and 600, in which more events fulfil the coherency criterion, could indicate an interval of increased natural signal activity. The distribution of the MRFs in the complex plane appears almost as random, and after the third decimation step in Fig. 8(b), only eight out of 1267 events are acceptable. These eight events are eventually reduced to four after all eight iteration steps.

Comparison of the total number of events in Table 1 with the amount of accepted events in Table 2 shows how significantly

Table 2. The total number of recorded events in comparison with the number of accepted events after application of the source-field criterion. The amount of rejected data varies considerably between the observation frequencies. Note the high number of accepted data for frequencies which are multiples of the Schumann resonance.

	evaluation frequency or period/accepted events						
Band 0	128 Hz	90 Hz	64 Hz	45 Hz	32 Hz	22 Hz	16 Hz
total: 1267	2	3	98	4	513	79	308
Band 1	16 Hz	11 Hz	8 Hz	5.6 Hz	4 Hz		
total: 2902	493	91	432	24	7		
Band 2	4 Hz	2.8 Hz	2 Hz	1.4 Hz	1 Hz		
total: 2441	38	58	111	136	131		
Band 3	1 s	1.4 s	2 s	2.8 s	4 s		
total: 509	24	23	37	18	25		
Band 4	4 s	5.6 s	8 s	11.3 s	16 s		
total: 151	10	8	8	7	36		
Band 5	16 s	22.7 s	32 s	45.5 s	64 s		
total: 35	7	17	14	10	13		
Band 6	32 s	45.5 s	64 s	90 s			
total: 16	5	5	6	5			

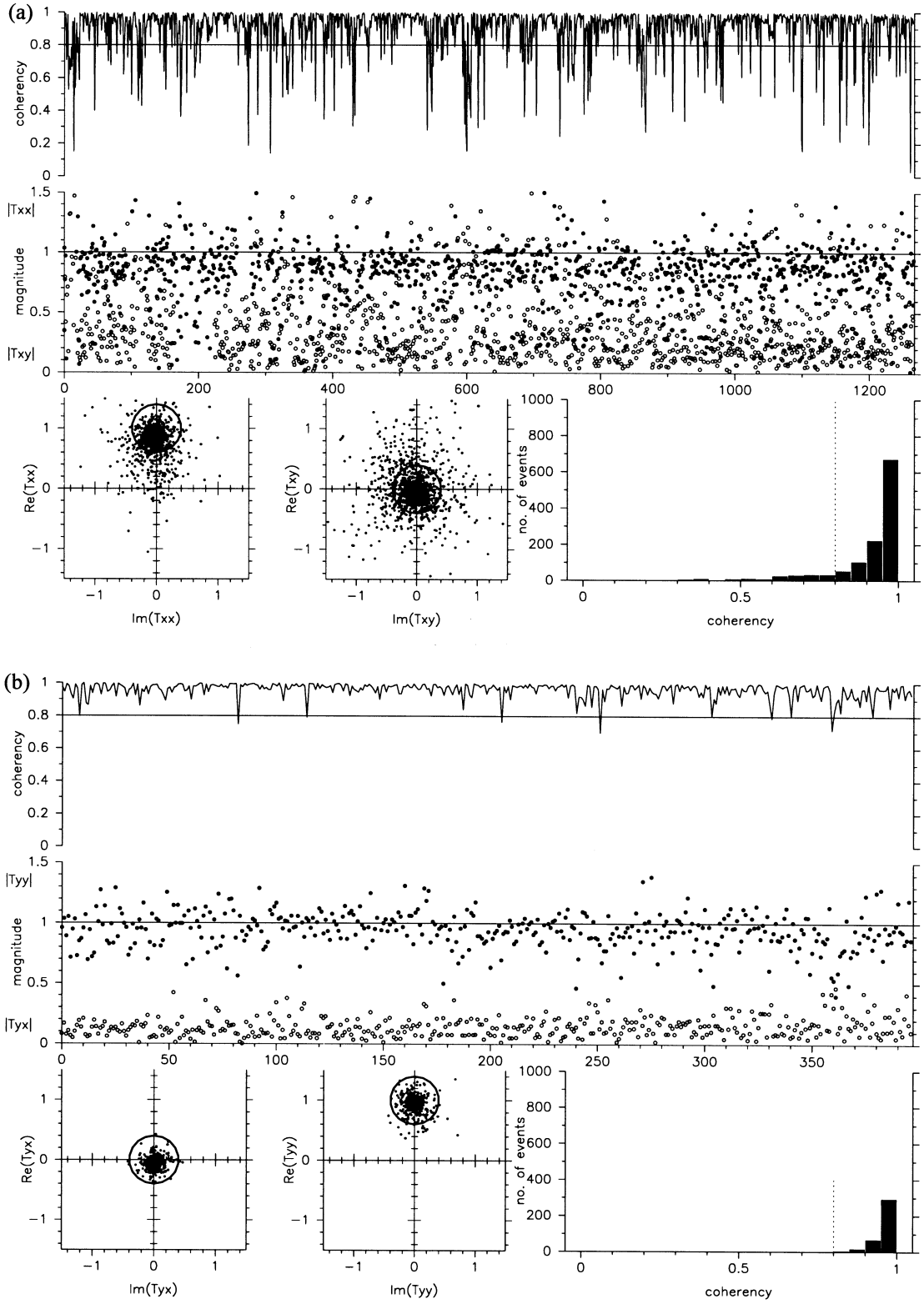

Figure 7. The effects of the source-field criterion at 16 Hz: coherencies and MRFs (a) between B_x(L008) and $B_{x,y}$(BASE); (b) between B_y(L008) and $B_{x,y}$(BASE). All estimates are derived from 1267 time-series segments (events) of 512 samples each. The top diagram shows the multiple coherency; the threshold is 0.8. Plotted just below are the magnitudes of the MRFs. The two smaller diagrams at the bottom left show the MRFs in the complex plane; the circles indicate areas of acceptance. The histogram at the bottom right gives the distribution of the coherencies. After the third decimation step in (b), more than 50 per cent of the data are rejected (see text).

GJI000 18/2/98 09:10:09 3B2 version 5.20
The Charlesworth Group, Huddersfield 01484 517077

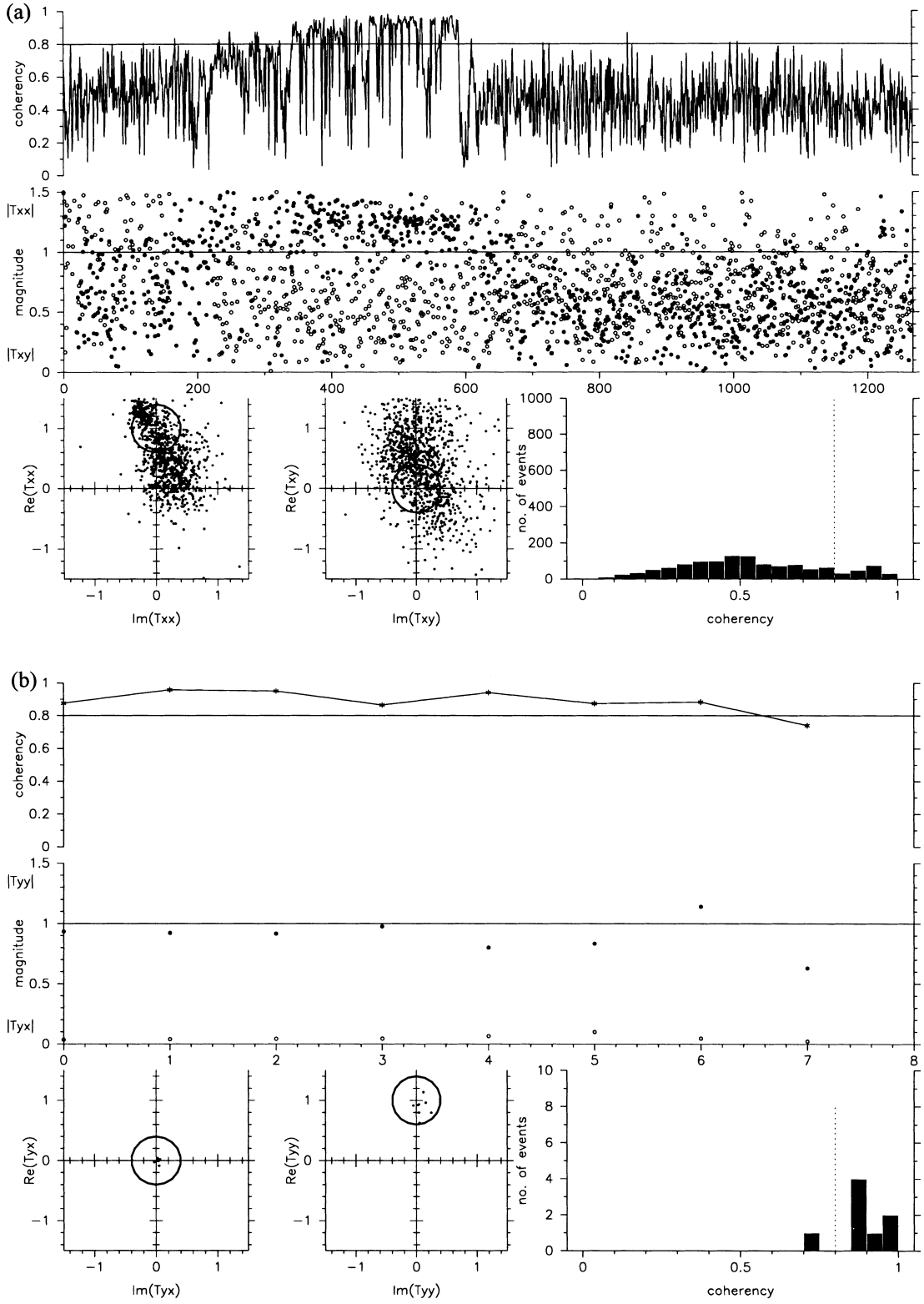

Figure 8. The effects of the source-field criterion at 45 Hz; see Fig. 7 for an explanation of the diagrams. The centre frequency of 45 Hz is close the frequency of the mains power supply (50 Hz), which is known to be generated very locally and to dominate the natural signal. More than 1000 events fail to reach the required coherency of 0.8. The distribution of the MRFs in the complex plane appears almost as random. Only eight events out of 1267 are taken over to the third decimation step in part (b) of the figure.

the data are reduced by the source field criterion. As expected, the amount of accepted data depends strongly on the natural signal activity. In frequency bands 0 and 1, all those frequencies that are multiples of 8 have a high volume of accepted events, very probably because they are centred around the energy maxima of the Schumann resonances. The frequency range of minimal natural signal activity, the so-called *dead band*, between 0.1 and 10 s is recognizable by the low number of accepted events. The reprocessing results of the MRFs using the cleaned data set are plotted in Figs 6(c) and (d). The curves show that the application of the source field criterion can recover a close-to-unity response over the whole frequency range at both local sites.

Generally, we find that a lot more data are rejected than accepted by the source field criterion, which means that we reduce the number of degrees of freedom. In the example in Table 2, the effect is so strong that it becomes statistically questionable to calculate variances for the highest and lowest evaluation frequencies. In practice, the method is probably most useful in audiomagnetotelluric applications for which huge data sets can be collected in short periods of time. However, the main point is that we must not feed the robust algorithm with invalid data (noise on the dependent channels). This is clearly proven in Figs 9 and 10, which show robust single site and remote reference reprocessing results using the cleaned data sets. The results of the two local sites have changed from effectively being useless to curves that can be interpreted. The error bars of the remote reference processed data in Fig. 10 are clearly larger than those of Fig. 9. The error bars are larger because the remote reference method is minimizing the covariance between the residuals estimated using both the local and remote magnetic fields. In a single site processing, the variance of the residual using local fields only is being minimized, which will usually result in smaller error bars, but not necessarily a better answer. However, the greatly improved response function results and cleaned MRFs suggest that the source field criterion can also help to reduce effectively the influence of coherent noise.

5 CONCLUSIONS

In this paper we stress the importance of high-quality horizontal magnetic field components for a meaningful estimation of geomagnetic and magnetotelluric response functions. We introduce the source-field quality criterion as a simple but efficient method to remove noise from magnetic channels in data sets of synchronously recorded sites.

Typically, all observed electromagnetic field components are contaminated to some extent with noise. The outcome of automatic data-processing schemes will therefore often be disappointing, even if robust remote reference procedures are applied. Robust (and least-squares) algorithms work generally on the basis that the input channels are free of noise, otherwise the results will be biased. The remote reference method in combination with robust processing alone cannot always improve the situation, as its successful application requires low-noise, coherent magnetic field channels from both local and remote sites. The processing of the field data from Scotland, which comprise two strongly disturbed local sites in combination with a moderately noisy remote site, results in strongly biased and scattered single site and remote reference response function estimates, which could not be interpreted.

The source-field criterion aims to find and isolate all those time segments with non-physical or strongly inhomogeneous source fields. By examining the intersite coherencies and magnetic response functions between all horizontal magnetic field components, events with poor properties are excluded from the subsequent robust stacking. The reprocessing of the remaining, strongly decimated data set results in dramatically improved vertical magnetic field response function curves for both the single site and the remote reference cases. Of course,

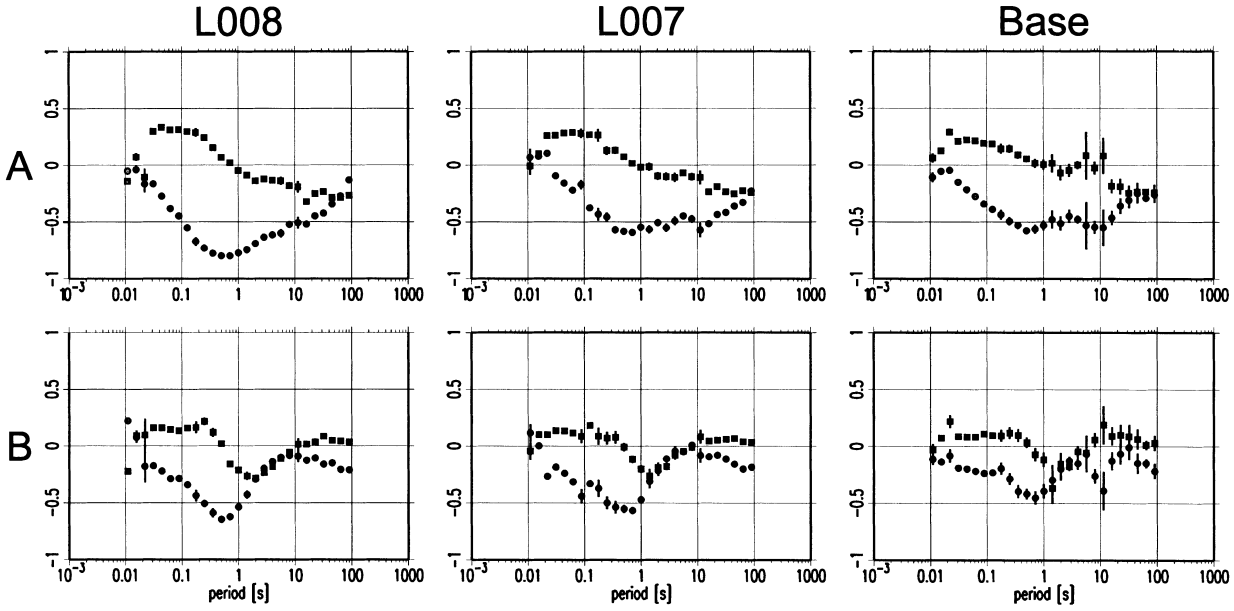

Figure 9. Robust single-site reprocessing of all sites with cleaned source fields. The results of all sites are tremendously improved over those from Fig. 3. The results of the two local sites have changed from being effectively useless, to curves that can be interpreted.

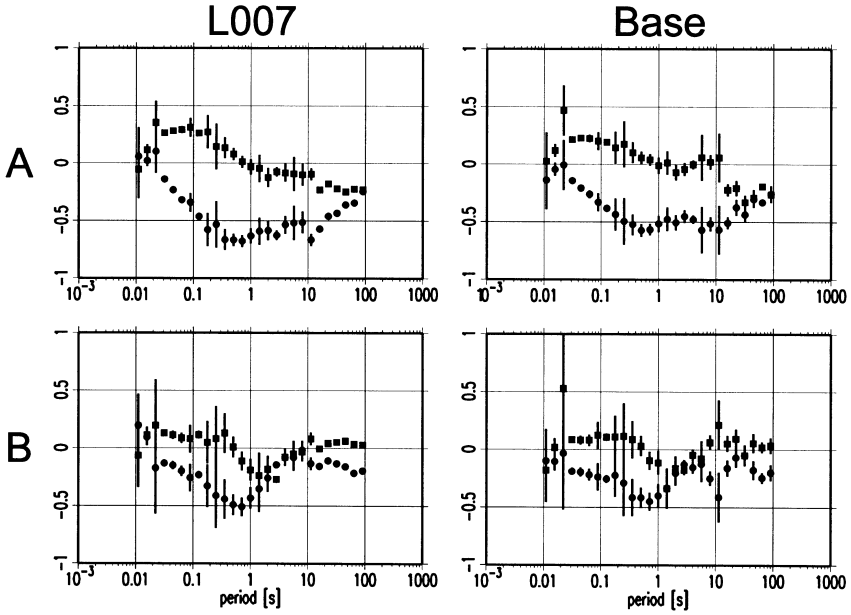

Figure 10. Robust remote reference processing of sites L007 and BASE using the cleaned data; L008 is used as the reference site. A clear improvement when compared with Fig. 4. The curves are in good agreement with the single-site reprocessing results of Fig. 9.

robust processing of the cleaned data set is still required, as the source-field criterion cannot consider outliers in the output channels.

In the past, it was often difficult to collect synchronous, multichannel recordings of high-frequency data because of hardware restrictions. Electromagnetic noise is often generated very locally, hence the noise situation can change within an area of only a few hundred metres across. On many occasions it will be possible to identify such noisy locations prior to long-term recordings with S.P.A.M. MkIII's real-time facilities. However, it is still essential to be able to record large volumes of synchronous time-series data in order to improve the results with post-processing. The multisensor capabilities are particularly interesting in applications in which data are collected on dense grids or profiles.

ACKNOWLEDGMENTS

We thank Darcy Nascimento for all the work he put into the design and construction of S.P.A.M. MkIII. OR was supported by an EEC research grant in the field of non-nuclear energies (B/JOUG 900018). We are grateful to Randy Mackie and an anonymous reviewer for their very helpful comments.

REFERENCES

Banks, R.J., Irving, A.A.K. & Livelybrooks, D.W., 1993. The simulation of magnetic variation anomalies using single-station data, *Phys. Earth. planet. Inter.,* **81,** 85–97.

Beaton, A. & Tukey, J., 1974. The fitting of power series, meaning polynomials, illustrated on band-spectroscopic data, *Technometrics,* **16,** 147–185.

Chave, A.D. & Thomson, D.J., 1989. Some comments on magnetotelluric response function estimation, *J. geophys. Res.,* **94**(B14), 14 215–14 225.

Chave, A.D., Thomson, D.J. & Ander, M.E., 1987. On the robust estimation of power spectra, coherencies, and transfer functions. *J. geophys. Res.,* **92**(B1), 633–648.

Dawes, G.J.K., 1990. Feasibility study for a transputer-based upgrade of the Short-Period Automatic Magnetotelluric (S.P.A.M.) system, *University of Edinburgh, NERC report F3/G6/S43.*

Egbert, G.D., 1997. Robust multiple-station magnetotelluric data processing, *Geophys. J. Int.,* **130,** 475–496.

Egbert, G.D. & Booker, J.R., 1986. Robust estimation of geomagnetic transfer functions, *Geophys. J. R. astr. Soc.,* **87,** 173–194.

Gamble, T.D., Goubau, W.M. & Clarke, J., 1979. Magnetotellurics with a remote reference, *Geophysics,* **44,** 53–68.

Goubau, W.M., Gamble, T.D. & Clarke, J., 1978. Magnetotelluric data analysis: removal of bias, *Geophysics,* **43,** 1157–1166.

Hampel, F.R., Ronchetti, E.M., Rousseeuw, P.J. & Stahel, W.J., 1986. *Robust Statistics*, Wiley, New York, NY.

Huber, P.J., 1981. *Robust Statistics,* Wiley, New York, NY.

Jones, A.G., Chave, A.D., Egbert, G., Auld, D. & Bahr, K., 1989. A comparison of techniques for magnetotelluric response function estimation, *J. geophys. Res.,* **94**(B10), 14 201–14 213.

Junge, A., 1990. Robust estimation of bivariate transfer functions, in *Protokoll Kolloquium Elektromagnetische Tiefenforschung,* pp. 75–86, eds Haak, V. & Homilius, H., DGG, Hornburg, Germany (in German).

Junge, A., 1992. On the effective number of degrees of freedom in magnetotelluric transfer function estimation, in *Protokoll Kolloquium Elektromagnetische Tiefenforschung,* pp. 139–158, eds Haak, V. & Rodemann, H., DGG, Borkheide, Germany (in German).

Junge, A., 1994. Induced telluric fields—new observations in North Germany and the Bramwald, *Habilitation Thesis,* Faculty of Physics, University of Göttingen, Germany (in German).

Junge, A., 1996. Characterization of and correction for cultural noise, *Surv. Geophys.,* **17,** 361–391.

Larsen, J.C., 1989. Transfer functions: smooth robust estimates by least-squares and remote reference methods, *Geophys. J. Int.,* **99,** 645–663.

Larsen, J.C., Mackie, R.L., Manzella, A., Fiordelisi, A. & Rieven, S., 1996. Robust smooth magnetotelluric transfer functions, *Geophys. J. Int.,* **124,** 801–819.

Nascimento, D., 1997. Magnetotelluric instrument development and application, *PhD thesis,* University of Edinburgh.

Park, J. & Chave, A.D., 1984. On the estimation of magnetotelluric response functions using the singular value decomposition, *Geophys. J. R. astr. Soc.,* **77,** 683–709.

Ritter, O., 1995. An audiomagnetotelluric investigation of the Southern Upland Fault: novel instrumentation, field procedures and 3D modelling, *PhD thesis,* University of Edinburgh.

Ritter, O. & Dawes, G., 1992. A transputer-based multi-station multi-technique geophysical data acquisition system—S.P.A.M. MkIII, in *Protokoll Kolloquium Elektromagnetische Tiefenforschung,* pp. 423–435, eds Haak, V. & Rodemann, H., DGG, Borkheide, Germany.

Szarka, L., 1988. Geophysical aspects of man-made electromagnetic noise in the earth—a review, *Surv. Geophys.,* **9,** 287–318.

Weaver, J.T., 1994. *Mathematical Methods for Geo-Electromagnetic Induction*, Research Studies Press, Taunton.

APPENDIX A: THE ROBUST ALGORITHM

A1 The χ^2 criterion

A1.1 Initial guess of response function estimates

The frequency-domain observations of the electromagnetic field components X, Y and Z are recorded in $l=1\ldots L$ time segments (=events). Z will be expressed as a linear combination of the components X and Y, plus an additional noise term δZ:

$$Z_l = a_l X_l + b_l Y_l + \delta Z_l \,. \tag{A1}$$

The response functions a_l and b_l are obtained as the solution of eq. (A1) by solving the normal equations for selected frequency bands containing at least five Fourier coefficients each. Then, we derive for the residuals S_l the following:

$$S_l^2 = \langle |\delta Z_l|^2 \rangle = \langle |Z_l - a_l X_l - b_l Y_l|^2 \rangle \,, \tag{A2}$$

where $\langle\ \rangle$ denotes the arithmetic mean over the products of Fourier coefficients of the respective frequency band.

A1.2 Initial guess of variance

$\hat{\sigma}_{\mathrm{M}}$ is the initial guess for the variance based on the median estimator:

$$\hat{\sigma}_{\mathrm{M}} = 1.483\ \mathrm{med}\,[|S_l - \mathrm{med}(S_l)|] \,. \tag{A3}$$

The median is more robust against outliers than the arithmetic mean (Hampel *et al.* 1986). We use $\hat{\sigma}_{\mathrm{M}}$ to define an upper limit c_{M}:

$$c_{\mathrm{M}} = 1.5\hat{\sigma}_{\mathrm{M}} \,, \tag{A4}$$

where the factor 1.5 in the above equation is a widely used value (Hampel *et al.* 1986) . The c_{M} values must be adjusted if the assumed amount of *bad* data is larger than $\approx$20 per cent outliers. c_{M} is used to calculate Huber weights w_l for each event l (Huber 1981):

$$w_l^{\mathrm{M}} = \begin{cases} 1 & \text{for } S_l \le c_{\mathrm{M}} \\ \dfrac{c_{\mathrm{M}}}{S_l} & \text{for } S_l > c_{\mathrm{M}} \end{cases} . \tag{A5}$$

Using the weights w_l^{M}, we sum up over all events,

$$\overline{\langle XY^* \rangle}^{\mathrm{M}} = \sum_{l=1}^{L} (w_l^{\mathrm{M}} \langle XY^* \rangle_l^0) \,, \tag{A6}$$

to calculate preliminary response functions a^{M} and b^{M} according to eq. (4).

A1.3 Robust estimation of response functions

To estimate the variance of the robust solution above, we must take into account the weights w_l. Using the Huber weights, the variance $\hat{\sigma}_{\mathrm{H}}$ becomes

$$\hat{\sigma}_{\mathrm{H}}^2 = \frac{L}{L_c^2} \sum_{l=1}^{L} (w_l^{\mathrm{M}} S_l^2) \,, \tag{A7}$$

where L_c is the number of weighted events with $w_l^{\mathrm{M}} = 1$ which fulfil the condition $S_l \le c_{\mathrm{M}}$ in eq. (A5).

To proceed, we replace c_{M} in eq. (A4) with $c_{\mathrm{H}} = 1.5\hat{\sigma}_{\mathrm{H}}$ and calculate the weights w_l^{H} in accordance with eq. (A5). Together with the Huber weights and using eq. (A6), we obtain new estimates for the response functions (a_{H} and b_{H}, respectively). The Huber function, used to compute the weights, cannot always sufficiently eliminate the effects of extreme outliers (Hampel *et al.* 1986).

A1.4 Tukey weights (reduction of extreme outliers)

To get rid of extreme outliers, the data are weighted again. This time, the weights w_l^{T} are calculated using Tukey's biweight function (Beaton & Tukey 1974). First we compute the variance $\hat{\sigma}_{\mathrm{T}}$ (Junge 1994, Appendix A.1):

$$\hat{\sigma}_{\mathrm{T}}^2 = \frac{\dfrac{1}{L} \displaystyle\sum_{l}^{L} (w_l^{\mathrm{H}} S_l)^2}{\dfrac{1}{L_{\mathrm{c}}} \displaystyle\sum_{l}^{L} \left(1 - \left(\frac{S_l}{c_{\mathrm{H}}}\right)^2\right)\left(1 - 5\left(\frac{S_l}{c_{\mathrm{H}}}\right)^2\right)} \,, \tag{A8}$$

and with the limit $c_{\mathrm{T}} = 6\hat{\sigma}_{\mathrm{T}}$ we obtain Tukey weights w_l^{T}:

$$w_l^{\mathrm{T}} = \begin{cases} \left(1 - \left(\dfrac{S_l}{c_{\mathrm{T}}}\right)^2\right)^2 & \text{for } S_l \le c_{\mathrm{T}} \\ 0 & \text{for } S_l > c_{\mathrm{T}} \end{cases} . \tag{A9}$$

If the assumption is correct that, except for a few outliers which had to be removed, the weighted δZ are normally distributed with variance σ_Z^2, then $\langle \delta Z \delta Z^* \rangle / \sigma_Z^2$ is a χ^2 distributed quantity with v degrees of freedom. The number of degrees of freedom of a χ^2 distributed quantity can be estimated from the observations, as the ratio of the expected value to its variance:

$$v = \frac{2E\{\langle \delta Z \delta Z^* \rangle\}^2}{\mathrm{var}\{\langle \delta Z \delta Z^* \rangle\}} \approx \frac{2\left(\dfrac{1}{L}\displaystyle\sum_{l} \langle \delta Z \delta Z^* \rangle\right)^2}{\dfrac{1}{L-1}\displaystyle\sum_{l} (\langle \delta Z \delta Z^* \rangle_l - \overline{\langle \delta Z \delta Z^* \rangle})^2} \,. \tag{A10}$$

The noise distributions of the observations and their theoretical expectations are consistently in better agreement if the number of degrees of freedom is computed using eq. (A10) instead of being derived directly from the equivalent bandwidth of the spectral smoother (Junge 1994). The latter method usually leads to systematically overestimated values for v and hence to underestimated error bars. The confidence limits are calculated using the weighted spectra, corrected number of degrees of freedom and the $F_{4,v-4}$ distribution.

A2 Consistency criterion

In the last section we declared single-event spectra data as *bad* if they had large errors based on single-event transfer functions. The influence of these outliers was reduced by down-weighting (removing) the whole event. The algorithm is founded on the assumption that the distributions of the derived response functions are constant in time. However, the response functions could be non-stationary owing to changing quality (inhomogeneity) of the source fields or to varying amounts of correlated noise which cannot be removed by the data-processing procedures.

The algorithm works iteratively; the superscript $j=0\ldots J$ denotes the iterations. The following abbreviations are used: $S_{xx}=\langle XX^*\rangle$, $S_{zx}=\langle ZX^*\rangle$ and $S_{zy}=\langle ZY^*\rangle$.

A2.1 Calculation of response functions

The response functions a and b and their related errors δZ_l are calculated from the $l=1\ldots L$ single-event spectra, for example using the χ^2 method of the previous section. For each iteration, we define a limit $c^{(j)}$:

$$c^{(j)}=1.5\sqrt{\mathrm{var}\{S^{(j)}_{\delta Z,l}\}}\,. \tag{A11}$$

A2.2 Calculation of weights

For the next iteration, weights less than 1 are calculated for events with errors greater than $c^{(j)}$:

$$(w_l^{(j+1)})^2=\begin{cases}1 & \text{for } S^{(j)}_{\delta Z,l}<c^{(j)}\\ \dfrac{c^{(j)}}{S^{(j)}_{\delta Z,l}} & \text{otherwise}\end{cases}\,. \tag{A12}$$

A2.3 Prediction of new spectra

In order to compute better response function values, we calculate new estimates for the cross- and auto spectra. An algorithm which works in a similar manner was developed by Egbert & Booker (1986) but predicts spectra instead of individual Fourier coefficients and is therefore faster. It can be shown to be similar to a Gauss–Newton scheme for solving non-linear systems. New estimates—or predictions—for single-event spectra are obtained by comparison with the stacked results from all events. The results for the $(j+1)$th iteration are

$$\langle|S^{(j+1)}_{zz,l}|^2\rangle_l=(w_l^{(j)})^2\langle|S^{(j)}_{zz,l}|^2\rangle_l+2w_l^{(j)}(1-w_l^{(j)})\,\mathscr{R}e\{\langle S^{(j)}_{zz,l}\hat{S}^{(j)*}_{zz,l}\rangle_l\}$$
$$+(1-w_l^{(j)})^2\langle|\hat{S}^{(j)}_{zz,l}|^2\rangle_l\,, \tag{A13a}$$

$$\langle S^{(j+1)}_{zx,l}\rangle_l=w^{(j)}\langle S^{(j)}_{zx,l}\rangle_l+(1-w_l^{(j)})\langle\hat{S}^{(j)}_{zx,l}\rangle_l\,, \tag{A13b}$$

$$\langle S^{(j+1)}_{zy,l}\rangle_l=w^{(j)}\langle S^{(j)}_{zy,l}\rangle_l+(1-w_l^{(j)})\langle\hat{S}^{(j)}_{zy,l}\rangle_l\,. \tag{A13c}$$

The previous jth iteration cross- and auto-spectra are calculated from the stacked results, using eq. (4):

$$\hat{S}^{(j)}_{zx}=a^{(j)}S^{(j)}_{xx}+b^{(j)}S^{(j)}_{xy}\,, \tag{A14a}$$

$$\hat{S}^{(j)}_{zy}=a^{(j)}S^{(j)}_{xy}+b^{(j)}S^{(j)}_{yy}\,, \tag{A14b}$$

$$\hat{S}^{(j)}_{zz}=|a^{(j)}|S^{(j)}_{xx}+|b^{(j)}|S^{(j)}_{yy}+2\,\mathscr{R}e\{a^{(j)}(a^{(j)})^*S^{(j)}_{xy}\}\,. \tag{A14c}$$

Steps 1 to 3 are repeated until the changes of $a^{(j)}$ and $b^{(j)}$ are less than a certain limit, e.g. <5 per cent. The algorithm works in a way that the smaller the weights $c^{(j)}$, the more a single-event spectrum is replaced by the value predicted from the response function (averaged over all spectra). For $w^{(j)}=1$ the observed spectra in eqs (A13a)–(A13c) are taken over to the next iteration unchanged, while for $w^{(j)}=0$ they are entirely replaced by those calculated in eqs (A14a)–(A14c).

The number of degrees of freedom is reduced to the same extent as the result of an event is replaced by its prediction:

$$v_l^{(j+1)}=v_l^{(j)}w_l^{(j)}\,. \tag{A15}$$

The consistency criterion is computationally more costly than the χ^2 procedure because it is based on an iterative algorithm. In practice, we found it often sufficient to rely solely on the χ^2 criterion.

Geophys. J. Int. (2003) **155,** 456–468

Images of the magnetotelluric apparent resistivity tensor

Ute Weckmann, Oliver Ritter and Volker Haak

GeoForschungsZentrum Potsdam, Telegrafenberg, D-14473 *Potsdam, Germany*

Accepted 2003 May 27. Received 2003 May 26; in original form 2002 July 18

SUMMARY

We present a method for converting the magnetotelluric (MT) impedance tensor into an apparent resistivity tensor. The inclusion of anisotropic permittivity and conductivity into Maxwell's equations leads to a tensor expression for the propagation constant. To solve Maxwell's equations we assume exponentially decreasing electric fields in the vertical direction, which implies that the subsurface is regarded as homogeneous but anisotropic. This approach effectively makes use of an anisotropic substitute model, in which contrasts and strike directions of conductivity anomalies are transformed into equivalent amounts and directions of anisotropy. We call this method propagation number analysis (PNA). Rotationally invariant parameters calculated from the resistivity tensor are physically meaningful quantities that are directly applicable to imaging methods. Imaging results of PNA are compared with Egger's eigenstate analysis and LaTorraca's singular-value decomposition method using synthetic data from 3-D MT modelling. With PNA, we obtain a comprehensive image of the subsurface that uniquely images structural details of the anomalies. Contrary to other methods, the results of PNA are stable and significant under extreme 3-D conditions. Application of PNA to MT data from the Waterberg Fault in Namibia unravels a complicated 3-D impedance and reveals a clear correlation between the resistivity tensor and the surface geology.

Key words: apparent resistivity tensor, imaging method, invariants, magnetotelluric.

1 INTRODUCTION

The magnetotelluric (MT) impedance tensor reflects the 3-D distribution of magnetic and electric field variations within the Earth. MT practitioners attempt to determine the electrical conductivity structure of the subsurface by interpreting the impedance tensor as a function of position and frequency. For practical reasons we are often limited to 2-D modelling of the data, which means that the diagonal components of the impedance tensor are not considered in the interpretation. Eggers (1982) presented an approach for analysing impedances using an eigenstate parametrization, which uses all elements of the impedance tensor. His eigenstate formulation implies that electric and magnetic field polarizations are always orthogonal. This, however, is not necessarily true in a complex geoelectric environment. The singular-value decomposition (SVD) introduced by LaTorraca *et al.* (1986) overcomes this obstacle. Both methods result in sets of eigenvalues and eigenvectors (characteristic vectors). Their graphical presentation shows the orientation of the electromagnetic field defined by the principal directions of the polarization ellipses. Plots of the polarization ellipses thus provide geometrical insight into the 3-D information contained in the impedance tensor.

Another approach utilizing all four elements of the impedance tensor is the analysis of invariants. Invariant quantities are independent of the coordinate system and are most suitable to illustrate the internal structure of the impedance tensor. Fischer & Masero (1994) argued that a four-element complex tensor should possess eight real invariants. Weaver *et al.* (2000) identified seven independent invariants. The algebraic relations between the various invariants were also examined systematically by Szarka & Menvielle (1997). Several authors have suggested that these tensor invariants can be presented as Mohr circles in the complex plane (Lilley 1993; Weaver *et al.* 2000). Images of the invariants, for example as plots in the horizontal plane for a certain frequency, result in seven different views of tensor properties. Their relation to physical properties of the subsurface is not always obvious.

Over the last few years tensor decomposition methods (Bahr 1991; Smith 1995; McNeice & Jones 2001, and references therein) have been widely used to condition the impedance tensor for subsequent 2-D interpretation. The basic idea is to decompose the impedance tensor into a 2-D complex tensor and a frequency-independent real distortion matrix. The complex tensor is related to a so-called regional conductivity structure, whereas the real matrix represents the galvanic response of small-scale, local heterogeneities. Upon decomposition, the regional tensor is generally interpreted using 2-D (inversion) modelling programs. The resulting conductivity model depends strongly on the validity of the galvanic assumption. It is often difficult to decide, however, to what extent small-scale and regional structures are connected by inductive coupling (Lezaeta & Haak 2003).

Imaging methods provide a different approach to understanding the conductivity distribution of the subsurface. They are based upon a direct conversion of measured data into physically meaningful

properties. The method described in this paper is comparable to the presentation of an apparent resistivity tensor introduced by Caldwell & Bibby (1998) for transient electromagnetics (TEM). Caldwell & Bibby present invariants of the measured resistivity tensor in form of ellipses, which was proposed earlier by Bibby (1986). In contrast with TEM or DC geoelectric sounding methods, however, we do not measure a resistivity tensor in MT. Upon taking the absolute values of the impedance to derive apparent resistivities, we lose the tensor character of our observations (see Appendix A). A direct application of this method to MT is therefore not straightforward but requires some considerations.

2 USING PROPAGATION NUMBER ANALYSIS TO OBTAIN AN APPARENT RESISTIVITY TENSOR IN MAGNETOTELLURICS

The method presented here was inspired by an internal report by Reilly (1979) on anisotropy tensors in magnetotelluric interpretation, which describes a theoretical concept formulated in terms of tensor algebra. An application to MT was demonstrated by Caldwell *et al.* (1998). In this section, we develop an alternative formulation of the problem, which should be more familiar for the MT community. Additionally, it more clearly shows the limitations of the method.

Below, we develop a true resistivity tensor by means of a substitute anisotropic half-space, which generates the same impedance tensor as the observed one. The commonly used MT apparent resistivity

$$\rho_{a,ij} = \frac{\mu_0}{2\pi f}|Z_{ij}|^2 \tag{1}$$

with $i, j = x, y$ and frequency f, is not a tensor as shown in Appendix A. As a function of rotation the apparent resistivity is therefore not suitable for imaging properties of the MT impedance.

In MT a second-order tensor connects the electric and magnetic fields represented by the impedance $\boldsymbol{Z}$ or its inverse, the admittance tensor $\boldsymbol{Y}$:

$$\mathbf{B} = \mu\mathbf{H} = \hat{\boldsymbol{Y}}\mathbf{E} = \begin{pmatrix} Y_{xx}E_x + Y_{xy}E_y \\ Y_{yx}E_x + Y_{yy}E_y \end{pmatrix}, \tag{2}$$

where $\mathbf{B}$ is the magnetic flux density [T], $\mathbf{H}$ is the magnetic field intensity [A m^{-1}] $\mathbf{E}$ is the electric field intensity [V m^{-1}] and μ is the relative magnetic permeability of the medium [T m A^{-1}]. This tensor relation between electric and magnetic fields originates from Maxwell's equations. Assuming a harmonic time dependence proportional to $e^{i\omega t}$, the electric and magnetic fields take the following form:

$$\nabla \times \mathbf{E} = -i\omega\mathbf{B} \tag{3}$$

$$\nabla \times \mathbf{H} = \mathbf{j} + i\omega\mathbf{D}, \tag{4}$$

where $\mathbf{D}$ is the electric displacement [C m^{-2}], $\mathbf{j}$ is the current density [A m^{-2}] and ω is the angular frequency [Hz]. To transform Amperè's law (4) into a tensor relationship requires anisotropic permittivity ϵ[F m^{-1}] and conductivity σ[S m^{-1}]. This means that both parameters must be promoted from scalars to tensors. For physically realizable materials the tensors $\hat{\boldsymbol{\epsilon}}$ and $\hat{\boldsymbol{\sigma}}$ are symmetric (Negi & Saraf 1989). Using the material parameters for anisotropic media we can rewrite Maxwell's equations:

$$\nabla \times \mathbf{E} = -i\omega\mu\mathbf{H} \tag{5}$$

$$\nabla \times \mathbf{H} = \hat{\boldsymbol{\sigma}}\mathbf{E} + i\omega\hat{\boldsymbol{\epsilon}}\mathbf{E}. \tag{6}$$

Multiplying Amperè's law by $i\omega\mu$ we can combine the right-hand side of eq. (6), thereby introducing the propagation constant γ in a similar way as in the general form of the Helmholtz equation:

$$\begin{aligned} -i\omega\mu\nabla \times \mathbf{H} &= -i\omega\mu(\hat{\boldsymbol{\sigma}} + i\omega\hat{\boldsymbol{\epsilon}})\mathbf{E} \\ &= -\omega\mu(i\hat{\boldsymbol{\sigma}} - \omega\hat{\boldsymbol{\epsilon}})\mathbf{E} \\ &= -\hat{\boldsymbol{\gamma}}\mathbf{E}. \end{aligned} \tag{7}$$

The propagation constant $\hat{\boldsymbol{\gamma}}$ is equivalent to the square of the wavenumber multiplied by $\sqrt{-1}$. Obviously though, $\hat{\boldsymbol{\gamma}}$ is not a constant quantity. We therefore referring to $\hat{\boldsymbol{\gamma}}$ as the propagation number analogue to the term wavenumber.

Replacing the magnetic field $\mathbf{H}$ with $\hat{\boldsymbol{Y}}\mathbf{E}$ in eqs (7) and (5), we obtain equations only dependent on the electric field $\mathbf{E}$,

$$-i\omega\nabla \times \hat{\boldsymbol{Y}}\mathbf{E} = -\hat{\boldsymbol{\gamma}}\mathbf{E} \tag{8}$$

$$\nabla \times \mathbf{E} = -i\omega\hat{\boldsymbol{Y}}E. \tag{9}$$

To solve these equations we assume an exponentially decreasing electric field in the z direction (vertical). Formally, this is equivalent to the general solution of the wave equation for a vertically downward-propagating plane wave but neglecting the term describing the upward-propagating part. This solution implies that the subsurface is regarded as homogeneous but anisotropic in terms of conductivity and permittivity. In this case all spatial derivatives in the x and y directions are zero. Furthermore, a restriction to purely azimuthal anisotropy is justified as in MT we have no sensitivity to the vertical conductivity component.

Using above assumptions, Faraday's and Amperè's laws eqs (9) and (7) can be written as

$$\nabla \times \begin{pmatrix} E_x \\ E_y \\ 0 \end{pmatrix} = \begin{pmatrix} -\dfrac{\partial}{\partial z}E_y \\ \dfrac{\partial}{\partial z}E_x \\ 0 \end{pmatrix} = -i\omega \begin{pmatrix} Y_{xx}E_x + Y_{xy}E_y \\ Y_{yx}E_x + Y_{yy}E_y \\ 0 \end{pmatrix} \tag{10}$$

$$i\omega \begin{pmatrix} -\dfrac{\partial}{\partial z}(Y_{yx}E_x + Y_{yy}E_y) \\ \dfrac{\partial}{\partial z}(Y_{xx}E_x + Y_{xy}E_y) \\ 0 \end{pmatrix} = -\hat{\boldsymbol{\gamma}} \begin{pmatrix} E_x \\ E_y \\ 0 \end{pmatrix}. \tag{11}$$

In the following discussion, we omit the vanishing z component of electric fields for clarity. The admittance tensor is not a function of depth, hence $\frac{\partial}{\partial z}(Y_{xy}E_x) = Y_{xy}\frac{\partial}{\partial z}E_x$, and we can substitute the partial derivatives of E_x and E_y using the right-hand side of eq. (10),

$$\begin{aligned} &-(i\omega)^2 \begin{pmatrix} -Y_{yx}(Y_{yx}E_x + Y_{yy}E_y) + Y_{yy}(Y_{xx}E_x + Y_{xy}E_y) \\ Y_{xx}(Y_{yx}E_x + Y_{yy}E_y) - Y_{xy}(Y_{xx}E_x + Y_{xy}E_y) \end{pmatrix} \\ &= -\hat{\boldsymbol{\gamma}} \begin{pmatrix} E_x \\ E_y \end{pmatrix}. \end{aligned} \tag{12}$$

The vector on the left-hand side of this equation can be decomposed into the dot product of a 2 × 2 matrix (containing combinations of all entries of the admittance tensor) and an electric field vector,

$$\begin{aligned} &-\omega^2 \begin{pmatrix} Y_{yy}Y_{xx} - Y_{yx}Y_{yx} & Y_{yy}\cdot(Y_{xy} - Y_{yx}) \\ Y_{xx}\cdot(Y_{yx} - Y_{xy}) & Y_{yy}Y_{xx} - Y_{xy}Y_{xy} \end{pmatrix} \cdot \begin{pmatrix} E_x \\ E_y \end{pmatrix} \\ &= \hat{\boldsymbol{\gamma}} \begin{pmatrix} E_x \\ E_y \end{pmatrix}. \end{aligned} \tag{13}$$

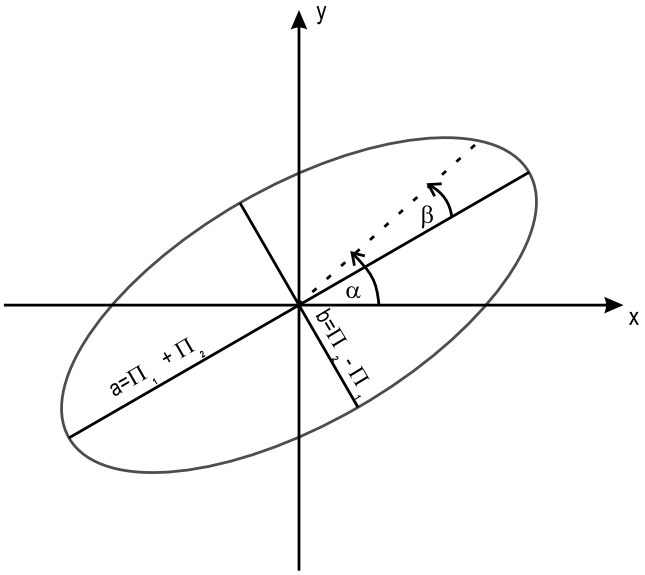

Figure 1. Construction of an apparent resistivity ellipse: Π_1 and Π_2 define the lengths of the major and minor axes. These quantities, along with the rotation angles α and β are obtained by separating the apparent resistivity tensor into symmetric and asymmetric parts (Bibby 1986).

The tensor $\boldsymbol{\gamma}$ takes the following form:

$$\begin{pmatrix} \gamma_{xx} & \gamma_{xy} \\ \gamma_{yx} & \gamma_{yy} \end{pmatrix} = -\omega^2 \begin{pmatrix} Y_{yy}Y_{xx} - Y_{yx}Y_{yx} & Y_{yy} \cdot (Y_{xy} - Y_{yx}) \\ Y_{xx} \cdot (Y_{yx} - Y_{xy}) & Y_{yy}Y_{xx} - Y_{xy}Y_{xy} \end{pmatrix}. \quad (14)$$

The propagation number is defined as $\hat{\boldsymbol{\gamma}} = -\omega^2\mu\hat{\boldsymbol{\epsilon}} + i\omega\mu\hat{\boldsymbol{\sigma}}$. The real part of this complex tensor is a function the permittivity $\hat{\boldsymbol{\epsilon}}$, whereas the imaginary part is dependent upon the conductivity $\hat{\boldsymbol{\sigma}}$. Thus, the MT apparent resistivity tensor is

$$\hat{\boldsymbol{\varrho}} = \hat{\boldsymbol{\sigma}}^{-1} = \mu\omega[\mathrm{Im}(\hat{\boldsymbol{\gamma}})]^{-1}. \quad (15)$$

The real and imaginary parts of complex tensors are also tensors. Our newly obtained quantity $\hat{\boldsymbol{\varrho}}$ is therefore a true tensor, in contrast to the apparent resistivity matrix derived by taking the squared absolute values of Z_{ij} (see eq. 1 and Appendix A).

In this paper, we are interested in developing a method for imaging the conductivity distribution of the subsurface. We therefore concentrate on the interpretation of the resistivity tensor as defined in eq. (15). It should be noted, however, that the real part of $\hat{\boldsymbol{\gamma}}$ is related to the permittivity tensor $\hat{\boldsymbol{\epsilon}}$. The electrical permittivity is typically not considered in MT applications because it is associated with vanishing displacements currents. In spite of this, the real part of $\hat{\boldsymbol{\gamma}}$ contains some aspects of the admittance tensor and a more systematic inspection of $\hat{\boldsymbol{\epsilon}}$ would be interesting but is beyond the scope of this paper.

In the following, we refer to this method as propagation number analysis (PNA). When we apply PNA, we effectively substitute the subsurface conductivity structure by an anisotropic model. In other

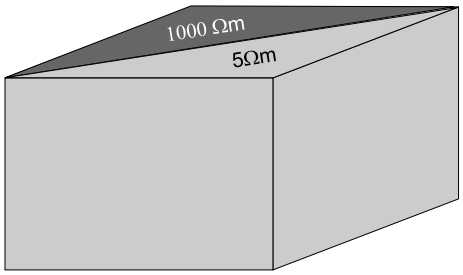

Figure 3. Model of a simple 2-D conductivity contrast striking 45°.

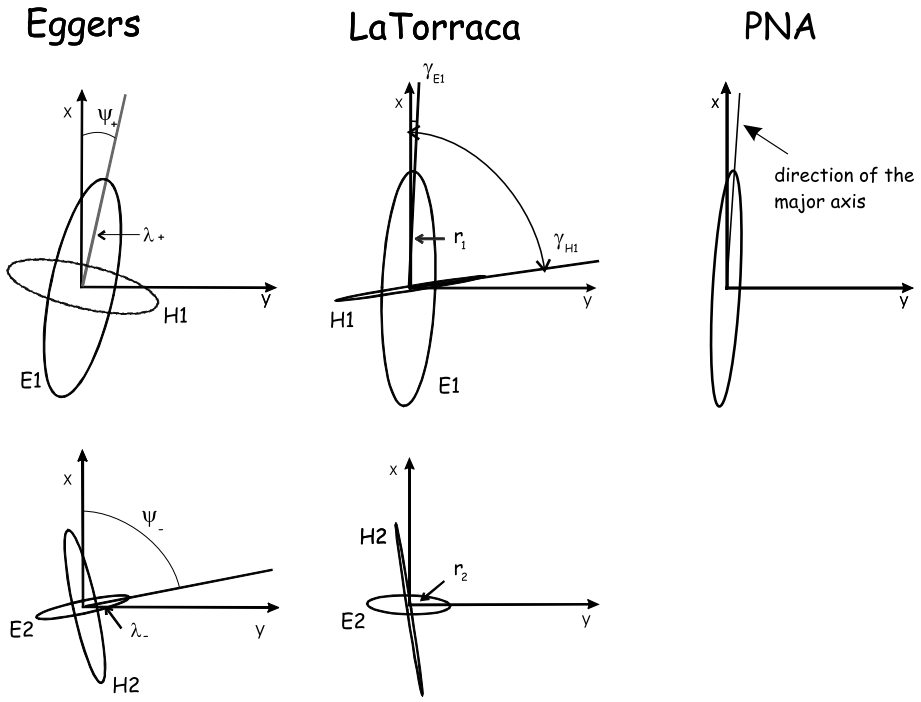

Figure 2. The impedance tensor of eq. (20) is plotted for Eggers' method, the LaTorraca SVD and PNA. The magnetic field amplitude is always unity. Note, that we obtain only one apparent resistivity ellipse with PNA, which is related to the electric field. ($\lambda, r \hat{=}$ eigenvalues; $\Psi, \gamma \hat{=}$ principal axis directions).

words, at each frequency of the measured impedance tensor we seek a homogeneous anisotropic subsurface that generates the same impedance tensor. We thereby transform the contrasts and strike directions of conductivity anomalies into their equivalent amounts and directions of anisotropy. It is important to understand that we do not attempt to model an anisotropic crust for the Earth with PNA. We use anisotropy only as a tool to resolve both the conductivity and geometry of an anomaly. However, in the presence of a truly anisotropic subsurface we can likewise image this anisotropy in terms of its strike.

Appendix B outlines a proof demonstrating that PNA truly recovers an arbitrary horizontal anisotropy from the electric and magnetic fields in a chosen coordinate system.

For the graphical representation of the resistivity tensor we use ellipses following the notation of Bibby (1986). Each tensor is split into its symmetric and asymmetric parts, Π_1 and Π_2, respectively:

$$\Pi_1 = \frac{1}{2}\left[(\varrho_{11} - \varrho_{22})^2 + (\varrho_{12} + \varrho_{21})^2\right]^{1/2} \tag{16}$$

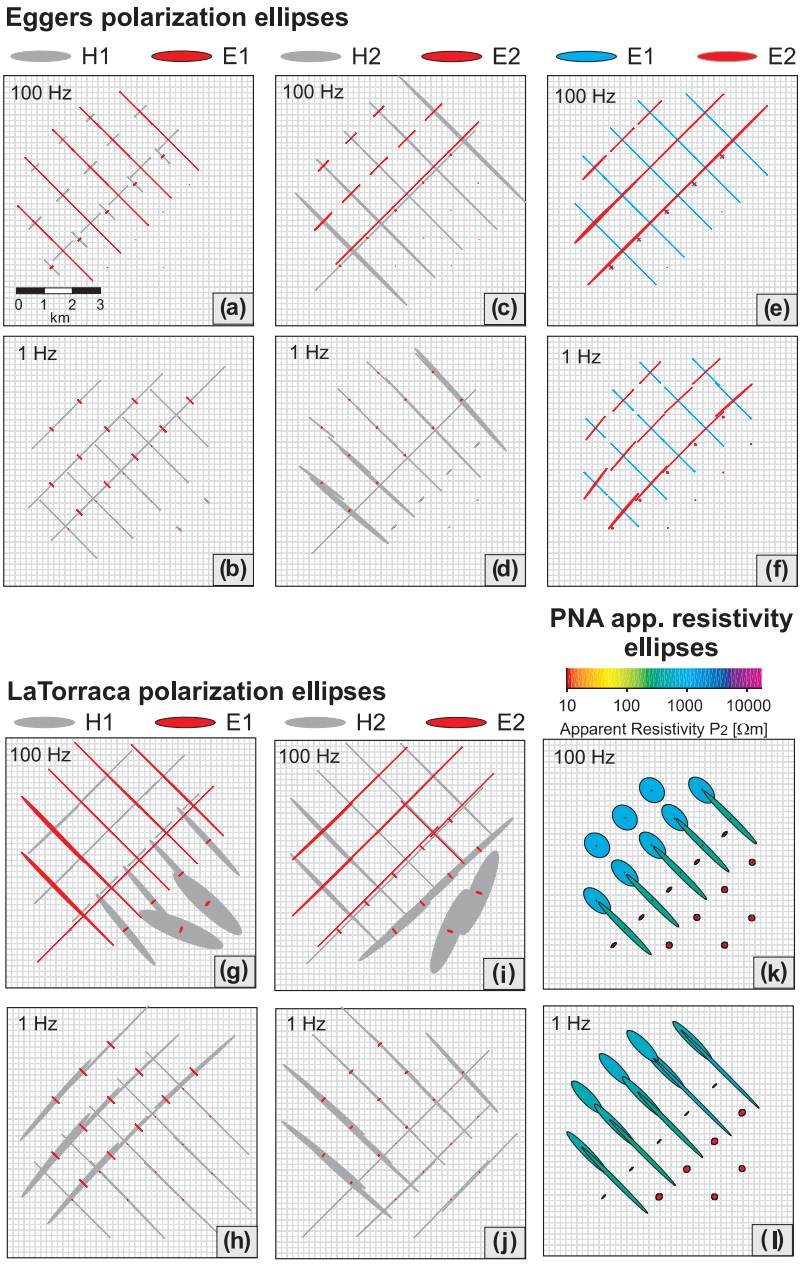

Figure 4. The upper left-hand panel [(a), (b)] shows the first set of Eggers' polarization ellipses (eigenvectors) at frequencies of 100 and 1 Hz. The second set [(c), (d)] at both frequencies is displayed in the middle panel. Both sets clearly indicate the conductivity contrast. Electric and magnetic eigenvectors are orthogonal by definition. A presentation of both electric polarization ellipses [(e), (f)] provides therefore a more comprehensive image of the subsurface. The first set of LaTorraca's polarization ellipses [(g), (h)] maps the conductivity contrast well. By definition the magnetic eigenvectors and the electric eigenvectors are orthogonal, so that the second set of polarization ellipses [(i), (j)] does not provide additional information. The apparent resistivity ellipses [(k), (l)] show a more comprehensive image of the model, as only the shape and direction of one ellipse has to be interpreted. Furthermore, the colour code gives a good estimate of the conductivity of the subsurface.

$$\Pi_2 = \frac{1}{2}\left[(\varrho_{11}+\varrho_{22})^2 + (\varrho_{12}-\varrho_{21})^2\right]^{1/2} \quad (17)$$

$$\alpha = \frac{1}{2}\arctan\left(\frac{\varrho_{12}+\varrho_{21}}{\varrho_{11}-\varrho_{22}}\right) \quad (18)$$

$$\beta = \frac{1}{2}\arctan\left(\frac{\varrho_{12}-\varrho_{21}}{\varrho_{11}+\varrho_{22}}\right). \quad (19)$$

Fig. 1 shows that the principal axes of a tensor ellipse are expressed as combinations of Π_1 and Π_2. The parameters Π_1 and Π_2 and the angle β are rotationally invariant quantities of the resistivity tensor. The angle α which determines the orientation of the ellipse is not rotationally invariant and thus represents the reference (measurement) coordinate system. Because the ellipses are plotted on top of a site location map (see Fig. 13 in Section 5, for example) with the *y*-axis in a northerly direction, the reference frame agrees with the geographic coordinate system.

3 COMPARISON BETWEEN PNA, EGGERS' EIGENSTATE ANALYSIS AND LATORRACA SVD

Eggers' eigenstate analysis (Eggers 1982) and LaTorraca's singular-value decomposition (LaTorraca *et al.* 1986) have both been used to analyse the MT impedance. Both methods result in two magnetic and two electric eigenvectors, and two eigenvalues. From these quantities, a total of four polarization ellipses can be constructed: a major (H1) and minor (H2) magnetic and a major (E1) and minor (E2) electric polarization ellipse. Similar to PNA, both methods use the complete impedance tensor information and also use ellipses for graphical presentation.

Eq. (20) shows an example impedance tensor, which Eggers introduced to illustrate his polarization ellipses. Since then, this example tensor has been frequently cited (e.g. LaTorraca *et al.* 1986) and we also use it to compare the three methods in Fig. 2:

$$\hat{\boldsymbol{Z}} = \begin{pmatrix} 0.097 + 0.208i & 1.140 + 0.957i \\ -0.274 - 0.457i & 0.297 - 0.138i \end{pmatrix}. \quad (20)$$

Using the graphical presentation for tensors, as shown in Fig. 1, we obtain only one ellipse for PNA. Because resistivity (or its inverse, conductivity) is related to the electric field, the apparent resistivity ellipse is comparable to the major electric polarization ellipses (E1) of the other two methods. To demonstrate the full potential of PNA, we test and compare all methods with real and synthetic 3-D data in the next sections.

4 APPLICATION OF PNA TO SYNTHETIC DATA

4.1 2-D synthetic example

We demonstrate the general behaviour of resistivity ellipses using the model shown in Fig. 3. The model comprises two quarter spaces of 1000 and 5Ωm striking at 45°. Although the conductivity distribution is 2-D, we calculated the model using the 3-D forward modelling code from Mackie *et al.* (1993) and generated an array of stations, evenly distributed on a grid, with a site spacing of approximately 2000 m. For all models described here, we have chosen a grid with 80 horizontal cells in each direction and 35 vertical cells. The horizontal cell is approximately 50–100 m in the vicinity of the conductivity contrast. The central part of the model has a depth extent of 60 km and is underlain by a homogeneous half-space of 100 Ωm.

After calculation of the full 3-D impedance tensors at two different frequencies (100 and 1 Hz), we applied Eggers', LaTorraca's and PNA methods. The results are compared in Fig. 4 in the form of polarization and apparent resistivity ellipses. For the 2-D case, the polarization ellipses as defined by Eggers and LaTorraca appear as thin lines, which are aligned parallel or perpendicular to the conductivity contrast. The upper left-hand column of Fig. 4 shows Eggers' first set of electric and magnetic polarization ellipses at both frequencies. The lengths of the ellipses are dependent on frequency, but in general, the electric ellipses above the poor conductor are perpendicular to the contrast, while they are aligned in parallel on top of the good conductor. Magnetic and electric ellipses are orthogonal by definition. For the 2-D case, the second set of eigenvectors, and therefore polarization ellipses, are perpendicular to the first one (Figs 4c and d). The angle between major axes of the electric polarization ellipses provides the most useful information concerning the structure of the anomalies. A combination of both electric ellipses, which is plotted on the upper right-hand side of Fig. 4, is therefore adequate for gathering information on the dimensionality and strike direction of the subsurface. This method of presentation also avoids scaling difficulties that arise because the sizes of magnetic and electric polarization ellipses depend strongly on frequency.

LaTorraca's polarization ellipses in Figs 4(g) and (h) appear to be comparable to Eggers' ellipses. Because LaTorraca's method is not restricted to orthogonal electric and magnetic fields, the presentation of the first set of polarization ellipses is already an indication of the geometry of the subsurface. In the case of a 2-D conductivity contrast, the angle between electric and magnetic ellipses is 90°. We would expect to see this behaviour at all frequencies due to the self-similarity of the model. However, at 100 Hz we observe unstable ellipses above the conductive side of the model. This is a numerical artefact already reported by LaTorraca *et al.* (1986). The first and second set of eigenvectors are orthogonal by definition and therefore, the ellipses in Figs 4(i) and (j) contains no additional information.

So far we have seen that both methods can be used to image the strike angle of a (simple) conductivity contrast, but without any indication of the subsurface conductivity. The images show that the

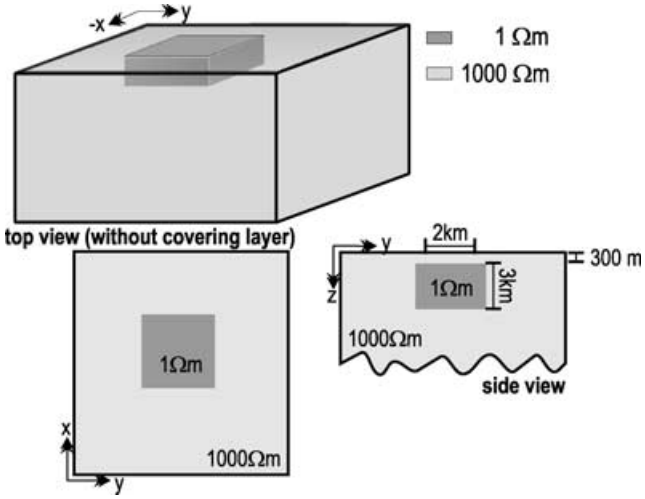

Figure 5. 3-D model of a conductive block (1 Ωm) embedded in a resistive host (1000 Ωm).

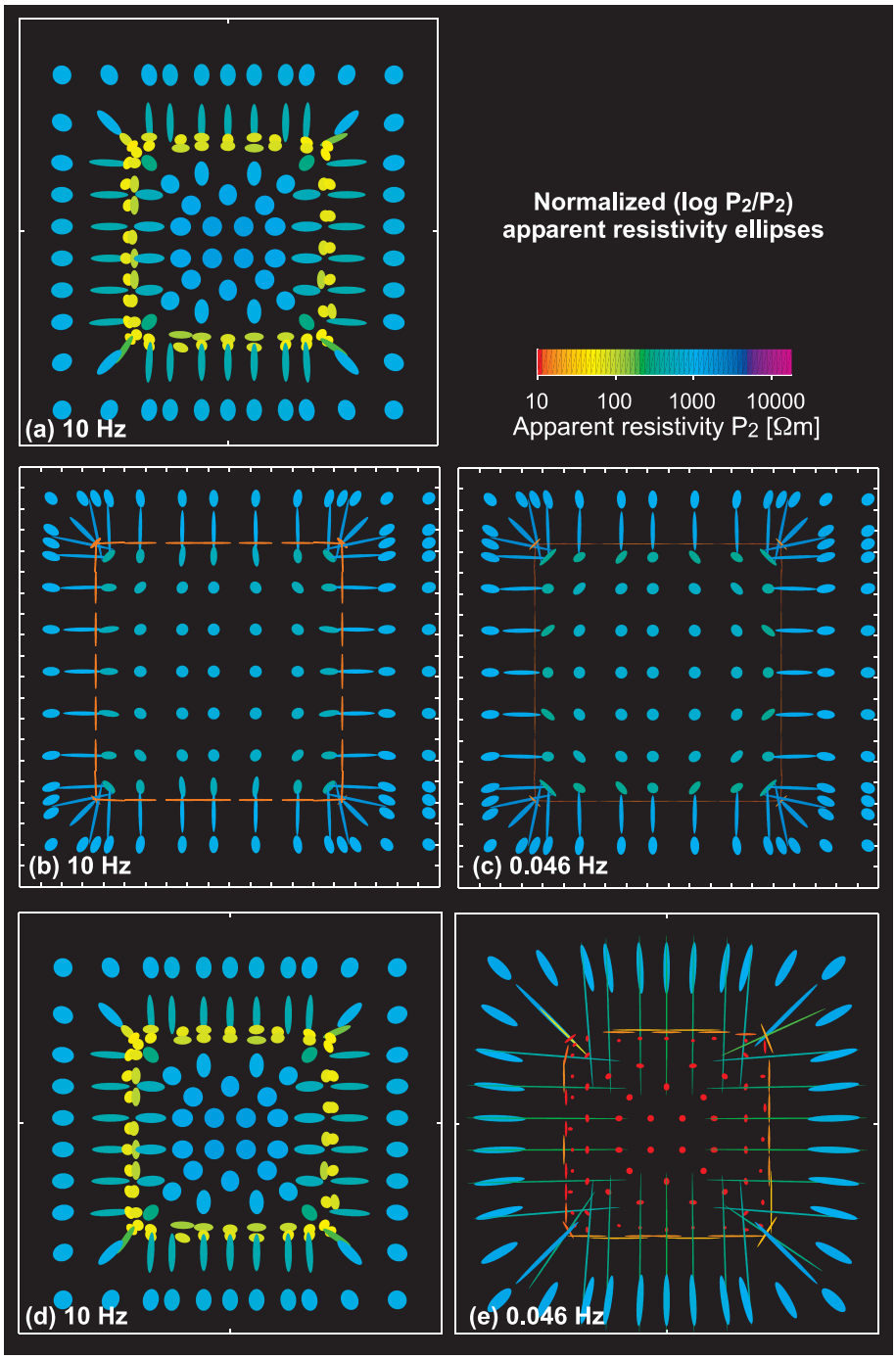

Figure 6. (a) Apparent resistivity ellipses for a station array above the conductive block (see Fig. 5) at 10 Hz. The light green ellipses clearly indicate the dimensions the block. Also a first impression of the conductivity is possible. (b) and (c) Apparent resistivity ellipses for a station array above the conductive ring (see Fig. 7) at 10 and 0.046 Hz. The extremely elongated ellipses in red indicate the conductive frame. The blue and green ellipses represent the resistive host material. For lower frequencies we observe a similar image. (d) and (e) Apparent resistivity ellipses for a station array above the conductive box (see Fig. 11) at 10 Hz and 0.046 Hz. At high frequencies the brim of the box is indicated by yellow ellipses. At a frequency of 0.046 Hz elongated ellipses in red enclose the frame, whereas more circular ellipses in red represent the conductive bottom. We can clearly distinguish that the frame has a bottom.

lengths of the ellipses appear to be dependent upon both the conductivity of the subsurface as well as the site distance from the conductivity contrast. With PNA we retrieve only one ellipse. Its size and orientation are, similarly to the other methods, indicators of the geometry of the conductivity distribution. However, we can gain additional information on the conductivity of the subsurface by colour coding the ellipses with the determinant of the resistivity tensor (P2). The bottom right-hand corner of Figs 4(k) and (l) shows the apparent resistivity ellipses derived from PNA. Above the poor conductor they are aligned perpendicular to the contact, while above the good conductor they are aligned parallel to it. At some distance from the contrast, dependent on the induction length

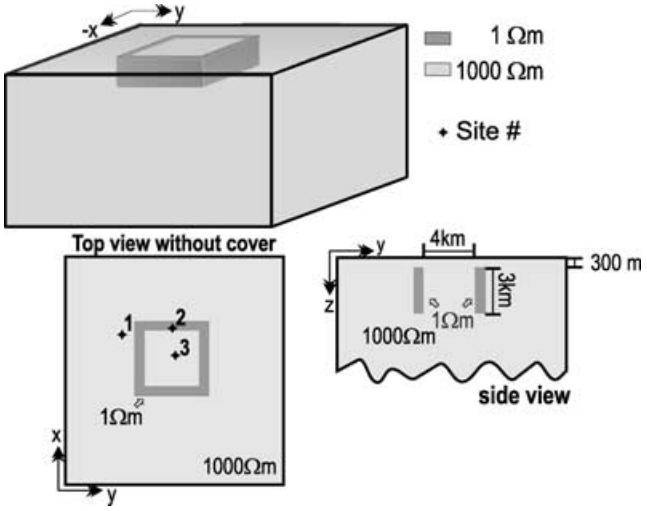

Figure 7. 3-D model of a conductive rectangular ring (1 Ωm) embedded in a resistive host (1000 Ωm). The walls of the conductive frame are 500 m thick.

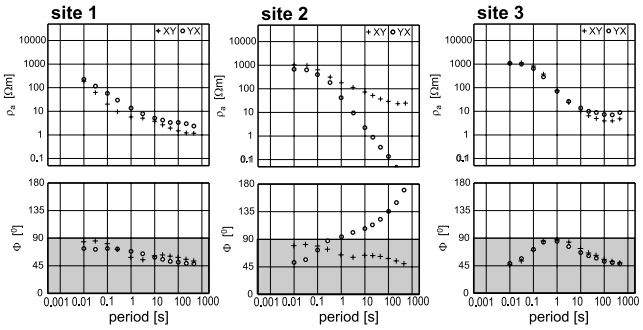

Figure 8. For the ring model we computed ρ_a and phase curves at the three sites marked in Fig. 7. Site 2, which is above the conductive ring exhibits phases above 90°. At sites 1 and 3 inside and outside the ring we do not observe such 3-D effects.

at the particular frequency for the conductivity under consideration, we observe more circular ellipses. For PNA, circular ellipses indicate a 1-D (layered or homogeneous) field distribution. Elongated ellipses are generated close to a conductivity contrast, and generally hint at a 2-D or 3-D field distribution.

4.2 3-D synthetic examples

Now we use the resistivity ellipses to image more complicated conductivity distributions. The next model contains a conductive block of 1 Ωm embedded in a resistive host of 1000 Ωm (Fig. 5). The thickness of the block is 3 km, while the horizontal extent is 2 km. The anomalous block is covered by a 300 m thick layer of resistive host material. Fig. 6(a) shows an image of the resistivity ellipses at a frequency of 10 Hz. The light green and yellow ellipses clearly follow the extensions of the conductive block. Close to all four boundaries, we observe elongated ellipses, while more circular ones are imaged towards the centre of the anomaly and at some distance from the block. The colours of the ellipses reflect resistive and conductive parts of the model.

For the next model we turn the anomalous block into a rectangular frame of conductive material (see Fig. 7).

All other dimensions and the conductivity contrast remain the same. Above the edges of the conductive frame we used a dense

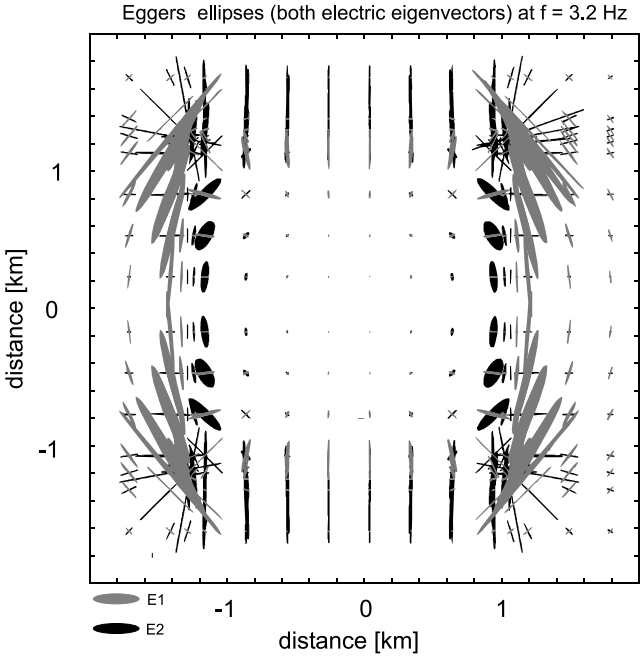

Figure 9. Image of the conductive ring model obtained by Eggers' electric polarization ellipses at 10 Hz: without knowledge of the true conductivity distribution, it is difficult to recover the conductive ring model.

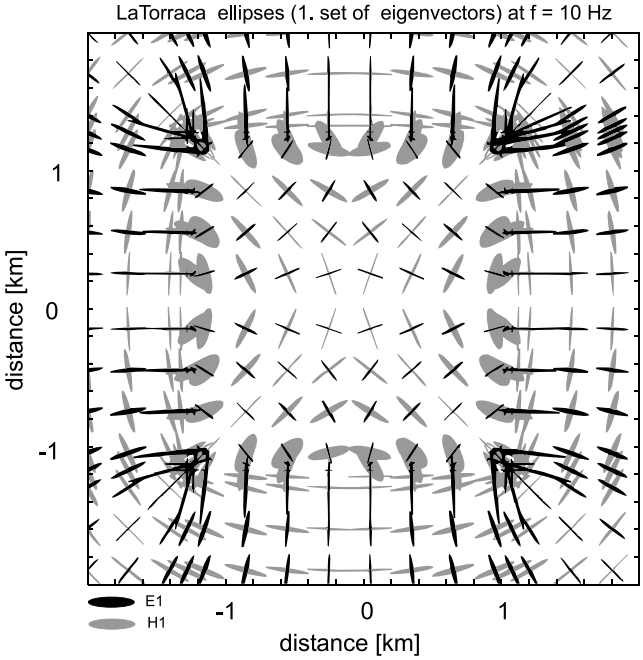

Figure 10. LaTorraca's polarization ellipses reflect the symmetry of the ring model. We obtain the image of a rectangular conductivity anomaly, but it is hard to resolve the thickness of the sides of the box.

grid of 25–50 m cell length for the forward calculations. An image of the apparent resistivity ellipses for this ring model is shown in Fig. 6 for frequencies of 10 Hz (b) and 0.046 Hz (c). At the higher frequency the conductive ring is imaged by extremely elongated red ellipses, whereas green and less elongated ellipses are observed at some distance from the conductivity contrast. PNA delivers a very focused image of the given structure and conductivity distribution. At the lower frequency the image looks quite similar, which

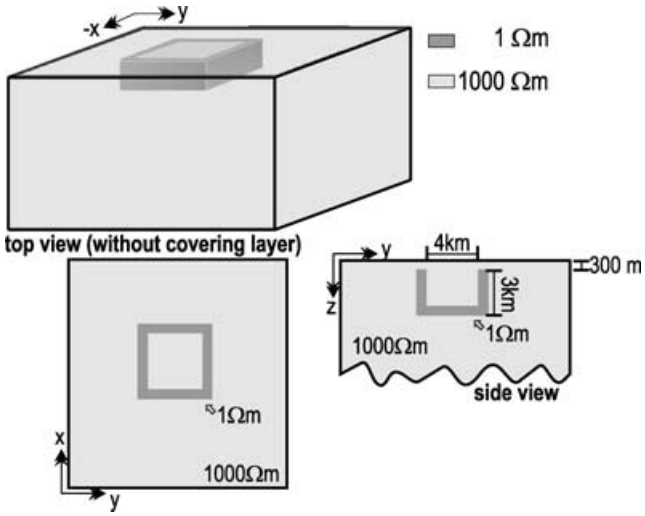

Figure 11. 3-D model of a conductive open box with bottom (1 Ωm) in a resistive host (1000 Ωm). The thickness of the bottom and the walls is again 500 m.

indicates that long-period data might also be effected by shallow anomalies.

Fig. 7 shows the locations of three sites for which the apparent resistivity and phase curves are plotted in Fig. 8. All the sites located above or in close vicinity to the conductive ring show phase values exceeding 90°. Site 2 is representative of this behaviour, which is a clear indication of a strongly 3-D field distribution. The sounding curves at site 1 and site 3, on the other hand, indicate that the 3-D effects are very local, concentrated directly above the ring. Nevertheless, PNA seems to produce stable and meaningful results even under these circumstances. Fig. 9 displays Eggers' polarization ellipses of both electric eigenvectors at a frequency of 10 Hz. The image is almost incomprehensible as it is impossible to recognize a rectangular conductivity anomaly. In contrast, the first set of LaTorraca's polarization ellipses image the expected rectangular anomaly. The general trend of the electric polarization ellipses is similar to that of the apparent resistivity ellipses. However, the resistivity ellipses provide a much better impression of the thickness of the conductor. From the LaTorraca ellipses alone, it is hard to conclude whether the object is a solid block or a conductive ring.

Fig. 11 shows the model of a conductive box (open), buried in a resistive host. All dimensions and conductivity contrasts remain the same but now the ring is closed by a conductive bottom at a depth of 3.3 km. Figs 6(d) and (e) shows the apparent resistivity ellipses for this model, again at frequencies of 10 and 0.046 Hz. As expected, we observe the image of a conductive rectangular ring at higher frequencies (10 Hz). At lower frequencies (greater penetration depth), the brim of the box is imaged by elongated red ellipses but now, the conductive bottom of the box becomes visible. It is expressed by the red circular ellipses inside the box.

5 APPLICATION OF PNA TO THE MT DATA SET FROM NAMIBIA

The above 3-D modelling studies illustrate both the capability of PNA to image complicated 3-D MT data and the importance of dense measurements in order to interpret ellipse plots. To apply PNA to field data, we chose a set of MT data from Namibia (Ritter *et al.* 2003; Weckmann *et al.* 2003). The data were recorded

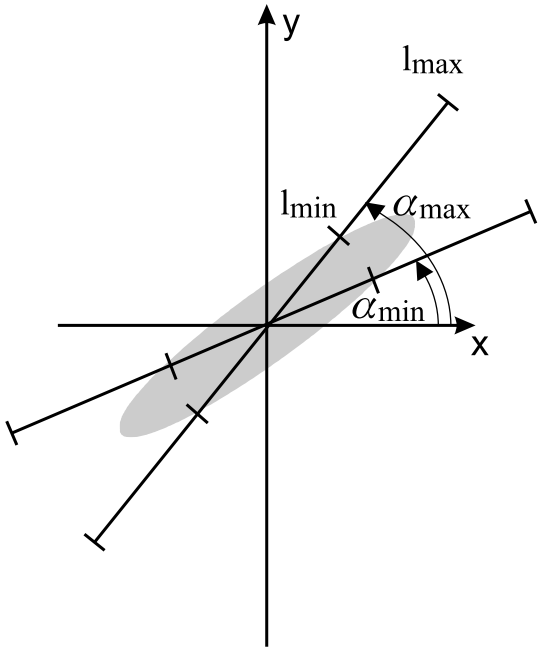

Figure 12. Presentation of the error bounds for a resistivity ellipse. The extremal orientations of the major axis are marked by two lines. The ticks indicate the maximum and minimum elongation of the major axis with respect to the data error.

at 60 sites with a site spacing of 500 and 2000 m across the Waterberg Fault/Omaruru Lineament (WF/OL), a major fault zone within the Damara Belt. In the vicinity of the WF/OL we observe strong 3-D effects, especially at long periods: very high skew, phases over 90° and three large (and one poorly determined) apparent resistivity components. In conjunction with real data it is important to show not only the resistivity ellipses but also their error margins. The latter demonstrate how stable and reliable the obtained ellipses are, when the transfer functions contain error bars. Developing rigorous error propagation for PNA is quite complicated, instead we follow a different approach: within the error bounds of each impedance tensor element, we computed a set of 500 random impedance tensor elements. Each individual tensor element is plotted in the complex plane to verify that a regular distribution of impedance estimates within their error margins is achieved. In such a map the error bound forms a circle around the complex tensor element. Subsequently, PNA is applied to each impedance tensor and the length and the angle of the major axis of the ellipse are computed. As a next step, we determine the minimum and maximum lengths as well as the minimum and maximum angles of the major axis. Fig. 12 shows an example of a resistivity ellipse together with its error margins. Minimum and maximum angles of the major axis are indicated by two lines, while tick marks denote the minimum and maximum elongation of the ellipses.

The resistivity ellipses of all sites in the Namibia data set are plotted in Figs 13(a)–(c) at three different frequencies. The location of the WF/OL is indicated in Fig. 13(b). At the highest frequency we observe elongated ellipses in the northern part of the profiles, whereas the ellipses in the southern part are less elongated. This behaviour is most distinct at 5.56 Hz where less elongated ellipses south of the WF/OL are orientated almost NS. At most sites north of the fault elongated ellipses can be observed. The orientation and shape of the ellipses indicate that the region to the north of the WF/OL consists of either a NNE–SSW-trending conductivity anomaly or an

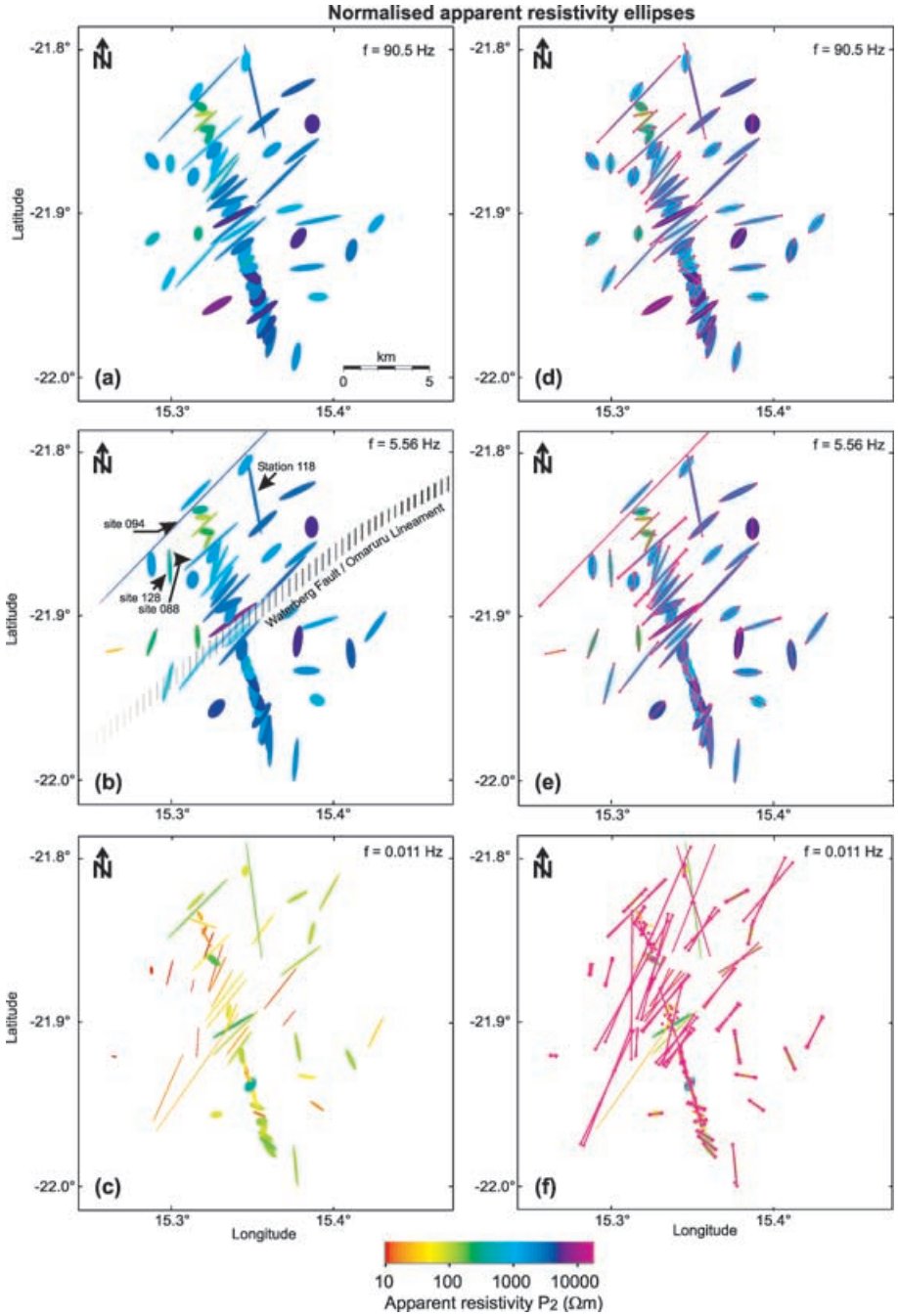

Figure 13. (a)–(c) Resistivity ellipses at three different frequencies for the MT data from Namibia. They indicate the location of the Waterberg Fault/Omaruru Lineament by a change in shape and orientation of the resistivity ellipses. The colour code indicates a resistive subsurface at high frequencies (90.5 and 5.56 Hz) and high conductivity at low frequencies (0.011 Hz). (d)–(f) The same ellipses overlain by error bounds for the resistivity ellipses at the same frequencies. At high frequencies where we observe vanishing data errors as the two error lines coincide. The MT impedances at low frequencies (f) have considerable data errors, but they generate only small deviations in the orientation and shape of the resistivity ellipses.

anisotropic region with enhanced conductivity parallel to the fault. Sites 118, 094, 128 and 088, which are marked in Fig. 13(b), are located on a conductive ring structure (see Weckmann *et al.* 2003). Their resistivity ellipses are extremely elongated and appear to follow this structure, which is comparable to the 3-D modelling results of the conductive box (see Fig. 8). At frequencies >5 Hz, the colours of the ellipses indicate a resistive shallow crust. However, at 0.011 Hz the orientations of the ellipses remain the same, but their colours reflect higher conductivity at greater depths. The right-hand column of Fig. 13 shows the resistivity ellipses at the same frequencies, but now with error margins. At the two highest frequencies both error lines as well as the minimum and maximum elongation coincide, indicating the vanishing error margins of the impedance estimates. At low frequencies, we observe phases over 90° and one poorly determined off-diagonal tensor element, which translates into larger errors for the ellipses. This observation demonstrates that PNA is robust and hence particularly useful for application to real data. A more complete interpretation of the data set based on 3-D and 2-D

anisotropic modelling and the geodynamic implications are given in Weckmann *et al.* (2003) and Ritter *et al.* (2003).

6 DISCUSSION

In order to make use of the tensor properties of the derived resistivity tensor, we choose invariants for presenting the resistivity tensor. A review of the meaning of impedance tensor invariants is not the goal of this work, but many papers have already dealt with their presentation and interpretation. Weaver *et al.* (2000) and Szarka & Menvielle (1997) propose the analysis of the seven invariants as a suitable method for imaging conductivity distributions and classifying distortion and dimensionality. The authors present invariants in the form of contour maps in the surface plane for a specific frequency. Weaver *et al.* (2000) demonstrate with synthetic data that a 3-D conductivity distribution can be imaged by invariants, although the relation to depth is difficult. In particular, the first four of invariants from Weaver *et al.* (2000) and Szarka & Menvielle (1997) can reproduce the geometry of the anomalies. However, the invariants are independent of conductivity, in contrast to PNA, where the conductivity of the subsurface can be assessed. In principle, the resistivity tensor derived by PNA could be displayed and analysed similarly in the form of contour plots. A major disadvantage of this approach though is that a dense regular station array is necessary to avoid interpolation or gridding effects. This is possible for synthetic MT data, but is difficult to achieve with the sparse and irregular spacing of real data. The presentation of the resistivity tensor in the form of ellipses overcomes this obstacle. Because the ellipses are plotted only at the site locations it is clearly shown where data and information are available. Additionally, with ellipses, the information of several aspects of the apparent resistivity tensor can be condensed into one meaningful parameter.

Weaver *et al.* (2000) discuss that three of their invariants can be compared with the galvanic distortion parameters twist and shear (Groom & Bailey 1989). Although PNA is not regarded as a tensor decomposition tool, we tested the influence of galvanic distortion by multiplying the example impedance tensor (see eq. 20) with a real distortion matrix. The distortion resulted mainly in a change of the direction of the main axis, but not in a change of the shape of the ellipses.

7 SUMMARY

We have introduced propagation number analysis as a method for deriving a resistivity tensor from the magnetotelluric impedance. For imaging purposes, the electrical resistivity is a physically meaningful parameter and the tensor characteristics allow the computation of rotationally invariant properties. We have demonstrated the potential of the method in comparison with two existing methods using synthetic 3-D data. The modelling study and the application of PNA to real data show that this method can produce focused images with stable results even if the electromagnetic fields are strongly 3-D. The method and its error estimation can easily be adapted to real data as it does not require any prerequisites. It can be used as an interpretation tool in combination with surface geological maps or as a computationally inexpensive way to obtain a starting model for a 3-D inversion.

The limitations of the method are common to similar imaging tools. The biggest problem is the difficulty in relating the observed images to depth. Because of the skin depth phenomena, the corresponding observation depths are always a function of both frequency and subsurface conductivity and like all imaging methods, PNA requires a dense station mesh so that images can be obscured or distorted by spatial aliasing.

ACKNOWLEDGMENTS

We are grateful to Grant Caldwell and Ian Reilly for providing his internal report to the authors. We also thank Peter Weidelt for his help on the mathematical background. We appreciate the critical and constructive comments from an anonymous referee and in particular from Josef Pek which helped to improve the manuscript.

REFERENCES

Bahr, K., 1991. Geological noise in magnetotelluric data: a classification of distortion types, *Phys. Earth planet. Inter.,* **66,** 24–38.

Bibby, H.M., 1986. Analysis of multiple source bipole–quadrupole resistivity surveys using apparent resistivity tensor, *Geophysics,* **51,** 972–983.

Caldwell, T.G. & Bibby, H.M., 1998. The instantaneous apparent resistivity tensor: a visualization scheme for lotem electric field measurements, *Geophys. J. Int.,* **135,** 817–834.

Caldwell, T.G., Bibby, H.M. & Reilly, W.I., 1998. Visualisation of 3D magnetotelluric data using apparent resistivity and apparent permittivity tensors, *14th Workshop on Electromagnetic Induction in the Earth*, Sinaia, Romania.

Eggers, D.E., 1982. An eigenstate formulation of the magnetotelluric impedance tensor, *Geophysics,* **47,** 1204–1214.

Fischer, G. & Masero, W., 1994. Rotational properties of the magnetotelluric impedance tensor: the example of the Araguainha impact crater, Brazil, *Geophys. J. Int.,* **119,** 548–560.

Groom, R.W. & Bailey, R.C., 1989. Decomposition of magnetotelluric impedance tensors in presence of local three-dimensional galvanic distortion, *J. geophys. Res.,* **94,** 1913–1925.

LaTorraca, G.A., Madden, T.R. & Korringa, J., 1986. An analysis of the magnetotelluric impedance for three-dimensional conductivity structures, *Geophysics,* **51,** 1819–1829.

Lezaeta, P. & Haak, V., 2003. Beyond MT decomposition: current channeling and magnetotelluric phases over 90°, *J. geophys. Res.,* **108,** 36, 2305, doi: 10.1029/2001 JB 000 990.

Lilley, F.E.M., 1993. Magnetotelluric analysis using Mohr circles, *Geophysics,* **58,** 1498–1506.

Mackie, R.L., Madden, T.R. & Wannamaker, P.E., 1993. Three-dimensional magnetotelluric modelling using difference equations—theory and comparisons to integral equation solutions, *Geophysics,* **58,** 215–226.

McNeice, G.W. & Jones, A.G., 2001. Multisite, multifrequency tensor decomposition of magnetotelluric data, *Geophysics,* **66,** 158–173.

Negi, J.G. & Saraf, P.D., 1989. *Anisotropy in Geoelectromagnetism, Methods in Geochemistry and Geophysics,* Vol. 28, Elsevier, Amsterdam.

Reilly, W.I., 1979. Anisotropy tensors in magnetotelluric application, *Technical Report,* Department of Scientific and Industrial Research, New Zealand, Wellington.

Ritter, O., Weckmann, U., Vietor, T. & Haak, V., 2003. A magnetotelluric study of the Damara Belt in Namibia. Part I: regional scale conductivity anomalies, *Phys. Earth planet. Inter.,* **138,** 71–90, doi: 10.1016/50031-9201 (03) 00078-5.

Smith, J.T., 1995. Understanding telluric distortion matrices, *Geophys. J. Int.,* **122,** 219–226.

Swift, C., 1967. A magnetotelluric investigation of an electrical conductivity anomaly in the southwestern United States, *PhD thesis,* MIT, Cambridge, MA.

Szarka, L. & Menvielle, M., 1997. Analysis of rotational invariants of the magnetotelluric impedance tensor, *Geophys. J. Int.,* **129,** 133–142.

Weaver, J.T., Agarwal, A.K. & Lilley, F.E.M., 2000. Characterization of magnetotelluric tensor in terms of its invariants, *Geophys. J. Int.,* **141,** 321–336.

Weckmann, U., Ritter, O. & Haak, V., 2003. A magnetotelluric study of the Damara Belt in Namibia. Part II: MT phases over 90° reveal the internal structure of the Waterberg Fault/Omaruru Lineament, *Phys. Earth planet. Inter.,* **138,** 91–112, doi: 10.1016/50031-9201 (03) 00079-1.

APPENDIX A: WHEN DOES A MATRIX CORRESPOND TO A TENSOR?

What are the differences between tensors and matrices? We attempt to give a concept, not a mathematically rigorous proof. Generally speaking, a matrix corresponds to a tensor if the following two procedures lead to the same result (see Fig. A1):

(i) Establishing the tensor in a given coordinate system and subsequent transformation into a second coordinate system.
(ii) Transformation of the tensor elements into the second coordinate system and subsequent establishment of the tensor.

To apply this concept to the $\boldsymbol{\rho}_a$ matrix, we first rotate the impedance tensor. Subsequently, the apparent resistivity values are calculated. For simplicity, we rotate a 2-D impedance tensor by angle θ.

$$\hat{\boldsymbol{Z}}' = \begin{pmatrix} \cos\theta & \sin\theta \\ -\sin\theta & \cos\theta \end{pmatrix} \begin{pmatrix} 0 & Z_\perp \\ Z_\parallel & 0 \end{pmatrix} \begin{pmatrix} \cos\theta & -\sin\theta \\ \sin\theta & \cos\theta \end{pmatrix}. \tag{A1}$$

The first two elements of the rotated impedance tensor are

$$\begin{aligned} Z'_{xx} &= \frac{1}{2}(Z_\perp + Z_\parallel)\sin(2\theta) \\ Z'_{xy} &= \frac{1}{2}(Z_\perp - Z_\parallel) + \frac{1}{2}(Z_\perp + Z_\parallel)\cos(2\theta). \end{aligned} \tag{A2}$$

The elements of the apparent resistivity matrix are derived by taking the absolute values squared of the impedance tensor elements. The matrix is then rotated similarly to eq. (A1)

$$\boldsymbol{\rho}'_a = \frac{\mu_0}{2\pi f} \begin{pmatrix} \cos\theta & \sin\theta \\ -\sin\theta & \cos\theta \end{pmatrix} \begin{pmatrix} 0 & |Z_\perp|^2 \\ |Z_\parallel|^2 & 0 \end{pmatrix} \begin{pmatrix} \cos\theta & -\sin\theta \\ \sin\theta & \cos\theta \end{pmatrix} \tag{A3}$$

and the elements of $\boldsymbol{\rho}_a$ take the following form:

$$\begin{aligned} \rho'_{a,xx} &= \frac{\mu_0}{2\pi f}\left[\frac{1}{2}\left(|Z_\perp|^2 + |Z_\parallel|^2\right)\sin(2\theta)\right] \\ \rho'_{a,xy} &= \frac{\mu_0}{2\pi f}\left[\frac{1}{2}\left(|Z_\perp|^2 - |Z_\parallel|^2\right) + \frac{1}{2}\left(|Z_\perp|^2 + |Z_\parallel|^2\right)\cos(2\theta)\right]. \end{aligned} \tag{A4}$$

If $\boldsymbol{\rho}_a$ is a tensor, then

$$\frac{\mu_0}{2\pi f}|Z'_{ij}|^2 \stackrel{?}{=} \rho'_{a,ij} \tag{A5}$$

with $i, j = x, y$. $\rho'_{a,ij}$ are summation terms of absolute values squared of $Z_\parallel$ or $Z_\perp$. Hence, $\boldsymbol{\rho}_a$ is generally *not* a tensor because $|a + b| \leq |a| + |b|$.

To decide if $\hat{\boldsymbol{\gamma}}$ is a tensor, we must rotate the admittance tensor $\hat{\boldsymbol{Y}}$ into a second coordinate system and then calculate $\hat{\boldsymbol{\gamma}}$. The rotated admittance tensor assumes the following form when we consider some substitutions for sums and differences of admittance tensor entries: $S_1 = Y_{xx} + Y_{yy}$, $S_2 = Y_{xy} + Y_{yx}$, $D_1 = Y_{xx} - Y_{yy}$ and $D_2 = Y_{xy} - Y_{yx}$:

$$\begin{aligned} \hat{\boldsymbol{Y}}' &= \begin{pmatrix} \cos\theta & \sin\theta \\ -\sin\theta & \cos\theta \end{pmatrix} \begin{pmatrix} Y_{xx} & Y_{xy} \\ Y_{yx} & Y_{yy} \end{pmatrix} \begin{pmatrix} \cos\theta & -\sin\theta \\ \sin\theta & \cos\theta \end{pmatrix} \\ &= \frac{1}{2}\begin{pmatrix} S_1 + D_2\cos(2\theta) + S_2\sin(2\theta) & D_2 + S_2\cos(2\theta) - D_1\sin(2\theta) \\ -D_2 + S_2\cos(2\theta) - D_1\sin(2\theta) & S_1 - D_1 cos(2\theta) - S_2\sin(2\theta) \end{pmatrix}. \end{aligned} \tag{A6}$$

Considering one element, e.g. γ_{xy}, we derive an analogue to eq. (A6),

$$\begin{aligned} \gamma_{xy}(\alpha) &= \frac{1}{2}[(\gamma_{xy} - \gamma_{yx}) + (\gamma_{xy} + \gamma_{yx})\cos(2\theta) - (\gamma_{xx} - \gamma_{yy})\sin(2\theta)] \\ &= -\frac{\omega^2}{2}\big\{[Y_{yy}(Y_{xy} - Y_{yx}) - Y_{xx}(Y_{yx} - Y_{xy})] + [Y_{yy}(Y_{xy} - Y_{yx}) + Y_{xx}(Y_{yx} - Y_{xy})]\cos(2\alpha) \\ &\quad - \left[\left(Y_{yy}Y_{xx} - Y_{yx}^2\right) - Y_{yy}Y_{xx} - Y_{xy}^2\right]\sin(2\alpha)\big\} \\ &= -\frac{\omega^2}{2}[D_2S_1 - D_2D_1\cos(2\alpha) - D_2S_2\sin(2\alpha)] \\ &= -\frac{\omega^2}{2}D_2[S_1 - D_1\cos(2\alpha) - S2\sin(2\alpha)] \\ &= -\omega^2 Y_{y'y'}(\alpha)[Y_{x'y'}(\alpha) - Y_{y'x'}(\alpha)] = \gamma_{x'y'}. \end{aligned} \tag{A7}$$

q.e.d.

APPENDIX B: CAN PNA RECOVER ARBITRARY ANISOTROPY?

To test if the propagation number analysis properly recovers the conductivity tensor of an arbitrary horizontally anisotropic, homogeneous medium in the chosen coordinate system, we describe the subsurface by a conductivity tensor for which principal axes are rotated by the angle β from the geographical coordinate system (see Fig. B1).

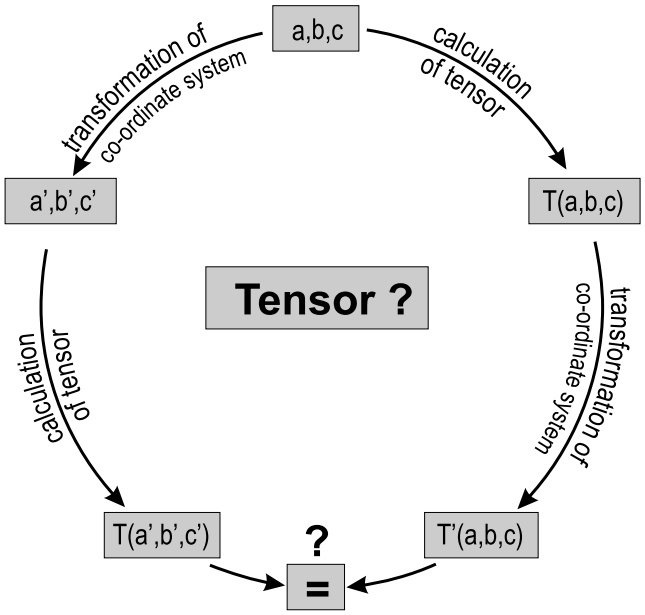

Figure A1. Examination of tensor properties: a quantity depending on a, b and c is defined in a coordinate system (x, y, z). It must be shown that $T(a', b', c') = T'(a, b, c)$.

At first we have to compute the electric and magnetic fields, which generate the admittance tensor. The wave equation for the electric fields in the case of azimuthal anisotropy and neglecting the displacement currents has the following form:

$$\begin{aligned} \frac{\partial^2 E_x}{\partial z^2} &= i\omega\mu_0(\sigma_{xx}E_x + \sigma_{xy}E_y) \\ \frac{\partial^2 E_y}{\partial z^2} &= i\omega\mu_0(\sigma_{yx}E_x + \sigma_{yy}E_y), \end{aligned} \tag{B1}$$

where $\sigma_{xy} = \sigma_{yx}$ and E_x, E_y only depend on the depth z. To solve these equations we assume a plane-wave solution:

$$E_x(z) = A_1 \mathrm{e}^{-kz} \quad E_y(z) = A_2 \mathrm{e}^{-kz} \tag{B2}$$

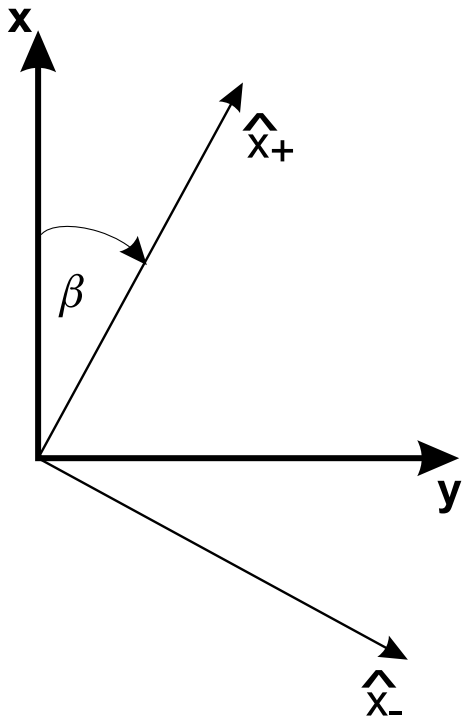

Figure B1. Conductivity tensor in a geographic coordinate system. $\hat{x}_+$ and $\hat{x}_-$ are the unit vectors of the conductivity tensor, which is rotated by β from the geographic coordinate system.

with the complex wavenumber $k = \sqrt{i\omega\mu_0\sigma}$. For this expression we need the eigenvalue of σ. Combining eqs (B2) and (B1) we obtain

$$\begin{aligned} \sigma A_1 &= \sigma_{xx} A_1 + \sigma_{xy} A_2 \\ \sigma A_2 &= \sigma_{xy} A_1 + \sigma_{yy} A_2. \end{aligned} \tag{B3}$$

If a solution of the equation system exists, the eigenvalue σ must be

$$\Rightarrow \sigma = \sigma_{\pm} = \frac{1}{2}\left[\sigma_{xx} + \sigma_{yy} \pm \sqrt{(\sigma_{xx} - \sigma_{yy})^2 + 4\sigma_{xy}^2}\right]. \tag{B4}$$

Using Vieta's theorem we can define

$$\sigma_+ + \sigma_- = \sigma_{xx} + \sigma_{yy}; \qquad \sigma_+ \cdot \sigma_- = \sigma_{xx}\sigma_{yy} - \sigma_{xy}^2. \tag{B5}$$

We can transform eq. (B3) into

$$\frac{A_2^{\pm}}{A_1^{\pm}} = \frac{\sigma_{\pm} - \sigma_{xx}}{\sigma_{xy}} = \frac{\sigma_{xy}}{\sigma_{\pm} - \sigma_{yy}} = \tan\beta \tag{B6}$$

using the geometric relations of Fig. 15.

To compute the admittance tensor (2) we consider two polarizations:

(a) $A_j^+ \neq 0$ and $A_j^- = 0$

(b) $A_j^- \neq 0$ and $A_j^+ = 0$ with $j = x, y$.

The magnetic field is given by Faraday's law (3),

$$B_x^{\pm} = -\frac{k^{\pm}}{i\omega} E_y; \quad B_y^{\pm} = \frac{k^{\pm}}{i\omega} E_x = \sqrt{\frac{\mu_0\sigma_{\pm}}{i\omega}} E_x. \tag{B7}$$

Together with

$$\hat{\boldsymbol{Y}} =: \frac{\sqrt{i\omega\mu_0}}{i\omega}\widetilde{\boldsymbol{Y}} = \sqrt{\frac{\mu_0}{i\omega}}\widetilde{\boldsymbol{Y}} \tag{B8}$$

the conditional equation for $\widetilde{Y}_{xx}$ and $\widetilde{Y}_{xy}$ can be written as

$$-\sqrt{\sigma_{\pm}} A_2^{\pm} = \widetilde{Y}_{xx} A_1^{\pm} + \widetilde{Y}_{xy} A_2^{\pm}. \tag{B9}$$

In consideration of eq. (B6) we have to solve the following system of equations:

$$-\sqrt{\sigma_{\pm}} = \frac{\sigma_{xy}}{\sigma_{\pm} - \sigma_{xx}}\widetilde{Y}_{xx} + \widetilde{Y}_{xy}. \tag{B10}$$

With regard to eq. (B6) the determinant of the system is given by

$$\frac{\sigma_{xy}}{\sigma_+ - \sigma_{xx}} - \frac{\sigma_{xy}}{\sigma_- - \sigma_{xx}} = \frac{\sigma_+ - \sigma_-}{\sigma_{xy}}. \tag{B11}$$

Therefore, $\widetilde{Y}_{xx}$ and $\widetilde{Y}_{xy}$ become

$$\widetilde{Y}_{xx} = -\frac{\sigma_{xy}}{\sqrt{\sigma_+} + \sqrt{\sigma_-}}; \qquad \widetilde{Y}_{xy} = -\frac{\sigma_{yy} + \sqrt{\sigma_-\sigma_+}}{\sqrt{\sigma_-} + \sqrt{\sigma_+}}. \tag{B12}$$

Similar considerations lead to expressions for $\widetilde{Y}_{yx}$ and $\widetilde{Y}_{yy}$.

$$\widetilde{Y}_{yx} = \frac{\sigma_{xx} + \sqrt{\sigma_-\sigma_+}}{\sqrt{\sigma_-} + \sqrt{\sigma_+}}; \qquad \widetilde{Y}_{yy} = \frac{\sigma_{xy}}{\sqrt{\sigma_-} + \sqrt{\sigma_+}}. \tag{B13}$$

Now, the admittance tensor can be written as

$$\hat{\boldsymbol{Y}} = \frac{\sqrt{\mu_0/(i\omega)}}{\sqrt{\sigma_-} + \sqrt{\sigma_+}} \begin{pmatrix} -\sigma_{xy} & -(\sigma_{yy} + \sqrt{\sigma_+\sigma_-}) \\ \sigma_{xx} + \sqrt{\sigma_+\sigma_-})\sigma_{xy} & \end{pmatrix}. \tag{B14}$$

This admittance tensor is used to compute the propagation number $\hat{\gamma}$ (eq. 14).

$$\gamma_{ij} = -i\omega\mu_0\sigma_{ij}, \quad \text{with} \quad i, j = x, y. \tag{B15}$$

Hence we have shown that the entries of the propagation number $\hat{\gamma}$ contain the related components of the conductivity tensor in the geographic coordinate system.

Scientific Technical Report STR 05/10

GeoForschungsZentrum Potsdam